



# PACIFIC EARTHQUAKE ENGINEERING RESEARCH CENTER

## **Seismic Performance of Well-Confined Concrete Bridge Columns**

**Dawn E. Lehman**  
University of Washington

and

**Jack P. Moehle**  
University of California, Berkeley

# **Seismic Performance of Well-Confined Concrete Bridge Columns**

**Dawn E. Lehman**

Department of Civil and Environmental Engineering  
University of Washington

**and**

**Jack P. Moehle**

Department of Civil and Environmental Engineering  
University of California, Berkeley

Research sponsored by the California Department of Transportation

PEER Report 1998/01  
Pacific Earthquake Engineering Research Center  
College of Engineering  
University of California, Berkeley

December 2000

## ABSTRACT

Recent earthquakes in California and abroad have provided performance data demonstrating that large losses can result from inadequate performance of highway bridges. An experimental and analytical research program was undertaken to characterize the response of well-confined, circular cross section, concrete bridge columns subjected to lateral loading. In the experimental investigation, columns with varying longitudinal reinforcement ratios and aspect ratios were tested in the laboratory to characterize the response of modern bridge columns to lateral loads. In the analytical investigation, methods to assess strength, force-displacement response, and element damage were evaluated using the experimental results. The research program results are used to delineate a performance-based seismic design framework for reinforced concrete bridge columns. Additional details about the study and results may be found in *Seismic Performance of Well-Confined Concrete Bridge Columns* (D. E. Lehman, University of Michigan dissertation AAT9922928, 1998).

## ACKNOWLEDGMENTS

The research reported herein was supported by the California Department of Transportation (Caltrans). The authors would like to thank the Caltrans design engineers for their evaluation of the research effort and their input. The project was meticulously monitored by Kelly Holden; her interest in all facets of the research program greatly improved the effort.

The work made use of the Pacific Earthquake Engineering Research (PEER) Center Shared Facilities supported by the Earthquake Engineering Research Centers Program of the National Science Foundation under Award Number EEC-9701568.

The contribution of the staff and students at the PEER center is gratefully acknowledged. The laboratory staff, Don Clyde and Wes Neighbor, are thanked for their advice and hard work. The testing was aided considerably by the help of fellow graduate students, in particular Laura Lowes, Frank McKenna, Anthony Calderone, and Sharon Elkin. Adrian Nacamuli deserves much of the credit for the success of the experiments. Special thanks go to Silvia Mazzoni, Abraham Lynn, and Wendy Taniwangsa for their help with all aspects of the research and their support.

The research was originally published as the dissertation of the first author. The contributions of Professors Stephen Mahin, Bruce Bolt, and Andrew Whittaker are gratefully acknowledged; their expertise and advice enhanced the technical and intellectual quality of the work.

Finally, the first author would like to thank her friends Paul Endres, Catherine Ribble Heeb, Amanda Simondson, and Caroline Fohlin; and her family, Marc Eberhard, Dara, Ralph, and Judy Lehman for their patience and encouragement during her graduate-school tenure.

## EXECUTIVE SUMMARY

In performance-oriented seismic design, a reinforced concrete bridge is designed to meet specified performance objectives. For example, an important bridge structure may be required to sustain some damage during a significant event, while a bridge that is not as critical may be designed to sustain more significant damage. This pairing of a structural performance level and a seismic demand level defines a performance objective. Performance-based seismic design differs from traditional design methods in that multiple performance objectives are specified and are designed for explicitly.

Additional, and in some cases more sophisticated, methods are required for performance-based design in that the damage state corresponding to each performance level must be quantified. For reinforced concrete bridges supported by columns, key aspects of structural performance include cracking, spalling, and cross-section fatigue. Development of performance-based seismic design provisions for reinforced concrete bridges requires engineering approaches that consider these aspects to define the state of structural performance.

Efforts to develop performance-oriented codes for the seismic design of bridges have begun. In the United States, the Applied Technology Council has issued a report entitled *ATC 32 Improved Seismic Design Criteria for California Bridges: Provisional Recommendations* [ATC 32, 1996]. Those guidelines recommend a performance-oriented seismic design framework. Two seismic hazard levels and three performance levels are specified; these levels specify the structural demand and capacity, respectively.

In performance-based seismic design, engineering limit states are used to quantify the structural performance. In the ATC 32 report, engineering expressions are provided to design and detail bridge columns for the significant damage state. However, methods to design and detail the bridge columns for minimum and intermediate damage states are not adequately specified. In part this is due to the fact that although previous research on the response of reinforced concrete bridge columns is extensive, these studies are not adequate to develop all aspects of performance-oriented design. Previous experimental research primarily has emphasized improving the design and understanding of reinforced concrete bridge columns subjected to significant cyclic plastic-displacement demands. Development of performance-based design methods requires further experimental and analytical investigations to evaluate intermediate damage levels and to develop analytical models and appropriate design methodologies.

Recognizing the shortcomings of current information, a research program was designed to develop improved methods to evaluate the performance of modern bridge columns over the range of typical geometries and range of performance levels. The objective of the research program was to characterize and quantify the seismic performance of reinforced concrete bridge columns. The research objective was achieved by designing an experimental and analytical investigation that would characterize the seismic performance of modern bridge columns at various damage states. The scope of the research program included reviewing the available literature, developing and carrying out an experimental research program, developing analytical models to represent observed response, and proposing a framework for performance-based design of bridges.

Previous research was reviewed and categorized to provide an understanding of the influence of individual parameters on the response of reinforced concrete elements. On the basis of the research review, column longitudinal reinforcement ratio and column aspect ratio were chosen as the experimental study parameters.

The experimental portion of the research program was designed to investigate the influence of these parameters on response and failure of modern bridge columns. The columns, representative of modern bridge construction, were detailed to represent a range of conditions that occur in modern bridge construction and to fill in gaps in the available information. Five columns were tested in two test series. The first test series studied the influence of longitudinal reinforcement ratio; three columns with aspect ratios of 4 and longitudinal reinforcement ratios of 0.75%, 1.5%, and 3.0% were tested. In the second test series, the influence of the column aspect ratio was considered. Three columns with longitudinal reinforcement ratios of 1.5% were constructed with aspect ratios of 4, 8, and 10. One column was common to both test series.

With the exception of the study parameters, the five columns were nominally identical. The columns were one-third of full scale. The column diameter was selected to be 2 feet, modeling a 6-foot diameter prototype column. The columns were reinforced longitudinally with No. 5 bars spaced evenly around the column circumference. The column spiral reinforcement ratio was 0.7%. The applied axial load of 147 kips was approximately 10 percent of the specified gross cross-sectional capacity. The lateral load was applied using a servo-controlled hydraulic actuator that was attached to the top of the column. Three cycles were imposed at each displacement level; a fourth, smaller cycle was imposed at the post-yield displacement levels. The primary displacement levels were monotonically increased to provide an indication of damage accumulation. The displacement histories used had nominally identical displacement ductility histories and were

determined for each column according to the column aspect ratio.

During testing, data were collected. The data provided a description of the visual observations, salient response quantities measured at the first peak displacement, and graphs of the force-displacement response history and the relative displacement components. Observations during testing suggest that the sequence of damage was similar in the five columns. The primary damage states included cracking, yielding of the longitudinal reinforcement, spalling, crushing of the core concrete, and fatigue of the cross section.

Typically, cracking was not detected during the initial displacement level but was initiated during the subsequent cycle. The crack spacing decreased at larger displacement demands. The crack spacing in the first 12 inches of the column height tended to stabilize following the yield displacement level.

Yielding of the extreme longitudinal reinforcing bar was noticeable in the force-displacement response or in the physical response. Yielding was detected using strain gauges that had been placed on the longitudinal steel prior to construction and were monitored during testing.

Spalling followed yielding; typically, initial spalling occurred above the column-footing interface. With continued loading, the spalling region increased in elevation, around the circumference, and into the column core, finally resulting in complete loss of the concrete cover, which exposed the spirals and longitudinal steel.

Subsequent loading resulted in a permanent displacement of the lower column spirals. Longitudinal bar buckling was evident visually. In all cases, the longitudinal bar buckled over more than one spiral spacing. The spirals located within the buckled length continued to extend as the bar continued to buckle until the spiral fractured. The lateral stiffness decreased as a result of spiral fracture which permitted the other longitudinal bars to buckle over a longer length. Fracture of the longitudinal bars occurred after bar buckling. Typically, fracture of one or more longitudinal bars resulted in strength loss significant enough to cause column failure.

The observed and measured responses were used to determine the influence of the study parameters. Results for the three columns with various levels of longitudinal reinforcement include differences in the crack widths (largest for the lightly reinforced column); spalled region (greatest for the heavily reinforced column); and displacement, curvature, and rotation ductility capacities. Similar contributions of bending, shearing, and slip were measured. Results for the three columns with different aspect ratios indicate differences in the height of the spalled region (increased with an increase in the column length); displacement ductility capacity (larger for the

shortest column); and the relative contributions of slip, shearing, and bending (the slender columns had a more significant bending component). The curvature ductility capacities of the three columns were approximately equal.

The experimental results were used to validate and develop mathematical models for use in strength-based and performance-based seismic design procedures. For strength-based design methods, initial estimates of the stiffness and strength are needed to assess the structural force demands. Performance-based seismic design requires a more accurate assessment of the deformation, energy, and cyclic demands and may require more sophisticated structural modeling techniques and analysis methods. Here, methods to compute the strength, the force-displacement response envelope, and the cyclic force-displacement response were developed and evaluated using the experimental data.

The maximum plastic flexural strength,  $M_p$ , was calculated by performing a moment-curvature analysis using the measured material properties. The ratio of the plastic strength,  $M_p$ , and the maximum measured moment  $M_{max}$  was calculated for each column; the average ratio was 1.0 with a standard deviation of 0.1. In some cases, such as initial design, a sophisticated analysis will not be warranted. As an alternative method, most codes provide factors to magnify the nominal moment strength to obtain the plastic moment strength, i.e.,  $M_p = \gamma M_n$ . In general, an increase in the longitudinal reinforcement ratio or the axial load ratio will result in an increase in the amplification factor. For axial load ratios less than  $0.2A_g f'_c$ , the maximum amplification factor ranges from approximately 1.15 for a longitudinal reinforcement ratio of 0.75% to 1.3 for a longitudinal reinforcement ratio of 3.0%. As an alternative to a detailed analyses, the plastic moment of columns with low axial load ratios may be assessed by amplifying the expected nominal moment strength by 1.3.

Evaluation of the deformation corresponding to different performance levels requires assessment of the force-displacement response envelope. In addition, the force-displacement envelope may be used as the backbone curve of a cyclic force-displacement model with additional rules to characterize the cyclic response. Both types of models were developed. This discussion will be limited to models used to assess the force-displacement response envelope; details of the cyclic model can be found in the report. The post-yield response of a column can be modeled directly or by lumping the inelastic response through use of a plastic hinge model. Both approaches were considered.

Force-displacement models are primarily used to determine the displacement corresponding

to failure, although other damage states may be assessed. Experimental results indicate that column failure was initiated by bar buckling, and, in most cases, directly results from longitudinal-bar fracture. This failure mode was, in part, induced by the cyclic nature of the loading. Therefore, in comparison with monotonic loading, fatigue effects may account for the limited displacement capacity. Since column failure was primarily due to the response of the longitudinal steel, the curvature capacity was predicted to correspond to a predefined tensile strain capacity; this method differs from methods that limit the compressive strain capacity of the core concrete [Priestley 1996]. The predicted maximum displacement corresponds to a tensile strain in the longitudinal steel of  $\epsilon_{max} = 0.5\epsilon_u$  where  $\epsilon_u$  is the strain corresponding to the maximum stress. For the columns that were tested, the ultimate curvature corresponded to a tensile steel strain of 0.08, implicitly accounting for the low-cycle fatigue effects. (Models that explicitly include fatigue effects were provided in the latter portion of the report.)

The direct approach accounts for the displacements results from slip ( $\Delta_s$ ), shear ( $\Delta_v$ ), and bending ( $\Delta_b$ ) deformations along the column length. Using a flexibility based approach, the tip displacement is the sum of the three components or  $\Delta = \Delta_b + \Delta_s + \Delta_v$ . Details of the model can be found in the report. The force-displacement envelope was determined for each column by using the limiting tensile strain and the direct-approach model. Comparing the predicted and measured response curves indicates that the response is well approximated over the entire displacement range. The initial stiffness, strengths, yield displacements, ultimate displacements, and overall shape of the response envelopes were similar.

In some cases, a more approximate method may be desirable to expedite the assessment of the force-displacement response. A widely used, more simplified model is the plastic hinge length model. Originally, the plastic hinge length method was used to assess lateral-load failure. Therefore, models were correlated to the measured displacement capacity. In a performance-based design environment, consideration of additional engineering limit states may be required. A plastic hinge length model that can reliably assess the appropriate limit states for performance-based seismic design was developed. The plastic hinge length was derived using the direct model and is given by  $l_p = \frac{l_y}{2} + \frac{(f_u - f_y)d_b}{(40 \sqrt{f_c'} \text{ psi})}$  where  $l_y = \frac{M_u - M_n}{M_u} L$ . The proposed plastic hinge length method and the limiting tensile strain value were used to predict the force-displacement response for the five columns. The displacement values approximately corresponding to the effective yield, spalling, and ultimate states were compared with the measured values. In the analysis, concrete spalling was estimated at a strain of 0.8% in the concrete cover. The ultimate displacement was

estimated at a tensile strain value of 8%. The proposed model capable of assessing intermediate post-yield limit states such as spalling and failure. However, for the two slender columns, the predicted displacement capacity exceeds the measured displacement capacity, likely a result of the linearization of the post-yield curvature diagram. For slender columns, the nonlinear shape of the curvature diagram is more pronounced and the proposed model overestimates the bending component.

The force-displacement response was compared using the plastic hinge length method given in ATC 32, which is the formulation by [Priestley 1996]. The plastic hinge length is approximately equal to  $l_p = 0.08L + 8d_b$ . The ultimate strain capacity corresponds to the compressive strain in the extreme fiber and is approximately equal to  $\epsilon_{cu} = 0.004 + 0.14(f_{ys}/(f'_c))$ . The ratios of the predicted to measured ultimate displacement capacities were calculated. The results indicate that the ratio is between 0.5 to 1.3 for the Priestley method and 0.8 to 1.1 for the proposed method. It is worthwhile noting that the two plastic hinge lengths are approximately equal if the flexural demand,  $M_{max}$ , is 16 percent greater than the yield strength,  $M_y$ , and the ultimate strength of the longitudinal steel is approximately twice the yield strength. Using the two plastic hinge lengths with the proposed limiting strain of half the maximum strain provides similar results.

Reversed cyclic loading influences the response and failure mode of a reinforced concrete element. The effect of cycling to large plastic demands must be considered when designing structures to withstand seismic demands. Recent research efforts have evaluated the response of columns designed to meet large cyclic displacement ductility demands. The progression of damage that has been observed during pseudo-static unidirectional testing of these columns is markedly similar to those noted previously [Stone 1989, Kunnath 1997, Calderone 1998]. Since the state of structural damage is indicative of the required repair effort and may influence the future performance, expressions are required to predict the state of structural or element damage. In this research project, a cumulative damage index was used to model the effect of cycling on structural damage.

A damage index capable of predicting complete spalling of the concrete cover and fatigue of the cross section was developed. Initially, fatigue curves were developed for each phase using a modification of the Coffin-Manson expression. The first equation (1) relates the number of cycles required to completely remove the concrete cover,  $(N_f)_c$ , at a strain ratio of  $\epsilon_c/\epsilon_{csp}$ . The second equation (2) calculates the number of subsequent cycles to failure,  $(N_f)_s$ , after complete spalling of the concrete cover; a single cycle to  $\epsilon_s = \epsilon_{su}$  results in failure.

$$(N_f)_c = 33 \left( \frac{\epsilon_c}{\epsilon_{csp}} \right)^{-5} \quad (1)$$

$$(N_f)_s = 0.08 \left( \frac{\epsilon_s}{\epsilon_{su}} \right)^{-5.5} + 0.92 \quad (2)$$

$$(DI)_c = \sum_i \frac{1}{(N_f)_{ci}} \quad \text{where } (DI)_c \leq 1 \quad (3)$$

The concrete and steel damage indices are calculated using Miner's rule, as shown by Equations 3 and 4.

$$(DI)_s = \sum_i \frac{1}{(N_f)_{si}} \quad \text{if } (DI)_c = 1 \quad (4)$$

The dual-phase damage index is employed in two stages. The steel fatigue index,  $(DI)_s$ , is equal to zero until the concrete damage index,  $(DI)_c$ , is equal to one. Element failure corresponds to a steel fatigue index value of one, i.e.,  $(DI)_s=1$ . The index was evaluated using the experimental results from the present study. The index correctly predicts failure for Column 407 (third cycle to 5 inches), for Column 415 (first cycle to 7 inches), and Column 815 (second cycle to 17.5 inches). Failure of Column 430 is predicted at the first cycle to 7 inches, rather than the second cycle to 7 inches. The damage index reaches a value of 0.92 at the measured failure of Column 1015. The dual-phase damage index predicted the failure of the five columns of the present study as well as those tested by [Kunnath 1997] and [Calderone 1998].

The expressions developed to assess the force-displacement envelope, cyclic force-displacement response, and element damage were used to assess the engineering limit states corresponding to each performance level in a performance-based design framework. Frameworks for performance-based seismic design have been established in the literature and code documents [e.g., Japan 1998, ATC 1996]. The framework in ATC 32 succeeded in defining performance levels that represent minimal, intermediate, and significant damage states. However, there are several shortcomings with the manner in which they are defined. Firstly, the document fails to explicitly define a minimal performance level that must be achieved for ordinary bridges. In addition, the performance levels are defined in terms of the required repair effort and serviceability; in some cases this definition may be too limiting.

To overcome these perceived shortcomings, the performance-based seismic design framework recommended herein adopts three performance levels. The three performance levels are the Fully Operational Performance Level, Delayed Operational Performance Level, and Stability Per-

formance Level. Each performance level is defined by the expected bridge serviceability, required repair effort, and the future performance.

A bridge designed to meet the requirements of the Fully Operational Performance Level is expected to respond essentially in the elastic range; repair is not required. To meet these requirements, residual crack widths are limited (e.g., less than 0.02 in.), and spalling, residual drift effects, and element fatigue are avoided.

A bridge designed to meet the requirements of the Delayed Operational Performance Level is expected to sustain moderate damage. Following the ATC 32 guidelines for repairable damage, post-earthquake repair may include concrete cracking, yielding of the longitudinal reinforcement, and spalling of the concrete cover; replacement of reinforcement or structural members is not permitted. The repair effort should be limited to limit closure of the bridge; therefore permanent offsets should be avoided. At this performance level, the cracking limit state may be exceeded. The spalling engineering limit state should be checked to ensure spalling is limited to the cover and does not extend into the core. Residual drifts should not exceed permissible construction offsets as defined by the local design provisions.

A bridge designed to meet the requirements of the Stability Performance Level is expected to sustain significant damage without imminent collapse. Exhaustion of the cross-section capacity must be avoided to ensure stability under gravity loading. However, the other limit states, including cracking, spalling, residual drift and fatigue, may be exceeded.

The limit states were quantified using the experimental results. In the following subsections, observed experimental response and numerical expressions are used to define and quantify structural performance.

Crack widths may be used to indicate if epoxy or other material must be used to restore the tensile strength. The residual crack widths measured during testing were used to postulate maximum permissible displacement ductility demand to ensure minimum crack widths. In general, the measured response indicates that the residual crack widths are 0.01 inches or less for displacement ductility demands less than 1.5 and are 0.02 inches or less for displacement ductilities less than 2. Therefore, to limit residual crack width, the displacement demand should be less than twice the effective yield displacement. Limiting the displacement demand to the effective yield displacement will ensure acceptable crack widths and essentially linear response.

Cover spalling may reduce the lateral stiffness of the cross section, durability in terms of corrosion, and lateral restraint on the longitudinal bar. Post-earthquake damage to the concrete

cover can require concrete patching; core damage can require partial or complete replacement of the structural element.

The experimental results from this study as well as studies by Calderone et al. [Calderone 1998] and Kunnath et al. [Kunnath 1997] were used to determine the compressive strain corresponding to spalling. The results indicate that the strain corresponding to initial spalling of the cover is in the range of 0.8% to 1.0%. For the provided data, the mean spalling strain is 0.9% with a standard deviation of 0.1%. For design, a compressive strain demand of 0.7% is suggested.

The response and failure of reinforced concrete elements subjected to seismic loading can be influenced by the load path. Fatigue of the concrete cover may require removal and replacement of the damaged concrete. Cross section failure, which includes longitudinal bar fatigue and/or fatigue of the core concrete, may require partial or full replacement of a structural element. Experimental evaluation of the use of such replacement techniques on modern bridge columns may be found in the literature [e.g., Elkin 1998, Nacamuli 1998].

The dual-phase damage index was used to predict column failure. Fatigue-induced failure of the concrete cover corresponds to approximately  $DI_c = 1$ . Fatigue-induced failure of the longitudinal steel corresponds to approximately  $DI_s = 1$ . The Fatigue Engineering Limit States are specified for the Delayed Operational Performance Level and the Stability Performance Level. Fatigue failure of the concrete is not permitted for a bridge designed to meet the Delayed Operational performance state. Repair (i.e., concrete patching) will be required if  $DI_c > 0$ . For the Life Safe Performance Level, failure of the concrete is permissible (i.e.,  $DI_c = 0$ ); however, failure of the longitudinal steel should be avoided (i.e.,  $DI_s < 0.9$ ).

# CONTENTS

ABSTRACT.....	iii
ACKNOWLEDGMENTS .....	iv
EXECUTIVE SUMMARY .....	v
TABLE OF CONTENTS .....	xv
LIST OF FIGURES .....	xix
LIST OF TABLES .....	xxv
CHAPTER 1 INTRODUCTION .....	1
1.1 Research Impetus and Background .....	1
1.2 Objective and Scope .....	2
1.3 Report Contents .....	3
CHAPTER 2 PREVIOUS RESEARCH RESULTS .....	5
2.1 Introduction .....	5
2.2 Member Behavior .....	6
2.2.1 Member Geometry and Reinforcement .....	7
2.2.1.1 Column Aspect Ratio and Length .....	8
2.2.1.2 Concrete Cover .....	9
2.2.2 Longitudinal Reinforcement Ratio .....	9
2.2.2.1 Confinement .....	10
2.2.2.2 Longitudinal Bar Diameter .....	11
2.2.3 Material Properties .....	12
2.2.3.1 Plain and Confined Concrete .....	12
2.2.3.2 Longitudinal Reinforcement .....	13
2.2.3.3 Transverse Reinforcement .....	14
2.2.4 Loading .....	14
2.2.4.1 Axial Load .....	14
2.2.4.2 Shear .....	15
2.2.4.3 Lateral Displacement History .....	16
2.3 Simplified Force-Displacement and Damage Models .....	17
2.3.1 Plastic Hinge Length Expressions .....	17
2.3.2 Force-Displacement Hysteresis Models .....	20
2.3.3 Damage Indices .....	21
2.3.3.1 Non-Cumulative Damage Indices .....	22
2.3.3.2 Fatigue-Based Cumulative Damage Indices .....	23
2.3.3.3 Energy-Based Cumulative Damage Indices .....	25
2.3.3.4 Evaluation of Damage Indices .....	26

CHAPTER 3 EXPERIMENTAL PROGRAM AND RESULTS .....	37
3.1 Research Impetus .....	37
3.2 Test Program .....	38
3.2.1 Test Matrix .....	38
3.2.2 Design Requirements .....	39
3.2.3 Geometry and Reinforcement .....	40
3.2.4 Material Properties .....	41
3.2.5 Loading .....	41
3.3 Overview of Experimental Observations .....	42
3.4 Column 407 .....	45
3.4.1 Progression of Observed Damage .....	45
3.4.2 Measured Response .....	46
3.5 Column 415 .....	46
3.5.1 Observed Response .....	46
3.5.2 Measured Response .....	48
3.6 Column 430 .....	48
3.6.1 Observed Response .....	48
3.6.2 Measured Response .....	49
3.7 Column 815 .....	50
3.7.1 Observed Response .....	50
3.7.2 Measured Response .....	51
3.8 Column 1015 .....	51
3.7.1 Observed Response .....	51
3.7.2 Measured Response .....	52
3.9 Comparative Summary .....	52
3.9.1 Test Series I: Longitudinal Reinforcement Ratio .....	52
3.9.2 Test Series II: Aspect Ratio .....	53
 CHAPTER 4 MODELING AND DESIGN IMPLICATIONS .....	 85
4.1 Introduction .....	85
4.2 Design Strength .....	85
4.2.1 Column Flexural Strength .....	86
4.2.2 Column Shear Strength .....	88
4.2.3 Joint Shear Strength .....	88
4.3 Response Envelope.....	89
4.3.1 Discrete Model .....	89
4.3.1.1 Bending .....	90
4.3.1.2 Slip .....	91
4.3.1.3 Shear .....	94
4.3.1.4 Comparison of Force-Displacement Response Envelopes .....	95
4.3.2 Simplified Model (Plastic Hinge Length Model) .....	96
4.3.2.1 Plastic Hinge Length by Priestley et al. ....	97
4.3.2.2 Proposed Plastic Hinge Length .....	98
4.4 Cyclic Response .....	100
4.4.1 Hysteresis Modeling .....	101
4.4.2 Damage Index .....	103

CHAPTER 5 PERFORMANCE-BASED SEISMIC DESIGN .....	133
5.1 Overview .....	133
5.2 Review of Existing Documents .....	134
5.3 Conceptual Framework for Performance-Based Seismic Design .....	136
5.3.1 Performance Levels .....	137
5.3.2 Seismic Hazard Levels .....	138
5.3.3 Performance Objectives .....	139
5.4 Engineering Approaches .....	140
5.4.1 Engineering Limit States Related to Performance Levels .....	141
5.4.1.1 Experimental Implications .....	142
5.4.2 Analysis Methods .....	147
CHAPTER 6 SUMMARY, CONCLUSIONS, AND FUTURE RESEARCH .....	159
6.1 Summary of Research Program .....	159
6.2 Conclusions .....	160
6.2.1 Future Research .....	163
APPENDIX A SPECIMEN DESIGN, MATERIALS, AND CONSTRUCTION .....	165
APPENDIX B EXPERIMENTAL SET UP, APPARATUS, AND PROCEDURES .....	187
APPENDIX C TEST DATA .....	211
APPENDIX D CRACK PATTERNS .....	281
REFERENCES .....	287

## LIST OF FIGURES

Figure 2.1:	Variation of Plastic Hinge Length with Column Aspect Ratio [Sakai 1989].....	28
Figure 2.2:	Force-Displacement Response of a Conventionally Reinforced Concrete Column and a Column with a Steel Jacket [Chai 1991] .....	28
Figure 2.3:	Axial Strain Capacity vs. Spiral Reinforcement Ratio [Saaticioglu 1994].....	29
Figure 2.4:	Column Displacement Resulting from Axial Deformation of the Embedded Portion of the Longitudinal Reinforcement.....	29
Figure 2.5:	Effect of Bar Diameter on Bond-Slip Response [Eligehausen 1993].....	30
Figure 2.6:	Influence of Axial Load on Column Response [Saaticioglu 1989] .....	31
Figure 2.7:	Force-Displacement Response of Members with Various Axial Load Ratios and Transverse Reinforcement Ratios [Wakabayashi 1984].....	31
Figure 2.8:	Variation of Shearing Deformation with Transverse Reinforcement Ratio and Axial Load Ratio [Atalay 1975].....	32
Figure 2.9:	Example Hysteresis Model .....	33
Figure 2.10:	Bi-linear Hysteresis Model .....	33
Figure 2.11:	Clough Hysteresis Model.....	34
Figure 2.12:	Takeda Hysteresis Model.....	34
Figure 2.13:	Evaluation of Various Damage Indices [Williams 1997].....	35
Figure 3.1:	Axial Load Ratio vs. Aspect Ratio for Columns .....	61
Figure 3.2:	Reinforcement Ratio vs. Aspect Ratio for Columns .....	61
Figure 3.3:	Test Matrix.....	62
Figure 3.4:	Specimen Geometry and Reinforcement .....	62
Figure 3.5:	Experimental Configuration .....	63
Figure 3.6:	Instrumentation .....	63
Figure 3.7:	Target Displacement History .....	64
Figure 3.8:	Column 407 Crack Pattern at 3-Inch Displacement Level .....	64
Figure 3.9:	Column 407 Spalled Region at 3-Inch Displacement Level.....	65
Figure 3.10:	Column 407 Buckled Bar and Fractured Spirals .....	65

Figure 3.11:	Column 407 Displaced to 5 Inches .....	66
Figure 3.12:	Column 407 Fractured Main Longitudinal Bars.....	67
Figure 3.13:	Column 407 Final Damage State .....	67
Figure 3.14:	Force-Displacement Response of Column 407 .....	68
Figure 3.15:	Column 407 Displacement Components .....	68
Figure 3.16:	Column 415 Crack Pattern.....	69
Figure 3.17:	Column 415 Spalled Region Following 5-Inch Displacement Level .....	69
Figure 3.18:	Column 415 Final Damage State .....	70
Figure 3.19:	Column 415 Force-Displacement Response.....	71
Figure 3.20:	Column 415 Displacement Components .....	71
Figure 3.21:	Column 430 Crack Pattern at 2-Inch Displacement Level .....	72
Figure 3.22:	Column 430 Spalled Region .....	72
Figure 3.23:	Column 430 Final Damage State .....	73
Figure 3.24:	Column 430 Force-Displacement Response.....	74
Figure 3.25:	Column 430 Displacement Components .....	74
Figure 3.26:	Column 815 Crack Pattern at 3.5-Inch Displacement Level .....	75
Figure 3.27:	Column 815 Spalled Region at First Cycle to 17.5 Inches.....	76
Figure 3.28:	Column 815 Fracture of Previously Buckled Longitudinal Bar .....	77
Figure 3.29:	Column 815 Fractured Main Longitudinal Bar .....	77
Figure 3.30:	Column 815 Displaced to 17.5 Inches .....	78
Figure 3.31:	Column 815 Final Damage State of North Face.....	79
Figure 3.32:	Column 815 Damaged Region on South Face After Testing .....	80
Figure 3.33:	Column 815 Force-Displacement Response.....	80
Figure 3.34:	Column 815 Displacement Components .....	80
Figure 3.35:	Column 1015 Crack Pattern at 5-Inch Displacement Level .....	81
Figure 3.36:	Column 1015 Spalled Region at 25-Inch Displacement Level.....	82
Figure 3.37:	Column 1015 Displaced to 25 Inches .....	83
Figure 3.38:	Column 1015 Damage State after Testing.....	83

Figure 3.39:	Column 1015 Force-Displacement Response .....	84
Figure 3.40:	Column 1015 Displacement Components .....	84
Figure 4.1:	Calculated Amplification Factor .....	113
Figure 4.2:	Joint Equilibrium .....	114
Figure 4.3:	Displacement Components for a Cantilever Column .....	114
Figure 4.4:	Measured and Predicted Longitudinal Steel Response .....	115
Figure 4.5:	Test Series I Measured and Predicted Moment-Curvature Response.....	115
Figure 4.6:	Test Series II Measured and Predicted Moment-Curvature Response .....	116
Figure 4.7:	Test Series I Measured and Predicted Force-Bending Response .....	116
Figure 4.8:	Test Series II Measured and Predicted Force-Bending Response .....	117
Figure 4.9:	Slip Displacement of Cantilever Column .....	117
Figure 4.10:	Predicted and Measured Bond Stress-Slip Response .....	118
Figure 4.11:	Test Series I Force-Slip Displacement Response: Bond-Slip Model .....	118
Figure 4.12:	Test Series II Force-Slip Displacement Response: Bond-Slip Model .....	119
Figure 4.13:	Bi-uniform Bond Slip Model: Measured and Predicted Response .....	110
Figure 4.14:	Measured and Predicted Force-Slip Response: Uniform Bond Model.....	120
Figure 4.15:	Computation of Secant Young's Modulus of Core Concrete .....	120
Figure 4.16:	Test Series I Measured and Predicted Force-Shearing Response .....	121
Figure 4.17:	Test Series II Measured and Predicted Force-Shearing Response .....	121
Figure 4.18:	Test Series I: Response Predicted Using Discrete Model.....	122
Figure 4.19:	Test Series II: Response Predicted Using Discrete Model .....	122
Figure 4.20:	Plastic Hinge Length Model .....	123
Figure 4.21:	Test Series I Predicted Response Using Plastic Hinge Model by Priestley .....	123
Figure 4.22:	Test Series II Response Predicted Using Plastic Hinge Model by Priestley .....	124
Figure 4.23:	Test Series I: Response Predicted Using Proposed Plastic Hinge Model.....	124
Figure 4.24:	Test Series II Response Predicted Using Proposed Plastic Hinge Model .....	125
Figure 4.25:	Trilinear Approximation of Force-Displacement Response Envelope .....	125
Figure 4.26:	Hysteresis Model .....	126

Figure 4.27:	Column 407 Force-Displacement Response Histories .....	126
Figure 4.28:	Column 415 Force-Displacement Response Histories .....	127
Figure 4.29:	Column 430 Force-Displacement Response Histories .....	127
Figure 4.30:	Column 815 Force-Displacement Response Histories .....	128
Figure 4.31:	Column 1015 Force-Displacement Response Histories .....	128
Figure 4.32:	Series I Predicted and Measured Values of Energy Dissipated in a a Single Cycle .....	129
Figure 4.33:	Series II: Predicted and Measured Values of Energy Dissipated in a Single Cycle .....	129
Figure 4.34:	Park-Ang Energy-Based and Mander-Cheng Fatigue-Based Damage Indices Evaluated for Columns Tested by Kunnath et al. [Kunnath 1997].....	130
Figure 4.35:	Failure Predicted by Dual-Phase Damage Index (Final Point Indicates Measured Failure) .....	131
Figure 5.1:	Current Seismic Design .....	153
Figure 5.2:	Performance-Based Seismic Design.....	153
Figure 5.3:	ATC 32 Hazard and Performance Levels for Ordinary and Important Bridges .	154
Figure 5.4:	FEMA 273 Performance Objectives.....	154
Figure 5.5:	Damage Descriptions by Performance Levels [FEMA 1997] .....	155
Figure 5.6:	Proposed Performance Objectives .....	155
Figure 5.7:	Correlation of Engineering Limit States and Performance Levels .....	155
Figure 5.8:	Test Series 1 Measured Crack Widths vs. Displacement Ductility Demand.....	156
Figure 5.9:	Test Series 1I Measured Crack Widths vs. Displacement Ductility Demand ....	156
Figure 5.10:	Force-Displacement Response of Original and Repaired Column [Elkin 1997]	157
Figure 5.11:	Average Residual Displacement Ratio [MacRae 1997] .....	158
Figure A.1:	Elevation of Prototype Structure.....	179
Figure A.2:	Prototype Structure: Column Cross Section .....	179
Figure A.3:	Test Specimen Geometry and Reinforcement .....	180
Figure A.4:	Test Specimen Geometry and Reinforcement .....	180
Figure A.5:	Cross Section of Anchor Block .....	181

Figure A.6:	Longitudinal Reinforcement Stress-Strain Response .....	181
Figure A.7:	Spiral Reinforcement Stress-Strain Response .....	182
Figure A.8:	Measured Plain-Concrete Stress-Strain Response for Column 407 .....	182
Figure A.9:	Measured Plain-Concrete Stress-Strain Response for Column 415 .....	183
Figure A.10:	Measured Plain-Concrete Stress-Strain Response for Column 430 .....	183
Figure A.11:	Measured Plain-Concrete Stress-Strain Response for Columns 815 and 1015 .....	184
Figure A.12:	Three Columns of Test Series I after Casting Anchor Blocks.....	184
Figure A.13:	Slump Test .....	185
Figure A.14:	Casting Concrete Cylinders .....	185
Figure A.15:	Casting Anchor Blocks .....	186
Figure A.16:	Sand Blasting of Exposed Joint Surface .....	186

## LIST OF TABLES

Table 3.1:	Specification of Main Test Parameters.....	55
Table 3.2:	Material Properties .....	55
Table 3.3:	Displacement Levels .....	55
Table 3.4:	Column 407 Measured Response Quantities .....	56
Table 3.5:	Column 415 Measured Response Quantities .....	57
Table 3.6:	Column 430 Measured Response Quantities .....	58
Table 3.7:	Column 815 Measured Response Quantities .....	59
Table 3.8:	Column 1015 Measured Response Quantities .....	60
Table 4.1:	Flexural Strength.....	109
Table 4.2:	Comparison of Nominal Flexural Capacity using Expected and Specified Strengths.....	109
Table 4.3:	Shear Strength Equations .....	109
Table 4.4:	Experimental Column Shear Demand and Demand/Capacity Ratios.....	110
Table 4.5:	Joint Shear Demand and Demand/Capacity Ratios.....	110
Table 4.6:	Measured Displacement at Top of Column (inches).....	110
Table 4.7:	Moment, Curvature, and Plastic Hinge Values for Priestley et al. Plastic Hinge Length Method.....	111
Table 4.8:	Displacement Values Computed by Priestley et al. Method (inches) .....	111
Table 4.9:	Displacement Values Computed by Proposed Method (inches) .....	111
Table 4.10:	Definition of Rules for Hysteresis Model .....	112
Table 4.11:	Results for Columns Subjected to Constant Amplitude Displacement Histories (translated from [Kunnath 1997]).....	112
Table 4.12:	Fatigue Analysis of Columns Subjected to Constant Displacement Amplitudes .....	128
Table 5.1:	Recommended Performance Levels.....	113
Table 5.2:	Results for Columns Subjected to Constant Amplitude Displacement Histories (translated from [Kunnath 1997]).....	150
Table 5.3:	Measured Displacement and Predicted Strain Corresponding to Initial Spalling.....	150
Table 5.4:	Correlation of Numerical Expressions and Performance Criteria.....	151
Table 5.5:	Minimum Required Analysis Procedures .....	152
Table A.1:	Specified, Expected, and Maximum Design Strengths .....	176
Table A.2:	Maximum Probable Moment .....	176
Table A.3:	Joint Shear Stress .....	176
Table A.4:	Column Shear Demand and Capacity Values .....	176

Table A.5: Test Specimen Geometry .....	177
Table A.6: Test Specimen Reinforcement .....	177
Table A.7: Concrete Mix Data .....	177
Table A.8: Development of Concrete Strength .....	178
Table A.9: Compressive and Tensile Strength on or near Day of Test .....	178

# 1 Introduction

## 1.1 RESEARCH IMPETUS AND BACKGROUND

In performance-oriented seismic design, reinforced concrete bridges are designed to meet specified performance objectives. A performance objective is a pairing of a structural performance level and a seismic demand level. A structural performance level is a specific damage state and is quantified using one or more engineering limit states. For reinforced concrete bridges supported by columns, key aspects of structural performance include cracking, spalling, residual drift, and cross-section fatigue. Development of performance-based seismic design provisions for reinforced concrete bridges requires engineering approaches that consider these aspects to define the state of structural performance.

Recent earthquakes, including the Loma Prieta and Northridge earthquakes, have provided preliminary data to study the seismic performance of bridges. In these earthquakes, damage was primarily focused in older bridge construction; damage to modern reinforced concrete bridges was predominantly in the form of cracking and minor spalling. As demonstrated by damage to older construction, damage to important bridges that results in delayed operation may be of significant economic cost.

Although past performance has indicated that modern bridges can perform well, the future performance of modern bridges is not known. Current seismic design standards for reinforced concrete bridges do not provide adequate performance design requirements. Most current codes specify seismic design force levels and standard details for key structural components. Likewise, previous seismic research has focused primarily on strength and detailing rather than structural performance. Although future earthquakes may result in damage to reinforced concrete bridges, it is possible that the damage may be limited; this result may indicate that current detailing requirements have resulted in overly conservative column design for the selected design earthquake.

Efforts to develop performance-oriented codes for the seismic design of bridges have begun. In the United States, the Applied Technology Council has issued a report entitled “ATC 32 Improved Seismic Design Criteria for California Bridges: Provisional Recommendations” [ATC 1996]. Those guidelines recommend a performance-oriented seismic design framework. Two seismic hazard levels and three performance levels are specified; these levels specify the struc-

tural demand and capacity, respectively. In performance-based seismic design, engineering limit states are used to quantify the structural performance. In the ATC 32 report, engineering expressions are provided to design and detail bridge columns for the significant damage state. However, methods to design and detail the bridge columns for minimum and intermediate damage states are not adequately specified.

Although previous research on the response of reinforced concrete bridge columns is extensive, these studies are not adequate to develop all aspects of performance-oriented design. Previous experimental research primarily has emphasized improving the design and understanding of reinforced concrete bridge columns subjected to significant plastic cyclic displacement demands. Development of performance-based design methods requires further experimental and analytical investigations to evaluate intermediate damage levels and to develop analytical models and appropriate design methodologies.

## **1.2 OBJECTIVE AND SCOPE**

Recognizing the shortcomings of current information, a research program was designed to develop improved methods to evaluate the performance of modern bridge columns over the range of typical geometries and range of performance levels. The objective of the research program was to characterize and quantify the seismic performance of reinforced concrete bridge columns. The research objective was achieved by designing an experimental and analytical investigation that would characterize the seismic performance of modern bridge columns at various damage states. The experimental investigation indicated the important aspects of structural damage. As a result, four engineering limit states were defined as cracking, spalling, residual drift, and cross-section fatigue. Analytical engineering expressions were developed to quantify each damage state. A performance-based seismic design framework for reinforced concrete bridges was developed using the analytical and experimental results.

The scope of the research program included reviewing the available literature, developing and carrying out an experimental research program, developing analytical models to represent observed response, and proposing a framework for performance-based design of bridges.

The previous research was reviewed and categorized to provide an understanding of the influence of individual parameters on the response of reinforced concrete elements. On the basis of the research review, column longitudinal reinforcement ratio and column aspect ratio were cho-

sen as the experimental study parameters.

The experimental study consisted of five columns that were representative of modern bridge construction; the columns were detailed to represent a range of conditions that occur in modern bridge construction and to fill in gaps in the available information. The columns were tested in two test series. In the first test series, three columns with different longitudinal reinforcement ratios were tested. An additional two columns with different aspect ratios were tested as part of the second test series.

In the analytical investigation, the experimental results were used to evaluate and modify analytical models to assess the strength, force-displacement response, and progression of damage of reinforced concrete bridge columns. The models were modified if discrepancies existed between the measured response and the predicted response.

Finally, a preliminary performance-based seismic design framework for reinforced concrete bridges was proposed. The investigation focused on defining and quantifying structural performance and corresponding engineering limit states. The three performance levels were termed Fully Operational, Delayed Operational, and Stability and were defined using the appropriate engineering limit states. The methods developed in the analytical investigation were used to assess each engineering limit state.

### **1.3 REPORT CONTENTS**

Chapter 2 summarizes previous seismic research on the experimental and analytical modeling of reinforced concrete elements. Chapter 3 summarizes the experimental program and results. The description of the experimental program and measured response summarized in Chapter 3 is intentionally terse; more detailed information is provided in the appendices. Analysis of the test results using available and newly proposed analytical models is provided in Chapter 4. Chapter 5 presents preliminary development of a performance-based seismic design framework for reinforced concrete bridges with ductile columns. The overall research program and its findings are summarized in Chapter 6.

## 2 Previous Research Results

### 2.1 INTRODUCTION

Significant changes in the seismic design of reinforced concrete bridges occurred following the San Fernando earthquake in 1971. However, structures built prior to the event remain at risk, and, as expected, existing bridge structures sustained significant damage during the Loma Prieta earthquake in 1989. Damage to the existing infrastructure prompted the State of California to investigate the seismic behavior of nonductile bridge structures as well as technologies for upgrading purposes. These studies were mainly funded by the California Department of Transportation (Caltrans) and were mainly conducted [e.g., Caltrans 1991, Caltrans 1994, Caltrans 1998] at California universities. The experimental and analytical results from these studies are being used to characterize the response of elements and structures detailed according to older codes as well as to determine suitable retrofit schemes for these structures. Experimental research considering the seismic response of modern bridge construction, including well-confined reinforced concrete elements, is more limited.

In modern seismic design, bridge columns are expected to form ductile, flexural hinges at specified locations. For a reinforced concrete element, the post-yield behavior is complex. From the outset, member response is inelastic. Models developed to estimate the post-yield response and damage state of a reinforced concrete member must be evaluated using measured response from laboratory and/or field testing.

Although experimental research focusing on the response of modern bridge columns has been limited, there is a substantial database of experimental research investigating the response of reinforced concrete elements subjected to cyclic loading. Typically, an individual study will characterize the influence of one or more important parameters. Section 2.2 summarizes the previous research findings emphasizing the influence of each parameter on the displacement capacity. The research review categorizes the study parameters into three groups: member geometry and reinforcement, material properties, and loading and strength.

There is a new focus in the seismic design of bridges on performance-oriented design. A recent effort, undertaken to improve seismic design practice in California [ATC 1996], has identi-

fied several research needs including establishing a quantitative basis for assessing qualitatively defined performance of bridge columns. Several researchers have proposed empirical models to assess structural performance in terms of the displacement capacity, hysteretic response, and damage [e.g. Priestley 1987, Saiidi 1979, Park 1985].

Plastic hinge length models were developed to approximate the post-yield displacement response; several are summarized in Section 2.3. Force-displacement models have been developed to assess element hysteresis; available models are summarized in Section 2.3.2. Damage indices are used to assess element damage; Section 2.3.3 reviews available damage indices.

## **2.2 MEMBER BEHAVIOR**

Research studies have investigated the response of bridge columns subjected to lateral loading. Earlier studies performed at the University of Canterbury in New Zealand have contributed much to the understanding of the behavior of bridge columns [e.g., Mander 1984, Ang 1985, Zahn 1986, Tanaka 1990, Wong 1990, Watson 1994]. Recent experimental efforts undertaken at the University of California, San Diego have focused on columns without ductile detailing [e.g., Verma 1992, Chai 1994]. Several research studies have focused on improving the design and upgrading of bridge beam-column joints [e.g., Ingham 1994, Stojadinovic 1995, Sriharam 1996, Lowes 1997, Mazzoni 1997]. The report by Taylor and Stone summarizes tests that have focused on the response of reinforced concrete bridge columns with circular cross sections [Taylor 1993].

The following summarizes experimental and analytical research studies focusing on the response of reinforced concrete elements to seismic loading. The focus parameters for each research program were identified. For each study, the focus parameters were categorized; categories included member geometry, material properties, and loading. The summaries of the research results were categorized accordingly.

The theoretical influence of each study parameter on the force-displacement response was considered. Using a method proposed by Sozen and Moehle [Sozen 1993] and adapted by Aschheim et al. [Aschheim 1997], the total displacement of a cantilever reinforced concrete column can be idealized as the sum of individual displacement components due to column bending ( $\Delta_{bending}$ ), shearing ( $\Delta_{shear}$ ), and slip of the longitudinal reinforcement out of the anchorage zone ( $\Delta_{slip}$ ), as shown in Equation 2.1. Equations 2.2 through 2.5 indicate expressions to approximate the post-yield bending, slip and shearing displacement components.

$$\Delta = \Delta_{bending} + \Delta_{slip} + \Delta_{shear} \quad (2.1)$$

$$\Delta_{bending} \cong \frac{1}{3}\phi_y L^2 + \frac{1}{2}(\phi_{max} - \phi_y)L_y(L - L_y/3) \quad (2.2)$$

$$\text{where } L_y = \frac{(M_{max} - M_y)}{M_{max}}L \quad (2.3)$$

$$\Delta_{slip} \cong \theta_{slip}L = \frac{u_t - u_c}{D''}L \quad (2.4)$$

$$\Delta_{shear} \cong \frac{V}{A_{eff}G_{eff}}L \quad (2.5)$$

The equation variables are defined as follows:

$L$  is the column length

$\phi_y$  and  $\phi_{max}$  are the yield and maximum curvature

$M_y$  and  $M_{max}$  are the yield and maximum moments

$\theta_{slip}$  is the slip rotation

$u_s$  and  $u_t$  are the slip extensions of the two extreme embedded longitudinal bars

$D''$  is the distance between the two extreme longitudinal bars

$V$  is the column shear demand

$A_{eff}$  is the effective shear area

$G_{eff}$  is the effective shear modulus

In the following discussion, the influence of each study parameter is studied using the previous expressions.

### 2.2.1 Member Geometry and Reinforcement

Important variables related to member geometry and reinforcement include aspect ratio, the ratio of the gross and the confined cross-sectional areas, longitudinal reinforcement ratio, transverse reinforcement ratio, and longitudinal bar diameter. Each of these variables can significantly influence the force-displacement response. In the following sections, the influence of each variable is characterized using the results of experimental and analytical studies.

### ***2.2.1.1 Column Aspect Ratio and Length***

Column aspect ratio is defined as the ratio of the column height,  $L$ , and the column diameter,  $D$ . For a constant column cross section, an increase or decrease in the aspect ratio increases or decreases the column length, respectively. The influence of the aspect ratio may be assessed using Equations 2.2 through 2.5. Theoretically, the total displacement depends on the square of the column length (Equations 2.2 and 2.3). This analysis suggests that an increase in the column length will increase the displacement for a specified curvature demand. For a constant column cross section, increasing (or decreasing) the column length will result in an increase (or decrease) in the maximum shear demand. According to Equation 2.5, the shearing deformation increases with the shear demand. However, increased shear demands can promote cracking and degradation of the concrete which can result in a smaller ultimate curvature capacity. See Section 2.2.4.2 for further discussion of the influence of shear on member response.

The effect of aspect ratio on column response has been considered in several experimental research studies. Iwasaki et al. [Iwasaki 1985] tested three columns with increasing aspect ratios ranging from 2.2 to 5.4. The columns with aspect ratios of 3.8 and 5.4 failed in an apparent flexure mode; the shortest column with an aspect ratio of 2.2 failed in an apparent shear mode. As predicted by theoretical analyses, the measured displacement capacity increased with an increase in column length. The reported displacement ductilities, which is the ratio of the maximum and yield displacements by definition, were approximately equal for the taller columns; however, the displacement ductility were lower for the shortest column.

Davey and Park [Davey 1975] tested three columns with the same physical aspect ratio. For a column in single curvature, the moment-to-shear ratio is equal to the aspect ratio. The researchers varied the moment-to-shear ratio by applying a fixed-end moment to the top of the column. For the columns tested by Davey and Park, moment-to-shear ratios of 1.75, 2.5, and 3.25 were used. The researchers reported that the column displacement ductility capacity increased with the moment/shear ratio.

Researchers at the National Institute for Standards and Technology (NIST) tested two full-scale circular bridge columns with aspect ratios of 3 and 6 [Stone 1989]. Both columns failed in an apparent flexure mode. The measured displacement capacity was largest for the slenderest column. The reported displacement ductility was smaller for the slendermost column. The NIST researchers also reported that the measured plastic hinge length increased with the moment-to-

shear ratio. Sakai and Sheikh [Sakai 1989] concur and state that analysis of experimental data from the University of Canterbury suggests that the effective plastic hinge length was approximately proportional to the column aspect ratio for columns aspect ratios of 4 or less (Figure 2.1).

### **2.2.1.2 Concrete Cover**

Theoretically, the thickness of the concrete cover influences the moment-curvature response of a cross section at large curvature; spalling of the cover concrete results in a loss of stress-carrying capacity. Spalling of the concrete cover will influence the conditions over the entire spalled length, not just at a single plane. Loss of the concrete cover can reduce the lateral restraint of the longitudinal bar thereby increasing the chance of bar buckling and worsening the bond condition of the longitudinal bars. Neither of these effects are accounted for in a theoretical cross-sectional analysis.

Experimental results of the response of a column encased with a steel jacket and a conventionally reinforced column were used to study the influence of concrete cover. When a jacket is placed, the concrete cover is retained over the jacketed region. This can improve the bond transfer mechanism and lateral restraint of the longitudinal bars. As a result column jacketing can alter the failure mode or postpone the column failure.

Experimental work by Chai, Priestley, and Seible demonstrates differences in the response of conventional and jacketed reinforced concrete columns [Chai 1991]. Figure 2.2 shows the force-displacement response of two circular bridge columns subjected to cyclic lateral loading tested by Chai et al. The columns were nominally identical except that a steel jacket was placed around one of the columns. The force-displacement response shown in Figure 2.2(a) is for the conventionally reinforced concrete column; the force-displacement response shown in Figure 2.2(b) is for the jacketed column. As expected, the jacketed column demonstrates increased displacement capacity and energy absorption. Therefore, although the longitudinal bars buckled during testing of both columns, the column jacket served to delay the onset of bar buckling and thereby increased the displacement capacity.

### **2.2.2 Longitudinal Reinforcement Ratio**

Failure of a ductile column with low shear stress demands may be due to exhaustion of the cross section in compression or tension. For constant values of axial load demand, geometry, and transverse reinforcement, varying the longitudinal reinforcement ratio can alter the compression and

tension demands which can alter the response and failure mode. The influence of the longitudinal reinforcement ratio will depend on the failure mode. Theoretically, increasing the longitudinal reinforcement ratio will reduce the ultimate curvature of a member failing in compression. The trend is the opposite for the case of tensile failure; increasing the longitudinal reinforcement ratio will increase the displacement capacity.

Experimental work by Iwasaki et al. [Iwasaki 1985] indicated that the column failure mode can depend on the quantity of longitudinal reinforcement. The authors tested three columns with axial load ratios approximately equal to 6% of the gross cross-sectional capacity that were reinforced with longitudinal reinforcing ratios of 0.48%, 0.87% and 1.79%. The maximum displacement capacity was reported for the column with a longitudinal reinforcing ratio of 0.87%. The displacement capacity for the column with a smaller reinforcing ratio (0.48%) was smaller. The displacement capacity for the column with a larger reinforcing ratio (1.79%) was also smaller. The results indicate that the failure modes of the three columns were not the same. The researchers also reported that the displacement ductility increased for columns with relatively less longitudinal reinforcement. In addition, the loading rate was changed. The most significant differences due to differences in the loading rates were noted for the column with the highest longitudinal steel ratio.

The influence of the longitudinal reinforcement ratio was also studied by Priestley and Benzoni [Priestley 1994]. Two columns were constructed with different both longitudinal reinforcement ratios (0.5% and 1%) and spiral reinforcement ratios (0.2% and 0.3%). The apparent failure mode for both columns was shear. The displacement ductility for the column reinforced with the larger longitudinal steel ratio was smaller. Therefore, it was not possible to directly draw conclusions regarding the influence of longitudinal reinforcement on the flexural ductility from these tests.

### ***2.2.2.1 Confinement***

The experimental response of reinforced concrete cylinders subjected to only axial load indicate that the concrete strain capacity increases with an increase in confinement (Figure 2.3). Several researchers have tested confined concrete cylinders and columns under monotonic and cyclic axial load [e.g., Mander 1984, Sheikh 1982]. Analytical models have been developed to account for the increase in strain capacity due to column confinement [e.g., Corley 1966, Scott 1982,

Mander 1988].

Several researchers have studied the response of columns with various transverse reinforcement ratios. Wong, Paulay, and Priestley [Wong 1990] tested short columns that had aspect ratios of 2 and spiral spacings that varied from  $0.075D$  to  $0.2D$  ( $D$  = the column diameter). The experimental results indicated that for a specific displacement demand, a column with a smaller transverse reinforcement ratio has a smaller curvature demand.

Other experimental studies on the behavior of bridge columns with circular cross sections have considered the influence of the spiral reinforcement ratio including [Potangaroa 1979, Ang 1981, Ang 1985, Zahn 1986, Stone 1989]. However, the influence of the spiral reinforcing ratio could not be identified directly since it was not an isolated study parameter.

### **2.2.2.2 Longitudinal Bar Diameter**

Conventional analyses of the flexural response of a cantilever reinforced concrete columns consider only the displacement due to column bending. This type of analysis neglects the displacement resulting from extension of the longitudinal reinforcement anchored within the footing. Of primary importance is the tensile stress in the reinforcement, which results in tensile strain of that reinforcement within the anchorage zone in the footing, and, hence, additional displacement of the column. This phenomenon is illustrated in Figure 2.4; the slip displacement at the top of the column is designated  $\Delta_{slip}$ .

Theoretical expressions suggest that the extension of the bar resulting from longitudinal stresses within the anchorage zone is inversely proportional to the main-bar diameter. For a value of slip equal to  $u_1$  at Point 1, the slip displacement at Point 2, a distance  $\Delta x$  away from Point 1, is expressed by Equation 2.6. The stress values of  $\sigma_1$  and  $\sigma_2$  correspond to the stresses at Points 1 and 2, respectively. A uniform bond strength of  $\mu$  over the bar length  $\Delta x$  is assumed:

$$u_2 = \frac{\epsilon_1 + \epsilon_2}{2} \left( \frac{4\mu}{d_b(\sigma_2 - \sigma_1)} \right) \Delta x + u_1 \quad (2.6)$$

Research efforts have been undertaken to develop expression for bond strength. Several researchers [e.g., Park 1975, Eligehausen 1983] have postulated that the bond capacity,  $\mu$ , depends on the bar diameter; Park and others have suggested that the bond capacity is directly proportional to the inverse of the bar diameter. However, experimental studies do not support such a strong correlation of bond strength and bar diameter. Eligehausen, Popov, and Bertero [Elige-

hausen 1983] performed pull-out tests on single bars anchored in reinforced concrete blocks. The tested bar sizes included No. 6, No. 8, and No. 10 bars (bar diameters of approximately 19, 25 and 32 mm). The measured response indicated that the bond capacity decreased slightly with an increase in bar diameter (Figure 2.5). The bond strength measured for the largest diameter bar was 10 to 20% lower than the bond strength measured for the smallest bar. As reported by Eligehausen et al., other experimental research has demonstrated that the bond strength does not depend on the longitudinal bar diameter.

If a uniform bond capacity is assumed over the entire bar, Equation 2.7 can be used to estimate the slip displacement at yield of the longitudinal steel. The expression indicates that the slip,  $u$ , increases with an increase in bar diameter,  $d_b$ .

$$u = \frac{f_y^2 d_b}{8E\mu} \quad (2.7)$$

### 2.2.3 Material Properties

The response of a composite section is influenced by response of the individual constituent materials. For a reinforced concrete element, individual materials include concrete, longitudinal reinforcing steel, and transverse reinforcing steel.

#### 2.2.3.1 Plain and Confined Concrete

Factors that can influence the effective stress-strain response of concrete include the unconfined stress-strain response, the amount, placement, and configuration of the transverse reinforcement, quantity and placement of the longitudinal reinforcement, ratio of the core and gross cross-sectional areas, strain gradient, and load history; [Sakai 1989] provides a more detailed discussion of each of these factors.

The compressive strain capacity of high-strength unconfined concrete, defined as concrete with a stress capacity  $f_c'$  exceeding 6000 psi [MacGregor 1992], is lower than the strain capacity of normal-strength concrete confined with equivalent transverse reinforcement [Sheikh 1994]. Recent experimental studies have shown that well-confined high-strength concrete columns possess strain capacities that are comparable to normal-strength specimens [Saatcioglu 1994, Sheikh 1994]. The quantity of transverse reinforcement required for strain ductility is a function of the strength of the concrete, strength of the transverse steel [Saatcioglu 1994], and axial load ratio [Sheikh 1994, Xiao 1998].

Experimental results indicate that the concrete tensile capacity increases the bond strength [Eligehausen 1983]. Therefore, increasing the concrete tensile strength may reduce the slip displacement.

### ***2.2.3.2 Longitudinal Reinforcement***

The response of a reinforced concrete member depends on the stress-strain response of the longitudinal steel. The distinct characteristics of the pre-yield response, the yield plateau, and the post-yield curve can influence the member response. Current seismic bridge design specifications in California do not permit the use of high-strength longitudinal reinforcement in yielding members [Caltrans 1992] and require that the longitudinal steel reinforcement meet the ASTM designation A 706, which is characterized by a distinct yield point, limits of the yield and ultimate strength, and minimum strain capacity. Typically, high-strength reinforcement does not display a distinct yield point or yield plateau, and has a lower ultimate strain capacity than normal-strength steel.

Post-yield response of high-strength steel can result in higher local bond demands or require longer development lengths, which may increase the relative contribution of the slip displacement (at a prescribed level of longitudinal steel strain). However, increased bond demands may also lead to bond failure. In an experimental study, Meli, Baeza, and Rodriguez investigated the response of columns reinforced with normal-strength and high-strength steel [Meli 1984] and found that the columns that were reinforced with similar longitudinal reinforcement ratio but different steel strengths had similar displacement ductility capacities.

Failure modes in confined columns include crushing of the concrete core, longitudinal bar buckling, and longitudinal bar fracture. Failure of ductile, well-confined columns may result from exhaustion of the cyclic capacity of the longitudinal steel [Zahn 1986, Hose 1996, Mazzoni 1997, Calderone 1998]. Typically, the longitudinal steel buckling is followed by bar fracture. Bars may buckle out-of-plane over many hoop spacings or along the spiral if the surrounding concrete has degraded. In all cases, the ultimate deformation capacity is influenced by the cyclic demands on the longitudinal steel.

### 2.2.3.3 Transverse Reinforcement

For columns that respond in a primarily flexural mode, the transverse reinforcement primarily serves to confine the core concrete and restrain the longitudinal bars. The role of column confinement has been tested by several researchers and summarized by Razvi and Saatcioglu [Razvi 1994]. Razvi and Saatcioglu define a confinement effectiveness ratio as  $(\rho_s f_{yh}) / (f'_c)$ , where  $\rho_s$  = the volumetric ratio of the transverse reinforcement,  $f_{yh}$  = the yield strength of the transverse reinforcement, and  $f'_c$  = the compressive strength of the concrete. Experimental results indicated that the axial strain ductility levels were approximately constant for a given confinement effectiveness ratio (Figure 2.3).

Review of previous research suggests that the compressive strain capacity of confined concrete cylinders depends on the yield strength,  $f_{yh}$ , and fracture strain of the transverse steel,  $\epsilon_{cu}$ .

$$\epsilon_{cu} = 0.004 + \frac{\rho_s f_{yh} \epsilon_{su}}{f'_c} \quad (2.8)$$

For example, the expression given in Equation 2.8 used to calculate the compressive strain capacity [Priestley 1996] was derived from tests on columns subjected to cyclic axial and cyclic lateral loadings [Mander 1984]. The expression does not explicitly account for bar buckling or compressive failure of the core concrete without spiral fracture.

## 2.2.4 Loading

Under seismic loading conditions, bridge columns may be subjected to variable axial load and lateral load. The following summarizes the influence of axial load and lateral displacement history. In addition, the influence of shear demand and shear strength on column response is discussed.

### 2.2.4.1 Axial Load

Application of the compressive axial load increases the compressive strain demand. As demonstrated by experimental research, higher axial loads may reduce the displacement capacity of columns failing in a compression (Figure 2.6) [Saatcioglu 1989]. Experimental results indicate that an increase in axial load may result in reduced member displacement ductility [e.g., Atalay 1975, Sheikh 1993]. Atalay et al. concluded that high axial stress demands may significantly alter the response. They advise careful attention to critical regions subjected to axial load greater than  $0.4A_g f'_c$  where  $A_g$  = gross cross-sectional area and  $f'_c$  = compressive stress capacity. However,

tests by Zahn, Park, and Priestley indicate that the response of some well-confined columns may be independent of axial load [Zahn 1986]. Zahn et al. tested two square columns with axial load ratios of 0.2 and 0.4 to provide approximately column flexural strengths. Both columns were well confined although the confinement ratios were slightly higher for the column with the higher axial load. The behavior of the two columns were similar.

#### **2.2.4.2 Shear**

As indicated previously, the lateral displacement of a reinforced concrete column can be idealized as the sum of the displacement components due to bending, slip and shear (Equation 2.1). Therefore, for a given lateral force, shear effects result in increased displacement. However, a column with high shear demands may fail in shear which may result in a smaller displacement capacity.

The behavior of a reinforced concrete element in shear is determined in part by the column shear demand. The allowable column shear may be limited to  $10\sqrt{f'_c}A_{eff}$ , regardless of the quantity of transverse reinforcement [ACI 1995]. For shear demands levels less than this limit, increasing the transverse reinforcement decreases the shearing deformation and occurrence for shear failure; experimental results by [Wakabayashi 1986] indicate that shear failure becomes more brittle with an increase in axial load and decrease in transverse reinforcement (Figure 2.7). Atalay and Penzien tested columns with various axial load ratios and transverse reinforcement ratios. The authors measured shearing deformations for all columns (Figure 2.8). The experimental results indicate shearing deformations are larger for columns with lower transverse reinforcement ratios and lower axial load ratios.

Although columns with high shear demands may not fail in a shear mode, shearing deformations may have a significant influence on the force-displacement response. In comparison to a column responding primarily in flexure, members with high shear stresses display pinched force-displacement hysteresis. It is likely that the energy dissipation of the column with high shear demands will be less than the flexural column [e.g., Celebi 1976]. Analytical studies show that the pinching response influences the force-displacement response of reinforced concrete structures subjected to seismic loading [e.g., Gupta 1998].

### ***2.2.4.3 Lateral Displacement History***

Seismic loading is cyclic and dynamic in nature. Several researchers have investigated the influence of loading pattern and rate on column response. Test methods include pseudo-static, pseudo-dynamic, and earthquake simulator tests. Influential characteristics include rate effects, directionality, and displacement pattern.

Several research efforts have compared the response of columns subjected to unidirectional and bidirectional loading [e.g., Otani 1981, Iwasaki 1985, Saatcioglu 1989]. The pre-yield response of columns subjected to bidirectional loading is similar to the response of columns subjected to unidirectional loading. However, significant differences in the strength and displacement ductility have been measured, in particular for columns with low levels of transverse steel.

Typical experimental displacement histories have monotonically increasing displacement levels with two or three displacement cycles at each level. Actual displacement histories imposed by seismic loading can vary substantially from this standard history. Several research studies have attempted to quantify the influence of displacement history on element response. The experimental research effort by Kunnath et al. evaluated low-cycle fatigue failure mode of reinforced columns using nominally identical columns [Kunnath 1997]. The columns were subjected to various displacement histories including monotonic, constant amplitude, and random displacement histories. The columns that were subjected to larger constant-amplitude displacement histories demonstrated that fewer cycles are required to reach failure. One of the constant-amplitude columns did not fail, even when over 150 displacement cycles were imposed. In this case, the imposed displacement was less than the displacement corresponding to the onset of spalling for monotonic loading which implies that more limited displacement demands may not be damaging. The test results also indicate that cycling at larger displacement demands can reduce the displacement capacity relative to that predicted by models based on monotonic test results.

Higashi, Ohkubo, and Ohtsuka studied columns subjected to different displacement histories including monotonic, asymmetric (i.e., increased cyclic displacement demand in one direction only), symmetric with three cycles at each displacement level (similar to a standard displacement history), and symmetric with ten cycles at each displacement level [Higashi 1977]. The results indicate that the response envelopes of the columns subjected to the monotonic and asymmetric displacement histories were similar; the displacement capacity of the columns subjected to standard displacement history was less. Cycling the column ten times at each displacement level fur-

ther reduced the displacement capacity. Displacement history has a strong influence on both the force-displacement response and the displacement capacity

## 2.3 SIMPLIFIED FORCE-DISPLACEMENT AND DAMAGE MODELS

Accurate assessment of the force-displacement response, displacement capacity, and energy dissipation capacity of a reinforced concrete element is difficult. As previously demonstrated, the influence of each parameter must be modeled. Both simplified and complex models have been developed to assess the displacement capacity, element hysteresis, and damage.

Simplified models to approximate the displacement capacity of a reinforced concrete member include the plastic hinge length method. Typically, the plastic hinge length is derived empirically and accounts for the influence of several parameters. Section 2.3.1 summarizes plastic hinge length expressions.

Consideration of the full cyclic force-displacement response requires modeling of element hysteresis. Available models include fiber, lumped-plasticity, and multilinear force-displacement models. Of these, the simplest are the multilinear force-displacement models, although the complexity of this model family does vary. Section 2.3.2 discusses several of these models.

Column damage primarily results from an increase in the displacement demand and cycling. Damage indices are used to quantify damage. A review of both member and system damage indices is provided by Williams and Sexsmith [Williams 1995]. Section 2.3.3 discusses local damage indices to evaluate bridge column performance.

### 2.3.1 Plastic Hinge Length Expressions

The total displacement of a reinforced concrete cantilever column may be idealized as the sum of the bending, slip, and shear displacement components (Equation 2.1). This calculation may require assessment of highly nonlinear behavior. The plastic hinge length method was developed to simplify the calculation of the plastic component of the total displacement. According to the plastic hinge length method, the plastic component of the displacement is

$$\Delta_p = (\phi_u - \phi_y)l_p(L - l_p/2) \quad (2.9)$$

where  $\phi_u$  = the ultimate curvature,  $\phi_y$  = the yield curvature,  $l_p$  = the plastic hinge length, and  $L$  = the length from the point of maximum moment to the point of inflection.

The plastic hinge length method is theoretically derived by replacing the inelastic (post-yield) area of the curvature diagram with an equivalent rectangle of height  $l_p$  and width  $(\phi_u - \phi_y)$ . However, as expressed in Equation 2.1, displacements due to slip and shear also contribute to the column tip displacement. To include these components, researchers have developed plastic hinge length expressions using experimental results. To do so, Equation 2.9 is rewritten in terms of the plastic hinge length,  $l_p$ , and measured values of the curvature, yield displacement, and column length are used to calculate  $l_p$ . Therefore, use of the methods relies on reasonable approximations of the yield and ultimate curvatures, yield displacement as well as the plastic hinge length.

The following subsections summarize plastic hinge length expressions developed for use in Equation 2.9.

### **Baker and Amarakone [Baker 1966]**

In 1956, Baker [Baker 1956] used  $l_p = 0.5D$  where  $D$  = the section depth to assess the response of reinforced concrete beams. Equations 2.10 and 2.11 were developed to calculate the plastic hinge length,  $l_p$ , and the compressive strain capacity,  $\epsilon_{cu}$ ; in the equations,  $\rho_s$  = transverse reinforcement ratio,  $L$  = columns length, and  $c$  = the neutral axis depth.

$$l_p = 0.8k_1k_3\frac{L}{D}c \quad (2.10)$$

$$\epsilon_{cu} = 0.0015\left(\left[1 + 150\rho_s + (0.7 - 10\rho_s)\frac{D}{c}\right] \leq 0.01\right) \quad (2.11)$$

Since the values of the plastic hinge length and compressive strain capacity depend on the neutral axis depth, they depend on the axial load and longitudinal reinforcement ratio. The parameters  $k_1$  and  $k_3$  in Equation 2.10 are defined as follows:  $k_1$  is equal to 0.7 for mild steel and 0.9 for cold-worked steel,  $k_3$  is equal to 0.6 for  $f'_c = 5100$  psi and 0.9 for  $f'_c = 1700$  psi. Therefore, for modern columns, the plastic hinge length is approximately  $l_p = 0.3(L/D)c$ .

### **Corley [Corley 1966]**

The expressions proposed by Corley to calculate the plastic hinge length and ultimate compressive strain were based on tests of simply supported beams (Equations 2.12 and 2.13).

$$l_p = 0.5D + 0.2\sqrt{D}\frac{L}{D} \quad (2.12)$$

$$\epsilon_{cu} = 0.003 + 0.02 \frac{b}{L} + \left( \frac{\rho_s f_y}{20} \right)^2 \quad (2.13)$$

Equation 2.13 provides a lower bound for the maximum concrete strain capacity. In the equation,  $b$  is the beam width and the other variables are as defined previously; the variable units are inches and psi. The plastic hinge length directly depends on the aspect ratio and member depth.

#### **Sawyer [Sawyer 1964]**

Sawyer proposed Equation 2.14 to calculate the plastic hinge length; the expression depends on only the member depth and length. The plastic hinge length exceeds  $0.5D$  for columns with aspect ratios of 3 or more.

$$l_p = 0.25D + 0.075L \quad (2.14)$$

#### **Priestley and Park [Priestley 1987]**

The plastic hinge length expression shown in Equation 2.15 was derived using measured displacement capacities of scaled bridge piers tests subjected to cyclic loading. The plastic hinge length depends on the column length,  $L$ , and the diameter of the main longitudinal bar,  $d_b$ .

$$l_p = 0.08L + 6d_b \quad (2.15)$$

#### **Zahn, Park, and Priestley [Zahn 1986]**

The previous expression was evaluated using additional data from model bridge piers that varied in cross-sectional shape, transverse reinforcement ratio and axial load ratio. The results were not conservative for axial load ratios less than 0.3. The expression was modified; Equation 2.16 shows the modified expression.

$$l_p = (0.08L + 6d_b) \left( 0.5 + 1.67 \frac{P}{A_g f'_c} \right) \quad (2.16)$$

#### **Priestley, Seible, and Calvi [Priestley 1996]**

Priestley, Seible and Calvi advocate the use of the plastic hinge length expression shown in Equation 2.17 for column plastic hinges forming against a supporting member (e.g., a column-footing

subassembly) [Priestley 1996]. The plastic hinge length depends on the column length, bar diameter, and yield strength of the longitudinal steel,  $f_y$ ; the variable units are inches ( $L$  and  $d_b$ ) and ksi ( $f_y$ ). Equation 2.18 provides an estimate of the curvature capacity.

$$l_p = 0.08L + 0.15f_y d_b \quad (2.17)$$

$$\epsilon_{cu} = 0.004 + \frac{1.4\epsilon_{uh}f_y h}{f'_{cc}} \quad (2.18)$$

In the expression, the first term primarily accounts for bending action and the second term accounts for the contribution due to slip of the anchored longitudinal reinforcement. The expression is identical to Equation 2.15 if  $f_y = 40$  ksi.

### 2.3.2 Force-Displacement Hysteresis Models

Seismic evaluation or design of a bridge structure may require a detailed representation of the complete hysteretic load-displacement relationship. Since the response of reinforced concrete elements is complex and influenced by several mechanisms, modeling the entire hysteretic response of each mechanism can be cumbersome. Simplified multilinear force-displacement models are commonly used to simplify the analysis.

Force-displacement hysteresis models are defined in terms of the response envelope, and the unloading and reloading curves. An example hysteresis model is described in Figure 2.9. The model is outlined by the response envelope curves; typically a multilinear curve is used. In Figure 2.9, the response envelope curves are indicated by thick grey lines in Quadrant 1 for positive loading and in Quadrant 3 for negative loading. In this example, the response envelope is trilinear. Each linear section, indicated by numbers 1, 2, and 3 in the example figure, is a single response loading rule. Curves to describe unloading from the response envelope and reloading from the unloading curve may also be defined by multilinear rules. In the example figure, each linear section of the unloading rules is numbered 4, 5, and 6. Most models follow a pattern similar to the example.

The bilinear model is the simplest hysteresis model (Figure 2.10). The bilinear model has a bilinear response envelope. The unloading curve is linear to the intersection point with the strain-hardening curve.

Clough [Clough 1966] developed the first stiffness-degrading hysteresis model. As shown in

Figure 2.11, the Clough model has a bilinear response envelope. The unloading stiffness is equal to the initial stiffness of the response envelope. Upon reaching the zero force point, the response targets the maximum displacement reached previously. Upon intersection with the envelope curve, the response continues along the envelope.

The Takeda hysteresis model [Takeda 1970] is a further modification of the Clough model (Figure 2.12) to include the use of a trilinear backbone curve with a degrading stiffness. The stiffness of the unloading curve depends on the maximum displacement ductility,  $\mu$ , (rule 4) as shown by Equation 2.19.

$$K_4 = K_y \mu^{-0.5} \quad (2.19)$$

Saiidi and Sozen simplified the Takeda model to develop the Q-hyst model [Saiidi 1979]. Other researchers have proposed similar models [e.g., Otani 1972, Mander 1984, Rothe 1984, Kunnath 1992].

The performances of different hysteresis models have been compared [e.g., Saiidi 1982, Stojadinovic 1995]. In the study by Saiidi, the nonlinear dynamic response of modeled single-degree-of-freedom systems was assessed by using five different hysteresis models including the elasto-plastic model, the bilinear model, the Clough model, the Q-hyst model, and the Takeda model. The results obtained using the Takeda model were used as a basis for comparison. The response predicted using the first three models were significantly different from the baseline response. The results using the Q-hyst models were comparable to the baseline response.

### 2.3.3 Damage Indices

Damage indices are used to quantify structural damage resulting from seismic loading. Damage may be assessed at the local, or element, level, or the global, or structure, level. For reinforced concrete structures, both local and global damage indices have been developed.

Damage indices may or may not account for cyclic load effect. In some cases, member deformation or stiffness are used as damage indicators; these formulations do not explicitly account for the effects of cyclic loading. Such damage indices are referred to as noncumulative damage indices. However, experimental research has indicated that cyclic loading can have an important effect on progression of damage and the failure mode. As an alternative, cumulative damage models have been developed; typically cumulative damage models use fatigue or energy

to assess cyclic damage. In addition, combined indices that include both noncumulative and cumulative damage components have been proposed.

The numerical value that indicates failure depends on the model formulation. For a dimensionless local damage index, it is common to restrict the model to range from 0 to 1. An index value of 0 indicates an undamaged state; an index value of 1 indicates a fully damaged state or failure.

The following subsections summarize noncumulative, cumulative, and combined local damage indices. Chung, Meyer and Shinozuka [Chung 1987] summarize local damage indices for both concrete and steel members. A comprehensive summary of both local and global damage indices for reinforced concrete structures is presented by Williams and Sexsmith [Williams 1995].

### ***2.3.3.1 Noncumulative Damage Indices***

Normalized deformations or stiffnesses have been used to assess local damage. Banon, Biggs and Irvine [Banon 1980, Banon 1981] developed damage indices that were based on rotational and curvature ductility. Similar damage indices based on total displacement ductility and member drift ratios have also been proposed [e.g., Oliveira 1975].

Damage indices based on normalized stiffness ratios include those by Lybas and Sozen [Lybas 1977], and Banon et al. [Banon 1981]. Damage is indicated by the ratio of the initial stiffness,  $k_o$ , and secant stiffness corresponding to the maximum displacement,  $k_r$ .

$$DI = \frac{k_o}{k_r} \quad (2.20)$$

Modifications by Roufaiel and Meyer [Roufaiel 1987] include using the secant stiffness corresponding to the displacement capacity,  $k_m$ .

$$DI = \frac{k_m (k_r - k_o)}{k_r (k_m - k_o)} \quad (2.21)$$

However, Banon et al. indicated that using stiffness-based or deformation-based damage ratios for test results did not provide a consistent indication of failure.

### 2.3.3.2 Fatigue-Based Cumulative Damage Indices

Failure of a ductile reinforced concrete member can result from compressive failure of the concrete core, spiral fracture, longitudinal bar buckling, and/or longitudinal bar fracture. At these large deformation demands, there may be significant cyclic loading effects. Low-cycle fatigue models were developed to assess the cyclic effects. Most low-cycle fatigue models are based either on displacement or strain.

Early fatigue models were developed for steel structures. Yao and Munse [Yao 1962] developed the displacement-based fatigue model shown in Equation 2.22.

$$DI = \sum_{i=1}^n \left( \frac{\Delta_i}{\Delta_{ui}} \right)^{1-0.86(\Delta'_i/\Delta_i)} \quad (2.22)$$

where  $\Delta_i$  = the maximum displacement of cycle  $i$ ,  $\Delta_{ui}$  = the maximum monotonic positive displacement capacity, and  $\Delta'_i$  = the minimum displacement of cycle  $i$ . For a symmetric loading history, the exponent is equal to 0.14 (i.e.,  $\Delta'_i$  is equal to  $\Delta_i$ ).

Similar indices for displacement-based fatigue of concrete structures have been developed. Banon et al. used a normalized cumulative rotation,  $NCR$  (Equation 2.23) where  $\theta_m$  = the maximum rotation and  $\theta_y$  = the member rotation at yield. (Note, the index range is not necessarily from 0 to 1.)

$$NCR = \frac{\sum |\theta_m - \theta_y|}{\theta_y} \quad (2.23)$$

Stephens and Yao [Stephens 1987] developed the displacement-based cumulative damage index shown in Equation 2.24 where  $\Delta\delta_f$  = the monotonic displacement capacity,  $\Delta\delta_p$  = the positive displacement demand,  $r$  = the ratio of the positive and negative displacements in a single displacement cycle, and  $b = 0.77$ .

$$DI = \sum \left( \frac{\Delta\delta_p}{\Delta\delta_f} \right)^{1-br} \quad (2.24)$$

Wang and Shah [Wang 1987] also developed a displacement-based cumulative damage index. An exponential expression, shown in Equations 2.25, was used to model strength and stiffness degradation due to cyclic effects. The rate of damage increases linearly with the cumulative normalized displacement,  $\beta$ . For a well-detailed member, the recommended values for the con-

stants  $s$  and  $c$  are 1.0 and 0.1, respectively.

$$DI = \frac{(\exp(s\beta) - 1)}{(\exp(s) - 1)} \quad (2.25)$$

$$\beta = c \sum_i \frac{d_{m,i}}{d_f} \quad (2.26)$$

Jeong and Iwan [Jeong 1988] proposed a fatigue formulation based on displacement ductility. For a given displacement ductility,  $\mu_i$ , the number of cycles to failure,  $N_f$ , is calculated using Equation 2.27. The constants  $c$  and  $s$  are empirical; values of 6 and 416 are recommended. The damage index was calculated using Miner's rule (Equation 2.28). Failure corresponds to a damage index,  $DI$ , of 1.

$$N_f = \frac{c}{\mu^s} \quad (2.27)$$

$$DI = \sum_i \left( \frac{n_i}{N(\mu_i)} \right) \quad (2.28)$$

Chung, Meyer, and Shinozuka [Chung 1989] concluded that a straight application of Miner's rule to assess damage is not supported by experiments. Therefore, they proposed a modified version. To develop the damage index, failure of a member subjected to cyclic loading was defined. It is common to define member failure to correspond with member strength loss. However, this definition may not be sufficient for a member that fails at a displacement level less than the maximum imposed displacement. For example, if a member is subjected to a drift of 1% following a drift of 3%, the resistance at the 1% drift level may be significantly less than the peak resistance. However, the member response may be stable. As an alternative, a failure envelope was defined. Chung et al. defined that failure occurred when the response curve intersected with the failure moment-curvature envelope defined by Equation 2.29 where  $M_f$  and  $\phi_f$  are the monotonic moment and curvature capacities. For a curvature of  $\phi_i$ , failure corresponds to a strength drop to the "failure" strength,  $M_{fi}$ .

$$M_{fi} = M_f \frac{2\Phi_i}{\Phi_i + 1} \quad (2.29)$$

$$\Phi_i = \frac{\phi_i}{\phi_f} \quad (2.30)$$

The damage index is based on a modified version of Miner's rule. The index is weighted for positive loading and negative loading (denoted with superscripts  $p$  and  $n$ , respectively),  $n$  is the number of cycles imposed at curvature  $\phi_i$ , and  $N_i$  is the number of cycles to cause failure at curvature  $\phi_i$ . The value of  $\Delta M_f$  is the strength reduction to the failure curvature, for example,  $\Delta M_f = 0.25M_f$ . The parameter  $\alpha_i$  is a damage modifier. The stiffness,  $k_{ij}$ , is the ratio of the flexural strength at cycle  $j$  and the curvature at cycle  $i$ .

$$DI = \sum_i \left( \alpha_i^p \frac{n_i^p}{N_i^p} + \alpha_i^n \frac{n_i^n}{N_i^n} \right) \quad (2.31)$$

$$N_i = \frac{M_i - M_{fi}}{\Delta M_i} \quad (2.32)$$

$$\Delta M_i = \left( \frac{\phi - \phi_y}{\phi_f - \phi_y} \right)^{1.5} \Delta M_f \quad (2.33)$$

$$\alpha_i = \frac{\frac{1}{n_i} \sum_{j=1}^{n_i} k_{ij} \phi_i + \phi_{i-1}}{N_i} \frac{1}{2\phi_i} \quad (2.34)$$

$$\frac{1}{N_i} \sum_{j=1}^{n_i} k_{ij}$$

$$k_{ij} = \frac{M_{ij}}{\phi_i} \quad (2.35)$$

### 2.3.3.3 Energy-Based Cumulative Damage Indices

The element or structure fatigue demand may be difficult to assess without knowledge of the ground motion; therefore, fatigue-based damage indices are difficult to use. With the availability of energy spectra, it is more common to use energy to estimate the influence of the cumulative demand on element damage.

Several energy-based damage indices have been proposed. A simple formulation, shown by Equation 2.36, normalizes the total energy demand,  $E_p$ , to the energy capacity of a column sub-

jected to monotonic loading,  $E_{mono}$ . The monotonic energy capacity may be approximated as  $E_{mono} \cong F_y \Delta_{mono}$ , where  $F_y$  = the yield force, and  $\Delta_{mono}$  = the monotonic displacement capacity.

$$DI = \frac{E_t}{F_y \Delta_{mono}} \quad (2.36)$$

Park and Ang [Park 1985] developed a combined damage index. Energy was used to characterize the cyclic effects; displacement was used to characterize the noncumulative effects. The cumulative term, based on energy, is the product of Equation 2.36 and a strength deterioration parameter,  $\beta$ .

$$DI = \frac{\Delta}{\Delta_{mono}} + \frac{\beta E_t}{F_y \Delta_{mono}} \quad (2.37)$$

Equations have been proposed to assess the strength deterioration factor,  $\beta$ . Using a regression analysis of 142 experimental results, Park and Ang proposed Equation 2.38 to calculate  $\beta$  as a function of the aspect ratio,  $L/D$ , axial load ratio,  $P/(A_g f_c')$ , longitudinal reinforcement ratio,  $\rho_l$ , and spiral reinforcement ratio,  $\rho_s$ .

$$\beta = \left( -0.447 + 0.73 \frac{L}{D} + 0.24 \frac{P}{A_g f_c'} + 0.314 \rho_l \right) 0.7 \rho_s \quad (2.38)$$

Others [e.g., Kunnath 1992, Stone 1994] have suggested alternate expressions for  $\beta$ .

Williams and Sexsmith noted difficulties in using the Park-Ang damage index, including the difficulty of estimating the monotonic displacement capacity and the difficulty of assessing strength deterioration factor  $\beta$ . Chai and Romstad [Chai 1995] observed that the Park-Ang index exceeded one for monotonic failure. To correct this, the plastic strain energy associated with monotonic loading was removed from the numerator of the cumulative term of Equation 2.37. Kunnath et al. [Kunnath 1992] also revised the Park-Ang index by removing a recoverable deformation,  $\delta_y$ , from the numerator and denominator of the noncumulative term.

#### 2.3.3.4 Evaluation of Damage Indices

There are discrepancies between failure predicted by damage models and failure measured using experimental methods. Scribner and Hwang [Scribner 1982] assessed the influence of high shear

ratios and displacement history on the response of cantilever beams. The authors found that the measured energy dissipation values did not correlate with normalized energy-based damage methods. Nishigaki and Mizuhata [Nishigaki 1983] concluded that results using linear, cumulative damage indices to predict failure of reinforced concrete columns do not correspond to the measured results.

Several researchers have evaluated the performance of the proposed indices using experimental results. Kunnath et al. [Kunnath 1997] used experimental results of scaled bridge columns subjected to different displacement histories to evaluate the modified Coffin-Manson fatigue-based damage index and the Park-Ang energy-based damage index. Although the fatigue-based index predicted damage for columns subjected to constant-amplitude displacements, it did not predict failure for columns subjected to random displacement histories. The Park-Ang index did not correctly predict failure.

Williams, Villemure, and Sexsmith [Williams 1997] evaluated eight damage indices including those developed by [Stephens 1987, Wang 1987, Jeong 1988, Park 1985] as well as noncumulative indices based on ductility and stiffness. The response of beams with high shear stress demand levels that were tested by Adebar et al. were used. As shown in Figure 2.13, there is a great deal of scatter for the results of any particular damage index.

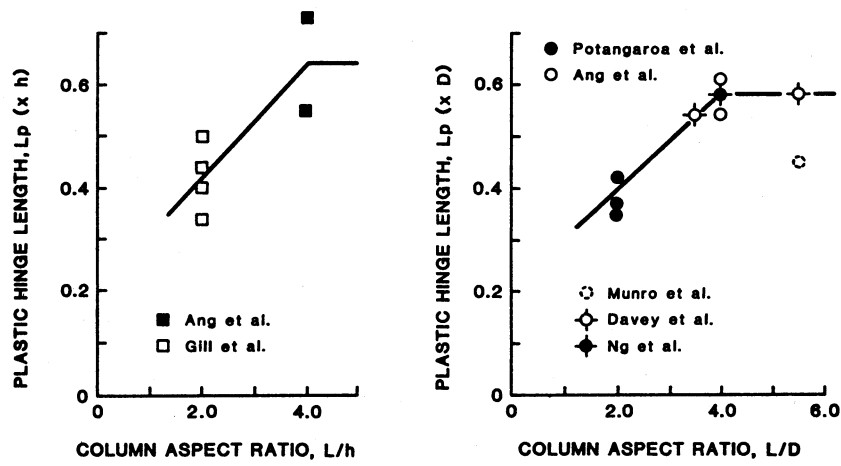


Figure 2.1: Variation of Plastic Hinge Length with Column Aspect Ratio [Sakai 1989]

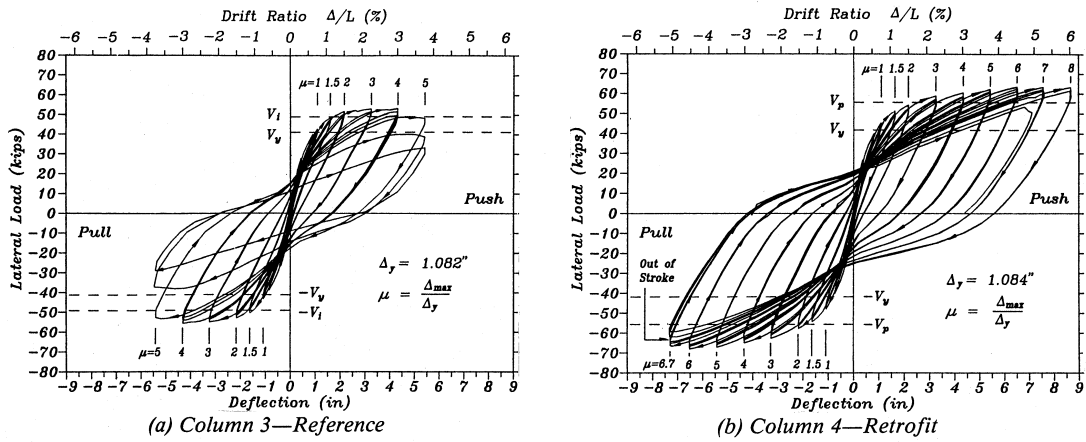
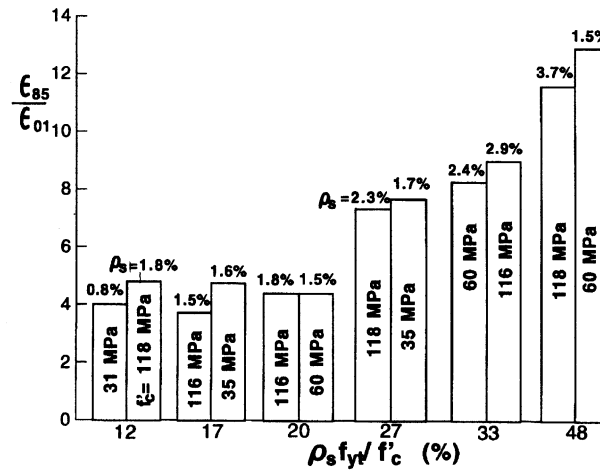


Figure 2.2: Force-Displacement Response of a Conventional Reinforced Concrete Column and a Column with a Steel Jacket [Chai 1991]



(a)

Figure 2.3: Axial Strain Capacity vs. Spiral Reinforcement Ratio [Saaticioglu 1994]

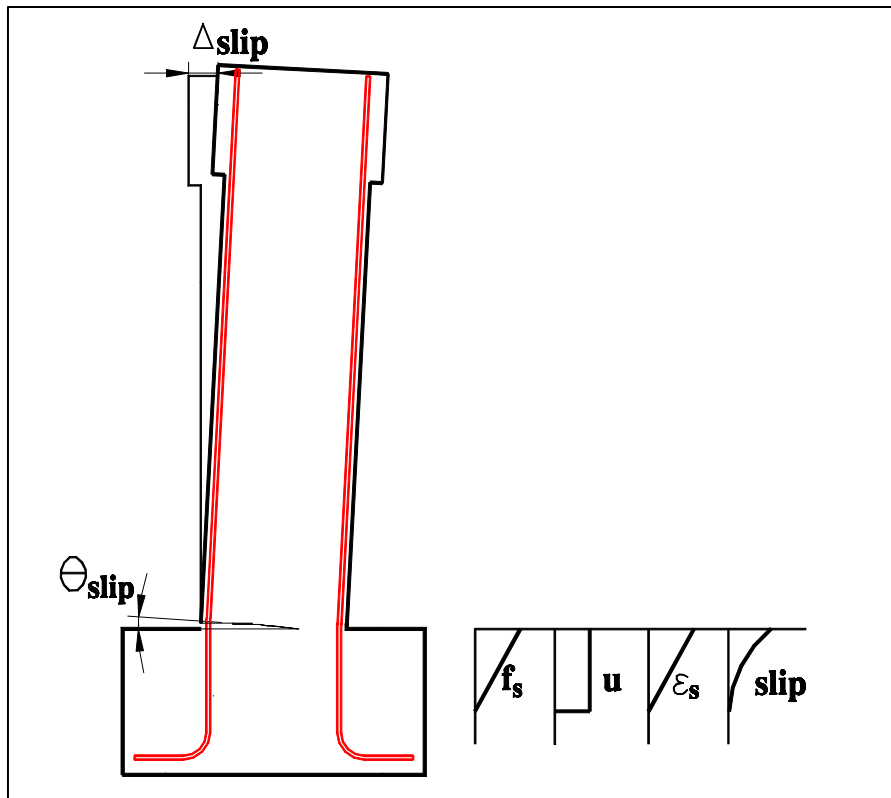


Figure 2.4: Column Displacement Resulting from Axial Deformation of the Embedded Portion of the Longitudinal Reinforcement

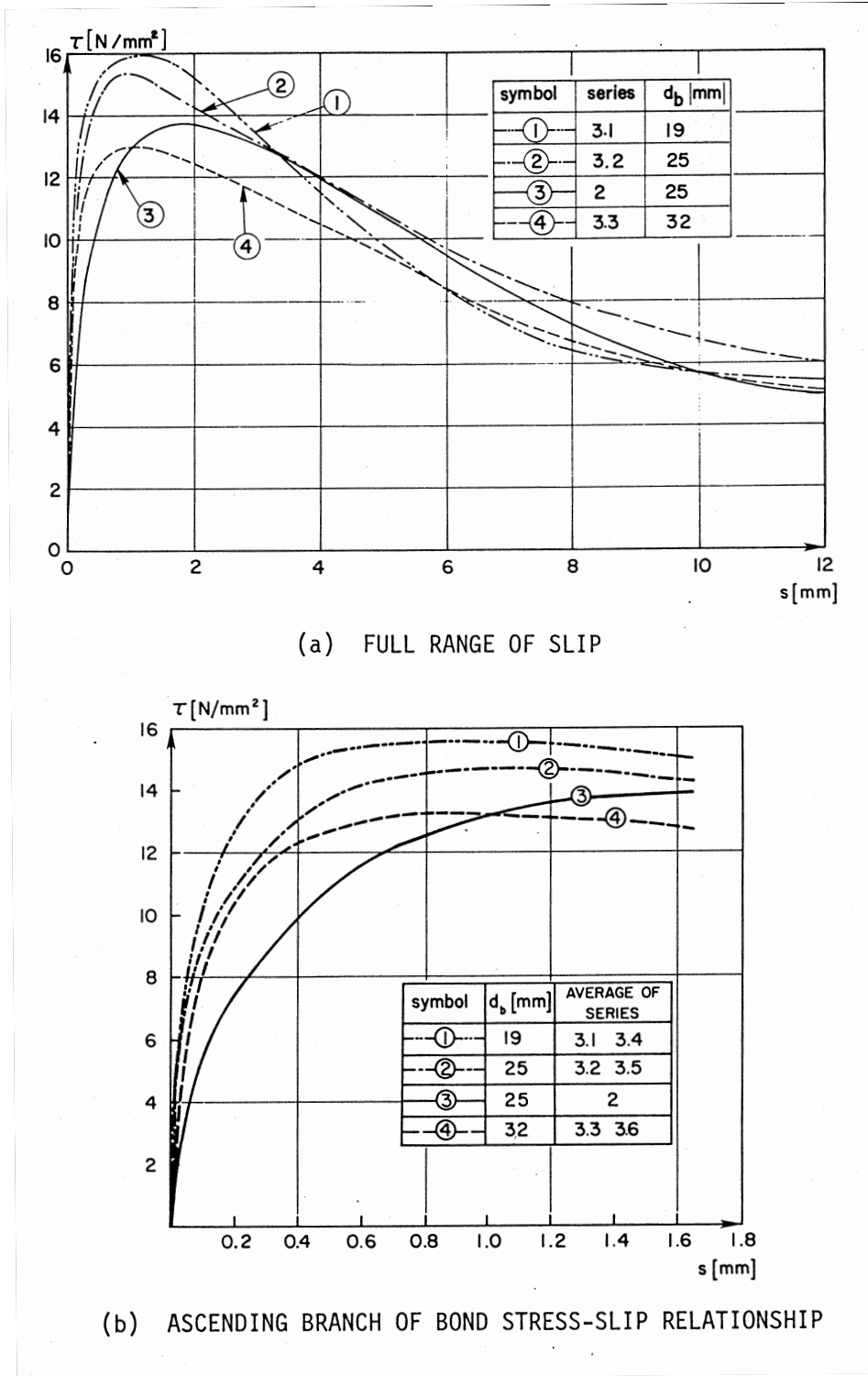
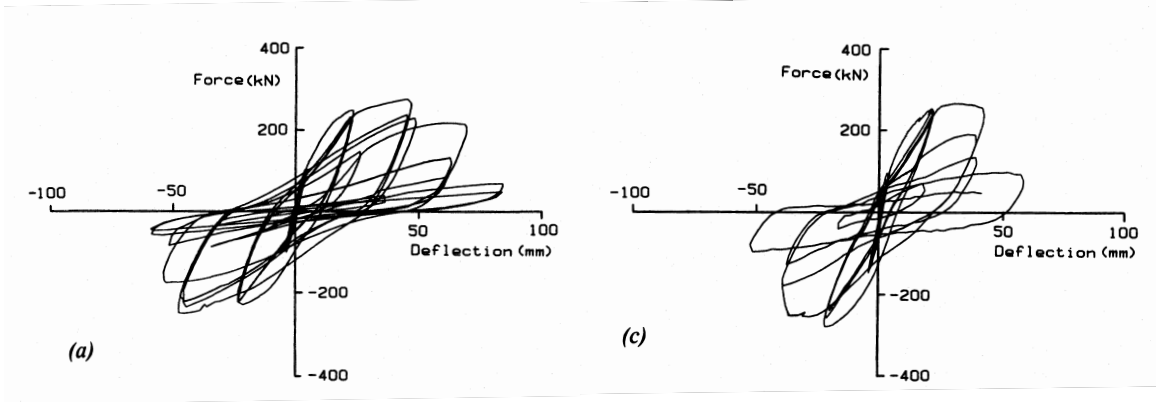


Figure 2.5: Effect of Bar Diameter on Bond-Slip Response [Eligehausen 1993]



(a)  $P/(A_g f'_c) = 0.0$

(b)  $P/(A_g f'_c) = 0.1$

Figure 2.6: Influence of Axial Load on Column Response [Saatcioglu 1989]

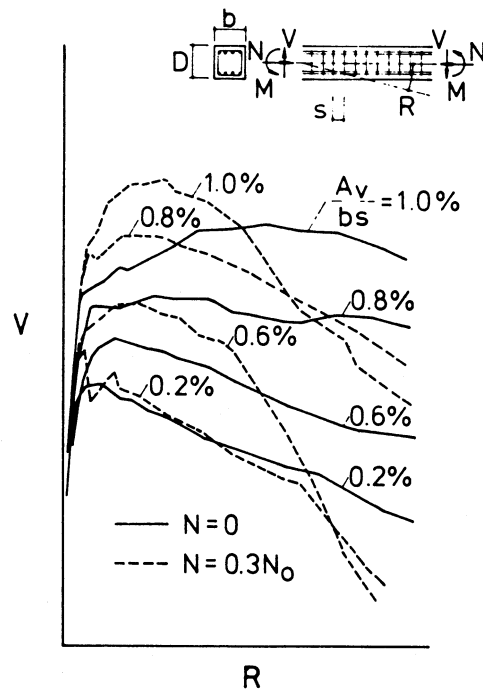


Figure 2.7: Force-Displacement Response of Members with Various Axial Load Ratios and Transverse Reinforcement Ratios [Wakabayashi 1984]

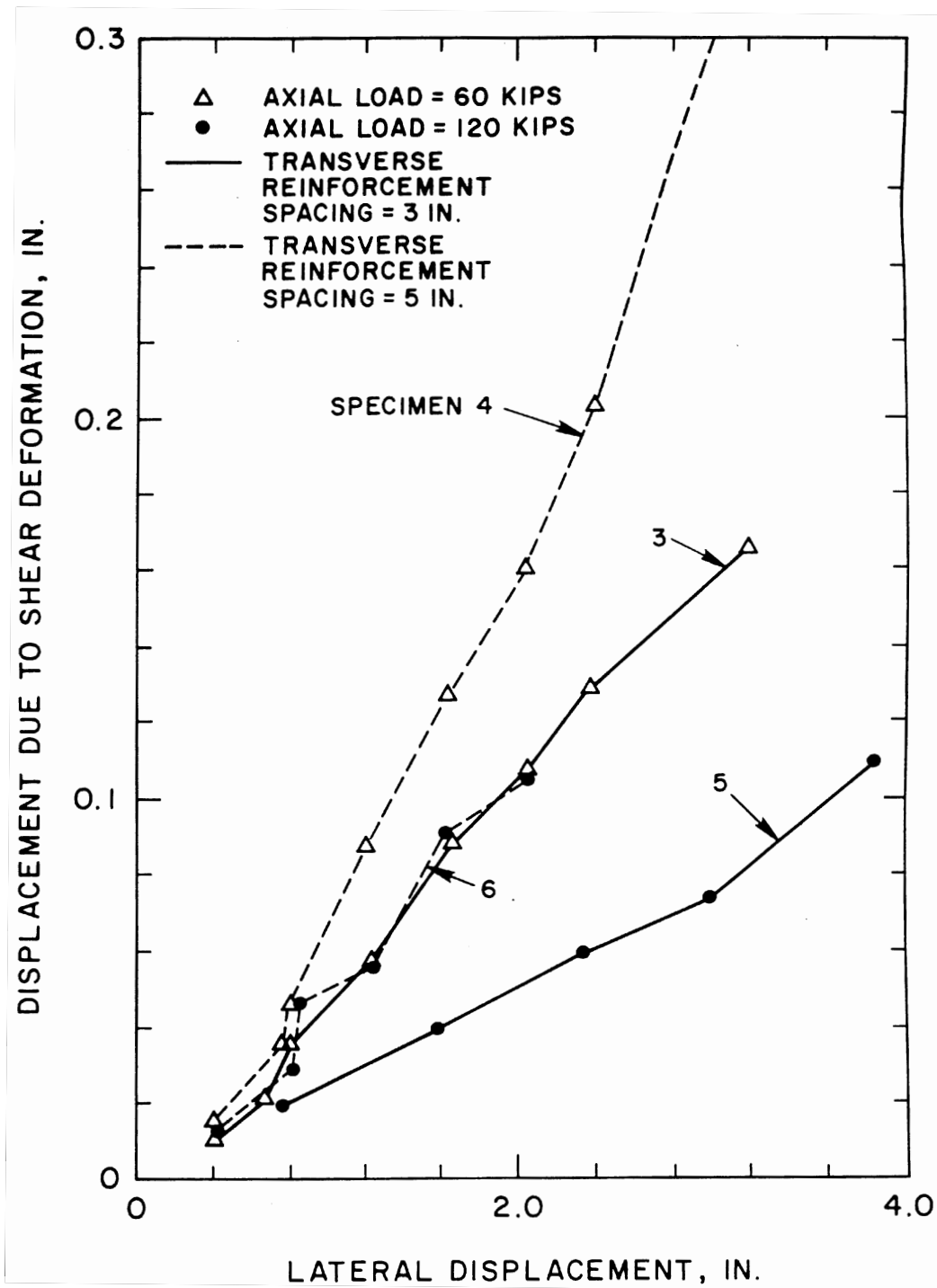


Figure 2.8: Variation of Shearing Deformation with Transverse Reinforcement Ratio and Axial Load Ratio [Atalay 1975]

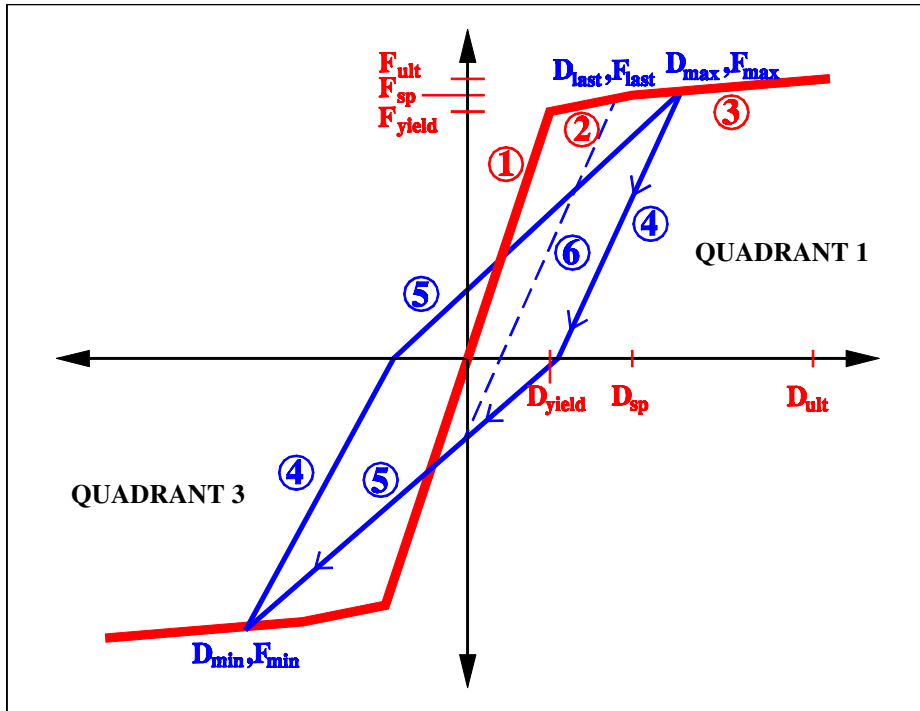


Figure 2.9: Example Hysteresis Model

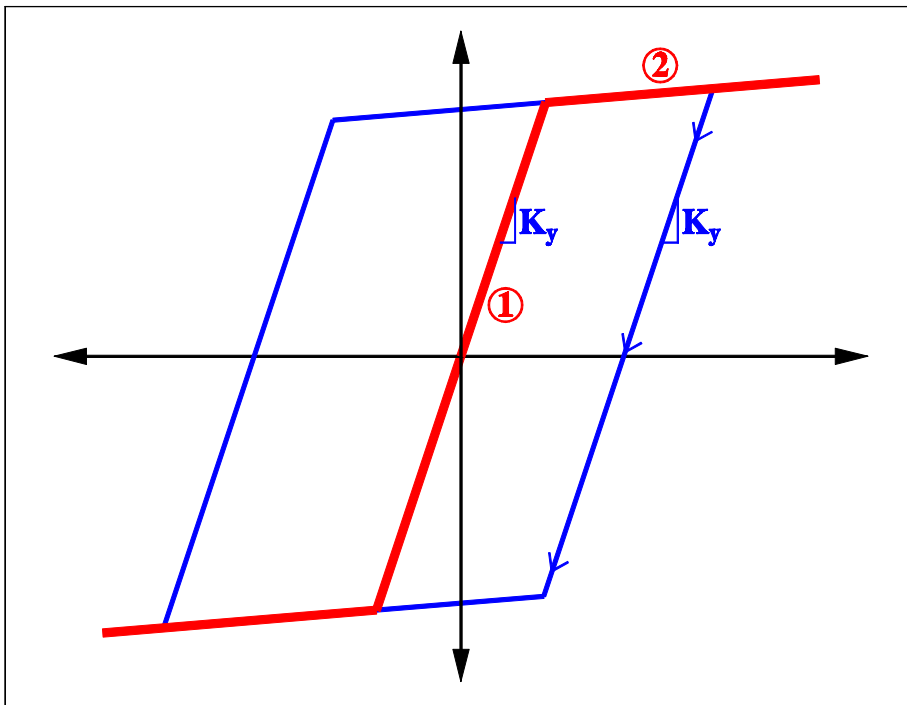


Figure 2.10: Bilinear Hysteresis Model

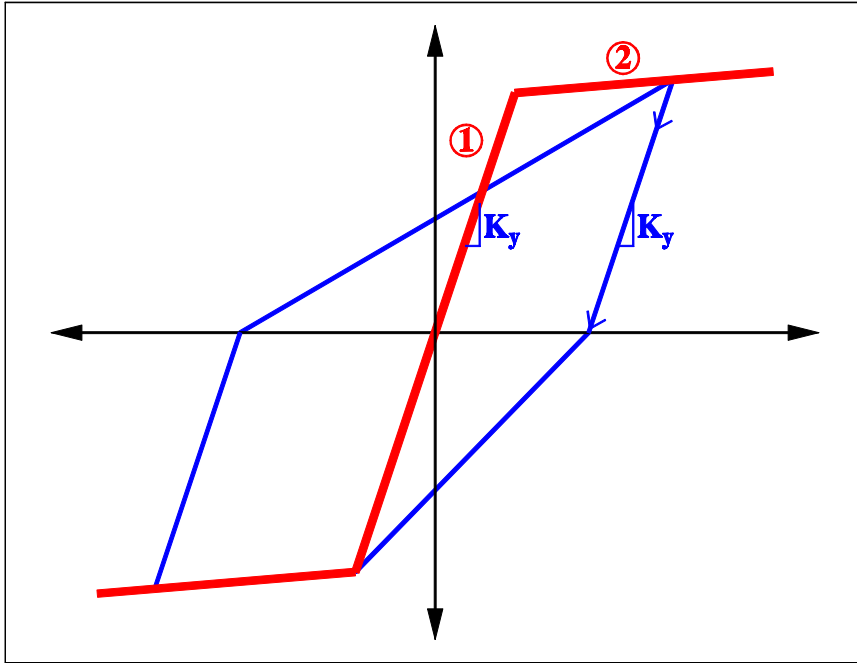


Figure 2.11: Clough Hysteresis Model

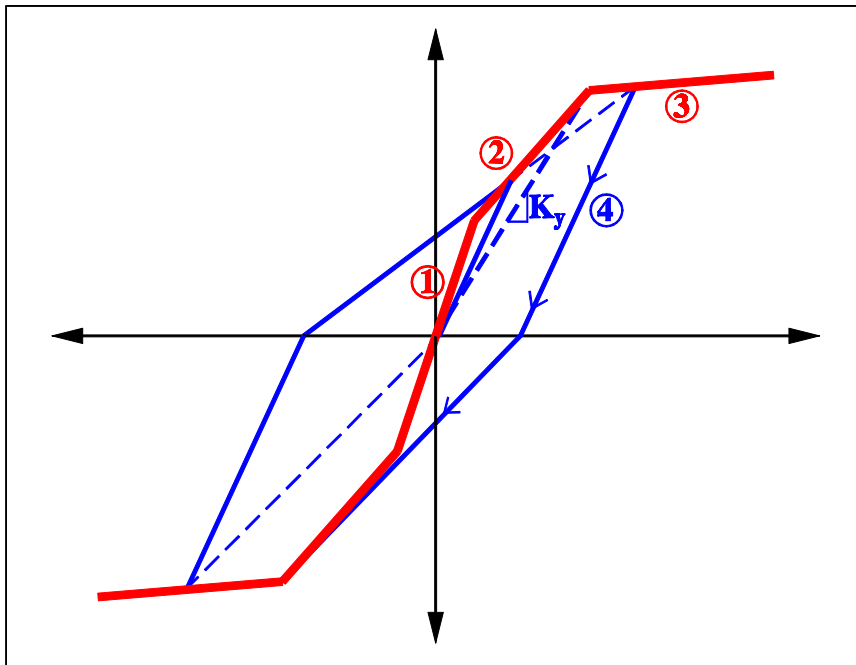
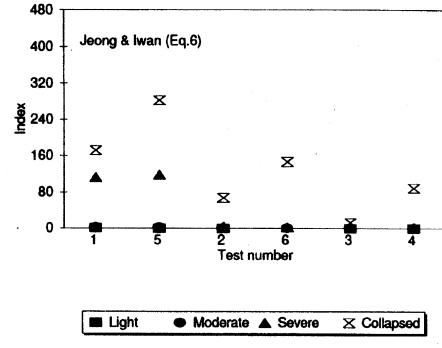
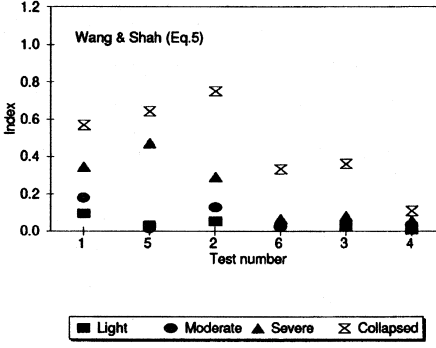
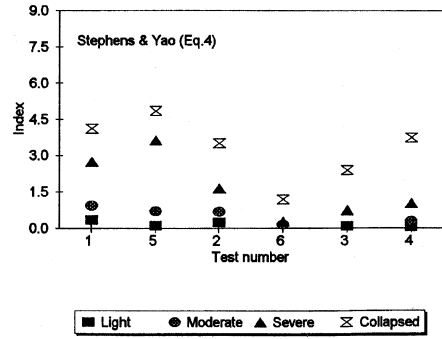
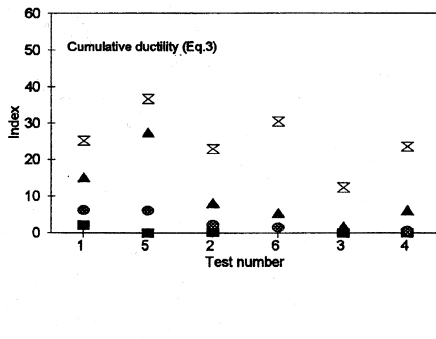
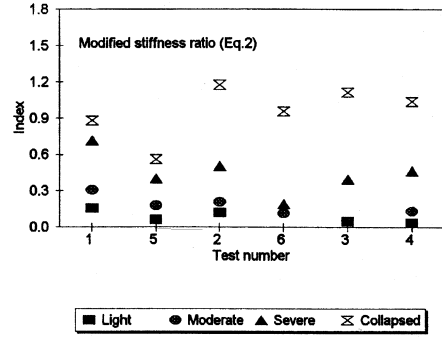
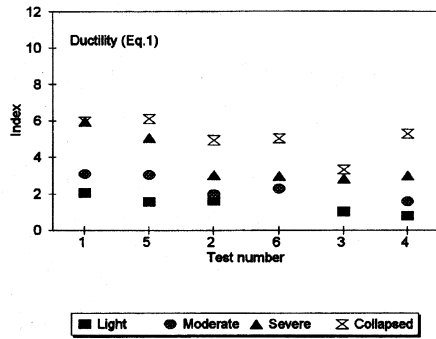


Figure 2.12: Takeda Hysteresis Model



Values of damage indices corresponding to light, moderate, severe, and collapse damage states

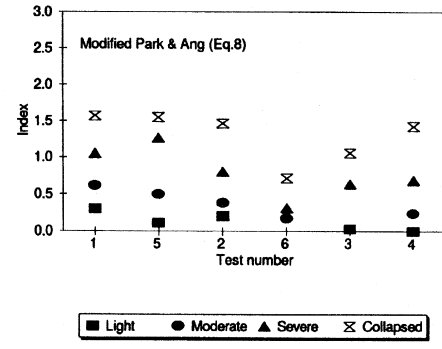


Figure 2.13: Evaluation of Various Damage Indices [Williams 1997]

## 3 Experimental Program and Results

### 3.1 RESEARCH IMPETUS

Many parameters can influence the inelastic cyclic behavior of a cantilever bridge column. Of those described in the previous chapter, the spiral reinforcement ratio, the column shear demand, the axial load ratio, the column aspect ratio, and the quantity of longitudinal reinforcement are the most significant. Modern code requirements restrict the ranges of these five parameters. As a result there are typical ranges of each parameter found in modern construction. For example, codes specify a minimum spiral reinforcement ratio. In capacity design, column shear demands are influenced primarily by aspect ratio and longitudinal reinforcement ratio; most seismic codes limit shear demands to  $10\sqrt{f'_c}\psi A_g$ . Axial load levels due to dead load are typically less than  $0.2f'_c A_g$ , where  $f'_c$  = the compressive strength of the concrete and  $A_g$  = the gross cross-sectional area. Column aspect ratios depend on bridge geometry and column diameter (typically sized to satisfy maximum axial load ratios) and typically vary between 1 and 10. On average, longitudinal reinforcement quantities fall between 2% and 4% of the gross cross-sectional area.

A study by Taylor et al. summarized the parameters and response histories of 92 columns tested as part of 15 research programs [Taylor 1993]. Evaluation of the variation in the aspect ratio, axial load ratio, and longitudinal reinforcement ratio indicated that a wide range of the parameters had been studied. The research gaps are emphasized in Figures 3.1 and 3.2. However, as is evident in Figure 3.2, slender columns, i.e., columns with aspect ratios of 4 or greater, have received limited attention. Results portrayed in Figure 3.2 indicate that the experimental studies on slender columns used longitudinal reinforcement ratios between 2% and 2.5%. Few of the columns had reinforcement ratios larger than this; none fell below. Although, axial load ratios varied between 0 and 0.7 of the gross cross-sectional capacity, the axial loads applied to the slender columns were less than  $0.1f'_c A_g$ , which is typical for bridge column design. The review of previous research efforts demonstrated that the influence of column aspect ratio and longitudinal reinforcement ratio on column response had not been investigated thoroughly.

An experimental research program was designed to investigate the influence of these parameters on response and failure of modern bridge columns. Using the research review as its basis,

the following points were emphasized in the development of the experimental investigation.

1. To study the effect of aspect ratio and longitudinal reinforcement ratio
2. To isolate the influence of each parameter, only one study parameter was varied for each test series.
3. To fully test the columns to failure, the actuator stroke was designed to be sufficient to ensure that each column reached its displacement capacity.
4. To permit adequate modeling of brittle mechanisms such as shear and bond, the specimens were constructed at one-third of full scale.
5. To model a column fixed into a column-footing joint, the system tested a cantilever column fixed into an anchor block. Both the joint and column regions were designed using current seismic design provisions. To the extent possible, realistic bond conditions in the joint were replicated; the embedded bar was loaded at one end only and prestressing was not permitted in the joint region.
6. To compare results with previous research, a “standard” displacement history was used to facilitate this comparison.

The following sections summarize the testing procedure and experimental results. Data provided included description of visual observations including photographs of each column at various stages of testing, salient response quantities measured at the first peak displacement, and graphs of the force-displacement response history and the relative displacement components.

## **3.2 TEST PROGRAM**

The test program was designed to model the behavior of a full-scale reinforced concrete bridge column assembly, measure local and global response quantities, and facilitate comparison with previous research studies. The following sections summarize the aspects of the research program including specimen details, loading, and instrumentation. Further details are found in *Seismic Performance of Well-Confined Concrete Bridge Columns* (Lehman 1998).

### **3.2.1 Test Matrix**

The experimental research study was developed to establish the effects of column aspect ratio and longitudinal reinforcement ratio on seismic behavior. Two test series were developed to individually study each focus parameter. The test series are shown in Figure 3.3; the two study parameters

are identified for each column. The column designations are indicated; each designation has three or four numerals. The latter two numerals denote the percentage of longitudinal steel; the first one or two numerals indicate the column aspect ratio (e.g., for column designation 815, the numeral 8 indicates that the column has an aspect ratio of 8 and 15 indicates that the column has a longitudinal reinforcing ratio of 1.5%).

The first test series, which will be denoted Test Series I for the remainder of the report, is depicted in the top row of the test matrix. Test series I consisted of three columns that varied in longitudinal reinforcement ratio; the aspect ratio of each column was 4 to 1. The center column, representing an “average” bridge column, was reinforced with 1.5% steel longitudinally and was denoted Column 415. Column 407, shown to the left of Column 415, had half the amount of longitudinal steel (0.75%); Column 430, shown to the right of Column 415, had twice the amount of longitudinal steel (3.0%) and was detailed with bundled bars. The three specimens of the second test series, which will be denoted Test Series II for the remainder of the report, are depicted in the center column of the matrix. The aspect ratios of the three specimens of Test Series II varied between 4 and 10; the columns were reinforced with 1.5% longitudinal steel. Therefore, Column 815 had an aspect ratio of 8 and Column 1015 had an aspect ratio of 10. The main test parameters for each specimen are summarized in Table 3.1.

### **3.2.2 Design Requirements**

Reinforced concrete bridge systems subjected to seismic loading are expected to sustain inelastic action; typical plastic design requires the formation of flexural plastic hinges at the column ends. To the extent possible, brittle response mechanisms, including inelastic response in shear and bond, should be repressed and the joint region should remain essentially elastic. Design guidelines developed by the California Department of Transportation [Caltrans 1991] are intended to ensure this behavior. Recent recommendations to improve the Caltrans specifications are provided in a report by the Applied Technology Council entitled *ATC 32 Improved Seismic Design Criteria for California Bridges: Provisional Recommendations* [ATC 1996]. The report provides a critical review of the California Bridge Design Specifications [Caltrans 1986] based on previous research efforts.

The five columns were designed to meet the bridge design specification requirements. For each specimen of the test program, the column and joint regions were designed in accordance with the Caltrans Bridge Design Specifications [Caltrans 1991]. In addition, the ATC 32 recom-

mentations were reviewed, and, in some cases, all or part of the provisions were adopted. For the column, shear demand levels varied according to column aspect ratio and longitudinal reinforcement ratio. Confinement requirements, intended to provide adequate curvature ductility, controlled the spiral design; the resulting spiral ratio (ratio of the volume of spiral to the volume of concrete within a single spiral spacing) for all columns was 0.7%.

The joint region was designed to meet or surpass the Caltrans standard practice [Caltrans Engineers 1996] and to limit inelastic response, although inelastic strain in the embedded longitudinal reinforcement was expected. To ensure the full development of the longitudinal reinforcement, the bars were embedded approximately 34 bar diameters into the joint; the embedment length was approximately 25% larger than that required by the Caltrans Specifications. Joint shear stress levels were assessed according to provisions in ACI 318-95 [ACI 1995]. For the five specimens tested, joint shear stress demands were expected to differ based on longitudinal reinforcement ratio. Analytical results indicated that the maximum joint shear stresses were less than  $12\sqrt{f'_c}$  (psi).

The response of the specimen footing was not expected to model an actual footing in the field. Since the specimen was prestressed to the laboratory floor, the footing boundary conditions in the laboratory were much different than those found in the field. The design of the footing in the test specimen did not follow standard design. The footing was designed to remain elastic under the demand that results from full inelastic action of the column. The maximum allowable tensile strain demands in the main longitudinal reinforcement of the footing were limited to 75% of the yield strain. Placement of ties in the footing followed standard detailing procedures.

### **3.2.3 Geometry and Reinforcement**

The experimental specimens were constructed at one-third of full scale. Column and joint details of the test specimens are shown in Figure 3.4.

The column diameter was selected to be 2 feet to model a 6-foot diameter prototype column. The three columns of Test Series I had lengths of 8 feet each. The remaining columns of Test Series II, Columns 815 and 1015, had column lengths of 16 feet and 20 feet, respectively.

The columns were reinforced longitudinally with No. 5 bars. The longitudinal reinforcement was spaced evenly around the column circumference. The longitudinal reinforcement was embedded into the joint to a depth of 21.5 inches, approximately equivalent to 34 bar diameters. The bars were terminated with a 90-degree hook that extended 12.5 bar diameters parallel to the bot-

tom of the footing.

The column spiral reinforcement ratio was 0.7%. The spiral was 1/4 inches in diameter smooth wire and spaced at 1-1/4-inches. The spiral reinforcement was continuous throughout the column height and joint depth.

Footing ties were sized and spaced to model the size and spacing of ties in full-scale footing applications. Footing ties were 1/4 inch in diameter spaced at 4 inches on center.

### **3.2.4 Material Properties**

The material properties specification met the requirements in the Caltrans Standard Specifications [Caltrans 1992]. According to the specification, column longitudinal reinforcement must conform to the ASTM designations: A 615, Grade 60 or A 706; the longitudinal steel met the ASTM designation: A 706. The available 1/4-inch diameter spiral reinforcement did not meet either ASTM designation; reinforcing wire meeting the ASTM designation A 82 was used, which is permitted for pile applications.

The concrete mix was designed to model a full-scale mix. To match the parameters of the prototype without compromising its workability, the aggregate size was scaled from 1-inch maximum (full-scale mix) to 3/8-inch maximum (scaled mix). The concrete mix was designed to reproduce the specified compressive strength, fracture energy, and modulus of elasticity.

Table 3.2 shows the specified, expected and actual strengths of the longitudinal steel, spiral steel, and the concrete. The values shown in the table were determined using the recommendations in the ATC 32 report. The specified strength is the minimum permissible strength. The expected strength is used in capacity design to predict the upper-bound demand from inelastic action of adjacent elements. The actual strength shown in Table 3.2 is the strength measured from the actual materials used in the test specimens. The yield strength for the high-strength A 82 wire used for the spiral was defined according to the ASTM specification as the strength corresponding to a strain of 0.005. Details of the testing procedures and the measured stress-strain response for each material can be found in *Seismic Performance of Well-Confined Concrete Bridge Columns* (Lehman 1998).

### **3.2.5 Loading**

Axial and lateral loads were applied to the top of the column. Figure 3.5 depicts the experimental configuration. The applied axial load of 147 kips is approximately  $0.1f_c'A_g$ , where  $f_c'$  = the specified concrete compressive strength and is approximately  $0.07f_c'A_g$ , where  $f_c'$  = the actual con-

crete compressive strength. The axial load ratio chosen corresponded to average axial load ratios found in single-column bent bridge construction. The axial load was applied through a spreader beam using a post-tensioning rods placed on either side of the column.

The lateral load was applied using a servo-controlled hydraulic actuator that was attached to the top of the column. The imposed displacement history included three cycles at each displacement level. The primary displacement levels were monotonically increased to provide an indication of damage accumulation. The imposed displacement pattern of three cycles at each displacement level provides an indication of degradation characteristics. The magnitude of the subsequent displacement level was determined by multiplying the current level by a factor ranging from 1.33 to 2. This smaller cycle was equal to one-third of that in the previous cycle. Both pre-yield and post-yield displacement levels were imposed. The pre-yield displacement levels are defined to include a displacement level prior to cracking, two levels between cracking and yielding, and a level approximately corresponding to the first yield of the longitudinal reinforcement. The post-yield displacement levels are defined to include all subsequent cycles. For the post-yield displacement levels, a small displacement cycle was imposed following the three main cycles. The displacement history is shown in Figure 3.7. Imposed displacement histories were determined for each column according to the column aspect ratio from nominally identical displacement ductility histories. As a result, the three columns of Test Series I were subjected to the same displacement history.

### **3.3 OVERVIEW OF EXPERIMENTAL OBSERVATIONS**

Observations during testing of the five columns suggest that the sequence of damage in the five columns was similar. This section provides a general description of the progression of damage listing each category of damage chronologically. A brief description of the visual indications are provided. Specific occurrences of each stage of damage are provided for each column in subsequent sections.

1. **Cracking** Typically, cracking was not detected during the initial displacement level but was initiated during the subsequent cycle. The crack spacing decreased at larger displacement demands. The crack spacing in the first 12 inches of the column height tended to stabilize following the yield displacement level.
2. **First yield of longitudinal steel** Yielding of the extreme longitudinal reinforcing bar

was noticeable in the force-displacement response or in the physical response. Yielding was detected using strain gauges that had been placed on the longitudinal steel prior to construction and that were monitored during testing.

3. **Spalling** Typically, initial spalling occurred above the column-footing interface. With continued loading, the spalling region increased in elevation, around the circumference, and into the column core.
4. **Spirals and longitudinal steel exposed** Complete loss of the concrete cover exposed the spirals and longitudinal steel.
5. **Visual extension of spiral and longitudinal bar buckling** Subsequent loading resulted in a permanent displacement of the lower column spirals. Longitudinal bar buckling was visually evident. In all cases, the longitudinal bar buckled over more than one spiral spacing.
6. **Spiral fracture** The spirals located within the buckled length continued to extend as the bar continued to buckle until the spiral fractured. The lateral stiffness decreased as a result of spiral fracture which permitted the other longitudinal bars to buckle over a longer length.
7. **Longitudinal bar fracture** Fracture of the longitudinal bars occurred after bar buckling. Typically, fracture of one or more longitudinal bars resulted in strength loss significant enough to cause column failure.

The following sections summarize the response of each of the five columns. In addition to written descriptions, photographs, graphs, and a summary table of salient response quantities are included for each column.

Displacement ductility values were calculated using the effective yield displacement. The effective yield displacement was determined using the method in Priestley 1996. The measured displacement corresponding to first yield of the longitudinal steel,  $\Delta_y$ , was determined using the strain measured by the Level 4 strain gauge on the main south longitudinal bar (see *Seismic Performance of Well-Confined Concrete Bridge Columns* (Lehman 1998) for details of the instrumentation scheme). The flexural strength corresponding to first yield of the longitudinal steel,  $M_y$ , and the flexural strength corresponding to a compressive strain demand of 0.004 in./in. in the extreme fiber,  $M_n$ , were calculated using the method described in Chapter 4. The effective yield displacement,  $\Delta_y'$ , was determined by magnifying the yield displacement by the moment ratio, as shown in Equation 3.1.

$$\Delta_y' = \frac{M_x}{M_y} \Delta_y \quad (3.1)$$

Sections 3.4 through 3.8 describe the response of each column and include the following data:

1. Observations recorded during testing including crack spacings, crack widths, height and width of the spalled regions, longitudinal bar buckling, spiral fracture, and longitudinal bar fracture.
2. Photographs showing the marked crack pattern, spalled region, and final damage state.
3. Column force-displacement response
4. Relative contribution of the bending, slip, and shear components to the total displacement measured by the external displacement gauges. Since the slip contribution was monitored using external vertical displacement gauges that measured vertical extension from the interface to a 6-inch elevation, the slip displacement includes the extension in the column within this region (strain gauge measurements were not reliable to use to compute the difference).
5. Specific peak measurements corresponding to the first cycle to the north are tabulated. Measurements provided include displacement ductility and numerical quantification of individual component contributions. Average compression strain, measurements resulting from vertical external displacement gauges placed from the interface to 6 inches interpreted at the column face, are provided. Tensile strain demands measured by strain gauges placed on the longitudinal steel and spiral approximately 6 inches above the interface are indicated. The fixed-end rotation (measured over 6 inches from the interface) and average curvature (measured from an elevation of 6 to an elevation of 12 inches above the interface) are also indicated. In addition, damage observed during testing is quantified. Crack widths at the column-footing interface and 12 inches above the interface are indicated. Height of the spalled region is also given.

Individual response quantities, including average curvature, shearing deformations, and longitudinal strain distribution, are presented in *Seismic Performance of Well-Confined Concrete Bridge Columns* (Lehman 1998).

### 3.4 COLUMN 407

Column 407 was reinforced with 0.75% longitudinal steel and had an aspect ratio of 4. Column 407 was the first column tested. An effective yield displacement of 0.8 inches was calculated using Equation 3.1. Table 3.4 summarizes response quantities for the column measured during the latter displacement levels.

#### 3.4.1 Progression of Observed Damage

Initial cracking was observed during the 0.3-inch displacement cycle. Horizontal cracks were observed to a height of 45 inches (approximately half the column height). The crack spacing was approximately 12 inches on the south face and 6-12 inches on the north face (Figure 3.8). During the cycle to 0.75 and 1.0 inches, new crack formation decreased the minimum crack spacing to 4 inches. In elevation, cracks were observed to approximately 65 inches. The cracks were primarily oriented horizontally.

Concrete spalling was observed during the displacement cycle to 1.5 inches. Initial spalling occurred approximately 4.5 inches above the interface, and the width of the spalled region was less than 1 inch. The spalled region extended during the 2-inch and the 3-inch cycles, reaching an elevation of 10 inches on the north face and 5 inches on the south face (Figure 3.9). With increased cycling, the spalled region extended radially, up to 7 inches on each side of the centerline. The force-displacement response (Figure 3.14) does not indicate strength loss at this cycle.

Extensive damage resulting in column failure occurred during the displacement cycles to 5 inches (corresponding displacement ductility of 6). During the first cycle to 5 inches (Figure 3.11), the spalled region extended in height, to 10 inches, and into the column core, exposing the main north and south longitudinal bar (during loading to north and south, respectively). Bar buckling was observed while loading to the south. The subsequent cycles to the north and south resulted in buckling of the center bars over approximately three tie spacings. Increased lateral displacement of the buckled bar occurred with increased displacement demand. At 0.75 inches south (moving to 5.0 inches south), the displacement demand imposed on the spiral by the buckled bar resulted in fracture of spirals located within the buckled length, approximately 1.25 and 2.5 inches above the interface (Figure 3.10). Similar behavior was noted on the north face during the third cycle to 5 inches north. Fracture of the spirals on the north face resulted in loss of transverse stiffness, permitting bar buckling without subsequent spiral fracture. The central longitudinal bar on

the south face fractured during the loading to 5 inches north at a displacement demand of 4 inches. Fracture of the center bar resulted in a loss of 5 kips of the lateral load capacity. The final cycle to 5-inches south resulted in additional bar buckling, spiral fracture and finally fracture of the central north longitudinal bar (at 4.3 inches south) (Figure 3.12). Figure 3.13 indicates the final damage state.

### **3.4.2 Measured Response**

Figure 3.14 presents the force-displacement response of Column 407. The response was stable until the 5-inch displacement cycle approximately corresponding to a ductility of 6 was reached, as the experimental observations indicate. (Stable response is indicated by a strength loss of less than 10% when comparing second cycle response to the first. The difference in strength for the second and third cycles is negligible.) The hysteretic behavior is pinched in comparison with an elastic-plastic response.

As indicated in Figure 3.15, the column response was dominated by slip and bending. Measurement of individual components was done with a maximum error of approximately 10%. During the initial displacement levels, slip accounted for up to 40% of the displacement. Slip contributed up to 50% of the total displacement during the latter cycles. The shearing deformation accounted for less than 1% of the overall response. Table 3.4 indicates some quantities measured during testing.

## **3.5 COLUMN 415**

Column 415 was reinforced with 1.5% longitudinal steel and had an aspect ratio of 4. Column 415 was the second column tested. An effective yield displacement of 0.92 inches was determined using Equation 3.1. Table 3.5 provides a summary of measured response quantities.

### **3.5.1 Observed Response**

Initial cracking was observed during the cycle to 0.10 inches. Cracking continued during the cycles to 0.30 inches, where the average spacing in lower portion of the column of 4 inches, and the cycles to 0.75 inches, where the average crack spacing in the lower portion of the column decreased to 2.5 inches. Horizontal cracks were observed to a height of 55 inches, just over half the column height (Figure 3.16).

Concrete spalling commenced during the cycle to 1.5 inches (displacement ductility of

approximately 1.5). The spalled region was less than 1 inch in width and was located approximately 4 inches above the interface. During the 2-inch displacement cycles, the spalled region extended vertically 6 inches and 5 inches in circumference (2.5 inches either side of the centerline). As was typical during the early stages of spalling, additional damage was not observed during the latter two displacement cycles. Cycling to ductility demand of 3 increased the height of the spalled region to 10 inches on the north face and to 7 inches in circumference. Examination of the force-displacement response (Figure 3.19) does not show signs of strength loss at this cycle.

During the first cycle to 5 inches north, the targets used to position the bottom instruments debonded, indicating bulging of the anchor block concrete. The spalled region on the north face increased in elevation to 12 inches and radially to 16 inches. Continuing to load in the south direction resulted in additional spalling. At completion of the first cycle, the lower three spirals (to 4 inches in elevation) on the south face and lower five spirals on the north face (to 6.25 inches in elevation) were exposed. At this displacement level, additional damage was observed in the footing. For example, loading to the north, the concrete 3 inches off the column face was observed to lift up one quarter of an inch. Similar behavior was observed during the loading to 5 inches south. Figure 3.17 shows the spalled region.

Observation of the force-ductility response (Figure 3.19) indicates that the column was able to sustain its capacity at the 5-inch displacement level during the second and third cycles. (Data accidentally were not recorded for the first quarter cycle to 5 inches north.) However, consideration of the “fourth” cycle to 5 inches north, that is, a displacement demand of 5 inches during first displacement cycle to 7 inches north, graphically reveals column damage. Five percent of the lateral load capacity was lost from the second cycle to the fourth. The observed damage reveals the cause. The center bar on the north face and the adjacent west bar buckled over a 3.5 inch length located approximately 1 inch over the interface. At 4.6 inches (while loading to 7 inches north) the two spirals, located 1.25 and 2.5 inches above the column/block interface, fractured. Again, the spiral fracture was observed to result from bar buckling (fracture points were located within the buckled length of the longitudinal bar). A third bar, the eastern adjacent one, buckled and spiral fracture, at an elevation of 3.75 inches, resulted at a displacement of 6.2 inches. Severe damage to the concrete core was measured 1.5 inches from the spiral (i.e., 2.25 inches from the column face).

Loading to 7 inches south resulted in a similar pattern of damage. The center three bars buckled. In this case the bars buckled over four spiral spacings. The additional buckled length

resulted from the loss in lateral stiffness (a result of the fractured spiral). At a displacement of 2.3 inches south (while traveling to 7.0 inches south), the center north bar fractured 3 inches above the interface. Note this fracture location is approximately located at midspan of the buckled length. A second north bar fractured at 6.65 inches. Consideration of the force-ductility response indicates significant load loss following bar fracture.

The final two 7-inch displacement cycles were imposed to complete the load history. All visible bars on both faces buckled. Final cycling buckled all but the extreme east and west bars. Figure 3.18 shows the final damage state.

### **3.5.2 Measured Response**

The measured force-displacement response of Column 415 is presented in Figure 3.19. The response was stable until the displacement cycle of 5 inches. The measured response is closer to elastic-plastic response in comparison with the response of Column 407.

As indicated in Figure 3.20, the column response was dominated by bending and slip. The error was approximately 15%. During the initial displacement levels, the slip displacement accounted for up to 35% of the displacement. Slip contributed up to 50% of the total displacement during the latter cycles. The shearing deformation accounted for less than 3% of the overall response. Table 3.5 indicates some quantities measured during testing.

## **3.6 COLUMN 430**

Column 430 was reinforced with 3% longitudinal steel and had an aspect ratio of 4. Column 430 was the third column tested. An effective yield displacement of 1 inch was determined using Equation 3.1. Table 3.6 provides a summary of measured response quantities.

### **3.6.1 Observed Response**

The cracked region extended to approximately 3 feet in height during the initial cycle to 0.10 inches. The minimum crack spacing was 6 inches. Crack orientation was primarily horizontal. In circumference the bottom crack (at the interface) extended 22.5 inches (11.25 inches in either direction). Cracking continued during the cycles to 0.3 inch and 0.75 inch and the cracked region extended to 7 feet in elevation. The cracks extending beyond the east or west centerline were inclined. Minimum crack spacing decreased to 2.5 inches below the 24-inch elevation (one column diameter). During the displacement cycle to 1.0 inch, the cracks migrated toward the center

of the east and west faces causing the opposite cracks to meet. Lower cracks on the east and west faces (below 24 inches) inclined 20 to 45 degrees. Minimum crack spacing decreased slightly to 2 inches. The crack pattern established during the earlier cycles stabilized during the displacement cycle to 1.5 inches. Figure 3.21 shows the marked crack pattern during the 2-inch displacement level.

Spalling was initiated during the 1.5-inch displacement cycle. The spalled region was noted to increase as the actuator traveled from 1.5 inches to 2.0 inches north. The spalled region on the south face measured 4 inches by 4 inches (in elevation and circumference, respectfully). During the displacement cycles to 3.0 inches, the spalled region extended 11 inches in circumference and 5 inches in elevation (Figure 3.22). Examination of the force-ductility response (Figure 3.24) indicated negligible strength loss as a result of the physical damage. Cycling the column at a 5 inch displacement level resulted in elongation of the spalled region on the north face to 13 inches in elevation and to 25 inches in circumference. The first cycle to 7.0 inches north resulted in an increase in the spalled region on the north face. Both the spirals and longitudinal bars were exposed. Bar buckling was not observed during this half cycle.

Loading to 7.0 inches south resulted in buckling of the center and adjacent east and west longitudinal bars on the south face. For this column, the longitudinal bars were placed in bundles and the bundled bars were observed to buckle together. The force-displacement response reveals loss of lateral load corresponding to buckling of the longitudinal bars. The second and third cycles to 7.0 inches resulted in additional buckling of the buckled bars. Significant load-carrying capacity was lost. However, this strength loss was not associated with bar fracture, as had been observed for the previous columns, since none of the longitudinal bars fractured. Figure 3.23 shows the final damage state. At completion of testing, all longitudinal bars were exposed and had buckled. Damage to the concrete core was extensive. A total of eight of the spirals had fractured (including those on the north and south faces). All of the fracture points were located at a buckled bar, suggesting that spiral fracture was a direct result of bar buckling.

### **3.6.2 Measured Response**

The force-displacement response of Column 430 is shown in Figure 3.24. The hysteretic response of the column was stable until the second cycle to a displacement demand of 7 inches.

As indicated in Figure 3.25, the column response was dominated by slip and bending. Measurement error was approximately 10%. During the initial displacement levels, the deformation

due to slip accounted for up to 30% of the displacement. Slip contributed up to 50% of the total displacement during the latter cycles. The shearing deformation was approximately 3% of the total, higher than that measured for Columns 407 and 415. Table 3.6 indicates some quantities measured during testing.

### **3.7 COLUMN 815**

Column 815 was reinforced with 1.5% longitudinal steel and had an aspect ratio of 8. Column 815 was the last column tested. An effective yield displacement of 3.3 inches was determined using Equation 3.1. Table 3.7 provides a summary of measured response quantities.

#### **3.7.1 Observed Response**

Cracking was initially detected during the first cycle to 0.15 inches. Cycling to a displacement demand of 0.6 inches decreased the spacing to 8 inches. The cracked region continued to increase in height during the displacement cycles to 1.75 inches and 3.5 inches, beyond 8 feet (or half of the column height). On average, the crack spacing in the lower portion of the column was 4 inches (Figure 3.26).

Initial spalling was observed at completion of the three displacement cycles to 5.25 inches. Spalling continued during the displacement cycles to 7.5 inches and was concentrated primarily in the center of the north and south faces. Spalling was initiated above the column-footing interface at a height of approximately 5 inches. The height of the spalled region reached approximately 13 inches on the north face and 22 inches on the south face during the 10.5 inch displacement cycle (Figure 3.27). The spirals were visible following the second cycle to 10.5 inches.

The final displacement cycle of 17.5 inches was imposed and the spalled region increased to 23 inches in height (Figure 3.30). During the first unloading excursion from 17.5 inches north to 17.5 inches south, the three center longitudinal bars on the south face buckled. When the load was reversed again, the three center bars on the north face buckled. The lateral displacement of the buckled bar resulted in spiral fracture on the north face, specifically, spirals at 4 inches, 5.25 inches and 6.5 inches (Figure 3.29). Fracture of the north longitudinal bars was observed during the subsequent excursion to 17.5 inches south. Figure 3.31 and 3.32 indicate the final damage state of the column. The strength loss associated with the observed damage can be seen in Figure 3.33.

### **3.7.2 Measured Response**

The force-displacement response of Column 815 is shown in Figure 3.33. The hysteretic response of the column was full and stable, until the second cycle to a displacement of 17.5 inches.

As indicated in Figure 3.34, the column response was dominated by flexural mechanisms. During the initial displacement levels, the slip deformation accounted for up to 20% of the total displacement. Slip contributed up to 30% of the total displacement during the latter cycles. The shearing deformation was negligible. Table 3.7 indicates some quantities measured during testing.

## **3.8 COLUMN 1015**

Column 1015 was reinforced with 1.5% longitudinal steel and had an aspect ratio of 10. Column 1015 was the fourth column tested. An effective yield displacement of 4.6 inches was determined using Equation 3.1. Table 3.8 provides a summary of measured response quantities.

### **3.8.1 Observed Response**

Cracking of the concrete was visible after the first cycle to 0.80 inches. The minimum crack spacing was approximately 3 inches after application of the 2.5-inch cycle. The cracked region extended in height during the 5-inch displacement cycles, with limited new cracking in the lower region of the column (Figure 3.35). Crack orientation remained primarily horizontal. Stabilization of the crack pattern was noted during the 7.5-inch displacement cycle.

Spalling of the concrete cover was initiated during the 7.5-inch displacement cycle along a height from approximately 5 inches to 9 inches above the interface. The spalled region extended to 18 inches in elevation during the displacement cycle to 10 inches. The spalled region stabilized during the final two cycles. The spalled region increased to 24 inches during the first 15-inch displacement cycle and continued to extend during the second cycle, to 35 inches (Figure 3.36).

Failure occurred during the 25-inch displacement cycles (Figure 3.37). The initial cycle resulted in the height of the spalled region reaching 26 inches during the first cycle to 25 inches north with sufficient cover spalling to permit observation of the spiral. Reversing the direction of loading from north to south resulted in buckling of the south longitudinal bars. The lateral displacement of the bars resulted in fracture of two spirals located at 12 and 13 inches above the column-footing interface. The bars buckled over a length of approximately 5.5 inches. Reversing the loading direction a second time resulted in buckling of the longitudinal bars on the north face. The

center bar on the north face fractured during the second displacement cycle to 25 inches south at an imposed displacement of 15 inches. The corresponding strength loss can be seen in Figure 3.39. Figure 3.37 shows the column after completion of testing.

### **3.8.2 Measured Response**

The force-displacement response of Column 1015 is shown in Figure 3.39. The hysteretic response of the column was full and stable until the second cycle to an approximate ductility demand of 5.

As indicated in Figure 3.40, the column response was dominated by flexural mechanisms. The slip displacement contributed up to 30% of the total displacement. The shearing deformation was negligible. Table 3.8 indicates some quantities measured during testing.

## **3.9 COMPARATIVE SUMMARY**

Important understanding is gained from individual study of the column behavior. Since the study objective was to identify and quantify the influence of the two study parameters, namely longitudinal reinforcement ratio and aspect ratio, on the seismic response of circular columns; comparison of column behavior for each test series is warranted.

A comparative analysis is provided for each test series. Observed response quantities provided include crack width, spalled height, and column failure mode. Measured response quantities are used to provide an indication of similarities and differences in force-ductility response, the relative contribution of bending, slip and shear, ductility capacity including displacement, rotation and curvature and strain demand, with an emphasis on compressive response.

### **3.9.1 Test Series I: Longitudinal Reinforcement Ratio**

The imposed drift history for the three columns of Test Series I was nominally identical. For each, significant cracking was initiated during the 0.03% drift cycles. Minimum crack spacing was largest for Column 407 (approximately 4 inches) and smallest for Column 430 (approximately 2 inches). The crack widths measured for Column 407 were larger than those measured for Column 430 at comparable strain demand (comparison of the crack widths provided in Tables 3.4, 3.5, and 3.6). Comparing the widths of the crack located at 12 inches above the interface reveals the largest measurement for Column 407 of 0.13 in. and the smallest for Column 430 of 0.02 inches.

Theoretical analyses suggest spalling depends on the compressive strain demand. The height

of the spalled region is expected to increase with an increase in the compressive strain demand, using this hypothesis. Theoretical moment-curvature analyses indicate an increase in the compressive strain demand with an increase in longitudinal reinforcement ratio; experimental results also indicate that the length of the spalled region increased slightly with an increase in reinforcement ratio. The height of the spalled region measured 10 inches measured for Column 407; 13 inches for Column 430. The measured average compressive strain demands also increased with an increase in longitudinal reinforcement ratio. During the final displacement cycle, the strain measured at the base of column 407 was 0.03 in./in. The measured strain demands in Columns 415 and 430 were 0.05 and 0.06, respectively.

Column failure was initiated by bar buckling. The force-displacement response for the three columns indicates full and stable behavior prior to the onset of bar buckling. Failure of Columns 407 and 415, indicated by loss in strength of 20% or more, corresponded to longitudinal bar fracture. Experimental observations suggest that fracture of the column spiral located along the length of the buckled bar significantly reduced its lateral restraint. This loss of restraint permitted extensive lateral deformation of the longitudinal bar. When the direction of loading was reversed, the longitudinal bar fractured as a result of the combined normal and bending strain demands in tension. Failure of Column 430 resulted solely from buckling of the longitudinal bars, spiral fracture, crushing of the core concrete.

The estimated displacement ductility capacities of the three columns differ. Column 415 had the largest displacement ductility capacity of 8. The displacement ductility of Columns 407 and 430 was 6 and 7 respectively. The base rotation ductility is shown to increase with an increase in longitudinal reinforcement ratio, from 9 to 13. The average curvature ductility capacity levels follow the pattern of the displacement ductility capacity with the largest value of 11 measured for Column 415. The average curvature capacities of Column 407 and 430 were approximately 7.

Contributions of bending, slip and shearing deformations to the total displacement were similar for the three columns. Approximately 35% of the total displacement resulted from the fixed-end slip rotation. The bending deformation contributed up to 55% of the column tip displacement. The shearing deformation increased with an increase in longitudinal reinforcement ratio and contributed 1% to 3% of the total displacement.

### **3.9.2 Test Series II: Aspect Ratio**

The displacement histories used for Test Series II were designed to impose approximated equal

displacement ductility demands for the three columns; differences in the column lengths resulted in different imposed drift histories. The crack spacing was similar for the three columns, as would be predicted for columns with identical longitudinal steel ratios. Comparing the width of the crack located approximately 12 inches above the interface (corresponding to a base crack width of roughly 0.02) indicates similar response.

The height of the spalled region is expected to be proportional to the region where the compressive strain demand exceeded the spalling strain. For the three columns, theoretical moment-curvature analyses suggest that the height of the spalled region would increase with an increase in column length. The experimental results support this theory; the height of the spalled region was 12 inches for Column 415, and 26 inches for Column 1015. However, measured average compressive strains are not constant for the three columns. This may be due to the relative proportion of the lowest instrumented segment and the column height. Average compressive strain demands are provided in the tables.

The force-displacement response measured for the three columns are similar. The response prior to the onset of bar buckling was full and stable. Failure, as indicated by 20% strength loss, corresponded to fracture of the first longitudinal bar. The failure mode was similar to that described previously for Column 415; fracture of the column spiral resulted from bar buckling, reduced the lateral restraint on the bar, and permitted extensive lateral deformation of the longitudinal bar. Reversing the direction of loading resulted in longitudinal bar fracture.

The displacement ductility capacity of the three columns differed. Column 415 had the largest displacement ductility capacity of approximately 8. For Columns 815 and 1015, the displacement ductility capacities were approximately 5. In addition, the relative contribution of the slip and bending displacements differed. For Column 415, the contributions of the bending and slip components were approximately equal. For Columns 815 and 1015, column bending accounted for approximately 60% of the total displacement; the slip component was approximately 30%. Analysis of the data shows that the rotation ductility (the ratio of the maximum rotation to the rotation corresponding to the effective yield displacement) of the three columns decreases with an increase in aspect ratio (from 13 for Column 415 to 7 for Column 1015); the average curvature ductility measured at Level 5 (the ratio of the maximum average curvature to the average curvature corresponding to the effective yield displacement) for Columns 415 and 815 are similar (data for Column 1015 were not reliable).

**Table 3.1: Specification of Main Test Parameters**

Column	Steel Ratio	Aspect Ratio
407	0.75%	4
415	1.5%	4
430	3.0%	4
815	1.5%	8
1015	1.5%	10

**Table 3.2: Material Properties**

Material	Specified (ksi)		Expected (ksi)		Actual (ksi)	
	Yield	Ultimate	Yield	Ultimate	Yield	Ultimate
Longitudinal Steel	60	80	66	92.4	68.4	93.3
Spiral	80		88		96.9	98.9
	Peak	Confined	Peak	Confined	Peak	Confined
Concrete	3.3		4.2	6.3	Varies	N/M

**Table 3.3: Displacement Levels**

Displacement Level	L/D = 4	L/D = 8	L/D = 10
	0.06"	0.15"	0.2"
	0.15"	0.6"	0.8"
	0.3"		
First-Yield	0.75"	1.75"	2.5"
$\Delta_y$	1"	3.5"	5"
$1.5\Delta_y$	1.5"	5.25"	7.5"
$2\Delta_y$	2"	7"	10"
$3\Delta_y$	3"	10.5"	15"
$5\Delta_y$	5"	17.5"	25"
$7\Delta_y$	7"		

**Table 3.4: Column 407 Measured Response Quantities**

Measurement	0.75"	1"	1.5"	2.0"	3.0"	5.0"
Displacement Ductility	0.9	1.3	2	3	4	6
Bending Component (%)	54%	51%	45%	46%	45%	37%
Slip Component (%)	37%	40%	47%	46%	47%	53%
Shear Component (%)	0.7%	0.9%	1%	1%	1%	2%
Average Compressive Strain	-0.004	-0.005	-0.008	-0.01	-0.016	-0.032
Tensile Strain above Interface	0.007	0.018	0.02	0.027	N/M	N/M
Spiral Strain	0.0002	0.0002	0.0002	0.0003	0.0006	0.0017
Height of Spalled Region	0"	0"	1"	3"	10"	10"
Rotation Ductility (0-6 inches)	0.9	1.3	2.3	3.1	4.8	9
Curvature Ductility (6-12 inches)	0.9	1.4	2.2	3.7	5.6	7.5
Crack Width @ Interface (in.)	0.025	0.06	0.07	0.13	0.19	0.25
Crack Width @ 12 inches (in.)	0.016	0.016	0.03	0.06	0.06	0.06
Residual Crack @ Interface (in.)	0.005	0.009	N/M	0.02	0.02	N/M
Residual Crack @ 12 inches (in.)	0.000	0.003	N/M	0.003	0.005	N/M

Notes:

1. N/M: not measured
2. Displacement ductility calculated using effective yield displacement
3. Average compressive strain measured by interpreting measurements of the north vertical displacement gauges to the column face.
4. Tensile strain measured by longitudinal strain gauge at Level 4
5. Spiral strain measured by spiral strain gauge on the north face at Level 4
6. Rotation and average curvature yield values reported are values that correspond to effective yield displacement
7. Crack widths measured on the north face of the column

**Table 3.5: Column 415 Measured Response Quantities**

Measurement	1"	1.5"	2.0"	3.0"	5.0"	7.0"
Displacement Ductility	1	2	2	3	5	8
Bending Component (%)	52%	45%	38%	37%	35%	32%
Slip Component (%)	31%	37%	44%	47%	39%	45%
Shear Component (%)	1.3%	1.7%	2%	2.1%	2.7%	2.7%
Average Compressive Strain	-0.004	-0.007	-0.01	-0.018	-0.33	-0.053
Tensile Strain above Interface	0.003	0.006	0.01	0.028	N/M	N/M
Spiral Strain	.00004	0.0001	0.0002	0.0005	N/M	N/M
Height of Spalled Region	0"	0"	4"	5"	12"	12"
Rotation Ductility (0-6 inches)	1	2	3	5	7	11
Curvature Ductility (6-12 inches)	1	2	3	5	8	11
Crack Width @ Interface (in.)	0.025	0.025	0.125	0.125	0.18	N/M
Crack Width @ D/2 (in.)	0.013	0.02	0.04	0.063	0.125	N/M
Residual Crack @ Interface (in.)	0.005	0.02	0.016	0.02	N/M	N/M
Residual Crack @ D/2	0.002	0.002	0.005	0.013	0.02	N/M

Notes:

1. N/M: not measured
2. Displacement ductility calculated using effective yield displacement
3. Average compressive strain measured by interpreting the measurements of the north vertical displacement gauges to the column face
4. Tensile strain measured by longitudinal strain gauge at Level 4
5. Spiral strain measured by spiral strain gauge on the north face at Level 4
6. Rotation and average curvature yield values correspond to effective yield displacement
7. Crack widths measured on the north face of the column

**Table 3.6: Column 430 Measured Response Quantities**

Measurement	1"	1.5"	2.0"	3.0"	5.0"	7.0"
Displacement Ductility	1	2	2	3	5	7
Bending Component (%)	54%	49%	43%	38%	35%	31%
Slip Component (%)	31%	32%	39%	45%	48%	51%
Shear Component (%)	1.4%	1.4%	1.5%	1.7%	2%	2.4%
Average Compressive Strain	-0.005	-0.008	-0.012	-0.022	-0.039	-0.057
Tensile Strain above Interface	0.0029	0.01	0.016	0.024	N/M	N/M
Spiral Strain	N/M	0.0001	0.0005	0.0009	0.0013	0.0024
Height of Spalled Region	0"	0"	0"	12"	12"	13"
Rotation Ductility (0-6 inches)	1	2	3	5	9	13
Curvature Ductility (6-12 inches)	1	2	2	4	6	7
Crack Width @ Interface	0.025	0.05	0.125	0.19	N/M	N/M
Crack Width @ D/2	0.013	0.025	0.03	0.02	N/M	N/M
Residual Crack @ Interface	N/M	0.016	0.03	N/M	N/M	N/M
Residual Crack @ D/2	N/M	0.003	0.009	N/M	N/M	N/M

Notes:

1. N/M: not measured
2. Displacement ductility calculated using effective yield displacement
3. Average compressive strain measured by interpreting the measurements of the north vertical displacement gauges to the column face
4. Tensile strain measured by longitudinal strain gauge at Level
5. Spiral strain measured by spiral strain gauge on the north face at Level 4
6. Rotation and average curvature yield values correspond to effective yield displacement
7. Crack widths measured on the north face of the column

**Table 3.7: Column 815 Measured Response Quantities**

Measurement	3.5"	5.25"	7"	10.5"	17.5"
Displacement Ductility	1	2	2	3	5
Bending Component (%)	70%	63%	59%	57%	57%
Slip Component (%)	23%	28%	30%	29%	28%
Shear Component (%)	0.3%	0.4%	0.4%	0.5%	0.4%
Average Compressive Strain	-0.006	-0.009	-0.012	-0.013	-0.019
Tensile Strain above Interface	0.02	0.02	0.03	0.04	N/M
Spiral Strain	0.0001	0.0002	0.0003	0.0008	0.0021
Height of Spalled Region	0"	0"	7"	22"	25"
Rotation Ductility (0-6 inches)	2	3	4	5	9
Curvature Ductility (6-12 inches)	1	2	4	7	13
Crack Width @ Interface (in.)	0.025	0.125	0.125	N/M	0.25
Crack Width @ D/2 (in.)	0.009	0.01	0.025	N/M	0.125
Residual Crack @ Interface (in.)	0.007	0.025	0.016	0.025	N/M
Residual Crack @ D/2 (in.)	0	0.0	0.009	0.007	N/M

Notes:

1. N/M: not measured
2. Displacement ductility calculated using effective yield displacement
3. Average compressive strain measured by interpreting measurements of the north vertical displacement gauges to the column face
4. Tensile strain measured by longitudinal strain gauge at Level 4
5. Spiral strain measured by spiral strain gauge on the north face at Level 4
6. Rotation and average curvature yield values correspond to effective yield displacement
7. Crack widths measured on the north face of the column

**Table 3.8: Column 1015 Measured Response Quantities**

Measurement	5"	7.5"	10"	15"	25"
Displacement Ductility	1	2	2	3	5
Bending Component (%)	55%	54%	56%	60%	64%
Slip Component (%)	24%	29%	31%	28%	26%
Shear Component (%)	0.3%	0.3%	0.3%	0.3%	0.2%
Average Compressive Strain	-0.005	-0.008	-0.01	-0.011	-0.012
Tensile Strain above Interface	0.02	0.02	0.04	N/M	N/M
Spiral Strain	0.0003	0.0005	0.0006	0.0015	0.0043
Height of Spalled Region	0"	1"	18"	24"	26"
Rotation Ductility (0-6 inches)	2	3	4	5	7
Curvature Ductility (6-12 inches)	1	2	N/M	N/M	N/M
Crack Width @ Interface (in.)	0.025	0.13	.13	.13	.25
Crack Width @ D/2 (in.)	0.025	0.063	0.09	.13	.13
Residual Crack @ Interface (in.)	0.005	0.016	0.013	0.04	N/M
Residual Crack @ D/2 (in.)	0.002	0.02	0.02	N/M	N/M

Notes:

1. N/M: not measured
2. Displacement ductility calculated using effective yield displacement
3. Average compressive strain measured by interpreting the measurements of the north vertical displacement gauges to the column face
4. Tensile strain measured by longitudinal strain gauge at Level 4
5. Spiral strain measured by spiral strain gauge on the north face at Level 4
6. Rotation and average curvature yield values correspond to effective yield displacement
7. Crack widths measured on the south face

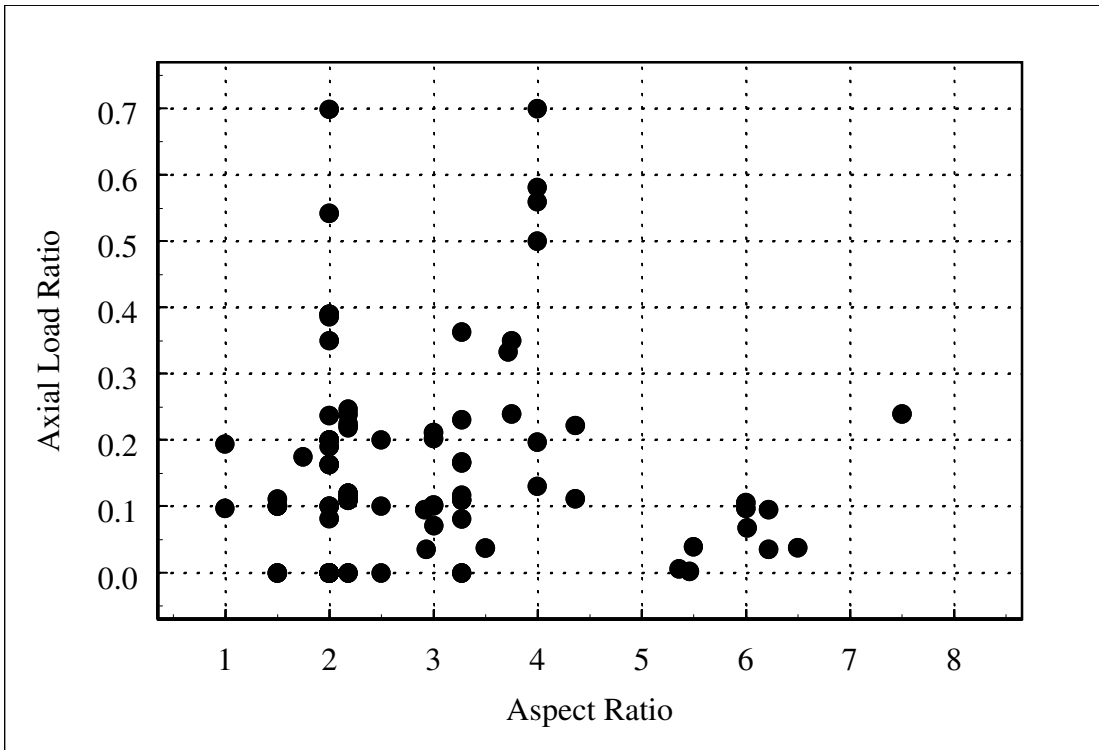


Figure 3.1: Axial Load Ratio vs. Aspect Ratio for Columns in [Taylor 1993] Study

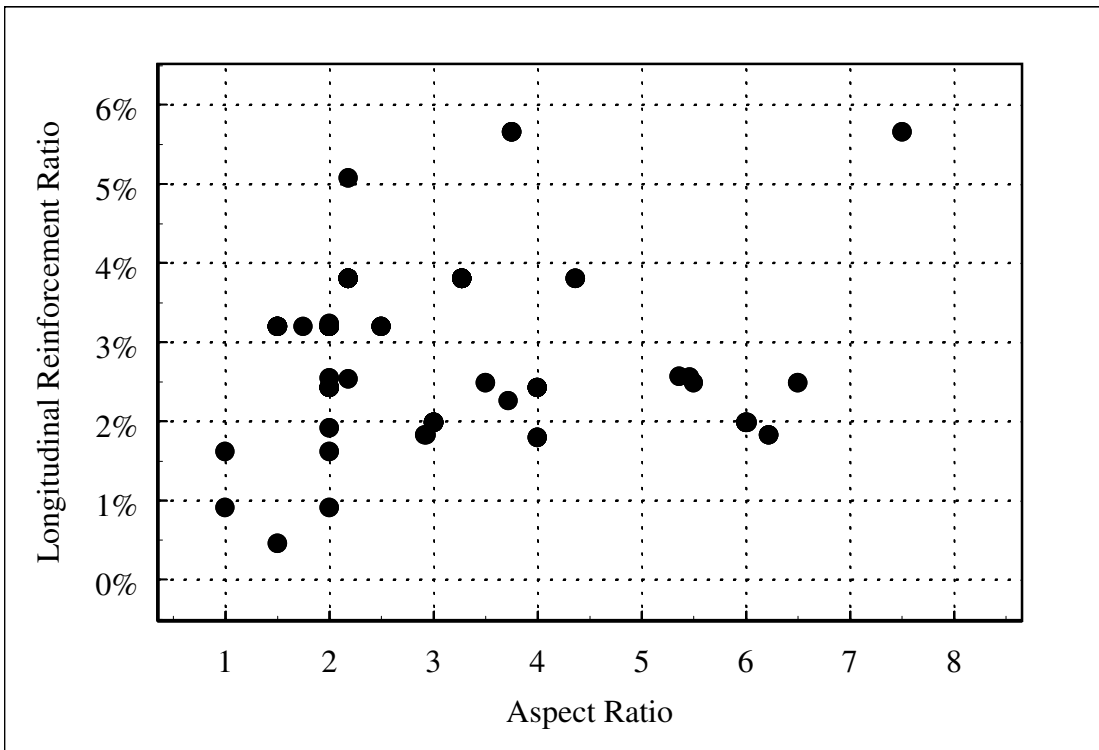
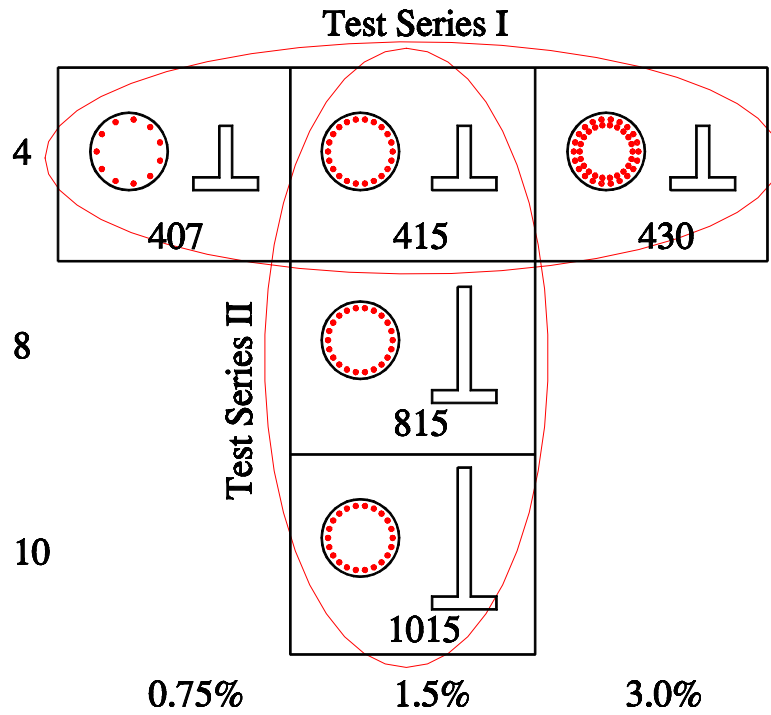
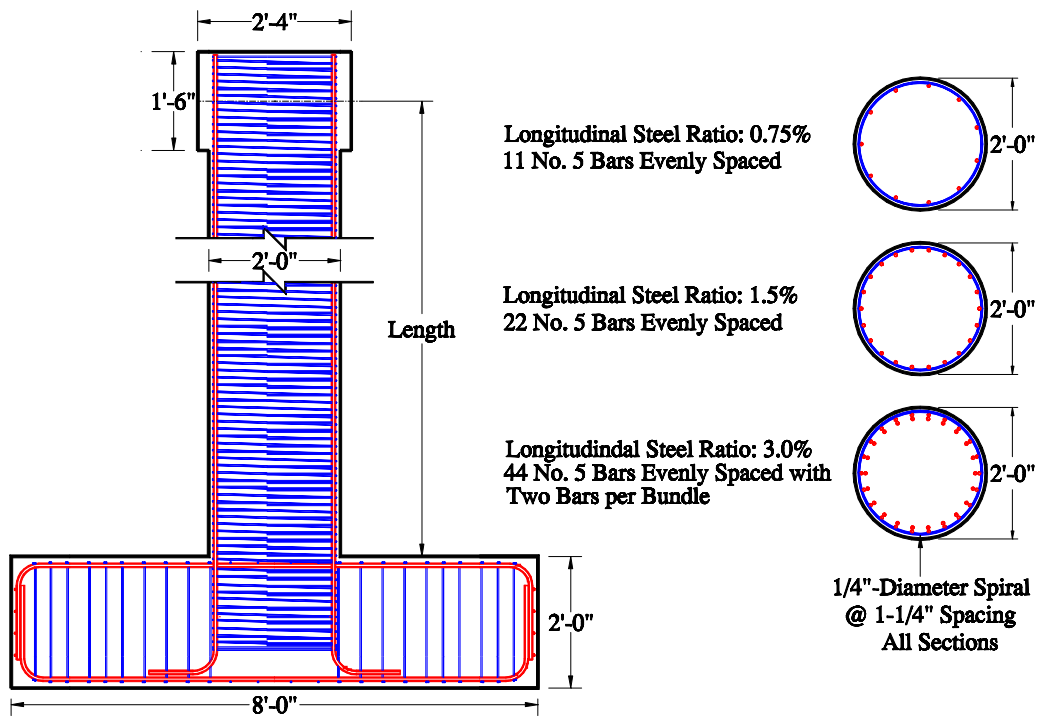


Figure 3.2: Reinforcement Ratio vs. Aspect Ratio for Columns in [Taylor 1993] Study



**Figure 3.3: Test Matrix**



**Figure 3.4: Specimen Geometry and Reinforcement**

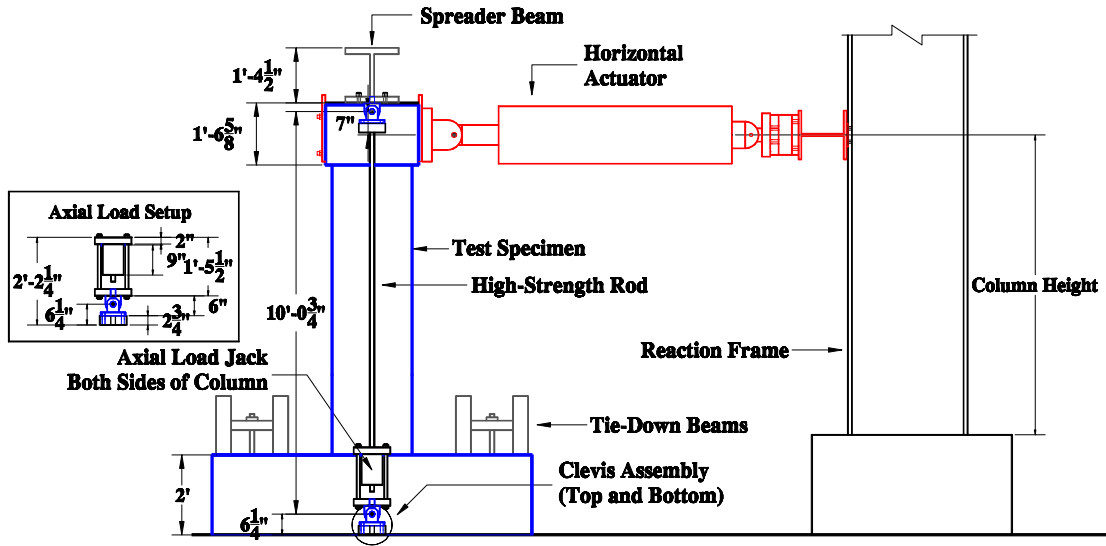


Figure 3.5: Experimental Configuration

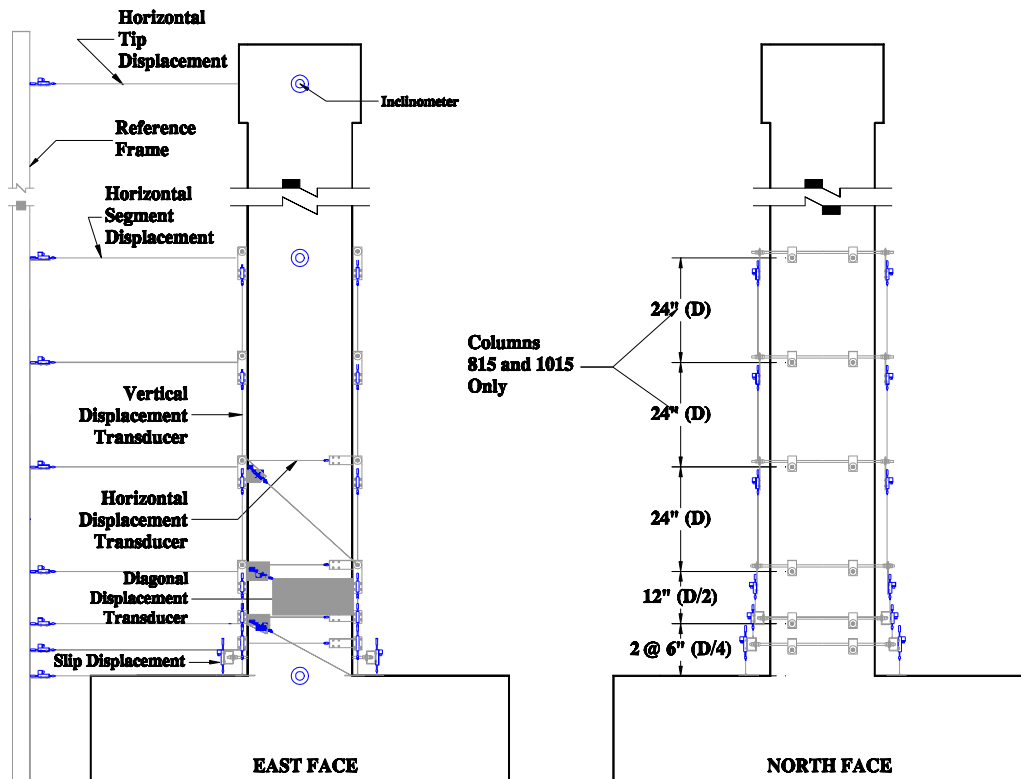
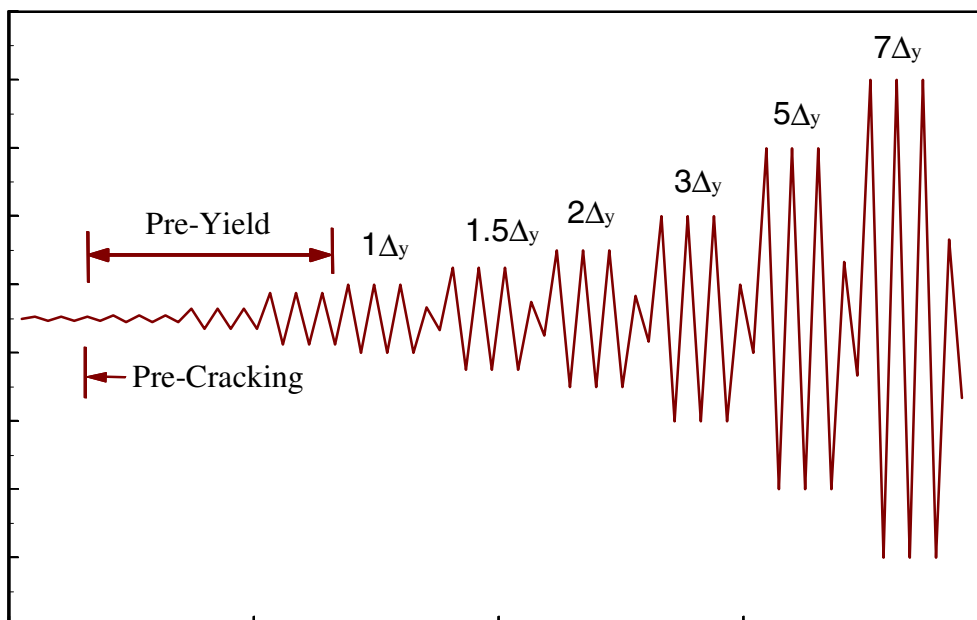
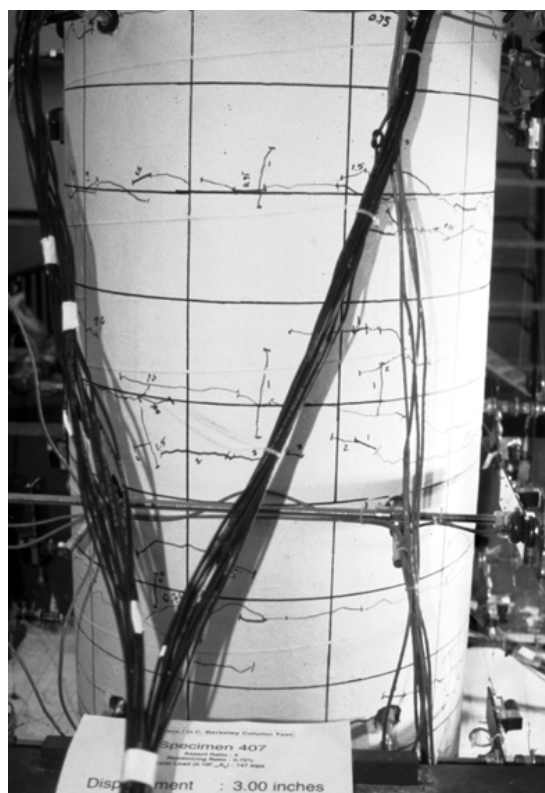


Figure 3.6: Instrumentation



**Figure 3.7: Target Displacement History**



**Figure 3.8: Column 407 Crack Pattern at 3-Inch Displacement Level**



**Figure 3.9: Column 407 Spalled Region at 3-Inch Displacement Level**



**Figure 3.10: Column 407 Buckled Bar and Fractured Spirals**

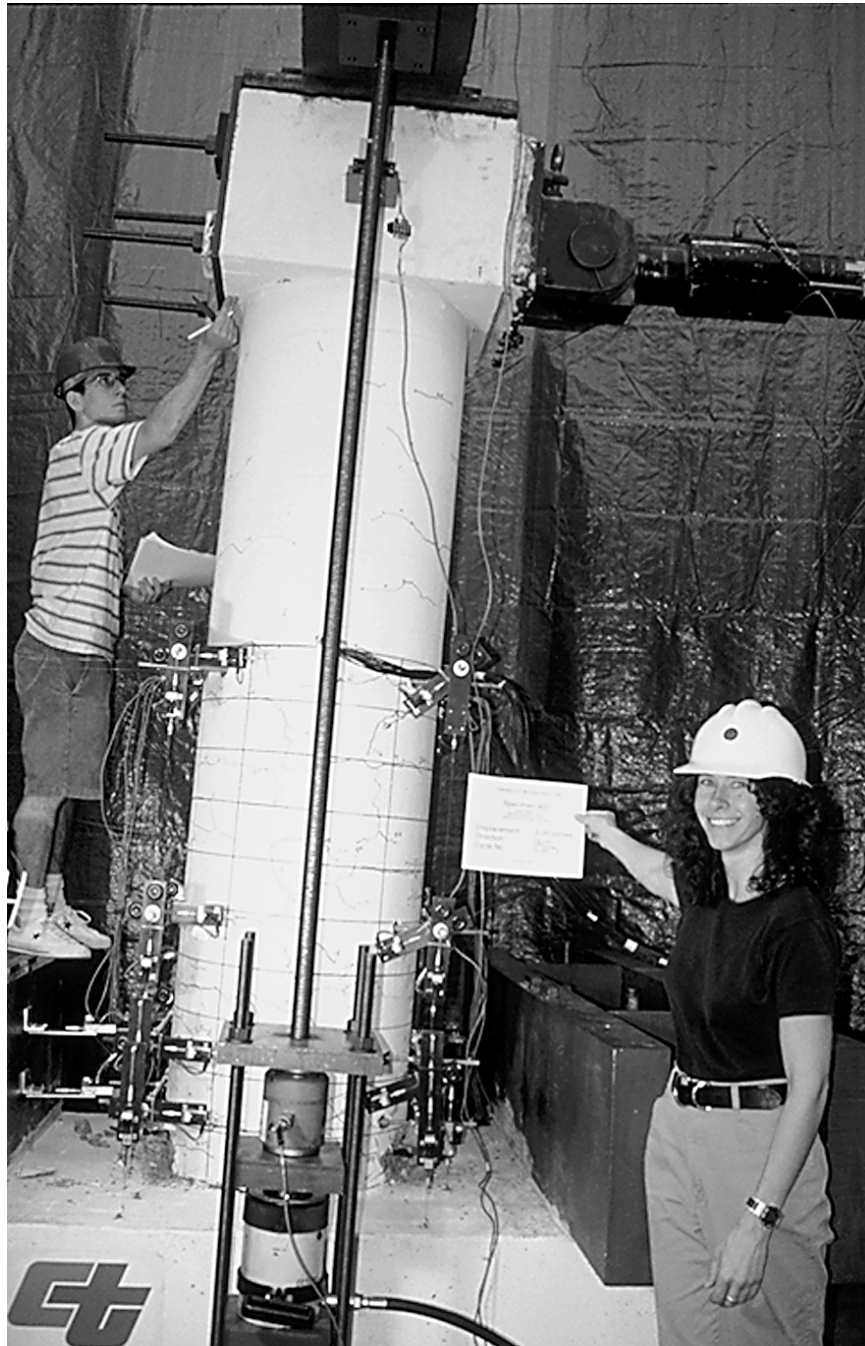


**Figure 3.11: Column 407 Displaced to 5 Inches**



**Figure 3.12: Column 407 Fractured Main Longitudinal Bars**



**Figure 3.13: Column 407 Final Damage State**

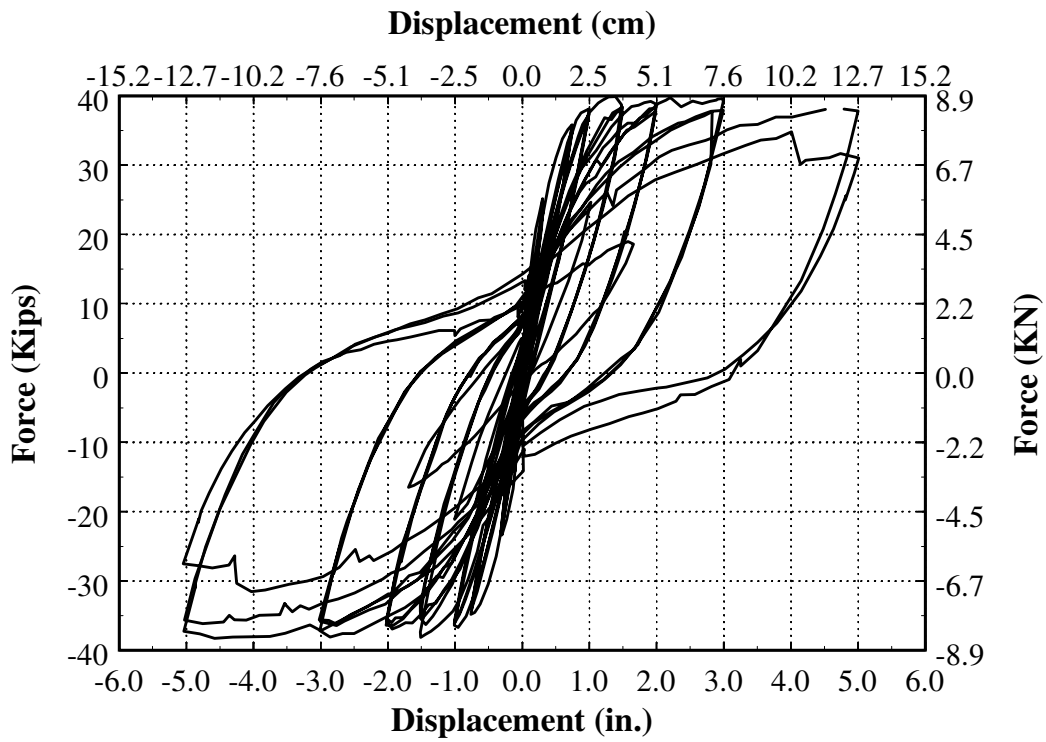


Figure 3.14: Force-Displacement Response of Column 407

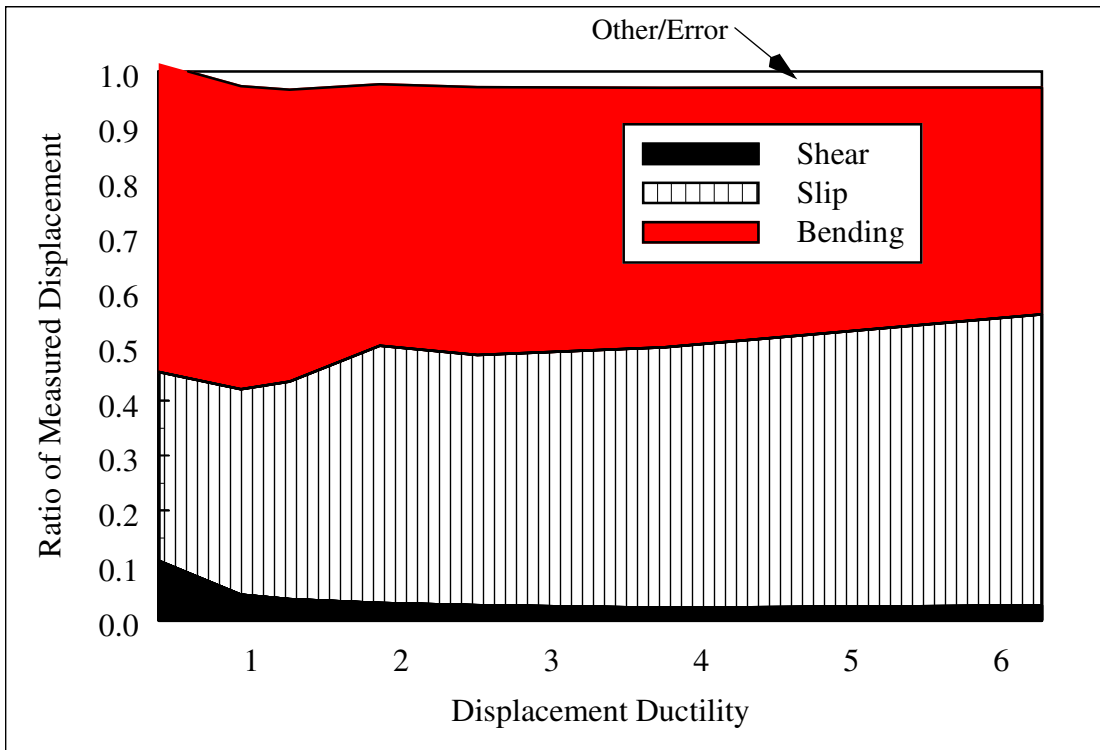


Figure 3.15: Column 407 Displacement Components

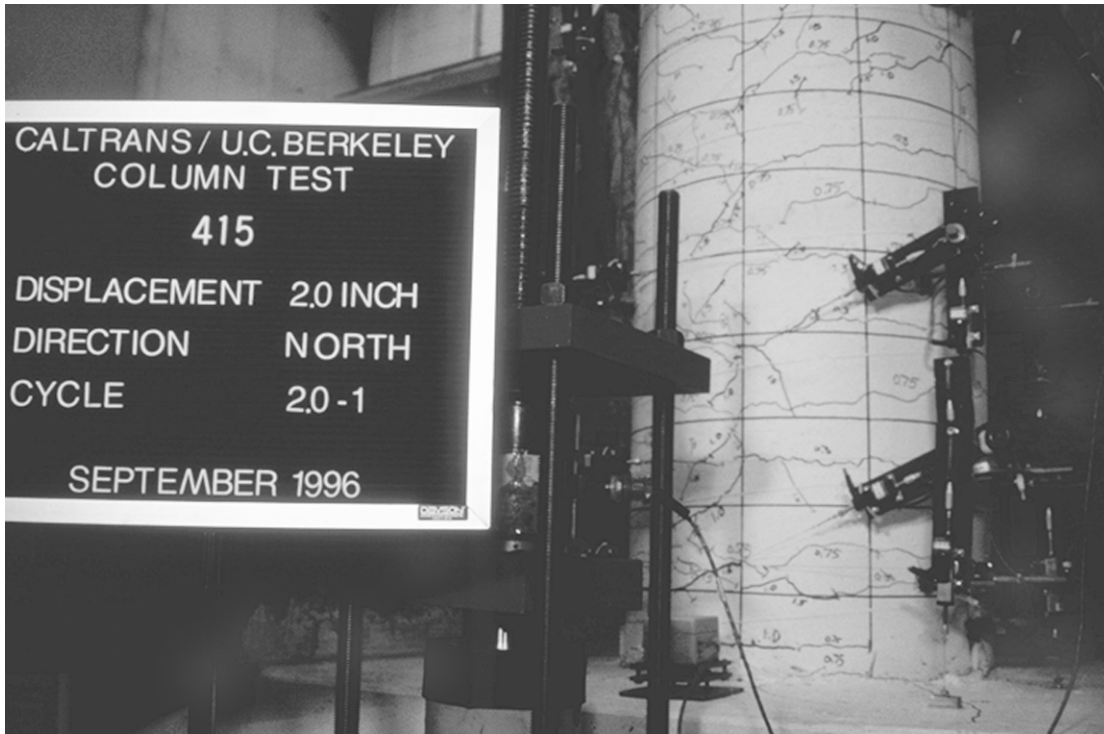


Figure 3.16: Column 415 Crack Pattern

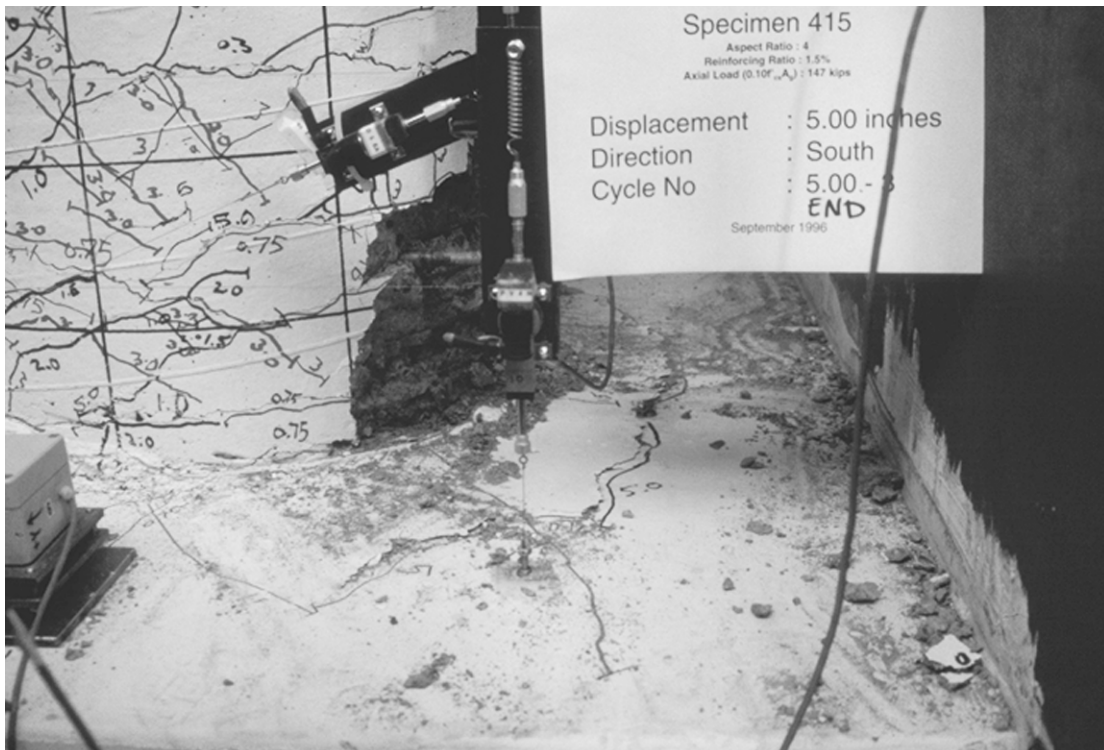
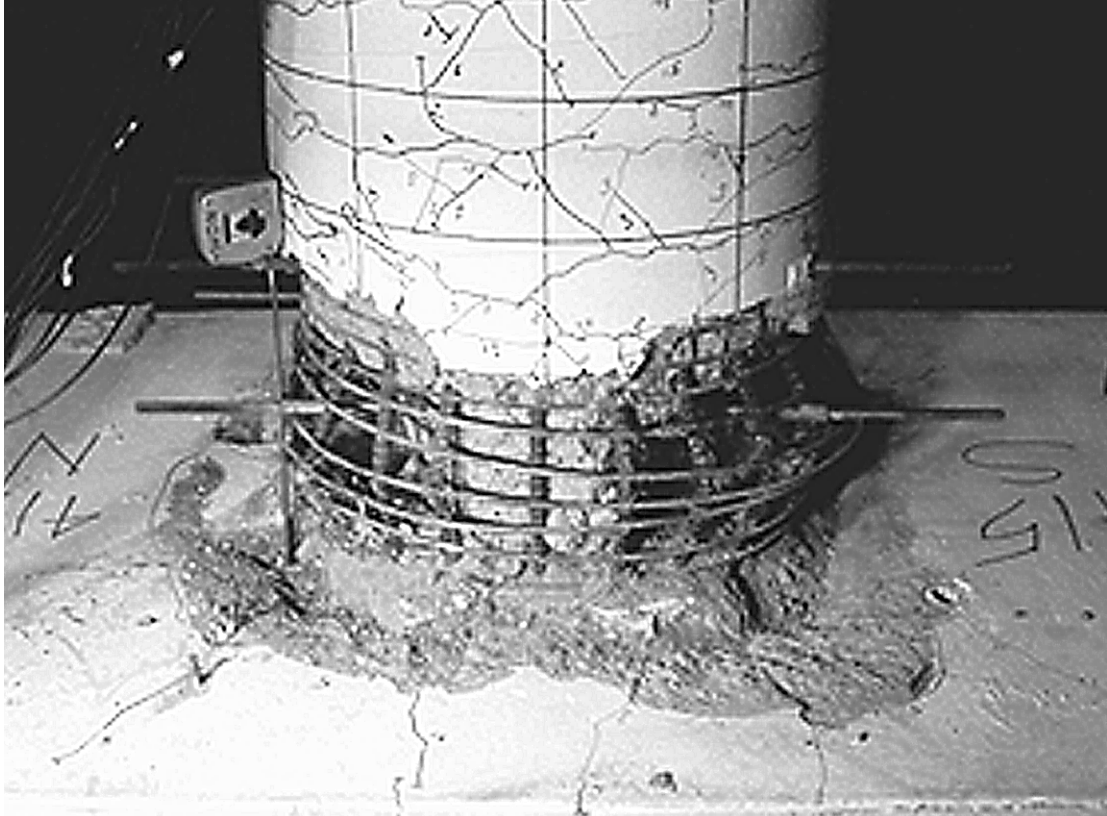


Figure 3.17: Column 415 Spalled Region Following 5-Inch Displacement Level



**Figure 3.18: Column 415 Final Damage State**

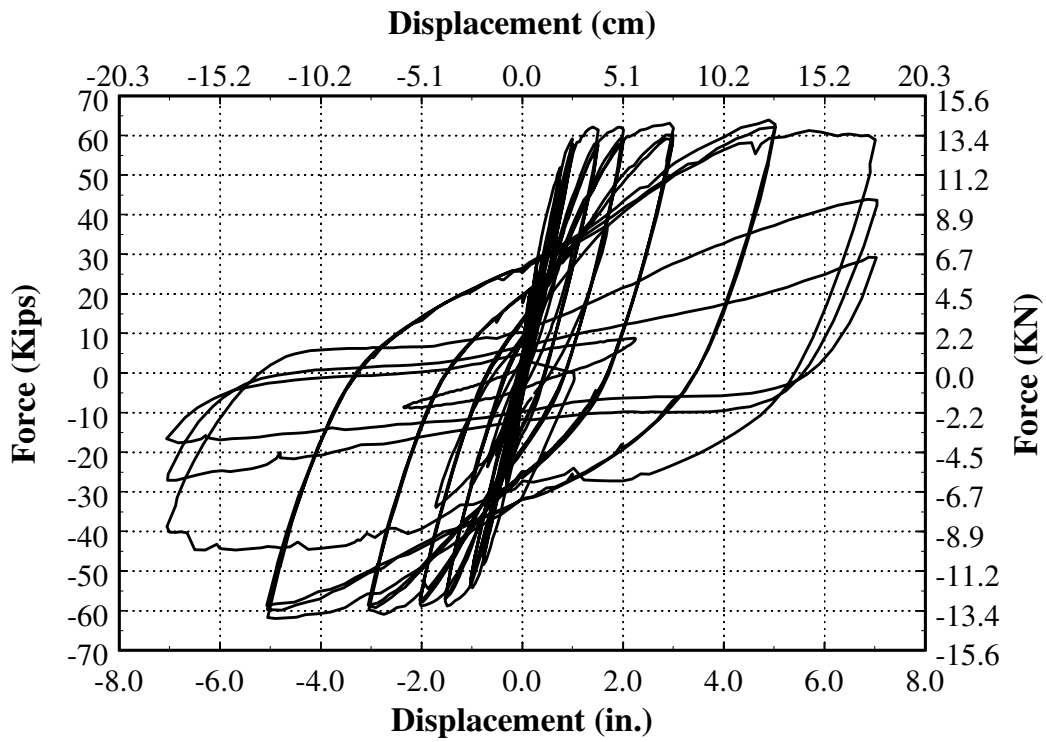


Figure 3.19: Column 415 Force-Displacement Response

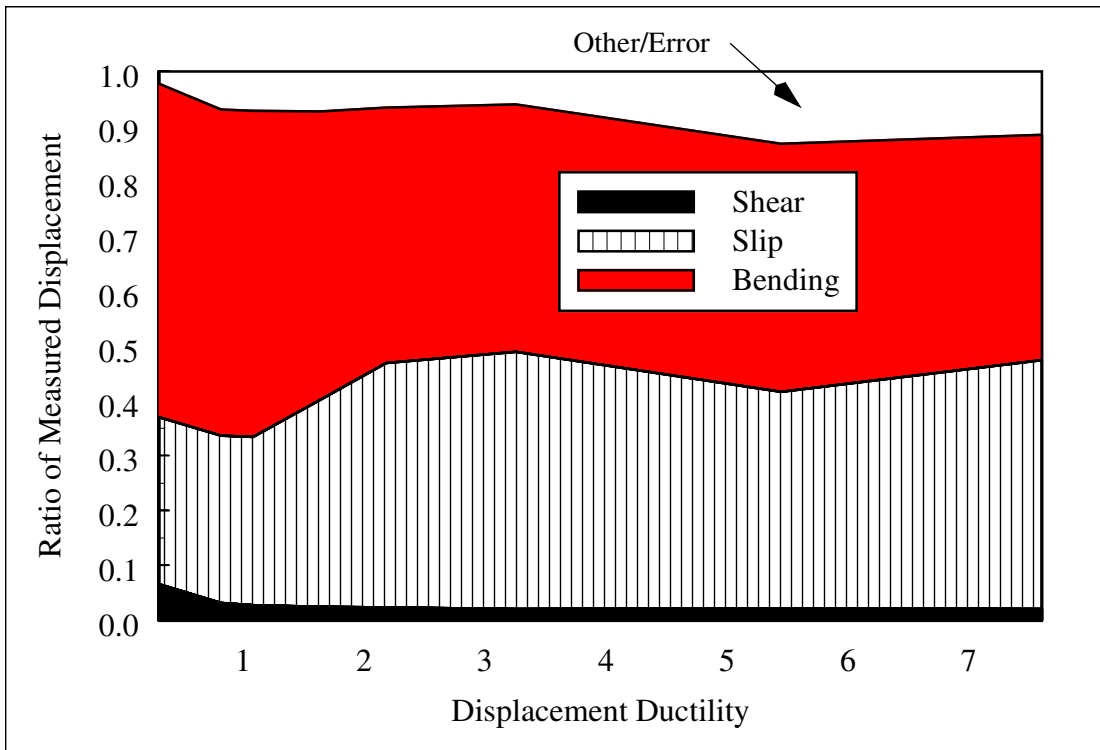


Figure 3.20: Column 415 Displacement Components





**Figure 3.23: Column 430 Final Damage State**

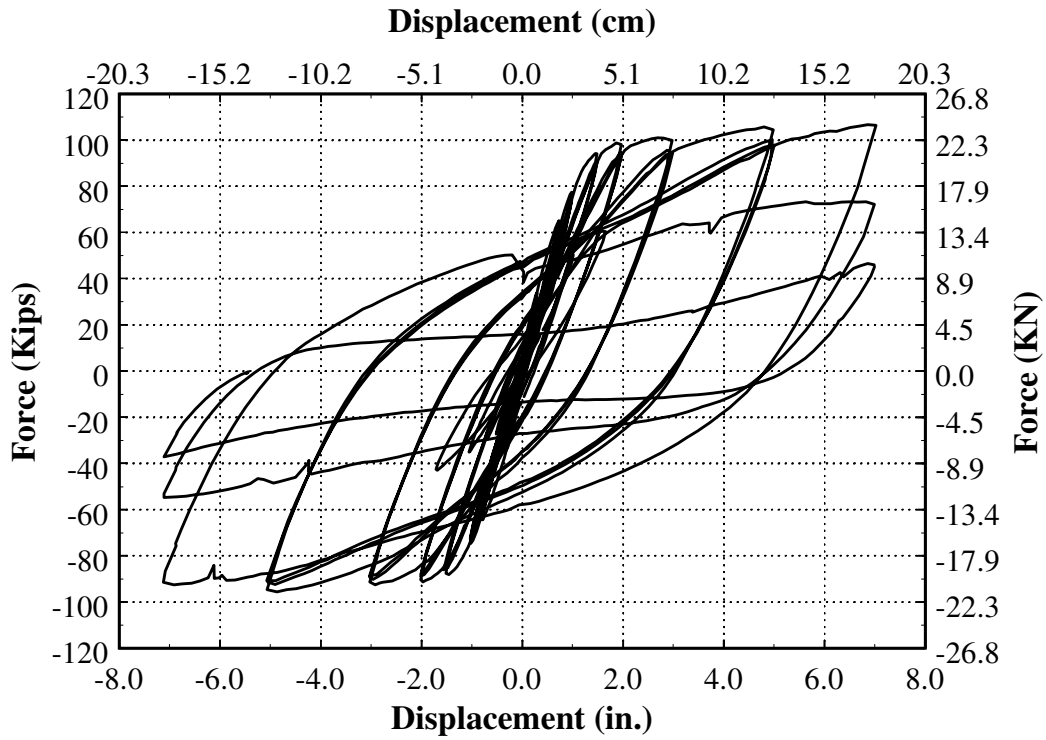


Figure 3.24: Column 430 Force-Displacement Response

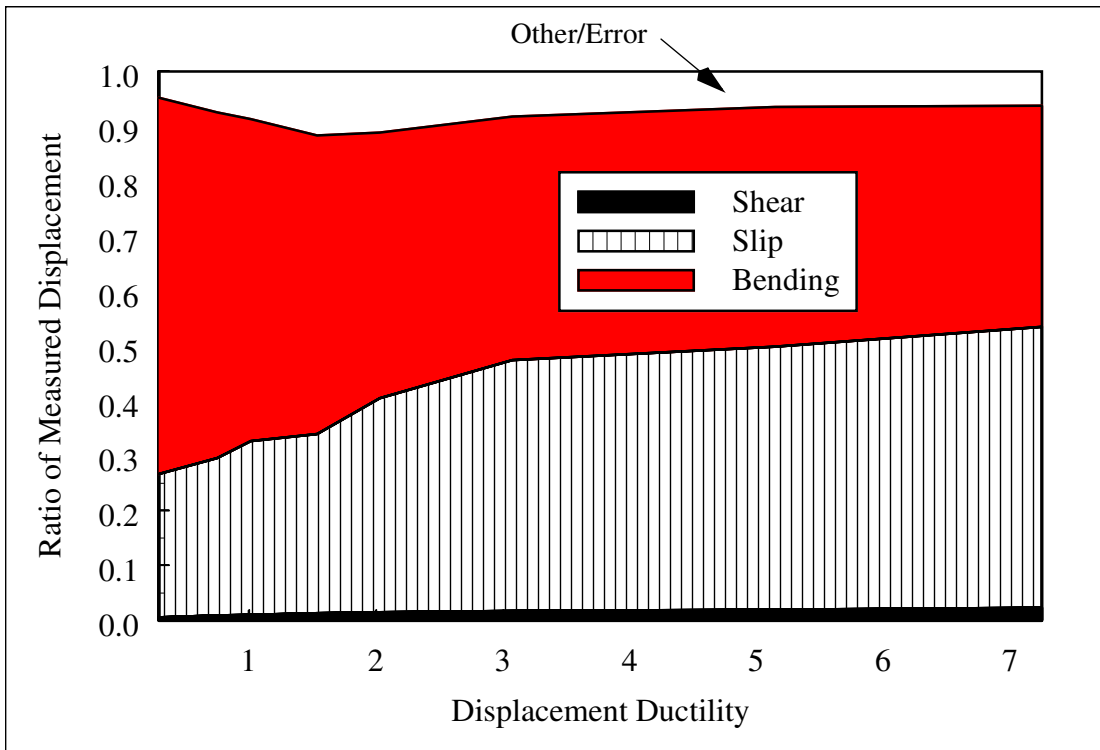


Figure 3.25: Column 430 Displacement Components



**Figure 3.26: Column 815 Crack Pattern at 3.5-Inch Displacement Level**



**Figure 3.27: Column 815 Spalled Region at First Cycle to 17.5 Inches**



**Figure 3.28: Column 815 Fracture of Previously Buckled Longitudinal Bar**

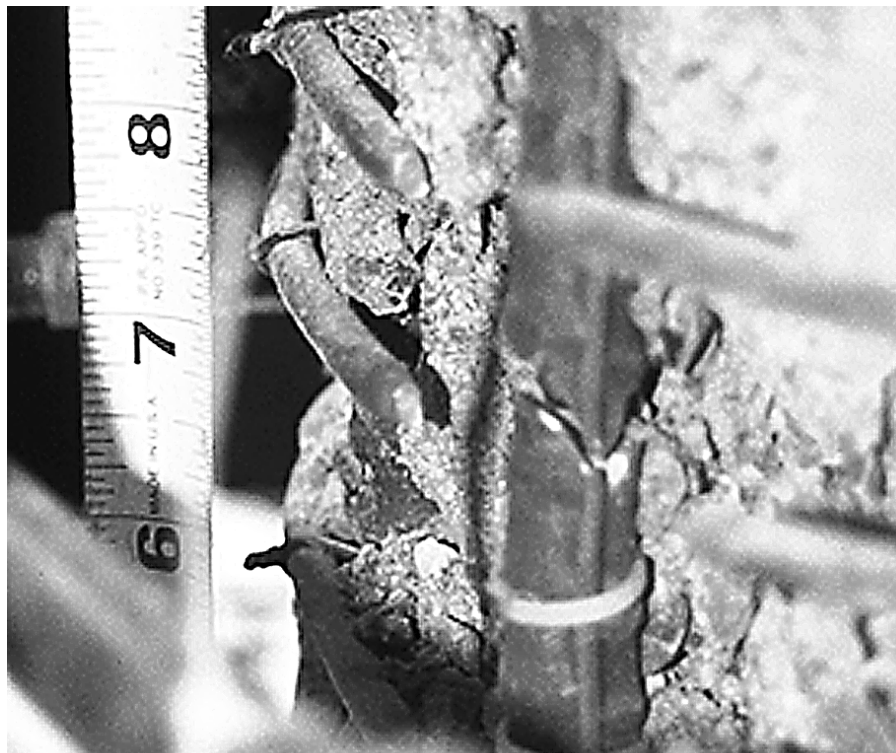


**Figure 3.29: Column 815 Fractured Main Longitudinal Bar**



**Figure 3.30: Column 815 Displaced to 17.5 Inches**

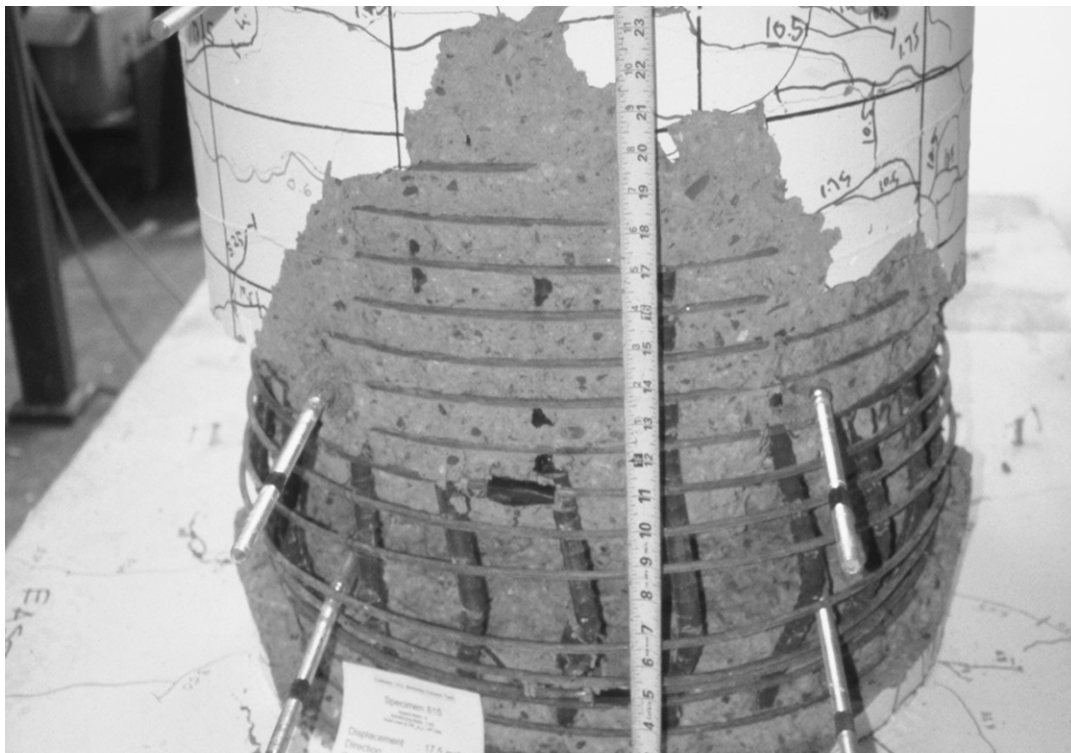


**Figure 3.31: Column 815 Final Damage State of North Face**

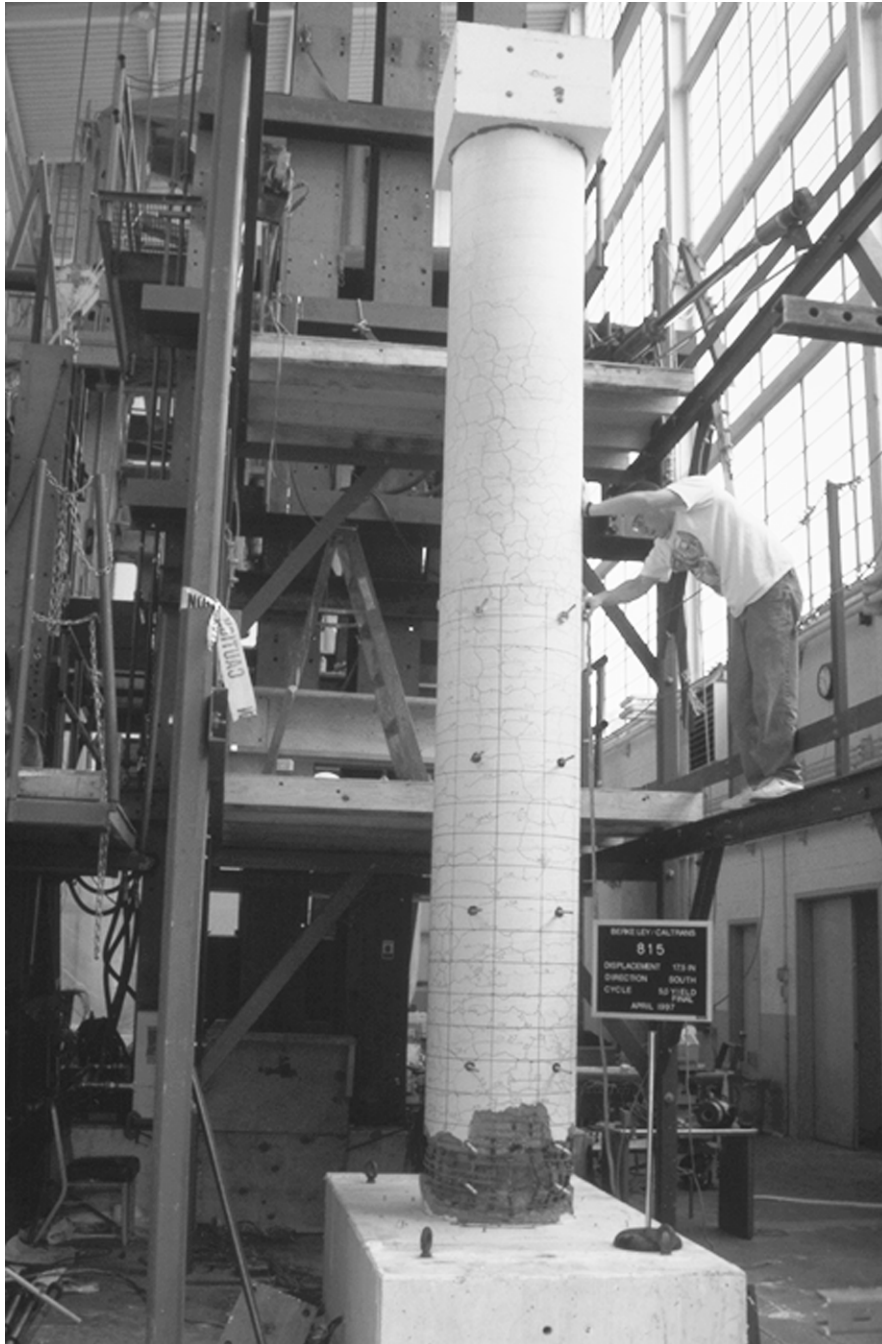


**Figure 3.32: Column 815 Damaged Region on South Face After Testing**

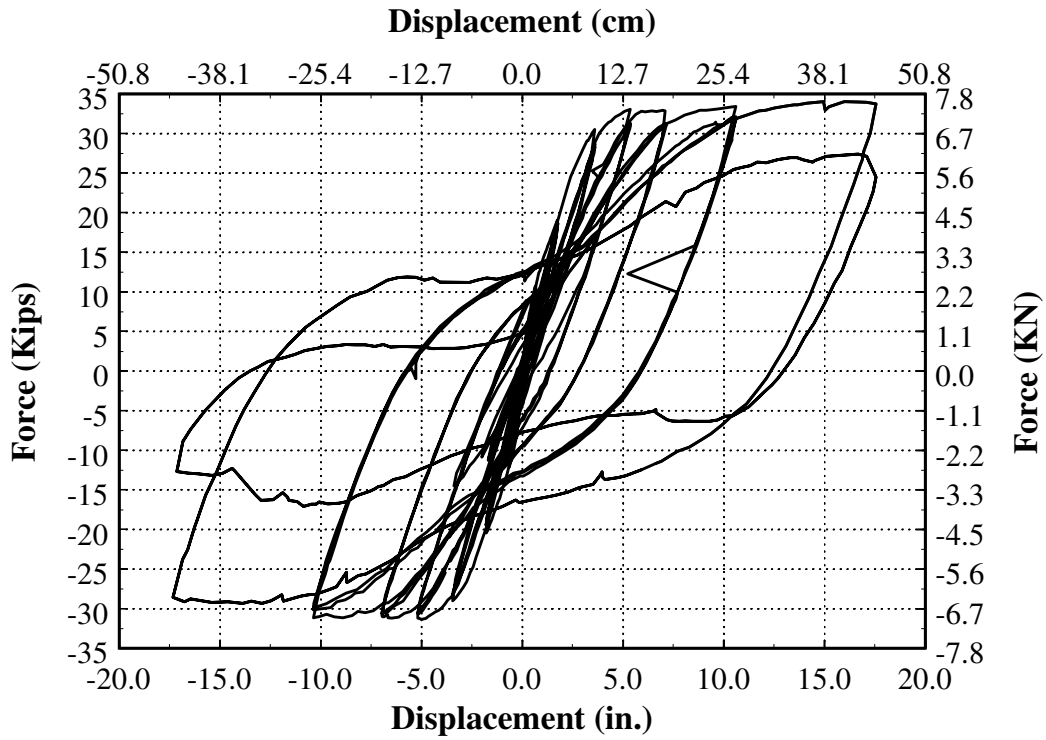


Figure 3.33: Column 815 Force-Displacement Response

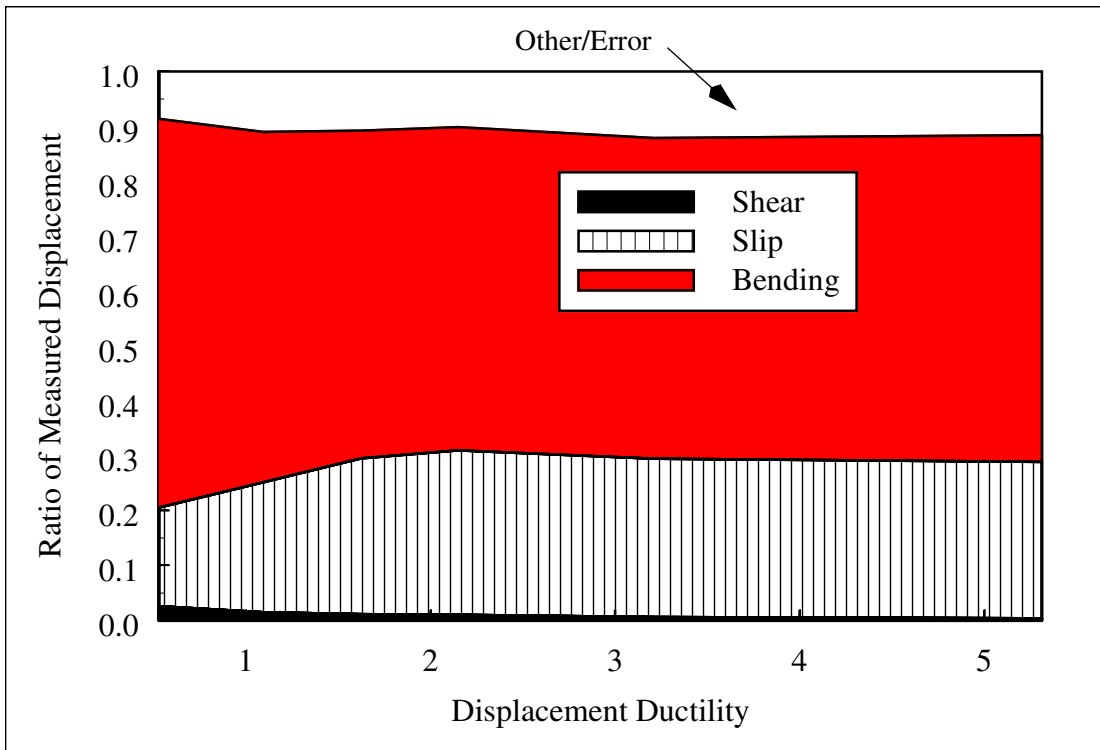
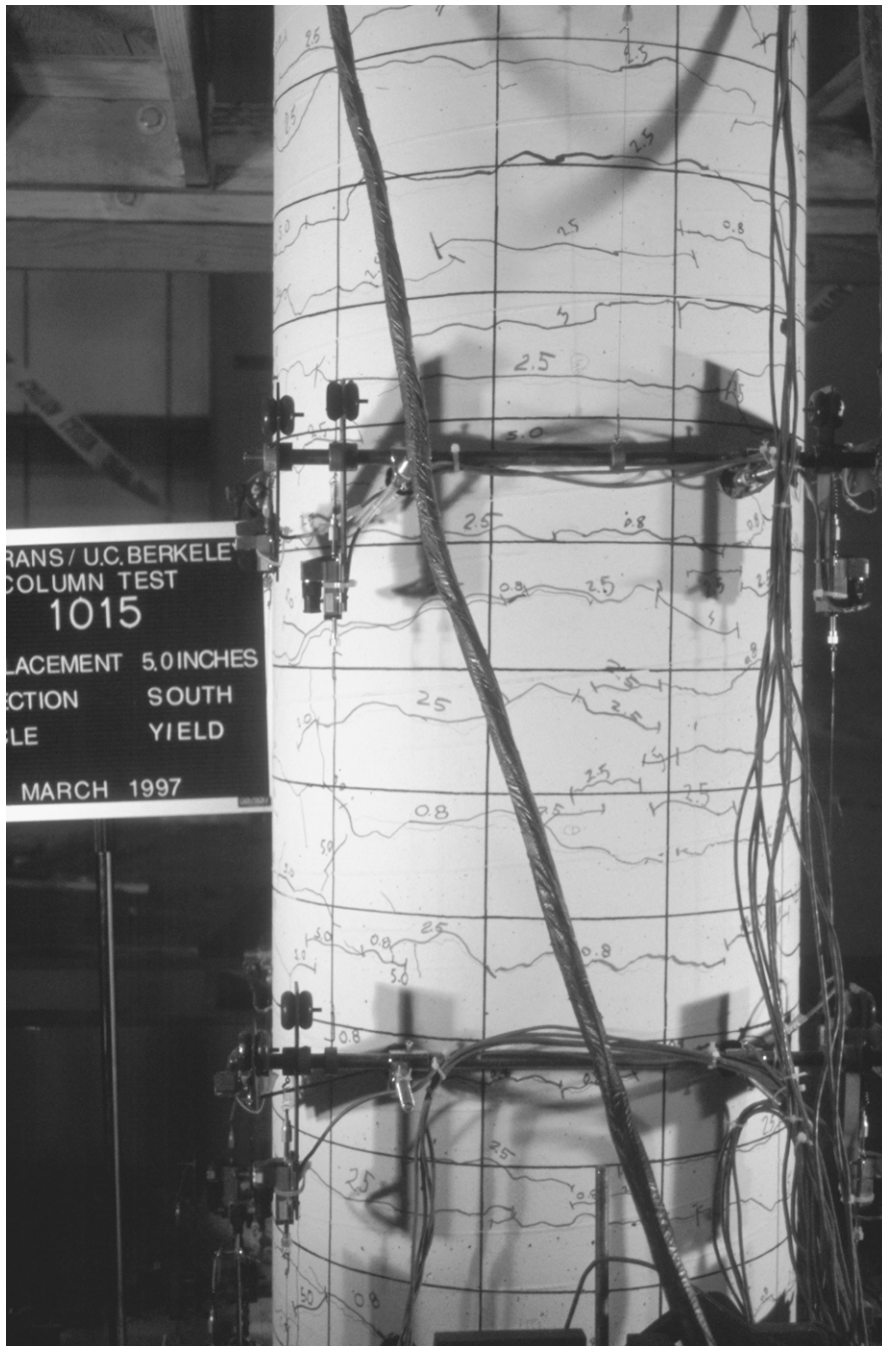
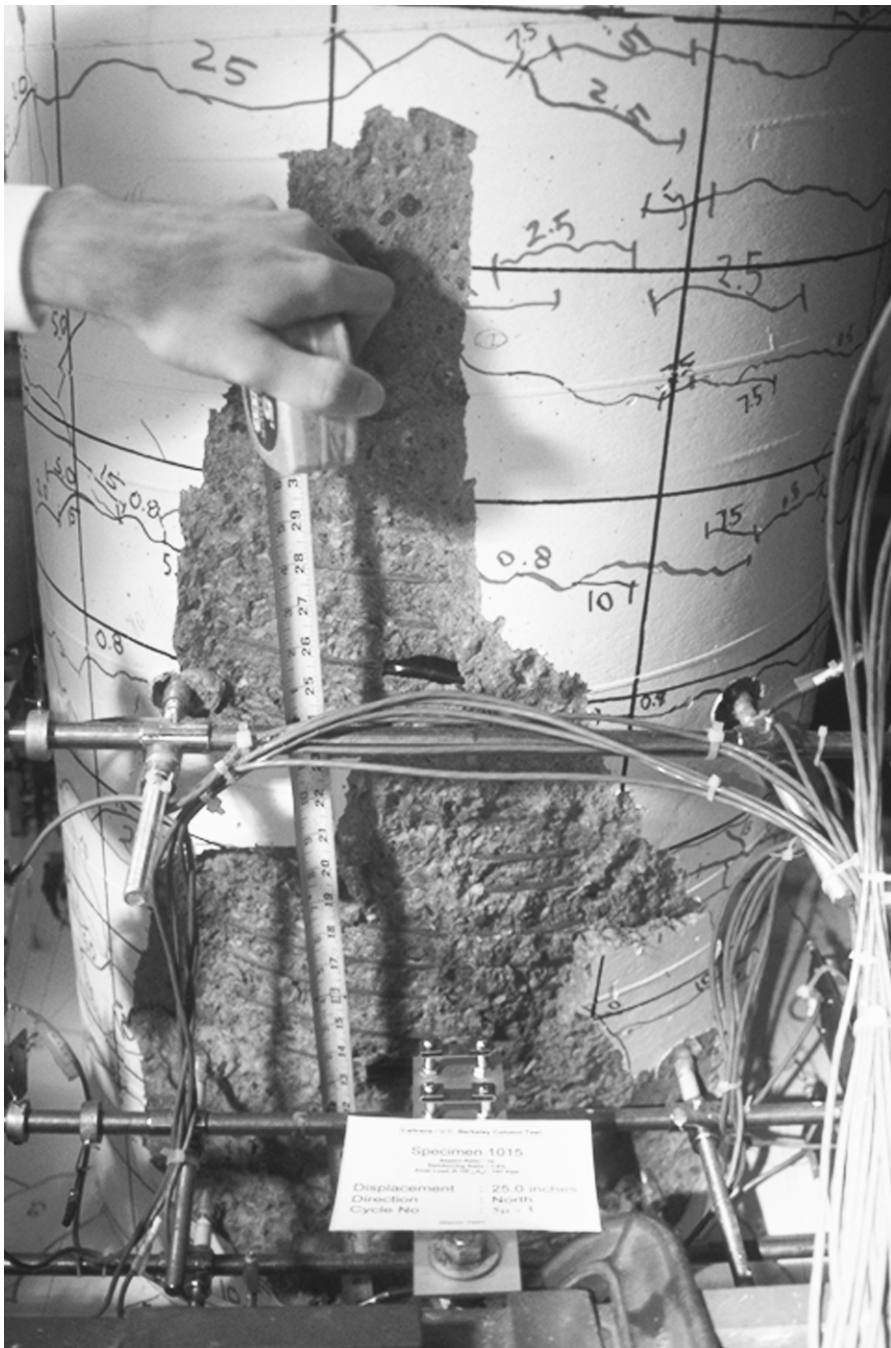


Figure 3.34: Column 815 Displacement Components



**Figure 3.35: Column 1015 Crack Pattern at 5-Inch Displacement Level**



**Figure 3.36: Column 1015 Spalled Region at 25-Inch Displacement Level**



**Figure 3.37: Column 1015 Displaced to 25 Inches**



**Figure 3.38: Column 1015 Damage State after Testing**

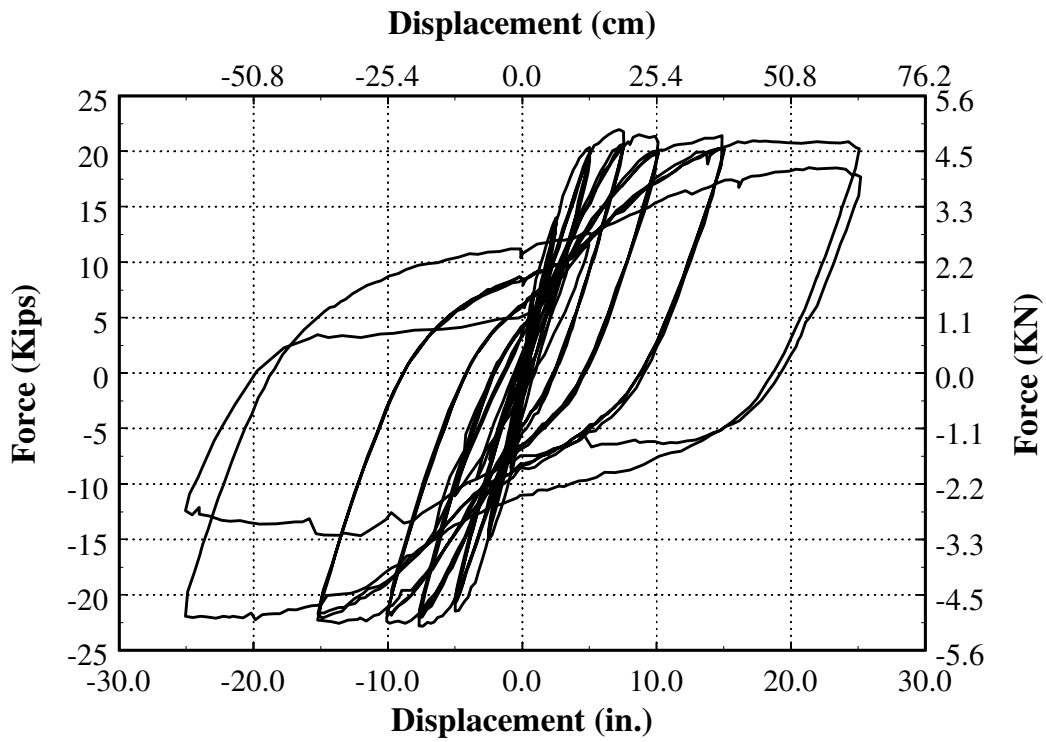


Figure 3.39: Column 1015 Force-Displacement Response

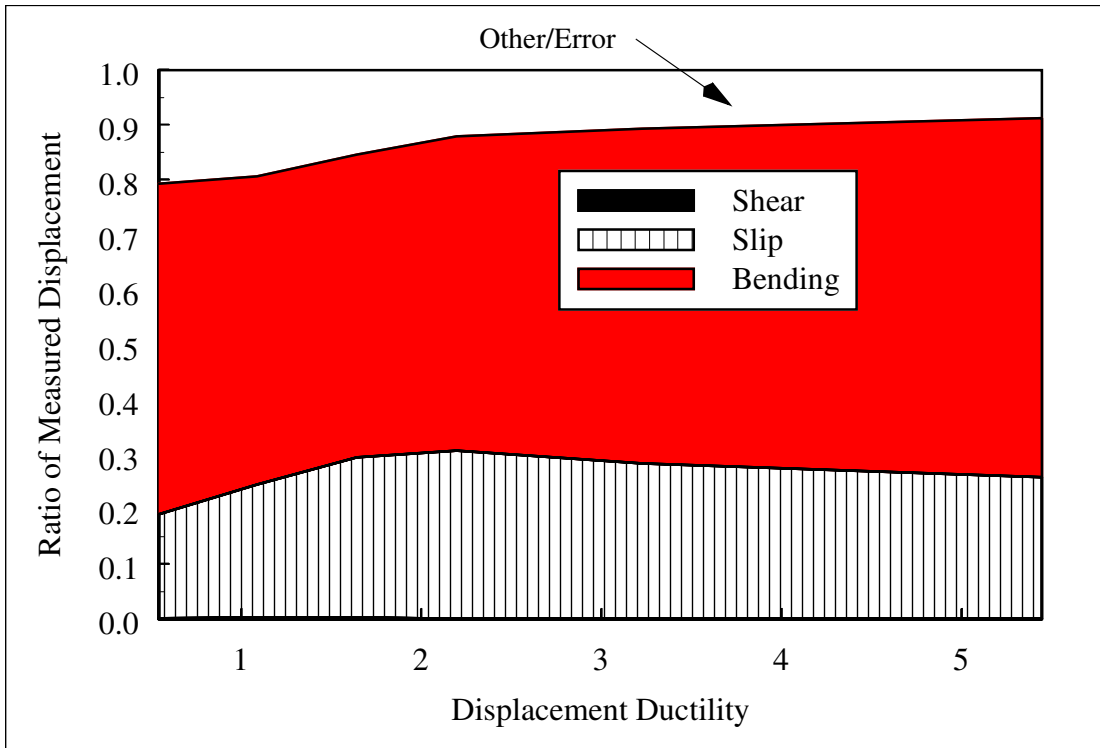


Figure 3.40: Column 1015 Displacement Components

# 4 Modeling and Design Implications

## 4.1 INTRODUCTION

Seismic design of reinforced concrete bridges requires that yielding elements withstand the expected cyclic deformation demand. Sophisticated numerical modeling may be required to fully characterize the cyclic response of the structure. The inelastic response of reinforced concrete elements, such as columns, joints, and beams is complex, and even the most sophisticated modeling of an element can require simplification. Therefore, analysis and design methods must be evaluated using experimental results.

The seismic design process has numerous phases; the procedures used for seismic design vary from simple to complex. For strength-based design methods, initial estimates of the stiffness and strength are used to perform an elastic analysis to assess the structural force demands. In the process the design may be refined and the structure reanalyzed. More accurately assessment of the deformation, energy, and cyclic demands may require more sophisticated structural modeling techniques and analysis methods. As a minimum, the design, modeling, and analysis procedures must meet those specified by the governing seismic design standard. For complex structures, further refinement of the seismic analysis may be warranted or required.

Design and analysis models of varying complexity have been developed. In this chapter, methods to compute the strength, the force-displacement response envelope, and the cyclic force-displacement response will be evaluated. For each method, comparison of the measured and predicted responses is made, and, if appropriate, modifications are suggested. Methods to estimate the column flexure and shear strengths, joint shear strength, force-displacement response envelope, element hysteresis, and element damage are included.

## 4.2 DESIGN STRENGTH

Seismic design standards specify methods to assess column flexural strength, column shear strength, and joint shear strength. The following sections evaluate the expressions found in common design standards including the Caltrans Bridge Design Specification [Caltrans 1991], pro-

posed modifications to this design standard as found in the ATC 32 document entitled *Improved Seismic Design Criteria for California Bridges: Provisional Recommendations* [ATC 1996], and the New Zealand Concrete design standard [NZS 1995].

#### 4.2.1 Column Flexural Strength

Seismic design standards specify methods to assess the nominal and ultimate flexural strengths of yielding elements. Typically, the plastic moment strength,  $M_p$ , can be approximated as the product of the nominal moment strength,  $M_n$ , which corresponds to a maximum extreme fiber strain of 0.003, and an amplification factor,  $\alpha$ . Previous studies have shown that the amplification factor depends on the longitudinal reinforcement ratio, spiral reinforcement ratio, axial load ratio, and material strengths [e.g, Aschheim 1997].

Following testing, the columns were analyzed using the cross-sectional analysis program ArCS [Thewalt 1994]. The measured geometry, measured longitudinal bar locations, and measured material properties were used in the analysis. Using measured properties gives an indication of the analysis method. In the analysis program, the column cross section was modeled using material-specific fibers. For each column cross section a mesh was developed using a 26 by 12 mesh. The model developed by Mander et al. [Mander 1984] was used to model the unconfined and confined concrete sections.

Table 4.1 indicates the analytical results for the five columns. The maximum plastic flexural strength,  $M_p$ , corresponds to a limiting longitudinal tensile strain of  $0.5\epsilon_{max}$  where  $\epsilon_{max}$  is the strain corresponding to the maximum steel stress designated. For the test columns, the strain limit was calculated using the measured stress-strain response of the longitudinal steel. The measured  $\epsilon_{max}$  was 0.15 in./in.; therefore the flexural strength was assessed at a strain corresponding to half of the maximum strain or 0.075 in./in. The maximum flexural strength measured during testing,  $M_{max}$ , is indicated in the fourth column of Table 4.1. The ratio of the plastic strength,  $M_p$ , and the maximum measured moment  $M_{max}$  is provided in the last column of Table 4.1. The results for the five column sample set indicate an average ratio of 1.0 and a standard deviation of 0.1. The analysis provides reliable results. In an actual design situation, it is unlikely that the as-built geometry or actual material properties will be available to the designer. An actual design should account for the uncertainty in the bridge material and construction.

In some cases, such as initial design, a sophisticated analysis will not be warranted. As an

alternative method, most codes provide factors to magnify the nominal moment strength to obtain the plastic moment strength, i.e.,  $M_p = \gamma M_n$  [Caltrans 1991, ATC 1996, NZS 1995]. The amplification factor varies. In the Caltrans specifications, an amplification factor of 1.3 is specified; the ATC 32 report recommends an amplification factor of 1.4.

Results from cross-sectional analyses were used to evaluate the recommended amplification factors. The effects of material strength, axial load, and longitudinal reinforcement ratio were identified.

To study the effect of material strength, cross sections were analyzed using the specified material strengths and the expected material strengths. The specified strength is the minimum strength; the expected strength includes the material overstrength to approximate the actual strength. The three cross sections tested as part of the experimental study were analyzed using the analysis program ArCS [Thewalt 1994] using the specified and expected material strength. An axial load of 147 kips was applied (axial load used in testing). The specified and expected material strengths used are those indicated in Chapter 3. The results are shown in Table 4.2. The ratio of the nominal flexural strengths calculated using expected and specified material strengths is approximately 1.1. This ratio is the same as the ratio of the expected strength to the specified strength of the longitudinal steel. The results indicate that for low axial load ratios (below  $0.2A_g f'_c$ ), the longitudinal steel amplification factor can be used to obtain the expected flexural strength from the nominal flexural strength.

It has been demonstrated that the ratio of the plastic moment capacity to the nominal moment capacity depends on the longitudinal reinforcement ratio and axial load ratio [Aschheim 1997, ATC 1996]. Figure 4.1 indicates the variation in the amplification factor as a function of the axial load ratio and the longitudinal reinforcement ratio. A general trend is that an increase in the longitudinal reinforcement ratio or the axial load ratio will result in an increase in the amplification factor. For axial load ratios less than  $0.2A_g f'_c$ , the maximum amplification factor ranges from approximately 1.15 for a longitudinal reinforcement ratio of 0.75% to 1.3 for a longitudinal reinforcement ratio of 3.0%. As an alternative to a detailed analyses, the plastic moment of columns with low axial load ratios may be assessed by amplifying the expected nominal moment strength by 1.3.

### 4.2.2 Column Shear Strength

Table 4.3 summarizes the shear strength expressions specified in the Caltrans design standard, ATC 32 document, the NZS concrete design standard, as well as proposed revisions to ACI 318 [Moehle 1998]. In the standards, the nominal shear strength,  $V_n$ , is specified to be the sum of the shear strength attributed to the concrete,  $V_c$ , and the shear strength attributed to the transverse steel,  $V_s$ . The concrete shear strength is a function of the square root of the compressive strength of the concrete,  $\sqrt{f'_c}$ , the effective area,  $A_e$ , and the axial stress,  $P/A_g$ . The nominal shear strength attributed to the spiral,  $V_s$ , is a function of the area of the spiral,  $A_s$ , spiral yield strength,  $f_{yh}$ , column diameter,  $D$ , and spiral spacing,  $s$ .

The expressions were evaluated using the five columns tested. For Column 430, the column with the highest shear demand, the values resulting from the four shear strength equations vary from approximately 150 kips (33 kN) to 230 kips (51 kN). Experimental observations revealed little signs of shear distress for the five columns. Table 4.4 tabulates the ratios of the measured shear demand,  $V_{pm}$ , to the shear strength,  $V_n$ , for each column. For Column 430, the ratio of  $V_n/V_{pm}$  ranges from 1.4 to 2. All four expressions correctly indicate that shear failure was suppressed.

### 4.2.3 Joint Shear Strength

Figure 4.2 shows an idealized free-body diagram of the joint region of a typical test specimen. The upper bound of the joint shear demand is estimated from tensile force demand,  $T$ , in column. The tensile force is approximated using Equation 4.1.

$$V_j \cong T = \frac{M_p}{0.9D} \quad (4.1)$$

The magnitude of the joint shear stress,  $v_j = V_j/A_j$ , depends on the definition of the joint area. The ACI and New Zealand standards define the joint area as the product of the column depth,  $D$ , and the joint depth,  $H_j$ , that is,  $A_j = D*H_j$ . The joint area specified in the ATC 32 document is larger; for a footing-column joint, the maximum joint area,  $A_j$ , is equal to the product of the joint depth,  $H_j$ , and an effective joint width. The model specifies that the joint width is three times that of the joint depth, i.e.,  $D*3H_j$ . However, the anchor block used in the test columns had a width of

two times the depth. Therefore, the joint area used was  $A_j = 2D*H_j$ .

The allowable joint shear stresses specified in the ACI standard, the New Zealand standard, and the ATC 32 document are given in Table 4.5. The resulting demand/capacity ratios for each standard are listed. The joint shear strength would be deemed adequate using any of the three provisions.

### **4.3 RESPONSE ENVELOPE**

Design methods may require modeling of the force-displacement response envelope or the full, cyclic response of the system. The response envelope may be used for pushover analyses or to define the limits of element hysteresis. Hysteresis force-displacement models may use a backbone curve based on the monotonic force-displacement response with additional rules to characterize the cyclic response.

The post-yield response of a column can be modeled either by integrating the inelastic deformations over the height directly or by lumping effects using a plastic hinge model. Difficulties computing the shear and slip contributions to the overall displacement have made direct modeling of the individual deformations components impractical for most design problems. Although recent efforts have improved modeling techniques, simplified models such as the plastic hinge length model are convenient for initial design. In some cases, further refinement may be warranted. The following section develops two models, one based on discrete modeling of deformation components and another based on a simplified plastic hinge approach.

#### **4.3.1 Discrete Model**

Displacement components that contribute to the tip displacement of a reinforced concrete column fixed into a joint are assumed to be bending along the column length, shearing along the column length, and fixed end rotation resulting from slip of the longitudinal reinforcement out of the joint. Figure 4.3 shows a cantilever column subjected to a lateral load. Approximate shapes of the slip ( $\Delta_s$ ), shear ( $\Delta_v$ ), and bending ( $\Delta_b$ ) deformations along the column length are shown. Using a flexibility based approach, the tip displacement is the sum of the three components, as indicated by Equation 4.2.

$$\Delta = \Delta_b + \Delta_s + \Delta_v \quad (4.2)$$

In the following sections, the models used to calculate the response of displacement components are evaluated using the experimental results.

#### 4.3.1.1 Bending

Bending along the column length may contribute a significant portion of the tip displacement. Analysis of the bending displacement component requires knowledge of the complete moment-curvature response. The bending displacement,  $\Delta_b$ , is computed by integrating curvature,  $\phi$ , over the length of the column,  $L$ .

$$\Delta_b = \int_0^L \phi(x) x dx \quad (4.3)$$

To compare the measured and predicted results, each test column was analyzed. For each column cross section, a moment-curvature analysis was performed using the analysis program ArCS [Thewalt 1994]. The software program uses a displacement-based finite element approach. The cross-section mesh was developed. Unconfined and confined concrete and longitudinal steel were specified for each segment when appropriate; the measured material properties were used when possible including the stress-strain relationship of the longitudinal steel and the stress-strain relationship of the unconfined concrete. The effects of confinement on the concrete were modeled using the confined concrete stress-strain model from [Mander 1988]. Figure 4.4 shows the measured and predicted stress-strain responses of the longitudinal steel; the predicted response was modeled to a strain of  $\epsilon_{max} = 0.08$  in./in.

Figures 4.5 and 4.6 show the predicted moment-curvature response and the measured moment-average curvature response for each column of Test Series I and the Test Series II. Since the measured rotation at the column base included both slip and bending deformations, the response measured for the adjacent instrumented segment, which extended from 6 inches to 12 inches, was used. This analysis assumes the curvature distribution is uniform over the lower 12 inches of the column. The average curvature of this segment was plotted against the maximum moment (this assumes that the curvature distribution is approximately uniform over the lower 12 inches of the column). Theoretically, the moment capacities of the three columns of Test Series II (Columns 415, 815, and 1015) are identical. However, as indicated in Figure 4.6, the flexural

strength of the three columns is different. However, the trend does not indicate that the differences were simply due to second-order effects. Initially, it was thought that the load cells used in the testing of Columns 815 and 1015 (which were different than those used in testing of the three other columns) were not calibrated correctly. However, the data were thoroughly reviewed and no errors were found.

Finally, the predicted and measured responses at the top of the column are compared. Figures 4.7 and 4.8 show the predicted and measured response envelopes. The measured bending displacement is calculated by summing the product of the measured segment rotation and the rotation arm to the top of the column without readings from the bottommost instrument. The predicted and measured response envelopes are similar.

#### 4.3.1.2 Slip

In modern construction, the column longitudinal reinforcement is well anchored into the joint region. As shown in Figure 4.9, axial deformation of the longitudinal bar into the joint region results in a rotation at the column-joint interface. For a column subjected to axial load and flexure, the longitudinal reinforcement displaces both in tension,  $u_{st}$ , and in compression,  $u_{sc}$ , where  $u_{st}$  and  $u_{sc}$  are the vertical displacements in the extreme bars at the column joint interface resulting from straining of the embedded bars (and are defined to be positive in tension). The fixed-end rotation,  $\theta_{slip}$ , is the difference in the two displacements divided by the distance between the two column bars,  $D''$  (Equation 4.4).

$$\Delta_{tip} = \theta_{slip} L; \theta_{slip} = \frac{u_{st} - u_{sc}}{D''} \quad (4.4)$$

The slip displacement,  $u_{st}$  or  $u_{sc}$ , is calculated by summing the axial strains over the anchored bar length. Mathematically the strain distribution may be assessed using a one-dimensional model. The governing differential equation expressing equilibrium along an infinitesimal portion of the bar is shown in Equation 4.5 where  $\tau(x)$  describes the bond stress distribution over the length of the bar and  $\sigma(x)$  describes the axial stress distribution over the length of the bar.

$$\frac{d\sigma}{dx} - \alpha\tau(x) = 0 \quad (4.5)$$

The variable  $\alpha$  is the ratio of the bar circumference to the bar area or

$\alpha = (\pi d_b)/((\pi d_b^2)/4) = 4/d_b$  where  $d_b$  = the longitudinal bar diameter. Strain-slip compatibility is expressed in Equation 4.6, where the strain in the reinforcing bar is denoted  $\varepsilon$  and the slip displacement is denoted  $u$ . The influence of the concrete deformation on the slip displacement is assumed to be negligible.

$$\varepsilon(x) = \frac{du}{dx} \quad (4.6)$$

The steel constitutive law (Equation 4.7) is used to relate the bond force to the slip.

$$\sigma = \sigma(\varepsilon) \quad (4.7)$$

The fully anchored bar is studied in Figure 4.8. The bar is divided into numerous segments of length  $x$ . Figure 4.9 shows a discrete bar length,  $x$ , with ends  $i$  and  $i+1$ . The bar force at each end is  $N_i = \sigma_i A_b$  and  $N_{i+1} = \sigma_{i+1} A_b$ . The boundary conditions on the bar are  $u = u_i$  at end  $i$  and  $u = u_{i+1}$  at  $i+1$ . The slip response of the segment is analyzed using Equations 4.8, 4.9, and 4.10. The bond stress and steel modulus are constant over the discrete bar segment.

$$u_{i+1} = \frac{(\varepsilon_{i+1} + \varepsilon_i)}{2} x + u_i \quad (4.8)$$

$$\sigma_i = \sigma(\varepsilon) \quad (4.9)$$

$$\tau = \frac{(\sigma_{i+1} - \sigma_i)}{\alpha x} \quad (4.10)$$

The slip at the column-joint interface is the summation of the segment slip displacements. The boundary conditions at the fully developed end are known, i.e., at  $x=0$ ,  $u=0$  and  $\varepsilon=0$ , the expression for the total slip at the end of segment  $n$  follows.

$$u_n = \int \varepsilon(x) dx \cong \sum_{i=1}^n \left( \frac{(\varepsilon_{i+1} + \varepsilon_i)}{2} \cdot x \right) \quad (4.11)$$

The preceding expressions were adopted and used to establish the bond-slip response of the longitudinal bars anchored in the test specimens using the strain gauge data. Three strain gauges were placed on the longitudinal steel with an 8-inch spacing, approximately 12 bar diameters. (For the locations, see *Seismic Performance of Well-Confined Concrete Bridge Columns* (Lehman

1998).) Average bond stress and slip values were computed at the end of each gauged segment using Equations 4.10 and 4.11. Using the measured longitudinal strains in Equation 4.11, the steel stress values corresponding to the strain readings were evaluated using the reinforcing steel model by Filippou et al. [Filippou 1983].

Figure 4.10 shows the resulting experimental bond-slip response for Column 415. The bond-slip response was assessed for the entire development length. Since the measured strain readings from the lowest strain gauge were less than yield strain, the development length (or the zero strain point) was linearly interpolated using the readings of the lower two longitudinal strain gauges. (Note, the strain gauge readings for all three gauges from Column 415 were reliable enough to assess the bond-slip response.) A model of the bond-slip response envelope was developed using the experimental results; the model is shown in Figure 4.10. The shape of the model was adapted from the model proposed by Eligehausen et al. [Eligehausen 1983]. As indicated in the figure, there are four transition points where the slope of the bond stress-slip response curve changes. The bond-slip response is linear to a slip value of 0.008 in. (0.2 mm). In the range of slip values from 0.008 to 0.015 in. (0.4 mm), the bond stress is a constant and equal to 0.9 ksi (6.2 MPa). In the range of slip values from 0.015 in. to 0.04 in. (1 mm), the bond stress linearly decreases from 0.9 ksi to 0.2 ksi (1.4 MPa). For slip values exceeding 0.04 in., the bond-stress is constant and is equal to 0.2 ksi. In compression, the assumed bond stress-slip response is linear with a slope of 0.9 ksi/0.008 in. (6.2MPa/0.2 mm).

The tip displacement resulting from slip of the embedded reinforcement requires an estimate of the magnitude of the tensile and compressive slip values (Equation 4.4). The strain distribution over the development length can be calculated using the bond distribution over the development length and the maximum strain demand. The slip value is determined by directly integrating the strains. The maximum strain demand,  $\epsilon_n$ , is assessed from the results of the moment-curvature analysis.

The slip values in the two extreme longitudinal bars were calculated using Equations 4.8 through 4.11. The measured and predicted force-slip displacement envelopes for each column are shown in Figures 4.11 and 4.12. The measured response is assessed using the lower vertical displacement gauges (Level 4).

Simplification of the bond-slip model resulted in the bi-uniform bond model shown in Figure 4.13. In the model, the transition slip value,  $u_y$ , corresponds to the yield strain in the bar and is approximated as 0.017 in. (0.4 mm). For slip values less than  $u_y$ , the bond stress capacity is

$12\sqrt{f'_c \text{ psi}}$ . For slip values exceeding  $u_y$ , the bond stress capacity is  $6\sqrt{f'_c \text{ psi}}$ . For  $u < u_y$ , Equations 4.12 and 4.13 are used. For  $u > u_y$ , Equations 4.14 and 4.15 are used. In the expressions,  $d_b$  is the longitudinal bar diameter,  $E$  and  $E_{sh}$  are the secant elastic modulus and secant strain hardening modulus of the steel, respectively,  $\varepsilon$  is the maximum strain,  $\varepsilon_y$  is the yield strain,  $l_{de}$  and  $l_{di}$  are the development lengths over the elastic and inelastic portions of the bar, and  $l_{dy}$  is the length required to develop the yield stress. The concrete compressive strength,  $\sqrt{f'_c}$ , is in units of psi. Equation 4.4 is used to determine the slip displacement at the tip of the column.

$$\text{for } \varepsilon \leq \varepsilon_y \quad l_{de} = \frac{E\varepsilon d_b}{48\sqrt{f'_c}} \quad (4.12)$$

$$u_{se} = 0.5\varepsilon l_{de} \quad (4.13)$$

$$\text{for } \varepsilon > \varepsilon_y \quad l_{di} = \frac{E_{sh}(\varepsilon - \varepsilon_y)d_b}{24\sqrt{f'_c}} \quad (4.14)$$

$$u_{si} = 0.5(\varepsilon + \varepsilon_y)l_{di} + 0.5\varepsilon_y l_{dy} \quad (4.15)$$

Figure 4.14 shows the force-slip displacement response curves predicted for the three columns of Test Series I. The measured response envelopes are shown with a solid line. As expected, the results obtained from using the four-transition bond-slip model better approximate the measured bond-slip response than the results obtained from using the bi-uniform model; in particular, the initial response is better. However, the bi-uniform model is efficient computationally. For initial design, use of the bi-uniform bond model is appropriate.

#### 4.3.1.3 Shear

For columns with low levels of shear, an intricate shear model is not warranted. Of the columns tested, the largest shear demand was for Column 430 and was  $v = 3.9\sqrt{f'_c \text{ psi}}A_g$ . A shear model based on elastic principles was used to assess the overall shear displacement. Typically, the shearing deformation of uncracked reinforced concrete member is assessed using an elastic model based on the principles of elasticity, i.e.,

$$\Delta_v = \frac{VL}{AG}; \quad G = \frac{E}{2(1 + \mu)} \quad (4.16)$$

where  $V$  is the shear demand,  $L$  is the column length,  $G$  is the bulk modulus,  $E_c$  is the elastic modulus of the concrete, and  $\mu$  is Poisson's ratio.

The shear model uses an adaptation of the approach as shown in Equation 4.17. At each plane, the bulk modulus  $G_{eff}(x)$ , the effective shear area,  $A_{eff}$ , and the elastic modulus,  $E_c(x)$ , are determined;  $\mu$  is approximated as 0.3. The bulk modulus distribution,  $G_{eff}(x)$ , is determined using Equation 4.18;  $E_c$  is assessed from the corresponding normal compressive stress and strain demands at the extreme fiber of the concrete core as shown in Figure 4.15. The effective shear area,  $A_{eff}(x)$ , is approximated as the area of concrete subjected to compressive strains, where  $R$  = the column radius,  $\phi(x)$  = the curvature,  $\epsilon_{cu}(x)$  = maximum compressive strain corresponding to  $\phi(x)$ .

$$\Delta_v = \int_L \frac{V(x)dx}{G_{eff}(x)A_{eff}(x)} = V \int_L \frac{dx}{G_{eff}(x)A_{eff}(x)} \quad (4.17)$$

$$G_{eff}(x) = \frac{E_c(x)}{2(1 + \mu)} \quad (4.18)$$

$$A_{eff} = \frac{1}{2}R^2(\psi(x) - \sin(\psi(x))) \text{ where } \psi(x) = \arccos\left(\frac{R - (\epsilon_{cu}(x))/(\phi(x))}{R}\right) \quad (4.19)$$

Figures 4.16 and 4.17 show the measured and predicted force-shear displacement response using the expression for each test series.

#### 4.3.1.4 Comparison of Force-Displacement Response Envelopes

The discrete modeling method was used to compute the predicted curve. Figures 4.18 and 4.19 indicate the predicted and measured force-tip displacement response envelopes for Test Series I and Test Series II, respectively.

Experimental results indicate that column failure was initiated by bar buckling and in most cases, a direct result of longitudinal bar fracture. This failure mode was, in part, induced by the cyclic nature of the loading. Therefore, in comparison with monotonic loading, fatigue effects may account for the limited displacement capacity. Since column failure was primarily due to the response of the longitudinal steel, the curvature capacity was predicted to correspond to a pre-defined tensile strain capacity; this method differs from methods that limit the compressive strain capacity of the core concrete [e.g., Priestley 1996]. Therefore, in the figures, the predicted maxi-

imum displacement corresponds to a tensile strain in the longitudinal steel of  $\epsilon_{max} = 0.5\epsilon_u$  where  $\epsilon_u$  is the strain corresponding to the maximum stress. For the columns that were tested, the ultimate curvature corresponded to a tensile steel strain of 0.08. The model implicitly accounts for fatigue effects. Models that explicitly include fatigue effects are provided in Section 4.4.2.

Comparing the predicted and measured response curves of Test Series I, as shown in Figure 4.18, indicates that the response is well approximated over the entire displacement range. The strengths, ultimate displacements, and shapes of the response envelopes are similar. The predicted and measured force-displacement response curves for the Test Series II columns are comparable. However, the strengths of the three columns are not predicted as well as for the Test Series I columns. The predictive model assumes identical moment-curvature response for the three columns. However, the experimental results indicate different flexural strengths. The model overestimates the strength of Column 1015 and underestimates the strength of Column 815. However, other aspects of the predicted results of the Test Series II columns, including initial stiffness, yield displacement, and ultimate displacement, are similar to the comparable measured responses.

### 4.3.2 Simplified Model (Plastic Hinge Length Model)

As shown in Figure 4.20, the post-yield bending response of a reinforced concrete member is highly nonlinear. In addition to bending, the force-displacement model must also include contributions of the other components, e.g., shear and slip. In some cases, a more approximate method may be desirable to expedite the assessment of the force-displacement response. A widely used simplified model is the plastic hinge length model. Originally, the plastic hinge length method was used to perform a simplified failure analysis. Therefore, models were correlated to the measured displacement capacity. In a performance-based design environment, consideration of additional engineering limit states may be required. Development of a plastic hinge length model that can reliably assess additional limit states is useful. Additional discussion of the plastic hinge length method can be found in Chapter 2.

The plastic hinge length method uses Equations 4.20 and 4.21 to calculate the total and plastic displacements,  $\Delta$  and  $\Delta_p$ . For circular columns, the post-yield displacement is the sum of the effective yield displacement,  $\Delta_y'$ , and the plastic displacement,  $\Delta_p$ . For curvatures greater than the yield curvature, Equation 4.21 is used to compute the plastic displacement. In the expression,  $l_p$  is the plastic hinge length.

$$\Delta = \Delta_p + \Delta_y' \quad (4.20)$$

$$\Delta_p = (\phi - \phi_y)l_p(L - l_p/2) \quad (4.21)$$

Several plastic hinge length models were discussed in Chapter 2. A plastic hinge length model similar to the method described in [Priestley 1996] was adopted in the ATC 32 report for the seismic design of bridge columns. In this chapter, the method from Priestley et al. [Priestley 1996] was evaluated using the experimental results. The method is limited in that it was intended for use in the failure analysis of bridge columns. Herein, a new model is proposed to assess the entire force-displacement response. The model is based on the discrete modeling approach. The model permits the evaluation of intermediate displacement levels.

#### 4.3.2.1 Plastic Hinge Length by Priestley et al.

The Priestley et al. method was derived using experimental results of reinforced concrete bridge piers. The equations form the basis of methods used in the ATC 32 report. Equations 4.22, 4.23, and 4.24 specify expressions to calculate the yield displacement, plastic hinge length, and ultimate compressive strain capacity.

$$\Delta_y' = \frac{M_n}{M_y}\Delta_y; \Delta_y = \frac{\phi_y}{3L^2} \quad (4.22)$$

$$l_p = 0.08L + 0.15f_yd_b \quad (f_y \text{ in ksi}) \quad (4.23)$$

$$\epsilon_{cu} = 0.004 + 1.4 \frac{\rho_s f_{yh} \epsilon_{fs}}{f_{cc}'} \quad (4.24)$$

Equation 4.22 defines the effective yield displacement,  $\Delta_y'$ . In the expression  $\Delta_y$  = the displacement at first yield of the longitudinal reinforcement,  $M_y$  is the calculated moment at first yield, and  $M_n$  is the nominal strength corresponding to a maximum compressive strain of 0.004 in the concrete cover. The factor  $M_n/M_y$  amplifies the value  $\Delta_y$  to account for the progressive yielding of a circular cross section.

The plastic hinge length,  $l_p$  (Equation 4.23) has two components. The first term mainly accounts for column bending; the second mainly accounts for bar slip. In Equation 4.23, the vari-

ables are  $L$  = the column length,  $f_y$  = the yield strength of the longitudinal steel, and  $d_b$  = the longitudinal bar diameter. The curvature capacity is limited by the capacity of the core concrete, as specified in Equation 4.24. The compressive strain capacity is approximated as the sum of the unconfined strain capacity, 0.004, and the enhanced strain capacity due to confinement effects. In Equation 4.24, the variables are defined as follows:  $\rho_s$  = the spiral reinforcement ratio,  $f_{yh}$  = the spiral yield strength, and  $\epsilon_{fs}$  = the spiral fracture strain. The product of the three variables,  $\rho_s f_{yh} \epsilon_{fs}$ , is normalized to the enhanced strength of the concrete due to confinement effects,  $f_{cc}'$ , which may be approximated as  $1.7f_c'$ .

Figures 4.21 and 4.22 show the force-displacement response predicted using the equations. Values of the yield and ultimate curvatures, yield and ultimate moments, and the plastic hinge lengths for each column are provided in Table 4.7. Table 4.8 presents the yield, spalling and ultimate displacement values predicted of the five test columns. The model adequately predicts the secant stiffness to the yield displacement. The predicted displacement capacity for all five columns is underestimated. In addition, the displacement capacities measured for the three columns of Test Series I indicate an increasing trend, that is, an increase in the longitudinal reinforcement ratio results in an increase in the displacement capacity (Figure 4.21). However, the predicted responses do not follow this trend. On average, the method underestimates the displacement capacity by half (the average is shown in the last row).

#### 4.3.2.2 Proposed Plastic Hinge Length

An alternative plastic hinge length based on the discrete model was proposed. The method permits calculation of pre-yield and post-yield displacements. For curvature demands less than the effective yield curvature,  $\phi_y'$ , the expressions shown in Equations 4.26 through 4.29 are used to compute the displacement. As with the discrete model, the elastic displacement,  $\Delta$  is the sum of three components: bending ( $\Delta_{be}$ ), slip, ( $\Delta_{se}$ ), and shear, ( $\Delta_{ve}$ ). The effective yield curvature, as defined in Equation 4.25, was adopted from Priestley et al. [Priestley 1996]. The variables used in the expressions have been defined previously.

$$\phi_y' = \frac{M_n}{M_y} \phi_y \quad (4.25)$$

$$\Delta_e = \Delta_{be} + \Delta_{se} + \Delta_{ve} \quad (4.26)$$

$$\Delta_{be} = \frac{\phi L^2}{3} \quad (4.27)$$

$$\Delta_{se} = \phi L \frac{d_b f_y}{96 \sqrt{f'_c} psi} \quad (4.28)$$

$$\Delta_{ve} = \frac{M}{0.4 E_{cs} A_{eff}} \quad (4.29)$$

$$\Delta_y' = \frac{M_n}{M_y} \Delta_y; \Delta_y = \Delta_e(\phi_y) \quad (4.30)$$

At section yield, the secant modulus of the concrete,  $E_{cs}$ , may be estimated as  $(f'_c)/0.002$ .

For displacements beyond yield, Equation 4.21 is used. The plastic displacement capacity is the sum of the plastic bending,  $\Delta_{bp}$ , and the plastic slip,  $\Delta_{sp}$ , contributions, i.e.:

$$\Delta_p = (\Delta_u - \Delta_y) \cong \Delta_{bp} + \Delta_{sp} \quad (4.31)$$

Using a linear approximation of the post-yield curvature distribution, the plastic flexural displacement is calculated using Equation 4.31. Equation 4.32 uses a simplified version of the bi-uniform bond model. The expression for the plastic slip displacement is similar to its elastic counterpart (Equation 4.28); a uniform bond strength of  $6 \sqrt{f'_c} psi$  for 5000 psi concrete is used for the portion of the embedded bar for which the strain exceeds the yield strain.

$$\Delta_{bp} = \frac{1}{2}(\phi_u - \phi_y') l_y (L - l_y / 3) \text{ where } l_y = \frac{(M_u - M_n) L}{M_u} \quad (4.32)$$

$$\Delta_{ps} \cong \frac{(\phi_u - \phi_y')(f_u - f_y) d_b L}{48 \sqrt{f'_c}} \quad (4.33)$$

The plastic hinge length is obtained by rewriting the proposed model for the ultimate displacement (Equation 4.34). The plastic slip displacement is approximated by assuming  $(\phi_u - \phi_y') \cong (\phi_u + \phi_y')$ . The longitudinal steel strength,  $f_u$ , and moment strength,  $M_u$ , corresponding to the curvature  $\phi_u$  are used.

$$l_p = \frac{l_y}{2} + \frac{(f_u - f_y) d_b}{(40 \sqrt{f'_c} psi)} \quad (4.34)$$

$$\phi_{max} = \frac{0.5 \epsilon_u}{D' - c} \quad (4.35)$$

The ultimate displacement capacity is assessed at a curvature of  $\phi_{max}$  corresponding to a limiting tensile steel strain equal to half of the strain corresponding to the maximum stress,  $\epsilon_u$  (Equation 4.35). This limiting strain value implicitly accounts for the cyclic effects of the imposed displacement history.

Figures 4.23 and 4.24 show the measured and predicted force-displacement response curves; the predicted response is shown with a dashed line for each column. The proposed plastic hinge length method predicts the force-displacement response for the five columns.

Table 4.9 provides the displacement values approximately corresponding to the effective yield, spalling, and ultimate states. In the analysis, concrete spalling was estimated at a strain of 0.008 in the concrete cover. The ultimate displacement was estimated at a tensile strain value of 0.08 in/in. The proposed model is capable of assessing intermediate post-yield limit states such as spalling and failure. However, for the two slender columns, the predicted displacement capacity exceeds the measured displacement capacity, likely a result of the linearization of the post-yield curvature diagram. For slender columns, the nonlinear shape of the curvature diagram is more pronounced and the proposed model overestimates the bending component.

The results using the plastic hinge length method formulation by Priestley et al. and that proposed herein are shown in Tables 4.8 and 4.9. The average ratios range from 0.5 to 1.3 for the Priestley methods. The range of the ratios calculated using the proposed method range is smaller and is from 0.8 to 1.1. The two methods are approximately equal if the flexural demand,  $M_{max}$ , is 16% greater than the yield strength,  $M_y$ , and the ultimate strength of the longitudinal steel is twice the yield strength (which may be a high estimate). Comparison of the displacement values corresponding to the limiting curvature in Equation 4.35 reveals similar values (column 4 in Table 4.8 and column 3 in Table 4.9). Therefore, the two plastic hinge length expressions are similar in the large displacement range.

#### 4.4 CYCLIC RESPONSE

Cyclic loading has a significant effect on the response, damage sequence, and failure mode of a reinforced concrete bridge column. In earthquake engineering design, a bridge is expected to respond in the post-yield range. The cyclic nature and severity of the seismic loading may require techniques to model the structural response and performance.

Various types of models are available to determine the cyclic force-displacement history of a reinforced concrete structure. Simpler models include single-degree-of-freedom models that model the force-displacement response as a single-degree-of-freedom oscillator. This type of modeling is convenient for multiple column bridges although it is limited to unidirectional seismic excitation which may require independent analyses in each response direction. In Section 4.4.1, the experimental results are used to evaluate the models.

Previous experimental results have demonstrated the influence of displacement history on column performance [Kunnath 1997]. As discussed in 2, research studies have focused on methods to assess damage of reinforced concrete elements (e.g., beams and columns) and structures subjected to seismic loading. The expressions are typically called damage indices. A damage index provides an estimate of the element performance, particularly in reference to column failure. In Section 4.4.2, a new damage index is developed considering experimental observations.

#### **4.4.1 Hysteresis Modeling**

During an earthquake, a structure may experience numerous displacement excursions beyond yield. Because the load path can be complex, the response of a yielding structure subjected to seismic excitations is usually described using a hysteresis model. Dynamic analysis requires that the hysteresis model adequately model the element stiffness and energy dissipation, particularly in the post-yield range. In addition, the cyclic displacement history affects the damage sequence and column failure mode. Typically, damage ratio expressions combine noncyclic and cyclic loading components, requiring assessment of cyclic effects and appropriate hysteresis modeling techniques. (See Chapter 2 for discussion of damage indices).

Figure 4.26 shows the hysteresis model developed during the research investigation. The proposed model is similar to previously developed models [e.g., Saiidi 1979, Moehle 1980, Takeda 1970]. The model consists of a backbone curve, and unloading and reloading curves. Six distinct rules are defined, numbered 1 through 6, and are indicated by the circled numbers in the figure. Three rules define the trilinear backbone curve, indicated by the thick grey line. The break-points in the curve roughly correspond to yield, concrete spalling, and element fatigue. The primary unloading and reloading curves, indicated by thin black lines in the figure, are bilinear. The transition point of the unloading curve occurs when the force is zero. The secondary unloading and reloading curve, indicated by the dashed line, are linear to the intersection point with the

unloading curve from the maximum point.

The three break-points approximately correspond to yield (yield), spalling (sp), and ultimate (ult). The yield point is defined by the effective yield displacement and force (Equations 4.25 to 4.29). The spalling point is defined by the displacement and force that correspond to a cover concrete compressive strain of 0.008 in./in. The ultimate point is defined by the displacement and force that correspond to a tensile steel strain in the extreme reinforcement equal to half the strain corresponding to the maximum stress under monotonic loading (in the case of the experimental columns, this strain limit was 0.08 in./in.). The analysis requires tracking of several history variables, including the displacement and force for the two previous loading steps, the maximum displacement and force ( $D_{max}$ ,  $F_{max}$ ), the minimum displacement and force ( $D_{min}$ ,  $F_{min}$ ), and the unloading displacement and force ( $D_{last}$ ,  $F_{last}$ ). Table 4.10 defines the stiffness, unloading rule, displacement limits, and exceedance criteria for each of the size rules. The rules are presented for loading in the direction of increasing displacement (i.e., the backbone curve values are positive) and unloading in the direction of decreasing displacement. The rules are easily adapted for the opposite case using the minimum values.

The unloading stiffness, shown in the table as  $k_4$  for Rule 4, is:

$$k_4 = k_1(\mu)^{-0.25} \quad (4.36)$$

where  $k_1$  is the pre-yield stiffness and  $\mu$  is the displacement ductility ( $\mu = (D_{max}/D'_y)$ ) where  $D_y$  = the effective yield displacement. The displacement ductility is based on the maximum displacement,  $D_{max}$ , when unloading from the positive backbone curve and the minimum displacement,  $D_{min}$ , when unloading from the negative backbone curve. The same holds for Rule 6 where the unloading point is less than the maximum (or greater than the minimum for the negative case). Therefore, the displacement ductility is the absolute value of  $D_{max}/D_y$  when unloading from the positive loading curve and the absolute value of  $D_{min}/D_y$  when unloading from the negative loading curve.

The hysteresis model was used to evaluate the cyclic force-displacement response of the five test columns. The results are shown in Figures 4.27 through 4.31. The results demonstrate that the model adequately represents the measured force-displacement response. Figures 4.32 and 4.33

indicate that the energy dissipation in a single cycle,  $E_{hi}$ , predicted using the hysteresis model (dashed line) and calculated from the experimental results (solid line); the energy dissipated in a single cycle,  $E_{hi}$ , is normalized with respect to the energy of a plastic response, i.e.,  $4*V_{max}D_{max}$  where  $V_{max}$  is the shear demand and  $D_{max}$  is the maximum displacement. In the figures, the cycle displacement is normalized with respect to the effective yield displacement. The results of the predicted and measured response envelopes are similar.

#### 4.4.2 Damage Index

Reversed cyclic loading influences the response and failure mode of a reinforced concrete element. The effect of cycling to large plastic demands must be considered when designing structures to withstand seismic demands.

Recent research efforts have evaluated the response of columns designed to meet large cyclic displacement ductility demands. The progression of damage that has been observed during pseudo-static unidirectional testing of these columns is markedly similar [Stone 1989, Kunnath 1997, Calderone 1998]. Chapter 3 provides a summary of the progression of damage.

The state of structural damage is indicative of the required repair effort and may influence the future performance. Damage indices are used to predict the state of structural or element damage, in particular the failure state. A cumulative damage index models the effect of cycling on structural damage using fatigue or energy models. Such models were reviewed in the latter part of Chapter 2. Since available test data were used, most models have been calibrated to the response of reinforced concrete elements subjected to standard displacement histories (i.e., increased displacement demand with cycling).

The experimental study described herein was not designed to study the effect of displacement history; nominally identical displacement histories were used for testing of the five test columns. Since the performance of a reinforced concrete element depends on the imposed displacement history, an experimental study designed to evaluate the effect of cycling on structural performance must include intermediate and extreme damage levels. The experimental investigation conducted by Kunnath et al. [Kunnath 1997] was designed to investigate the effect of displacement history on structural response and damage. As described previously, the researchers subjected 12 nominally identical columns to various displacement histories. Monotonic, standard, constant amplitude, and random displacement histories were imposed.

In the test program by Kunnath et al., four columns were subjected to constant amplitude displacement histories (designated Column A3, A4, A5, and A6), one column was subjected to a standard displacement history (similar to the displacement history used in the present study), and one column was subjected to a monotonic loading; six additional columns were tested using random earthquake loading [Kunnath 1997]. However, since the use of random loading histories makes it difficult to isolate the damaging cycles, these results were not included in the current analysis. These test results were used to evaluate damage indices and to develop a new fatigue-based model. An understanding of the progression of damage is required to evaluate the performance of a damage model. The following briefly summarizes the reported observations during testing. The report should be consulted for more detailed information.

Table 4.11 summarizes the salient properties for the four columns subjected to constant amplitude displacement histories; tabulated quantities include the imposed displacement and the estimated displacement ductility, the damage was observed for a nominally identical column subjected to monotonic loading at the same displacement demand, Column A1, the number of cycles required to remove the entire cover, and the total number of cycles to failure.

At significant displacement demands column failure is influenced by cyclic loading. The displacement ductility capacity of Column A1 (column subject to monotonic loading) exceeded 11. However, the displacement capacities of Columns A4, A5, and A6 are markedly reduced from this capacity and differ from one another. It is evident that cycling had a significant effect on the performance. For Column A3, which was subjected to a constant amplitude displacement demand approximately corresponding to a ductility of two, the imposed cyclic displacement demand of 150 cycles did not result in failure. At completion of testing, the concrete cover was still partially intact around the entire circumference in the lower region of the column. This result suggests that the restraint provided by the cover was sufficient to restrain the longitudinal bars and the core by delaying both bar buckling and spiral yielding; low-cycle fatigue of the column was delayed.

At significant displacement demands, cyclic effects are important. For these cases, damage should be assessed using a cumulative damage index. Kunnath et al. evaluated four damage indices using their experimental results including the energy-based damage index developed by Park and Ang [Park 1985] and a fatigue-based damage index, based on the Coffin-Manson equation using Miner's rule, developed by Mander and Cheng. Results from the evaluation are provided in Figure 4.34.

The Park-Ang damage index is a linear combination of a noncumulative and cumulative

damage index (see Chapter 2 for further discussion). In the evaluation by Kunnath et al., the strength reduction factor beta,  $\beta$ , was determined from the response of Column A2 (subjected to a standard displacement history); this value of  $\beta$  was used in the analysis of the remaining columns. The results indicate that Column A3 fails which it did not. Normalized energy significantly contributes to column failure in the numerical analysis of Column A3. However the experimental results indicate that significant energy demand does not result in significant damage. Failure analysis of Columns A5 and A6 using the Park-Ang model indicated that the columns did not fail, again opposite to the measured result. The analysis results lead Kunnath et al. to conclude that the Park-Ang model is most appropriate for column failure resulting from large plastic displacement demands.

Mander and Cheng used the Coffin-Manson equation to predict the number of cycles,  $2N_f$ , to cause for a specific strain demand,  $\epsilon_t$ . Equation 4.37 was based on fatigue tests of steel reinforcing bars. Miner's rule was used (Equation 4.38) to predict failure of a column subjected to various displacement demands; Miner's rule correlates failure with a damage index of one (i.e.,  $DI = 1$ ).

$$\epsilon_t = 0.08(2N_f)^{-0.33} \quad (4.37)$$

$$DI = \sum_i \left( \frac{1}{2N_{fi}} \right) \quad (4.38)$$

Using the Mander-Cheng fatigue-based damage index, failure was predicted for Columns A2, A4, and A5. The index predicted that Column A3 does not fail. However, column failure was not predicted for Column A6.

Asserting that fatigue-based models are more promising, the Kunnath research team derived a fatigue-based damage index that was correlated to their experimental results; the Coffin-Manson equation was used to determine the number of cycles,  $2N_f$ , that cause failure at a tensile strain demand in the longitudinal steel of  $\epsilon_t$  (Equation 4.39); The damage index was calculated using Miner's rule. The columns subjected to the random earthquake loading histories were evaluated. The index predicted failure for only two of the six columns.

$$\epsilon_t = 0.06(2N_f)^{-0.36}; \quad DI = \sum_i \left( \frac{1}{2N_{fi}} \right) \quad (4.39)$$

The studies show that predicting failure of a reinforced concrete element is difficult at best. The performance of Column A3 suggests that the energy dissipation capacity of a reinforced concrete element depends on the imposed displacement history. The experimental results imply that the energy-dissipation capacity is difficult to use to characterize element performance. In their present state, fatigue-based damage indices only model fatigue of the longitudinal steel. However, experimental results indicate that fatigue-induced damage may also depend on the response of the concrete cover, the core concrete, and the spiral reinforcement. Experimental results from both the present study and the Kunnath et al. study suggest that response of a longitudinal bar subjected to low-cycle fatigue loading depends on the lateral restraint provided. The lateral bar restraint, in turn, depends on the condition of the surrounding concrete, and the stiffness and spacing of the spiral.

Herein, a preliminary study was undertaken to develop a new damage index to model the observed experimental response. Damage resulting from cyclic loading is modeled using a two-phase model. The first phase models damage to the lateral restraint on the longitudinal bar as damage to the concrete cover. The second phase models damage of the longitudinal steel. Each phase is modeled using a modified format of the Coffin-Manson equation as shown in Equation 4.40. The expression relates the number of complete cycles to failure,  $N_f$ , to a normalized strain,  $\epsilon_r = \epsilon/\epsilon_o$ .

$$N_f = a \left( \frac{\epsilon}{\epsilon_o} \right)^b + c \quad (4.40)$$

Miner's rule is employed to determine the damage index,  $DI$ , as shown by Equation 4.41. Failure corresponds to a damage index of 1 (one). Equations 4.42 and 4.43 were used to develop the expressions for the concrete damage phase and the steel damage phase.

$$DI = \sum_i \left( \frac{1}{N_{fi}} \right) \quad (4.41)$$

In the present study, the imposed displacement history was used to analyze failure of modern

bridge columns subjected to cyclic lateral loading and to facilitate comparison with previous research. Use of a single displacement history does not lend itself to development of fatigue models. Therefore, the coefficients of the dual-phase damage index were derived using the experimental results of the Kunnath et al. study.

The columns subjected to constant amplitude and monotonic displacement histories (Columns A1, A3, A4, A5, and A6) were used to develop the dual-phase damage index. The following quantities were assessed using experimental observations or predicted response for each column:

1. Compressive strain in the extreme fiber of the core concrete,  $\epsilon_c$ : *predicted*
2. Number of cycles to degrade the cover concrete,  $(N_f)_c$ : *experimental*
3. Tensile strain in the extreme longitudinal bar,  $\epsilon_{su}$ : *predicted*
4. Number of cycles to failure after cover spalling,  $(N_f)_s$ : *experimental*

The values are summarized in Table 4.12. The compressive and tensile strain demands corresponding to the maximum displacement amplitude were predicted using the discrete modeling technique presented in Section 4.3.1.

Table 4.12 summarizes the maximum imposed displacement, compressive and tensile strain ratios, and number of cycles to failure of the concrete cover and the longitudinal steel. These values were used to develop Equations 4.42 and 4.43. The modified Coffin-Manson expression uses a normalized strain ratio to minimize dependence on the material response. The compressive strain,  $\epsilon_c$ , was normalized to the strain corresponding to spalling,  $\epsilon_{csp}$  ( $\epsilon_{csp} = -0.01$  for the columns tested by Kunnath et al., which was consistent with the results from the initial spalling analysis). The tensile strain,  $\epsilon_s$ , was normalized to the strain corresponding to the maximum steel stress,  $\epsilon_{su}$  ( $\epsilon_{su} = 0.09$  using measured response of the longitudinal steel).

$$(N_f)_c = 33 \left( \frac{\epsilon_c}{\epsilon_{csp}} \right)^{-5} \quad (4.42)$$

$$(N_f)_s = 0.08 \left( \frac{\epsilon_s}{\epsilon_{su}} \right)^{-5.5} + 0.92 \quad (4.43)$$

Equation 4.42 relates the number of cycles required to completely remove the concrete cover,  $(N_f)_c$ , at a strain ratio of  $\epsilon_c/\epsilon_{csp}$ . Equation 4.43 calculates the number of subsequent cycles to failure,  $(N_f)_s$ , following fatigue-induced failure of the cover. Equation 4.43 predicts that one cycle results in failure under monotonic loading if  $\epsilon_s = \epsilon_{su}$ . The concrete and steel damage indices are calculated using Miner's rule, as shown by Equations 4.44 and 4.45.

$$(DI)_c = \sum_i \frac{1}{(N_f)_{ci}} \quad \text{where } (DI)_c \leq 1 \quad (4.44)$$

$$(DI)_s = \sum_i \frac{1}{(N_f)_{si}} \quad \text{if } (DI)_c = 1 \quad (4.45)$$

The dual-phase damage index is employed in two stages. The steel fatigue index,  $(DI)_s$ , is equal to zero until the concrete damage index,  $(DI)_c$ , is equal to one. Element failure corresponds to a steel fatigue index value of one, i.e.,  $(DI)_s=1$ . The dual-phase damage index was evaluated using the experimental results from the present study. For these columns, a concrete spalling strain,  $\epsilon_{csp}$ , of -0.008 and ultimate steel strains,  $\epsilon_{su}$ , of 0.14 were used. The analytical results are shown in Figure 4.35. The progression of damage predicted by the concrete fatigue model is shown by a line marked with circles. The progression of damage predicted by the longitudinal steel fatigue model is shown by a line marked with squares. The maximum value of both indices is 1.0. The dual-phase index correctly predicts failure for Column 407 (third cycle to 5 inches), for Column 415 (first cycle to 7 inches), and Column 815 (second cycle to 17.5 inches). Failure of Column 430 is predicted at the first cycle to 7 inches, rather than the second cycle to 7 inches. The damage index reaches a value of 0.92 at the measured failure of Column 1015. The dual-phase damage index predicted the failure of the five columns of the present study as well as those tested by Kunnath et al.

**Table 4.1: Flexural Strength**

Column	$M_p$ calculated		$M_{max}$ measured		$M_{max}/M_p$
	kip-ft.	kN-m	kip-ft.	kN-m	
407	318	433	319	431	1.0
415	523	694	512	709	1.0
430	852	1157	853	1156	1.0
815	524	739	545	711	1.0
1015	507	597	440	688	1.2
Average					1.04
Standard Deviation					0.09

**Table 4.2: Comparison of Nominal Flexural Capacity Using Expected and Specified Strengths**

Column	$M_{ns}$ Specified	$M_{ne}$ Expected	Ratio $M_{ne}/M_{ns}$
407	257	289	1.1
415	392	438	1.1
430	603	668	1.1

**Table 4.3: Shear Strength Equations**

Code/Document	$V_c$	$V_s$	$V_n$ (value)
Caltrans 1992	$2\left(1 + \frac{P}{2000A_g}\right)\sqrt{f'_c}A_e$	$\frac{A_w f_{yh} D}{s}$	150 kips 34 kN
ATC 32 1995	$2\left(1 + \frac{P}{2000A_g}\right)\sqrt{f'_c}A_e$	$\frac{\pi A_w f_{yh} D'}{2s}$	193 kips 43 kN
NZS 1995	$\left(1 + \frac{3P}{A_g f'_c}\right)v_b A_e$ $v_b \cong (0.07 + 5\rho_l)\sqrt{f'_c}$	$\frac{A_w f_{yh} A_e}{s D'}$	105-149 kips 23-33 kN
ACI Proposed 1998	$2\left(1 + \frac{P}{2000A_g}\right)\sqrt{f'_c}A_e$	$\frac{2A_w f_{yh} D}{s}$	230 kips 51 kN

**Table 4.4: Experimental Column Shear Demand and Demand/Capacity Ratios**

Column	$V_{pm}$		Caltrans	ATC 32	NZS	ACI Proposed
	Kips	kN	$V_{pm}/V_n$	$V_{pm}/V_n$	$V_{pm}/V_n$	$V_{pm}/V_n$
407	39	9	0.2	0.2	0.4	0.2
415	64	14	0.3	0.3	0.5	0.3
430	107	24	0.7	0.6	0.7	0.5
815	34	8	0.2	0.2	0.3	0.2
1015	22	5	0.2	0.1	0.2	0.1

**Table 4.5: Joint Shear Demand and Demand/Capacity Ratios**

Column	$v_{jm} (A_j = D*H_j)$		$v_{jm} (A_j = D*2H_j)$		Caltrans $12\sqrt{f'_c}$	ATC 32 $0.3f'_c$	NZS $0.2f'_c$
	ksi	MPa	ksi	MPa	$v_j/v_{jm}$	$v_j/v_{jm}$	$v_j/v_{jm}$
407	0.3	2.2	0.2	1.1	0.4	0.1	0.4
415	0.5	3.6	0.3	1.8	0.7	0.2	0.6
430	0.9	6	0.4	3	1.1	0.3	0.9
815	0.6	3.8	0.3	1.9	0.7	0.2	0.6
1015	0.5	3.1	0.2	1.5	0.5	0.2	0.5

**Table 4.6: Measured Displacement at Top of Column (inches)**

Column	Effective Yield Displacement	Spalling Displacement	Ultimate Displacement
407	0.8	1.5	5
415	0.9	1.5	6
430	1	1.5	7
815	3.3	5.25	17.5
1015	4.6	7.5	25

**Table 4.7: Moment, Curvature, and Plastic Hinge Values for Priestley et al. Plastic Hinge Length Method**

Column	$M_y$ (k-in.)	$M_n$ (k-in.)	$\phi_y$ (1/in.)	$\phi_u$ (1/in.)	$l_p$ (in.)
407	2,634	3,503	0.00023	0.0022	14
415	3,994	5,456	0.00025	0.0018	14
430	6,226	8,758	0.00026	0.0014	14
815	3,949	5,425	0.00025	0.0018	22
1015	3,949	5,425	0.00025	0.0018	25

**Table 4.8: Displacement Values Computed by Priestley et al. Method (inches)**

Column	Computed Values				Ratio to Measured Displacement		
	$\Delta'_y$	$\Delta_{\epsilon = -0.008}$	$\Delta_u(\epsilon_s = 0.1)$	$\Delta_u(\epsilon_{core})$	Yield	Spalling	Ultimate
407	0.7	2.3	7.2	14	0.9	1.5	0.6
415	0.8	2.0	7.5	14.8	0.8	1.3	0.4
430	0.8	1.3	8.1	16	0.8	1.1	0.3
815	3.0	6.9	24.6	36	0.9	1.3	0.5
1015	4.7	10.4	36.5	53	1.0	1.4	0.5
Mean					0.9	1.3	0.5
Standard Deviation					0.08	0.13	0.1

**Table 4.9: Displacement Values Computed by Proposed Method (inches)**

Column	Computed Values			Ratio to Measured Displacement		
	$\Delta'_y$	$\Delta_{\epsilon = -0.008}$	$\Delta_u(\epsilon_s = 0.1)$	Yield	Spalling	Ultimate
407	0.9	1.2	5.1	1.1	1.0	1.0
415	0.9	1.2	6.3	1.0	1.0	1.1
430	1.0	1.2	7.5	1.0	0.9	1.1
815	3.3	4.3	20.4	1.0	0.9	1.2
1015	5.1	6.5	30.4	1.1	1.0	1.2
Mean				1.0	0.8	1.1
Standard Deviation				0.05	0.08	0.08

**Table 4.10: Definition of Rules for Hysteresis Model**

Rule	Stiffness	Limits	Unloading	Exceedance
1	$k_1 = \frac{F_y}{D_y}$	$D_i \leq D_y < D_{max}$	Rule 1	Rule 2
2	$k_2 = \frac{F_{sp} - F_y}{D_{sp} - D_y}$	$D_y < D_i < D_{sp}$	Rule 4	Rule 3
		$D_y < D_i \leq D_{max} < D_{sp}$	Rule 6	
3	$k_3 = \frac{F_u - F_{sp}}{D_u - D_{sp}}$	$D_{sp} > D_i$	Rule 4	N/A
		$D_{sp} < D_i < D_{max}$	Rule 6	
4	$k_4 = k_1(\mu_{max})^{-0.25}$	$D_i > D_o = D_{max} - (F_{max})/k_4$	Rule 4	Rule 5
5	$k_5 = \frac{F_{min}}{D_{min} - D_o}$	Backbone Curve	Rule 4	$f(D_{min})$
6	$k_4 = k_1(\mu_{max})^{-0.25}$	Intercept with Unloading Curve From Maximum Point	Rule 6	Unloading Curve From Max.

**Table 4.11: Results for Columns Subjected to Constant Amplitude Displacement Histories (translated from [Kunnath 1997])**

Column	Reported Displacement Ductility	Corresponding Damage under Monotonic Loading	Cycles to:	
			No Cover	Failure
A3	2 (1.1 inches)	Yield	>150	N/A
A4	3 (2.2 inches)	Initial Spalling	8	25
A5	4 (3 inches)	Initial Spalling	6	9
A6	5 (3.8 inches)	Significant Spalling	1	3

**Table 4.12: Fatigue Analysis of Columns Subjected to Constant Displacement Amplitudes**

Column	Displacement	$\epsilon_c/\epsilon_{sp}$	$(N_f)_c$	$\epsilon_s/\epsilon_{su}$	$(N_f)_s$
A1	5.9 in. (monotonic)	N/A	N/A	1	1
A3	1.1 inches	0.74	>150	N/A	N/A
A4	2.2 inches	1.27	8	0.40	17
A5	3.0 inches	1.55	6	0.48	3
A6	3.8 inches	1.93	1	0.58	2

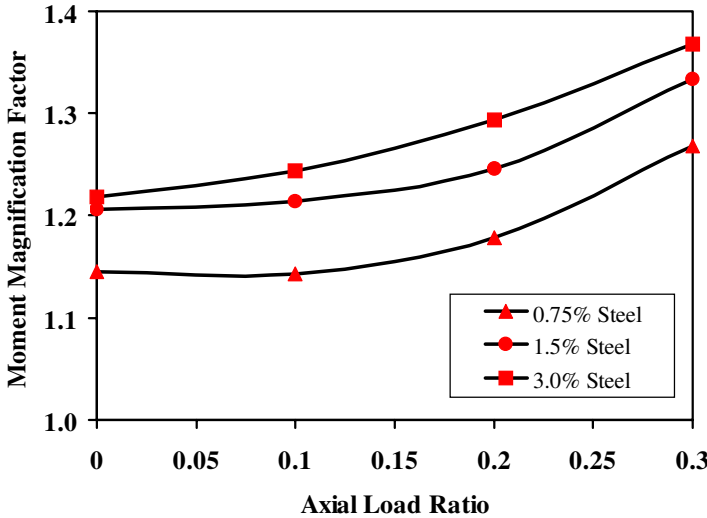


**Figure 4.1: Calculated Amplification Factor**

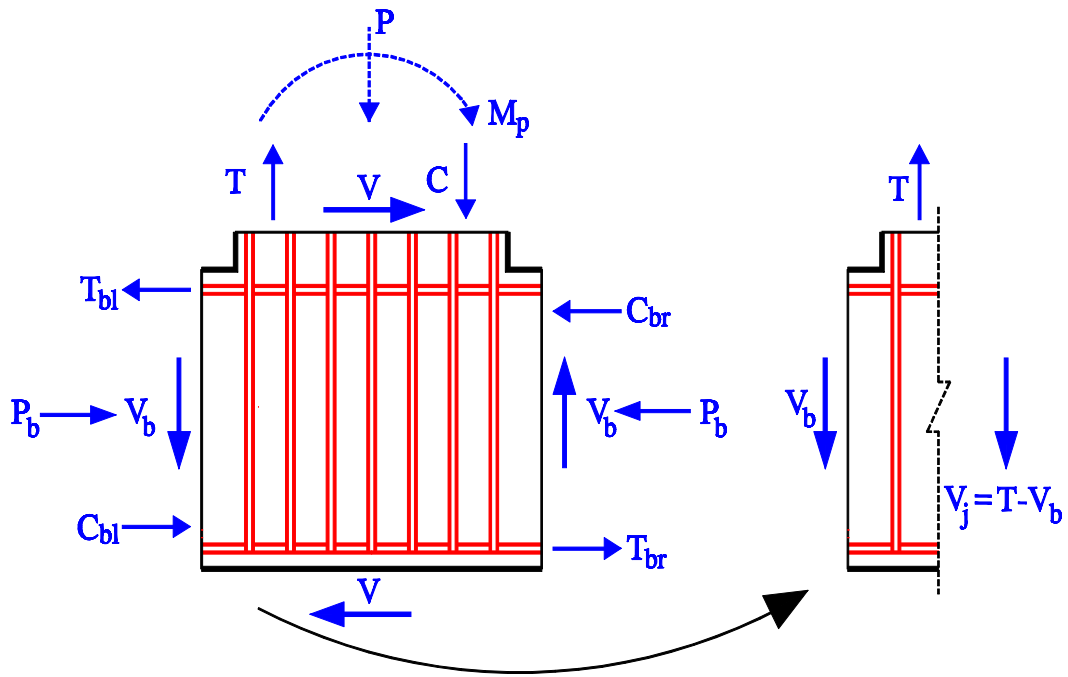


Figure 4.2: Joint Equilibrium

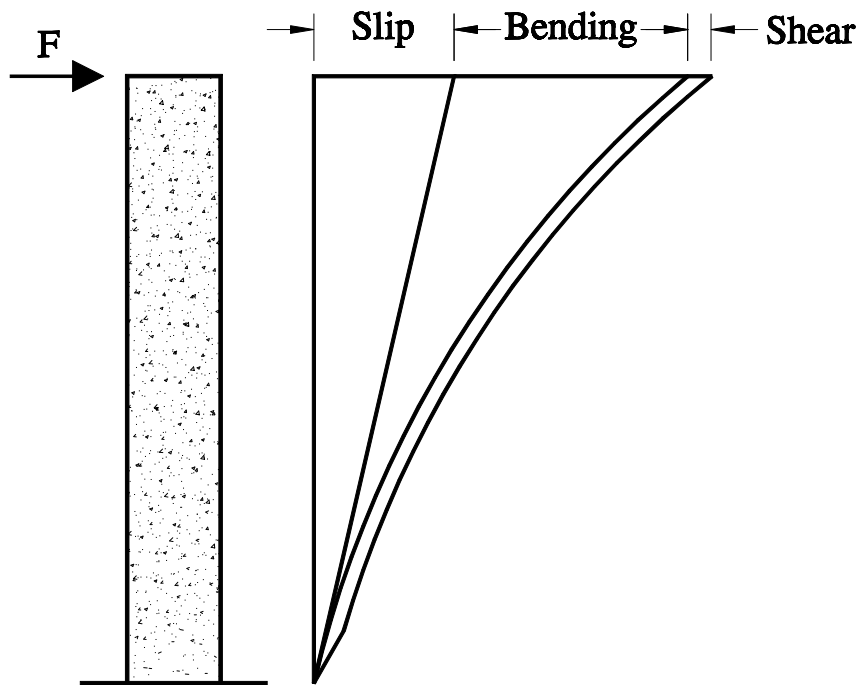


Figure 4.3: Displacement Components for a Cantilever Column

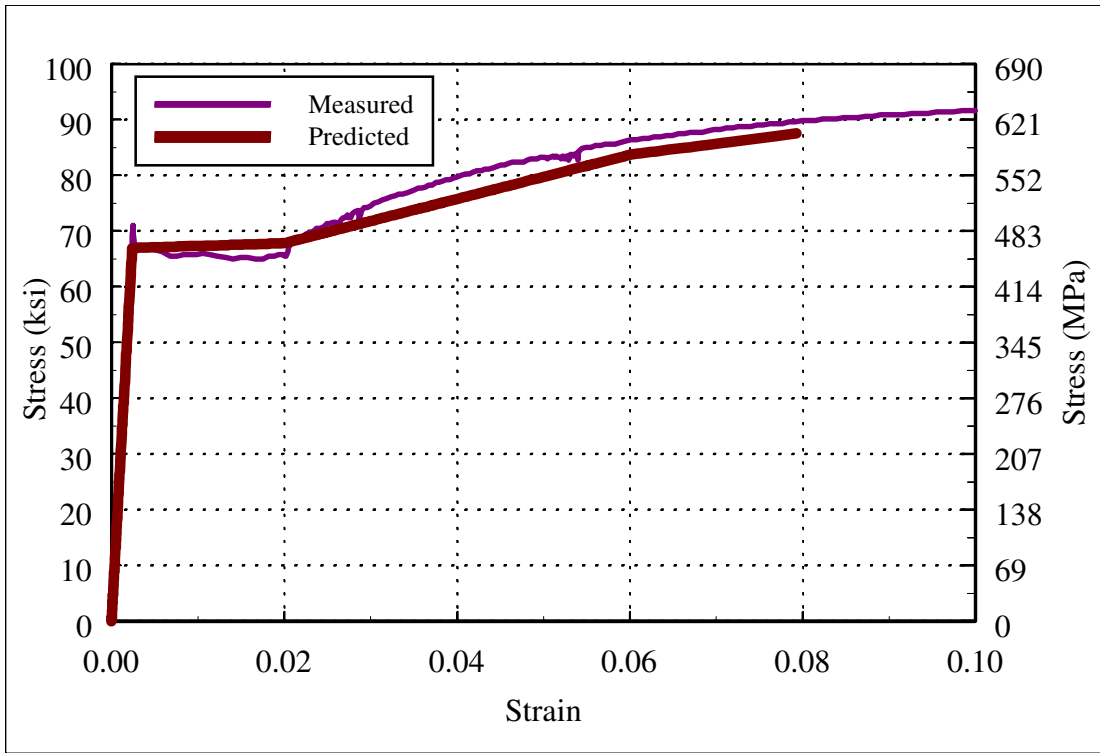


Figure 4.4: Measured and Predicted Longitudinal Steel Response

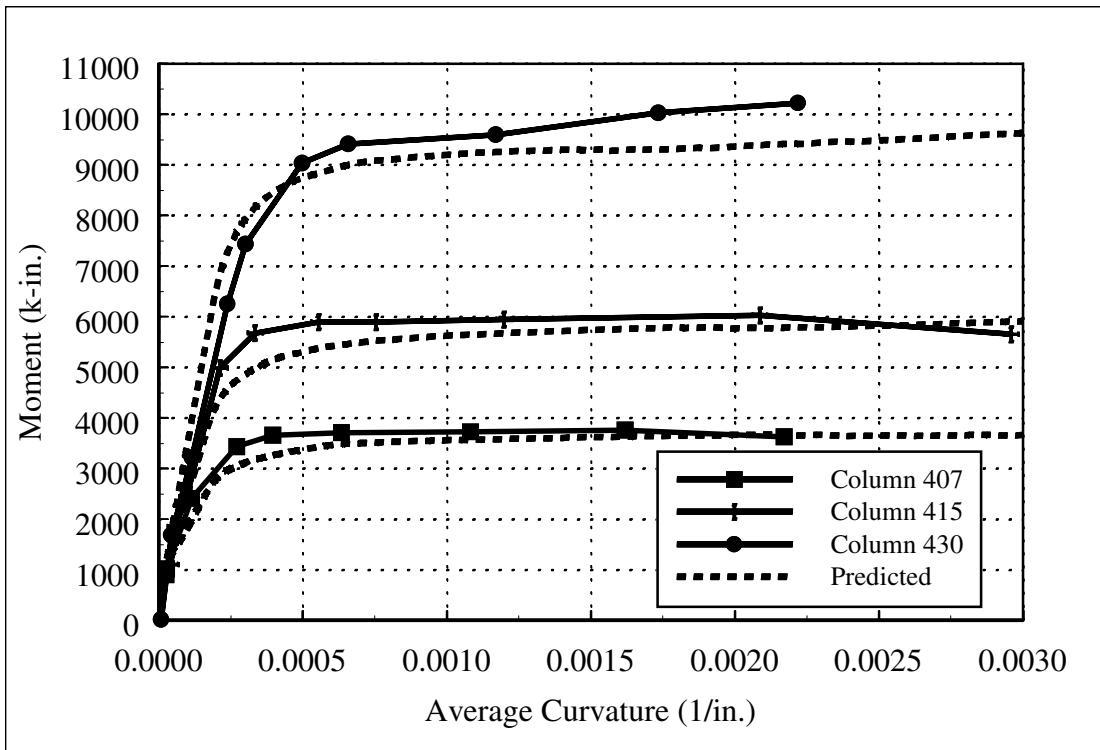


Figure 4.5: Test Series I Measured and Predicted Moment-Curvature Response

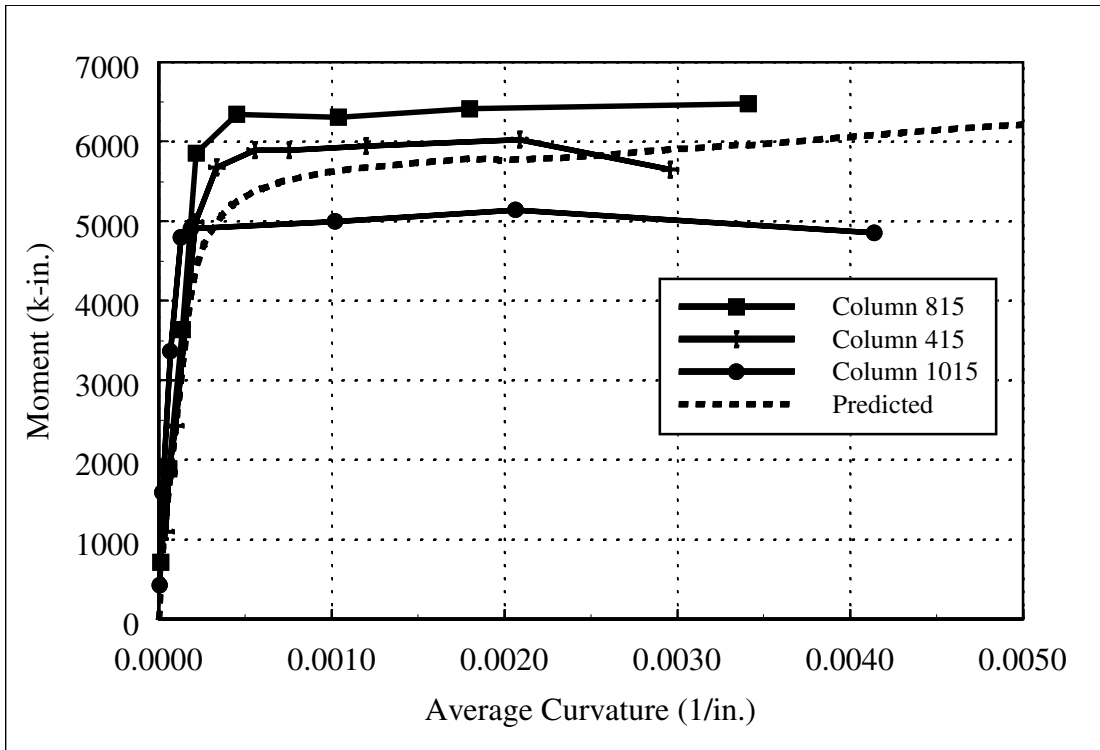


Figure 4.6: Test Series II Measured and Predicted Moment-Curvature Response

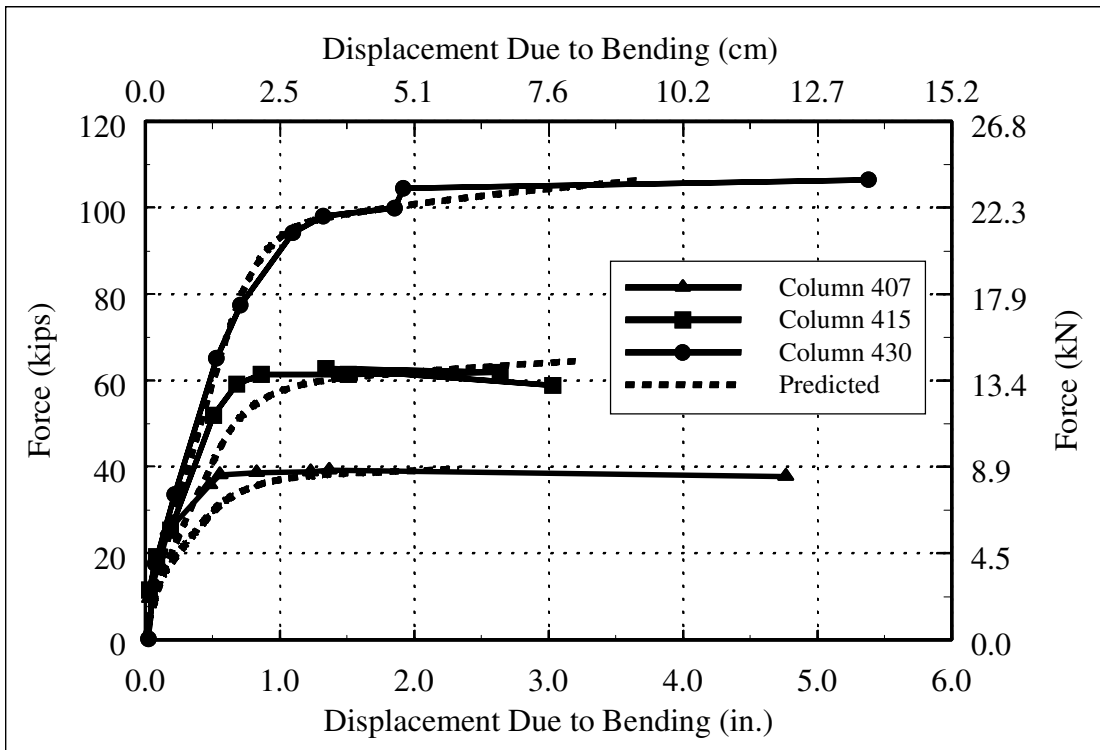


Figure 4.7: Test Series I Measured and Predicted Force-Bending Displacement Response

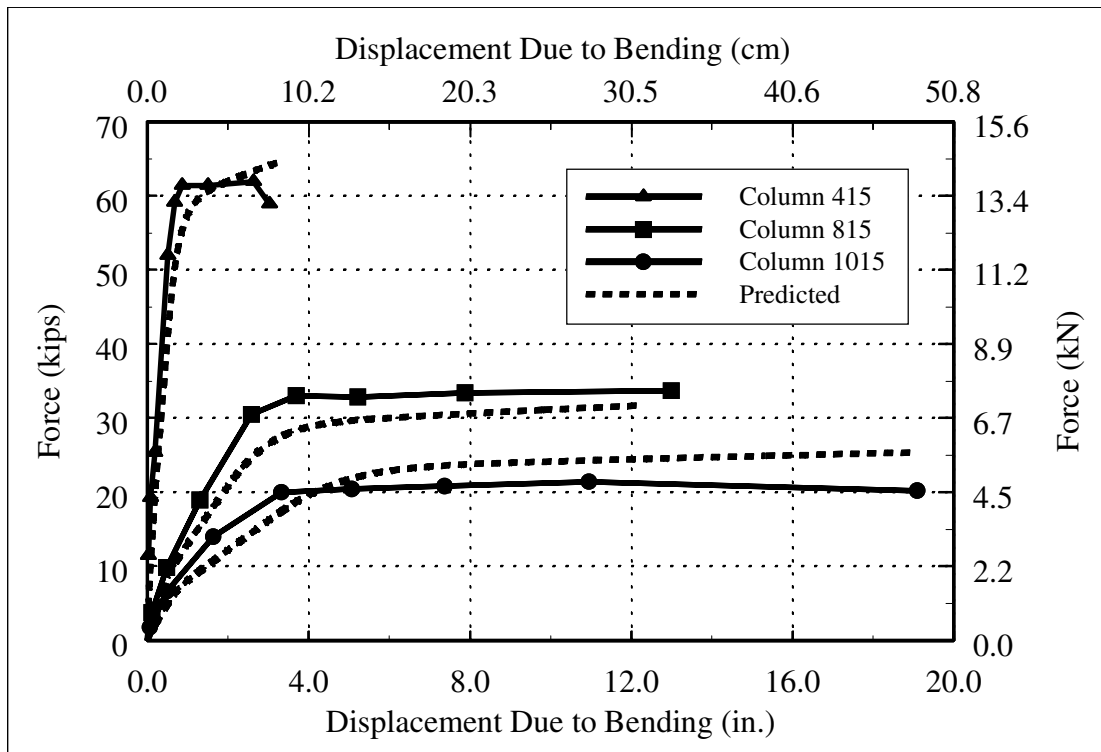


Figure 4.8: Test Series II Measured and Predicted Force-Bending Displacement Response

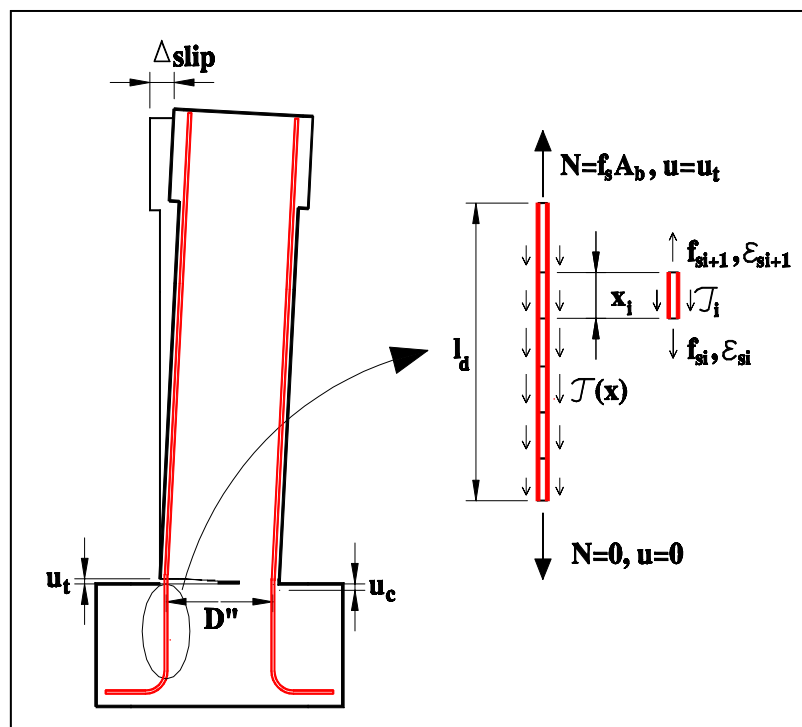


Figure 4.9: Slip Displacement of Cantilever Column

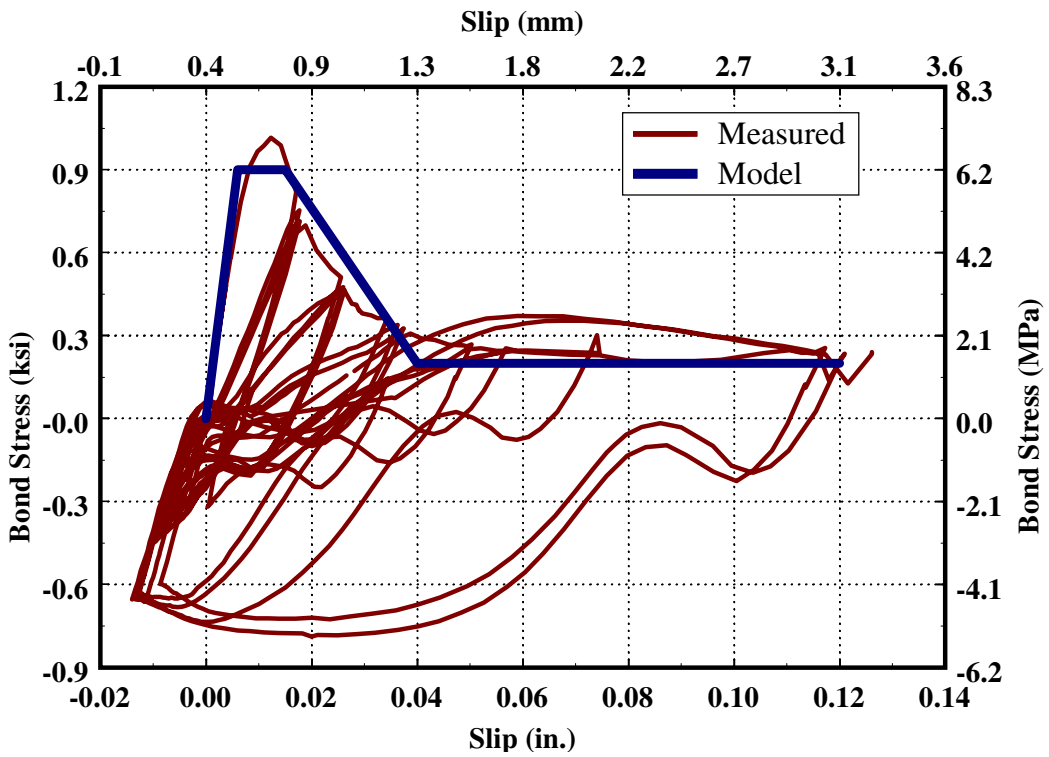


Figure 4.10: Predicted and Measured Bond Stress-Slip Response

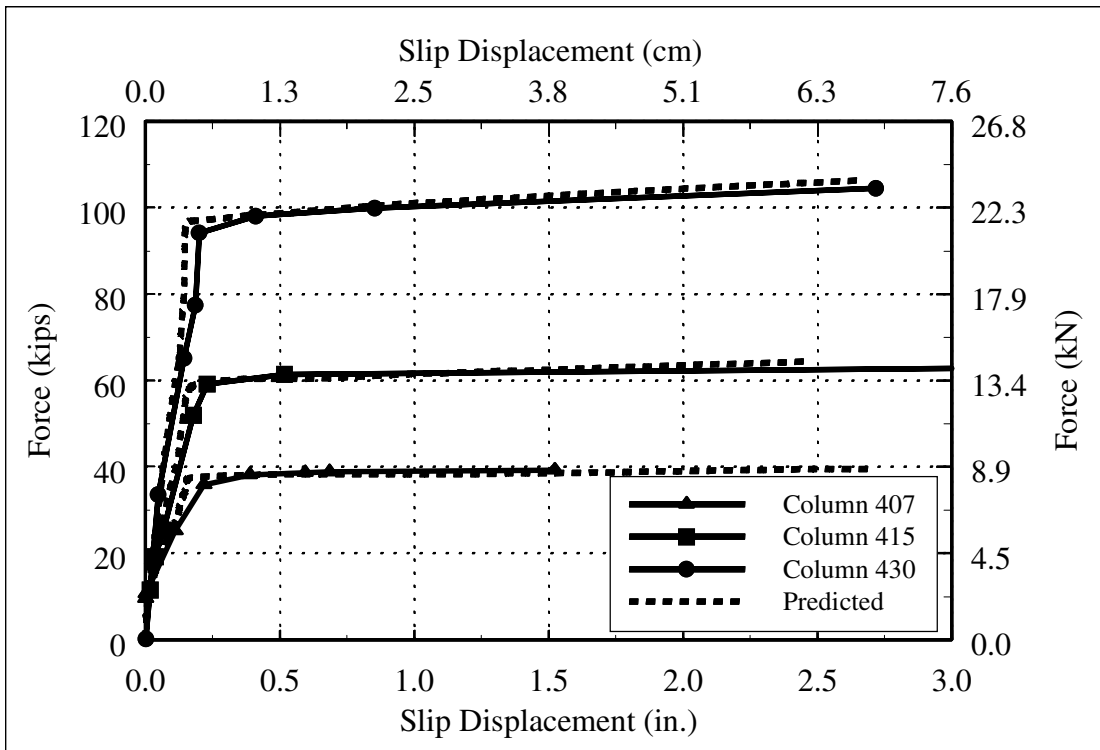


Figure 4.11: Test Series I Force-Slip Displacement Response: Bond-Slip Model

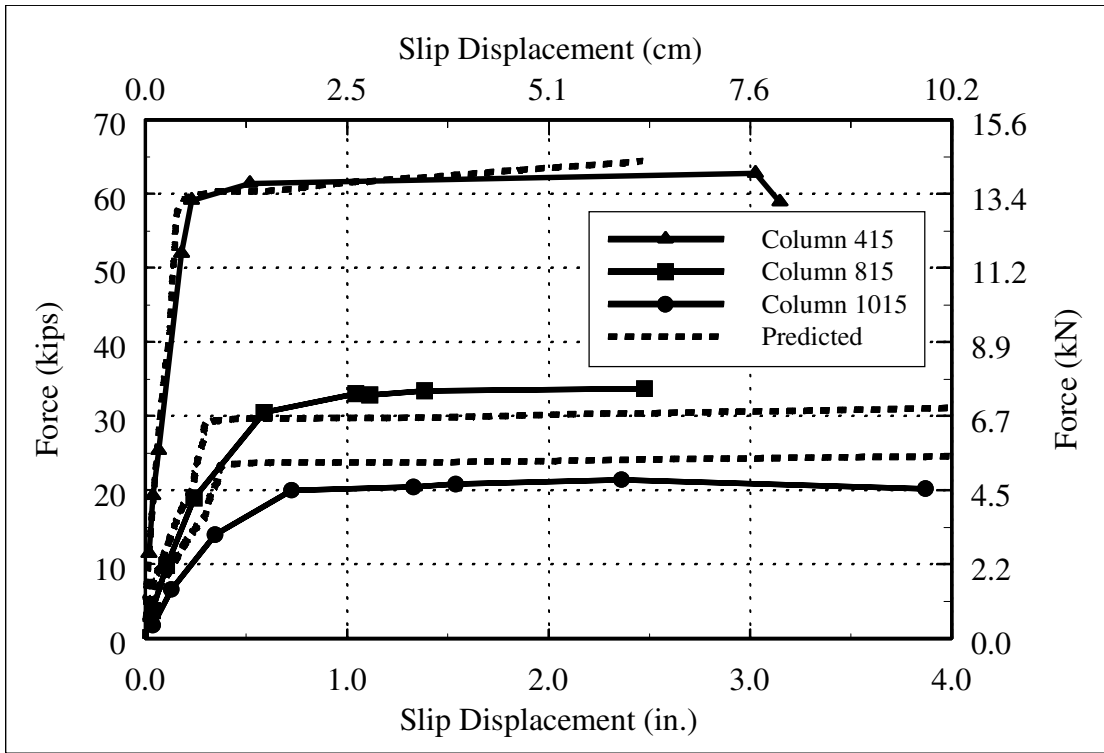


Figure 4.12: Test Series II Force-Slip Displacement Response: Bond-Slip Model

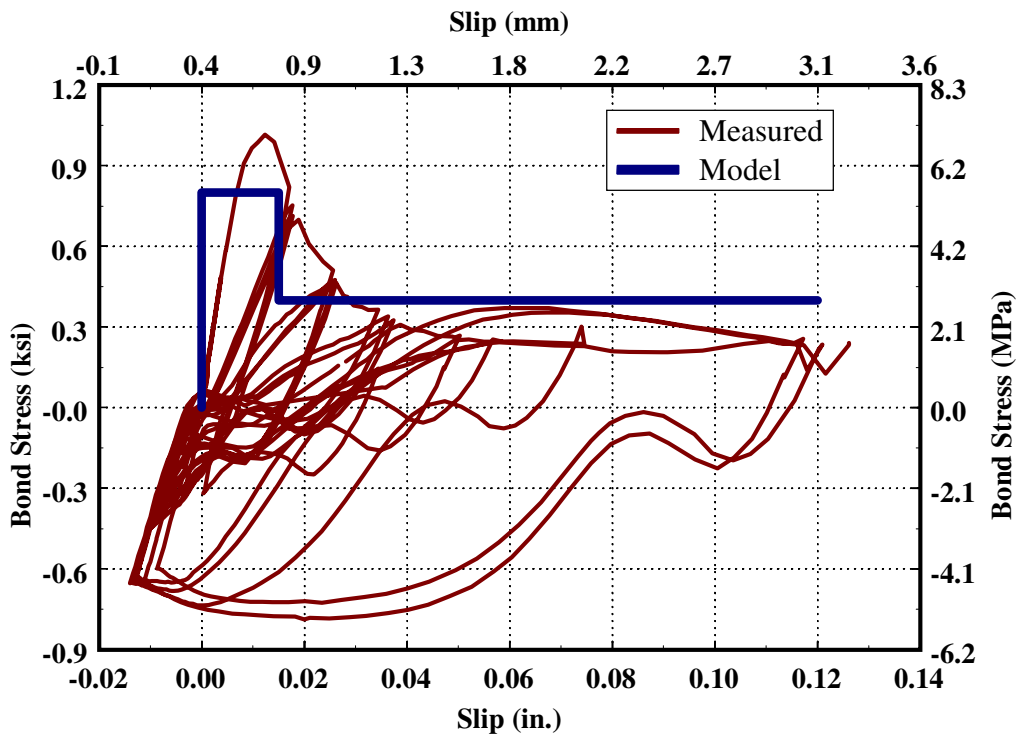


Figure 4.13: Bi-Uniform Bond Slip Model: Measured and Predicted Response

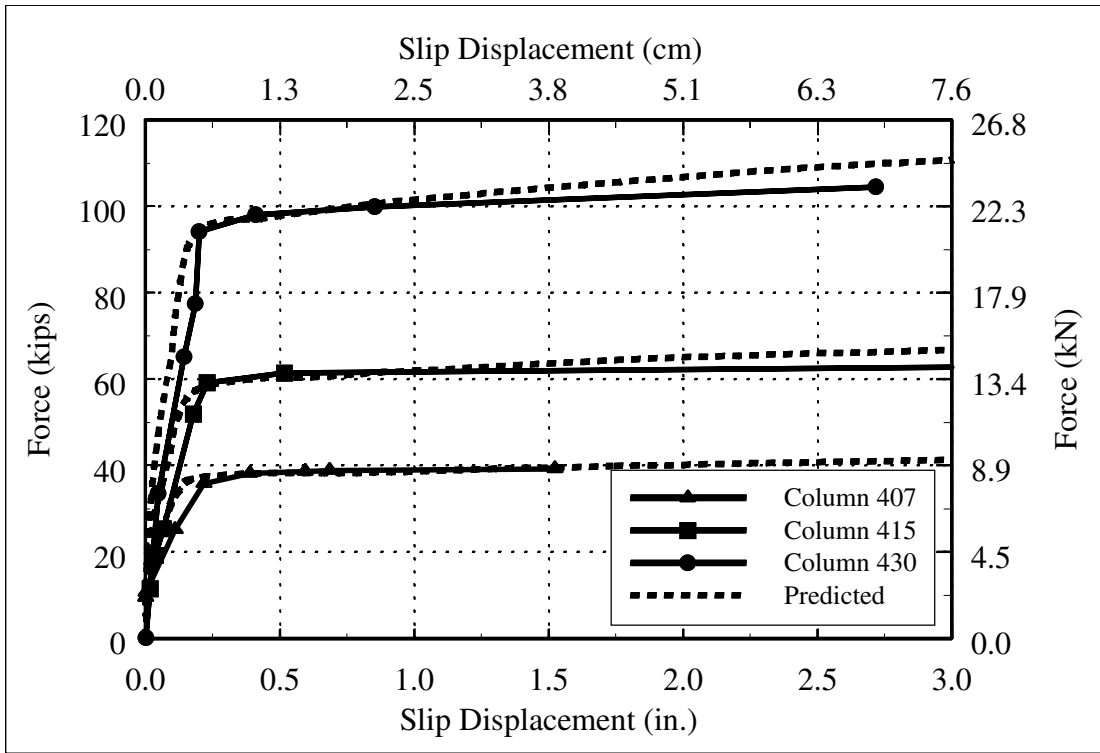


Figure 4.14: Measured and Predicted Force-Slip Response: Uniform Bond Model

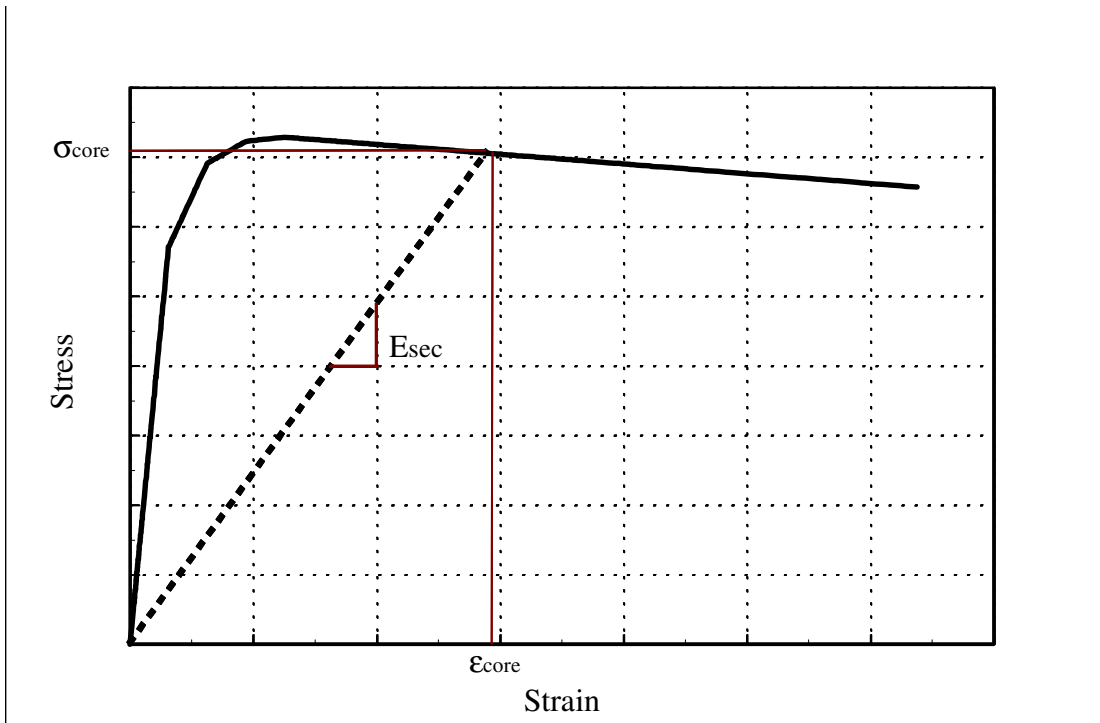


Figure 4.15: Computation of Secant Young's Modulus of Core Concrete

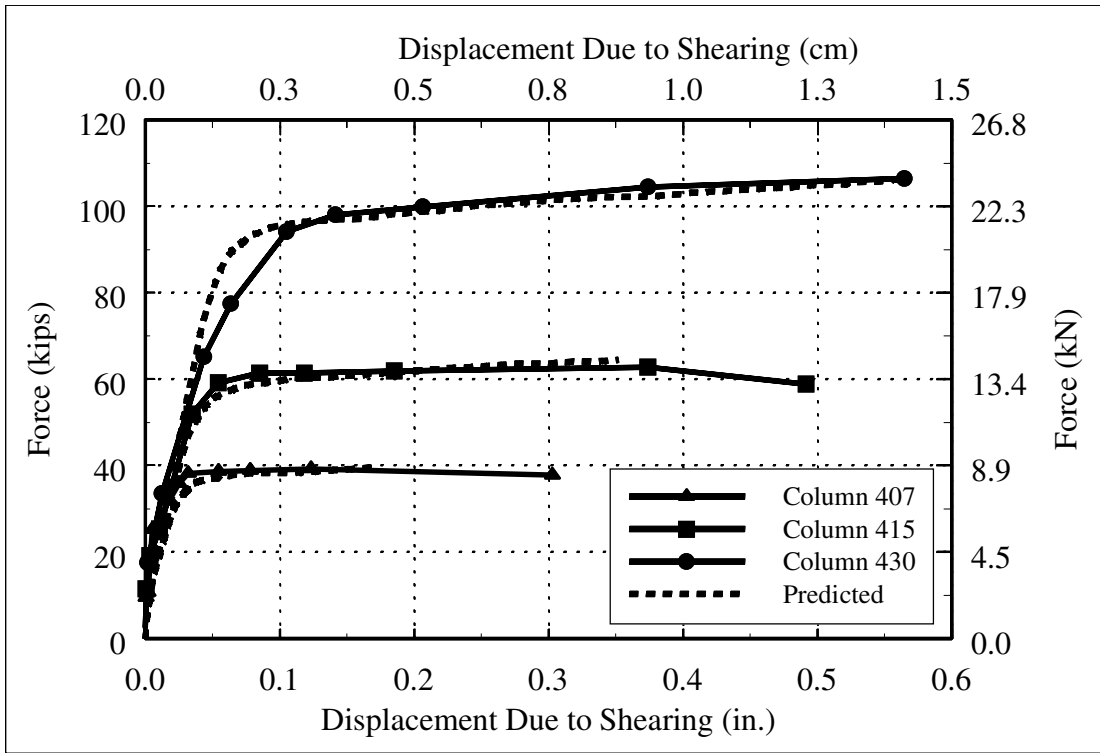


Figure 4.16: Test Series I Measured and Predicted Force-Shearing Response

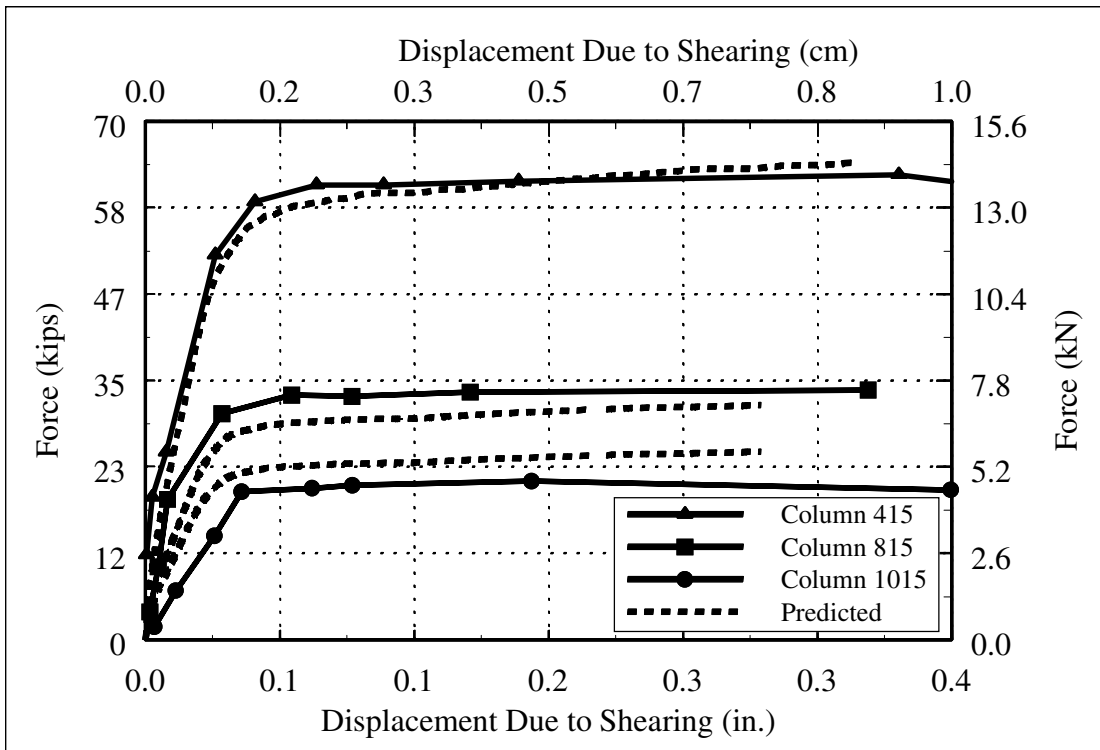


Figure 4.17: Test Series II Measured and Predicted Force-Shearing Response

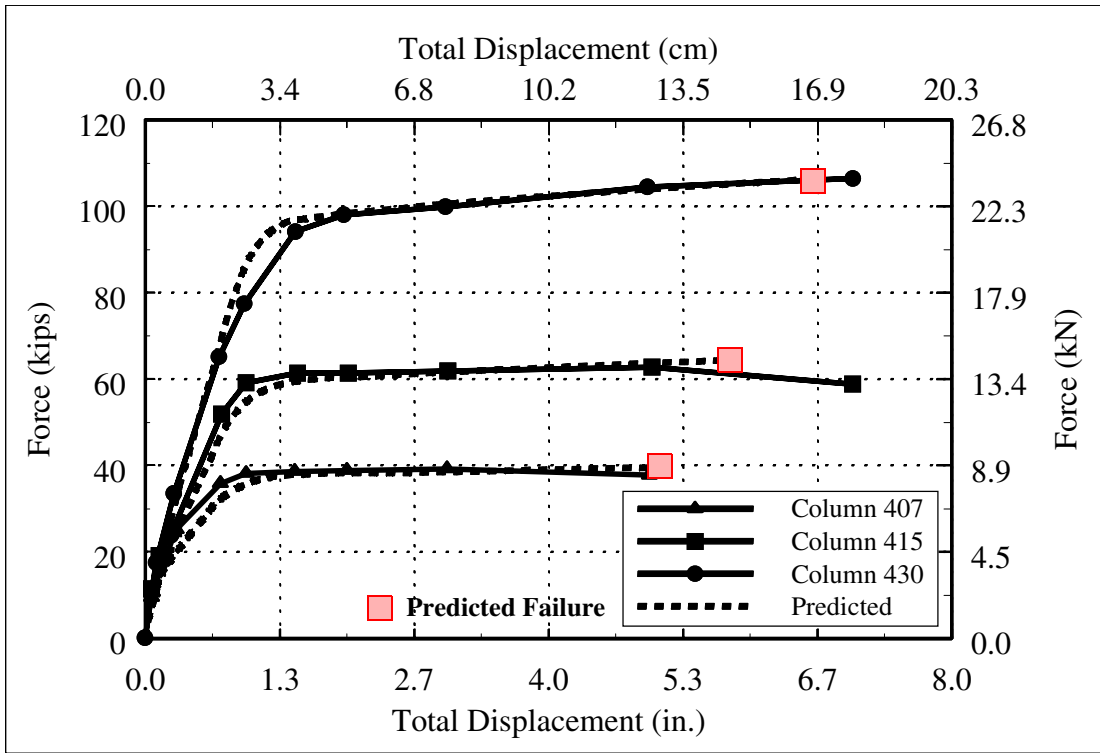


Figure 4.18: Test Series I: Response Predicted Using Discrete Model

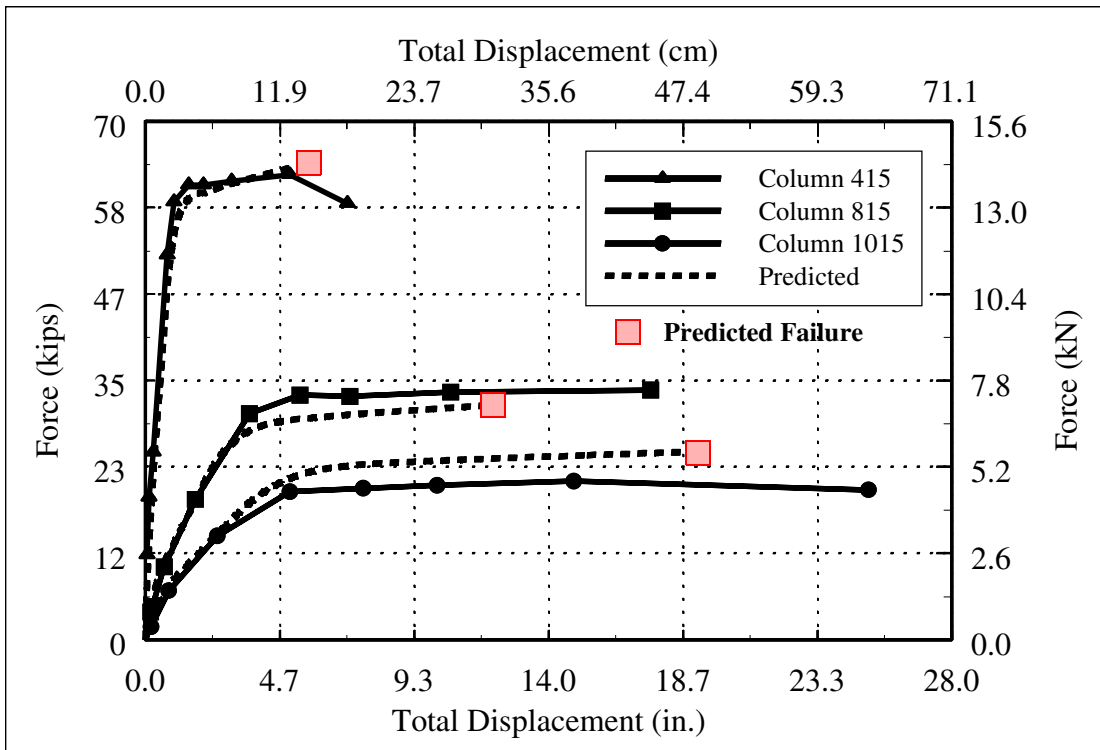


Figure 4.19: Test Series II: Response Predicted Using Discrete Model

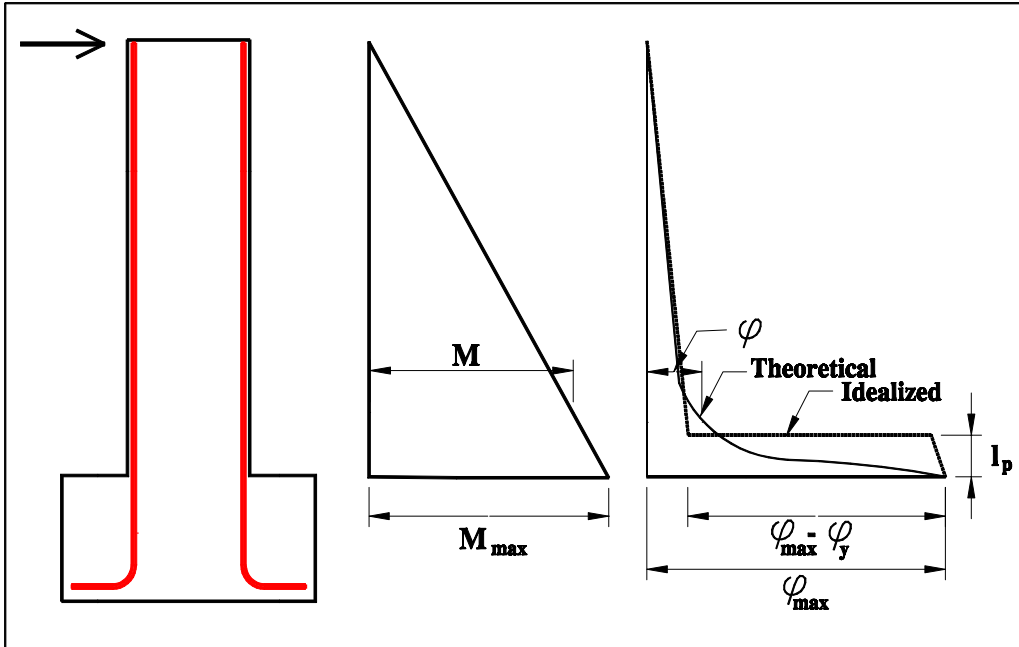


Figure 4.20: Plastic Hinge Length Model

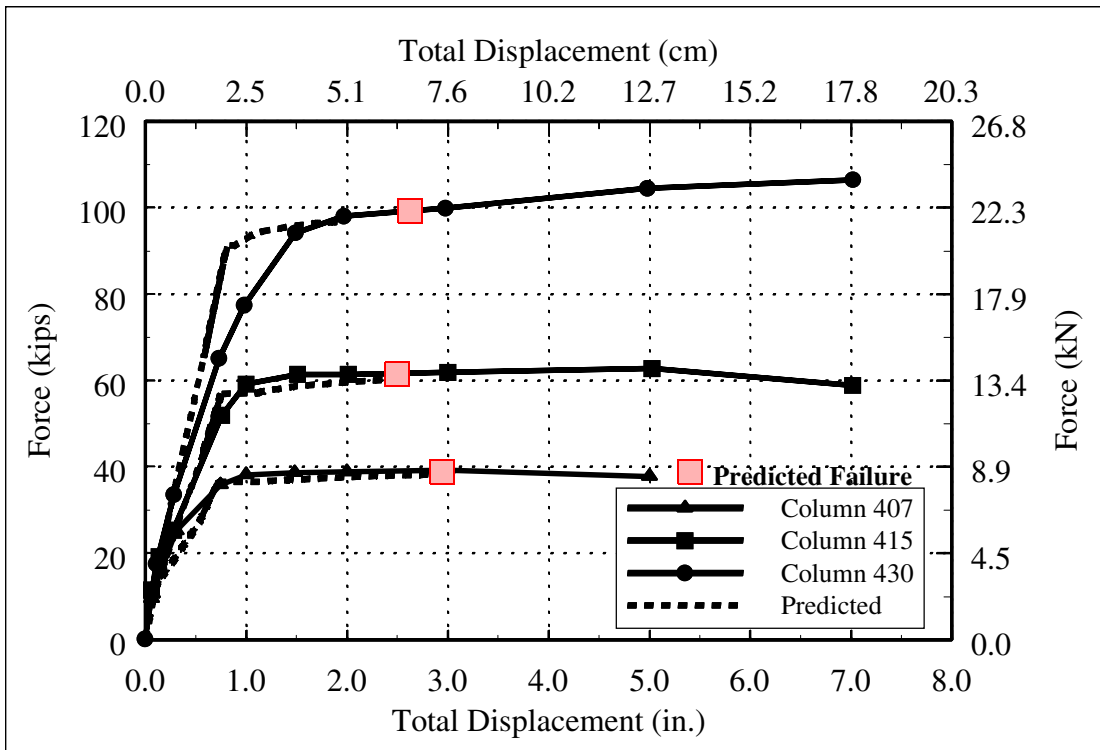


Figure 4.21: Test Series I Predicted Response Using Plastic Hinge Model by Priestley

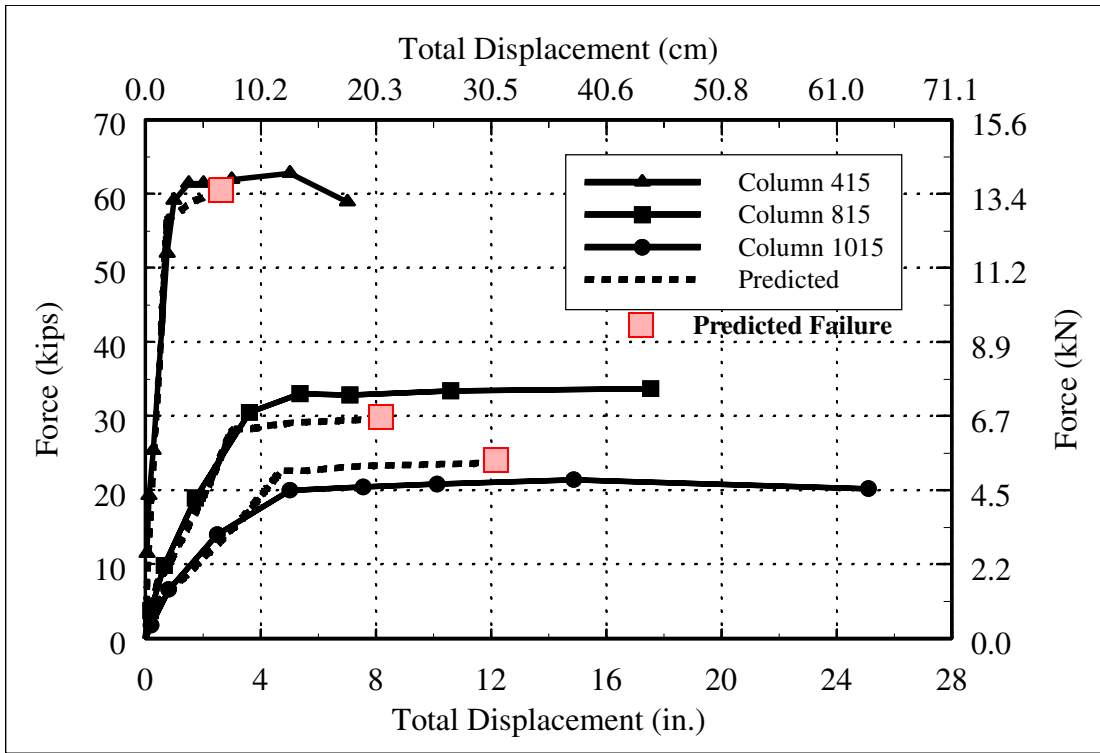


Figure 4.22: Test Series II Response Predicted Using Plastic Hinge Model by Priestley

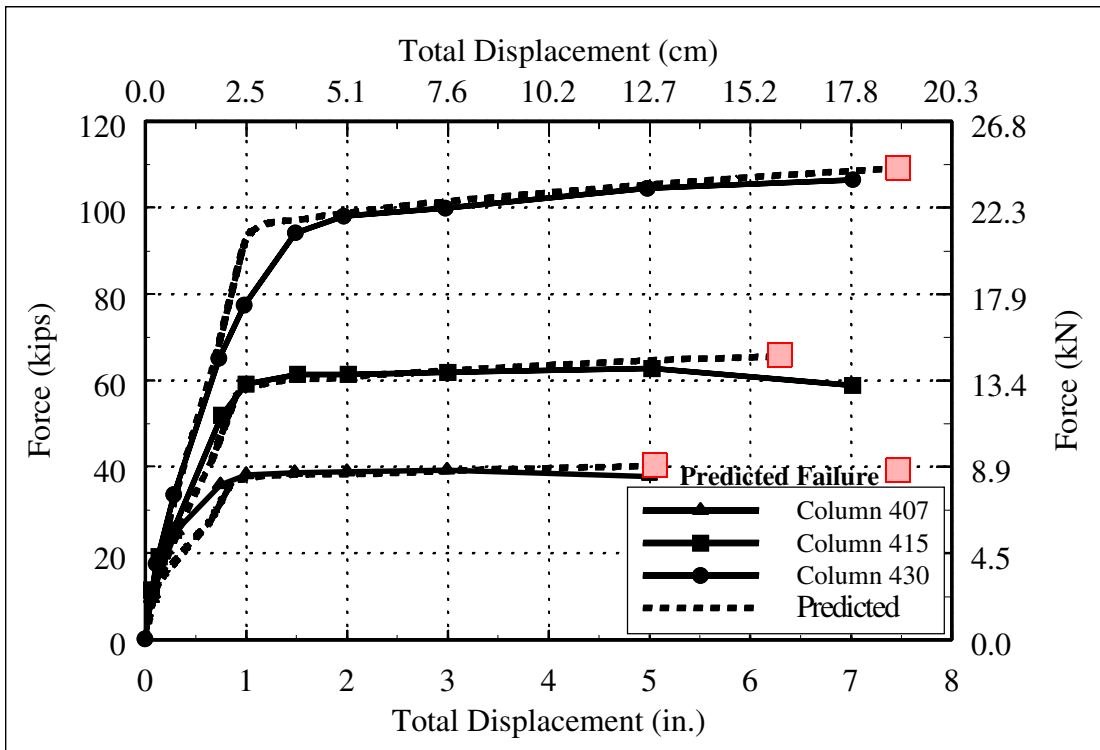


Figure 4.23: Test Series I: Response Predicted Using Proposed Plastic Hinge Model

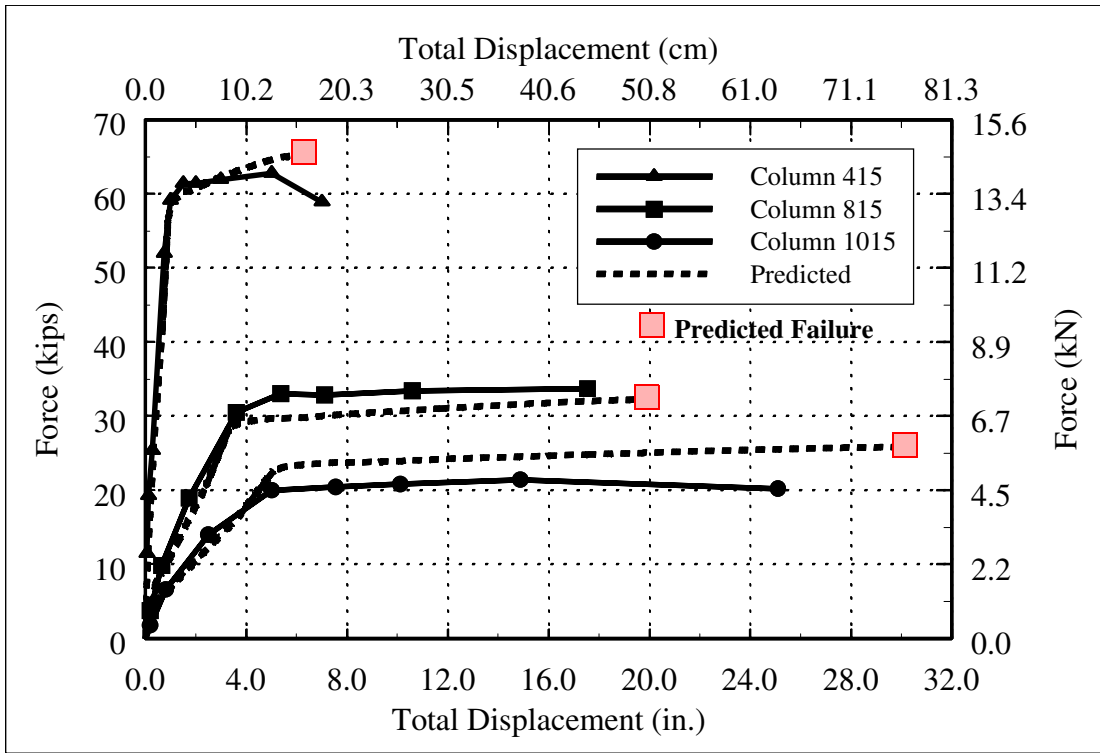


Figure 4.24: Test Series II Response Predicted Using Proposed Plastic Hinge Model

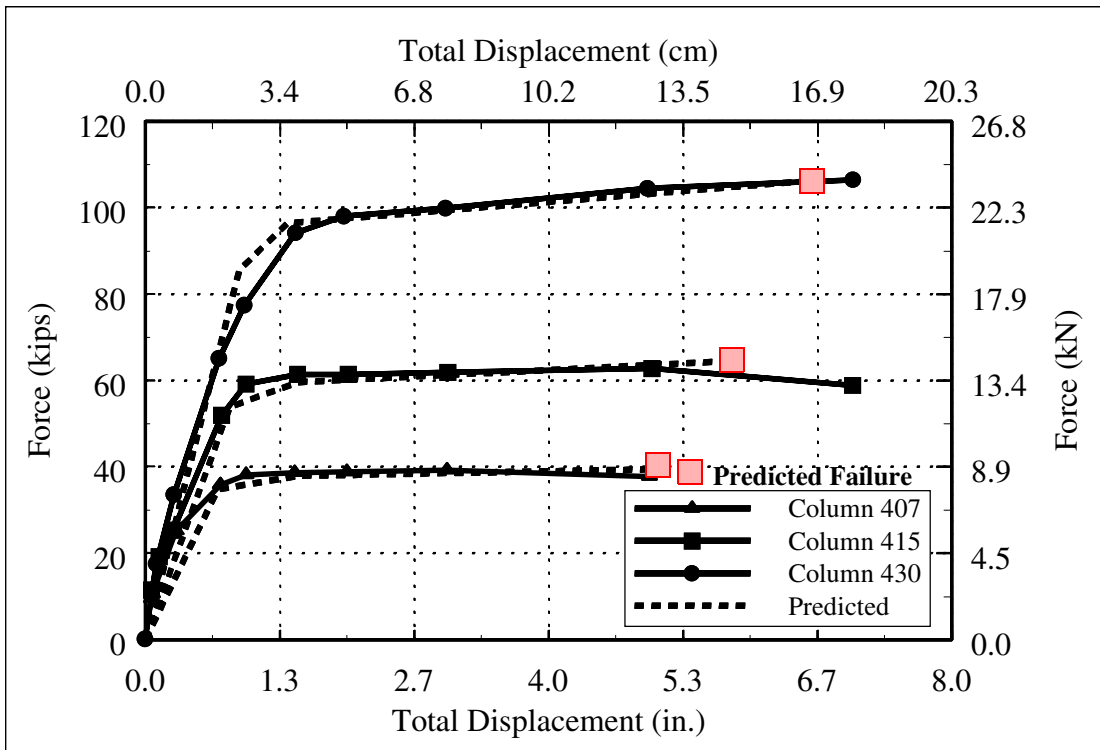


Figure 4.25: Trilinear Approximation of Force-Displacement Response Envelope

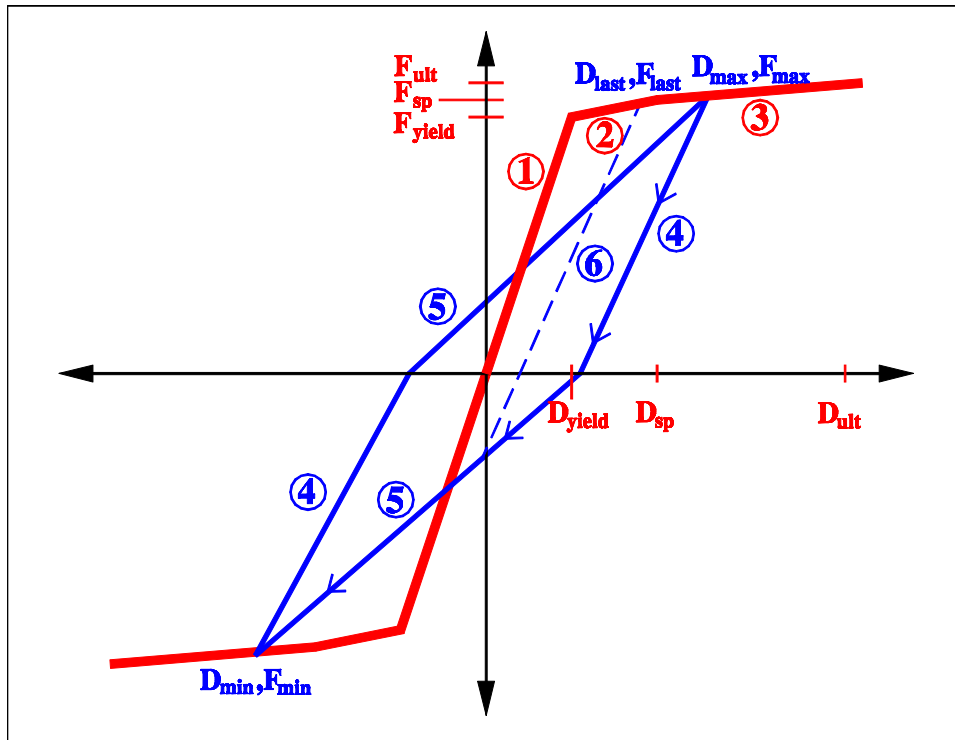


Figure 4.26: Hysteresis Model

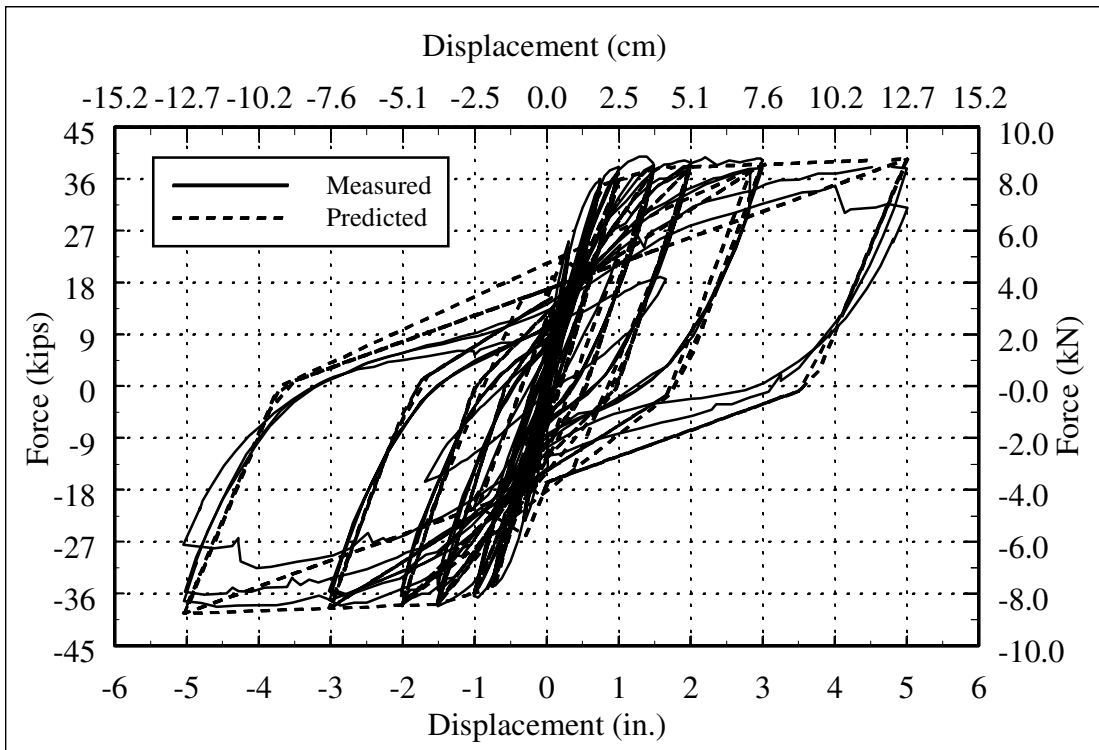
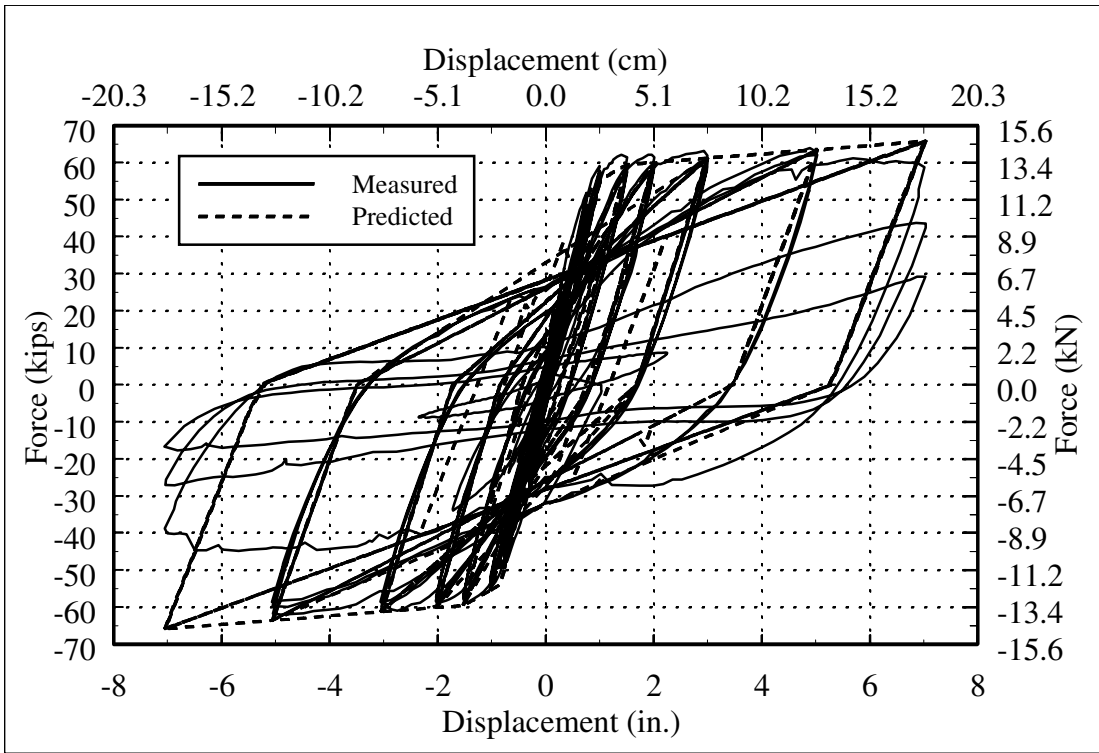
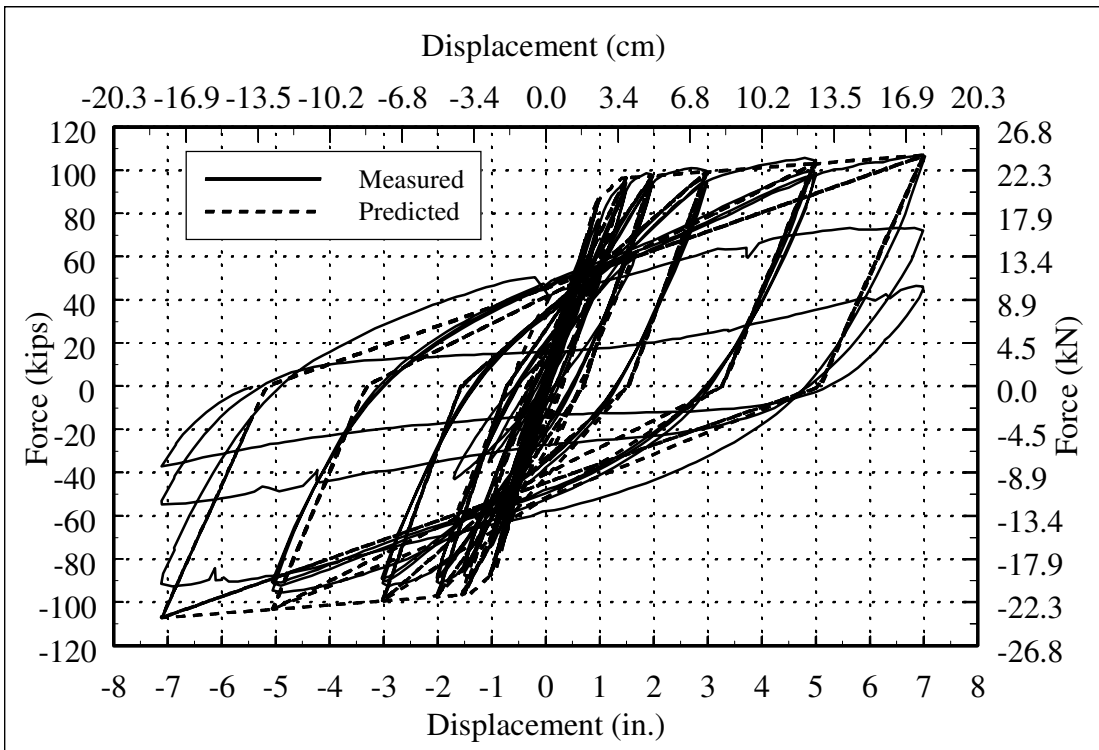


Figure 4.27: Column 407 Force-Displacement Response Histories



**Figure 4.28: Column 415 Force-Displacement Response Histories**



**Figure 4.29: Column 430 Force-Displacement Response Histories**

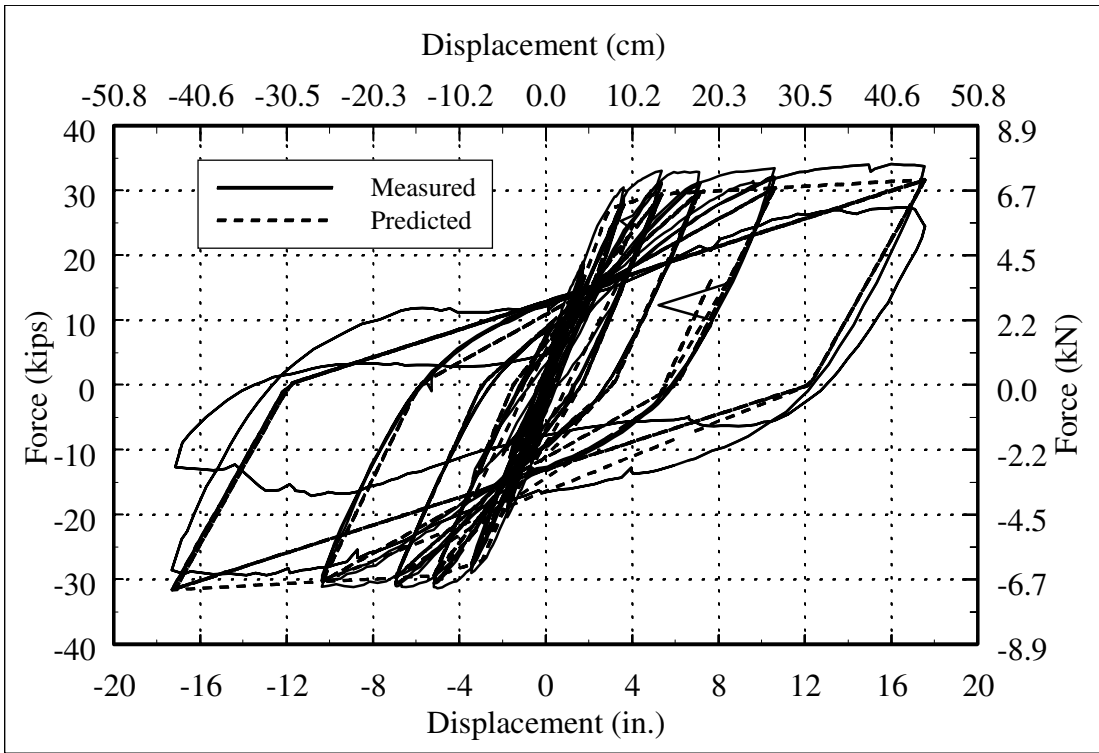


**Figure 4.30: Column 815 Force-Displacement Response Histories**

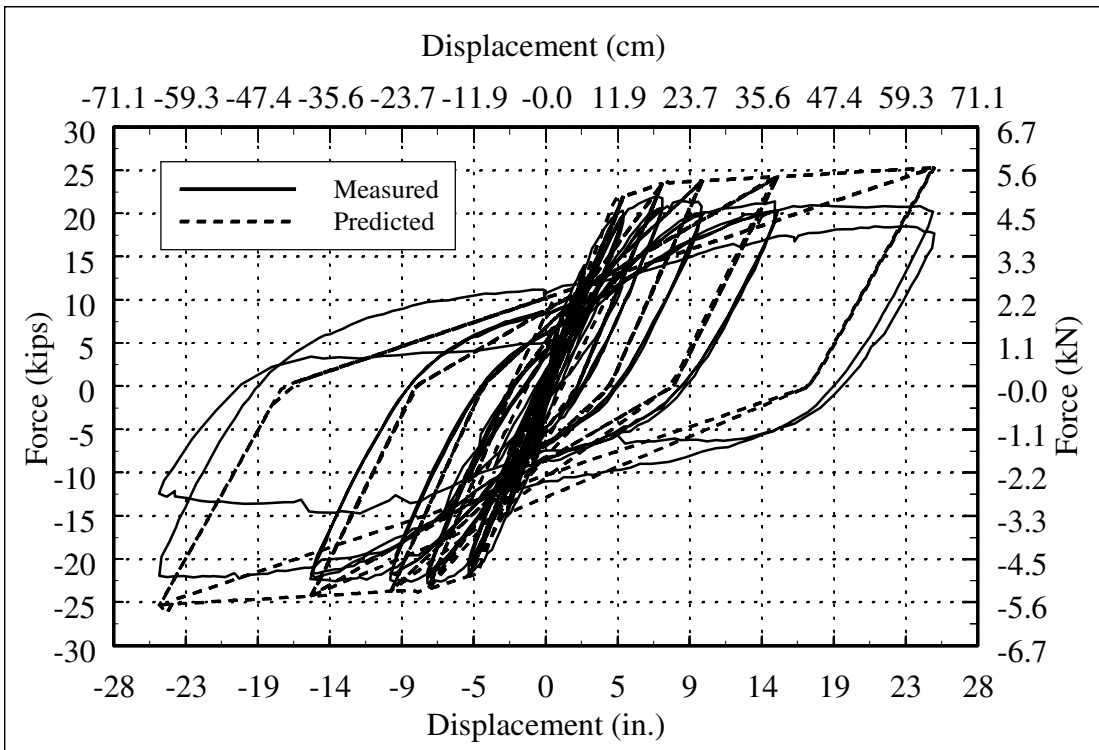


**Figure 4.31: Column 1015 Force-Displacement Response Histories**

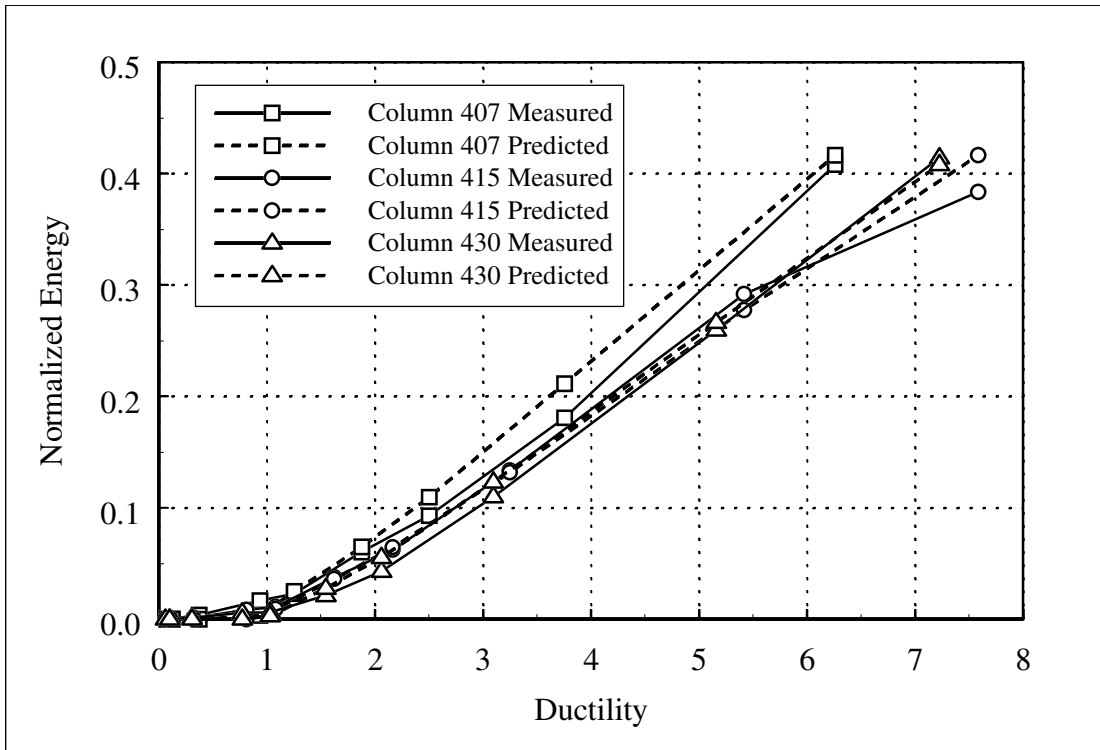


Figure 4.32: Series I Predicted and Measured Values of Energy Dissipated in a Single Cycle

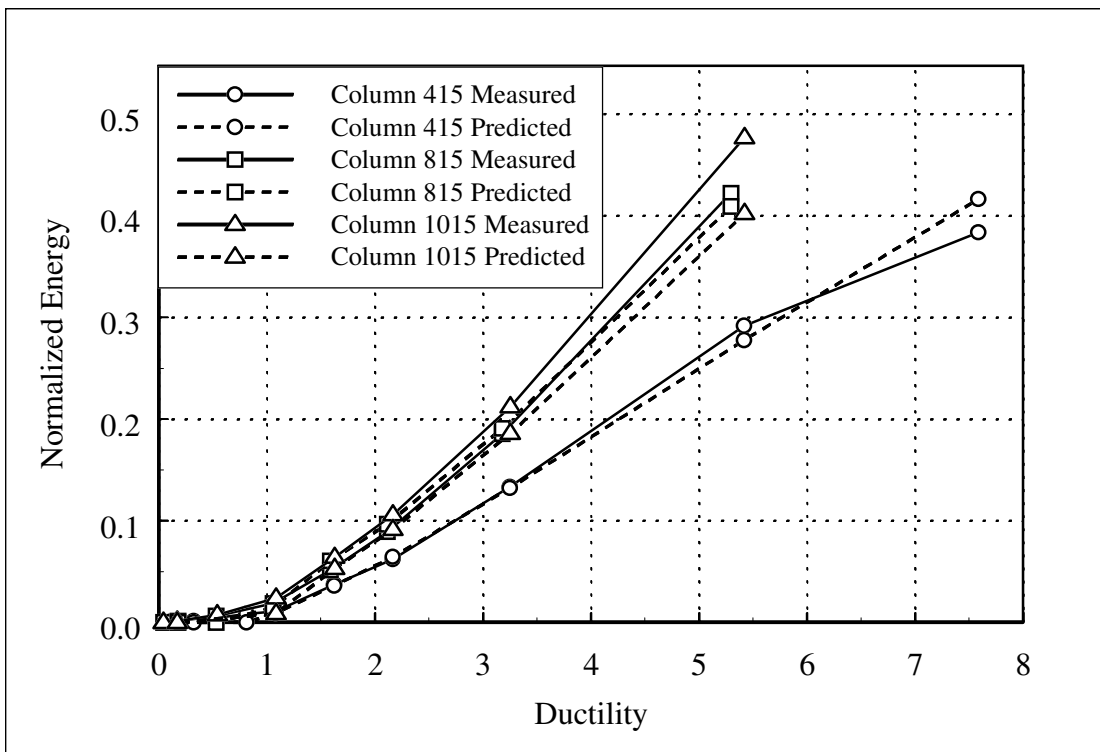
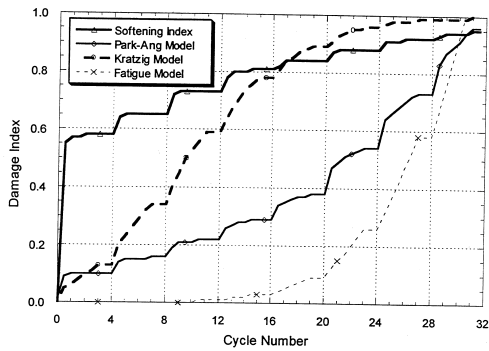
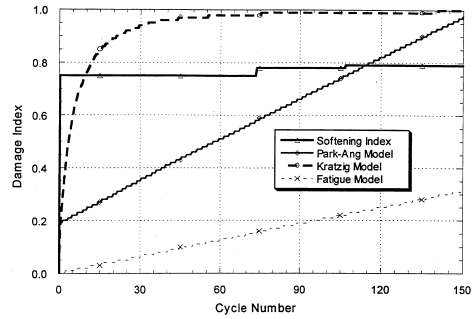


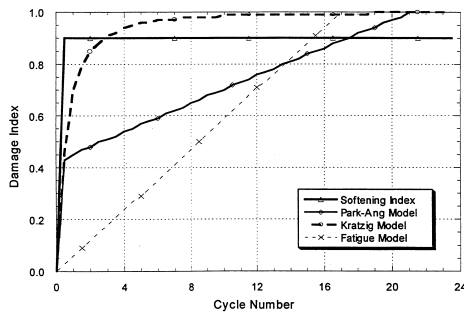
Figure 4.33: Series II: Predicted and Measured Values of Energy Dissipated in a Single Cycle



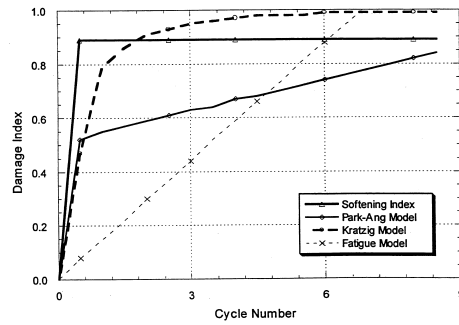
Comparative Evaluation of Progressive Damage for Specimen A2



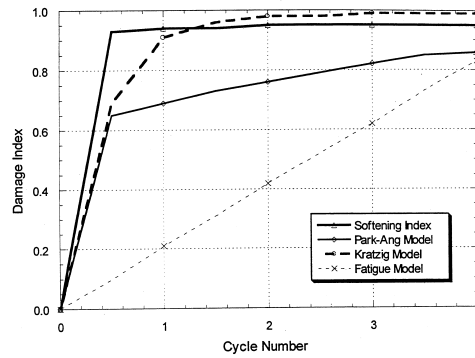
Comparative Evaluation of Progressive Damage for Specimen A3



Comparative Evaluation of Progressive Damage for Specimen A4



Comparative Evaluation of Progressive Damage for Specimen A5



Comparative Evaluation of Progressive Damage for Specimen A6

**Figure 4.34: Park-Ang Energy-Based and Mander-Cheng Fatigue-Based Damage Indices Evaluated for Columns Tested by Kunnath et al. [Kunnath 1997]**

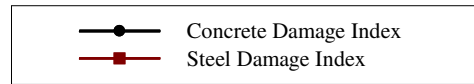
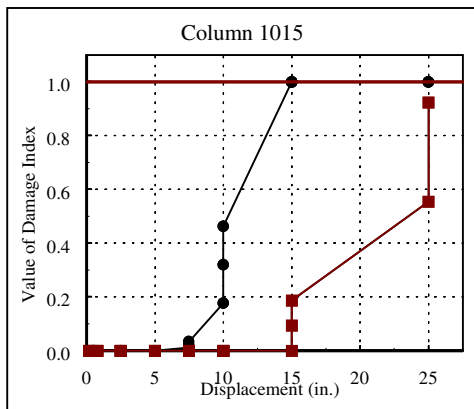
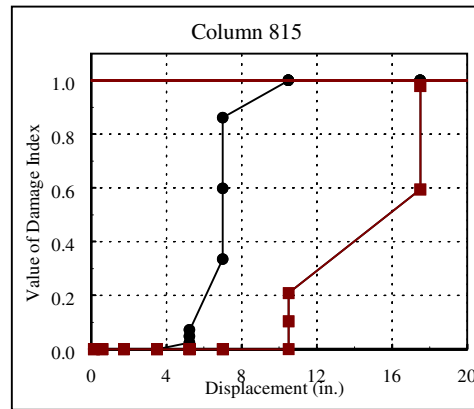
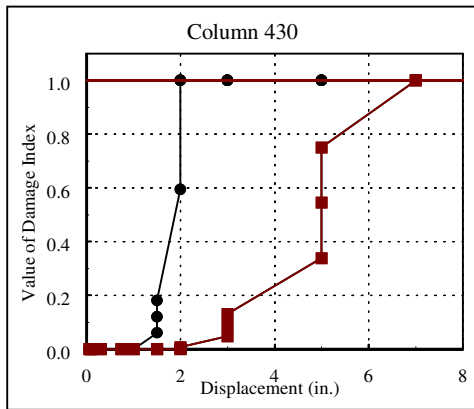
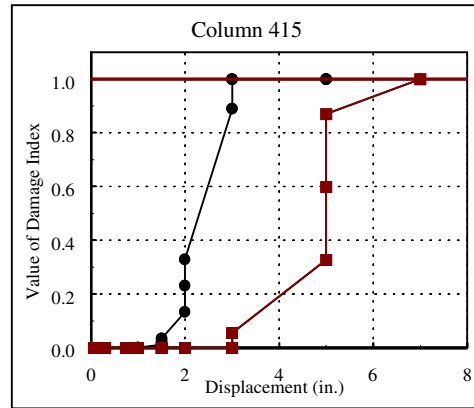
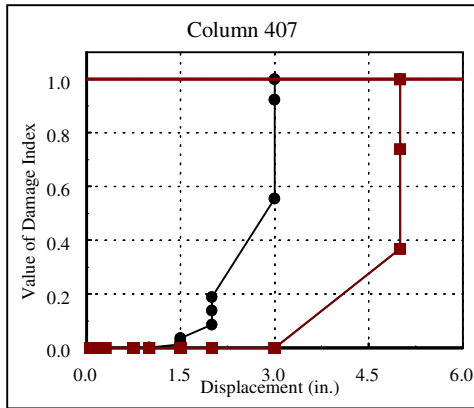


**Figure 4.35: Failure Predicted by Dual-Phase Damage Index (Final Point Indicates Measured Failure)**

# 5 Performance-Based Seismic Design

## 5.1 OVERVIEW

Performance-based seismic design may be defined as design to reliably achieve targeted performance objectives. This design approach contrasts with most current design approaches (e.g., AASHTO for bridges and UBC for buildings). Those codes define a single level of seismic hazard (e.g., ground shaking hazard level with a 10% chance of exceedance in 50 years [SEAOC 1995]) and a single level of performance that is generally understood to be life-safety. Furthermore, those codes use indirect methods such as base shear strength and linear-elastic analysis to define the performance state, which can be expected to be relatively inaccurate. Performance objectives other than the life-safety are not evaluated explicitly; whether these performance objectives are achieved depends somewhat randomly on the seismic environment characteristics of the structural and nonstructural components.

As illustrated in Figures 5.1 and 5.2, performance-based seismic design differs from the current seismic design provisions. Where current seismic design provisions specify design requirements for a single hazard and performance level, performance-based seismic design can specify performance for a range of hazard levels. Performance can be defined in terms of structural component parameters (e.g., spalling), structural parameters (e.g., stability), or functionality. Engineering limit states are used to quantify each aspect of performance. A performance objective pairs a single hazard level with a single performance level. Categorizing structures as “ordinary” or “important,” the example performance based-seismic design framework as illustrated in Figure 5.2 has three performance objectives for ordinary structures and two performance objectives for important structures.

Recent events have emphasized the need for performance-based seismic design. The economic cost associated with structural damage caused by both the Loma Prieta earthquake and the Northridge earthquake exceeded public expectations [EERI 1990, EERI 1995]. Loss of function of critical bridges and highways impaired emergency operations and caused considerable traffic delays over months and years. Performance-based seismic design would permit the engineer to directly address functionality in design and is expected to reduce losses in future events.

## 5.2 REVIEW OF EXISTING DOCUMENTS

Numerous efforts have been undertaken to identify, define, and quantify aspects of performance-based seismic design. The efforts described in *Vision 2000: Performance-Based Engineering* [SEAOC 1995] and *FEMA 273 NEHRP Guidelines for the Seismic Rehabilitation of Buildings* [FEMA 1997] provide the most comprehensive work on performance-based design of buildings, with FEMA 273 being the most complete work to date on the subject. The Applied Technology Council has issued a report entitled *ATC 32 Improved Seismic Design Criteria for California Bridges: Provisional Recommendations* [ATC 1996] and has recommended performance-oriented design guidelines for bridges. The ATC 32 report provides the most complete effort in the U.S. on performance-based seismic design of bridges. The subsequent discussion summarizes performance objectives, hazard levels, and performance levels recommended in ATC 32 and FEMA 273.

Figure 5.3 shows the performance objectives outlined in the ATC 32 report. Independent performance objectives are defined for Ordinary bridges and Important bridges. A bridge is categorized as Important if it is required to provide secondary life safety, it creates significant impact if closure exceeds a few days, or it is formally designated as critical by local authority. All other bridges are categorized as Ordinary.

In the ATC 32 framework, two hazard levels are defined; the hazard levels are termed as the Functional-Evaluation ground motion and the Safety-Evaluation ground motion. The Functional-Evaluation ground motion has a 60% probability of not being exceeded during the useful life of the bridge. The Safety-Evaluation ground motion may be assessed in a deterministic or a probabilistic manner and corresponds to the Maximum Credible Earthquake defined in the Caltrans Bridge Design Specification [BDS 1986] with an expected return period of 1000–2000 years.

In ATC 32, three performance levels are defined; the three performance levels are defined as Minimum, Intermediate, and Maximum damage states. The performance levels are defined by the bridge service level and the required repair effort. The post-earthquake service level is either an Immediate service level requiring full access to traffic immediately following the earthquake or a limited service level requiring limited access within days following the earthquake with full service restorable within months. The required repair effort immediately following an earthquake is categorized as Minimum, Repairable, or Significant. A bridge requiring Minimum repair will perform in an essentially elastic manner and require no structural repair. A bridge meeting Repairable

state requirements will have cracking and minor spalling of the concrete cover following the earthquake with minimal permanent offsets. A bridge meeting the Significant repair requirements will have significant spalling, and may have permanent offsets requiring repair or replacement of certain structural components or the entire structure.

The performance-oriented design framework outlined in ATC 32 is an important step in developing a performance-based seismic design code for bridges. However, limitations exist. The performance levels are not explicitly quantified using engineering limit states. Further verification of Minimum, Repairable and Significant damage using experimental and analytical methods is required.

FEMA 273 was developed for seismic rehabilitation design of existing buildings. The FEMA 273 report provides a more comprehensive definition of performance-based seismic design. A range of hazard levels and performance levels are described. The document emphasizes three structural performance levels and two seismic hazard levels; detailed guidance is provided for both.

The three structural performance levels are termed Immediate Occupancy, Life Safety, and Collapse Prevention. For the Immediate Occupancy performance level, the building is expected to sustain minimal or no damage to structural elements and nonstructural components; minimal repair required. For a building meeting the Life Safety Performance Level, extensive damage to structural components is expected; repairs will be required prior to re-occupancy although this may not be economical. A structure meeting the requirements at the Collapse Prevention Performance level may pose hazard to life safety resulting from nonstructural elements; structural collapse should be prevented to avoid loss of life.

In the FEMA 273 report, four seismic hazard levels are defined. The Basic Safety Earthquake 2 (BSE-2), also termed Maximum Considered Earthquake, has a 2% probability of exceedance in 50 years except that reduced shaking is defined near known faults with significant slip rates and characteristic earthquakes with magnitudes in excess of about 6. The Basic Safety Earthquake 1 (BSE-1) has a 10% probability of exceedance in 50 years. Two lesser seismic hazard levels that may also be considered include the 50% probability of exceedance in 50-year earthquake and the 20% probability of exceedance in 50-year earthquake.

Sample FEMA 273 performance objectives are shown in Figure 5.4. The document defines a Basic Safety Objective, which corresponds to designs satisfying the performance level-hazard level combinations designated by letters k and p. Satisfaction of additional performance objec-

tives, specifically Performance Objectives a, e, i, m, b, f, j, or n, is defined as enhanced design. A design that satisfies only Performance Objectives k or p (or c, g, d, or h) is defined to be a limited design. Figure 5.5 provides quantitative descriptions of engineering limit states for vertical concrete elements for each performance level. Current seismic design procedures for buildings target Performance Objective k.

Comparison of the ATC 32 and FEMA 273 approaches reveals similarities and differences. The primary similarity is the pairing of multiple performance levels with selected hazard levels. A main difference is that FEMA 273 more explicitly defines performance levels, the corresponding hazard levels, and the engineering limit states. Although FEMA 273 is specifically intended for buildings, many aspects appear relevant to bridges. Still, further work is needed to define performance levels relevant to bridge performance-based seismic design.

### **5.3 CONCEPTUAL FRAMEWORK FOR PERFORMANCE-BASED SEISMIC DESIGN**

Performance-based seismic design of bridges requires that the engineer complete the following tasks:

1. Select performance objective(s)
2. Define performance level using engineering limit states
3. Define hazard level at site
3. Perform structural design and evaluation using engineering approaches
4. Quality assurance

The following sections summarize recommendations for each task within the context of a performance-based seismic design framework for the design of reinforced concrete bridges. Performance levels and seismic hazard levels are defined. Performance objectives are developed by pairing a single performance level and a single seismic hazard level. Design approaches appropriate for each performance level are discussed. Expressions to assess the engineering limit states are provided to quantify each performance level; the engineering expressions used were developed in the analytical study and were evaluated using the experimental results described herein.

### 5.3.1 Performance Levels

For performance-based design of bridges, ATC 32 succeeds in defining performance levels that represent minimal, intermediate, and significant damage states. However, there are several shortcomings with the manner in which they are defined. Firstly, the document fails to explicitly define a minimal performance level that must be achieved for ordinary bridges. In addition, the performance levels are defined in terms of the required repair effort and serviceability; in some cases this definition may be too limiting.

To overcome these perceived shortcomings, the performance-based seismic design framework recommended herein adopts three performance levels. The three performance levels outlined in Table 5.1 are designated as Fully Operational Performance Level, Delayed Operational Performance Level, and Stability Performance Level. Each performance level is defined by the expected bridge serviceability, required repair effort, and the future performance.

For a bridge meeting the Fully Operational Performance Level, repair is not required and the bridge is expected to be fully serviceable immediately following the earthquake. To meet the minimum repair requirements, residual crack widths must be small and spalling should not occur. In addition to limits on local damage, such as cracking and spalling, there should be no disturbance of the bridge alignment. The future seismic performance will essentially be unaffected, which requires negligible damage accumulation.

A bridge meeting the Delayed Operational Performance Level requirements is expected to have sustained some damage during the earthquake. The bridge should provide limited service to emergency vehicles. Closure of the bridge should be limited to several days provided sufficient resources are available. Therefore, damage should be limited to concrete cracking, yielding of the longitudinal reinforcement, and spalling of the concrete cover. The repair effort may include patching of the cover concrete and epoxy injection; repair efforts that include partial or full element replacement do not fall within this performance level. In future, more significant events, the bridge performance is expected to be close to the original performance. However, the influence of prior damage on performance under future moderate demand levels has not been well established.

A bridge meeting the Stability Performance Level is expected to have sustained significant damage. As a result, partial or full replacement of bridge elements (including columns and restrainers) may be required and the bridge may remain out of service for several weeks or months. The future performance of the structure is limited; however, in its damaged state, the

bridge is expected to survive an aftershock of lesser intensity.

### **5.3.2 Seismic Hazard Levels**

Ideally, seismic hazards should be considered in terms of ground motion, including temporal and spatial variation, pounding, liquefaction, lateral spreading, and landslides. Although all types of hazard levels, especially ground shaking and lateral spreading, may be critical for bridge design, seismic hazards are generally defined only in terms of ground shaking. Herein each seismic hazard will be addressed briefly. Seismic hazard levels will be defined in terms of ground shaking.

Structural pounding is defined as one structure pounding against another. Pounding effects are particularly important for adjacent bridges of different heights, where the superstructure of one bridge may collide with the column of the other. Pounding can also be important at in-span hinges [EERI 1995]. Design solutions to avoid pounding include separating structures by the maximum expected relative displacements.

Liquefaction and subsequent lateral spreading may induce large permanent displacement demands. If site liquefaction is likely to occur, mitigating measures may be taken including modifications to the structure (including the foundation) to sustain the expected demands, or improvement of the ground to reduce or eliminate the liquefaction potential.

Similarly, landslides may induce large displacement demands. The following solutions may be appropriate to reduce earthquake-induced landslides: regrading, drainage, buttressing, structural improvements, soil modification, or resiting the bridge.

Typically, ground shaking is characterized using acceleration spectra, displacement design spectra, site-specific acceleration response spectra, site-specific displacement response spectra, and/or site-specific ground-motion records. Typically, the ground shaking is characterized by the site location, history and distance of faults of interest (this information may be obtained using a seismic hazard map), mean return period or exceedance criteria, soil conditions, and structural period. Further discussion of methods to characterize site-specific ground motion may be found in the FEMA 273 document. Seismic hazard maps may be obtained from the United States Geological Survey.

Herein, three performance levels are defined; each performance objective requires a pairing of a performance level and a minimum seismic hazard level. Therefore, three seismic hazard levels are defined. Within the state of California, the ATC 32 recommendations for ordinary bridges

may be adopted; the Intermediate and Significant Level Earthquakes corresponding to the Functional-Evaluation Earthquake and Safety-Evaluation Earthquake, respectively, as defined in ATC 32. These recommendations may not be appropriate for other regions. Ideally, the return period for the seismic hazard level will depend on the seismicity of the region and the site, and is defined to match an acceptable level of uniform risk.

Although defining a single return period for each hazard level may expedite the design process, it may be more realistic to consider the risk for each performance level. However, defining a uniform level of risk for each performance level depends on the seismicity of the region, economic factors, and structural importance of the bridge. In the context of the performance-based design framework proposed (Figure 5.2), the expected performance levels for ordinary structures are expected to be Fully Operational for the Minimum Level event, Delayed Operational for the Intermediate Level event and Life Safe for the Significant Level event. Therefore, the earthquake levels are defined in a broad sense, without specific reference to uniform risk or hazard levels. The three seismic hazard levels are defined as a Minimum Level Earthquake, Intermediate Level Earthquake, and Significant Level Earthquake. The return period for the Minimum Level Earthquake is defined to be in the range of 75 to 225 years. The return period for the Intermediate Level Earthquake is defined to be in the range of 225 to 475 years. The return period of the Significant Level Earthquake is defined to be in the range from 475 to 2500 years.

### **5.3.3 Performance Objectives**

A performance objective is the pairing of a performance level and a seismic hazard level. Typically, the performance objective is defined for a specific seismic hazard level. However, it is possible (and may be more realistic) to define performance objectives for the lifetime of the structure. This continuum approach estimates the life cycle costs by integrating the seismic performance in all seismic events over the lifetime of the bridge. This approach may provide a better estimate of the costs associated with the structural damage. However, the life cycle costs are more difficult to quantify and apply in design than the single hazard level approach. Therefore, the discrete method is adopted herein.

In addition to the performance level and seismic hazard level, a performance objective may also depend on the bridge category. For the purposes of this report, the ATC 32 recommendations are adopted and bridges are categorized as Ordinary and Important.

Five performance objectives are defined within the performance-based design framework (Figure 5.6). Three are defined for Ordinary bridge structures. Two are defined for Important bridge structures. Some of the performance objectives are similar to the performance objectives defined in the ATC 32 document. Ordinary bridges are structures expected to meet the objectives of the Fully Operational Performance Level for the Minimum hazard level, the objectives of the Delayed Operational Performance Level at the Intermediate hazard level, and the objectives of the Stability Performance Level at the Significant hazard level. Important bridges are expected to meet the objectives of the Fully Operational Performance Level at the Intermediate hazard level (and therefore, for the Minimum hazard level as well) and the objectives of the Fully Operational Performance Level at the Significant hazard level. Closure of important bridges is not permitted for the hazard levels specified.

## **5.4 ENGINEERING APPROACHES**

In conventional practice, structural design is achieved by performing a demand/capacity analysis. The structural demands and capacities are measured in terms of structural forces and strengths. Typically, the structural demand is assessed from a reduced elastic acceleration design spectrum. Using elastic analysis techniques, the forces are calculated and a demand/capacity analysis is performed for each element. A similar analysis is made for the drift. However, the drift demand is not necessarily the maximum drift demand the structure would experience during the design earthquake.

The engineering procedure in a performance-based environment is similar in that a demand/capacity approach is adopted. The parameters defining the structural capacity depend on the performance level. The performance level is intimately linked to the required method of seismic hazard assessment and structural analysis. Therefore, engineering approaches and limit states are specified explicitly for each performance level. The following sections summarize the engineering limit states and analysis methods applicable to the performance-based seismic design of reinforced concrete bridges.

### 5.4.1 Engineering Limit States Related to Performance Levels

In the proposed matrix, structural performance is defined in terms of service, repair effort, and future performance. For reinforced concrete bridges, the engineering limit states used to define each performance level are:

1. Cracking
2. Spalling
3. Residual Drift
5. Fatigue and Cross-Section Failure

The acceptable range of each engineering limit state must be defined for each performance level. Figure 5.7 identifies the engineering limit states that must be checked for each performance level.

A bridge designed to meet the requirements of the Fully Operational Performance Level is expected to respond essentially in the elastic range; repair is not required. To meet these requirements, residual crack widths are limited (e.g., less than 0.02 in.), and spalling, residual drift effects, and element fatigue are avoided. As indicated in Figure 5.7, the cracking engineering limit state is checked at the Fully Operational Performance Level.

A bridge designed to meet the requirements of the Delayed Operational Performance Level is expected to sustain moderate damage. Following the ATC 32 guidelines for repairable damage, post-earthquake repair may include concrete cracking, yielding of the longitudinal reinforcement, and spalling of the concrete cover; replacement of reinforcement or structural members is not permitted. The repair effort should be limited to limit closure of the bridge; therefore, permanent offsets should be avoided. At this performance level, the cracking limit state may be exceeded. The spalling engineering limit state should be checked to ensure that spalling is limited to the cover and does not extend into the core. Residual drifts should not exceed permissible construction offsets as defined by the local design provisions. (Note that the issue of residual drifts for the Delayed Operational Performance Level may need to be researched further. It may be permissible to allow limited drift ratios that meet the repair requirements.) Figure 5.7 indicates the acceptable limit states of cracking and spalling.

A bridge designed to meet the requirements of the Stability performance level is expected to sustain significant damage without imminent collapse. Exhaustion of the cross-section capacity must be avoided to ensure stability under gravity loading. However, the other limit states, includ-

ing cracking, spalling, residual drift and fatigue, may be exceeded.

#### ***5.4.1.1 Experimental Implications***

The limit states were quantified using the experimental results. In the following subsections, observed experimental response and numerical expressions are used to define and quantify structural performance. Where applicable, appropriate repair techniques are recommended.

##### ***5.4.1.1.1 Cracking***

Crack widths and crack patterns may be used to indicate the required repair effort. Large residual crack widths (from 0.01-0.02 in.) may need to be filled with epoxy or other material to restore the tensile strength.

The residual crack widths measured during testing were used to postulate maximum permissible displacement ductility demand to ensure minimum crack widths. Although strain demands should provide a more uniform assessment of crack widths, observations of the post-yield response of the longitudinal strain gauges indicated the measurements were not reliable when the yield plateau was reached. In addition, since yielding of the cross section is progressive, local strain readings do not indicate cross-section crack widths.

Figures 5.8 and 5.9 provide the maximum crack widths, residual crack widths, and corresponding displacement ductility demands measured during testing; the crack that was measured for the columns was located approximately 6 inches above the interface on the North face of the column (see Chapter 3 for further details of the test results). The displacement ductility is the ratio of the measured displacement,  $\Delta$ , and the effective yield displacement,  $\Delta_y'$ . The reader is cautioned to note that the residual crack width measurements correspond to the zero displacement point upon completion of a displacement cycle and not the zero force point.

In general, the measured response indicates that the residual crack widths are 0.01 inches or less for displacement ductility demands less than 1.5 and are 0.02 inches or less for displacement ductilities less than 2. Therefore, to limit residual crack width, the displacement demand should be less than twice the effective yield displacement. Limiting the displacement demand to the effective yield displacement will ensure acceptable crack widths and essentially linear response.

#### ***5.4.1.1.2 Spalling***

Cover spalling may reduce the lateral stiffness of the cross section, the durability in terms of corrosion, and the lateral restraint on the longitudinal bar. Post-earthquake damage to the concrete cover can require concrete patching; core damage can require partial or complete replacement of the structural element.

An important research study on the effects of displacement history on spalling was reported by Kunnath et al. [Kunnath 1997]. In that study, 12 columns were constructed and subjected to various displacement histories including monotonic, constant amplitude cyclic, and random pseudo-static earthquake loadings. The subset of columns tested under constant amplitude response provide important information on low-cycle fatigue response. Four nominally identical columns were constructed and cycled to repeated displacements. The four constant amplitude drift ratios were 2%, 4%, 5.5%, and 7%; the drift ratios corresponded to estimated displacement ductilities of 2, 3, 4, and 5. In addition, a nominally identical column was subjected to monotonic loading. Table 5.2 presents salient aspects of the column testing program including the physical damage due to monotonic loading at the displacement level, number of cycles to spalling of the entire cover (estimated from the documented observations of physical damage), and the number of cycles to failure. Three of the columns failed; one did not. The column that did not fail, Column A3, was subjected to a constant amplitude history of 2% drift. At this drift level, the column subjected to monotonic loading (Column A1) had cracked but cover spalling had not occurred. Using these results, it is postulated that fatigue-induced failure is likely if damage incurred by the imposed displacement demands results in complete spalling of the concrete cover. This result implies that initial spalling is not influenced by earthquake-type fatigue loading. Therefore a non-cumulative, strain-based damage index may be sufficient to predict initial spalling of the concrete cover.

Numerous studies have focused on the behavior, performance, and repair of modern ductile columns. The experimental observations made during this study, which are relevant to the behavior of modern columns, are used to correlate physical damage and predicted response. Additional observations from experimental research by Elkin and Moehle [Elkin 1998], which focused on the repair of modern bridge columns, and experimental research by Kunnath et al. [Kunnath 1997] and Calderone and Moehle [Calderone 1998], both of which focused on the performance of modern bridge columns, are included to substantiate the findings.

The experimental results from the study by Calderone and Moehle, the study by Kunnath et al., and the present study were used to evaluate the feasibility of using concrete strain to indicate initial spalling of the concrete cover. A predictive analysis was performed for each test specimen. The columns were analyzed using the discrete modeling technique described in Section 4.2 using the measured material properties. Table 5.3 summarizes the results. The measured initial spalling displacement is recorded in the second column of the table. The predicted compressive strain in the extreme fiber corresponding to the initial spalling displacement is recorded in the third column of the table. The results indicate that the strain corresponding to initial spalling of the cover is in the range of -0.008 to -0.01. For the provided data, the mean spalling strain is -0.009 with a standard deviation of 0.001. Although spalling is not uniquely related to strain demand, the results indicate that compressive strain may provide a reasonable estimate of initial concrete spalling. For design, a compressive strain demand of mean plus two standard deviations, or a compressive strain of -0.007, is suggested. Given the size of the sample set however, further analysis of experimental results including a study of model reliability is warranted.

A repair technique for the spalling limit state was evaluated by Elkin and Moehle by investigating the influence of previous damage on the response of repaired columns with different levels of damage. The study was an extension of the present study. Column 415, which was tested as a part of this study, was repaired using a reinforced concrete jacket. A second column, nominally identical to Column 415, was constructed and tested to a more moderate damage level that included concrete cracking, initial spalling of the concrete cover, and yielding of the longitudinal steel. The displacement history used in the repair study was the same as used in the present study. To impose a moderate damage level, the displacement history was terminated at the displacement level corresponding to a displacement ductility of three; the physical damage state included cracking and limited spalling of the concrete cover such that the longitudinal bars and spirals were not visible. The column was repaired as follows: the column was plumbed to its original position, the loose concrete was removed, the spalled region was patched, and the open cracks were injected with epoxy. The repaired column was retested by imposing the original displacement history until column failure was reached. The force-displacement responses for Column 415 and the repaired column are given in Figure 5.10. Salient observations include:

1. The initial stiffness of the repaired column was less than that of the undamaged column.
2. The strength of the repaired column approaches the strength of the original column at the maximum displacement imposed during the initial displacement history.

3. The unloading stiffness of the repaired column is less than the unloading stiffness of the original column.
4. The strength loss during the first cycle to 7 inches is larger for the repaired column than for that for the original column.

The results indicate that the repair technique of concrete patching and crack injection may be necessary for environmental and aesthetic reasons; however, its effectiveness in restoring the original stiffness is limited.

#### 5.4.1.1.3 Fatigue and Cross-Section Failure

The response and failure of reinforced concrete elements subjected to seismic loading can be influenced by the load path. Fatigue of the concrete cover may require removal and replacement of the damaged concrete. Cross section failure, which includes longitudinal bar fatigue and/or fatigue of the core concrete, may require partial or full replacement of a structural element. Evaluations of the experimental use of such replacement techniques on modern bridge columns may be found in the literature [e.g., Elkin 1998, Nacamuli 1998].

The dual-phase index proposed in Chapter 4 was used to predict column failure. The index models fatigue of the concrete and the fatigue of the longitudinal steel in two phases.

$$DI_c = \sum_i \frac{1}{(N_f)_{ci}}; DI_c \leq 1 \quad (5.1)$$

$$DI_s = \sum_i \frac{1}{(N_f)_{si}} \text{ if } DI_c = 1; DI_s \leq 1 \quad (5.2)$$

Fatigue-induced failure of the concrete cover corresponds to approximately  $DI_c = 1$ . Fatigue-induced failure of the longitudinal steel corresponds to approximately  $DI_s = 1$ . Further description of the model may be found in Chapter 4.

The Fatigue Engineering Limit States are specified for the Delayed Operational Performance Level and the Stability Performance Level; each corresponds to the required repair effort specified in Table 5.4. Fatigue failure of the concrete is not permitted for a bridge designed to meet the Delayed Operational performance state. For the Life Safe Performance Level, failure of the concrete is permissible (i.e.,  $DI_c = 0$ ); however, failure of the longitudinal steel should be avoided (i.e.,  $DI_s < 0.9$ ). Repair (i.e. concrete patching) will be required if  $DI_c > 0$ .

#### 5.4.1.1.4 Residual Drift

Post-earthquake damage of yielding structures often includes residual drift. Residual drift is a direct indication of the required repair effort. In the case of large residual drifts, repair may not be feasible. On the basis of residual drift considerations, Japanese engineers have proposed limiting the allowable residual drift to 1.67% [PWRI 1998].

Several researchers have studied this problem using single-degree-of-freedom oscillators with various earthquake ground motions. MacRae and Kawashima [MacRae 1997] investigated the response of bilinear oscillators. In the study, ductility demand, ratio of the post-yield stiffness to the initial stiffness, type of soil, and structural period were varied. The research results indicate that the residual displacement ratio primarily depends most heavily on the stiffness ratio. For oscillators with moderate stiffness ratios (0.05 to 0.5), the ductility demand also influenced the residual displacement. Figure 5.11 provides charts available to quickly assess the residual drift ratio (ratio of the residual drift demand to the maximum displacement demand).

The present experimental results were used to provide insight into the likelihood of meeting various residual drift requirements, such as those suggested by PWRI. Using the charts developed by MacRae and Kawashima, the properties of Column 415 were used to evaluate the expected residual drift. As indicated in the force-displacement response shown in Chapter 3, the ratio of the post-yield stiffness and the initial stiffness of Column 415 is small. The stiffness ratio (the ratio of the elastic and yielding stiffness of the bilinear response envelope) was estimated as 0.05. The chart shown in Figure 5.11a was developed for a displacement ductility of four. The mean plus one standard deviation curve residual drift ratio is 0.6 times the maximum drift ratio or in this case 2.4%. This residual drift greatly exceeds the suggested drift ratio of 1.67%. In fact, according to the chart, the stiffness ratio of the column would have to be 0.1 or greater to ensure the residual drift ratio was less than 1.67%.

The PWRI document suggests Equation 5.3 to assess the residual displacement,  $\delta_r$ :

$$\delta_r = (\mu_{\Delta} - 1)(1 - r)\Delta_y' \quad (5.3)$$

where  $\mu_{\Delta}$  is the displacement ductility demand,  $r$  is the ratio of the post-yield stiffness to the secant stiffness to yield, and  $\Delta_y'$  is the yield displacement. The expression was used to predict the displacement ductility demand that would meet the PWRI requirements using the properties of

Column 415. The analysis indicates the displacement ductility should be limited to 3 to meet the drift limitations. In comparison with limitations due to cross-section fatigue, the allowable displacement ductility for the residual drift limit state may be less than the fatigue limit state. This suggests that acceptable residual drifts may be as or more limiting than specimen fatigue.

### **5.4.2 Analysis Methods**

Each single performance objective matches a performance level and a seismic hazard level. The structural capacity is defined for each performance level using engineering limit states. The structural demand is defined by the seismic hazard level that is described by a response spectrum or a ground-motion history. The structural demand and capacity are related by performing a structural analysis. Basic analysis procedures to relate the seismic hazard level to the structural capacity include linear analysis and nonlinear analysis methods; either may use static or dynamic procedures.

The analysis method used should capture the expected nonlinearity of the structural response and its effect on the seismic demand. The degree of structural nonlinearity is related to engineering limit state, i.e., cracking, spalling, and cross-section fatigue. The required analysis procedure depends on the degree of nonlinearity; likewise the appropriate choice of the analysis procedure depends on the performance level. Table 5.5 relates the analysis procedures and the engineering limit states.

Static analyses may be appropriate for all performance levels. Static analysis procedures use either response or design spectra to estimate seismic demands to estimate the maximum seismic force and drift demands. To account for element hysteresis, the response spectrum is reduced using effective damping or structural displacement ductility factors. The available static analysis procedures include the force-based design procedure [e.g., FEMA 1997], the displacement-based design procedure [e.g., Moehle 1985, Kowalsky 1995], and the energy-based design procedure [e.g., Teran-Gilmore 1996]. The referenced papers provide method details, appropriate applications, and limitations. In some cases, for example large displacement demand levels or longer earthquake durations, cyclic effects can impact the structural response. Nonlinear static or nonlinear dynamic procedures may be required to properly account for cyclic effects.

Table 5.5 pairs each design procedure with the appropriate performance level. For Fully Operational performance, the strength-based design procedure may be used. The displacement-based design procedure may be used for bridges meeting the Delayed Operational Performance Level. The Stability Performance Level requires that a fatigue-based design procedure be employed. The proposed analysis methods used include linear static, nonlinear static, and nonlinear dynamic. A design method that uses static analysis procedures consists of the following five, general steps:

1. Construct response spectrum for desired response quantity (e.g., force, drift, energy, f fatigue).
2. Estimate the gross secant stiffness and damping of structure.
3. Determine the structural demand from the response spectrum.
4. Determine the distribution of demands using a modal analysis.
5. Analyze the structure to determine the local element demands for the desired engineering limit state.

A structure designed to meet the Fully Operational Performance Level is expected to be essentially elastic, i.e., yielding of the longitudinal reinforcement is restricted. In this case the force-displacement response is approximately linear; a force-based analysis procedure is used. Force-based methods use strength to characterize the structural response. The structural displacement should not exceed the effective yield displacement. The base shear demand is estimated using an acceleration response spectrum (or design spectrum if a site-specific response spectrum is not available) for the appropriate seismic hazard level. The structural geometry and stiffness must be considered to determine the appropriate number of modes of response required for analysis. A demand/capacity analysis is performed using element forces and strengths.

A structure designed to meet the Delayed Operational Performance Level is expected to yield and should be modeled using nonlinear analysis procedures. Depending on the compressive strain demand, cyclic effects at this level may be negligible; for such cases, use of a displacement-based design approach is appropriate. Since there is not yet general consensus on the details of the displacement-based design approach, only a general outline of the method is provided. Herein, the substitute structure method is adopted [Shibata 1976]. The method is outlined as follows.

1. Estimate the force-displacement response envelope of the structure. A general purpose nonlinear analysis program may assist in this step.
2. Approximate the allowable displacement to restrict crushing of the concrete core.

3. Using this curve, estimate an equivalent structural damping ratio and secant stiffness. The expression developed by Gulkan and Sozen [Gulkan 1974] may be used to correlate the displacement ductility demand with structural damping ratio.
4. The structural displacement demand is estimated, preferably using a site-specific response spectrum for the appropriate seismic hazard level.
5. A demand/capacity analysis is performed. A redesign may be required if the structural displacement demand exceeds the capacity.

At the Stability Performance Level, the structural response is expected to be highly nonlinear. The structure is expected to sustain permanent offsets (Residual Drift Limit State) and cyclic response effects must be assessed. Previous researchers have proposed the energy-based approach to achieve this objective [Teran-Gilmore 1996]. The energy-based design approach is similar to the displacement-based design approach. However in the energy-based design approach the displacement capacity is limited due to cyclic effects. Energy demand is used to characterize the cyclic effects. The energy-based design approach employs an energy-based damage index, such as the Park-Ang damage index, to relate the displacement capacity to the energy demand. This allows that the displacement-based design method can be used with two substitutions:

1. In addition to estimating the displacement demand using a displacement response spectrum, estimate the energy demand using an energy-response spectrum.
2. Assess the displacement capacity using an energy-based damage ratio (e.g. the Park-Ang Damage Index)

As demonstrated in Chapter 4, energy does not reliably characterize the cyclic response of a reinforced concrete element; therefore an alternative, dual-phase fatigue-based damage index was developed to assess the effects of cyclic loading. To date, fatigue-based static design methods have not been fully developed (in comparison with energy-based design methods) and it is not possible to fully implement (or advocate) any fatigue-based design method. However, it may be postulated that a fatigue-based design approach would be similar to the energy-based method using a fatigue response spectrum instead of an energy response spectrum. Currently, it is possible, although more computationally expensive, to use a nonlinear dynamic analysis procedure to assess the cyclic strain demands on each element and the dual-phase damage index to assess the element capacity.

**Table 5.1: Recommended Performance Levels**

Performance Level	Required Repair Effort Serviceability	Future Performance
Fully Operational	Minimal Damage Fully Serviceable	Original Level
Delayed Operational	Repairable Damaged Delayed Service	Slightly Reduced from Original
Stability	Significant Damage Significantly Delayed	Minimum Level (Aftershock)

**Table 5.2: Results for Columns Subjected to Constant Amplitude Displacement Histories (translated from [Kunnath 1997])**

Column	Reported Displacement Ductility	Monotonic Damage	Cycles to:	
			No Cover	Failure
A3	2 (1.1 inches)	Yield	>150	N/A
A4	3 (2.2 inches)	Initial Spalling	8	25
A5	4 (3 inches)	Initial Spalling	6	9
A6	5 (3.8 inches)	Significant Spalling	1	3

**Table 5.3: Measured Displacement and Predicted Strain Corresponding to Initial Spalling**

Research Team	Column	Measured Initial Spalling Displacement	Corresponding Predicted Spalling Strain
Lehman and Moehle	407	1.5 in.	-0.008
	415	1.5 in.	-0.008
	430	1.5 in.	-0.01
	815	5.25 in.	-0.009
	1015	7.5 in.	-0.008

**Table 5.3: Measured Displacement and Predicted Strain Corresponding to Initial Spalling**

Research Team	Column	Measured Initial Spalling Displacement	Corresponding Predicted Spalling Strain
Kunnath et al.	A1	1.1 in.	-0.01
Calderone and Moehle	328	0.8 in.	-0.01
	828	5.25 in.	-0.01
	1028	7.5 in.	-0.01
Mean			-0.009
Standard Deviation			0.001

**Table 5.4: Correlation of Numerical Expressions and Performance Criteria**

Numerical Expression		Physical Damage	Repair
Displacement Ductility Demand/ Tensile Strain in Steel		Cracking	Epoxy Injection
Compressive Strain in Cover		Initial Spalling	Patching
Residual Drift		Residual Drift	Plumb Structure
Dual-Phase Damage Index	$(DI)_c = 1$ $(DI)_s = 0$	Complete Spalling	Concrete Replacement
	$(DI)_s \leq 0.9$	Bar/Spiral Failure	Fully Damaged Replacement Only

**Table 5.5: Minimum Required Analysis Procedures**

Performance Level	Engineering Limit State	Analysis Method	Design Procedure
Fully Operational	Cracking	Linear Static	Force-Based Design
Delayed Operational	Spalling	Nonlinear Static	Displacement-Based Design
Life Safe	Fatigue Residual Drift	Nonlinear Static or Nonlinear Dynamic	Fatigue-Based Design

Seismic Hazard Level	Structural Performance Level	
		Life-Safety
	Hazard Level: 10% Exceedingly in 50 Years	

**Figure 5.1: Current Seismic Design**

	Structural Performance Level			
Seismic Hazard Level	<div style="display: flex; align-items: center;"> <div style="width: 15px; height: 15px; background-color: black; margin-right: 5px;"></div> Ordinary Structure         </div> <div style="display: flex; align-items: center; margin-top: 5px;"> <div style="width: 15px; height: 15px; background-color: gray; margin-right: 5px;"></div> Important Structure         </div>	Maximum Performance Level (e.g. Fully Operational)	Intermediate Performance Level (e.g. Delayed Operational)	Minimum Performance Level (e.g. Life Safety)
	Minimum Hazard Level			
	Intermediate Hazard Level			
	Maximum Hazard Level			

**Figure 5.2: Performance-Based Seismic Design**

		Performance Level		
	<div style="display: flex; align-items: center;"> <div style="width: 15px; height: 15px; background-color: black; margin-right: 5px;"></div> Ordinary Structure         </div> <div style="display: flex; align-items: center; margin-top: 5px;"> <div style="width: 15px; height: 15px; background-color: gray; margin-right: 5px;"></div> Important Structure         </div>	Minimal Damage, Immediate Service	Repairable Damage, Immediate Service	Limited Damage, Limited Service
Hazard Level	Functional-Evaluation Ground Motion			
	Safety-Evaluation Ground Motion			

Figure 5.3: ATC 32 Hazard and Performance Levels for Ordinary and Important Bridges

		Building Performance Levels			
		Operational Performance Level (1-A)	Immediate Occupancy Performance Level (1-B)	Life Safety Performance Level (3-C)	Collapse Prevention Performance Level (5-E)
Earthquake Hazard Level	50%/50 year	a	b	c	d
	20%/50 year	e	f	g	h
	BSE-1 (~10%/50 year)	i	j	k	l
	BSE-2 (~2%/50 year)	m	n	o	p

k + p = BSO  
 k + p + any of a, e, i, m; or b, f, j, or n = Enhanced Objectives  
 o = Enhanced Objective  
 k alone or p alone = Limited Objectives  
 c, g, d, h = Limited Objectives

Figure 5.4: FEMA 273 Performance Objectives

**Table 2-4 Structural Performance Levels and Damage<sup>1</sup>—Vertical Elements**

Elements	Type	Structural Performance Levels		
		Collapse Prevention S-5	Life Safety S-3	Immediate Occupancy S-1
Concrete Frames	Primary	Extensive cracking and hinge formation in ductile elements. Limited cracking and/or splice failure in some nonductile columns. Severe damage in short columns.	Extensive damage to beams. Spalling of cover and shear cracking (< 1/8" width) for ductile columns. Minor spalling in nonductile columns. Joint cracks < 1/8" wide.	Minor hairline cracking. Limited yielding possible at a few locations. No crushing (strains below 0.003).
	Secondary	Extensive spalling in columns (limited shortening) and beams. Severe joint damage. Some reinforcing buckled.	Extensive cracking and hinge formation in ductile elements. Limited cracking and/or splice failure in some nonductile columns. Severe damage in short columns.	Minor spalling in a few places in ductile columns and beams. Flexural cracking in beams and columns. Shear cracking in joints < 1/16" width.
	Drift <sup>2</sup>	4% transient or permanent	2% transient; 1% permanent	1% transient; negligible permanent

**Figure 5.5: Damage Descriptions by Performance Levels [FEMA 1997]**

		Performance Levels		
		Fully Operational	Delayed Operational	Stability
Hazard Levels	Minimum	■ Ordinary Structure		
	Intermediate	■ Important Structure	■ Ordinary Structure	
	Significant		■ Important Structure	■ Ordinary Structure

**Figure 5.6: Proposed Performance Objectives**

		Performance Levels		
		Fully Operational	Delayed Operational	Stability
Engineering Limit States	Cracking	■ Check Limit State	■ Check Limit State	■ Check Limit State
	Spalling		■ Check Limit State	■ Check Limit State
	Residual Drift			■ Check Limit State
	Fatigue			■ Check Limit State
	Cross Section Failure			

**Figure 5.7: Correlation of Engineering Limit States and Performance Levels**

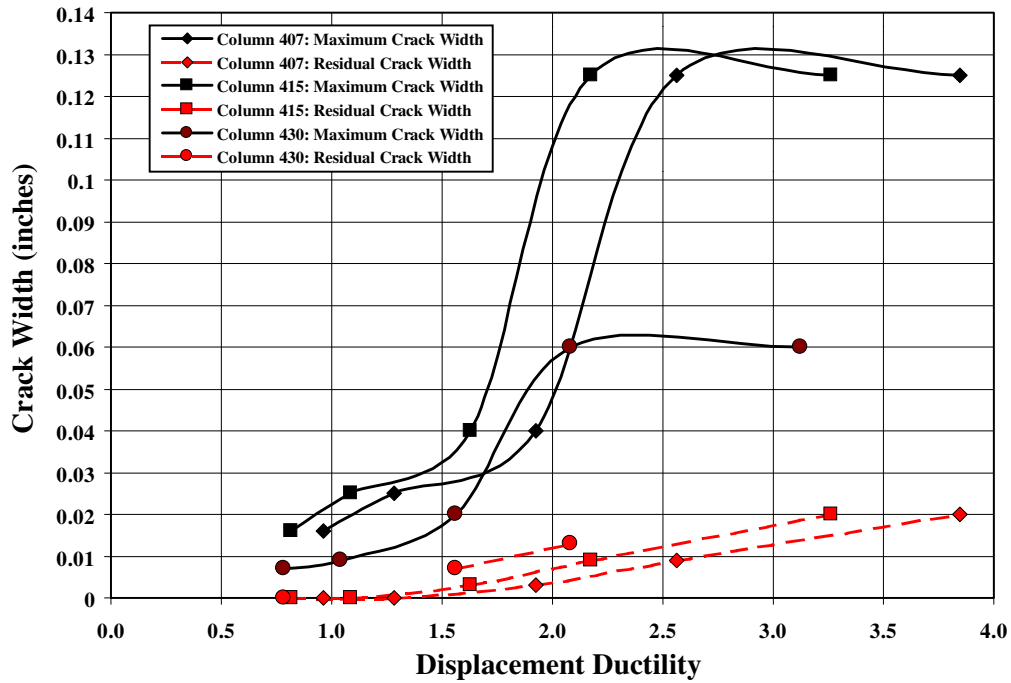


Figure 5.8: Test Series I Measured Crack Widths vs. Displacement Ductility Demand

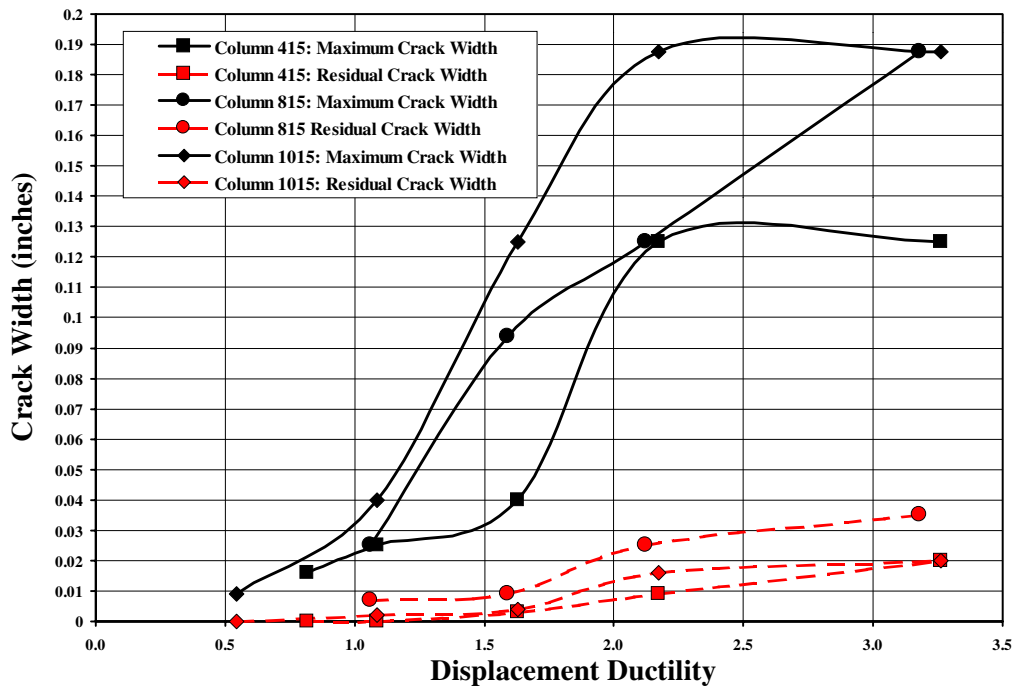


Figure 5.9: Test Series II Measured Crack Widths vs. Displacement Ductility Demand

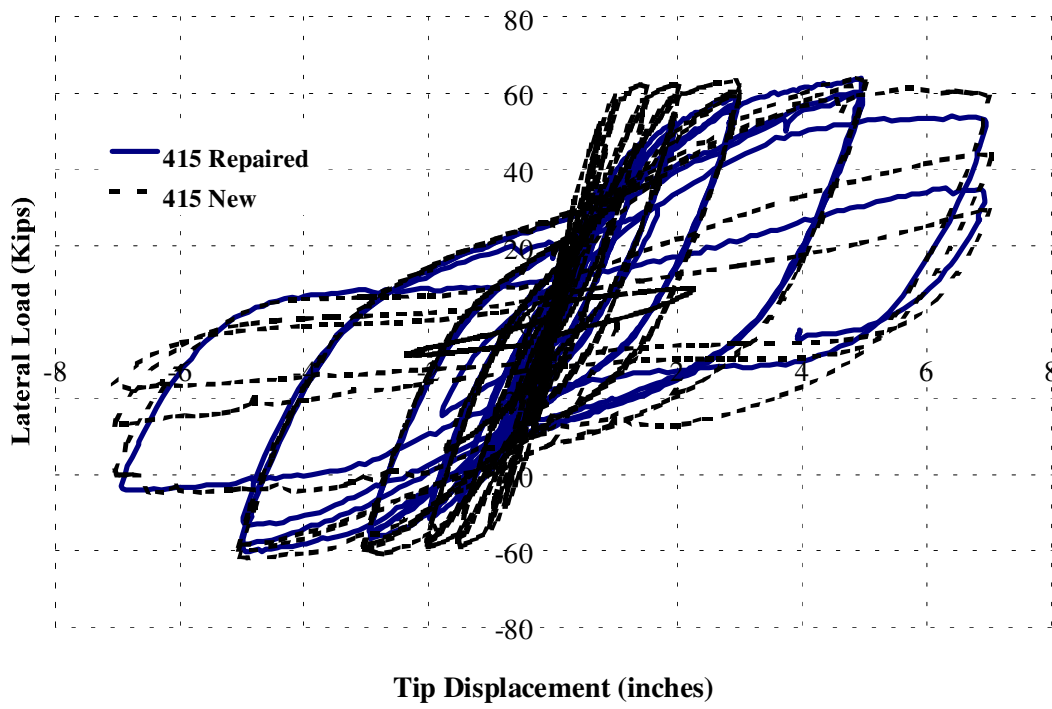
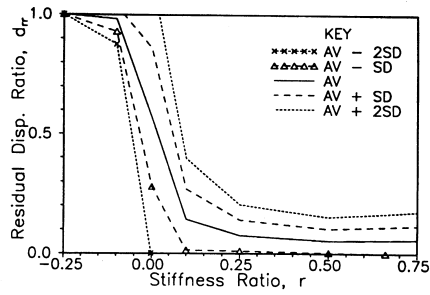
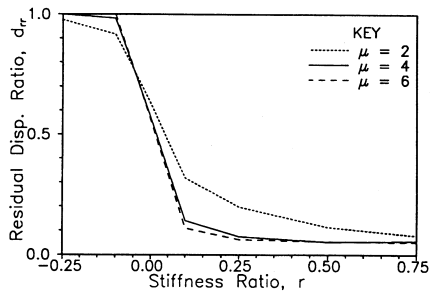


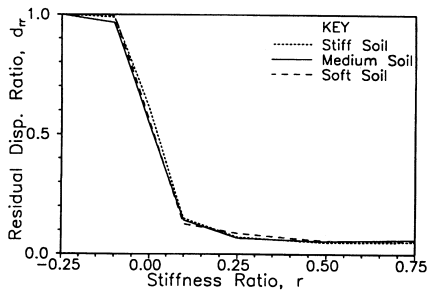
Figure 5.10: Force-Displacement Response of Original and Repaired Column [Elkin 1997]



Average residual displacement ratio,  $d_r$ , versus stiffness ratio,  $r$ , for all records ( $\mu=4$ )



Effect of peak ductility,  $\mu$ , on average residual displacement ratio,  $d_r$



Effect of ground type on average residual displacement ratio,  $d_r$  ( $h=2$  per cent,  $\mu=4$ )

**Figure 5.11: Average Residual Displacement Ratio [MacRae 1997]**

# 6 Summary, Conclusions, and Future Research

## 6.1 SUMMARY OF RESEARCH PROGRAM

In modern construction, the seismic performance of reinforced concrete bridge structures depends on the response of the ductile hinge regions. A research program was undertaken to characterize the response of well-confined, circular cross-section, concrete bridge columns. The research objectives included evaluating current design procedures and recommended performance-based design procedures for reinforced concrete bridges in seismic zones. The research was executed in three stages. The existing literature was reviewed and used to guide the design of the experimental and analytical components of the investigation. The results of the research study were used to develop a performance-based design framework for reinforced concrete bridges.

The following text summarizes each phase of the research program.

### *Literature Review*

Initially, parameters that influence the seismic response of reinforced concrete bridge columns were identified. For each parameter, previous research results were reviewed and summarized. As a result, aspect ratio and longitudinal reinforcement ratio were chosen as the study parameters.

### *Experimental Investigation*

An experimental investigation was designed to study the influence of the two study parameters on column response. A test matrix that consisted of five columns tested in two series was developed. The columns were constructed at one-third of full scale. With the exception of the study parameters, the columns were detailed with nominally identical geometries, reinforcement quantities, and material properties. The three columns of the first test series had aspect ratios of 4 and longitudinal reinforcement ratios of 0.75%, 1.5%, and 3.0%. The three columns of the second test series had longitudinal reinforcement ratios of 1.5% and aspect ratios of 4, 8, and 10.

In the laboratory, the columns were tested upright and subjected to a constant axial load and reversed cyclic lateral loading. The lateral load was applied using displacement control and followed a standard displacement history with increasing displacement demands for each cycle.

System response was monitored using load cells and displacement gauges. The system

response was expressed in terms of axial force, lateral force, and lateral displacement. In addition, the column and joint regions were extensively instrumented with internal strain gauges and external displacement gauges within the expected length of plastic action. At most locations the deformations were monitored to interpret average curvature, average shear strain, average normal strain, horizontal expansion, and horizontal displacement of the column. In addition, crack patterns, crack widths, and damage patterns were monitored during testing.

### ***Analytical Investigation***

Models to assess column and joint strengths, the force-displacement response envelope, the cyclic force-displacement response, and element damage were evaluated. Using the experimental results, modifications to the available methods were proposed as appropriate. In particular, strength design provisions specified in the California Department of Transportation Bridge Design Specification [Caltrans 1991] and the ATC 32 Improved Seismic Design Criteria for California Bridges: Provisional Recommendations were evaluated [ATC 1996]. In addition, methods to assess the force-displacement response envelope of a reinforced concrete element were evaluated. The response envelope may be calculated directly by integrating deformations along the column and the anchorage zone or indirectly using the plastic hinge length method. Available versions of these direct methods were evaluated and modifications suggested. Finally, the suitability of damage indices to assess damage of a reinforced concrete bridge element was evaluated. A new, fatigue-based damage index was proposed, based on the sequence of damage observed during testing.

## **6.2 CONCLUSIONS**

The experimental and analytical investigation was undertaken to characterize the response of modern reinforced concrete bridge columns. The following primary conclusions were obtained.

### ***Experimental Investigation***

1. The force-displacement response of the experimental columns was ductile and stable well beyond the elastic limit.
2. With one exception, the sequence of damage observed during testing was similar for the five columns, and followed the sequence of cracking, yielding of the longitudinal steel, initial spalling of the concrete cover, loss of the concrete cover, yielding of spiral reinforcement/longitudinal bar buckling, spiral fracture and longitudinal bar fracture. The

exception was that the longitudinal reinforcement did not fracture in the heavily reinforced column.

3. Longitudinal reinforcement ratio influenced the column failure mode. Columns having longitudinal reinforcement ratios of 0.75% or 1.5% failed due to bar fracture that was preceded by and appeared to result from prior bar buckling. Column 430, which was reinforced with 3.0% longitudinal steel, failed as a result of excessive bar buckling, spiral fracture, and extensive damage to the core concrete; the longitudinal bars of Column 430 did not fracture.
4. Experimental results demonstrated that shearing deformations of slender columns are less than 5% of the total displacement. The contribution of the bending displacement relative to the slip displacement increases with column slenderness.

### ***Analytical Investigation***

1. Plastic moment strengths were evaluated using two procedures. The more accurate of the two involved a direct, cross-sectional analysis assuming linear variation of strain across the section depth with actual material properties represented. As an alternative, the plastic moment strength,  $M_p$ , can be calculated as the product of the nominal moment strength,  $M_n$ , and appropriate magnification factors,  $m_1$  and  $m_2$ ; that is  $M_p = m_1 m_2 M_n$ . The first magnification factor,  $m_1$ , depends on the quantity of longitudinal reinforcement and axial load ratio. For axial load ratios less than 20% of the gross cross-sectional capacity,  $m_1$ , primarily depends on the longitudinal reinforcement ratio and ranges from 1.2 to 1.3. The second magnification factor,  $m_2$ , is equal to 1.0 unless the nominal moment strength was calculated using specified material strength. If this is the case, analytical results indicate that the magnification factor  $m_2$  can be approximated as the ratio of the expected yield strength,  $f_{ye}$ , to the specified yield strength,  $f_{ys}$ , that is  $m_2 = f_{ye}/f_{ys}$ .
2. The force-displacement response envelope can be assessed using a discrete modeling technique. Using a flexibility-based approach, models were proposed to individually calculate the flexural deformation, the shearing deformation, and deformation due to slip of the longitudinal reinforcement from the joint. Using actual material strengths to model the columns, the predicted response and measured response for the individual response mechanisms and the overall force-displacement response were similar, indicating that the modeling technique is suitable for the analysis of reinforced concrete bridge columns.
3. Analyses indicate that a simplified approach based on the plastic hinge length method may also be used to assess the force-displacement response envelope. The proposed model is a simplification of the models used to calculate the slip and bending components of the discrete modeling approach. The plastic hinge length,  $l_p$ , depends on the maximum steel stress and ratio of the maximum and nominal moments and therefore it lengthens with increased plastic demand. As such, the proposed model may be used to assess the entire force-displacement response envelope.
4. The cyclic force-displacement response of the columns was modeled using a hysteresis model. The proposed model, a modification of the Q-hyst model, consists of trilinear

backbone curves, and bilinear unloading and reloading curves. To assess the accuracy of the model, the quantities of energy dissipated during a single cycle were compared. The results were similar for the measured and predicted responses.

5. Reversed cyclic loading influences the response, the failure mode, and displacement capacity of reinforced concrete bridge columns. Both energy-based and fatigue-based cumulative damage have been proposed. However, columns tests indicate that the energy dissipation capacity of a reinforced concrete element depends on the imposed displacement history. As a result, energy dissipation capacity seems inappropriate as a way to characterize element performance. A new fatigue-based damage index was proposed. The proposed damage index models column damage in two phases. In the first phase, fatigue-induced damage to the concrete cover is modeled. In the second phase, fatigue-induced damage of the longitudinal steel is modeled. Both models use a modified format of the Coffin-Manson equation to assess the fatigue effects and employ Minor's rule to calculate the damage index. Using the dual-phase index, failure of the five experimental columns of the current study as well as the columns tested by Kunnath et al. [Kunnath 1997] were predicted.

### ***Performance-Based Seismic Design of Reinforced Concrete Bridges***

A performance-based seismic design framework for reinforced concrete bridges was developed. Three performance objectives were established; each performance objective was defined by a single performance level and a single hazard level. Engineering limit states, based on the results from the experimental and analytical investigations, were used to define each performance level. Guidelines for appropriate design methods for each performance level were also defined.

The following summarizes the performance-based design framework.

1. ***Performance Objectives*** Three performance objectives were defined as the Fully Operational Performance Objective, the Delayed Operational Performance Objective and the Life Safe Performance Objective. In general terms, a bridge designed to meet the Fully Operational Performance Objective is expected to be undamaged and fully operational, a bridge designed to meet the Delayed Operational Performance Objective is expected to be immediately repairable requiring limited delay in operation, and a bridge designed to meet the Life Safe Performance Objective is expected to sustain significant damage without impairing life safety and may not be able to be repaired.
2. ***Performance Levels*** A single performance level is associated with each performance objective. Therefore, the performance levels are designated using the same titles and intents as the performance objectives, i.e., Fully Operational, Delayed Operational and Life Safe Performance Level.
3. ***Engineering Limit States*** Engineering limit states define the state of element damage and thereby define the Performance Levels. Four limit states are defined: Cracking, Spalling, Residual Drift, and Cross-Section Fatigue. Expressions to approximate each limit state were evaluated using the response measured or observed during the experimental investi-

gation.

4. ***Seismic Hazard Levels*** The design framework proposed three seismic hazard levels with a defined range of exceedance. The appropriate value of exceedance will depend on the specified seismicity of the site.
5. ***Design Approaches*** Force-based, displacement-based, and fatigue-based design approaches were discussed. Use of a particular design approach directly depends on the engineering limit states. A force-based design approach is recommended for bridges that do not exceed the Cracking Limit State. A displacement-based design approach is recommended for bridges that do not exceed the Spalling Limit State. The fatigue-based approach is recommended for all other bridges.

### **6.2.1 Future Research**

The research program included an in-depth experimental and analytical investigation of specific aspects of modern, ductile reinforced concrete bridge columns. To further the state of performance-oriented bridge design, additional aspects should be included in future research. Specifically, the effect of the following parameters on the modeling procedures should be studied:

1. The effect of varying the load history from the standard history used in this study,
2. The effect of subjecting the column to biaxial lateral loading,
3. The effect of modifying the quantity of spiral reinforcement,
4. The influence of longitudinal bar diameter,
5. The effect of high strength concrete and steel

In addition, a comprehensive experimental study is required to study the fatigue-based failure mode. The proposed dual-phase damage index has proved to be successful to model failure of several test columns. Results from an experimental study designed to focus on fatigue-based failure modes would aid in further development of this approach. The following lists possible areas of study:

1. Low-cycle fatigue of the steel may depend on the extent of both the positive and negative excursions and spiral reinforcement ratio. Therefore, the index should be modified to account for these asymmetric excursions.
2. Experimental research indicates that degradation of the lateral bar restraint depends on biaxial loading [e.g., Mazzoni and Moehle 1997]; sufficient degradation of the concrete in all directions around the longitudinal bar may permit in-plane buckling of the longitudinal steel. Therefore, the damage index should account for biaxial loading effects.

3. Experimental research that focuses on the influence of displacement history is limited. To date, the dual-phase damage index has been evaluated using constant amplitude displacement histories or standard displacement histories with increasing displacement demands. Further analytical and experimental research is required to estimate the effect of cycling on the displacement capacity of damaged elements. Techniques to extrapolate from the element response to the system response are needed.
4. The form of the proposed index is strongly dependent on limiting strain values, i.e.,  $\epsilon_{sp}$  and  $\epsilon_{su}$ . In practical situations these values may be difficult to determine. Reformulation of the model may be required to minimize this dependence.
5. As has been noted previously, failure of a reinforced concrete element is difficult to define. Commonly, element failure has been related to strength loss as a fraction of the peak strength. Although this simple definition may be adequate for increasing displacement demands, it may not be sufficient for random displacement histories. Research is needed to define more broadly applicable definitions of element failure.

# Appendix A Specimen Design, Materials, and Construction

## A.1 INTRODUCTION

Reinforced concrete bridge columns resisting earthquake effects commonly are expected to form ductile hinges at predetermined locations and to sustain numerous inelastic reversed loading cycles. Nonductile response mechanisms, e.g., those associated with shear and bond distress, are suppressed and yielding in adjacent elements is restricted. The hinge regions are detailed to ensure adequate displacement capacity and stable response under reversed loading conditions.

Standards for the seismic design of ductile columns supporting reinforced concrete bridges are evolving. Recent recommendations to modify the bridge design standards in California [Caltrans 1991] are summarized in the ATC 32 document entitled *Improved Seismic Design Criteria for California Bridges: Provisional Recommendations* [ATC 1996]. That document recommends changes to the then-current design practices including maximum probable plastic moment, shear strength, minimum longitudinal reinforcement ratio, spiral reinforcement quantity, and development of deformed bars in tension. The changes aim to improve the design and modeling of ductile reinforced concrete columns and joints. The test specimens were designed to meet the Caltrans or the ATC 32 design procedures, or both, to explore issues of actual column performance using the current design standards. Generally, design criteria were according to the Caltrans design standard. In some cases the ATC 32 recommended procedures also were adopted.

Section A.2 outlines the design of the full-scale prototype column and joint regions. Details of the corresponding scaled test specimens are presented in Section A.3. Actual material properties and procedures used in the construction of the test specimens are described in Sections A.4 and A.5.

## A.2 PROTOTYPE DESIGN

Seismic design of reinforced concrete bridge columns typically locates plastic hinges at the column ends. The design objective is to ensure ductile response in predetermined hinge locations.

The design process includes proportioning and detailing the structure geometry and reinforcement for the estimated seismic demands and plastic action. The design procedure is as follows:

1. Select plastic hinge locations to form desired collapse mechanism
2. Estimate flexural strength and deformation demand in plastic hinges
3. Design plastic hinge regions for estimated force demands
4. Design plastic hinge regions for estimated displacement demands accounting for cyclic effects.
5. Estimate demand on all elements using plastic analysis. Perform plastic analysis using maximum probable flexural strength of plastic hinge regions.
6. Design all elements for demands from plastic analysis. This includes the yielding elements. In a typical bridge system the design will include:
  - a. For Column regions: shear strength, flexural demand outside of plastic hinge region, bond demand, curvature demand
  - b. For joint regions: shear strength, development length/bond demands
  - c. For beam regions: flexural strength, shear strength

The following sections summarize the design of the five prototype column and joint regions.

### **A.2.1 Column Geometry and Reinforcement**

The test columns were one-third of a full-scale prototype column. The full-scale columns were designed using the appropriate design standards. The experimental columns were scaled from the corresponding prototype using a geometric scale factor of one-third. The column longitudinal reinforcement ratio and aspect ratio were defined according to the test matrix. The columns were divided into two test series with longitudinal reinforcement ratio and aspect ratio as study parameters. The five columns were 6 feet in diameter and were reinforced longitudinally with No. 14 bars. The column longitudinal reinforcement ratio,  $\rho_l$ , is defined using Equation A.1 where  $A_g$  is the gross cross-sectional area and  $A_s$  is the total area of the longitudinal steel.

$$\rho_l = \frac{A_s}{A_g} \quad (\text{A.1})$$

The Test Series I columns had longitudinal reinforcement ratios,  $\rho_l$ , of .75%, 1.5%, and 3%; the three columns were 24 feet in length. The lengths of the three columns in Test Series II varied and

were specified as 24, 48, and 60 feet; the longitudinal steel reinforcement ratios were 1.5% for all columns. The schedule in Figure A.1 indicates the study variables for each column. The column designation indicates the aspect ratio (4, 8, or 10) and percentage of longitudinal reinforcement ratio (07, 15 and 30).

### **A.2.2 Loading**

The columns were modeled as cantilevers. During testing, the columns were subjected to a constant compressive axial force (to simulate gravity loading) and reversed cyclic lateral displacement (to simulate seismic loading effects). The applied axial load was 1323 kips (294 kN) which approximately corresponds to 10 percent of the specified gross cross-sectional capacity ( $0.1f_c'A_g$ ) with a specified concrete strength of 3.25 ksi (22.4 MPa).

### **A.2.3 Material Properties**

Design material strengths of the longitudinal reinforcing steel, spiral reinforcing steel, and concrete vary according to the design provisions. The Caltrans design specification uses the specified material strengths. The strengths used in the ATC 32 design procedures depend on the application and may be the specified, expected, or maximum-probable strengths. Table A.1 lists the specified, expected, and maximum probable strengths for the longitudinal reinforcement and the plain concrete.

### **A.2.4 Moment Strength for Plastic Analysis**

As described earlier, the columns are expected to form plastic hinges at predetermined locations. Using plastic analysis, the adjacent element demands are calculated using the maximum probable moment strengths of the plastic end regions. Both the Caltrans and ATC 32 design provisions provide procedures to assess the maximum probable moment strength.

Using the Caltrans procedure, the nominal moment capacity,  $M_n$ , is determined by assuming the maximum usable strain at the extreme compression fiber is 0.003 in./in. and a steel strength equal to the specified yield strength. The plastic moment capacity,  $M_p$ , is estimated by magnifying the nominal moment strength by a factor of 1.3, as shown in Equation A.2.

$$M_p = 1.3M_n \quad (\text{A.2})$$

In the ATC 32 procedure, the maximum plastic moment is defined as “the maximum moment that is expected to develop in the plastic hinge region of a ductile column at peak plastic rotation considering maximum feasible material strengths, effects of confinement of concrete, and strain-hardening of longitudinal reinforcement.” The nominal moment capacity,  $M_n$ , is determined by assuming the maximum usable strain at the extreme compression fiber is 0.004 in./in. The nominal moment capacity is computed using the expected concrete compression strength,  $f_{ce}' = 1.3f_c'$ , and the expected yield strength of the longitudinal steel,  $f_y = 1.1f_y$ . The plastic moment strength is estimated by magnifying the nominal moment by a factor of 1.4 (Equation A.3).

$$M_p = 1.4M_n \quad (\text{A.3})$$

An alternative procedure is also provided in the ATC 32 document. The flexural strength,  $M_p'$ , is determined using results from a moment-curvature analysis with the maximum probable material strengths,  $f_{cm}' = 1.7f_c'$  and  $f_{ym} = 1.25f_y$ . To account for possible overstrength effects, the plastic strength is magnified by a factor of 1.15, as shown in Equation A.4.

$$M_p = 1.15M_p' \quad (\text{A.4})$$

Table A.2 summarizes the maximum plastic moment values computed for the three column cross sections using the Caltrans procedure as well as both ATC 32 procedures. For design purposes herein, the maximum probable moment determined using the alternative ATC 32 procedure was used in the following ATC 32 design methods and the maximum probable moment determined using the Caltrans procedure was used in the following Caltrans design methods.

### **A.2.5 Design Adjacent Element: Joint Region**

Joint regions adjacent to yielding hinge zones are designed to restrict yielding and suppress non-ductile response mechanisms. Typically, code provisions specify the maximum allowable joint shear stress demand. Since limiting joint shear stress values are not given in the Caltrans bridge design specification, the ACI-318 [ACI 1989] recommendations were adopted. Equation A.5 is used to approximate the joint shear stress demand,  $v_j$ . The variables include the plastic moment

strength,  $M_p$ , the column diameter,  $D$ , and the joint depth,  $H_j$ , where  $T$  is the approximate tensile force in the column. The joint area is specified as  $A_j = DH_j$ .

$$T \cong \frac{M_p}{0.9D}; v_j = \frac{T}{DH_j} \quad (\text{A.5})$$

The method to suppress joint shear failure proposed in ATC 32 limits the principal compressive stress in the joint. The principal stress is a function of the shear stress (tensile demand in the column longitudinal steel) as well as the normal compressive and tensile stress demands. (Note that the joint area specified in the ATC 32 report is larger than that specified by ACI). For a footing-column connection, the maximum joint area,  $A_j$ , is equal to the product of the joint depth,  $H_j$ , and an effective joint width. Assuming 45-degree strutting action, the effective joint width is the sum of the column depth,  $D$ , and twice the joint depth i.e.,  $A_j = H_j(2H_j + D)$ . However, for the columns tested, the actual footing width was less than the allowable effective joint width. Therefore, the joint area is defined as follows:  $A_j = H_j(D + H_j)$ . Equation A.6 is used to calculate the principal compressive stress in the joint.

$$p_c = \frac{f_v}{2} + \sqrt{\left(\frac{f_v}{2}\right)^2 + v_j^2} \quad (\text{A.6})$$

In the expression,  $f_v$  = the normal stress due to the axial load and  $v_j$  = the joint shear stress. The principal stress is limited, in compression only, to a value of  $0.25f'_c$ . Table A.3 compares the capacity/demand ratios using both methods.

In the Caltrans Bridge Design Specification and the ATC 32 Design Provisions, the expressions to determine the required anchorage length of the longitudinal steel in the joint are similar. The Caltrans design specification expression is indicated by Equation A.7. The ATC 32 expression is indicated by Equation A.8.

$$\text{Caltrans } l_{dh} = \frac{1200d_b}{\sqrt{f'_c}} \quad (\text{A.7})$$

$$\text{ATC 32 } l_{dh} = \frac{0.028d_b f_y}{\sqrt{f'_c}} \quad (\text{A.8})$$

Using specified strengths, the ATC 32 expression results in an anchorage length of 50 inches, which is 40 percent larger than that required by the Caltrans specification. Typically, longitudinal reinforcement is fully anchored in the joint. For the design case, the footing depth is 6 feet, resulting in an anchorage depth of approximately 69 inches.

### A.2.6 Design of Yielding Element: Column Region

The column is designed to sustain the demands from the plastic analysis and flexural bond demands as well as to achieve the desired displacement capacity considering the cyclic nature of the loading.

Column confinement requirements are intended to ensure dependable section curvature ductility. Based on numerical modeling of cross-sectional response, the curvature capacity is a function of the strain capacity of the concrete core in compression, thereby increasing the curvature capacity with an increase in the column confinement. The required confinement is expressed in terms of spiral reinforcement ratio and is a function of the gross cross-sectional area,  $A_g$ , the axial load,  $P$ , the concrete strength,  $f_c'$ , and the yield strength of the transverse reinforcement,  $f_{yh}$ . In addition, the ATC 32 expression is written in terms of the longitudinal reinforcement ratio,  $\rho_l$ . Equations A.9 and A.10 give the Caltrans and the ATC 32 expressions, respectively.

#### Caltrans

$$\text{The greater of } \rho_s = 0.12 \frac{f_c'}{f_{yh}} \left( 0.5 + \frac{1.25P}{f_c' A_g} \right)$$

$$\text{or } \rho_s = 0.45 \left( \frac{A_g}{A_c} - 1 \right) \frac{f_c'}{f_y} \quad (\text{A.9})$$

#### ATC 32

$$\text{The greater of } \rho_s = 0.16 \frac{f_{ce}'}{f_{yhe}} \left( 0.5 + \frac{1.25P}{f_{ce}' A_g} \right) + 0.13(\rho_l - 0.01) \text{ or}$$

$$\rho_s = 0.09 \left( c \left( \frac{\theta_p}{l_p} + \phi_y \right) - 0.004 \right) \frac{1.5 f_{ce}'}{1000} \text{ with } l_p = 0.08L + 9d_{bl} \quad (\text{A.10})$$

A comparison of the first expressions of each specification facilitates a comparison of the requirements. For a longitudinal reinforcement ratio of 0.01, there is an increase of 33 percent in the ATC 32 requirement with respect to the original Caltrans standard. Using expected material strengths, as specified in the ATC 32 report, there is an increase of approximately 60 percent. The ATC 32 expression, using expected material strengths and neglecting the second term, results in a required spiral reinforcement ratio of 0.61%. The columns were detailed with a No. 6 spiral at 4 inches (spiral reinforcement ratio of 0.66%).

For a cantilever column, the column shear demand,  $V_p$ , is the ratio of the plastic moment demand,  $M_p$  and the effective length,  $L$  (Equation A.11).

$$V_p = \frac{M_p}{L} \quad (\text{A.11})$$

The nominal shear strength is the sum of the nominal shear strength provided by the concrete,  $V_c$ , and the nominal shear strength provided by the transverse reinforcement,  $V_n$ . The nominal concrete strength is a function of the applied axial load,  $P$ , concrete strength,  $f'_c$ , and the gross and effective cross-sectional area of the column,  $A_g$  and  $A_e$ , respectively. In the Caltrans and ATC 32 design procedures, the form of the nominal concrete shear strength expressions are similar, except that in the ATC 32 specification the coefficient amplifying the concrete strength was reduced by one half. The expressions are given in Equations A.12 and A.13.

$$\text{Caltrans } V_c = 2 \left( 1 + \frac{P}{2000A_g} \right) \sqrt{f'_c} A_e \quad (\text{A.12})$$

$$\text{ATC 32 } V_c = 2 \left( 0.5 + \frac{P}{2000A_g} \right) \sqrt{f'_c} A_e \quad (\text{A.13})$$

The nominal shear strength provided by the steel is a function of the area of the spiral,  $A_w$ , spacing,  $s$ , column diameter,  $D$ , and strength of the transverse steel,  $f_{yh}$ , provided. Equations A.14 and A.15, respectively, present the nominal steel shear strength expressions provided in the Caltrans design standard and the ATC 32 document.

$$\text{Caltrans } V_s = \frac{A_w f_{yh} D}{s} \quad (\text{A.14})$$

$$\text{ATC 32 } V_s = \frac{\pi A_w f_{yh} D'}{2s} \quad (\text{A.15})$$

In the ATC 32 expression,  $D'$  is the diameter at the centerline of the spiral. Table A.4 presents the resulting plastic shear demands, nominal shear strength, and demand-capacity ratios for both procedures.

### A.3 SPECIMEN GEOMETRY AND REINFORCEMENT

The test specimens are shown in Figure A.3. The scaled column and joint reinforcement of the test specimens were one-third of the prototype and therefore complied with the provisions used to

design the prototype column and joint regions.

Tables A.5 and A.6 present the specimen geometry and reinforcement. The test column and joint dimensions are one third of the prototype. Longitudinal and spiral reinforcement ratios are approximately the same. However, several parameters could not be scaled exactly; the longitudinal bar diameter, concrete cover, spiral spacing, and diameter of the joint ties were scaled to the nearest eighth of an inch.

The geometry and reinforcing of the anchor block were the same for all five columns. The size of the anchor block was 8 feet by 4 feet in plan and 2 feet deep. The anchor block plan dimensions were chosen to ensure an adequate transfer mechanism outside of the prestressed region and to facilitate construction (therefore, the dimensions of a single sheet of plywood were used for the plan dimensions). The reinforcement outside of the joint region was designed to prevent yielding under the highest demand (i.e., the shear demand of Column 430). The anchor block was longitudinally reinforced with approximately 1% reinforcing steel with the same mat top and bottom (Figure A.4). The footing ties were No. 2 bars and were spaced at 4 inches on center. The volume of tie steel scales to No. 5 bars at 12 inches in the prototype column (Figure A.5). PVC pipe were located in the anchor block to facilitate placement of hydostone prior to testing. Locations of PVC pipes are also shown in Figure A.4. Details of the testing procedures and specimen placement are described in *Seismic Performance of Well-Confined Concrete Bridge Columns* (Lehman 1998).

## **A.4 MATERIALS**

Longitudinal steel reinforcement, spiral steel reinforcement, and plain concrete cylinders were tested to determine the stress-strain response. Steel and concrete stress-strain relationships used in the column and joint modeling were based on the material testing.

### **A.4.1 Longitudinal Reinforcement**

Longitudinal reinforcement met the ASTM Designation A 706. The longitudinal reinforcement used for construction of the five test specimens and for material testing was specified to be from a single batch of steel and delivered in a single batch (to limit variation in steel properties). The reinforcing bars were tested using standard testing methods. A 24-inch bar length was cut and the center section was machined to localize bar yielding and permit precise measurement of the

machined bar diameter. The stress-strain response for the test specimens is shown in Figure A.6. The steel had a marked yield strength of approximately 70 ksi (483 MPa). The yield plateau extended from approximately 0.0025 in./in. to a strain of 0.02 in./in. The fracture strain was approximately 0.2 in./in.

#### **A.4.2 Spiral Reinforcement**

One-quarter inch diameter deformed spiral meeting the ATSM Designation A 706 was not available. Since the Caltrans design standards permits use of spiral reinforcement in piles meeting the ASTM Designation A 605 or A 82, steel with ASTM Designation A 82 was selected for the spiral reinforcement. (Grade A 605 steel was available in 20-foot lengths only, which would require splices within the column spiral.) Three coupons were tested to obtain the stress-strain response of the spiral. Figure A.7 shows the measured response. The yield strength, corresponded to a strain of 0.0035 and was determined to be 88 ksi (607 MPa). The apparent fracture strain was 0.07 in./in. The ultimate strength of the steel was approximately 98 ksi (676 MPa).

#### **A.4.3 Plain Concrete**

The concrete mix was designed to approximate the prototype mix. Table A.7 provides details of the prototype and scaled mix. The strength and water/cement ratio were retained for the scaled mix. However, matching coarse aggregate content of the prototype mix would have severely reduced its workability; therefore, the coarse aggregate content was increased.

The five columns were cast in two phases. The three test specimens of Test Series I were cast together in two stages outside the laboratory facility. The three anchor blocks were cast on May 13, 1996, from a single batch of concrete. The three columns were cast on May 24, 1996, from a single batch of concrete. Figure A.12 shows the three columns of Test Series I following placement of the anchor block concrete. The remaining two test specimens of Test Series II were cast together inside the laboratory facility. The two anchor blocks were cast together on November 15, 1996, and the two columns were cast

together on November 26, 1996.

During each casting, a slump test was performed to ensure that the concrete slump was between 3 and 5 inches (Figure A.13). Concrete cylinders, 12 inches in height and 6 inches in diameter, were cast with the anchor blocks and columns (Figure A.14). The cylinders were kept in the same location as the test specimens and wet cured with the parallel specimen concrete. The forms of the cylinder cast with the anchor blocks were not removed until testing to mimic the curing conditions of the joint concrete. The forms of the cylinders cast with the columns were removed when the column forms were removed. Cylinders from each batch were tested at 7, 14, 21, and 28 days to measure the compressive strength. Test results are shown in Table A.8.

Additional material tests were performed on the day of the test. The tensile and compressive strength of the anchor block concrete was measured; 3 split cylinder and 3 compressive tests were performed. Table A.9 gives the average results for the tests. The tensile, compressive, and stress-strain responses of the column concrete were measured. Three tests were performed for each. Figure A.8 through Figure A.10 gives the measured stress-strain response for each column.

## **A.5 CONSTRUCTION PROCEDURES**

Procedures to construct the test specimens were established to mimic the construction sequence in the field, adhering to the Caltrans Standard Specifications whenever possible. The construction process had four major phases: construction of the reinforcement cages, casting of the anchor blocks, preparation for column casting including preparation of the joint surface and plumbing the column reinforcement and forms, and column casting.

The columns were constructed outside the structural laboratory at the Earthquake Engineering Research Center, Richmond Field Station, of the University of California. A local contractor and steel fabricator constructed the specimens. Concrete formwork was constructed off-site and delivered. The reinforcing steel was cut and bent off-site and delivered to the job site. The bottom portion of the anchor block cages were constructed and placed inside the forms. The column cage was constructed, placed, and secured. The strain gauges were attached to longitudinal steel prior to construction of the column cage. The top portion of the anchor block cage was constructed in place. The anchor block ties were placed, completing the reinforcement cage construction.

Concrete from the shoot of the concrete truck was placed into the anchor block formwork and vibrated (Figure A.15). The concrete was placed in two 1-foot lifts. The exposed surface was

finished, wet cured for 7 days, and sand blasted prior to placing the new concrete (Figure A.16). Approximately 2 days after placement of the anchor block concrete, small rods were soldered to the longitudinal steel for placement of the vertical slip instruments and strain gauges were attached to the column spiral. A heavy-wall Burke Sonotube was placed over each column reinforcement cage to serve as formwork. Three-quarter inch dobies were use to space the reinforcement cage and formwork. Instrumentation rods were placed through holes in the formwork. One-half-inch diameter pipe insulation was placed into the holes to prevent leakage during concrete placement. Concrete was placed into the Sonotube forms in lifts of 4 feet or less. The exposed portion of the column was wet cured for a period of 7 days at which time the forms were stripped.

**Table A.1: Specified, Expected, and Maximum Design Strengths**

Material	Specified	Expected	Maximum
Reinforcement			
Yield	60 ksi (8.7 MPa)	66 ksi (9.6 MPa)	75 ksi (10.9 MPa)
Ultimate	90 ksi (13 MPa)	99 ksi (14.4 MPa)	112 ksi (16.2 MPa)
Concrete	3.25 ksi (0.47 MPa)	4.5 ksi (0.65 MPa)	5.5 ksi (0.8 MPa)

**Table A.2: Maximum Probable Moment**

Cross section	Caltrans	ATC 32	ATC 32 (Alt.)
0.75% steel	145,000 k-in	133,000 k-in	133,000 k-in
1.5% steel	170,000 k-in	203,000 k-in	212,000 k-in
3.0% steel	274,000 k-in	329,000 k-in	379,000 k-in

**Table A.3: Joint Shear Stress**

Cross section	Caltrans		ATC 32		
	$v_j$	$\alpha \sqrt{f'_c}$	$v_j$	$p_c$	Ratio
0.75% steel	0.34 ksi	6	0.2 ksi	0.2 ksi	0.31
1.5% steel	0.51 ksi	9	0.33 ksi	0.33 ksi	0.51
3.0% steel	0.82 ksi	14	0.56 ksi	0.57 ksi	0.87

**Table A.4: Column Shear Demand and Capacity Values**

Column	Caltrans			ATC 32		
	$V_p$	$V_n$	$\frac{V_p}{V_n}$	$V_p$	$V_n$	$\frac{V_p}{V_n}$
407	399 kips	849 kips	0.5	462 kips	922 kips	0.5
415	590 kips	849 kips	0.7	770 kips	922 kips	0.8
430	951 kips	849 kips	1.1	1315 kips	922 kips	1.4
815	295 kips	849 kips	0.4	385 kips	922 kips	0.4

**Table A.4: Column Shear Demand and Capacity Values**

Column	Caltrans			ATC 32		
	$V_p$	$V_n$	$\frac{V_p}{V_n}$	$V_p$	$V_n$	$\frac{V_p}{V_n}$
1015	236 kips	849 kips	0.3	309 kips	922 kips	0.3

**Table A.5: Test Specimen Geometry**

Column	Length	Diameter	Concrete Cover	Anchor Block
407	8'-0"	2'-0"	3/4"	8' x 2' x 4'
415	8'-0"	2'-0"	3/4"	8' x 2' x 4'
430	8'-0"	2'-0"	3/4"	8' x 2' x 4'
815	16'-0"	2'-0"	3/4"	8' x 2' x 4'
1015	20'-0"	2'-0"	3/4"	8' x 2' x 4'

**Table A.6: Test Specimen Reinforcement**

Column	Longitudinal Reinforcement			Spiral Reinforcement		
	$\rho_l$	Bar size	#	$\rho_v$	Size	s
407	0.75%	No. 14	11	0.70%	No. 2	1.25"
415	1.5%	No. 14	22	0.70%	No. 2	1.25"
430	3.0%	No. 14	44	0.70%	No. 2	1.25"
815	1.5%	No. 14	22	0.70%	No. 2	1.25"
1015	1.5%	No. 14	22	0.70%	No. 2	1.25"

**Table A.7: Concrete Mix Data**

Mix	Max. Aggregate	28-Day Strength	Slump	Water/Cement Ratio	Coarse Aggregate Weight	Fine Aggregate Weight
Prototype	1"	4.0 ksi	4"	0.53	1800 lb	1430 lb
Scaled	3/8" (pea gravel)	4.0 ksi	5" $\pm$ 1"	0.53	1250 lb	1900 lb

**Table A.8: Development of Concrete Strength**

	Cylinders	7-Day	14-Day	21-Day	28-Day
Test Series I	Anchor Blocks	3.16 ksi	3.89 ksi	4.05 ksi	4.4 ksi
	Columns	2.74 ksi	3.51 ksi	3.82 ksi	3.9 ksi
Test Series II	Anchor Blocks	3.35 ksi	4.22 ksi	4.25 ksi	4.54 ksi
	Columns	3.12 ksi	4.24 ksi	4.66	

**Table A.9: Compressive and Tensile Strength on or near Day of Test**

Column Designation	Columns		Anchor Blocks	
	Compression	Tension	Compression	Tension
407	4.3 ksi	0.42 ksi	5.2 ksi	0.48 ksi
415	4.4 ksi	0.42 ksi	4.9 ksi	0.51 ksi
430	4.6 ksi	0.46 ksi	5.0 ksi	0.43 ksi
815 and 1015	4.9 ksi	0.42 ksi	5.6 ksi	0.48 ksi

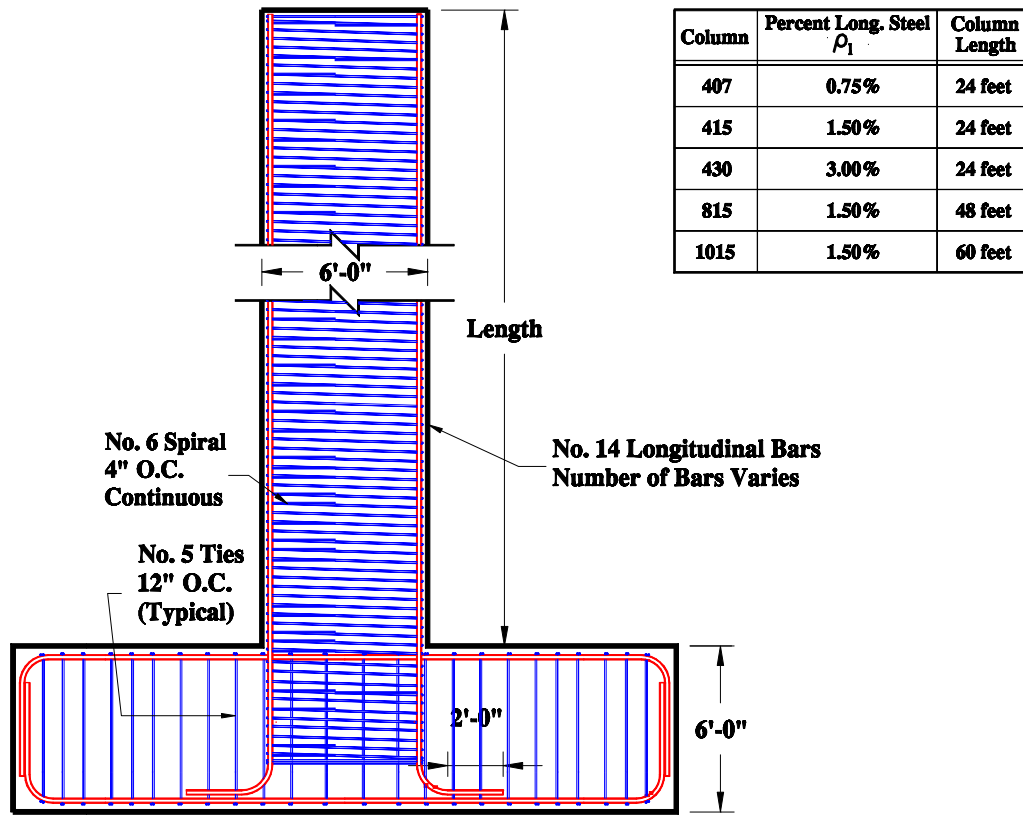


Figure A.1: Elevation of Prototype Structure

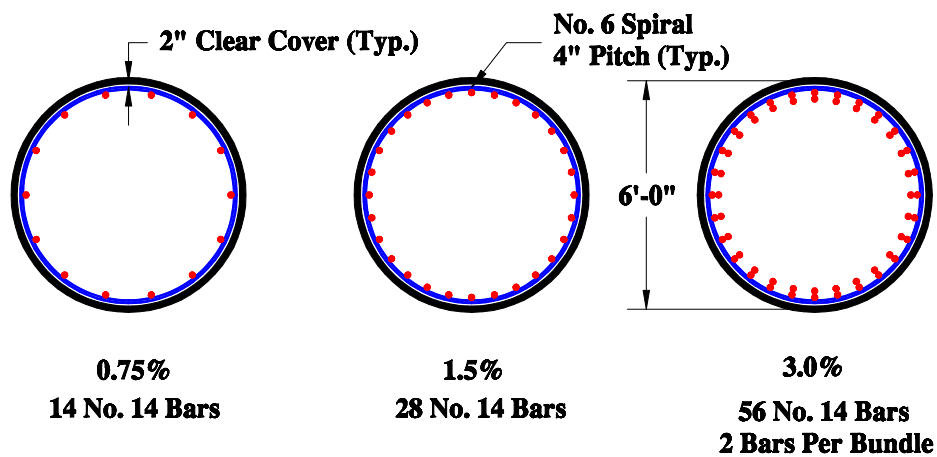


Figure A.2: Prototype Structure: Column Cross Section

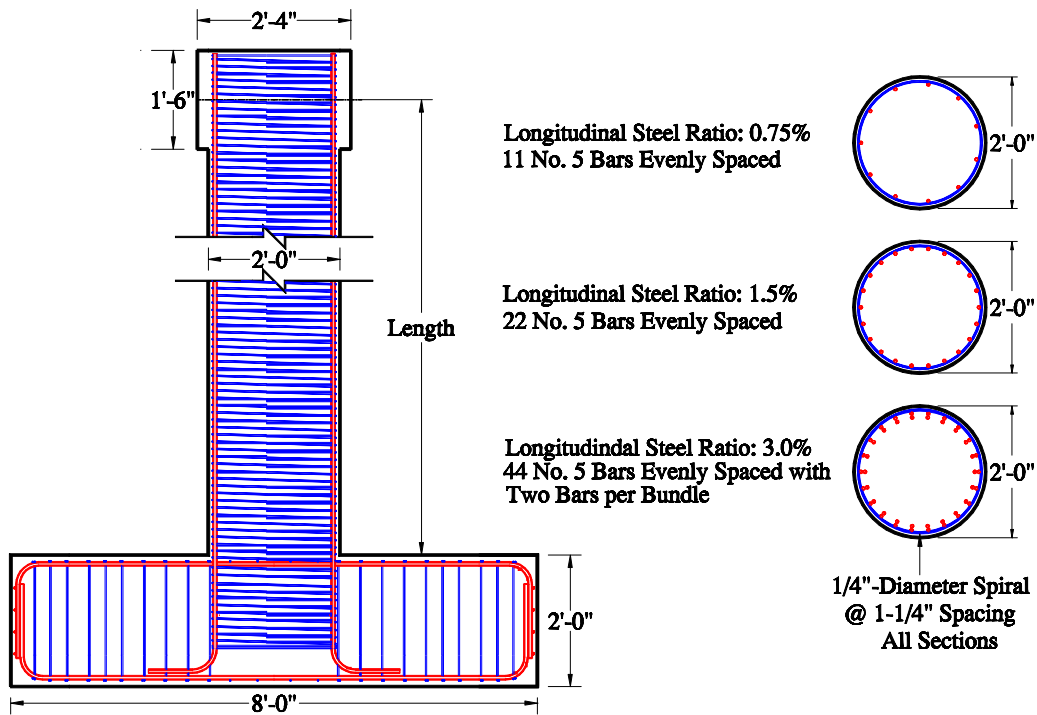


Figure A.3: Test Specimen Geometry and Reinforcement

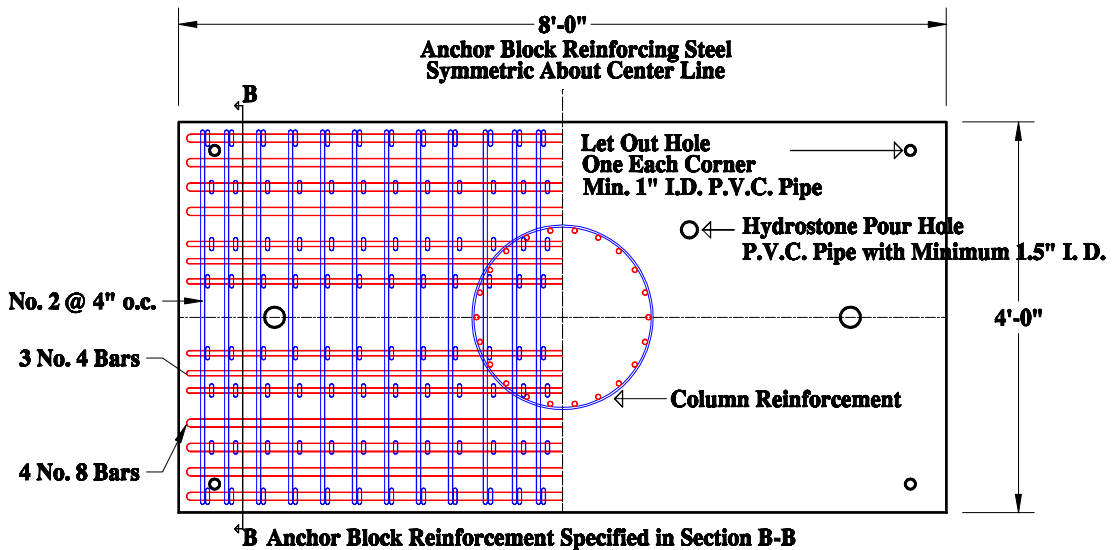
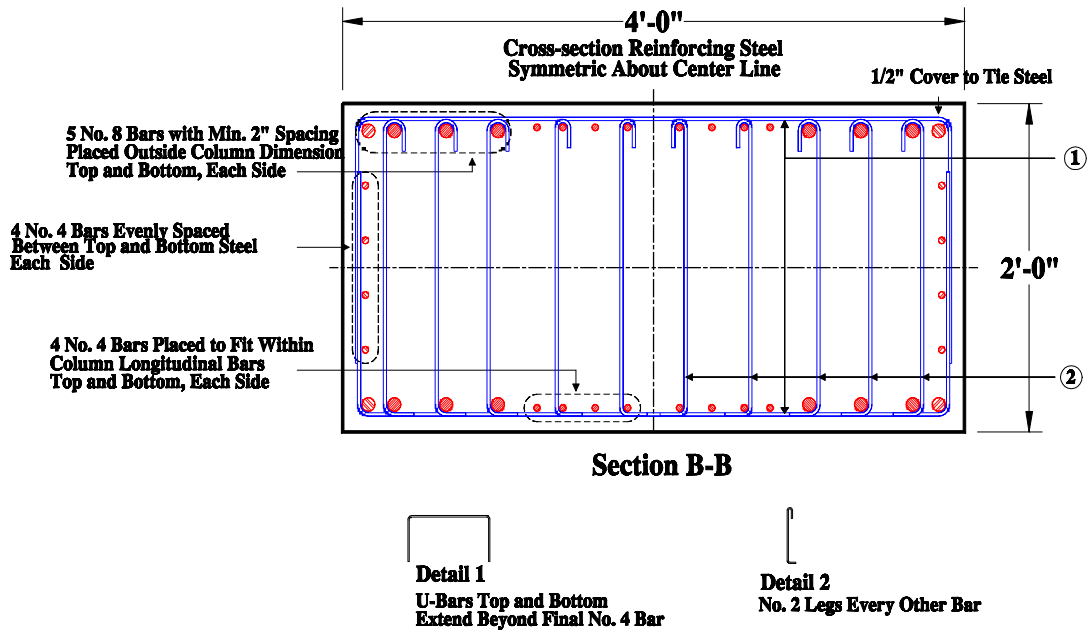
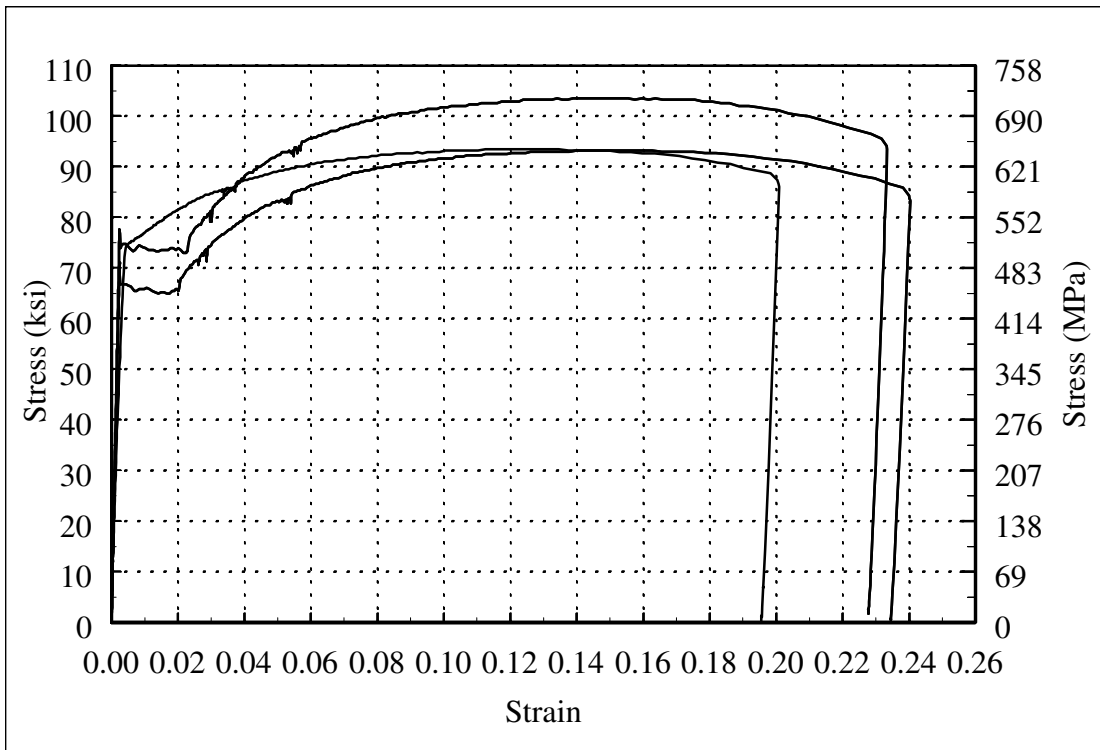


Figure A.4: Top and Bottom Mat of Reinforcement with Hole Locations



**Figure A.5: Cross Section of Anchor Block**



**Figure A.6: Longitudinal Reinforcement Stress-Strain Response**

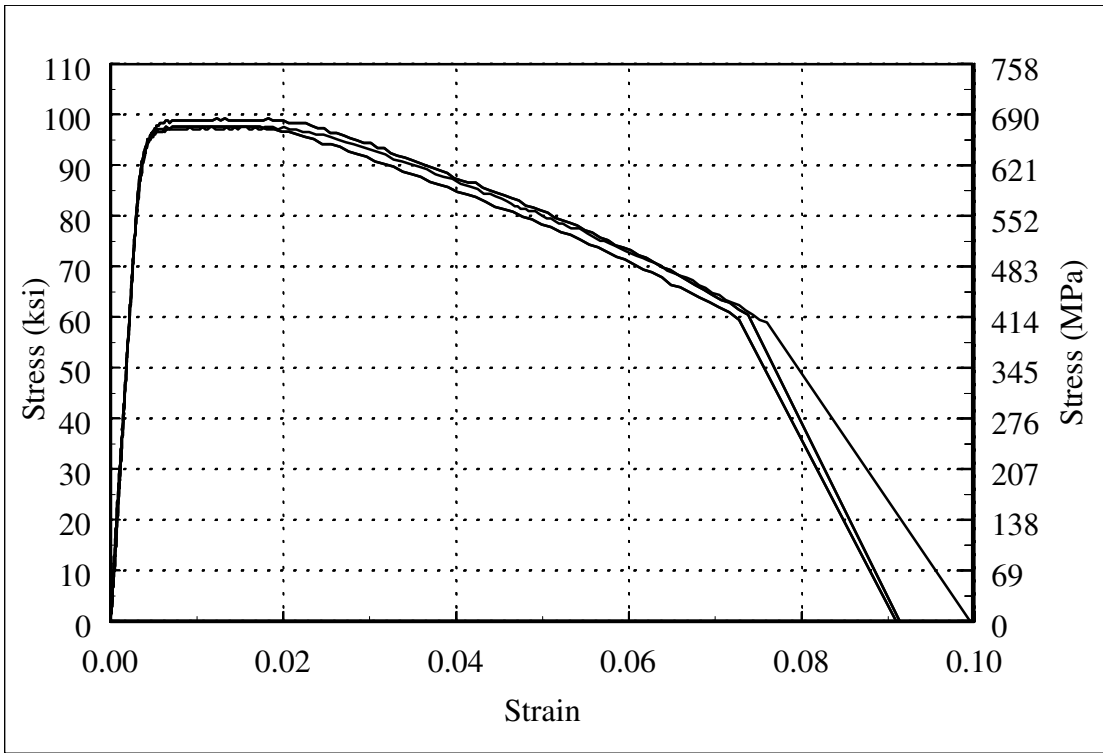


**Figure A.7: Spiral Reinforcement Stress-Strain Response**

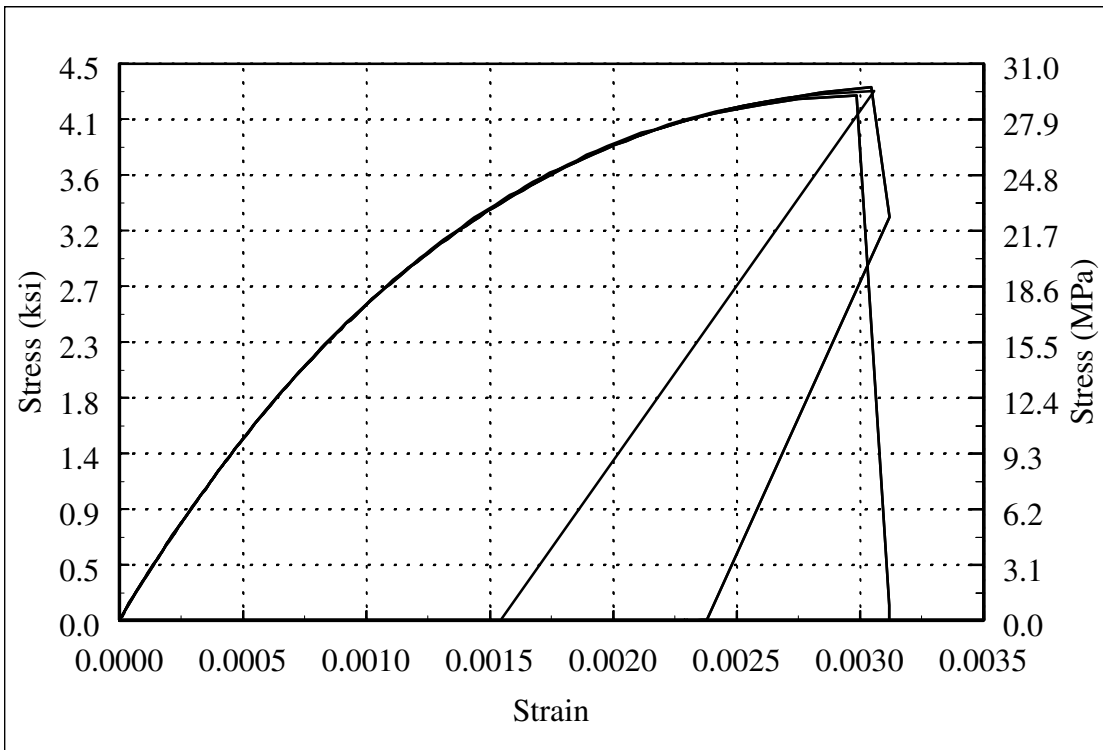


**Figure A.8: Measured Plain-Concrete Stress-Strain Response for Column 407**

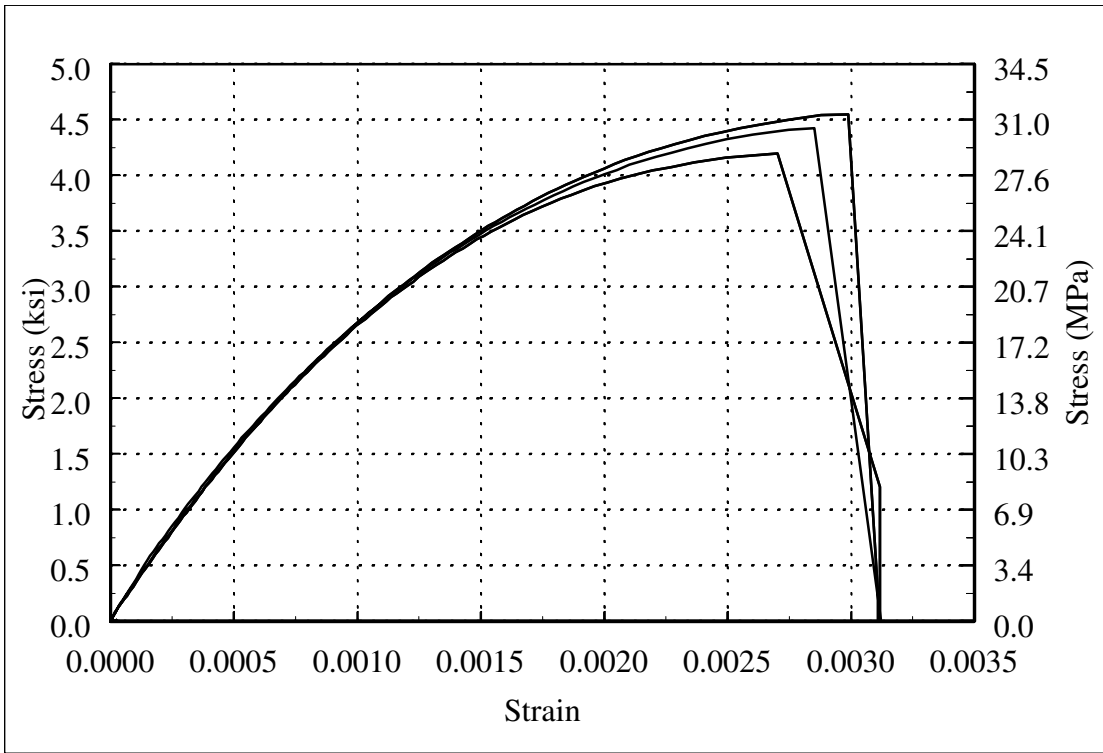


**Figure A.9: Measured Plain-Concrete Stress-Strain Response for Column 415**

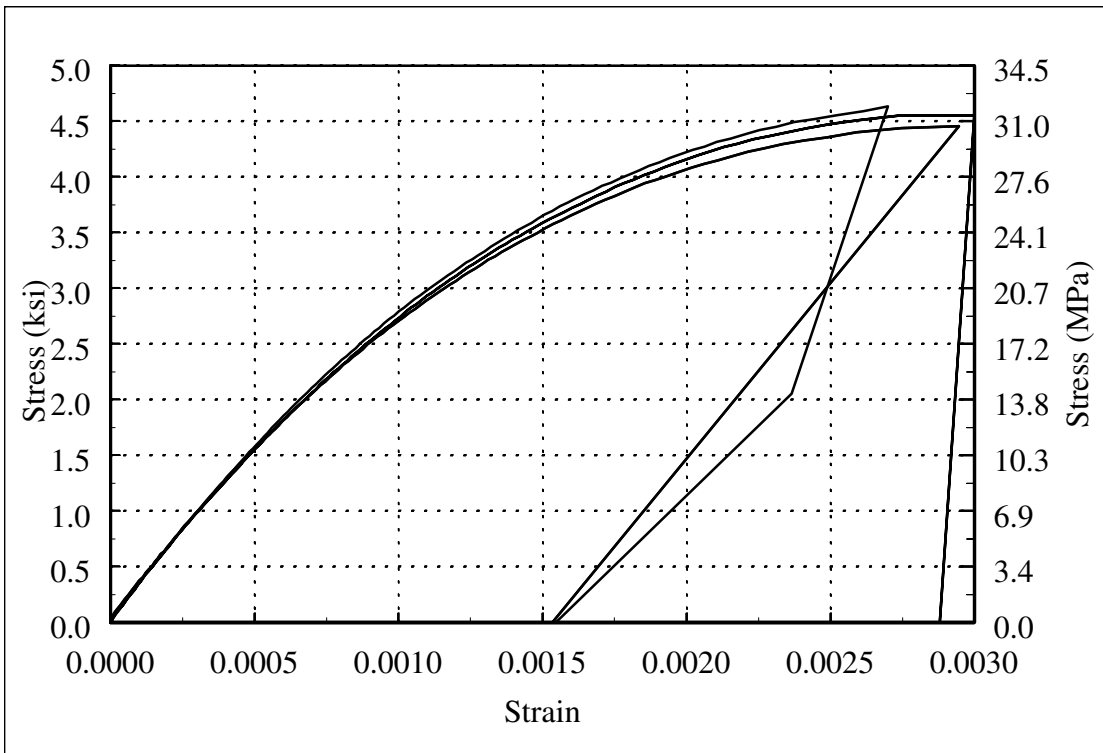


**Figure A.10: Measured Plain-Concrete Stress-Strain Response for Column 430**

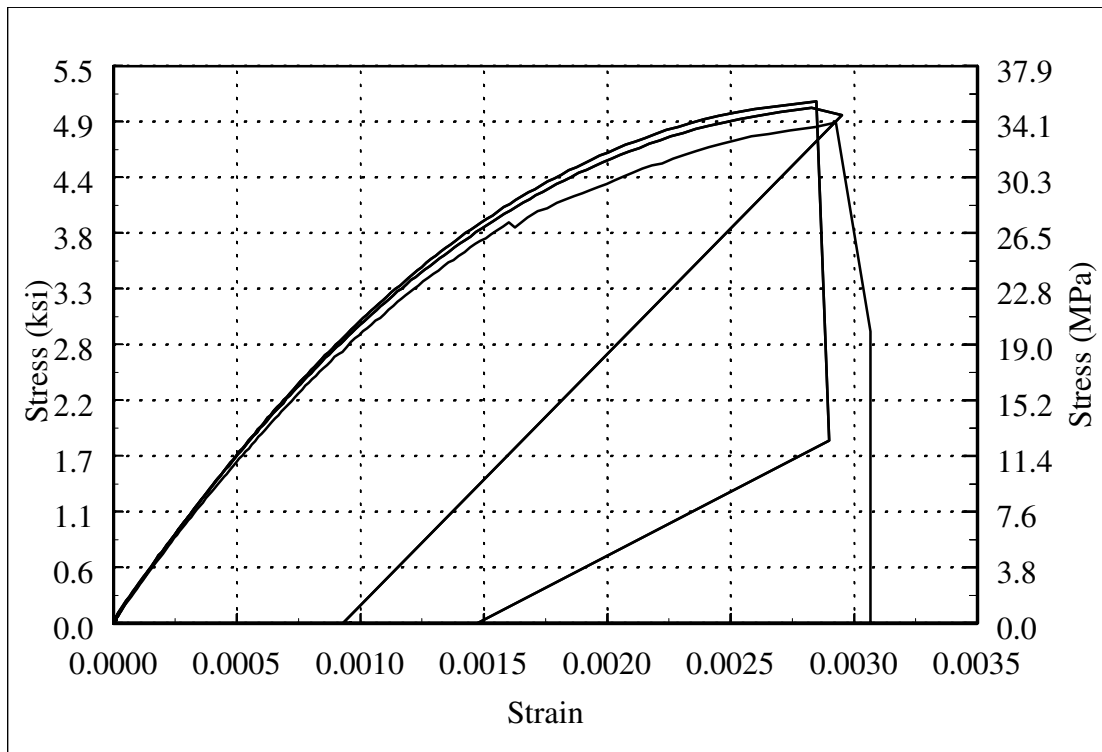


**Figure A.11: Measured Plain-Concrete Stress-Strain Response for Columns 815 and 1015**



**Figure A.12: Three Columns of Test Series I after Casting Anchor Blocks**



**Figure A.13: Slump Test**



**Figure A.14: Casting Concrete Cylinders**



**Figure A.15: Casting Anchor Blocks**



**Figure A.16: Sand Blasting of Exposed Joint Surface**

# **Appendix B Experimental Set Up, Apparatus, and Procedures**

## **B.1 INTRODUCTION**

The experimental portion of the research program was designed to characterize the cyclic response of circular cantilever bridge columns subjected to lateral loading. Single-column bent systems typically exist in the transverse direction, i.e., the transverse direction perpendicular to the superstructure span, in addition to the longitudinal direction. Such a system is depicted in Figure B.1. The column response can be approximated as single curvature under transverse loadings. In the test model, shown by the shaded region in Figure B.1, the actual column is idealized as a cantilever column that is fully fixed into the joint region. The test specimen was constructed to model the column only; the influence of the pile response or soil-structure interaction was not modeled. The column and joint regions were designed in accordance with standard bridge design practice as described previously in Appendix A.

The experimental apparatus, instrumentation, and procedures of the test program were designed to determine the response of the cantilever bridge column subjected to a cyclic lateral load at its end. The test specimens were attached to the laboratory floor with prestressing rods and constant axial load and cyclic lateral load were applied to the free end of the column. The column and joint instrumentation were designed to monitor both internal and external local deformation modes, and the system response. Data from the instruments were collected continuously during testing. In addition, observed response quantities, e.g., crack widths and area of spalled regions, were measured at the first peak displacements of each displacement cycle. The following sections provide details of the experimental set up and procedures.

## **B.2 EXPERIMENTAL SETUP**

The experimental specimen was constructed to model the column and joint regions of a full-scale, single-column bent bridge system. The specimen geometry and reinforcement were scaled to approximately one third of the full-scale system. The specimen was intended to adhere to the seis-

mic bridge design standards in the column and joint regions. Details of the specimen geometry and reinforcement are given in Appendix A. The specimens were modeled as cantilever columns. The columns were constructed and tested in the upright position. Prior to testing, the columns were moved into position in the laboratory. The setup procedure in the laboratory consisted of placing and plumbing the specimen, placing hydrostone and prestressing the anchor block to the laboratory floor, attaching the axial load set up and attaching the horizontal actuator. The following paragraphs summarized the procedure used to place the specimen in the laboratory.

The specimens were tested in the Structures Laboratory at the Richmond Field Station at the University of California, Berkeley. The elevation and plan of the specimen in-position in the laboratory are shown in Figures B.2 and B.3. The column was placed approximately 12 feet from the reaction frame and centered on a hole in the floor (holes in the laboratory floor were spaced at 3 feet on center). Placing the anchor block on 1/4-inch thick steel spacers, the column was plumbed by placing thin metal shims between the anchor block and the steel spacers. Once the column was plumb, the hydrostone was poured into holes that had been placed during construction; the holes were constructed by placing PVC pipe in the anchor block prior to casting the concrete (Figure A.4). The hole placed nearest to the column was used to pour the hydrostone; four smaller holes were placed at the four corners and were filled when the hydrostone overflowed after filling the 0.25-inch gap between the anchor block and the floor.

The hydrostone was allowed to cure for 24 hours after which the anchor block was then post-tensioned to the laboratory floor with six high-strength rods, as indicated in Figure B.3. The rods were post-tensioned to a force of 100 kips apiece. Figure B.4 shows equilibrium of the laboratory configuration. Using a 6-foot distance between the prestressed rods, the required prestressing force on each side of the anchor block,  $P_{applied}$ , to restrain specimen rotation was:

$$P_{applied} = \frac{150kips \times 8feet + -147kips \times 3feet}{6feet} = 127kips \quad (B.16)$$

In addition to restricting specimen rotation, the prestressing force was required to prevent sliding of the test specimen. Hydrostone was placed between the specimen and laboratory floor to provide a reliable shear transfer mechanism. Assuming a hydrostone friction coefficient of 0.2, the required prestressing force to apply was:

$$P_{applied} = \frac{(150kips - 0.2 \times 147kips)}{0.2} = 600kips \quad (B.17)$$

Therefore, 6 rods, 3 on each side of the anchor block, prestressed to 100 kips apiece, were used to apply the required force. This would require an 8-foot by 8-foot anchor block. To minimize the size of the anchor block, thereby reducing the construction cost, without disturbing the modeled region, tie-down beams were used to transfer the prestressing force to the test specimen. As shown in Figure B.B.3, the tie-down beams were placed on top of the anchor block and three prestressed rods were placed through each beam and the column anchor block. The rods were then prestressed to 100 kips apiece.

Each column was subjected to a constant axial load and a cyclic lateral load. The axial load was applied by prestressing two rods, one on each side of the specimen, to the designated force of 74 kips apiece. Each rod was attached to a clevis which transferred load to the column through a spreader beam (Figure B.2). The load was applied using manually controlled jacks. As shown in the photograph of Figure B.5, a cage bordered by an upper steel plate, the top plate of the lower clevis, and four 1-inch diameter rods was constructed around each jack and load cell pair. Hydrostone was placed between the lower clevis and the laboratory floor. A rod was threaded into the bottom plate of the lower clevis and prestressed to the laboratory floor. The entire axial load apparatus was attached following placement and prestressing of the main rods through the anchor block.

The lateral load was applied using a servo-controlled hydraulic actuator. The actuator applied the force to the top of the column and reacted against the reaction frame, as shown in Figures B.2 and B.3. The lateral load was applied using a single 500-kip load, 20-inch stroke capacity actuator for Columns 407, 415, and 430 (Figure B.6). For Columns 815 and 1015, the lateral load was applied by two 20-kip load, 100-inch stroke capacity actuators that were placed in parallel (Figure B.7). To facilitate attachment of the horizontal actuator, a square head, measuring 28 inches by 28 inches in plan, was constructed at the top of the column. The head extended 9 inches above and below the top of the column, to accommodate the width of the end plate of the actuator clevis. Four high-strength rods, measuring 1-1/8 inch in diameter, were placed through PVC pipe (inserted through the square column head during construction) and attached to a plate on the opposite face. The combined prestressing force was 240 kips (60 kips per rod), approximately twice the maximum expected shear force.

### **B.3 INSTRUMENTATION**

The column and joint instrumentation was placed to monitor both system and local response quantities. The system response monitored included the horizontal displacement (measured from a fixed reference frame), column and anchor block rotation, and the applied horizontal and axial loads. Local deformation modes were monitored along the column and into the joint. External displacement transducers, and internal strain gauges were used. The following subsections summarize the instrumentation used to measure the forces, displacements and local deformation modes.

#### **B.3.1 External Forces**

Load cells were used to measure the applied axial and lateral loads. To measure the axial load, load cells were placed between the axial load jacks and the upper steel plate (Figure B.5). The lateral load was measured using the load cell located between the clevis and the horizontal actuator. The exact locations of the axial load jacks and horizontal actuator are indicated in Figures B.2 and B.3.

#### **B.3.2 Global/System Displacements**

Measured system displacements included the horizontal displacement of the column at various locations along its length, horizontal displacement of the anchor block, rotation of the column, rotation of the anchor block and slip of the longitudinal reinforcement.

Horizontal displacements were measured at the midheight of the anchor block and at various locations along the column length. As depicted in Figure B.9, the column was divided into segments at which several deformations were monitored. The horizontal displacement of the anchor block was measured at midheight. For the three columns of Test Series I, horizontal instruments were placed at 6 inches, 12 inches, 24 inches, 48 inches, and 96 inches above the column/anchor block interface. In addition to these locations, two additional points were monitored for the two slender columns, Columns 815 and 1015. For Column 815, additional displacements were also monitored at 72 inches and 192 inches (column height). For Column 1015, additional displacements were also monitored at 72 inches and 240 inches (column height).

The horizontal displacements were measured at the top of each segment from a fixed reference column placed 13 feet from the face of the top column block. The reference frame consisted

of a steel H-section that had been previously welded to a steel plate. The bottom plate was post-tensioned to the laboratory floor. To attach the instruments to the reference frame, a series of channel-section unistrut pieces were attached to the reference column at the appropriate location (Figure B.8). Small aluminum plates were used to attach the instruments to the unistrut with two instruments attached at each plane. A 2-inch stroke linear potentiometer was used to monitor the initial displacement cycles. An instrument with a larger stroke, either a wire pot or a direct current displacement transducer, was used to monitor the latter displacement cycles. The instruments located at the 6-inch and 12-inch levels were attached to the hold-down beams. The instruments were mounted on small aluminum angles that were epoxy glued to the hold-down beams. Piano wire was drawn between the instruments and the targeted location.

Column and anchor block rotations were monitored using inclinometers. The anchor block instrument, used to measure rotation of the anchor block, was attached to the anchor block using bolts embedded into the concrete. A second inclinometer was attached to the centerline of the actuator block at the top of the column. The instrument was attached to a steel angle, which was then attached to bolts anchored into the block.

The anchored longitudinal reinforcement was expected to displace relative to the anchor block. As depicted in Figure B.10, a linear displacement transducer was placed vertically and attached to a 1/2-inch square rod that had been soldered to the longitudinal reinforcement, using low-temperature silver solder. Targets were placed into the anchor block to connect the instruments to the anchor block; therefore, the instrument measured the displacement of the longitudinal bar relative to the anchor block. The small square steel rods were soldered to the longitudinal reinforcing bar after casting the anchor block. In each case, the rod was placed approximately 3.5 inches above the anchor block.

### **B.3.3 Local Deformations**

Local column and joint deformations were monitored with internal and external instrumentation.

#### ***B.3.3.1 External Instrumentation***

Linear displacement transducers were placed to monitor local deformation modes, including shearing, horizontal extension, vertical extension, rotation and shearing. Vertical, horizontal and diagonal instruments spanned adjacent instrumented cross sections to monitor the relative move-

ment of adjacent planes.

The lower region of the column was segmented and instrumented, as shown in Figure B.9., where significant inelastic action was expected. In all cases, the column instrumentation extended beyond the theoretical yielded length,  $L_{iy}$ , where the theoretical yielded length was determined using Equation B.18 by predicting values of the ultimate and yield flexural strengths (denoted  $M_u$  and  $M_y$  respectively) using expected strengths, and the column length,  $L$ .

$$L_{iy} = 1.25 \frac{M_u - M_y}{M_u} L \quad (\text{B.18})$$

Local deformations were monitored over height of a 4 feet for the three columns of Test Series I and a height of 8 feet for Columns 815 and 1015 of Test Series II. To facilitate placement of the instrumentation and comparison of the measured response for each column, the same column instrumentation was used for the lower 4 feet for all.

The instrumented region was segmented in proportion to the column diameter (Figure B.9) with larger segment heights for the segments located away from the interface. Within the first 4 feet, the segments were spaced at 6 inches, 6 inches, 12 inches, and 24 inches (Figure B.9). These planes are numbered sequentially from Plane 4 to Plane 7. At these lower segments, four vertical and two diagonal linear potentiometers (placed in opposite directions on the east and west faces) were placed to monitor rotation, vertical extension, and shearing deformations. However, the lowest diagonal instrument spanned between the bottom of the column and Plane 5, located 12 inches above it, since the angle of the diagonal between Planes 4 and 5 or Planes 5 and 6 was determined to be too shallow to adequately monitor shearing deformations. In addition, two horizontal linear potentiometers were placed at each plane to measure average horizontal expansion.

The two additional segments that were monitored for Columns 815 and 1015 were spaced at 24 inches each. Since the number of channels available in the data acquisition system was limited, only the relative vertical movement was monitored. Since shear strains and horizontal expansion of the upper regions of the slender columns were expected to be minimal, monitoring only the vertical movement was deemed appropriate.

Rods were placed through the column cross section to attach the external instruments to the column. Figure B.11 describes the rod assembly and the attachment of the external displacement transducers. Each rod assembly consisted of a 3-foot long, 1/2-inch diameter threaded rod cut in

half and placed in a greased metal tube. Two rod assemblies were placed at each plane through the column core. The discontinuous rods were anchored to the core at two “bonding” points which were 2 inches long and were located at either end of the tube, as shown in the figure. This configuration permitted the rods to rotate and expand with the cross section without confining the core. On either side of the bonding points, the remainder of the rod was covered with a plastic sleeve to prevent it from bonding to the concrete.

The instruments were attached to a 5/8-inch smooth rod that was placed perpendicular to the embedded rods, as shown in Figure B.11. A connector was used to hold the smooth rod perpendicular to the threaded rods. The instruments were mounted as described in Figure B.12. Each instrument was mounted on a small aluminum plate which was placed on the 5/8-inch diameter rod. Small restraining collars were placed on either side of the aluminum plate to prevent translation of the plate but permit plate rotation. (The plate rotates with the column to prevent kinking of the wire.) As shown in the figure, a counterweight was placed opposite to the instrument to balance the assembly.

#### ***B.3.3.2 Internal Instrumentation***

Strain gauges were placed on the longitudinal and spiral steel to monitor the internal steel strains. The internal response was monitored at each plane to facilitate comparison with the external response, as indicated in Figure B.13.

Strain gauges were placed on the longitudinal and spiral reinforcement at each of the instrumented planes. At each plane, the north and south locations were monitored on the longitudinal bars and the spiral. In addition, the east and west locations were instrumented on the longitudinal bars and the spiral at the top of segments where the shear strain was monitored (that is, at the location of an external diagonal instrument).

The strain gauges were purchased from Texas Measurements Laboratory (TML). The longitudinal strain gauges were designated YFLA-5 High Elongation Gauges. In general, readings from the longitudinal strain gauges were reliable to 5% strain. The spiral gauges were TML FKL-1-11 gauges. Readings from these strain gauges were reliable to approximately 0.3% strain.

The joint was instrumented with spiral strain gauges, longitudinal strain gauges, and concrete strain gauges. The internal joint instrumentation was identical for all five columns. The joint was instrumented to a depth of 24 bar diameters (16 inches) below the column-joint interface. Longitudinal, spiral and concrete strains were monitored at Planes 1, 2 and 3 (indicated in Figure

B.13) which were located at the interface, at a depth equivalent to 12 bar diameters (8 inches) below the interface, and a depth equivalent to 24 bar diameters (16 inches) below the interface. At each plane, longitudinal and spiral steel strains were monitored at the four quadrant points.

Embeddable TML concrete strain gauges were used in the joint region only. Large discrete cracks expected within the column length made using concrete gauges an expensive and unreliable effort within the column. At each instrumented plane, two concrete gauges were placed adjacent to the longitudinal steel strain gauges on the north and south bars.

#### **B.4 EXPERIMENTAL PROCEDURE**

The testing procedure was established to ensure, to the extent possible, equal treatment of the five columns.

As described in Section B.2, the specimen was moved into the laboratory and placed in the location shown in Figure B.3. The specimen was plumbed, and hydrostone was placed and allowed to cure. Six rods were placed through holes in the anchor block and the laboratory floor, and were prestressed to 100 kips apiece. The axial load apparatus was then attached to the column. The instruments were placed on the column and attached to the data acquisition system. The instruments were then calibrated. Finally, the horizontal actuator was attached to the column at the top block. The horizontal actuator was then calibrated.

Figure B.15 provides the checklist used prior to testing. The data acquisition system was turned on and zeroed. The axial load was then applied using two manually controlled hydraulic pumps (one for each jack). The axial load was applied in approximately 30-kip increments until the target load of 147 kips was reached.

The column was displaced according to the prescribed displacement history (see Chapter 3 for details of displacement histories used). Figure B.17 shows the ideal displacement history in terms of yield displacement. The column was cycled three times at each displacement level where a single displacement cycle consisted of pulling the actuator north and pulling the actuator south. An additional displacement cycle equal to one-third the magnitude of the previous cycle was imposed for the post-yield displacement levels. The displacement history was imposed at a slow rate.

Measurements and photographs were taken at the first north peak and first south peak of each displacement level. Figure B.B.16 shows the checklist used for each displacement level. At

the first north and south displacement peaks, the widths of certain cracks were measured, dimensions of spalled regions were noted, the crack pattern on the north and south face (within the instrumented region) was recorded, and photographs of the observed damage and overall response were taken. In addition, widths of the cracks were measured after completion of all cycles at a displacement level. Additional photographs were taken during testing at stages of important damage (e.g., bar buckling, spiral fracture, bar fracture). Testing was terminated after a strength loss of 40% or more.

#### **B.4.1 Data Acquisition and Reduction**

The measurements made by each instrument were acquired by a data acquisition system periodically during testing. The readings were then reduced to interpret engineering response quantities.

##### ***B.4.1.1 Data Acquisition System and Procedure***

The Neff System 620 Data Acquisition system was used to interpret the instrument movements. A computer interfaced with the system was used to manually record the information. The internal strain gauges were calibrated by shunting a resistor across the strain gauge channels and verifying the resulting strain readings. Channels that did not properly interpret the calibration were removed.

The displacement transducers were calibrated using precisely measured calibration blocks. A linear calibration program was used. Three calibration readings were made for each instrument. The NEFF data acquisition software calculated the corresponding calibration factor from the three readings.

The instrument measurements were read manually. Numerous readings were made between the maximum and minimum displacement peaks of each cycle. After testing, the data was downloaded from the computer as a single matrix. The strain gauge readings are readily interpreted. However, the readings from the external instruments needed to be interpreted in terms of engineering response quantities. This was accomplished using the Matlab software program. The following section describes the expressions used to interpret the data.

##### ***B.4.1.2 Data Reduction***

The local vertical, horizontal, and diagonal measurements were used to calculate the average vertical strain, average horizontal strain, average curvature, and average shear strain of the segment.

Figure B.14 shows a typical instrumented column segment. The original segment configuration is shown in Figure B.14.a. The segment has a height,  $h$ , and a width,  $b$ . The length of the diagonal is  $d = \sqrt{h^2 + b^2}$ . The six external instruments are indicated by hollow rectangles. The instrument measurements are denoted by  $\Delta$ . Two vertical, two horizontal, and one diagonal measurement were made.  $\Delta N$  and  $\Delta S$  are the displacements measured by the north and south vertical instruments, respectively. The top and bottom horizontal displacements measured are denoted  $\Delta T$  and  $\Delta B$ .  $\Delta D$  is the measured extension of the diagonal instrument.

The instrument readings were used to interpret two displacements, vertical and horizontal, and two rotations, flexure and shear as indicated in Figures B.14.b–B.14.e. In each figure, the deformation mode is sketched using a dashed line and filled rectangles indicate the instruments that were extended.

#### AVERAGE VERTICAL STRAIN

Average vertical strain,  $\bar{\epsilon}_v$ , is the average vertical displacement divided by the original length (Equation B.19).

$$\bar{\epsilon}_v = \frac{\Delta_v}{h} \quad (\text{B.19})$$

As shown in Figure B.14.b, the vertical extension,  $\Delta_v$ , is the average of the two vertical displacements (Equation B.20). Note the diagonal instrument also extends, however the reading is redundant and is not used.

$$\Delta_v = \frac{(\Delta N + \Delta S)}{2} \quad (\text{B.20})$$

#### AVERAGE HORIZONTAL STRAIN

A similar expression was used to calculate the average horizontal strain,  $\bar{\epsilon}_h$ . The average horizontal strain is the horizontal extension,  $\Delta_h$ , divided by the original length (Equation B.21). The horizontal extension is the average of the measurements of the two horizontal displacement devices (Equation B.22). Likewise, the diagonal instrument also extends, however the reading is redundant and is not used.

$$\bar{\epsilon}_h = \frac{\Delta_h}{b} \quad (\text{B.21})$$

$$\Delta_h = \frac{\Delta T + \Delta B}{2} \quad (\text{B.22})$$

#### AVERAGE CURVATURE (SEGMENT ROTATION)

The average curvature for the segment approximated as the segment rotation divided by the segment height,  $h$ , as indicated by Equation B.23. As depicted in Figure B.B.14.c, segment rotation,  $\theta$ , was calculated using the two vertical instruments, as indicated by Equation B.24.

$$\bar{\phi} = \frac{\theta}{h} \quad (\text{B.23})$$

$$\theta = \frac{(\Delta S - \Delta N)}{b} \quad (\text{B.24})$$

#### AVERAGE SHEAR STRAIN

As indicated in Figure B.14.e, the shear deformation mode displaces the diagonal instrument. The extension due to horizontal and vertical extension must be removed to determine the shearing deformation. Therefore, the extension of the diagonal instrument,  $\Delta D$ , is resolved into two components: the component due to vertical and horizontal extension,  $\Delta D_{vh}$ , and the extension due to shear,  $\Delta D_s$ . The extension due to shearing is determined by subtracting the extension due to horizontal and vertical deformation of the segment from the instrument reading (Equation B.25).

$$\Delta D_s = \Delta D - \Delta D_{vh} \quad (\text{B.25})$$

The extension due to horizontal and vertical deformation of the segment is computed as shown in Equation B.26.

$$\Delta D_{vh} = \sqrt{(b + \Delta_h)^2 + (h + \Delta_v)^2} - d \quad (\text{B.26})$$

The shear strain,  $\gamma$ , is approximated using Equation B.27; the change in segment height due to the shearing deformation is assumed to be negligible.

$$\gamma = \frac{\sqrt{(d + \Delta D)^2 - (h + \Delta_v)^2} - (b + \Delta h)}{h + \Delta_v} \quad (\text{B.27})$$

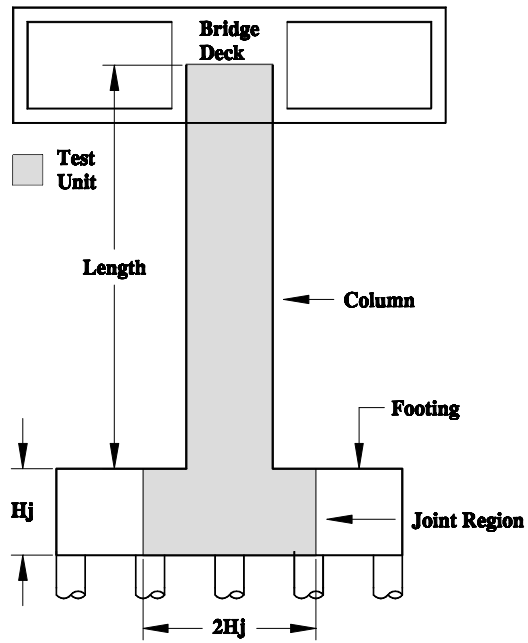


Figure B.1: Modeled Section of Prototype Structure

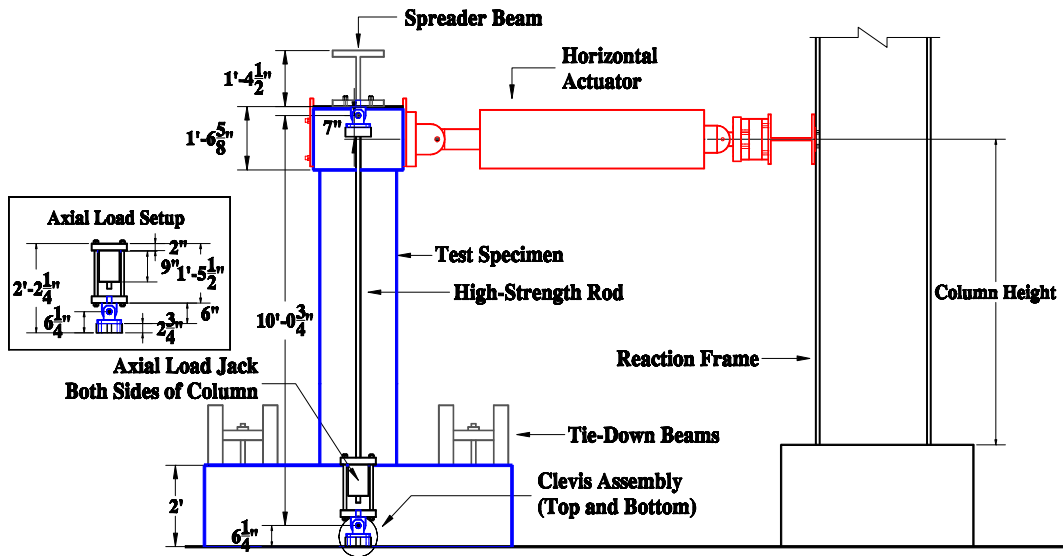


Figure B.2: Experimental Configuration: Elevation

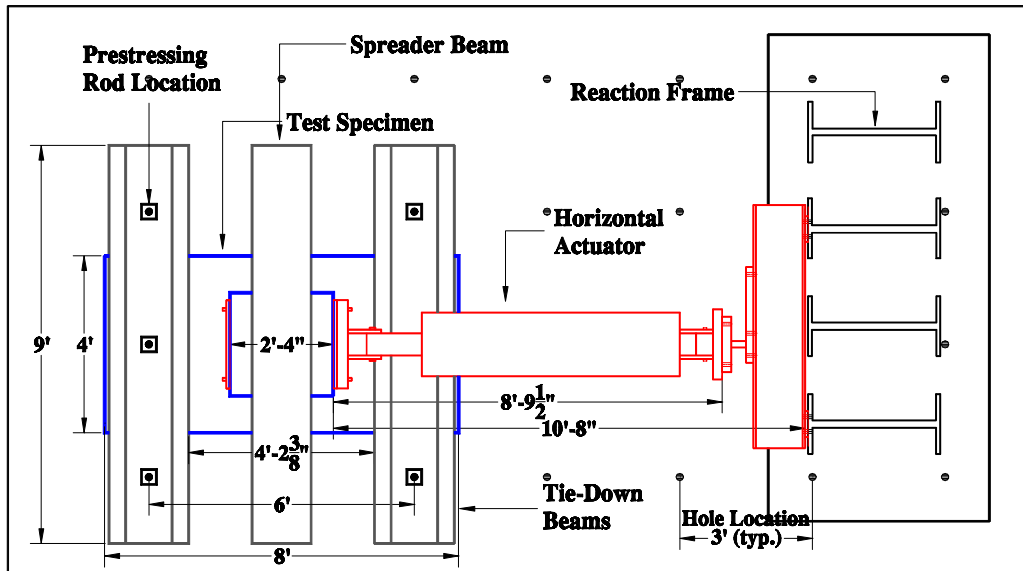


Figure B.3: Experimental Configuration: Plan

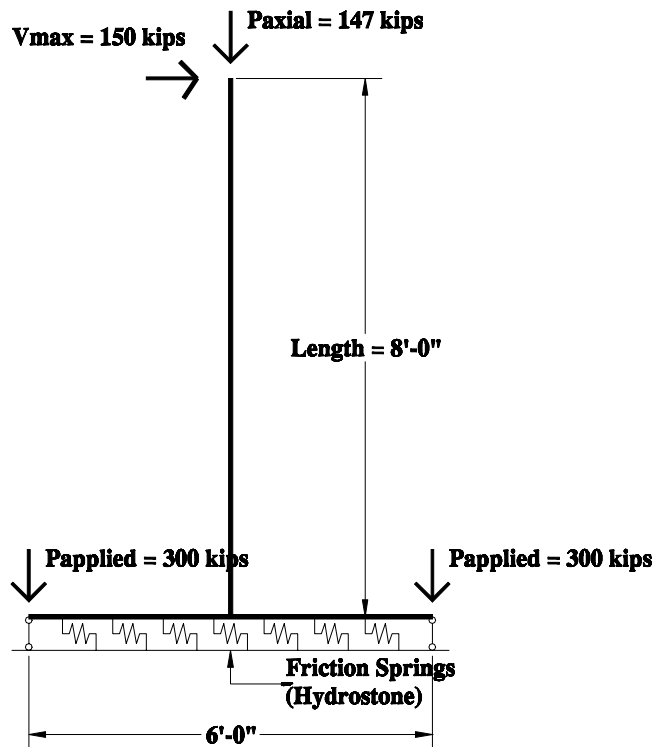
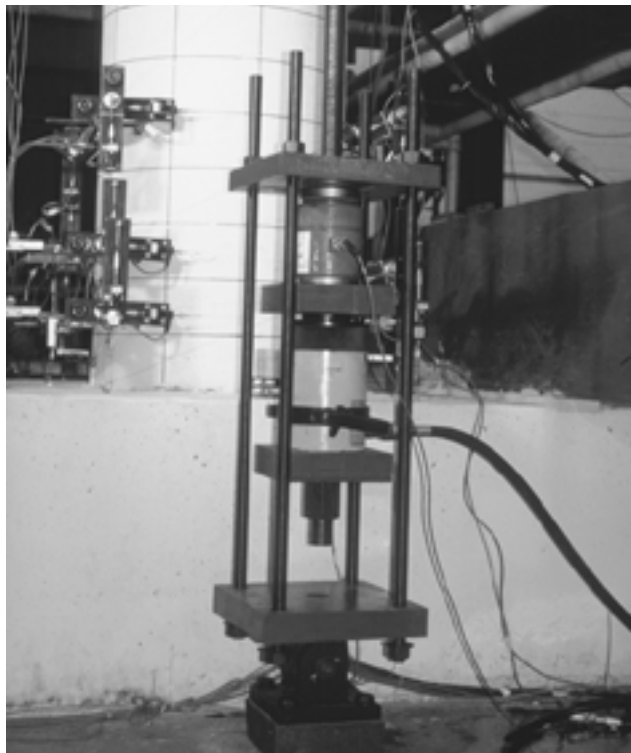
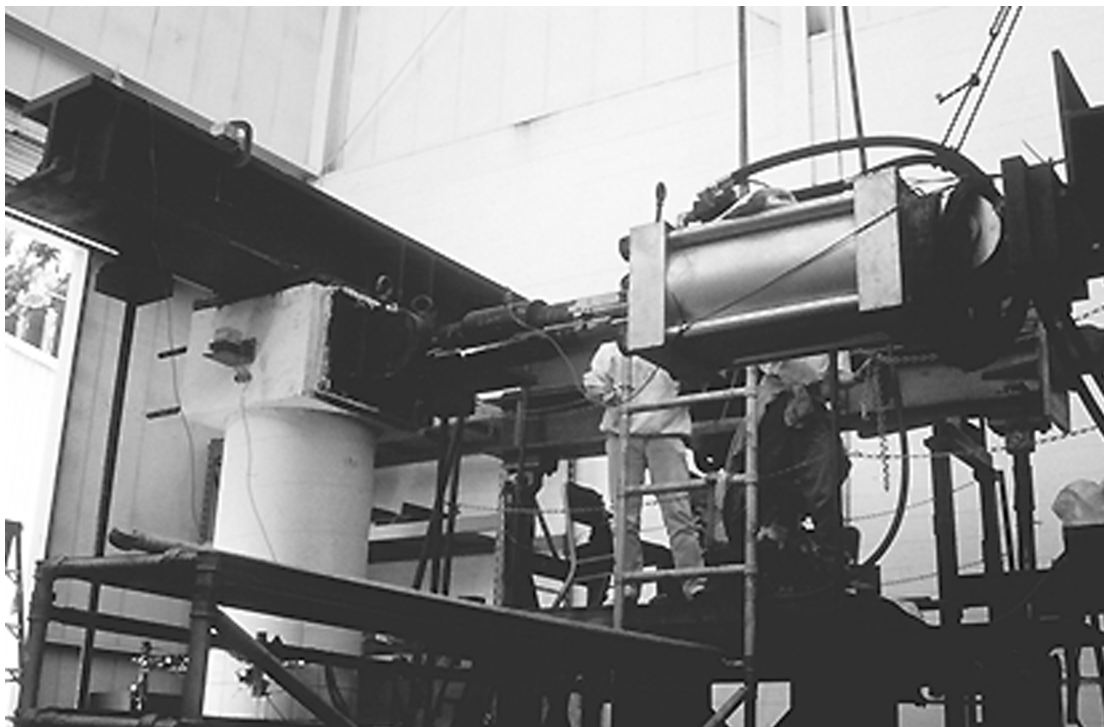


Figure B.4: Equilibrium of Laboratory Configuration



**Figure B.5: Axial Load Setup**



**Figure B.6: Actuator used for Testing of Columns 407, 415, and 430**



**Figure B.7: Actuators Used for Testing of Columns 815 and 1015**



**Figure B.8: Instruments Attached to the Reference Column**

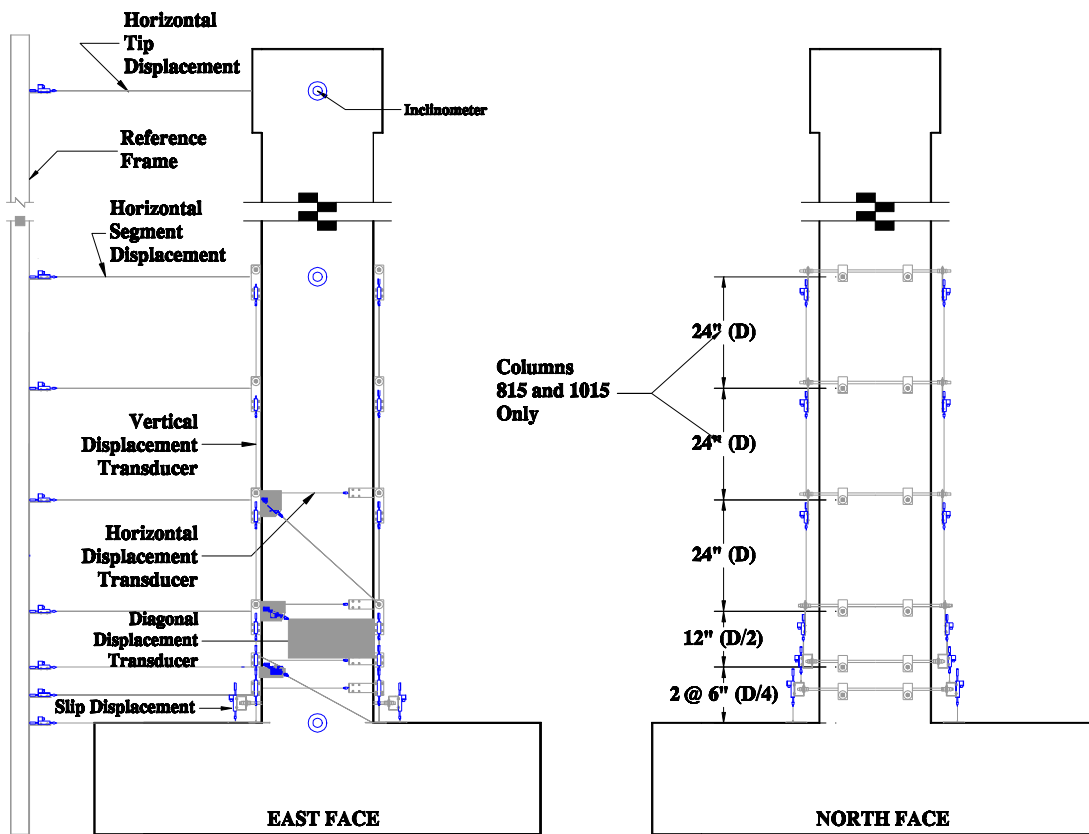


Figure B.9: External Instrumentation Layout: Elevation

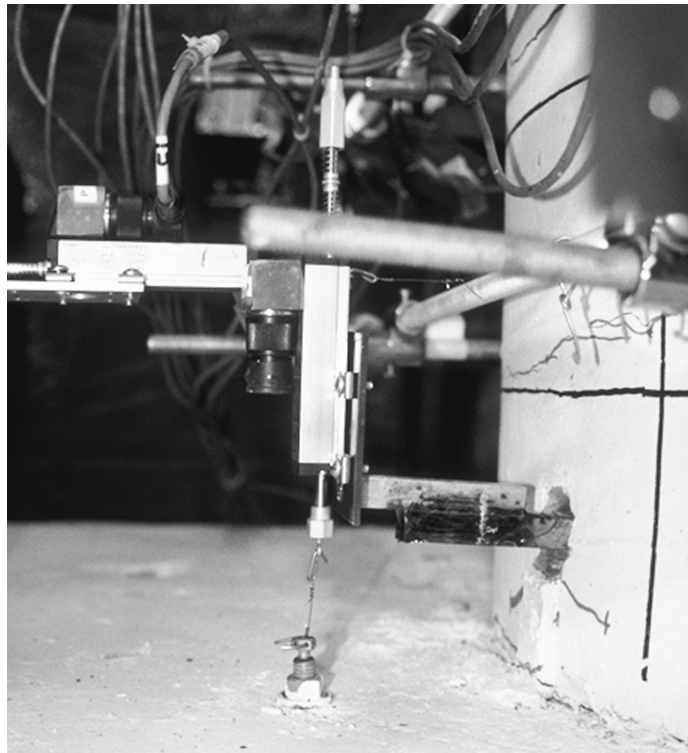


Figure B.10: Slip Instrumentation

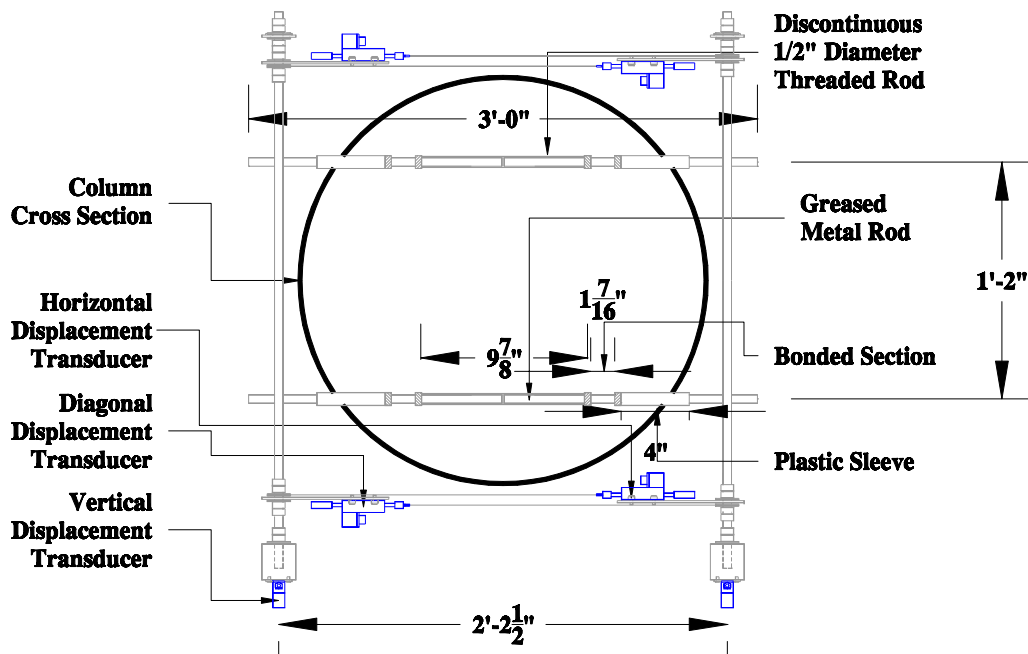


Figure B.11: External Instrumentation Layout: Plan

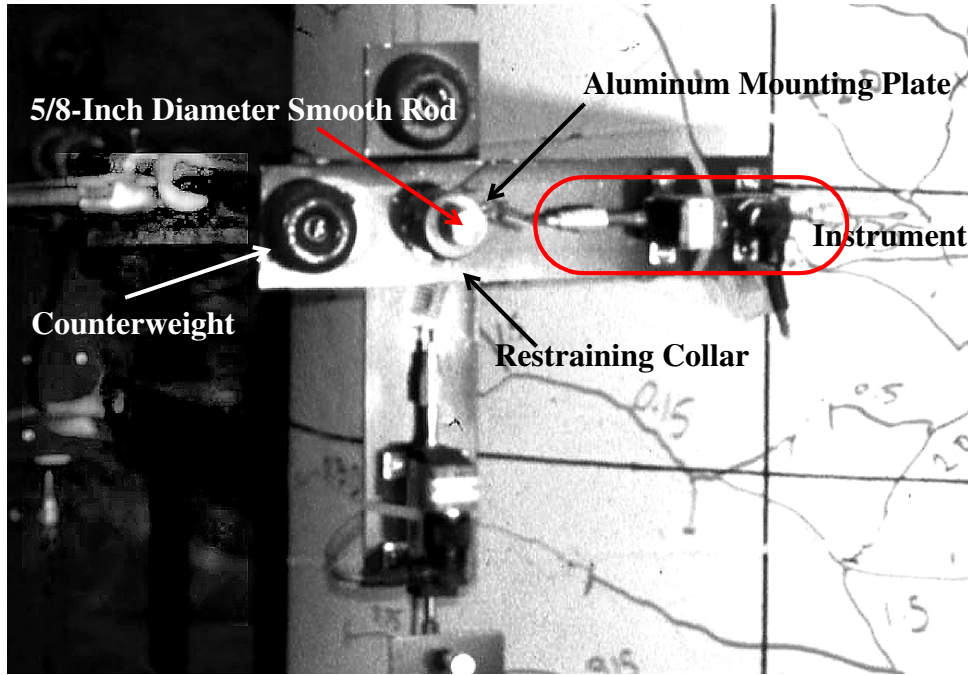


Figure B.12: Typical Attachment of External Instruments

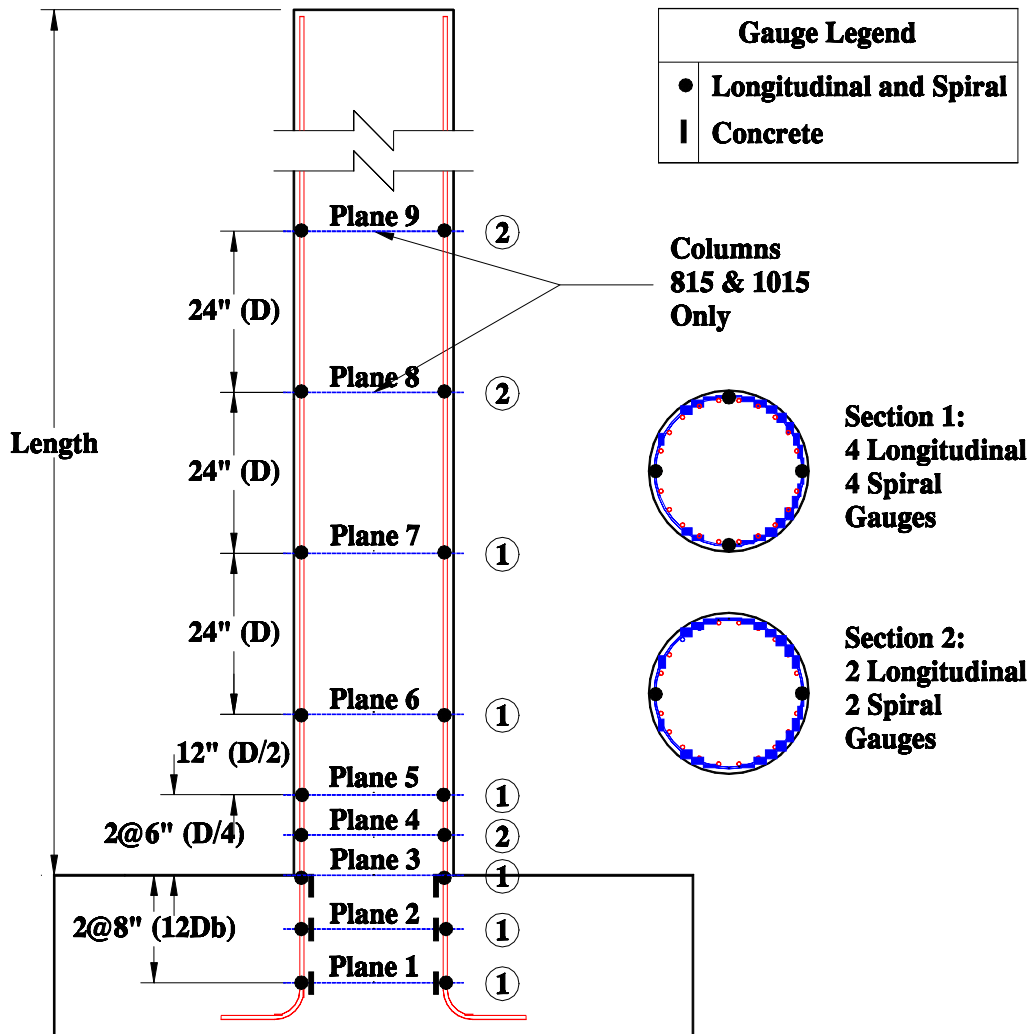


Figure B.13: Internal Instrumentation Layout

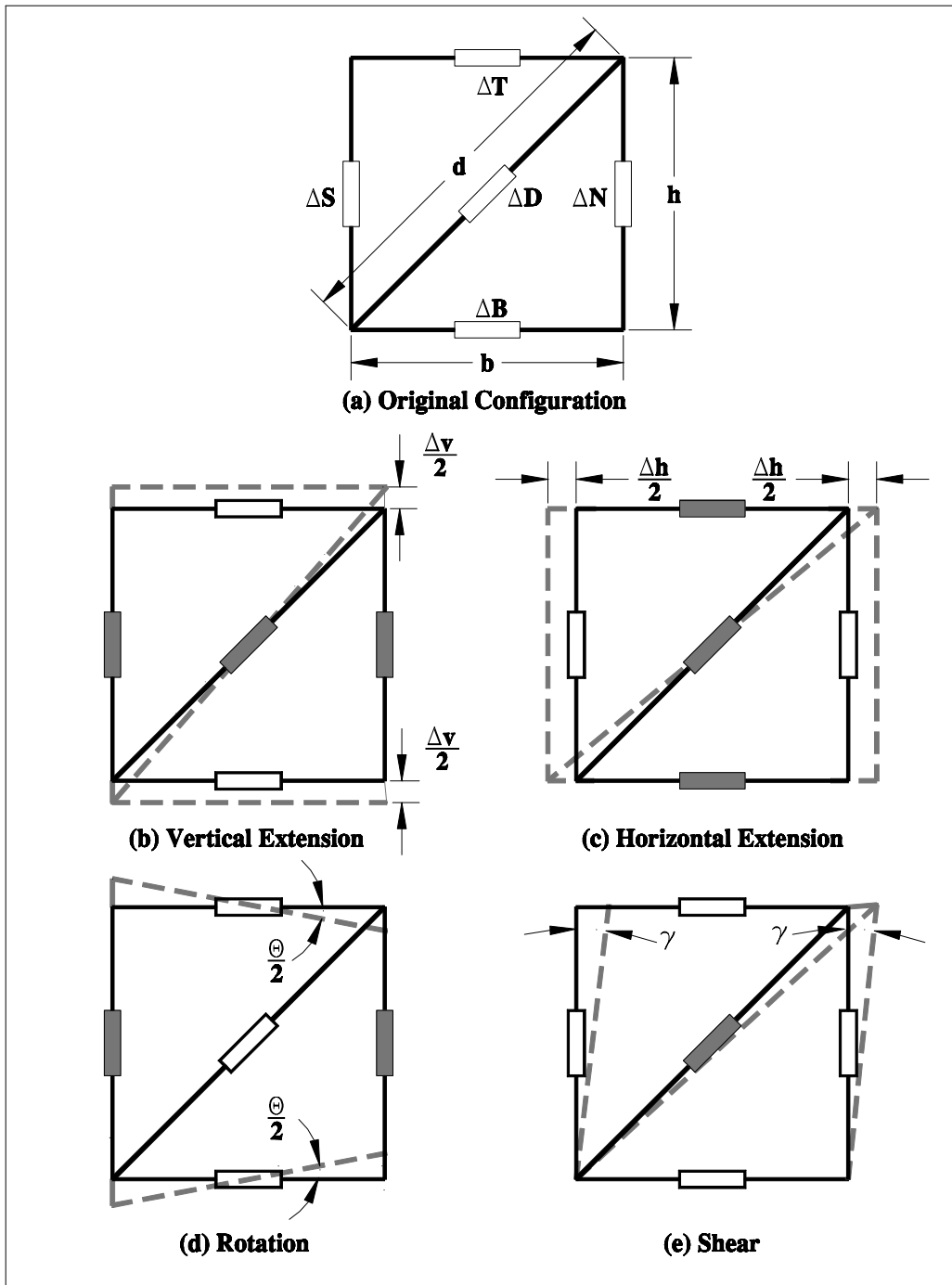


Figure B.14: Local Deformation Modes

U.C. Berkeley/Caltrans  
Task 5 - Behavior of Bridge Columns

Column \_\_\_\_\_  
Date \_\_\_\_\_

1. Initial Startup

HYDRAULICS ARE ON

a) SAFETY CHECKS

- i) Check that crane cables are connected to blue tarp \_\_\_\_\_
- ii) Helmets on for everyone \_\_\_\_\_
- iii) Caution tape on instruments and back of NEFF \_\_\_\_\_
- iv) Channel list for marking if something goes wrong with instruments \_\_\_\_\_
- v) Plug in lights. Must have their own outlet \_\_\_\_\_
- vi) Check Axial Load set-up. Are rods loose? \_\_\_\_\_

b) CONTROLLER OPERATION : Wes Neighbour

- i) Periodically check X-Y plotters for deviations from the norm

c) DATA ACQUISITION SYSTEM

i) Connect

- a) Neff System 620 to PC \_\_\_\_\_

- b) PC to printer \_\_\_\_\_

- c) Output Channels to Meter and XY recorders \_\_\_\_\_

ii) Power Up

- a) Neff System 620 \_\_\_\_\_

- b) PC \_\_\_\_\_

- c) Printer - make sure printer is on-line \_\_\_\_\_

- d) Goto directory \das85 \_\_\_\_\_

- e) run software nef621.exe \_\_\_\_\_

- (1) USE CAPS

- (2) calibration file: 430CAL

- (3) read all : R

- (4) open calibration file : DFILE

- (5) set watch channels: WATCH

- (6) read @ \_\_\_\_\_

- (7) pens down on x-y recorders \_\_\_\_\_

- (8) set automatic recording : AREC \_\_\_\_\_

- (9) take readings at appropriate steps : R

- (10) mark peaks and zeros on load history

....

- (11) end of test : DFILE to close data file

- (12) DFILE to open new data file

- (13) AREC to automatically record

- (14) exit program : STOP

D) VISUALS

- i) Lights on \_\_\_\_\_

- ii) First cycle sign \_\_\_\_\_

- a) Caltrans/U.C. Berkeley Bridge Column Test

- b) Specimen \_\_\_\_ :

- c) Ductility

- d) Displacement \_\_\_\_ in.

- e) Cycle No.

- f) Date

- iii) Tripod set with black and white camera \_\_\_\_\_

- iv) Mark any initial cracks prior to testing(black) \_\_\_\_\_

**Figure B.15: Checklist Prior to Testing**

### Testing Checklist : Each Cycle

- a) Call out cycle number
- b) Read data
- c) Check watch channels
- d) Mark reading number at peak on load history
- e) Mark points of interest on load history
- f) Mark cracks
- g) Measure 5 main cracks on north and south face first cycle
- h) Measure 5 main cracks on north and south face at end of third cycle
  - i) Mark damage to concrete and steel on drawings
  - j) Check wires
  - k) Photograph
- l) Place Signage for Next Cycle : change what is in bold
  - i) Sign
    - a) Caltrans/U.C. Berkeley Bridge Column Test
    - b) Specimen \_\_\_\_ :
  - c) Aspect Ratio \_\_\_\_ ; Longitudinal Reinforcement Ratio \_\_\_\_
  - d) Axial Load  $0.10A_g f'_c s = 147$  kips
  - e) Ductility
  - f) Displacement \_\_\_\_ in.
  - g) Cycle No.
  - h) Date
  - m) Copy crack drawing
  - n) Copy damage drawing

**Figure B.16: Testing Checklist for Each Cycle**

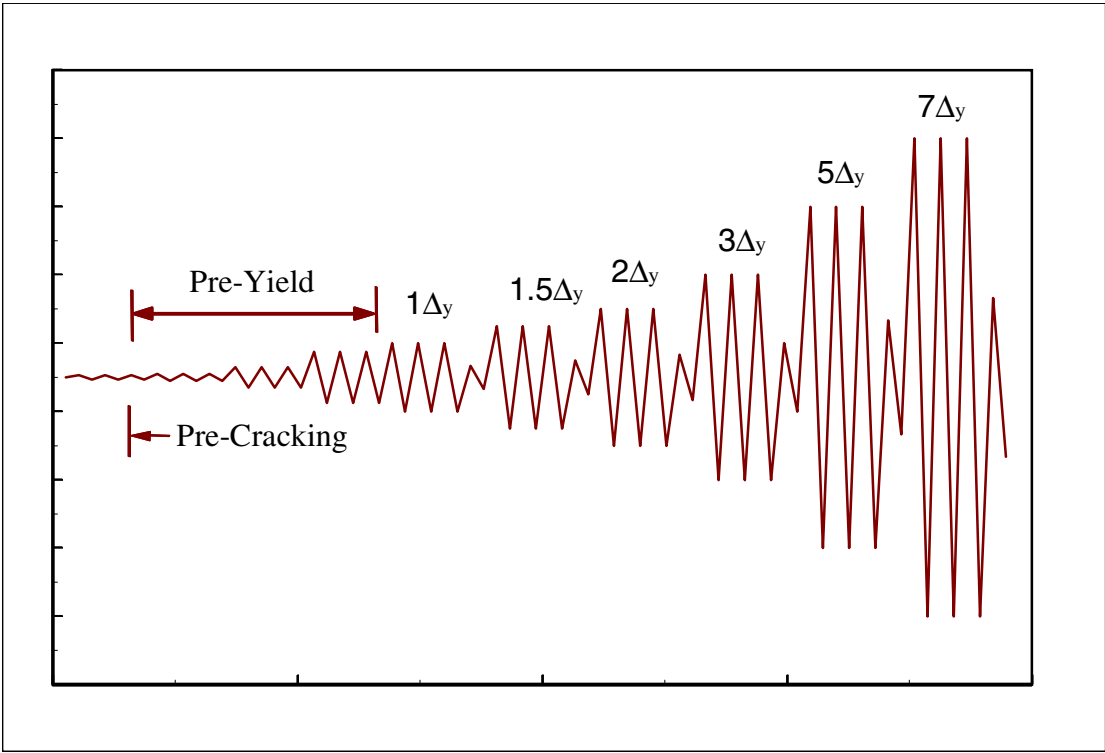


Figure B.17: Idealized Displacement History

# Appendix C Test Data

## C.1 INTRODUCTION

Measurements made during an experiment are crucial to its usefulness. Therefore, the instrumentation layout and measurements are of utmost importance. The instrumentation scheme used in this research program was developed to gain a better understanding of the inelastic behavior of reinforced concrete bridge columns and column-footing joints. Deformations were monitored globally and locally, including external and internal measurements.

Appendix C presents the measured response for the five specimens of the two test series. Interpreted results are provided in Chapters 3 and 4 with comparative analysis of the influence of each parameter and comparison with analytical response. This appendix is intended to be a resource document. The data are presented in an absolute form for each column providing a foundation for interpretation for both the present and future studies.

The instrumentation was placed to monitor the response of the column, joint, and system. Along the column length, bending and shearing deformations were measured using external instruments placed between adjacent planes. Additional instruments were placed to measure core expansion, steel longitudinal strains, and spiral strains. Monitored joint deformations include longitudinal steel strains, longitudinal concrete strain, and extension of the longitudinal steel at the column/joint interface. Global rotation and horizontal displacements at each monitored level were measured as well. The following sections summarize the column, joint, and global response for each experimental specimen.

## C.2 COLUMN REGION

Instrumentation was placed externally and internally to monitor the response of the column. External instrumentation was placed to monitor expected flexural and shearing deformation modes. These readings were correlated with internal deformation response quantities measured with strain gauges that had been placed on the longitudinal and spiral strain along the column height. For the column, the following measured response quantities are presented: internal longitudinal strains (cyclic and peak), external average longitudinal strains (cyclic and peak), peak spiral strain profiles, peak horizontal expansion profiles, cyclic moment-rotation relations, cyclic

moment-curvature relations, curvature profiles, cyclic shear stress-strain relations and shear strain profiles.

The column behavior was monitored externally and internally along a length where significant inelastic deformations were expected. Instrumented segments were located along the column length from the interface to 4 feet for the shorter columns (Columns 407, 415 and 430) or to 8 feet for the taller columns (Columns 815 and 1015). The length of the segments, which increased up the column height, was a percentage of the column diameter. The external and internal instrumentation layout is described in Figures B.5 and B.9 of Appendix B. For the 8-foot columns of Test Series I, four segments were monitored. Measuring from interface, the segment lengths were 0.25D (6 inches), 0.25D (6 inches), 0.5D (12 inches) and 1.0D (24 inches). For the slender columns (Columns 815 and 1015) two additional segments were monitored. The additional segments had lengths of 1.0D (24 inches). External instrumentation extended between the planes to monitor horizontal (expansion), vertical (bending), and diagonal (bending plus shearing) movement of adjacent planes. Internal longitudinal and spiral strains corresponding to the external response were monitored at the four cross-sectional quadrant points for segments in which diagonal extension was measured. For the plane in which only vertical and horizontal extensions were measured (6 inches above the interface), only the extreme points were monitored.

### **C.2.1 Local Longitudinal Steel Strains: Internal Strain Gauges**

Strain gauges placed on the longitudinal steel provide an indication of the strains in the longitudinal reinforcement. Readings extend over a finite length of the strain gauge and may be influenced by local bond loss and cracking. Therefore, the magnitude of the gauge reading should not be expected to correlate directly with analysis results.

The longitudinal strain response was monitored throughout the displacement history. Typically, the readings were reliable to a strain of 0.03 in./in. The data are presented in two forms. Figures C.1 through C.21 present the response history of the south gauges (while gauge remained active) at various heights above the column/joint interface. The strain is plotted as a function of the applied lateral force. The yield strain (approximately 0.0023) is indicated with a dashed-dotted line. Note that the north gauges (initially in compression) are presented for Column 815 in Figure C.20 (readings for the south gauges were not reliable).

Longitudinal strain profiles of the longitudinal strain gauges are indicated in Figures C.23

through C.31. Initial and final cycles are plotted. The peak strain at the first cycle to the ductility demand is indicated. Each marker indicates a single gauge reading. Profiles are plotted as a function of percentage of column height. For graphs showing final displacement cycles, the yield strain is indicated with a dashed-dotted line.

Readings from the initial cycles indicate nearly linear strain distribution above the lower 10% of the column height. Later cycles indicate yielding over a finite column length. Results for the three columns from Test Series I (Columns 407, 415, and 430) indicate the length over which the longitudinal strain exceeded the yield strain was similar for the three columns (approximately 25% of the column height at a displacement ductility of 2 to 2.5). The length over which the bar yielded increased with an increase in column length as indicated for the results of the columns of Test Series II (Columns 415, 815, and 1015). Bar yielding extended to approximately  $0.25L$  for Column 415,  $0.37L$  for Column 815, and  $0.4L$  for Column 1015 where  $L$  is the column length.

Additional strain gauges were placed on the two bars at the remaining two cross-section quadrant points. Strain profiles interpreted from the peak readings are presented in Figures C.32 through C.36. Yield strain is indicated by a dashed-dotted line. The yielded lengths were equal to or less than those obtained for the respective north and south gauges (Figure C.22 through C.31). The yielded lengths for the shorter columns (Test Series I) were approximately 25% of the column height. The yielded lengths of the slender columns (Test Series II) was approximately 20% of the column height.

## **C.2.2 Average Longitudinal Strains: External Displacement Gauges**

Although external vertical displacement gauges extended between planes primarily to monitor rotation, they were also used to interpret the longitudinal strain demand. Because the longitudinal reinforcement slips relative to the concrete they cannot provide a reliable indication of concrete strains. Therefore, the external displacement gauges are the only instruments available to assess the compressive strain demand in the concrete.

The vertical displacement gauges are placed outside of the column diameter. However, it is desirable to compare the strain measurements at the column face or at the longitudinal reinforcement. Assuming the distance from the displacement gauge to the desired location is  $e_i$ , the equivalent average strain  $\bar{\epsilon}$  at level  $i$  is assessed using Equation C.28.

$$\bar{\varepsilon}_i = \frac{\Delta_{vi} - \tan(\theta_i)e_i}{h_i} \quad (C.28)$$

The variables in the expression are defined as follows:  $\Delta_{vi}$  is the extension measured by the instrument extending vertically over segment  $i$ ,  $\theta_i$  is the local rotation measured for segment  $i$ , and  $h_i$  is the height of the segment.

Figures C.37 through C.41 indicate the response history of the vertical displacement gauges in terms of average strain at the extreme longitudinal bar. For each instrument, the entire average strain history is presented in relation to the applied lateral load. Each figure presents four plots, with each plot corresponding to a different segment. For the columns of Test Series I, all instruments are shown. For the remaining columns of Test Series II, instrument response shown includes the bottommost instrument (0 inches to 6 inches in elevation) and upper level instruments including those extending from 6 to 12 inches, 24 to 48 inches and 48 to 72 inches. Average strain profiles are shown in Figures C.42 through C.46, with average strain plotted on the horizontal axis. For each column, the average strain distribution as measured by the vertical displacement gauges is plotted as a function of column height. The figure plots the strain measured at the first peak loading north. For each segment, both the tensile and compressive strains are presented. The response is plotted corresponding to location as percentage of column height. Since the reading extends over a finite length (the segment height), the average strain measured is plotted over the entire segment height. The reference lines (shown as a dashed-dotted line) indicate the yield strain and the approximate spalling strain. (For the experiments, the strain corresponding to initial spalling was approximated as -0.006 in./in.)

Linear response is noted in the uppermost instrument. The area under the curve tends to be largest for the bottommost instrument. With the exception of the bottom vertical displacement transducer, the average strain measured by the external instruments was similar to the measurements made by the internal strain gauges. The average strain measured by the bottom instrument is larger than the strain measured by the longitudinal gauge. This difference may be a result of the compressive bar slip (recall the instruments at this level measure both the joint and column response).

Average strain profiles (Figures C.42 through C.46) reveal approximate yielded length and length of high compressive strain demand. Evaluation of the three columns in Test Series I indicates little difference in the overall response. Yielded length is equal to approximately  $0.25L$

(where L is the column length), a result that is similar to that obtained from the internal strain gauge readings. Compressive strain demands exceeding -0.006 are restricted to a height of less than 10% of the column height. Response of the slender columns (815 and 1015) show an increase in yielded length, which is similar to the results obtained from the strain gauges. As for the shorter columns, compressive strain demands exceeding -0.006 are restricted to a height of less than 10% of the column height.

### C.2.3 Spiral Strains

Strain gauges were placed on the spirals at locations corresponding to the placement of the longitudinal strain gauges. Strain gauges placed at the two extreme quadrant points (denoted north and south) are primarily believed to measure circumferential strain resulting from transverse expansion under the action of normal strain. Strain gauges placed at the remaining two quadrant points (denoted east and west) likely measure circumferential strain resulting from both transverse expansion and shearing. Spiral strain gauge measurements are expected to indicate strain distribution. Therefore, only strain profiles at peak displacement demands are provided.

Figures C.47 through C.50 indicate profiles on the north and south faces. Measured values are less than the yield strain. Strain demands are highest in the lower 20% of the column. Figures C.51 through C.55 display the peak responses of the strain gauges placed on the west face of the column. Each figure presents data corresponding to six peak displacement levels. Columns 407, 415, 815 and 1015 (all have shear demands of less than  $2\sqrt{f'_c psi}(0.8D^2)$ ) indicated higher levels of shear strain in the lower 20% of the column length. Although magnitudes of the maximum spiral strain are similar for all columns (approximately 0.001 in./in.), spiral strain profiles for Column 430 (Figure C.53) indicate this higher level of strain demand over a longer region of the column.

### C.2.4 Horizontal Expansion

Horizontal expansion of the column was measured at several planes along the length of the column. As described in Appendix B, measurement of horizontal expansion was achieved by extending horizontal displacement gauges between adjacent rods that had been bonded to the core concrete within the column cross section. Three-foot-long threaded rods were cut, placed through

the cross section at each plane, and bonded to the concrete at two distinct locations. The intention of the configuration is to ensure that the severed rod will move with the column cross section resulting in a movement of the horizontal instruments. Average horizontal expansion was measured in this manner at the lower planes (Planes 4 through 7) for the five columns.

Figures C.56 to C.60 provide profiles of the horizontal expansion measurements for the five columns. Peak measurements (corresponding to the first loading to the displacement ductility demand indicated) are indicated by markers on each plot. Expansion measurements were made to a height of 4 feet for all columns. For the columns of Test Series I (Columns 407, 415 and, 430), maximum expansion measurements (bottom instrument) were similar for all columns. However, a higher demand over the length of the column was noted with an increase in longitudinal reinforcement ratio. Profiles for the columns in Test Series II (Columns 415, 815, and 1015) were similar.

### **C.2.5 Average Curvature**

In experimental work, accurate measurement of actual curvature of a plane is not possible. The definition of curvature resides at a plane. Internal measurements of strain distribution can be used to interpret curvature, but the accuracy is limited to the accuracy of the strain gauge measurements and limited by the finite length of the gauges. Where bond loss occurs, use of a strain gauge reading to interpret curvature may not be realistic. Typically, the external vertical displacement devices are used to measure curvature. Although it is reasonable to assume that these devices provide reasonable estimates of the rotation of the segment over which they extend, extrapolation of these rotation measurements requires making assumptions about the curvature distribution. The resulting values may provide an estimate of the distribution of curvature over the column height; however accurate measures of the curvature demand at the cross section are difficult to obtain. The reader is advised to interpret the values given below with caution.

Rotation of a segment is approximated using the external vertical displacement gauges. Engineering expressions approximate the curvature of an infinitesimally small segment subjected to pure rotation as the strain divided by the rotation arm (or neutral axis depth). Experimentally, it is not possible to measure the curvature of an individual plane. Instead, average segment curvature is approximated from the measured segment rotation.

At each plane, vertical instruments measuring the extension and compression,  $v_n$  and  $v_s$ , of the segment were placed a width,  $w$ , apart. The rotation of Segment  $i$  is assessed using Equation

C-C.29.

$$\theta_i = \frac{\Delta_{vsi} - \Delta_{vni}}{w_i} \quad (\text{C.29})$$

Assuming that the change in moment over the segment is small (i.e., an approximately uniform curvature distribution), the average (or equivalent uniform) curvature of Segment  $i$  with depth,  $h_i$ , is assessed using Equation C.30.

$$\phi_i = \frac{\theta_i}{h_i} \quad (\text{C.30})$$

For the 8-foot tall columns, the depth of the bottom two segments is just over 6% of the column length (3% and 2.5% for the 18-foot and 20-foot columns). The upper segments are up to 25% of the column length. Longitudinal strain gauge readings indicate that the uppermost segments remain essentially elastic.

For the average curvature measurements, both the response history and peak values are presented. The response of the instruments at all levels except the bottommost level is presented. The moment-rotation response of this segment is presented in Section C.3.4. The measured response of the segment adjacent to the interface primarily captures the rotation resulting from joint deformation, in particular the strain penetration of the longitudinal steel into the joint.

Average moment-curvature response history is presented in Figures C.61 to C.79. For each, the average curvature is assessed as outlined above. The response history mimics the force-tip displacement response for the column. The second segment (from 6 to 12 inches) shows a “pinched” response, similar to the overall force-displacement response. Inelastic action is noted in the lower 24 inches of the column for the three columns in Test Series I. The response of the uppermost instruments (extending from 24 to 48 inches) is essentially linear. Linear response is noted in the two uppermost segments (above a height of 48 inches) for the two slender columns of Test Series II (Column 815 and 1015).

Curvature profiles are shown in Figures C.80 to C.89. Initial displacement cycles (typically less than or equal to a displacement ductility of 1) and final displacement cycles are provided separately. Curvature measurements are plotted over the entire segment height. The vertical axis indicates percentage of column height corresponding to each segment. Initial response shows essentially a linear curvature distribution up the column height (in particular, this trend is notice-

able for Columns 407, 815, and 1015. Discrepancies in distribution at these small displacement levels may be due to instrument error). Later cycles reveal a nonlinear curvature distribution for all columns.

### C.2.6 Average Shear Strain

Average shear strain is monitored over the lower 4 feet of the five columns. Shearing deformation of the segment is assumed to deform the diagonal instrument only. Assumptions made to compute the shearing strain include movement of the vertical displacement devices results solely from axial and flexural deformations (i.e., the vertical movement corresponding to segment shearing is negligible). These deformations must be removed to assess the average shear strain at each segments. Therefore, at each segment, five displacements measurements are required to assess the shear displacement. Therefore, instrumentation error is compounded and results should be interpreted with caution.

Figures C.90 to C.99 present shear strain response of the five columns. Both cyclic history and peak response profiles are presented. Shear stress-strain response histories are presented for the lowest instrument, extending to a height of 12 inches for all columns. The instrument angle was approximately 25 degrees. The shear stress is computed assuming an effective area equal to 80% of the gross cross-sectional area and normalized to  $v = (\sqrt{f'_c})ksi \left(0.8\pi\frac{D^2}{4}\right)$ . Only reliable readings are plotted (less than 25% change between individual readings), therefore, the entire response history is not presented). Similar response in all columns is noted.

For all columns, shearing deformations were monitored over the lower 4 feet. Differences in the response of the three columns in Test Series I are most evident in the upper regions of the column (2 feet to 4 feet in elevation). Increased shear distortion of this upper segment is evident as the longitudinal reinforcement ratio increased. (Increasing the steel quantity results in an increase in shear stress demand.) It is of interest to note the shear distortion profile of Column 815 is similar to Column 407.

## C.3 JOINT REGION

Joint deformation modes include shearing and vertical extension of the section. Extension of the footing beyond the joint region is significantly larger than would be found in a column/beam cap

connection, and it was difficult to place external instruments to measure the joint behavior. Instead, primary measurements include strains in the embedded longitudinal steel, embedded spirals, and in the adjacent concrete. Description of the joint instrumentation is provided in Appendix B.

### **C.3.1 Longitudinal Steel Strain Profile: Internal Strain Gauges**

Longitudinal strain gauges placed along the length of the embedded bar give an indication of the strain distribution and, in turn, the bond distribution in the joint region. The measurements may be influenced by the effects of local bond slip and cracking, and therefore should not automatically be assumed to be completely accurate.

Figures C.100 to C.109 illustrate the first peak strain profile reading for the lower three strain gauges placed on the north and south longitudinal bars. Initial and final displacement cycles are presented separately for each column. Each marker shows a single peak reading corresponding to the displacement ductility level indicated by the legend. The zero-inch level indicates the column/anchor block interface level. The location of the strain gauges is normalized to the bar diameter. The yield strain is indicated with a dashed-dotted line.

Readings from the initial displacement cycles indicate a nearly linear compressive strain distribution for the columns. Strain readings in tension imply larger bond demands in the upper portion of the bar. This is especially noted for strain profiles corresponding to peak strains equal to one half the yield strain. For example, Figure C.104 shows the strain profiles measured during the initial displacement cycles for Column 430. Differences in strain readings from 0 inches to 12 bar diameters below the interface were 0.008, while differences in strain readings from 12 to 24 bar diameters below the interface were only 0.002. Readings from the final displacement cycles indicate the longitudinal strain demand exceeds the yield strain within the joint.

Figures C.110 to C.114 indicate strain profiles over the cross-section depth for two planes, at the column/joint interface and 8 inches (12 bar diameters) below the interface. Three strain gauge readings are plotted for each displacement cycles, the strain reading at the two extreme (north and south) bars and the reading at the middle bar (east or west). Actual readings are indicated by small markers. Zero strain readings indicate an inactive gauge. The zero point on the cross section as indicated on the horizontal axis is the midpoint. Strain profiles at the interface are nearly linear for Columns 415 and 430. Nonlinearity is noted for Column 407. Strain distributions at the lower

plane appear similar for the three columns, and indicate nearly uniform strain distribution in tension, with the maximum tensile strains less than the yield strain.

### **C.3.2 Concrete Strain Profile**

Concrete strain gauges were oriented so that the vertical strain in the concrete adjacent to the longitudinal reinforcement in the core of the column cross-sectional dimension. Tensile readings of concrete strain gauges can be heavily influenced by local cracking. Concrete gauges span a length several times the aggregate size (6-inch gauge length for 3/8 aggregate). Therefore, local cracking distribution will be included in the measurements. Therefore, the strain gauges were placed in the joint region, where, in comparison with the column, cracking was expected to be less significant. Strain readings made for Columns 815 and 1015 were more reliable than the measurements for the remaining columns in that placement of the concrete gauges was improved for the slender columns.

Figures C.115 to C.119 present peak strain profiles measured by the concrete strain gauges. Markers indicate actual readings. At the column-joint interface, strain measurements are smaller than the steel strains (i.e., at ductility demands just greater than 1, the strains are approximately equal to the yield strain). The concrete strain demands at 12-bar diameters below the interface are similar to the steel strains. Measured compression strains are less than the approximate spalling strain for the presented measurements.

Evaluation of the columns of Test Series I indicates increased tensile strain demands with an increase in longitudinal reinforcement ratio; note strain measurements for Column 407 are relatively small. Tensile strain measurements for the Test Series II columns are similar for Column 415 and 815; however, an increase is noted for Column 1015 in relation to the others.

### **C.3.3 Steel Extension at Interface**

As described more fully in Appendix B, vertical instruments attached to the rods measured elongation of the bar out of and into the joint. The readings apparently were reliable until the significant elongation of the bar occurred (typically displacement ductility demands of about 3).

Figures C.120 and C.121 present the results for the instrument attached to the south bar. The slip extension is plotted as a function of longitudinal bar strain as measured by the strain gauge

just above the interface. Figure C.120 displays results for the columns of Test Series I. Results for the Test Series II columns are shown in Figure C.121. The slip extension is noted to be largest for Column 415 in comparison with Columns 407 and 430. Similar results are shown for Columns 415, 815, and 1015. Results for Columns 815 and 1015 are markedly similar, while the measured extension for Column 415 is larger. Reconsidering the response of the Test Series I columns without Column 415 indicates quite comparable response. Therefore the slip response of the four columns (and likely five) is similar.

### **C.3.4 Moment-Rotation Response at Base**

The external vertical displacement devices were used to measure average curvature. However, vertical measurements made over the segment extending from the footing include deformation of the column segment as well as the joint region. Reducing the segment depth minimizes the contribution of the column deformation so that the majority of the measured response may be assumed to result from the joint.

Figures C.122 through C.126 shows the rotation response history of the bottom segment as a function of base moment. The shape of the curve is similar to the overall force-displacement response suggesting that the joint response has a significant influence on the overall behavior.

## **C.4 GLOBAL RESPONSE**

Global response includes joint and column behavior. Horizontal displacements were monitored at instrumented levels along the column height and the free end. Horizontal displacements were measured at instrumented levels along the column height. Profiles for all columns are shown in Figures C.127 to C.131. Horizontal displacements are measured over the entire column height. Actual displacement measurements are indicated by markers. Initial displacement cycles are not shown. Some of the measurements made at these cycles were similar to the instrument precision.

Change in the slope of the displacement profiles gives an indication of column flexure. Results for Column 407 show significant deformations over approximately  $0.08L$ . Results for Columns 415 and 430 indicate this length increases to  $0.25L$ . Similar results are seen for Columns 815 and 1015 where the length is approximately  $0.25L$  to  $0.3L$ .

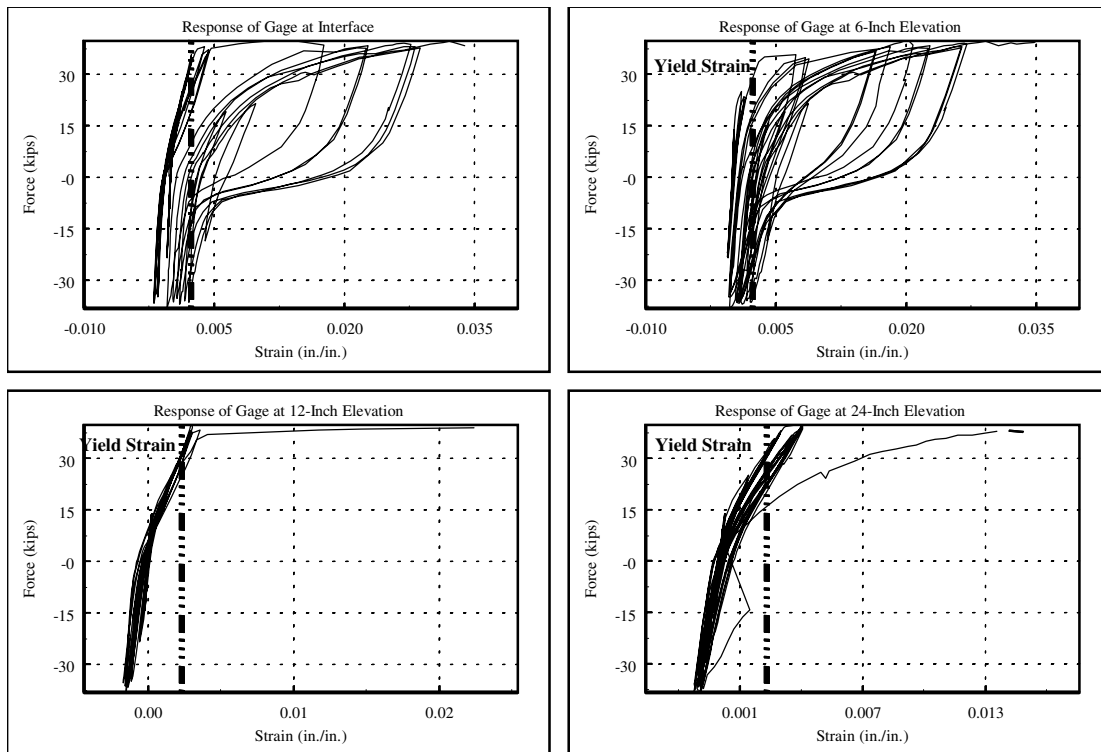


**Figure C.1: Column 407 Cyclic Response of South Longitudinal Strain Gauges**

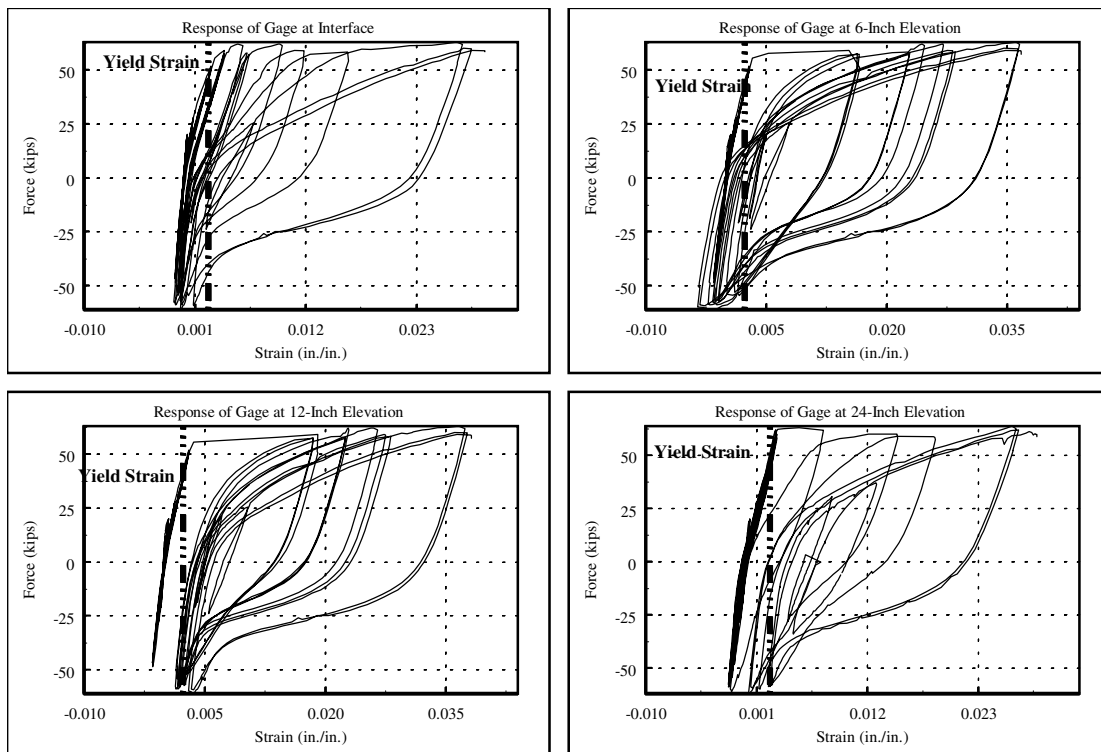


**Figure C.18: Column 415 Cyclic Response of South Longitudinal Strain Gauges**

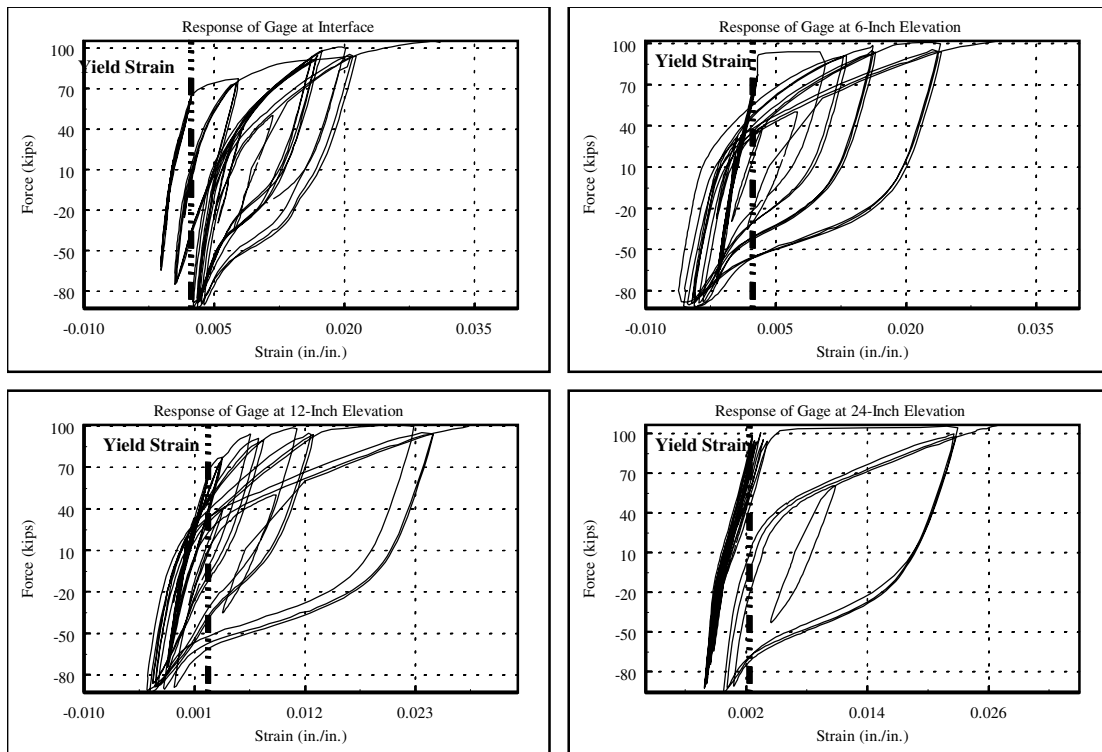


**Figure C.19: Column 430 Cyclic Response of South Longitudinal Strain Gauges**

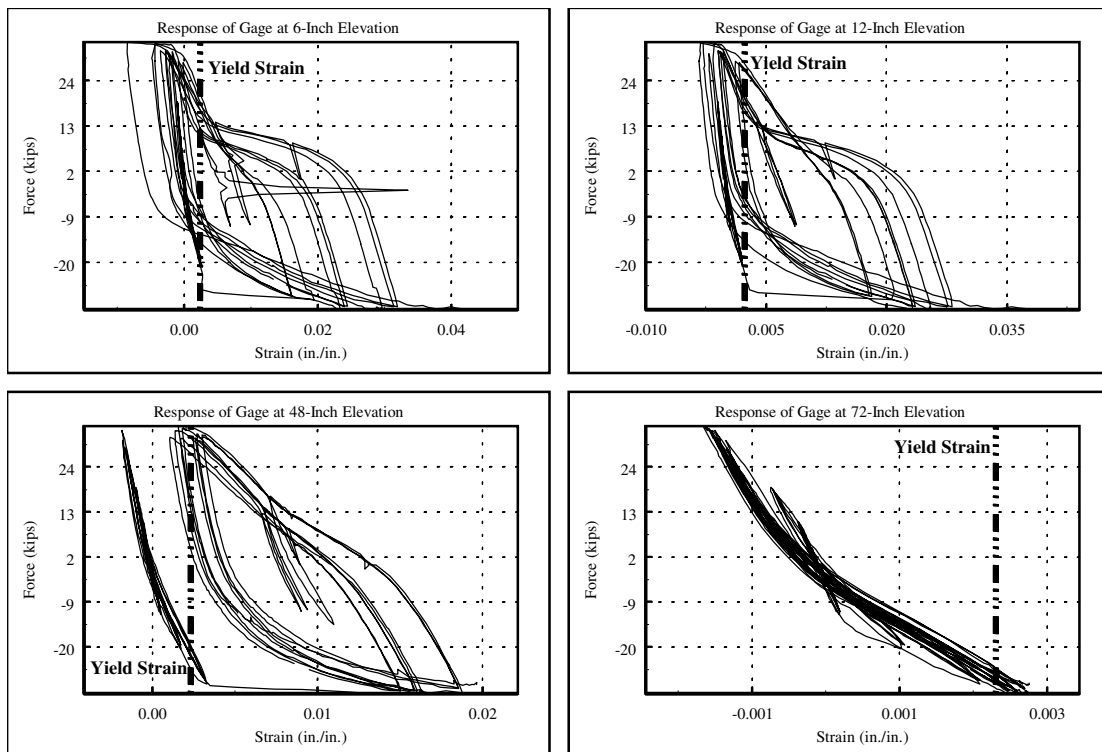


**Figure C.20: Column 815 Cyclic Response of North Longitudinal Strain Gauges**

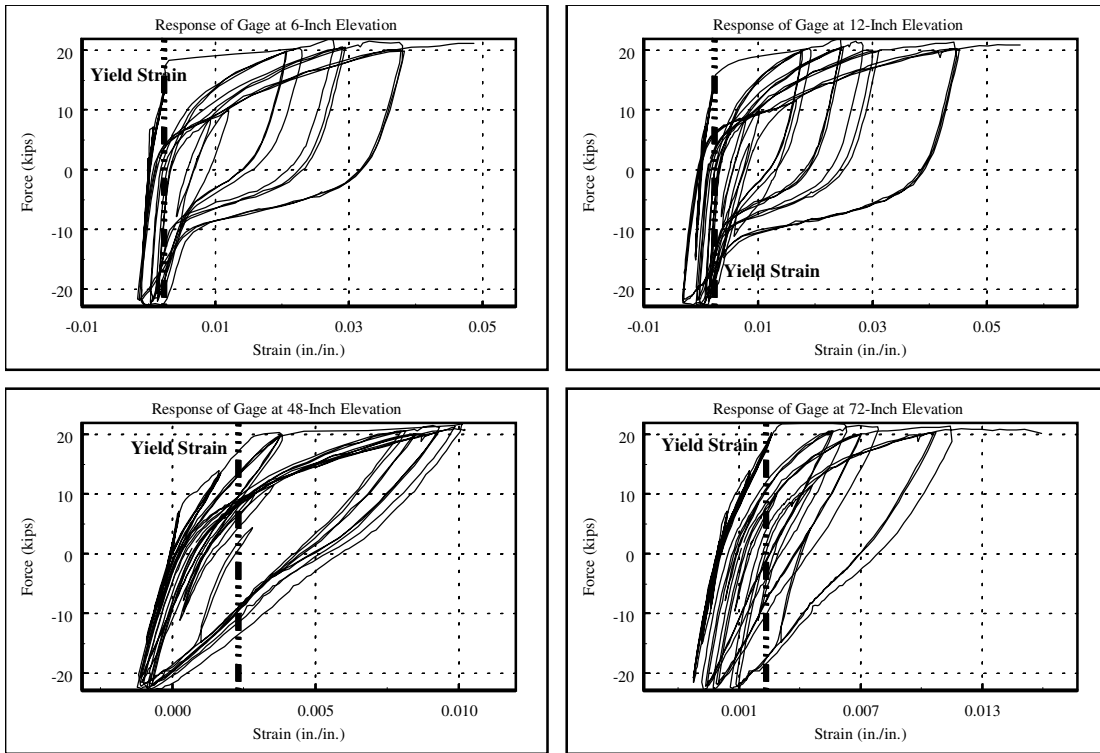


Figure C.21: Column 1015 Cyclic Response of South Longitudinal Strain Gauges

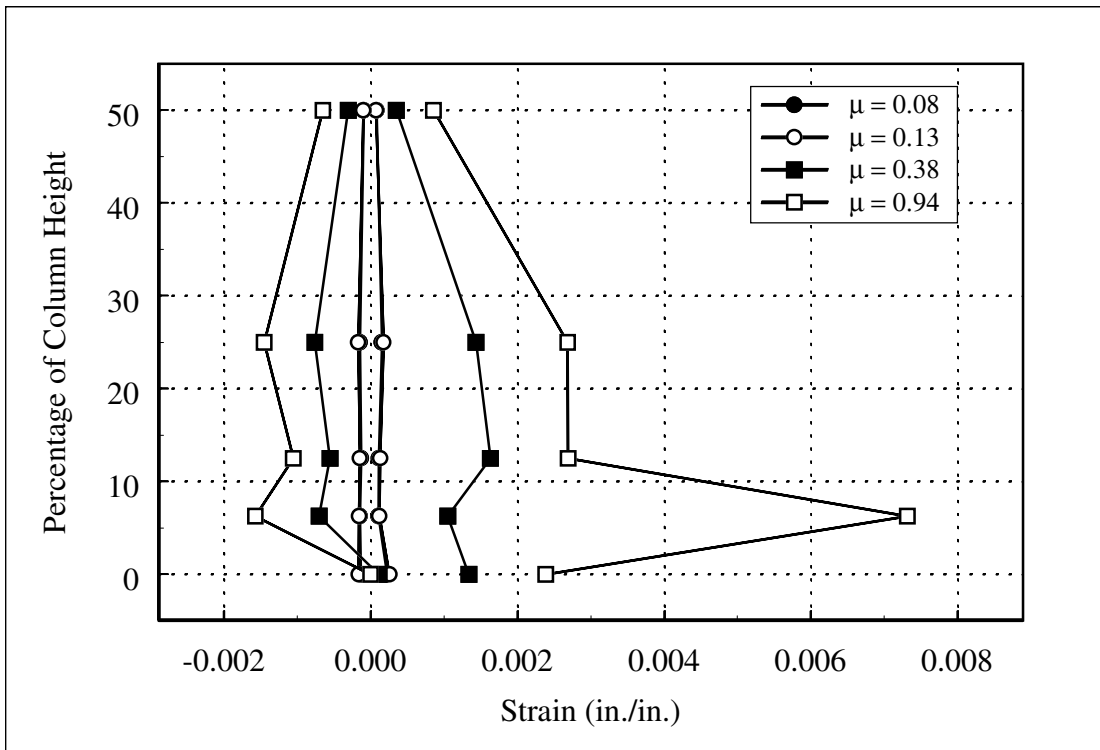
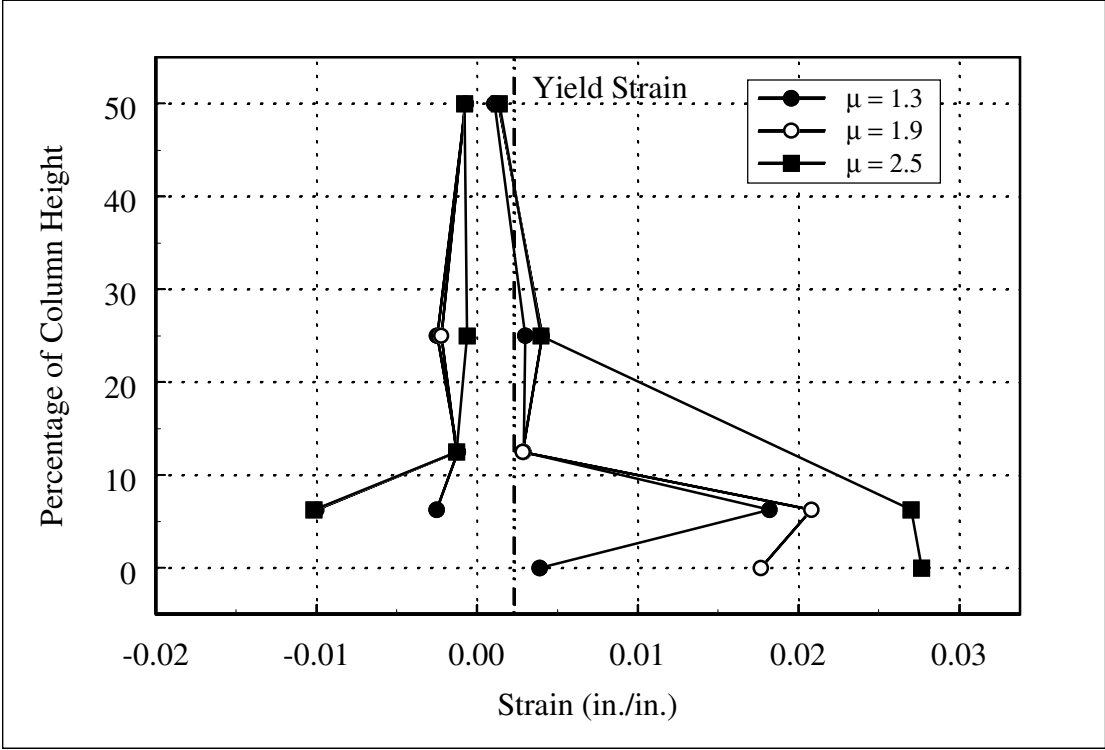
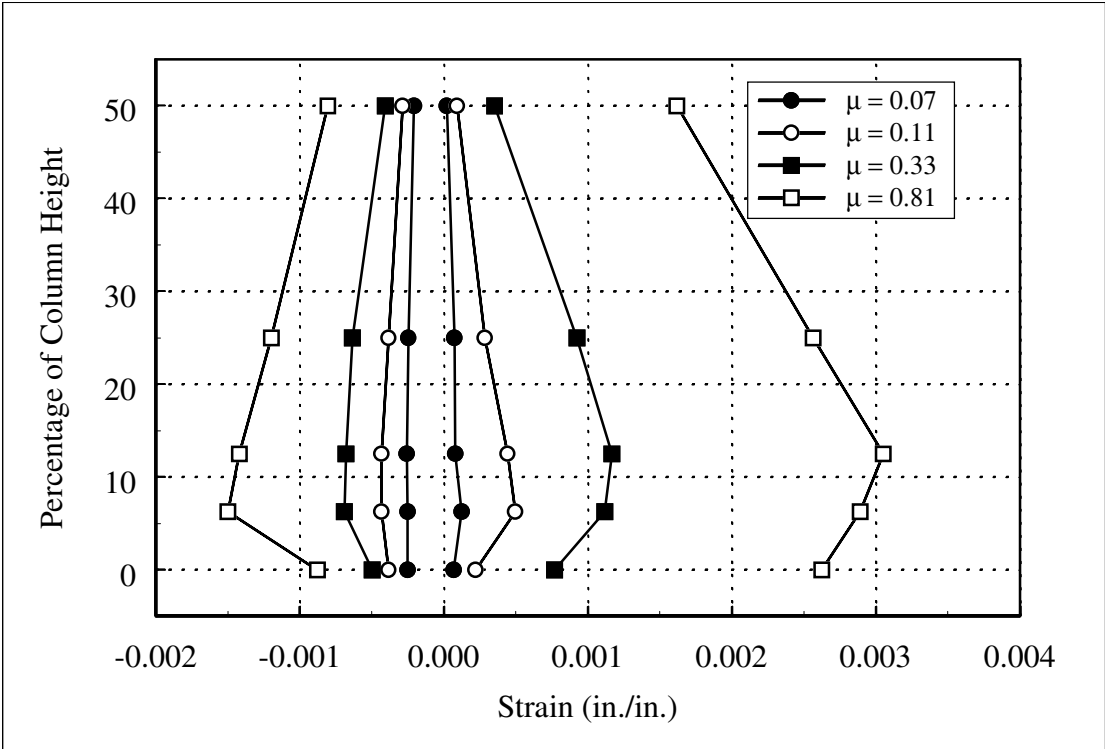


Figure C.22: Column 407 Longitudinal Strain Profile (Initial Cycles): North and South Gauges



**Figure C.23: Column 407 Longitudinal Strain Profile (Final Cycles): North and South Gauges**



**Figure C.24: Column 415 Longitudinal Strain Profile (Initial Cycles): North and South**

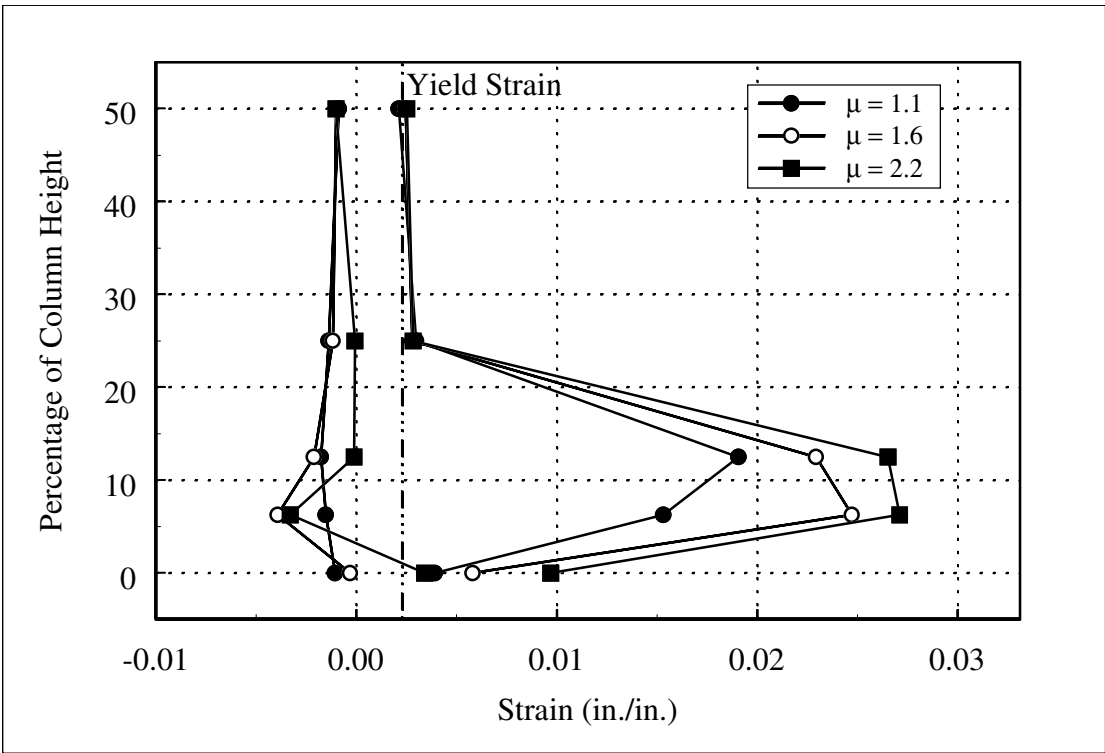


Figure C.25: Column 415 Longitudinal Strain Profile (Final Cycles): North and South Gauges

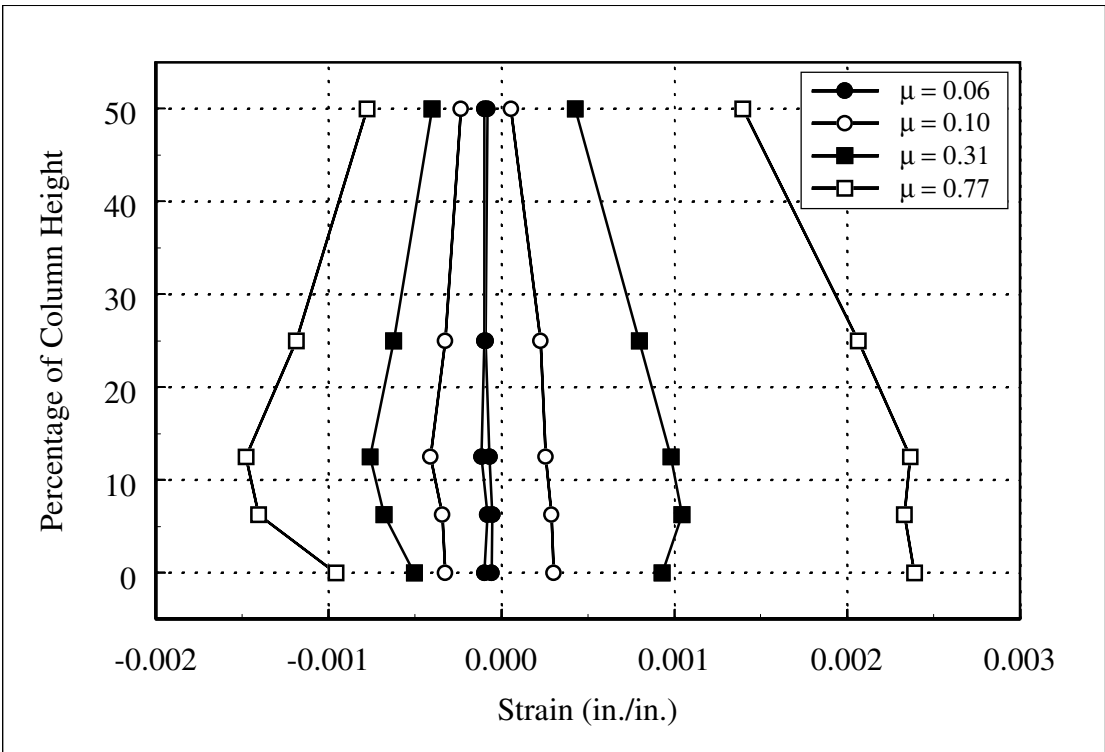


Figure C.26: Column 430 Longitudinal Strain Profile (Initial Cycles): North and South

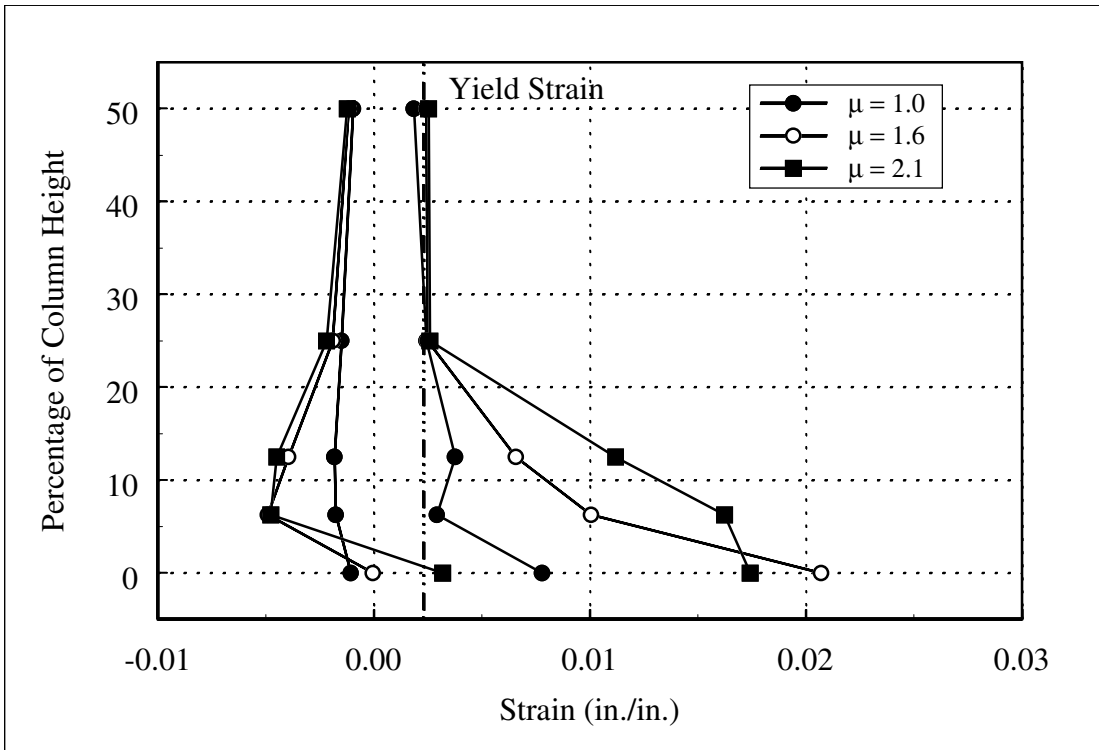


Figure C.27: Column 430 Longitudinal Strain Profile (Final Cycles): North and South Gauges

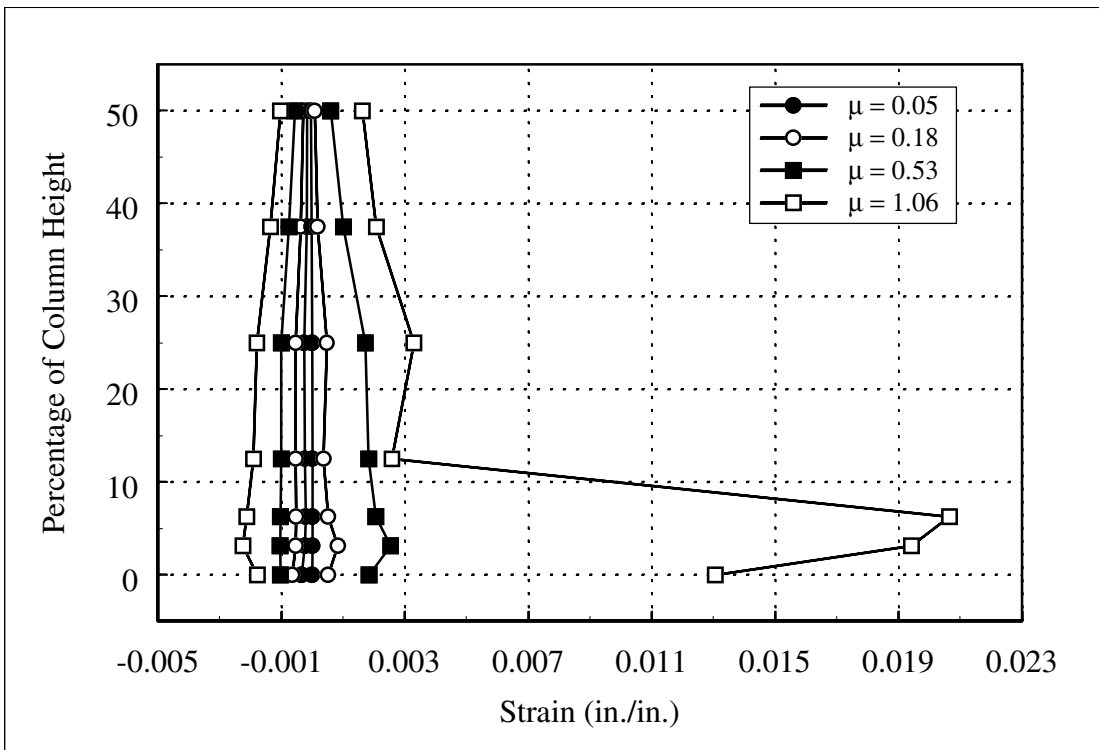


Figure C.28: Column 815 Longitudinal Strain Profile (Initial Cycles): North and South

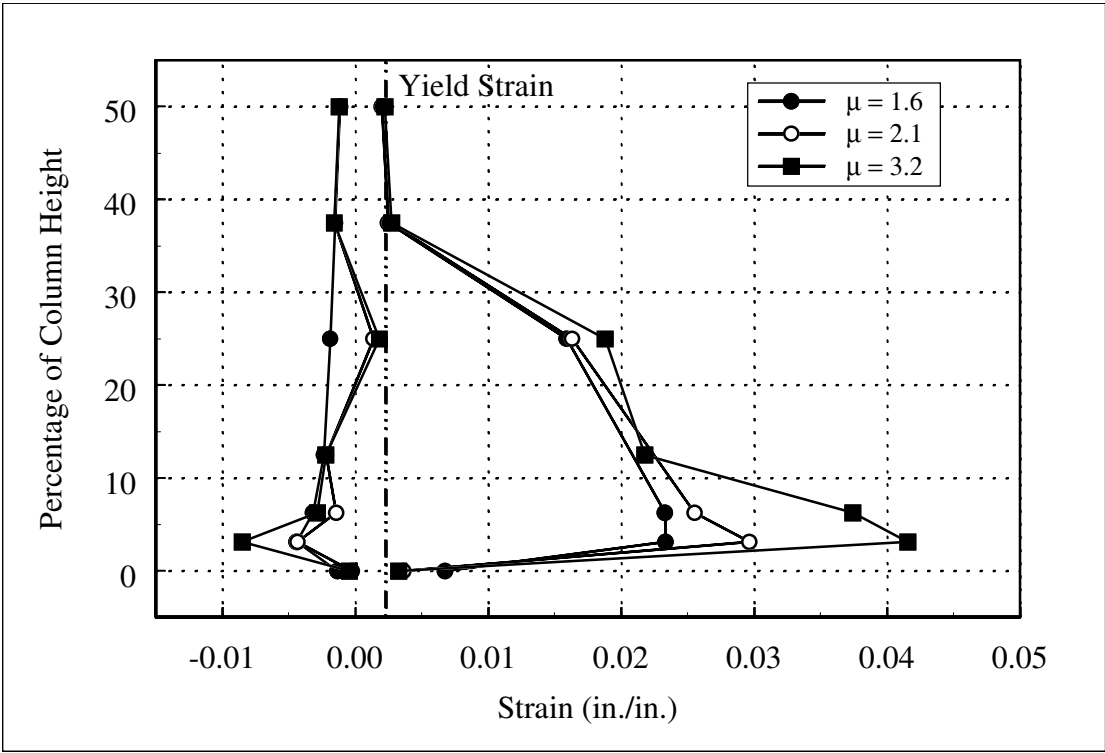


Figure C.29: Column 815 Longitudinal Strain Profile (Final Cycles): North and South Gauges

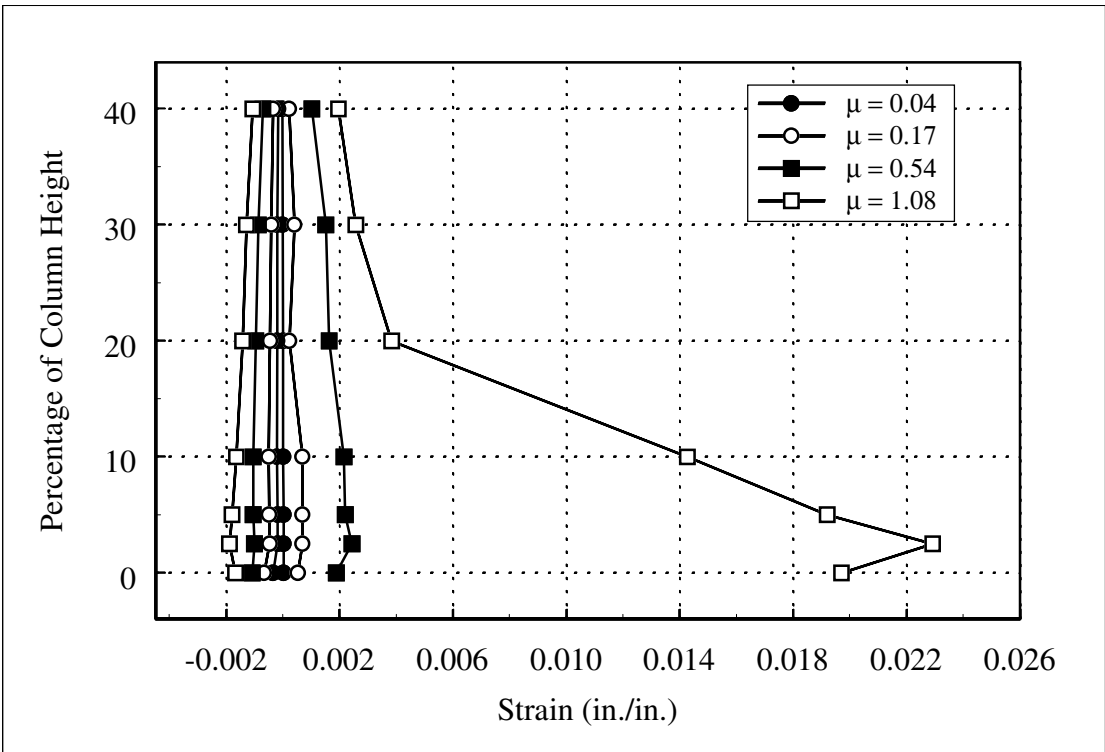


Figure C.30: Column 1015 Longitudinal Strain Profile (Initial Cycles): North and South

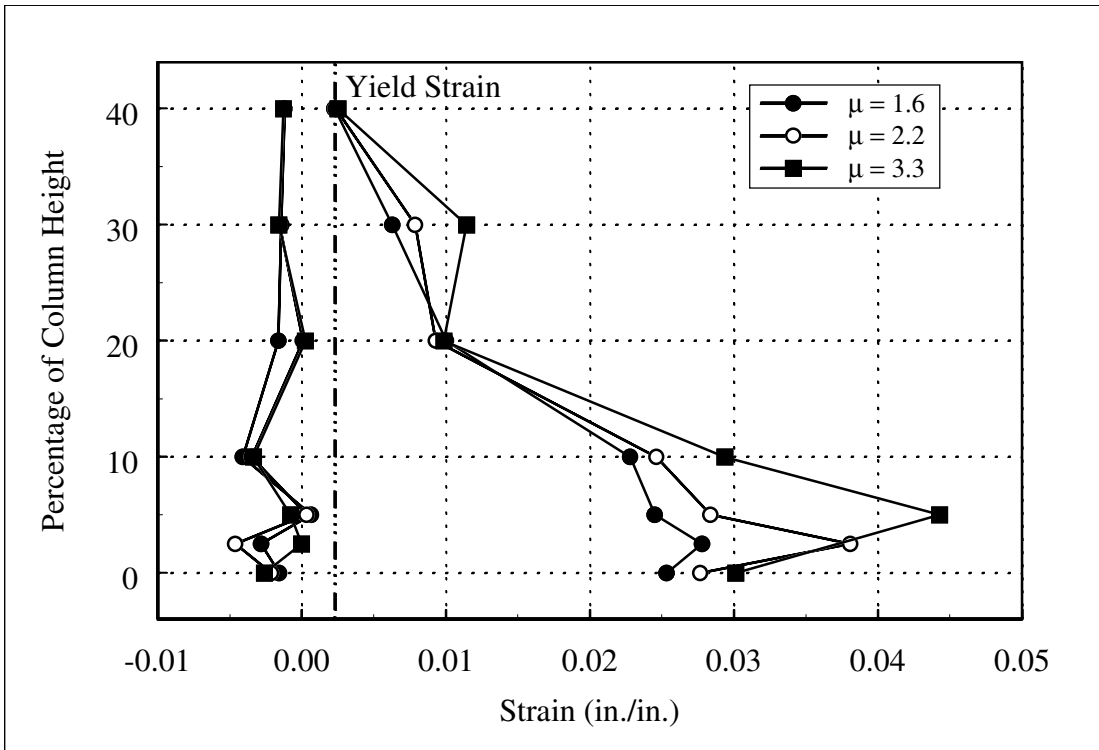


Figure C.31: Column 1015 Longitudinal Strain Profile (Final Cycles): North and South Gauges

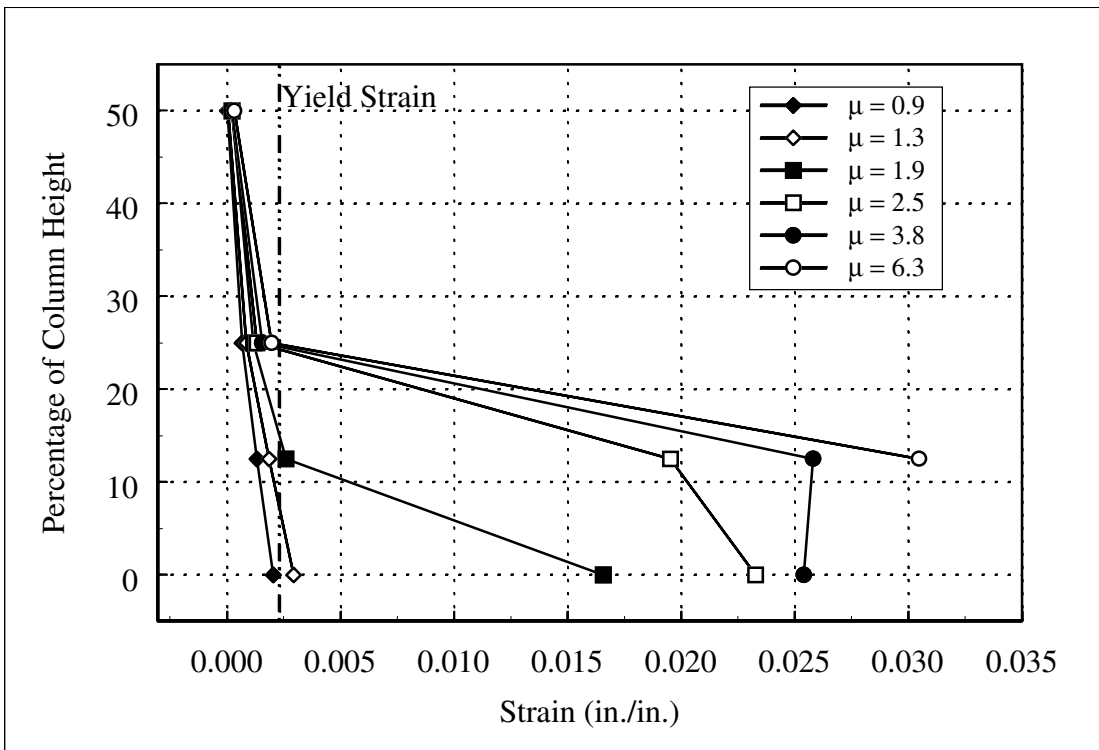


Figure C.32: Column 407 Profile of West Longitudinal Strain Gauge Readings

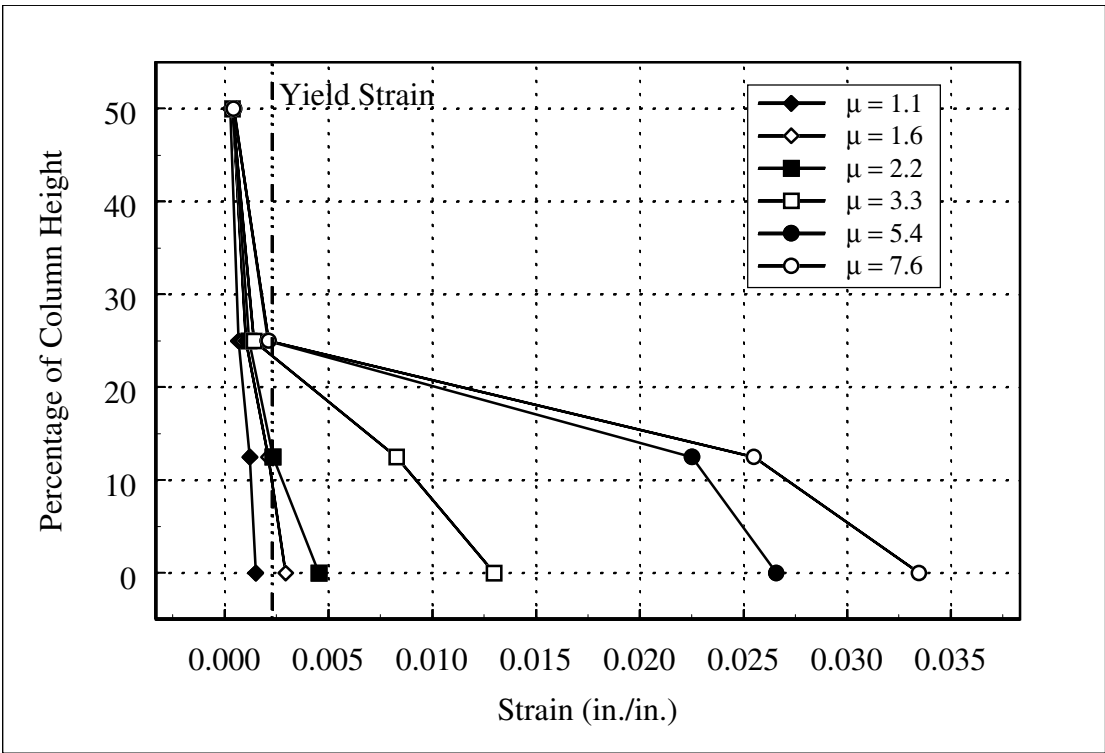


Figure C.33: Column 415 Profile of West Longitudinal Strain Gauge Readings

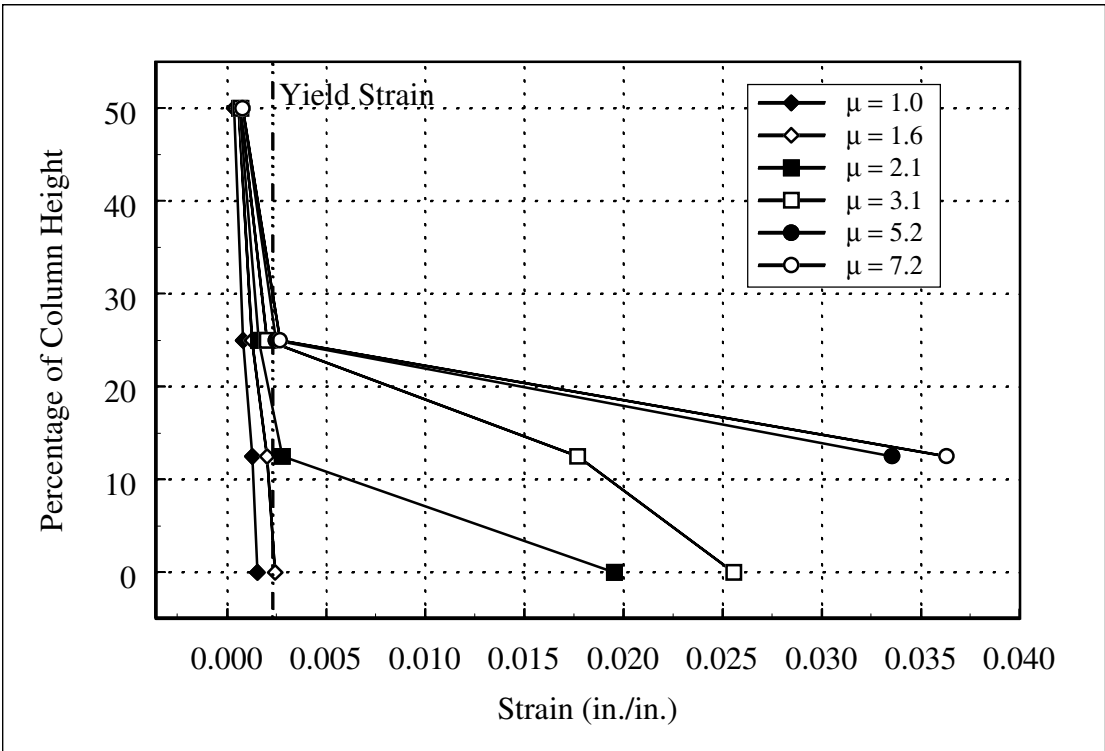


Figure C.34: Column 430 Profile of West Longitudinal Strain Gauge Readings

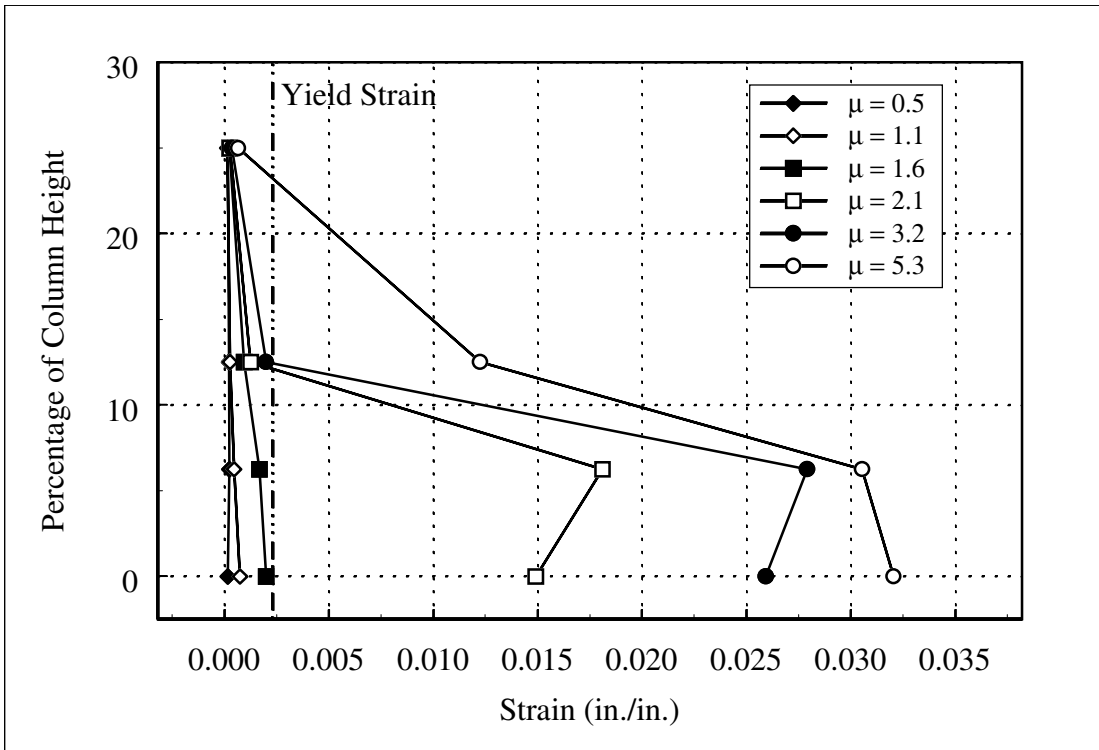


Figure C.35: Column 815 Profile of West Longitudinal Strain Gauge Readings

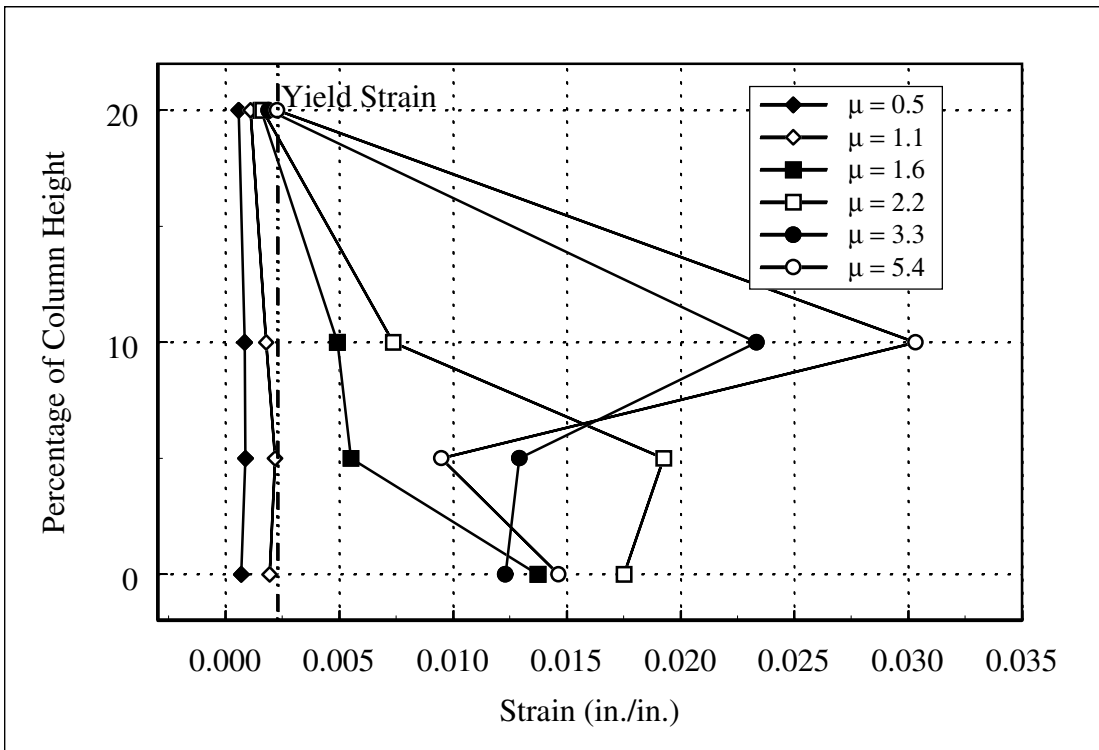
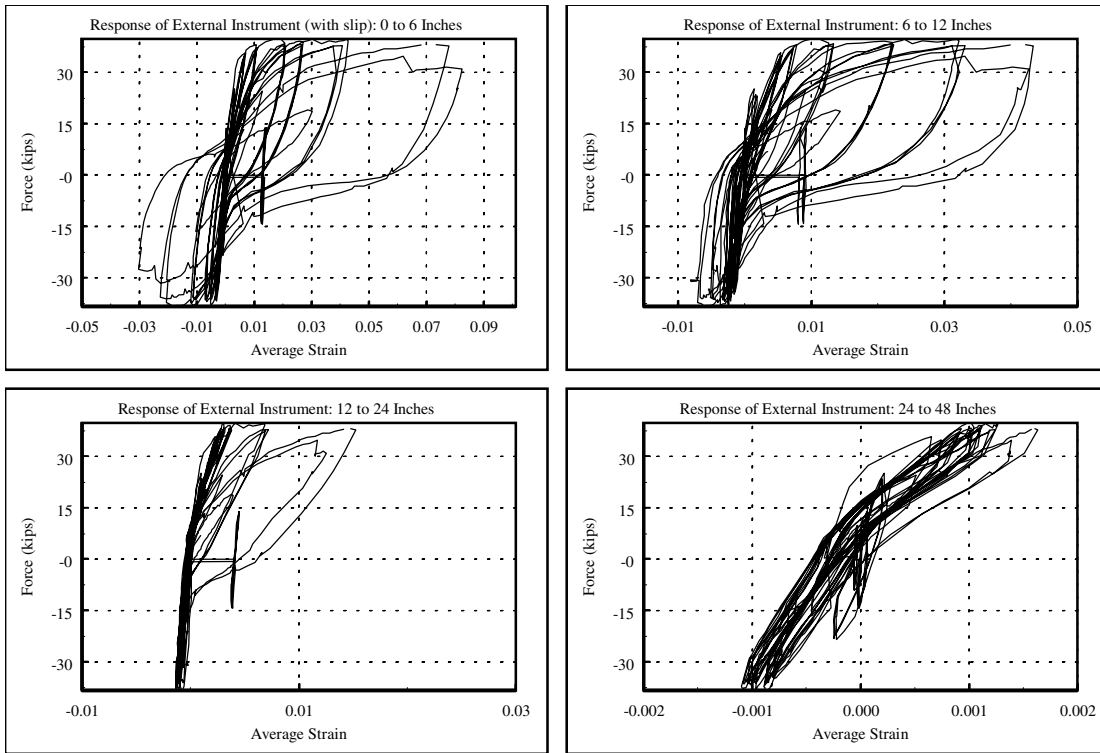
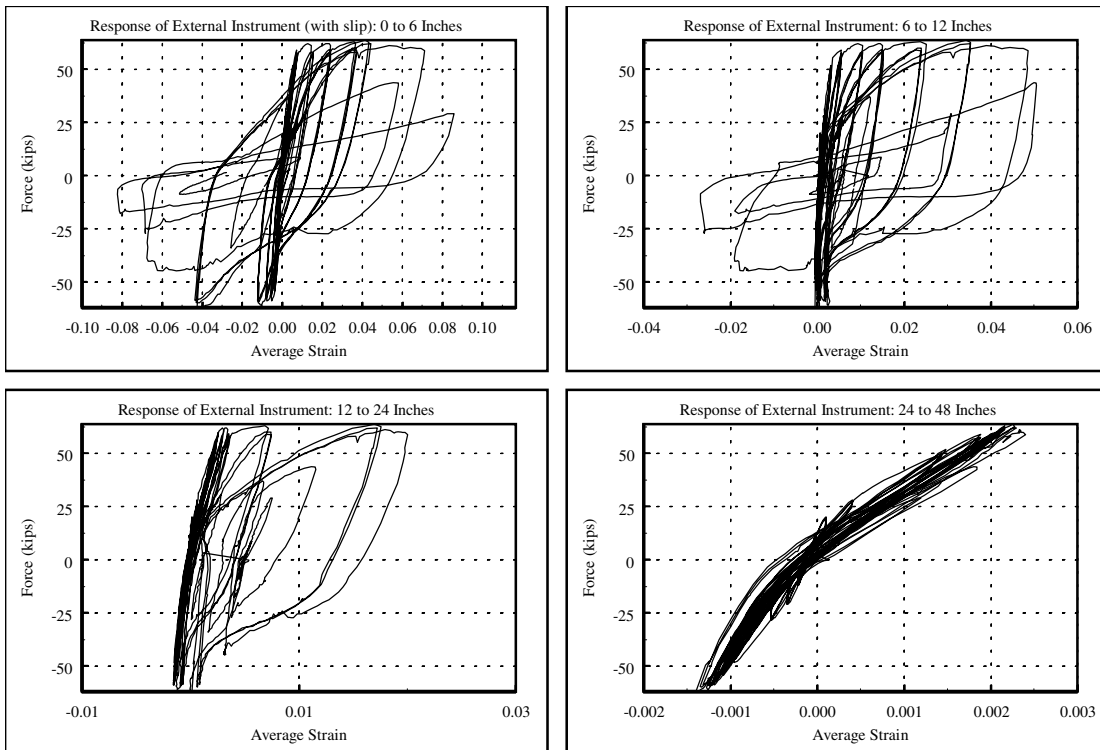


Figure C.36: 1015 Profile of West Longitudinal Strain Gauge Readings



**Figure C.37: Column 407 Cyclic Response of Average Longitudinal Strains**



**Figure C.38: Column 415 Cyclic Response of Average Longitudinal Strains**

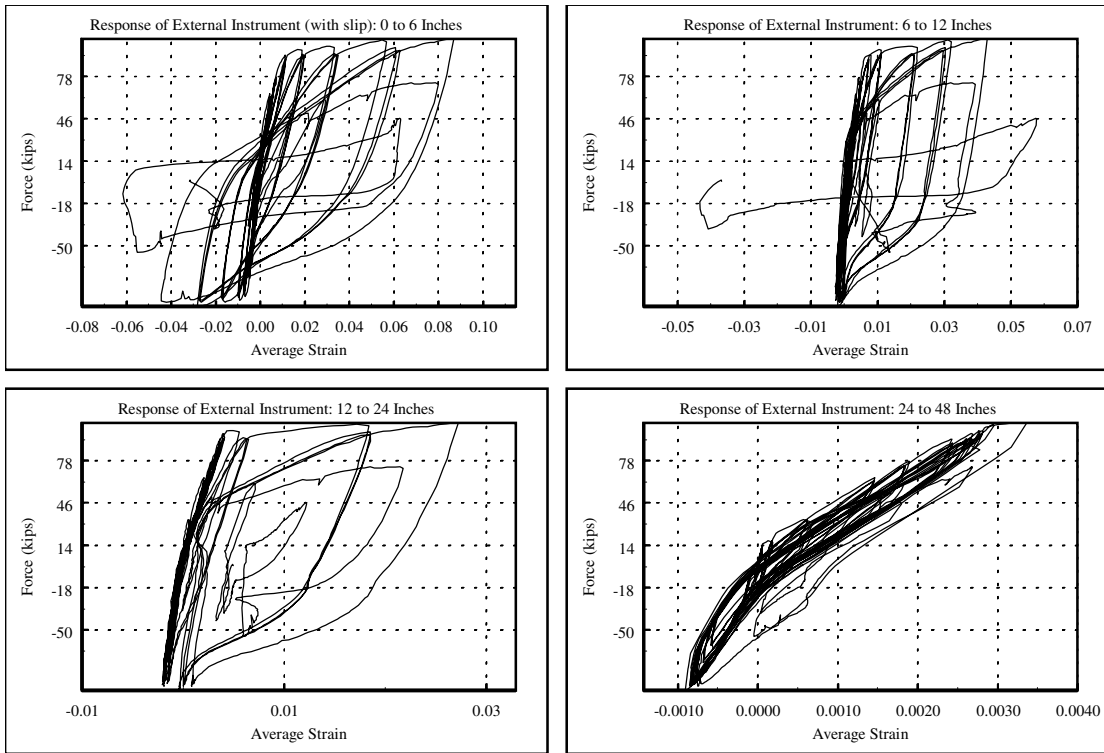


**Figure C.39: Column 430 Cyclic Response of Average Longitudinal Strains**

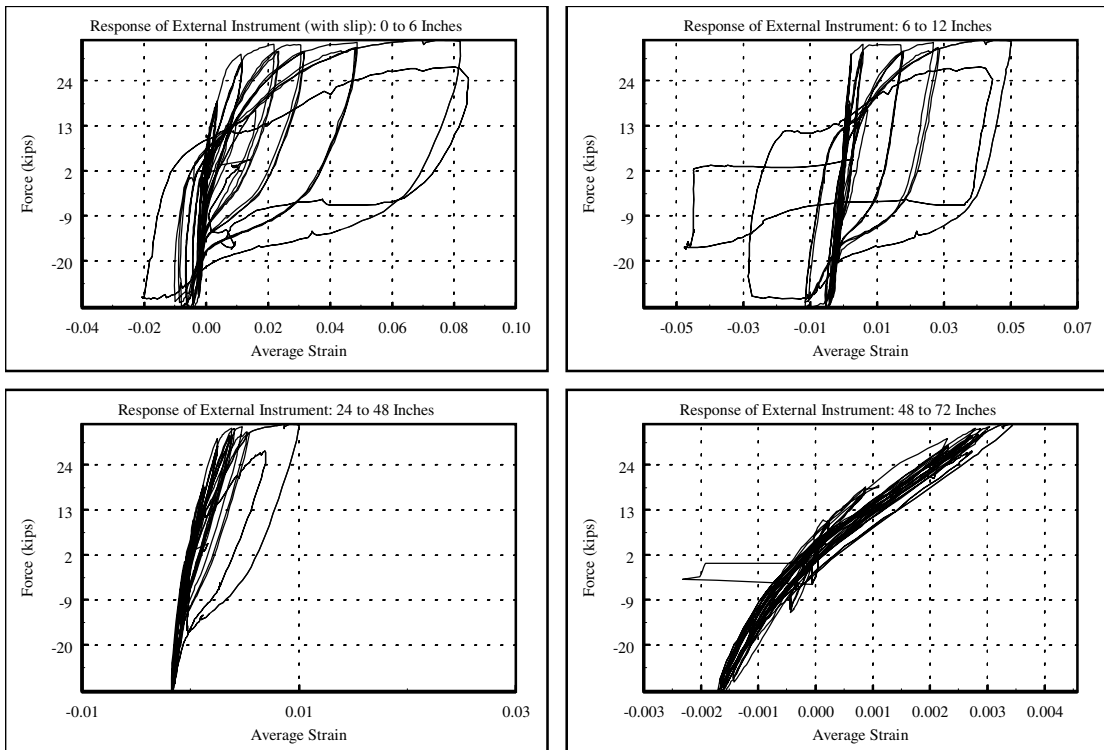


**Figure C.40: Column 815 Cyclic Response of Average Longitudinal Strains**

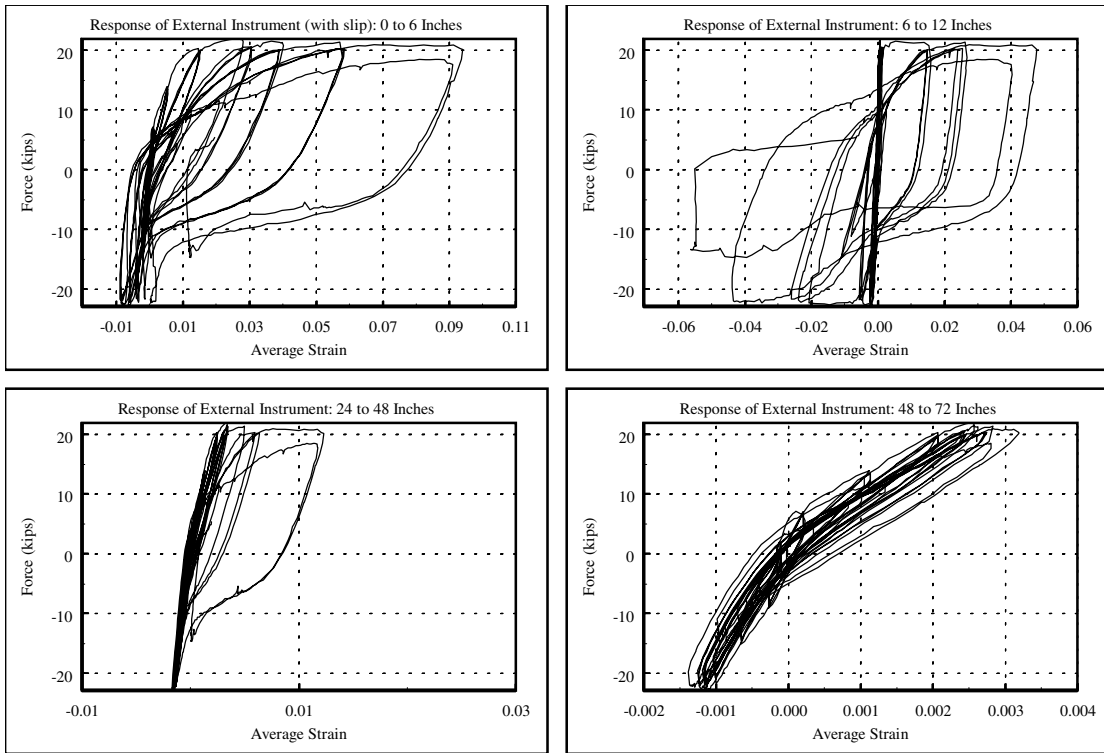


Figure C.41: Column 1015 Cyclic Response of Average Longitudinal Strains

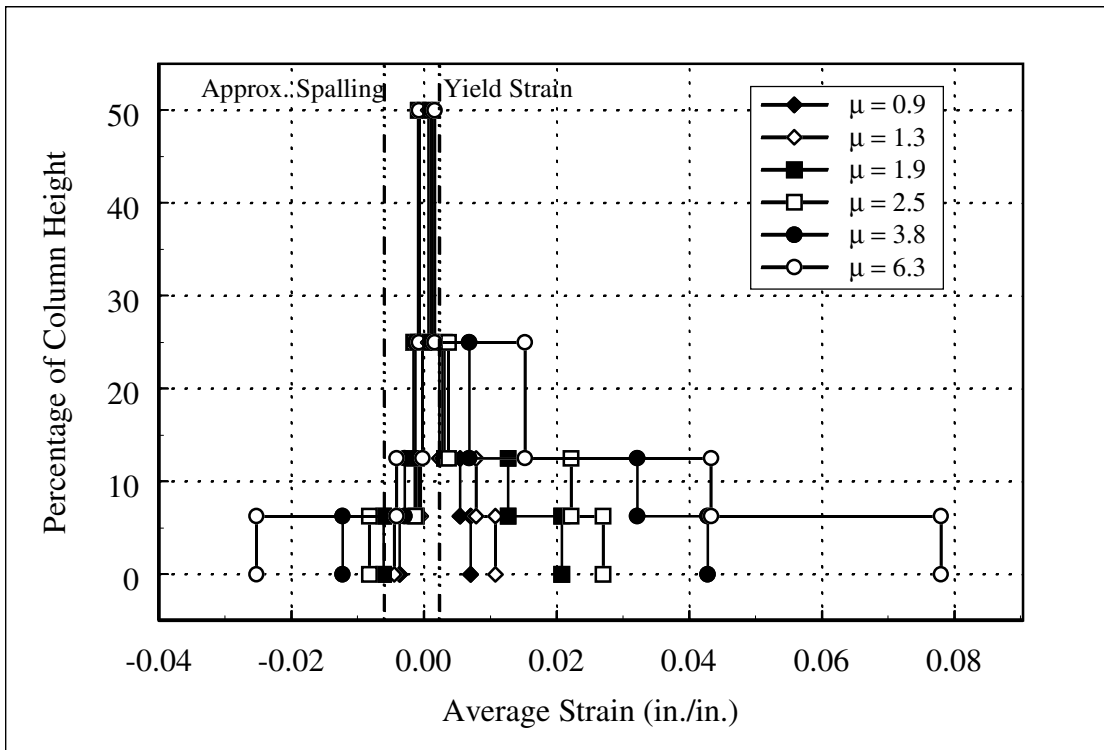


Figure C.42: Column 407 Profile of Average Strain Measurements (External Instruments)

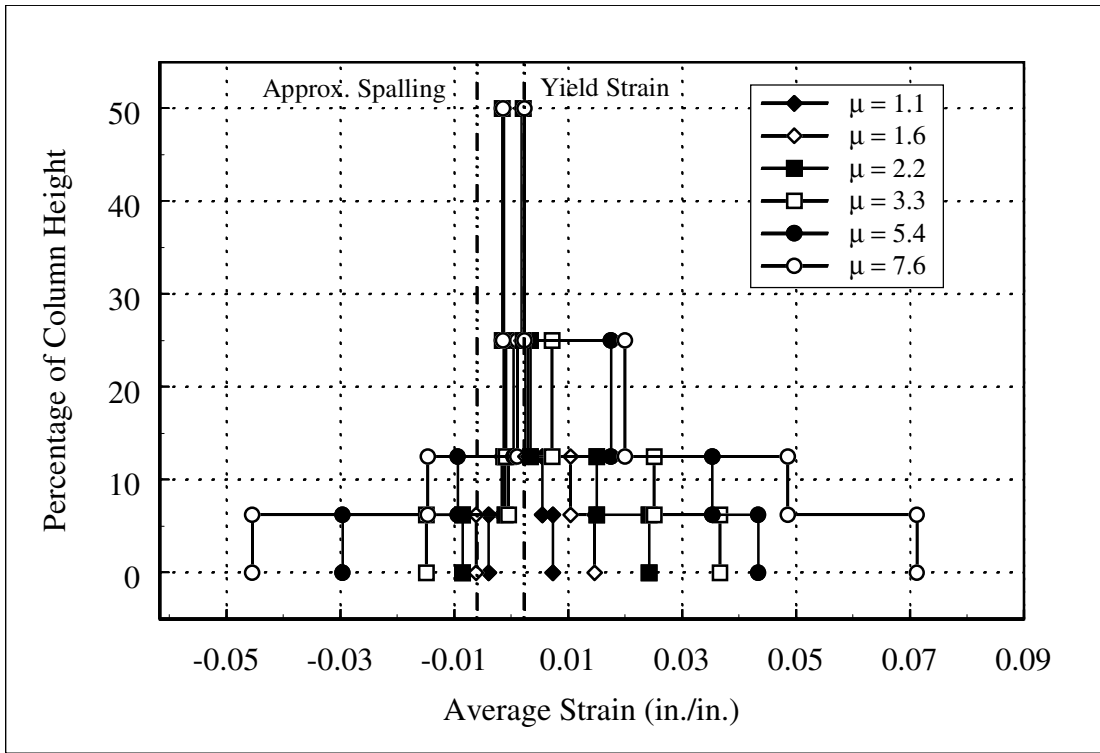


Figure C.43: Column 415 Profile of Average Strain Measurements (External Instruments)

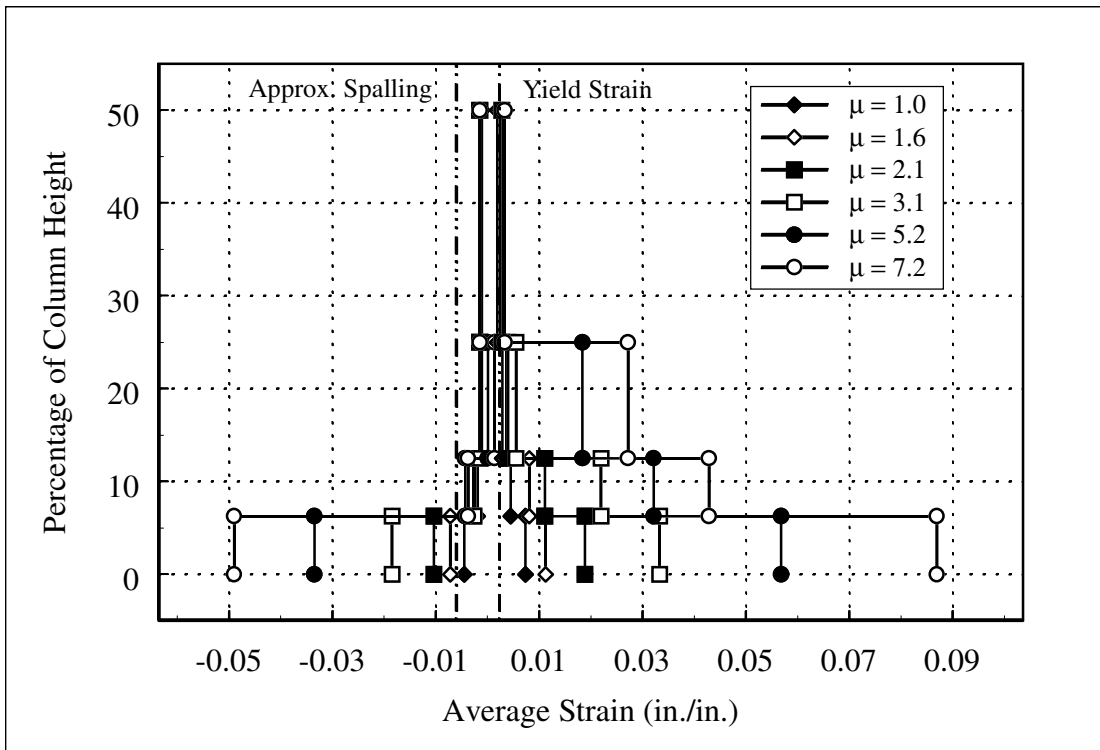


Figure C.44: Column 430 Profile of Average Strain Measurements (External Instruments)

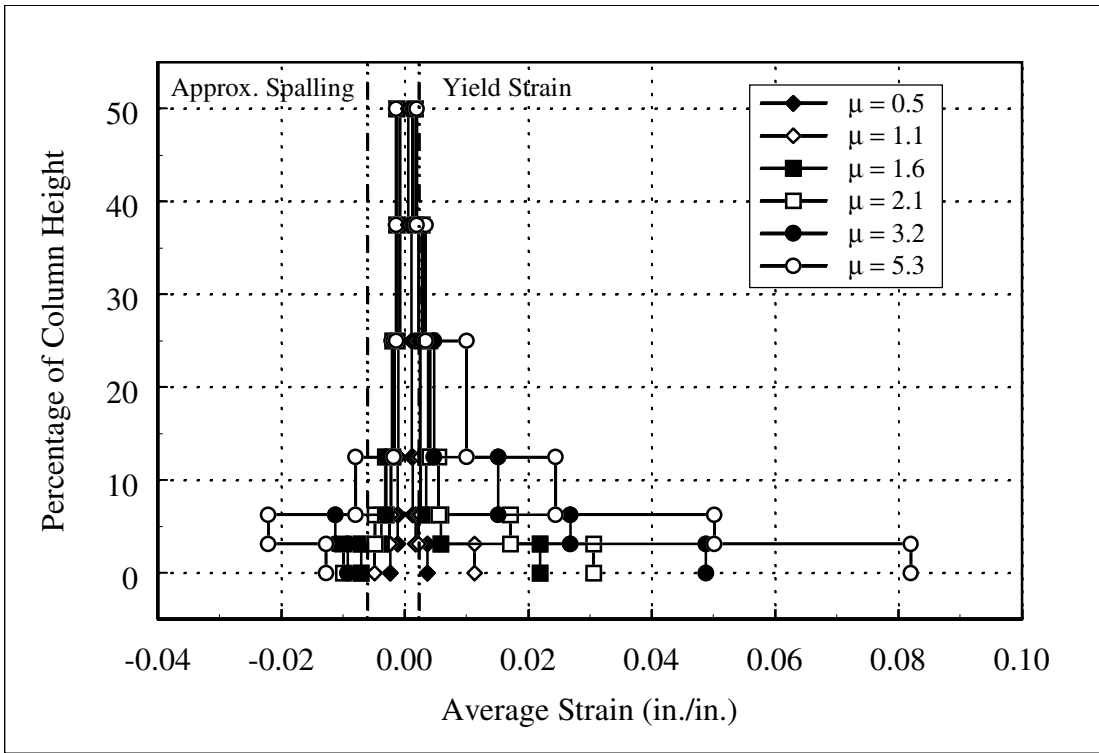


Figure C.45: Column 815 Profile of Average Strain Measurements (External Instruments)

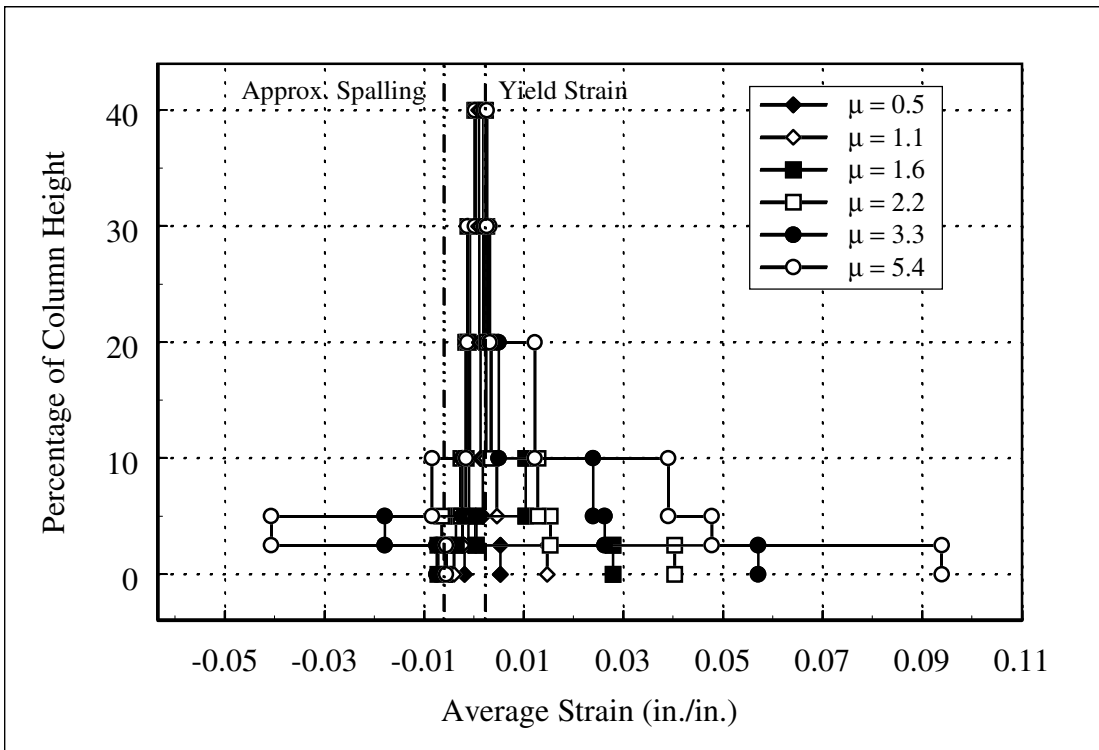


Figure C.46: Column 1015 Profile of Average Strain Measurements (External Instruments)

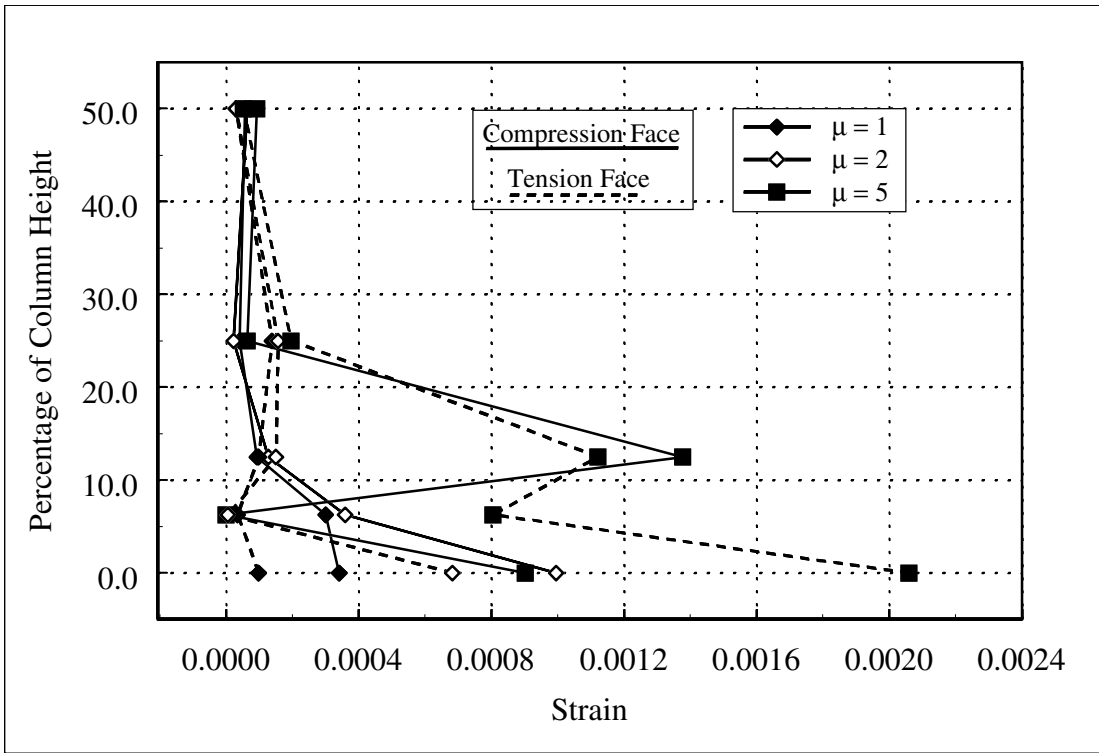


Figure C.47: Column 415 Spiral-Strain Profile: North and South Gauges

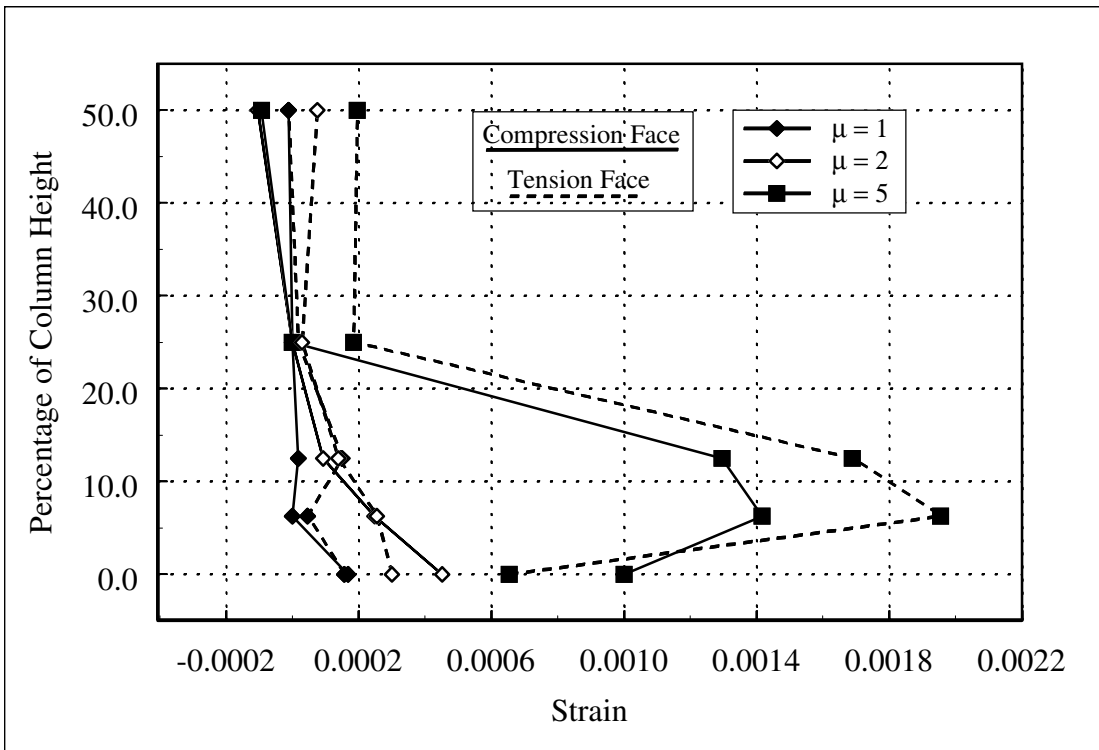


Figure C.48: Column 430 Spiral-Strain Profile: North and South Gauges

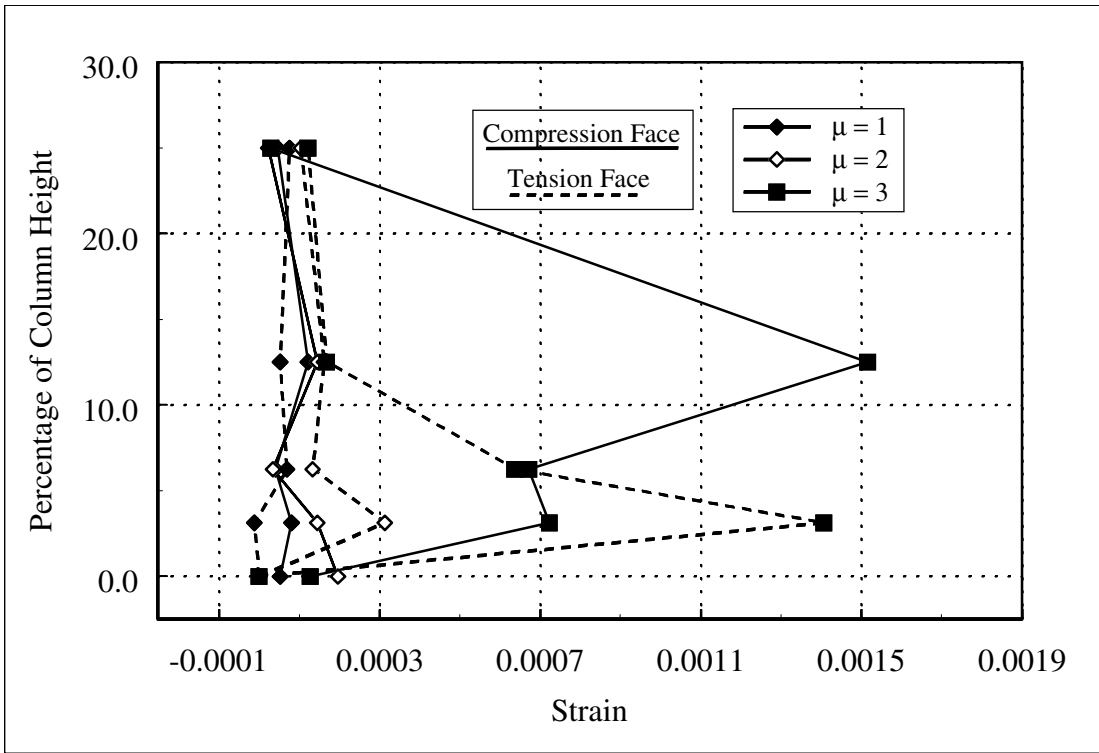


Figure C.49: Column 815 Spiral-Strain Profile: North and South Gauges

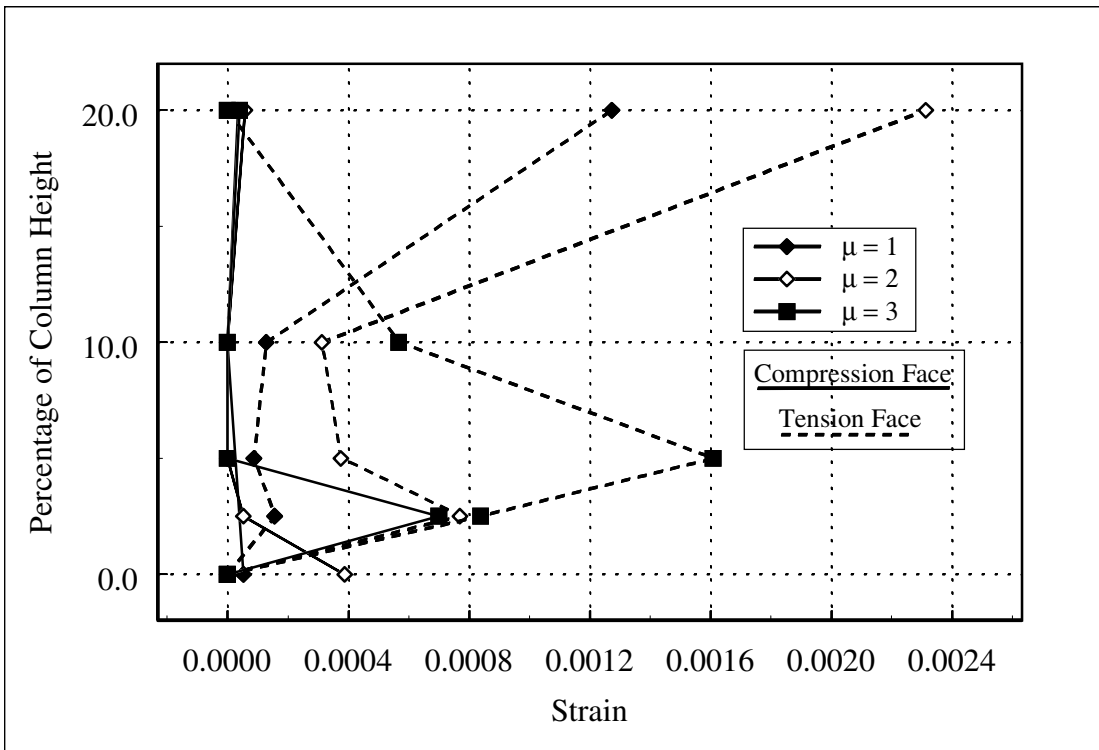


Figure C.50: Column 1015 Spiral-Strain Profile: North and South Gauges

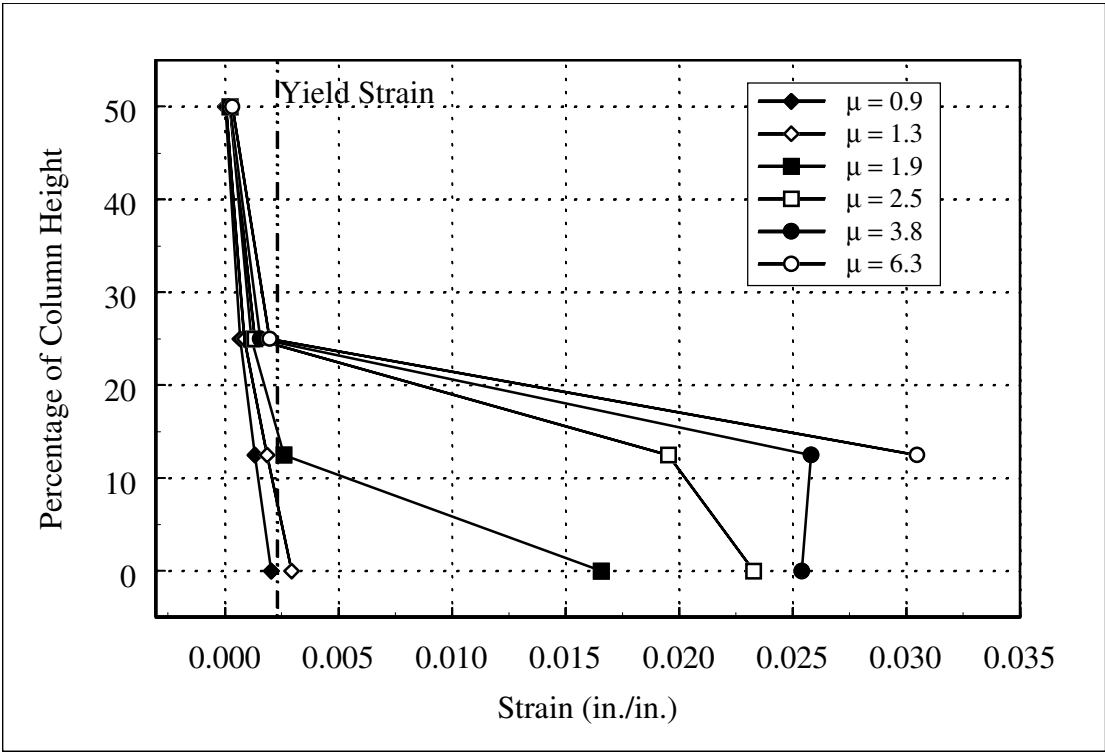


Figure C.51: Column 407 Spiral-Strain Profile: West Gauges

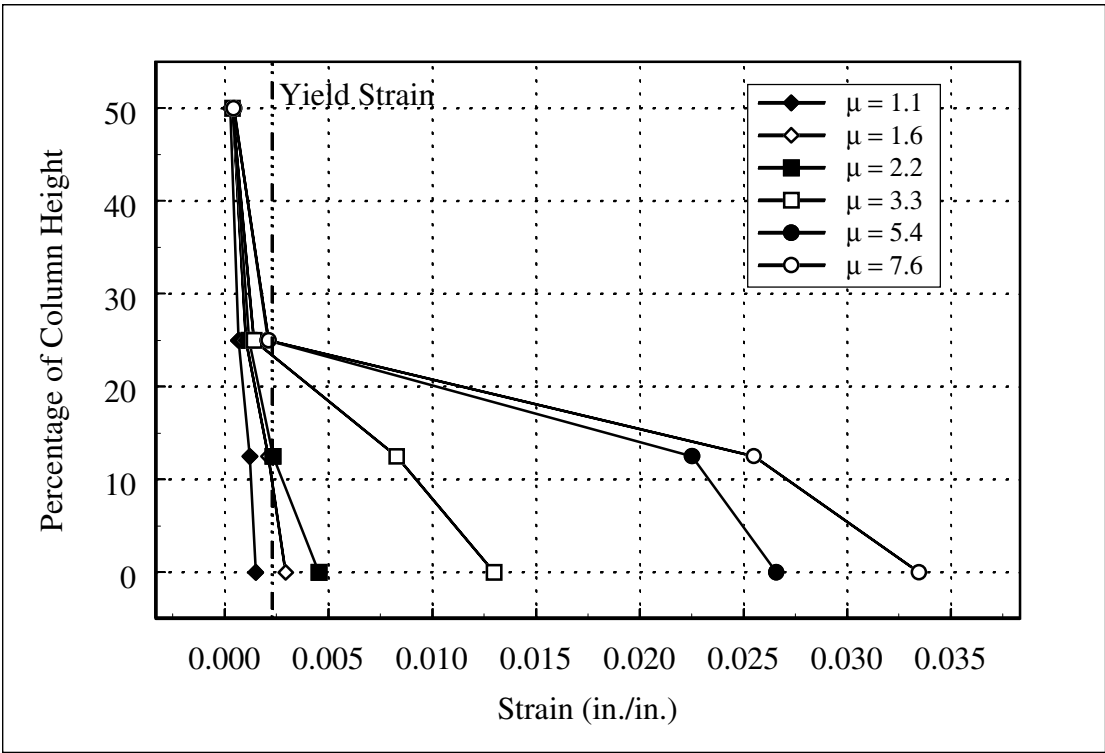


Figure C.52: Column 415 Spiral-Strain Profile: West Gauges

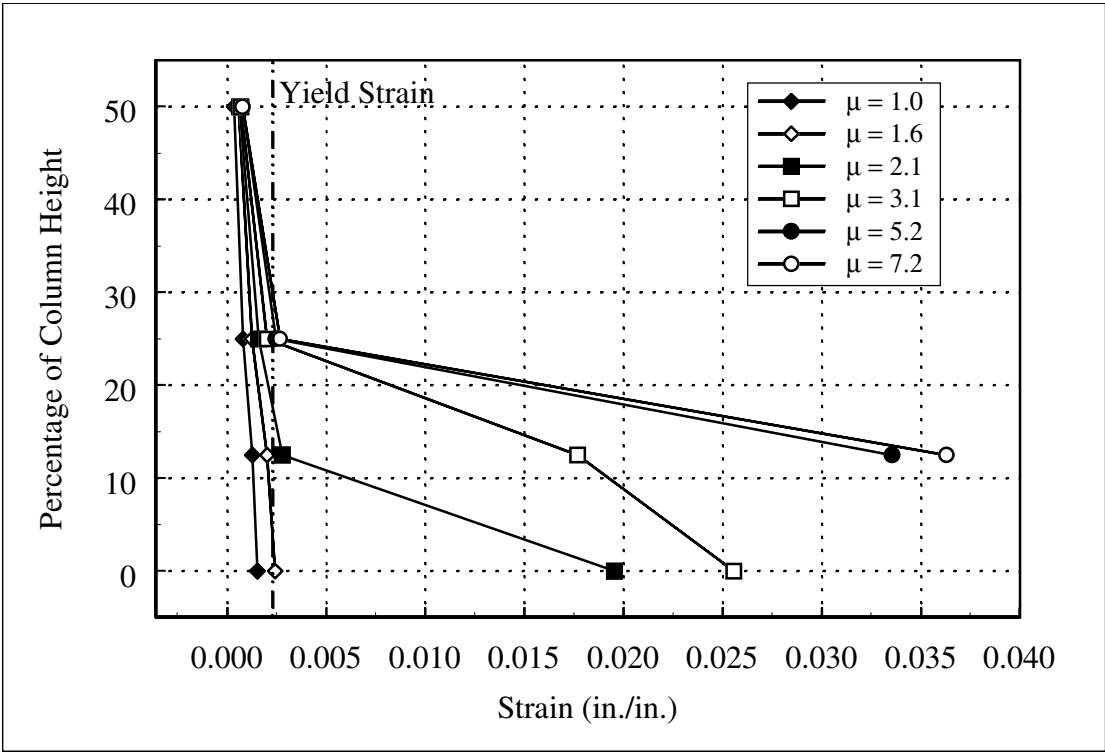


Figure C.53: Column 430 Spiral-Strain Profile: West Gauges

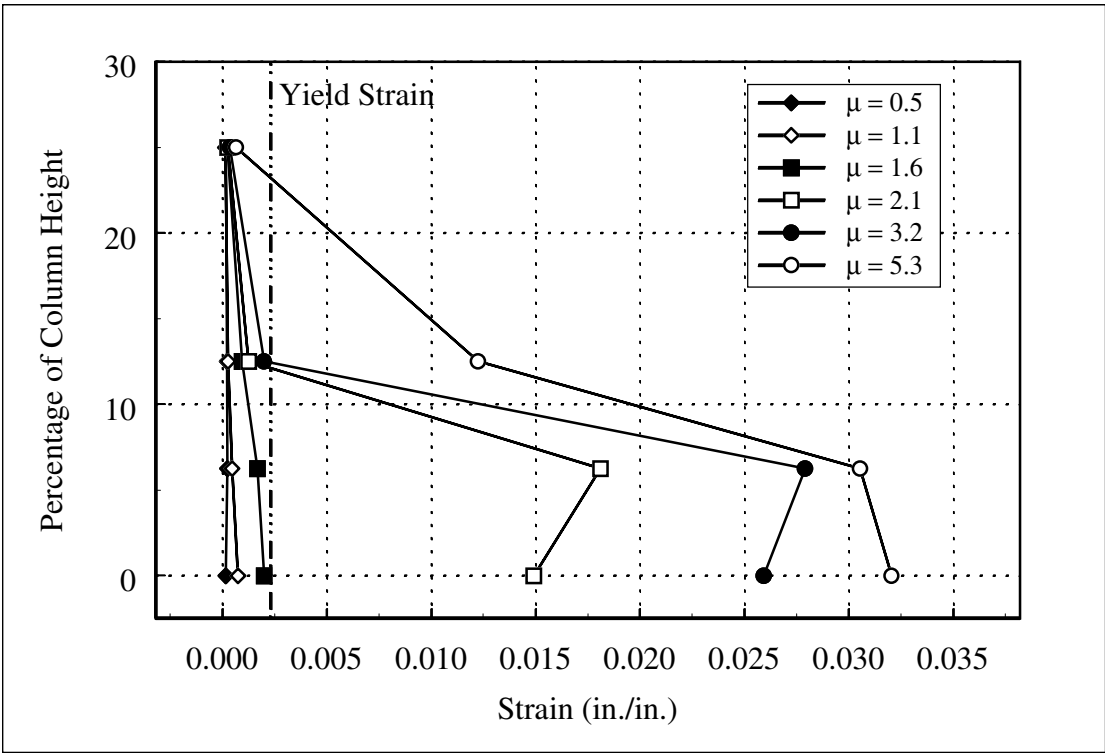


Figure C.54: Column 815 Spiral-Strain Profile: West Gauges

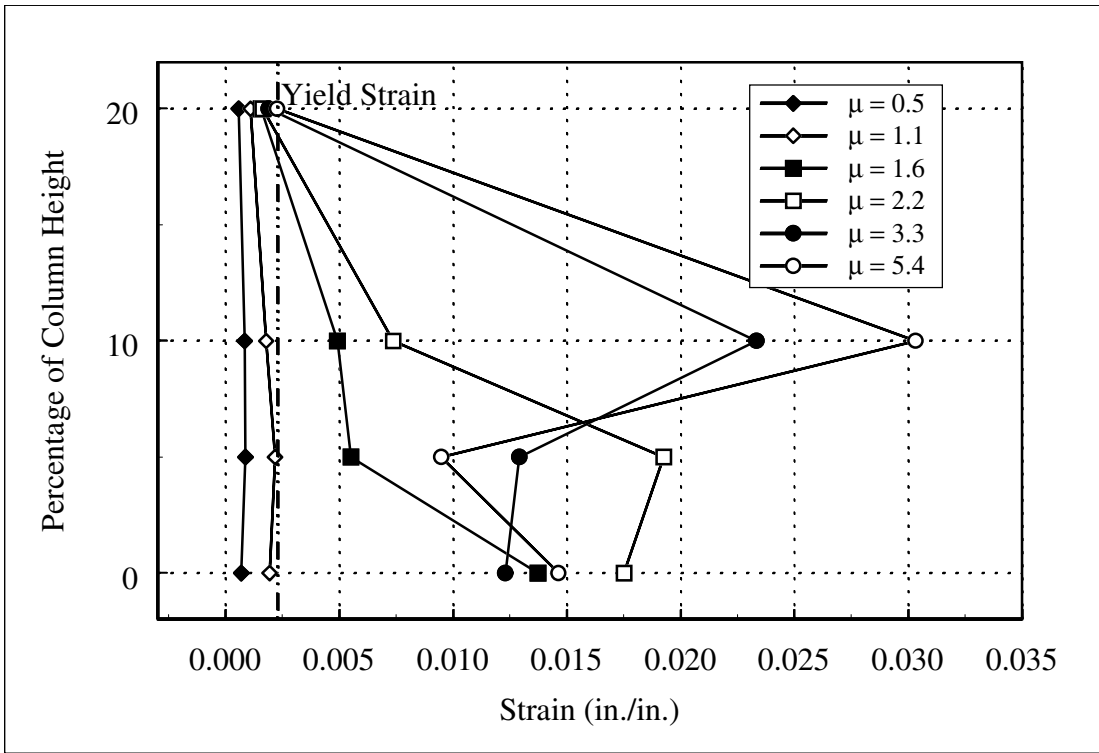


Figure C.55: Column 1015 Spiral-Strain Profile: West Gauges

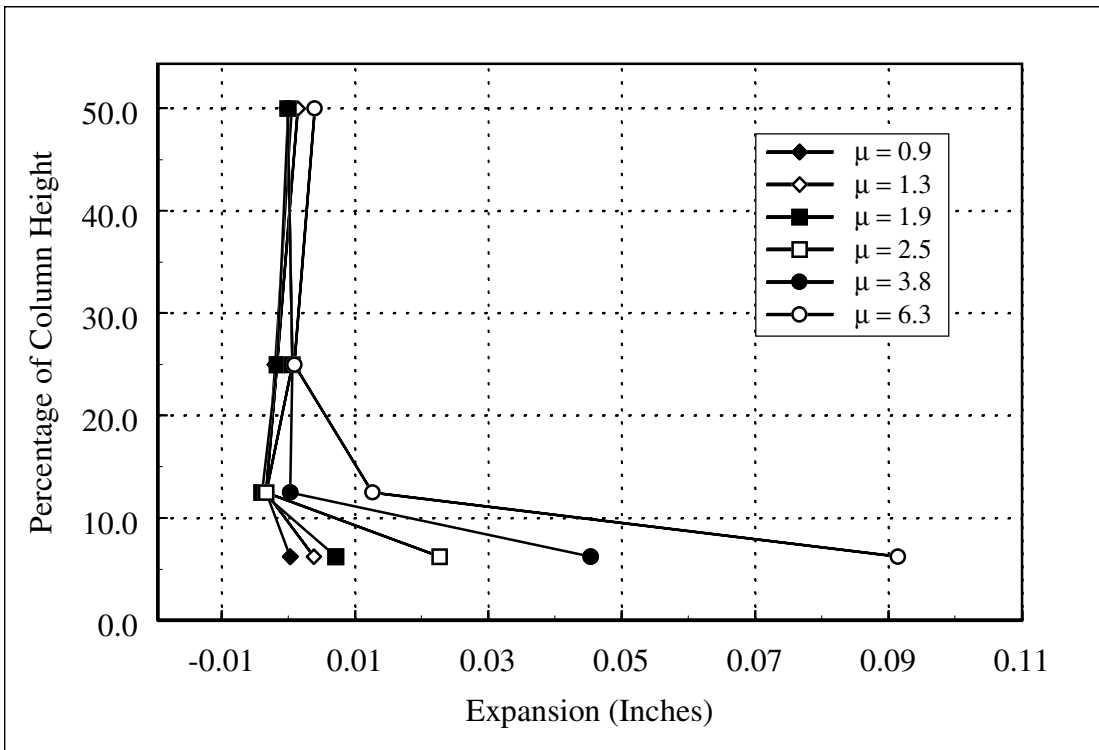
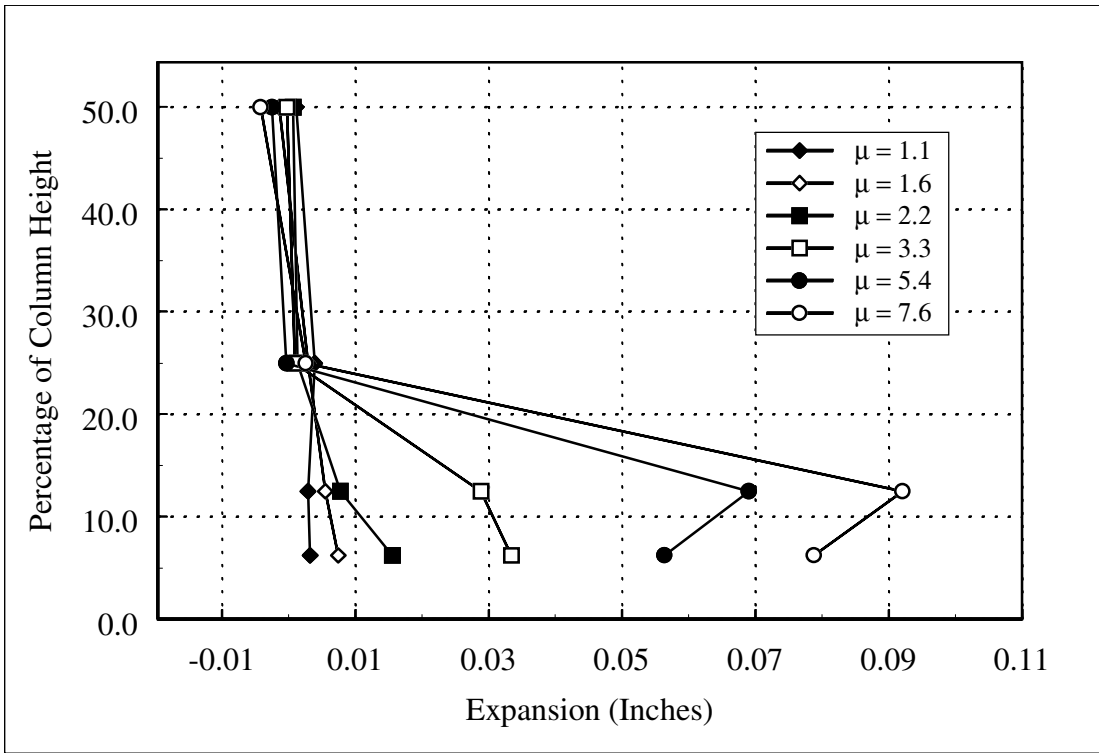
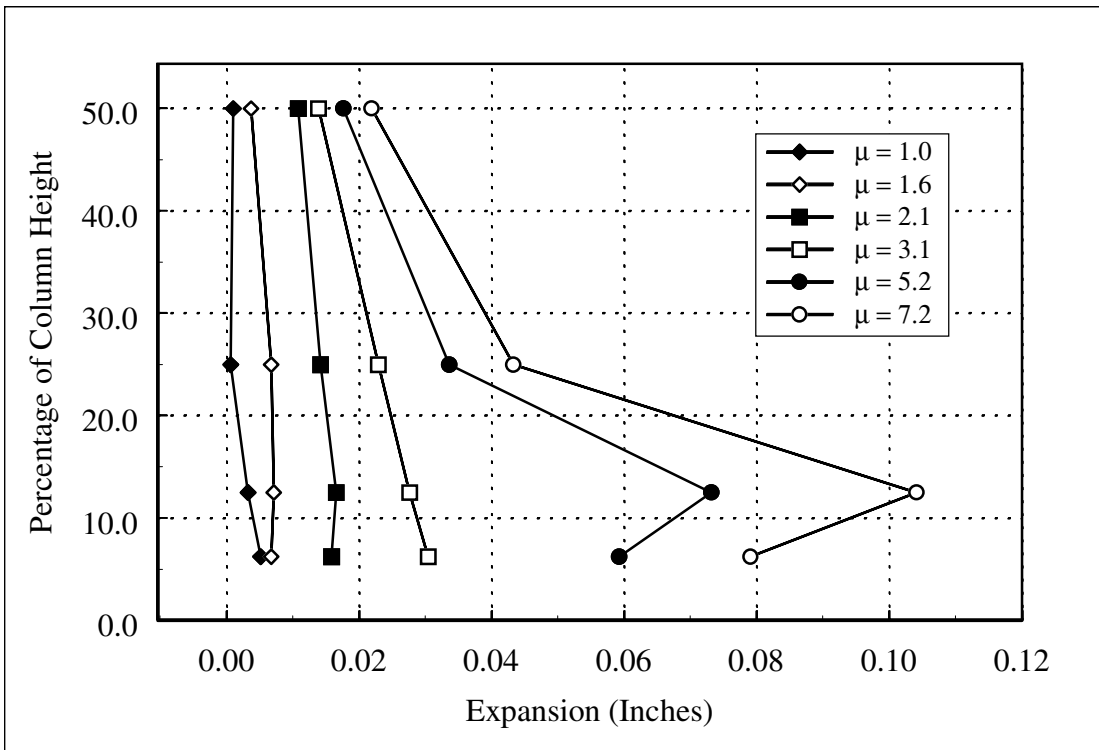


Figure C.56: Column 407 Profile of Horizontal Expansion



**Figure C.57: Column 415 Profile of Horizontal Expansion**



**Figure C.58: Column 430 Profile of Horizontal Expansion**

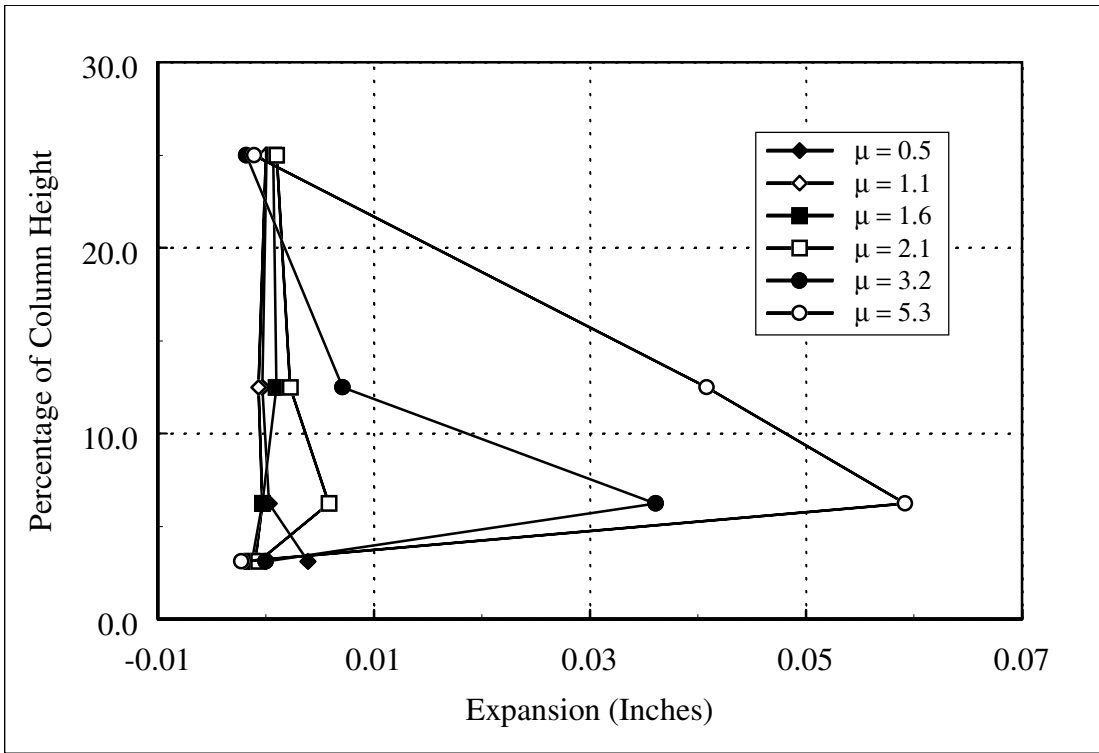


Figure C.59: Column 815 Profile of Horizontal Expansion

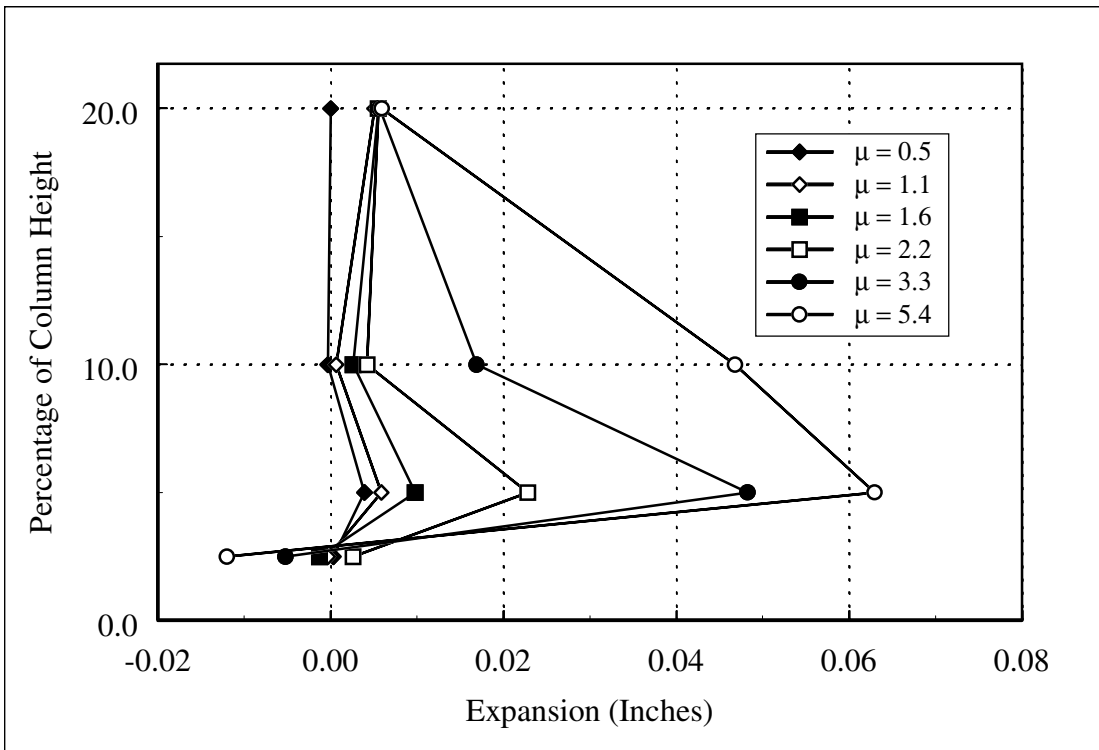
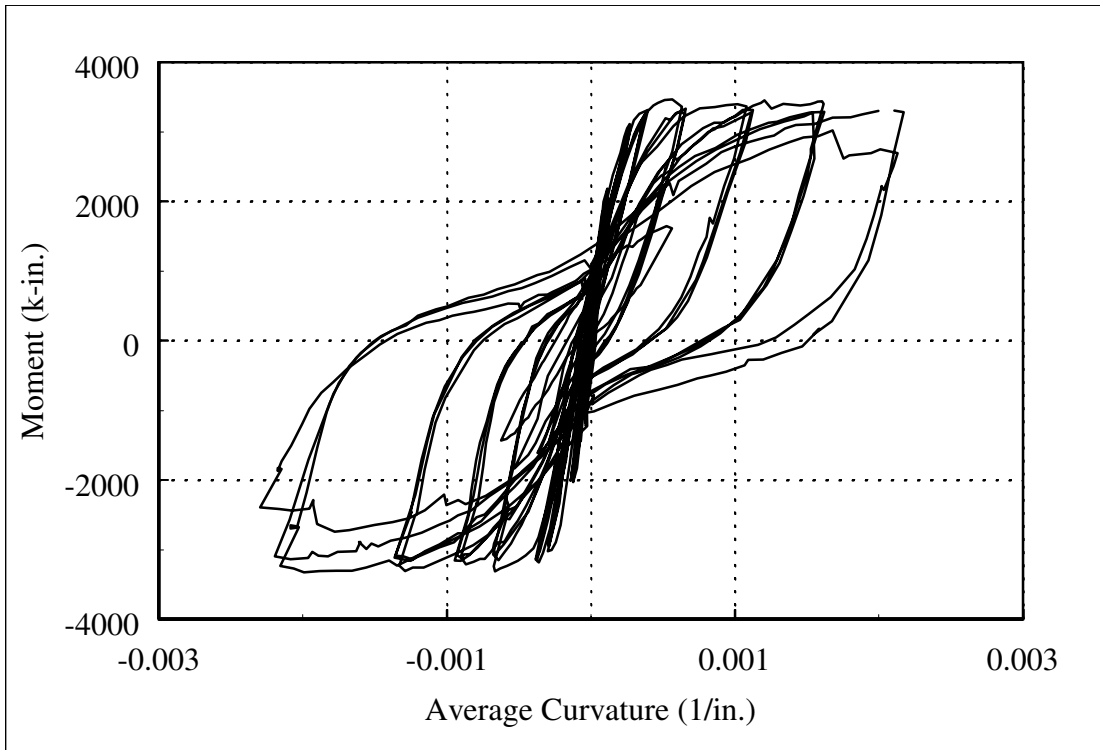
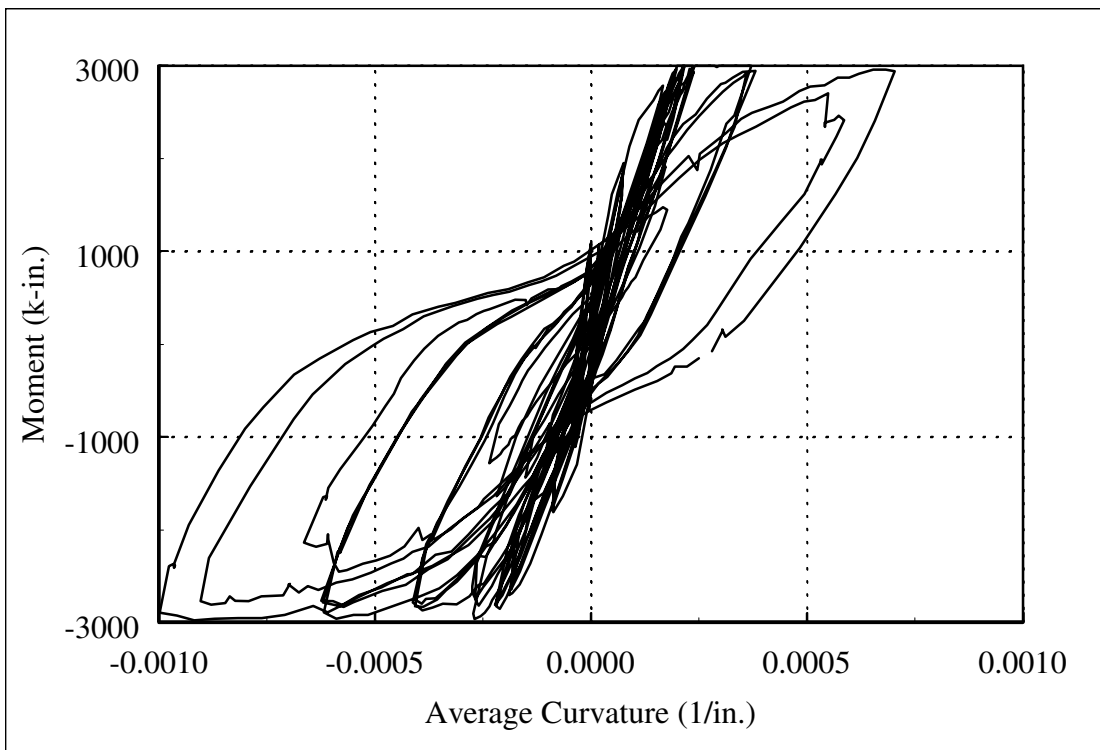


Figure C.60: Column 1015 Profile of Horizontal Expansion



**Figure C.61: Column 407 Average Moment-Curvature Response (Elevation: 6 to 12 Inches)**



**Figure C.62: Column 407 Average Moment-Curvature Response (Segment: 12 to 24 Inches)**

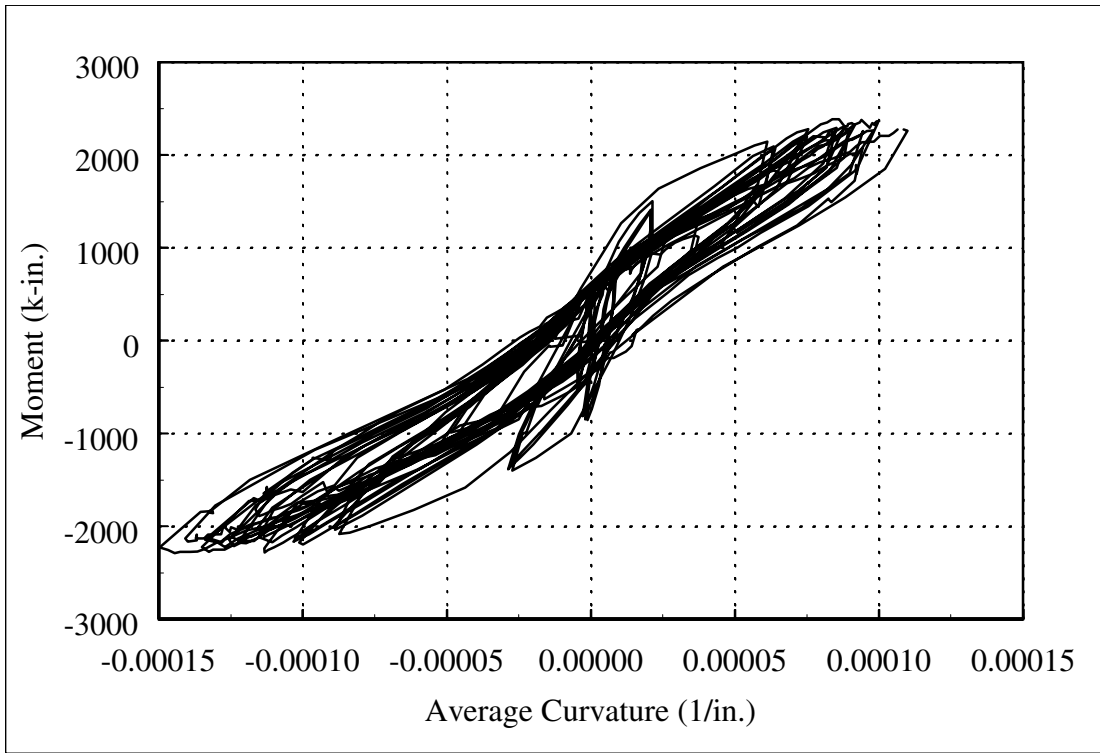


**Figure C.63: Column 407 Average Moment-Curvature Response (Elevation: 24 to 48 Inches)**

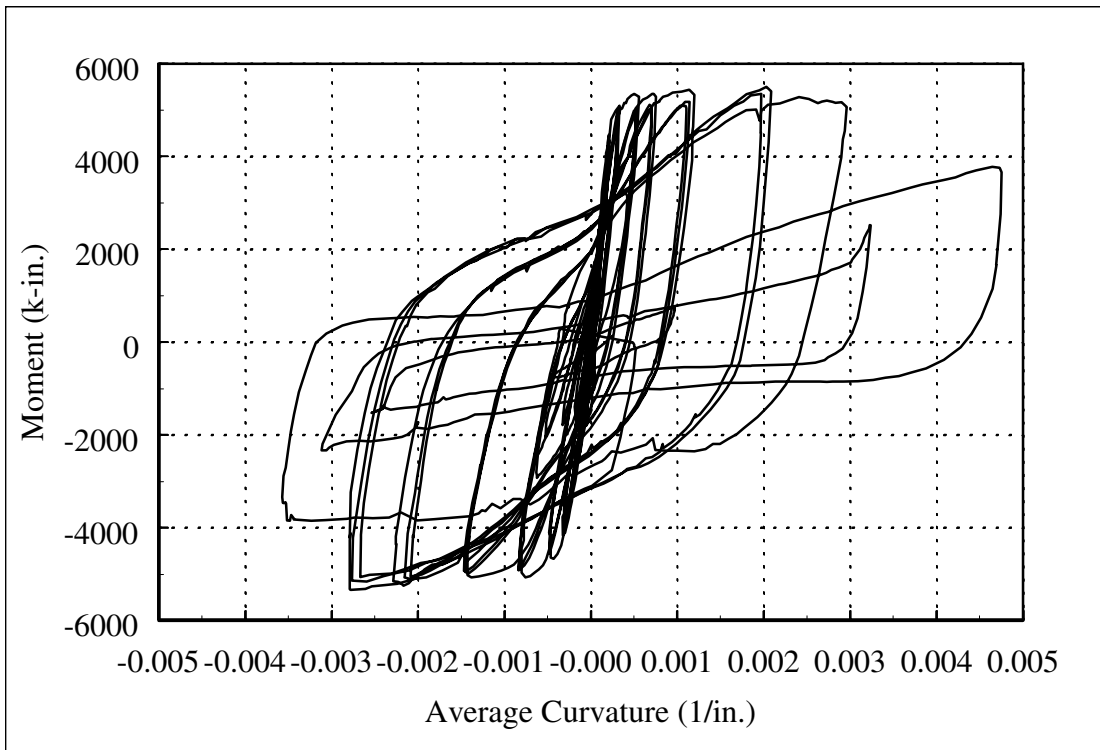


**Figure C.64: Column 415 Average Moment-Curvature Response (Elevation: 6 to 12 Inches)**

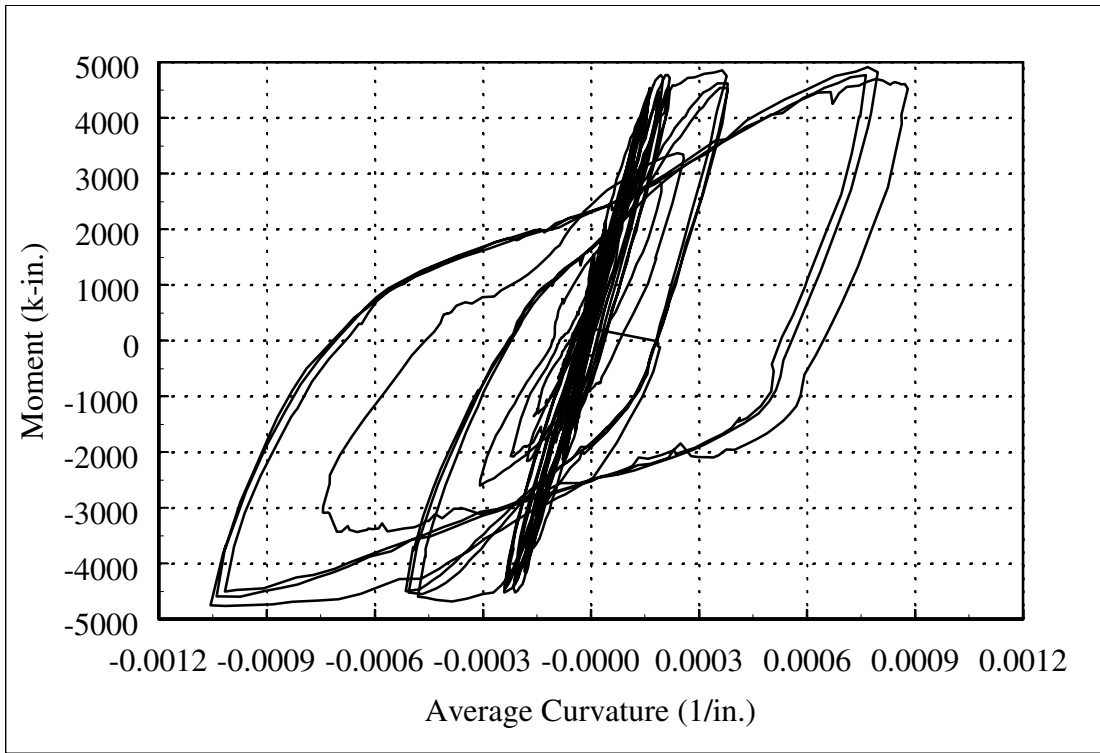


**Figure C.65: Column 415 Average Moment-Curvature Response (Elevation: 12 to 24 Inches)**

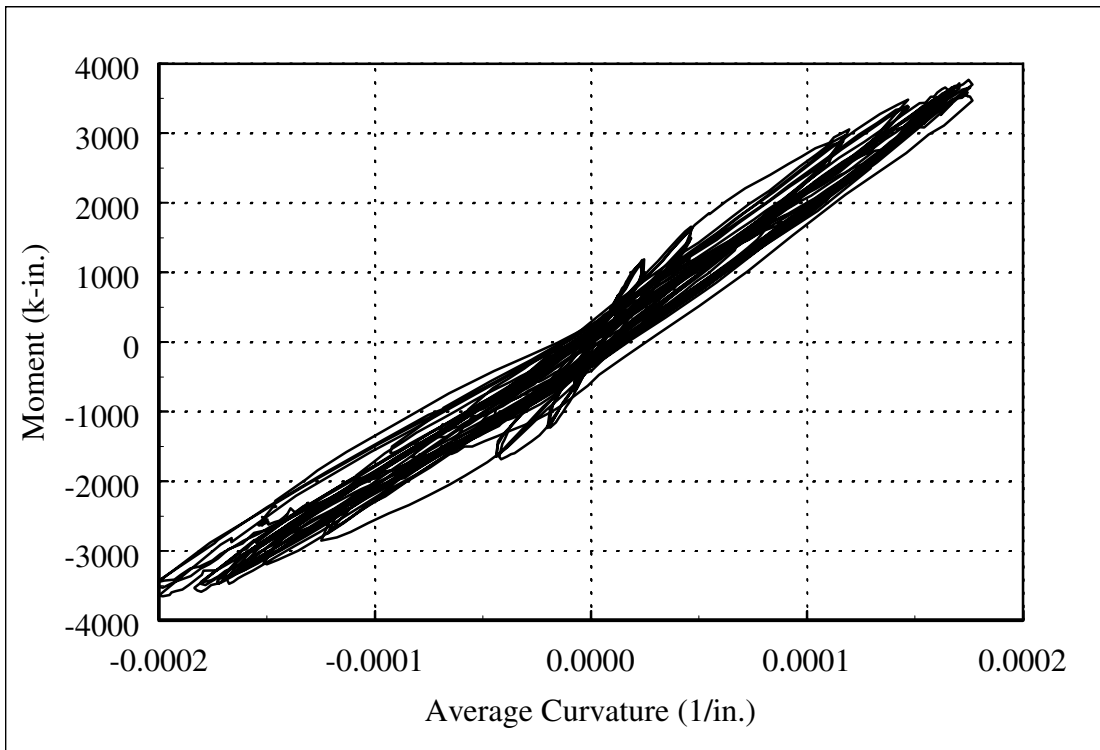


**Figure C.66: Column 415 Average Moment-Curvature Response (Elevation: 24 to 48 Inches)**

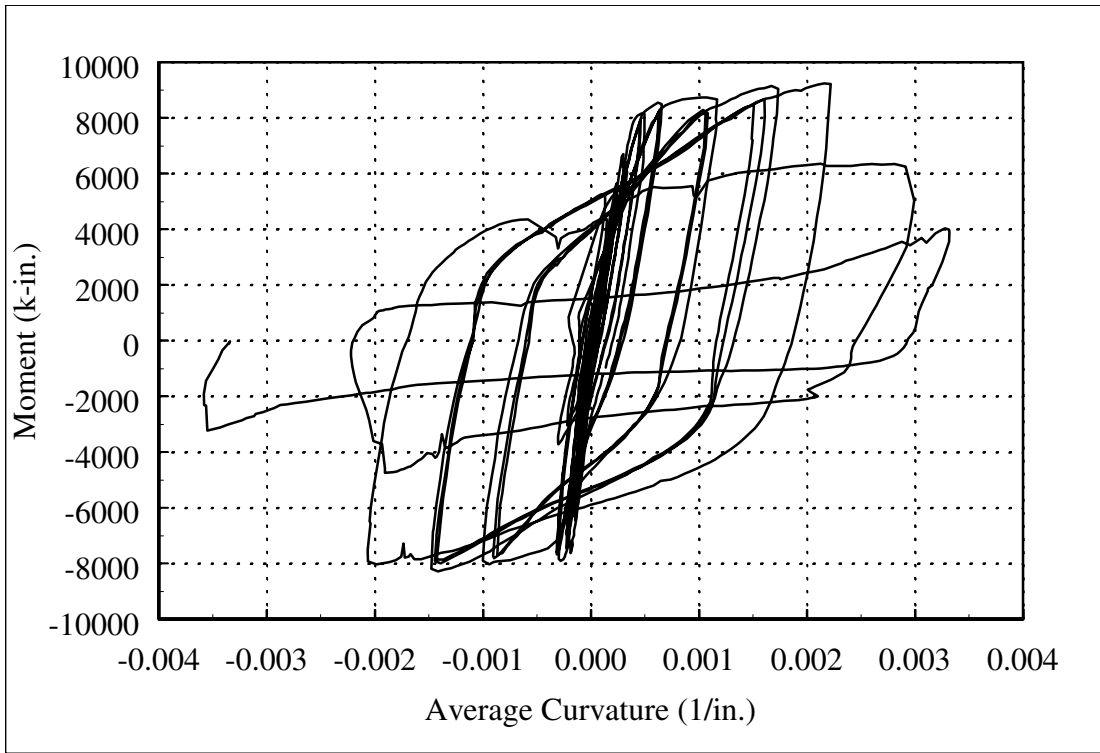


**Figure C.67: Column 430 Average Moment-Curvature Response (Elevation: 6 to 12 Inches)**

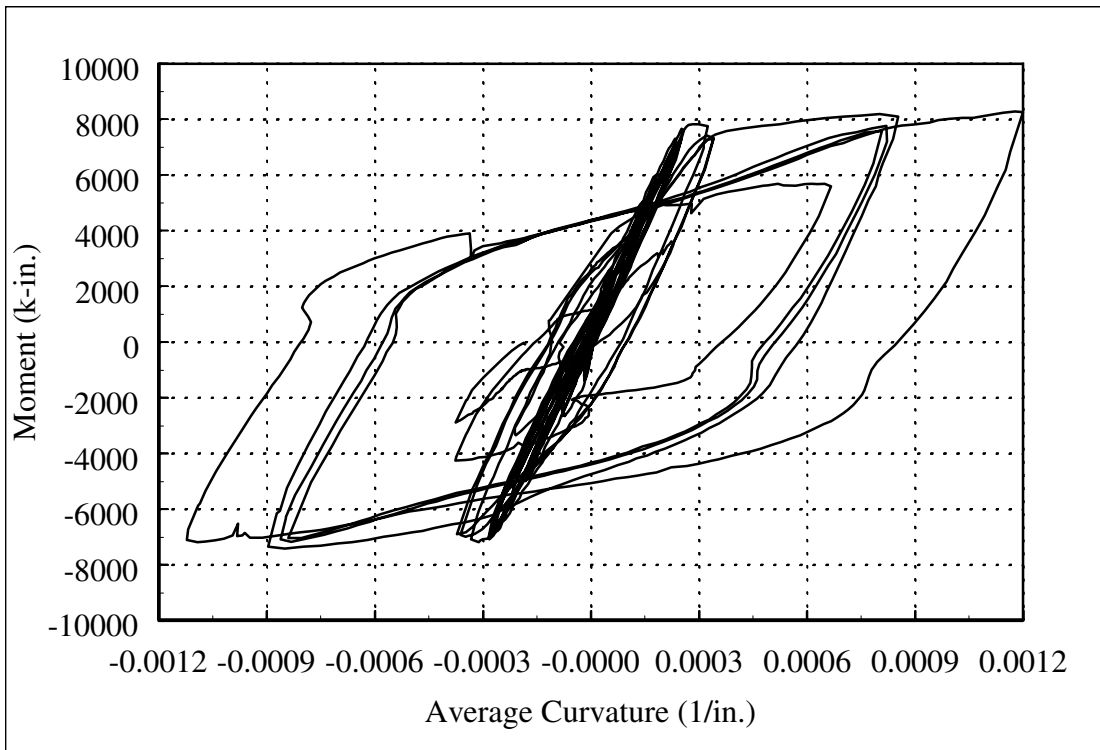


**Figure C.68: Column 430 Average Moment-Curvature Response (Elevation: 12 to 24 Inches)**

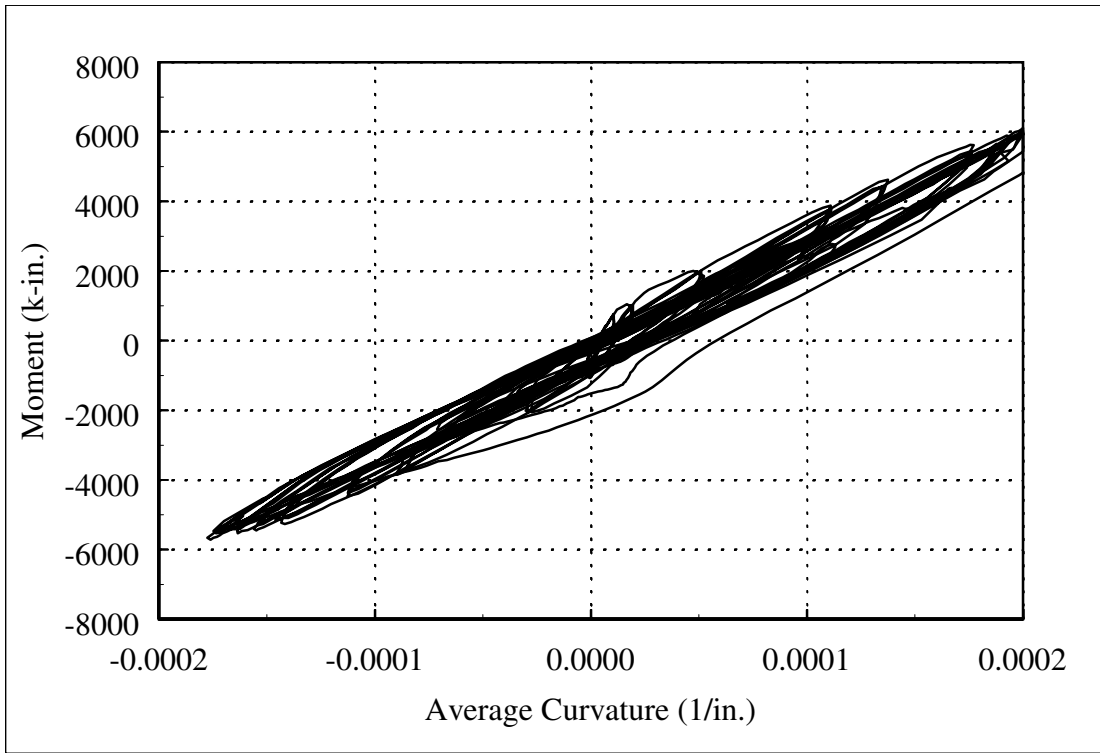


**Figure C.69: Column 430 Average Moment-Curvature Response (Elevation: 24 to 48 Inches)**

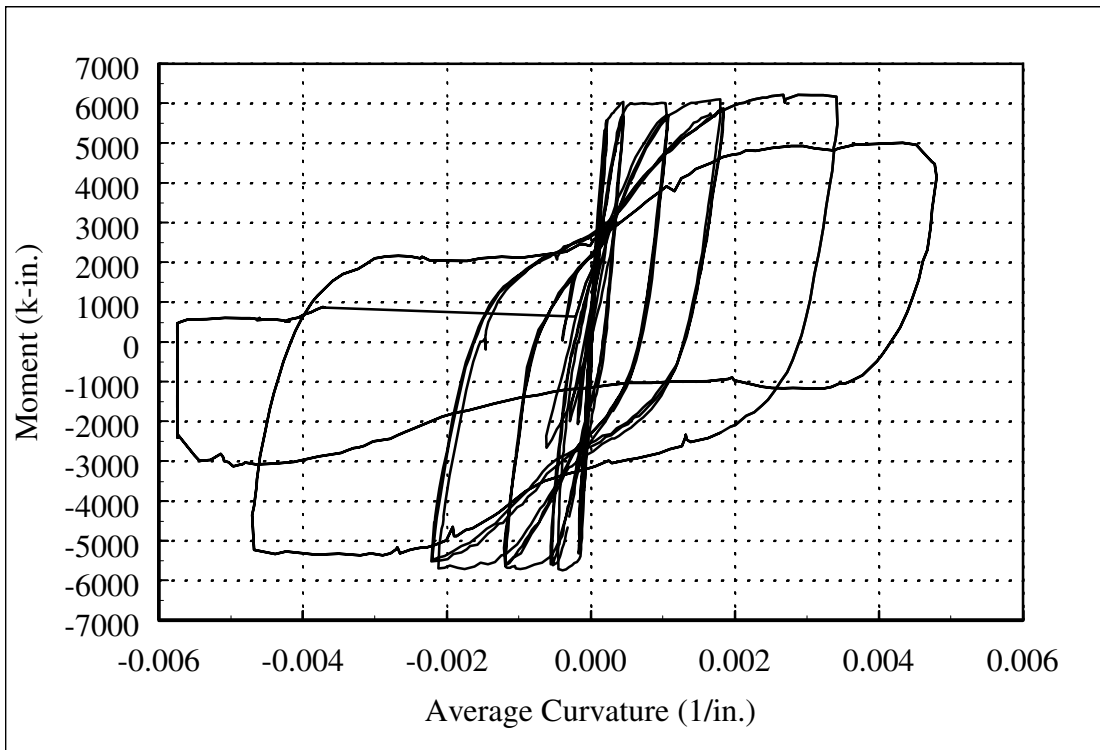


**Figure C.70: Column 815 Average Moment-Curvature Response (Elevation: 6 to 12 Inches)**

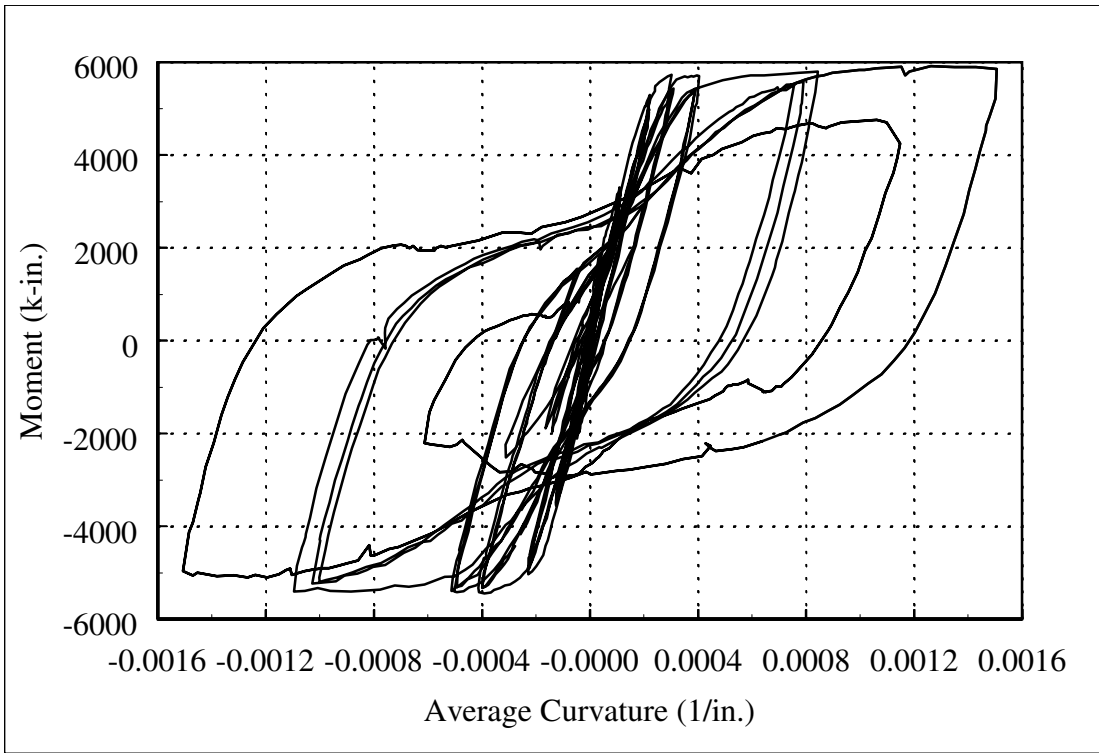


**Figure C.71: Column 815 Average Moment-Curvature Response (Elevation: 12 to 24 Inches)**

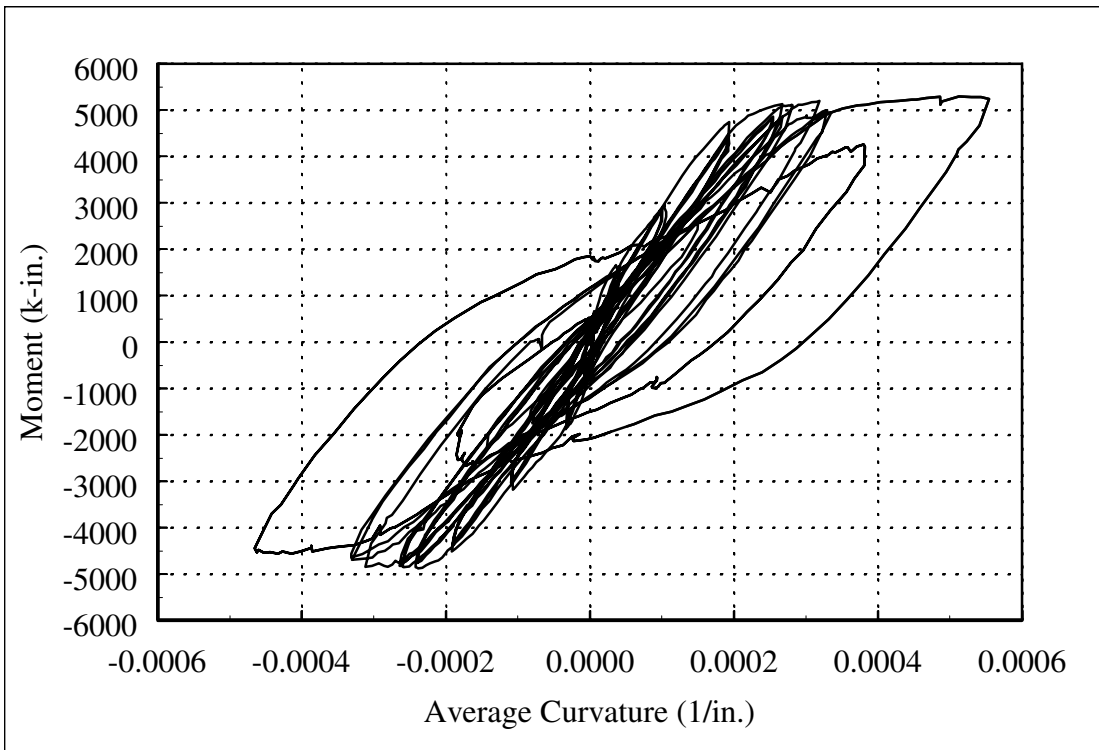


**Figure C.72: Column 815 Average Moment-Curvature Response (Elevation: 24 to 48 Inches)**

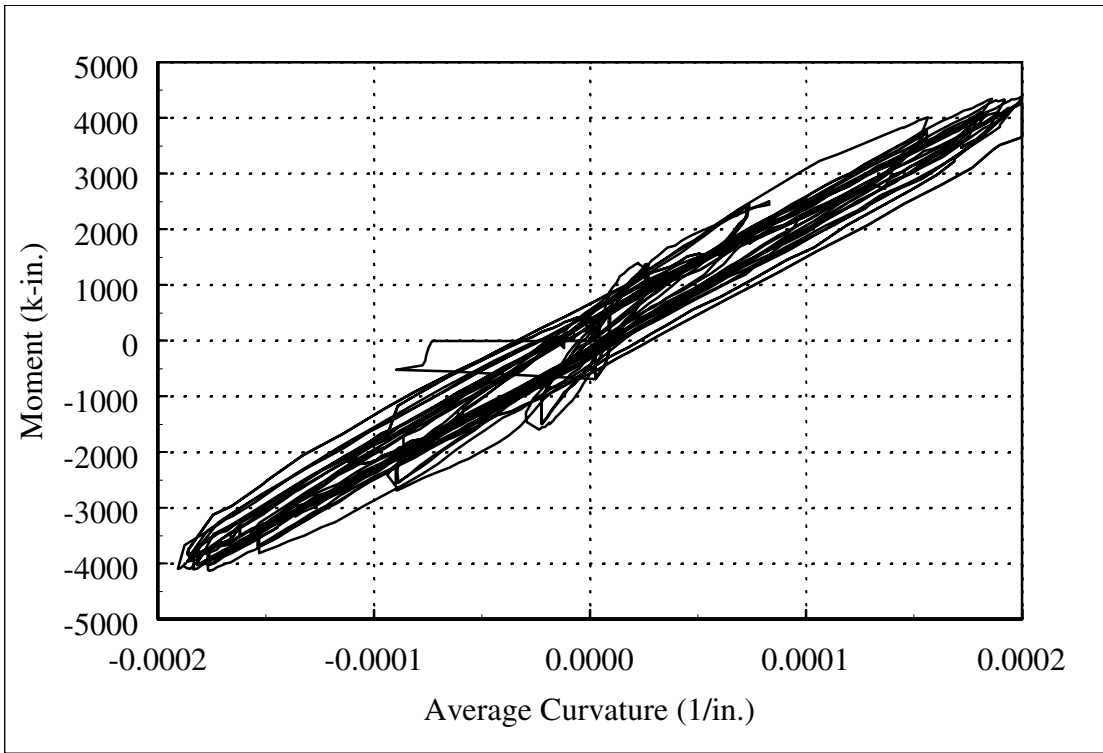


**Figure C.73: Column 815 Average Moment-Curvature Response (Elevation: 48 to 72 Inches)**

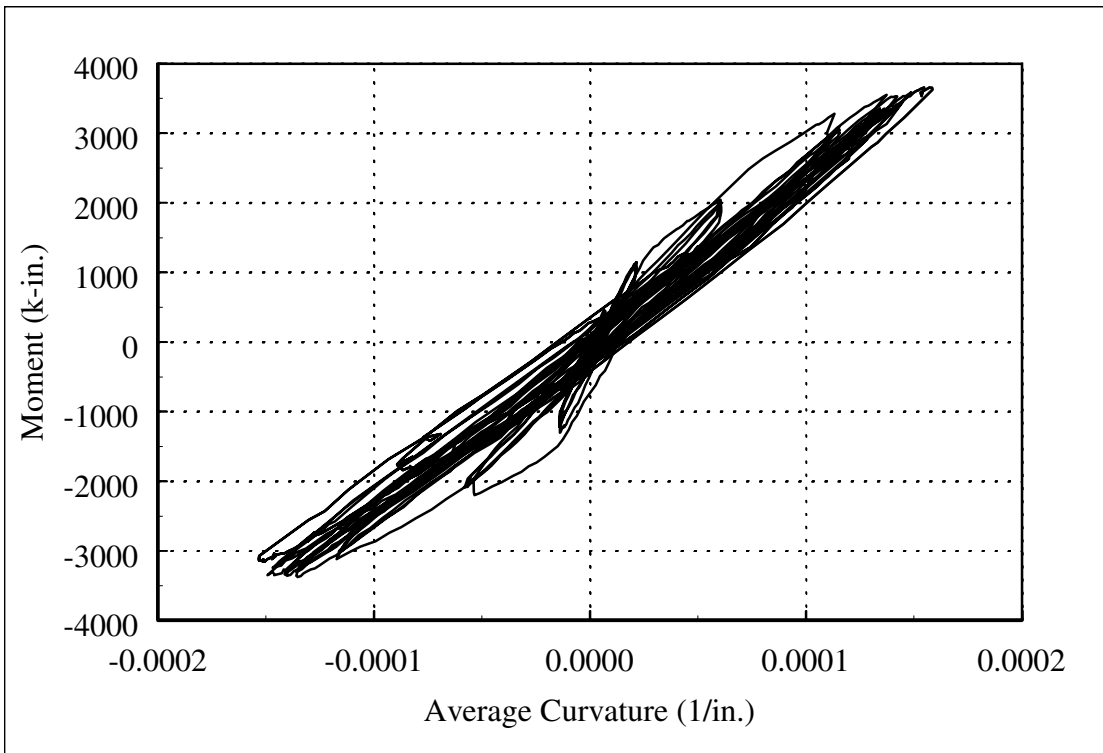


**Figure C.74: Column 815 Average Moment-Curvature Response (Elevation: 72 to 96 Inches)**

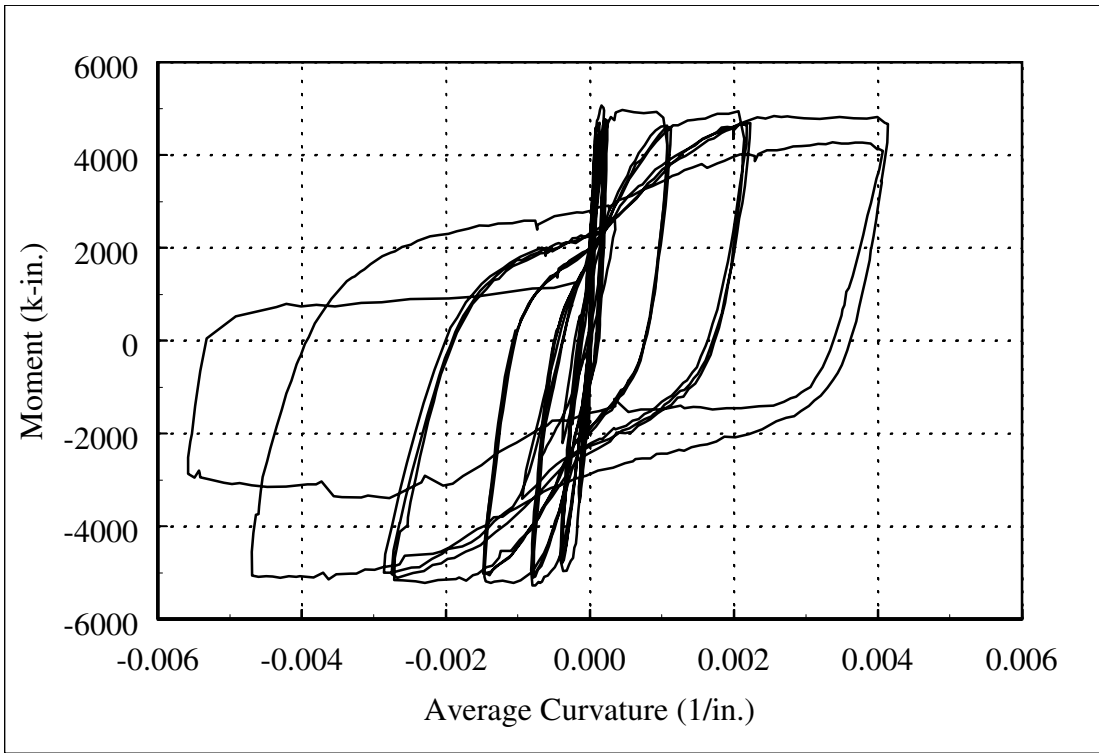


**Figure C.75: Column 1015 Average Moment-Curvature Response (Elevation: 6 to 12 Inches)**

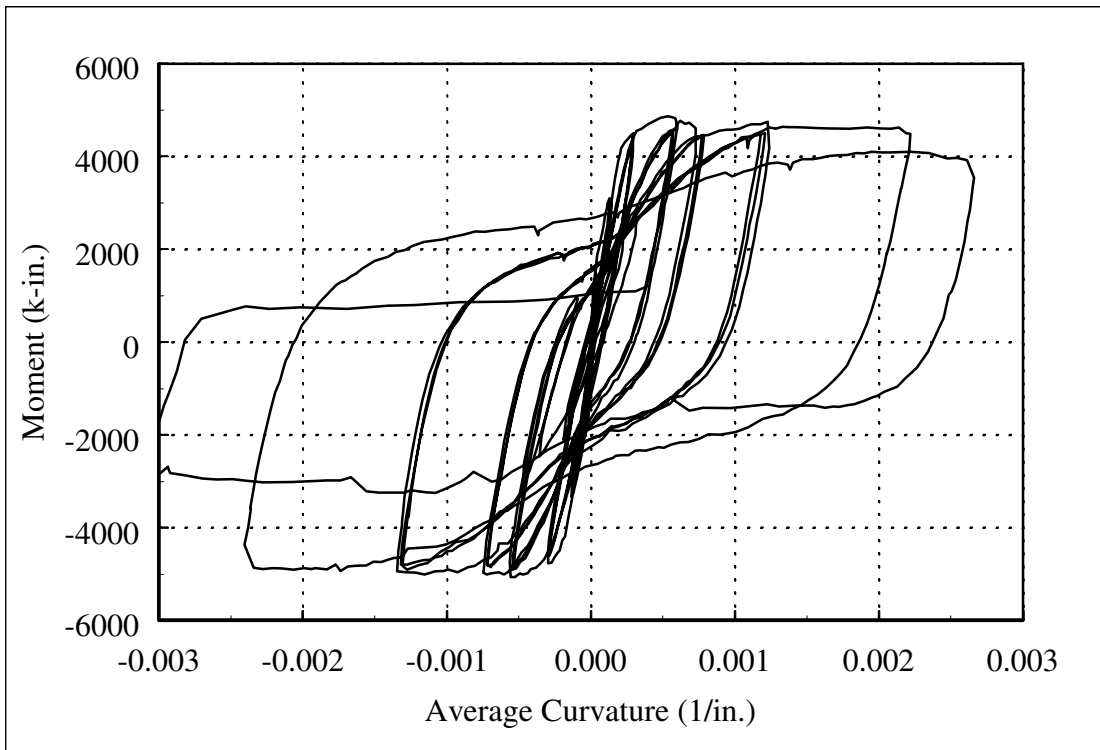


**Figure C.76: Column 1015 Average Moment-Curvature Response (Elevation: 12 to 24 Inches)**

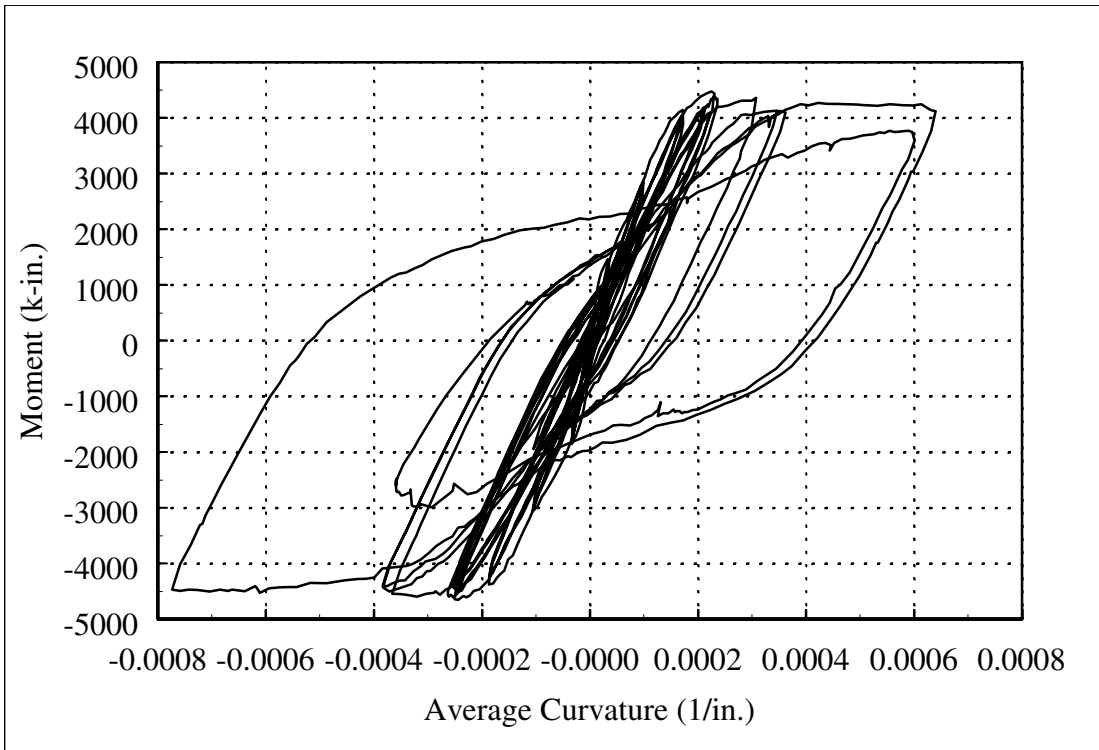


**Figure C.77: Column 1015 Average Moment-Curvature Response  
(Elevation: 24 to 48 Inches)**

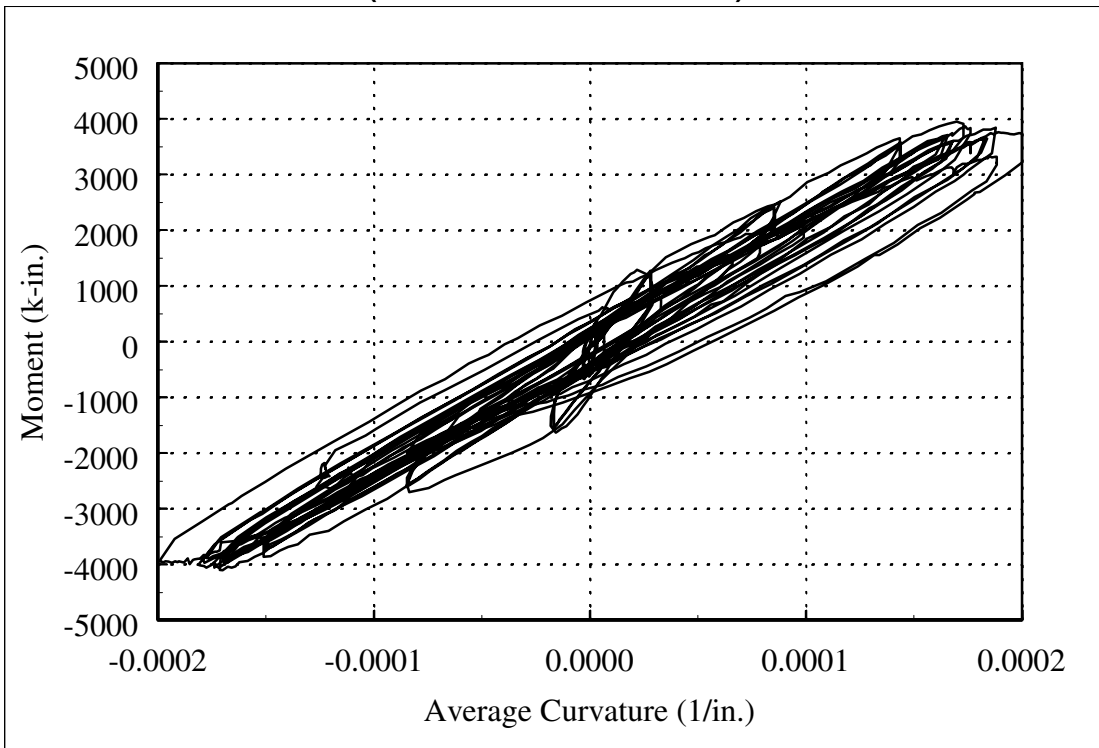


**Figure C.78: Column 1015 Average Moment-Curvature Response  
(Elevation: 48 to 72 Inches)**

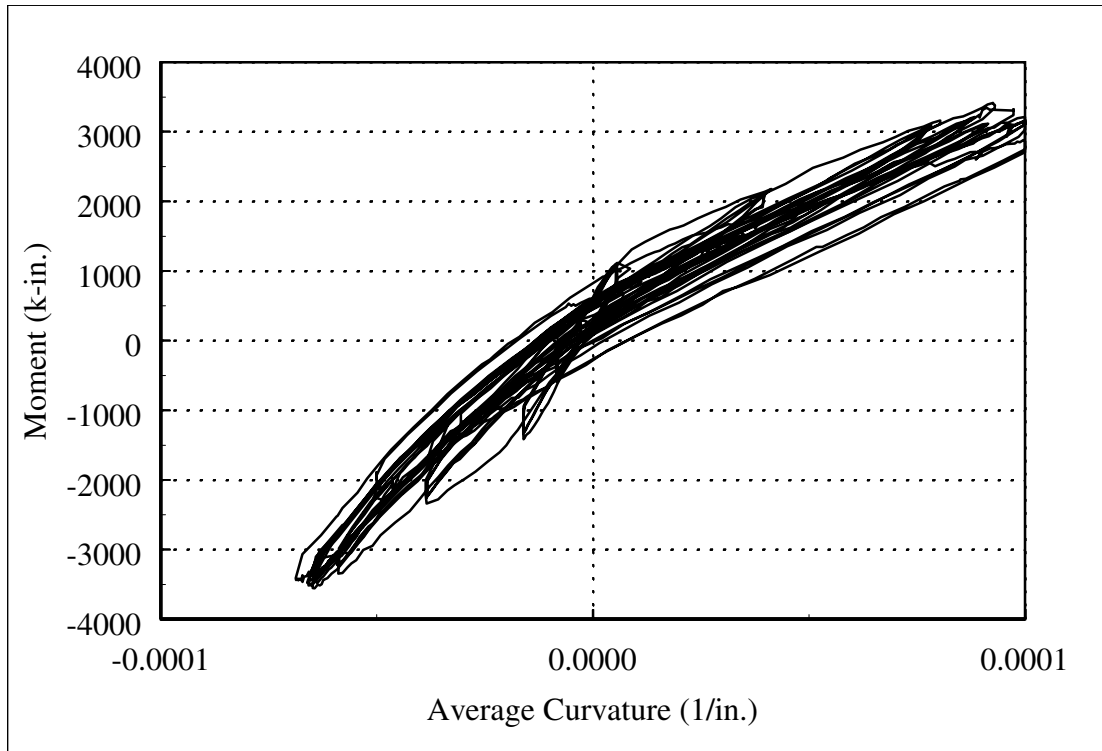


**Figure C.79: Column 1015 Average Moment-Curvature Response  
(Elevation: 72 to 96 Inches)**

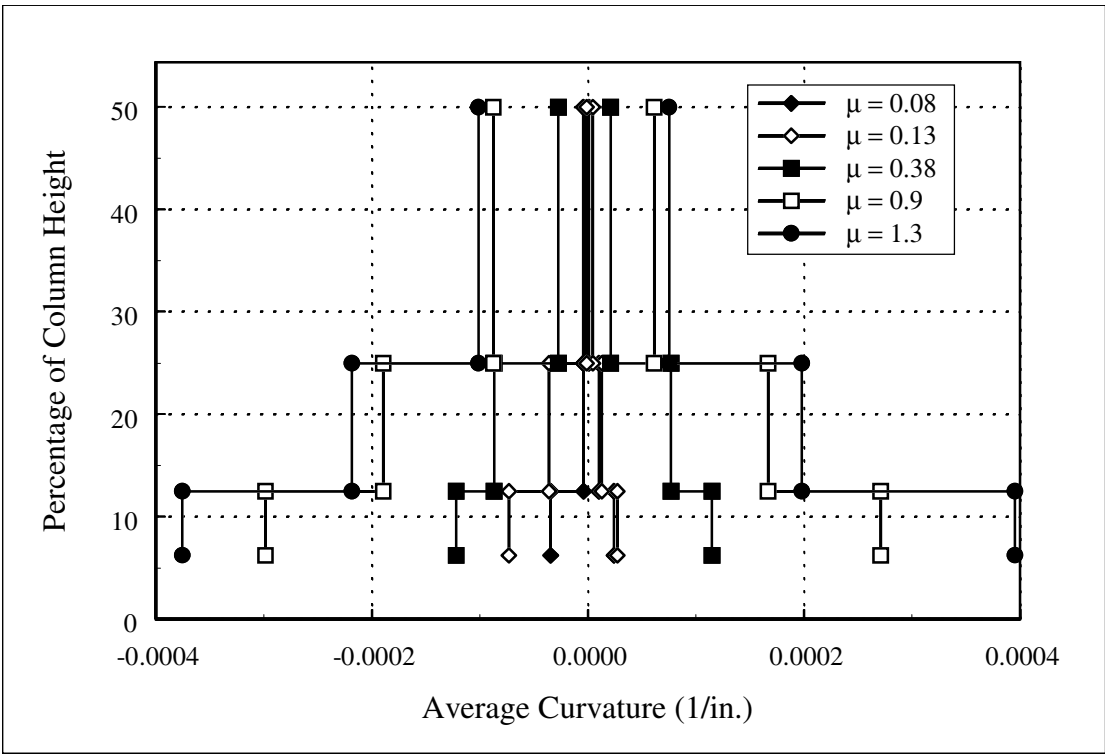


Figure C.80: Column 407 Curvature Profile (Initial Displacement Cycles)

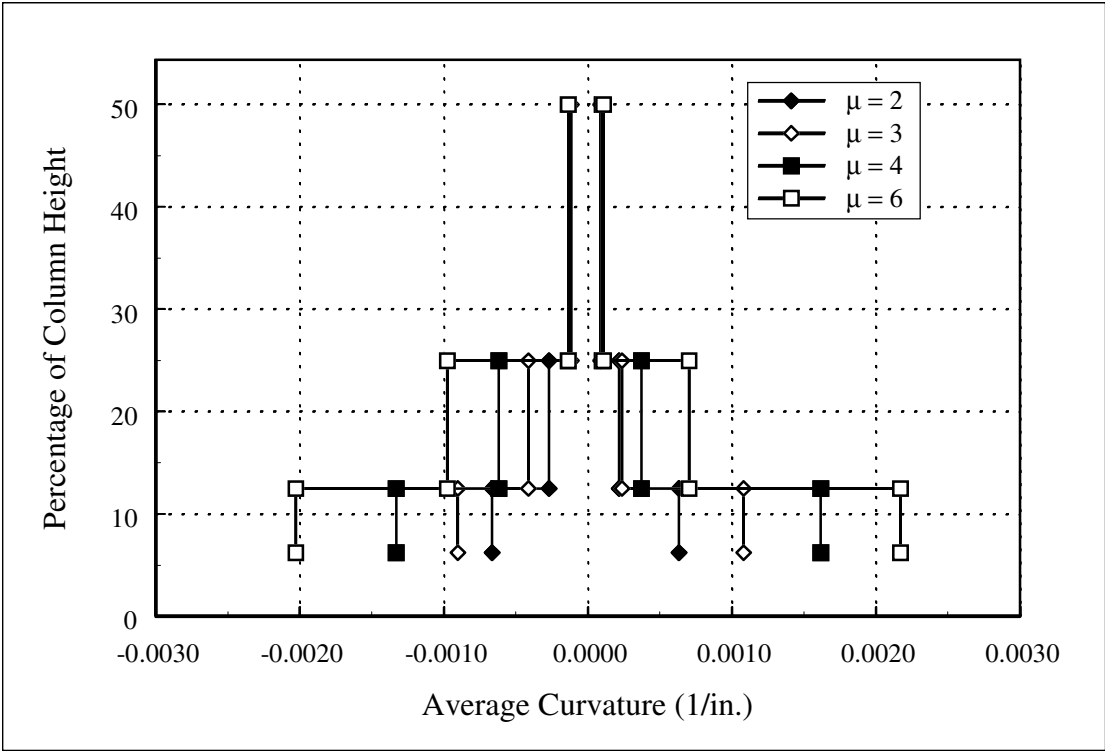


Figure C.81: Column 407 Curvature Profile (Final Displacement Cycles)

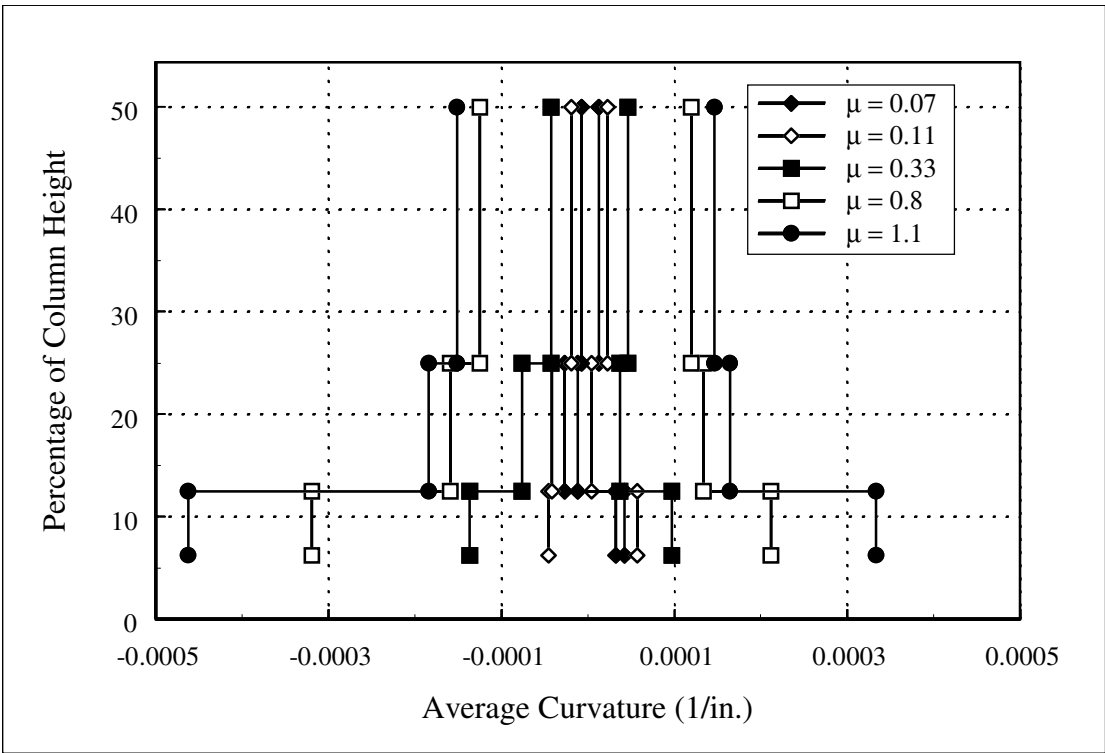


Figure C.82: Column 415 Curvature Profile (Initial Displacement Cycles)

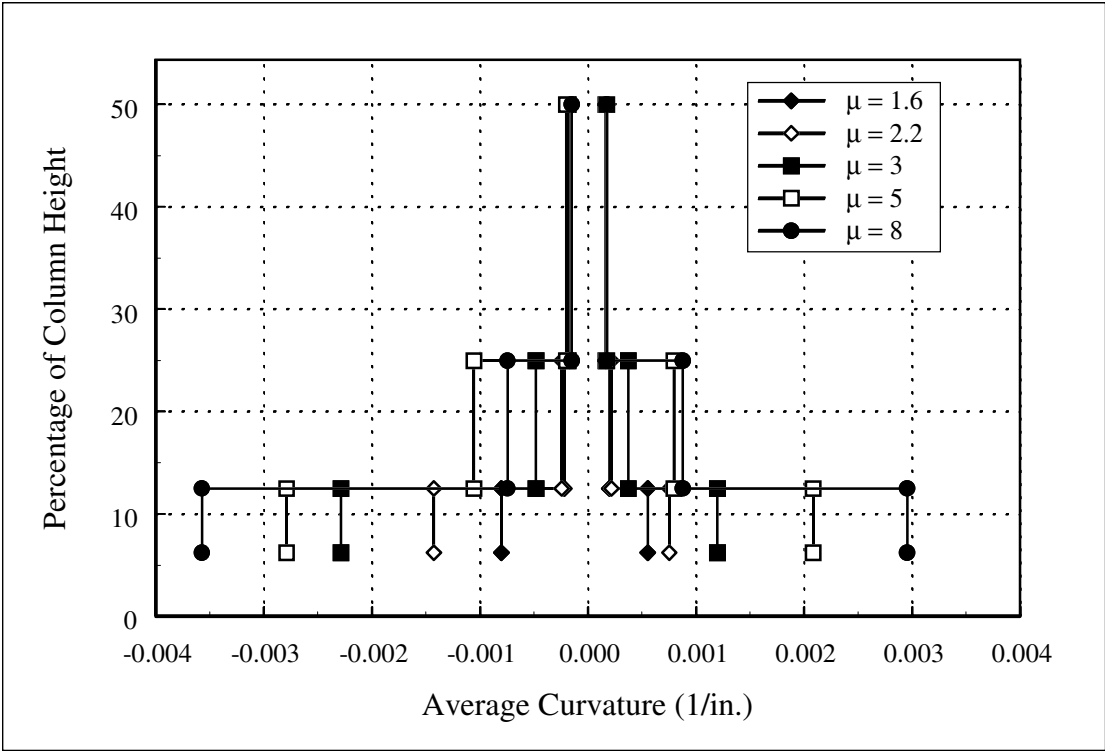


Figure C.83: Column 415 Curvature Profile (Final Displacement Cycles)

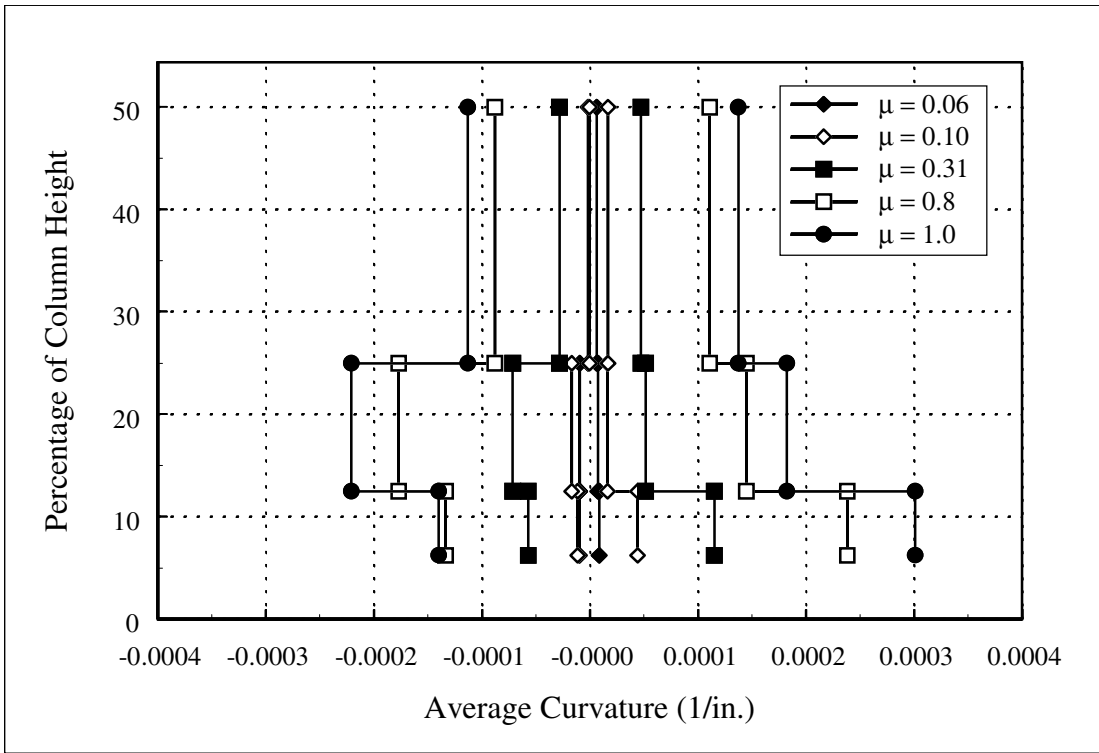


Figure C.84: Column 430 Curvature Profile (Initial Displacement Cycles)

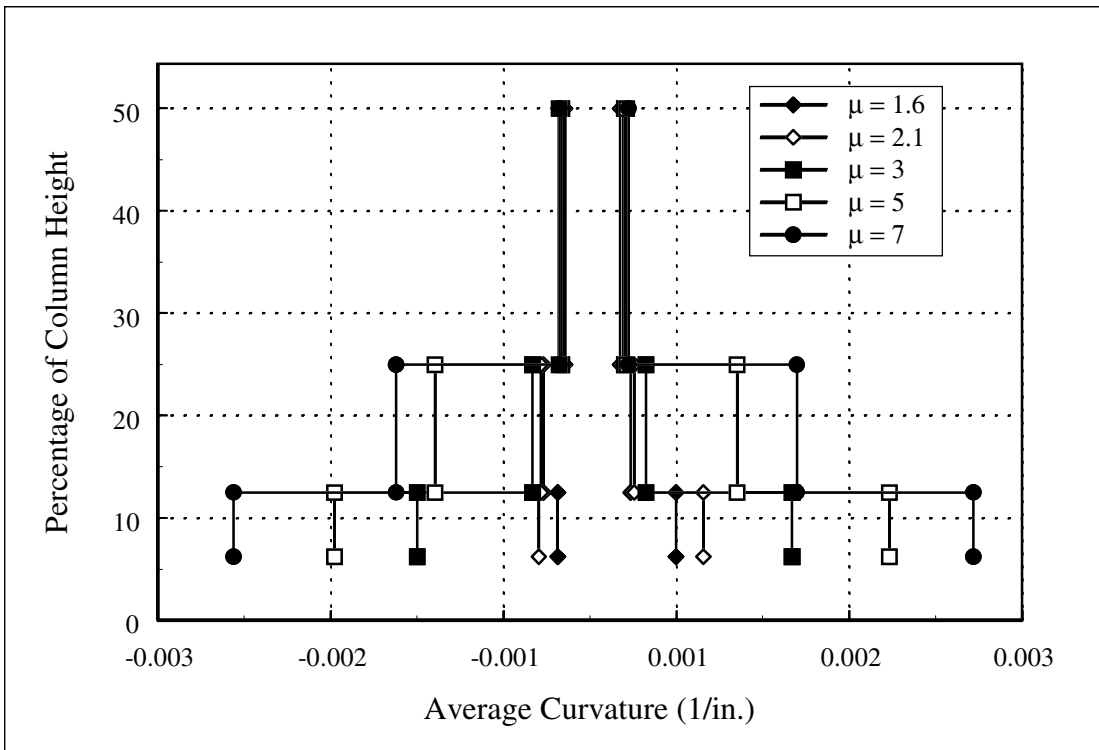


Figure C.85: Column 430 Curvature Profile (Final Displacement Cycles)

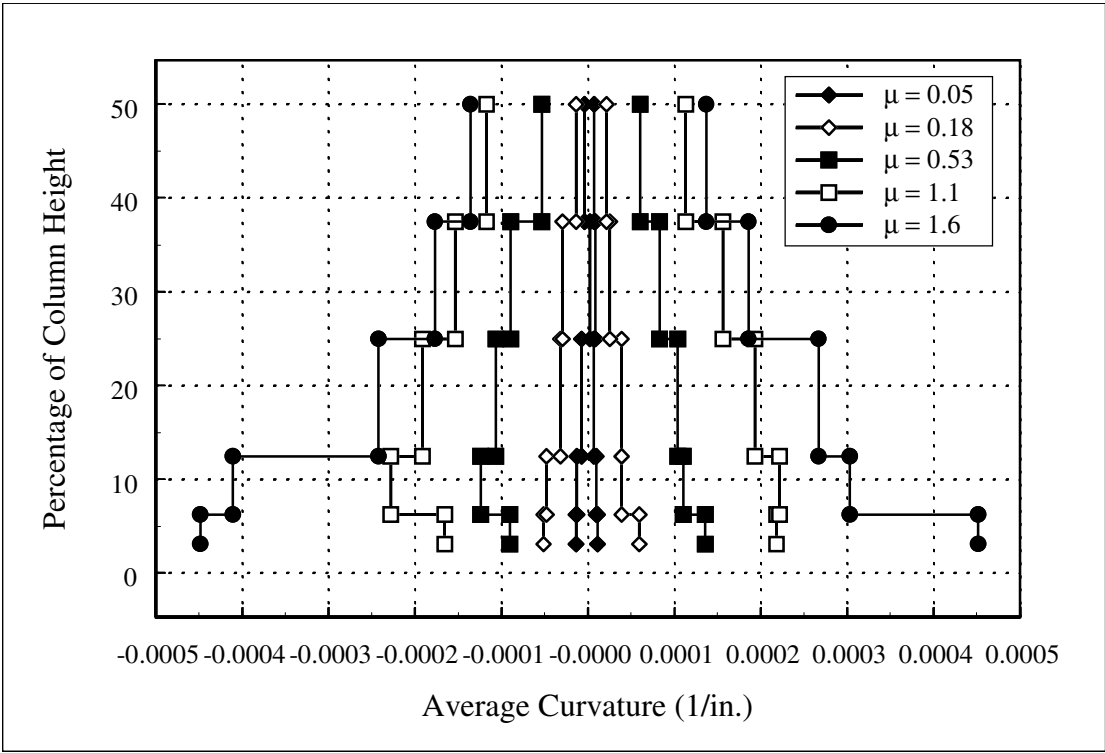


Figure C.86: Column 815 Curvature Profile (Initial Displacement Cycles)

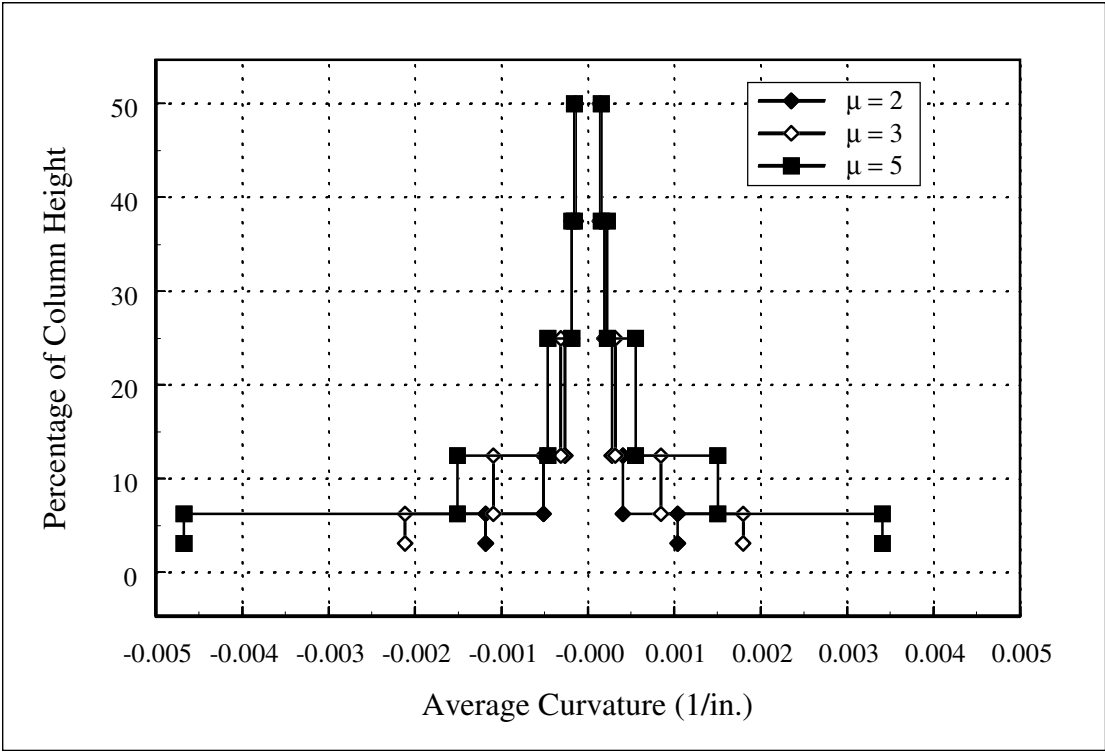
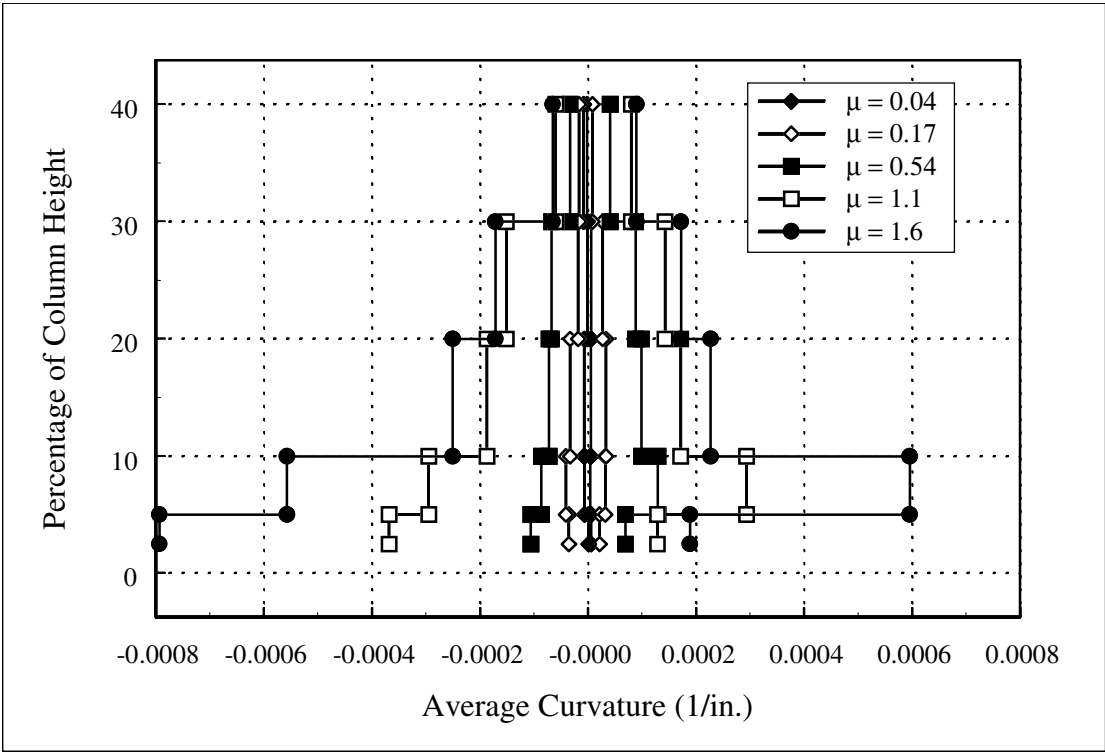
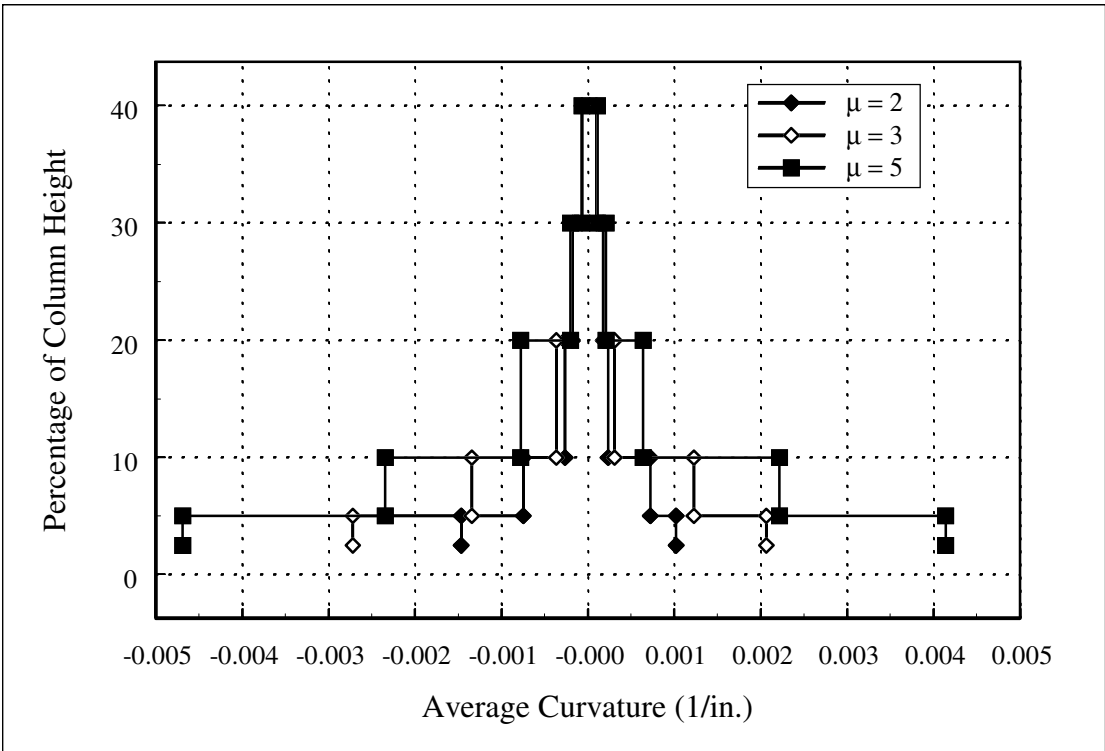


Figure C.87: Column 815 Curvature Profile (Final Displacement Cycles)



**Figure C.88: Column 1015 Curvature Profile (Initial Displacement Cycles)**



**Figure C.89: Column 1015 Curvature Profile (Final Displacement Cycles)**

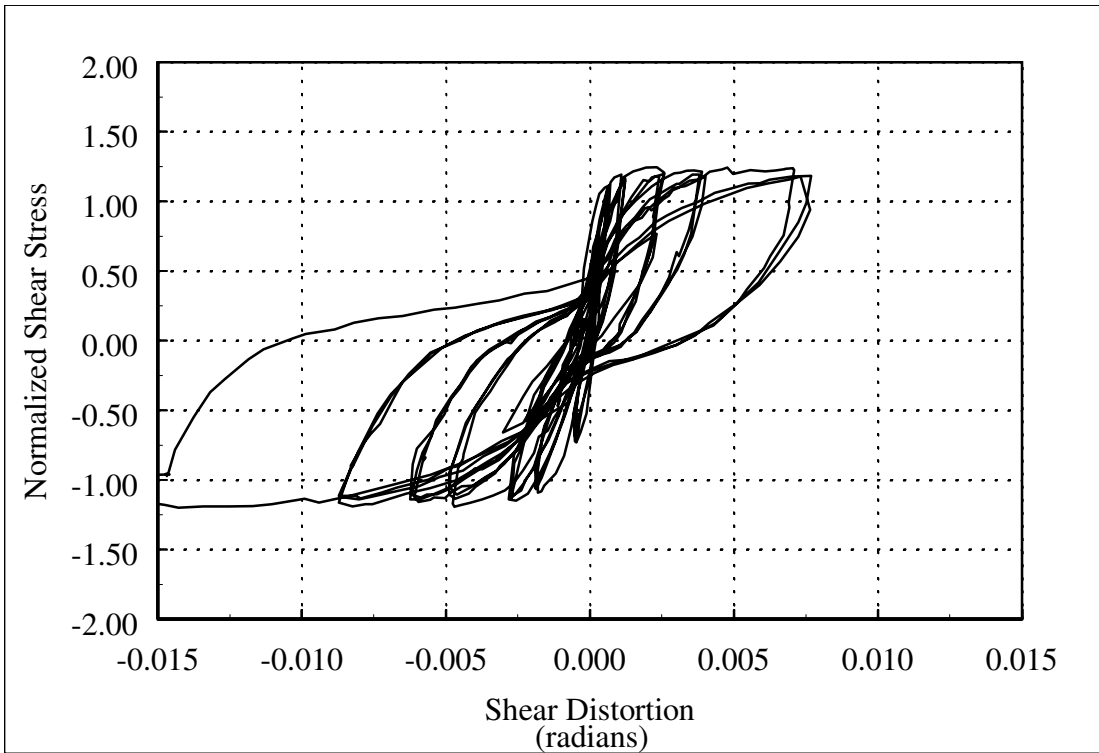


**Figure C.90: Column 407 Cyclic Shear Strain-Shear Stress, Elevation of D/2**

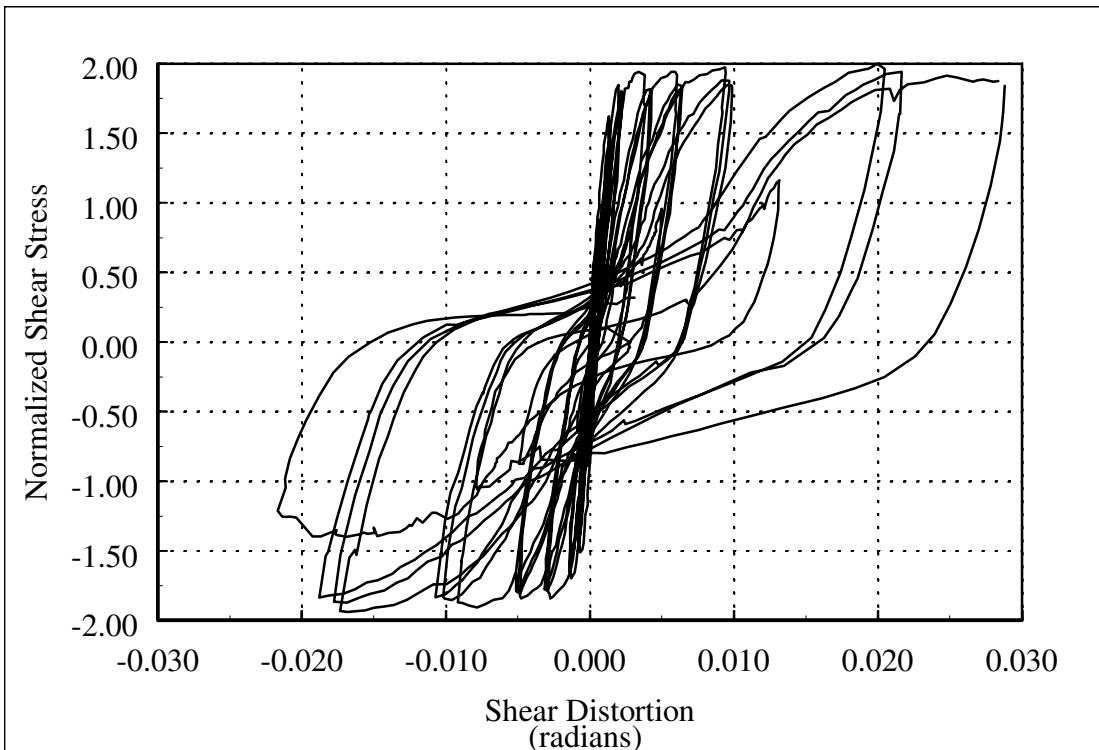


**Figure C.91: Column 415 Cyclic Shear Strain-Shear Stress, Elevation of D/2**

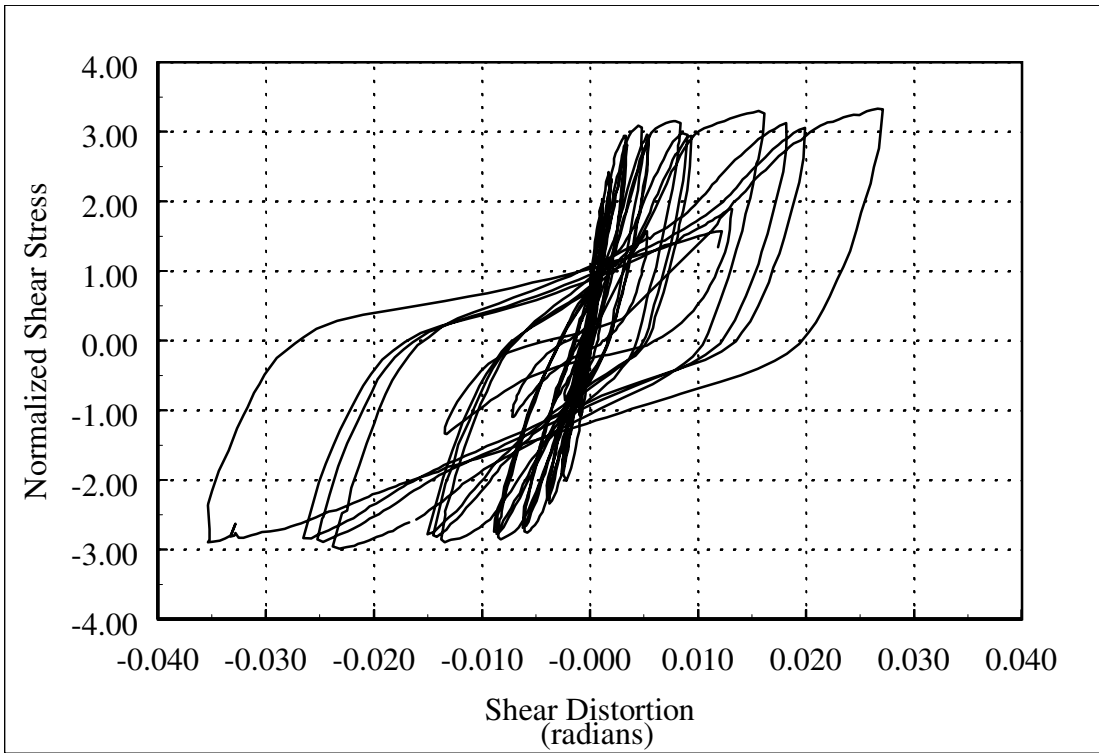


**Figure C.92: Column 430 Cyclic Shear Strain-Shear Stress, Elevation of D/2**

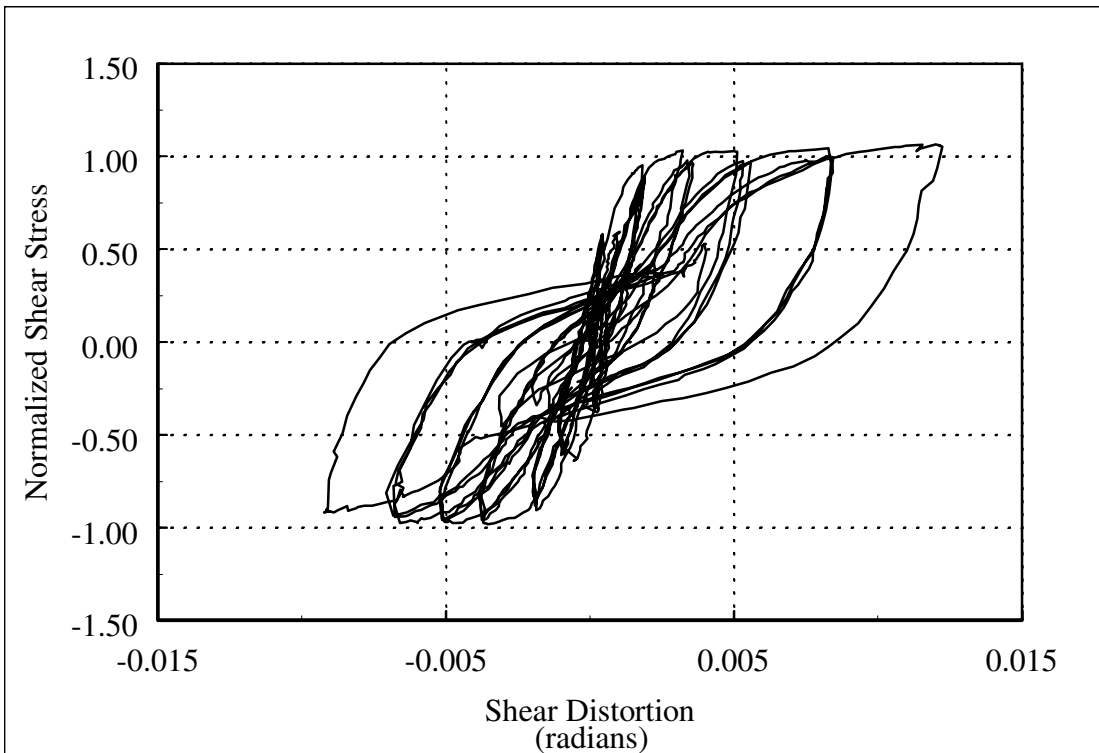


**Figure C.93: Column 815 Cyclic Shear Strain-Shear Stress, Elevation of D/2**

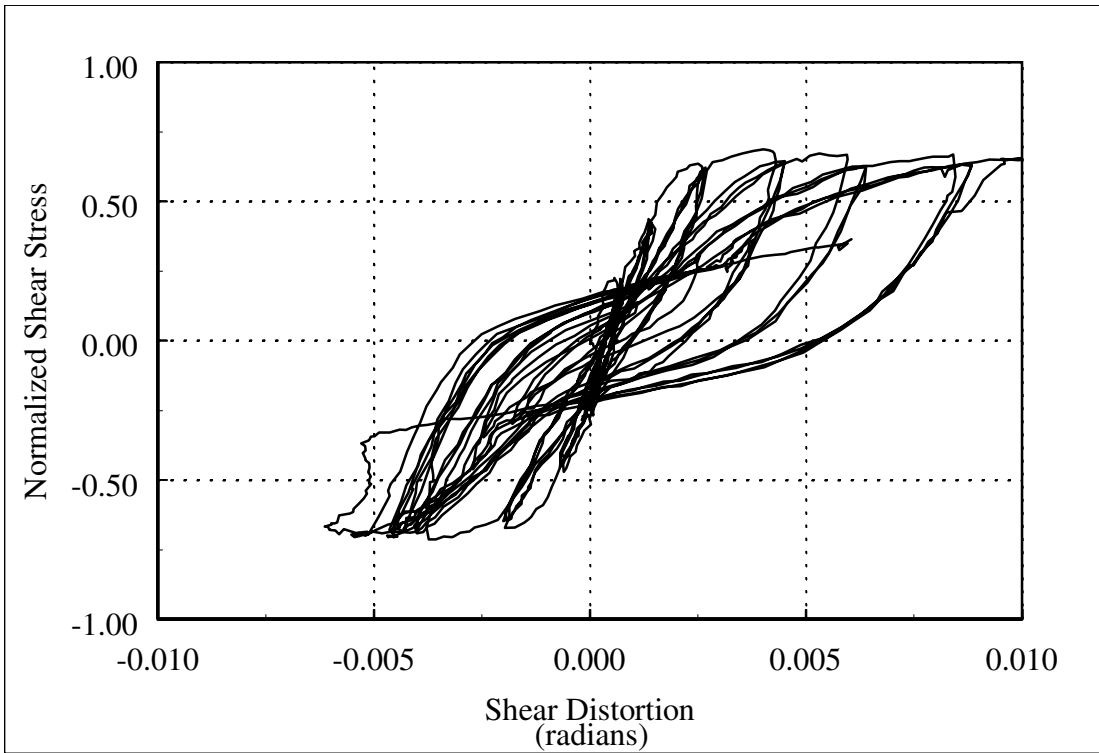


Figure C.94: Column 1015 Cyclic Shear Strain-Shear Stress, Elevation of D/2

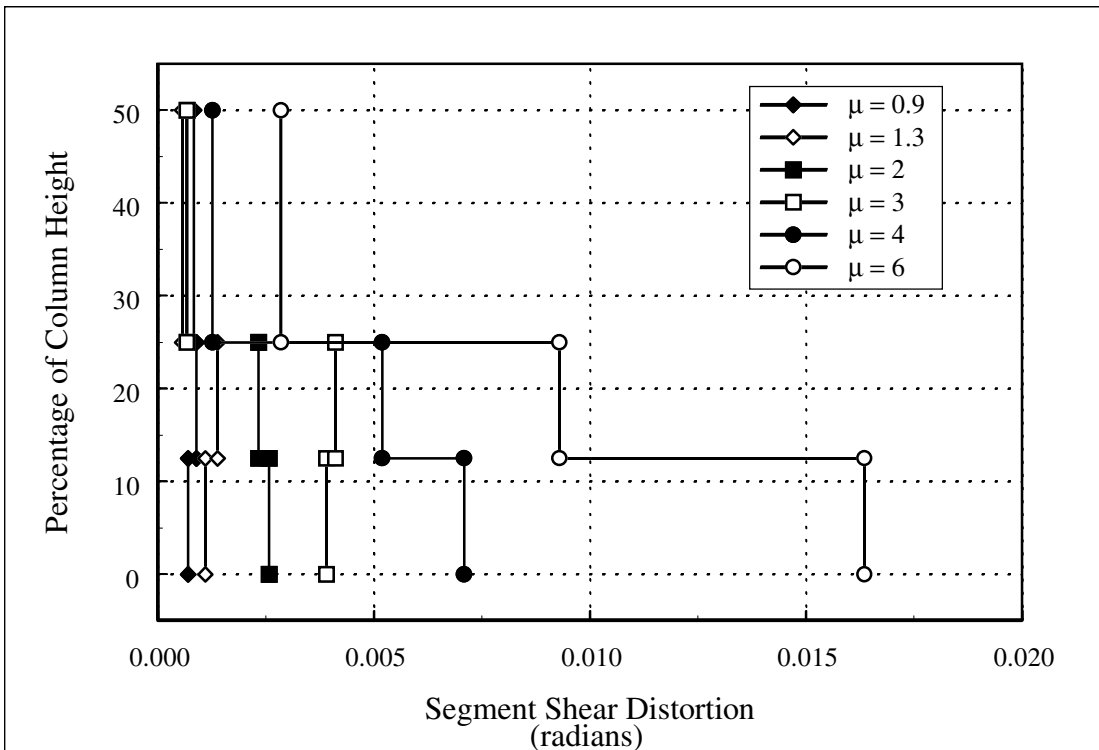


Figure C.95: Column 407 Shear-Strain Profile

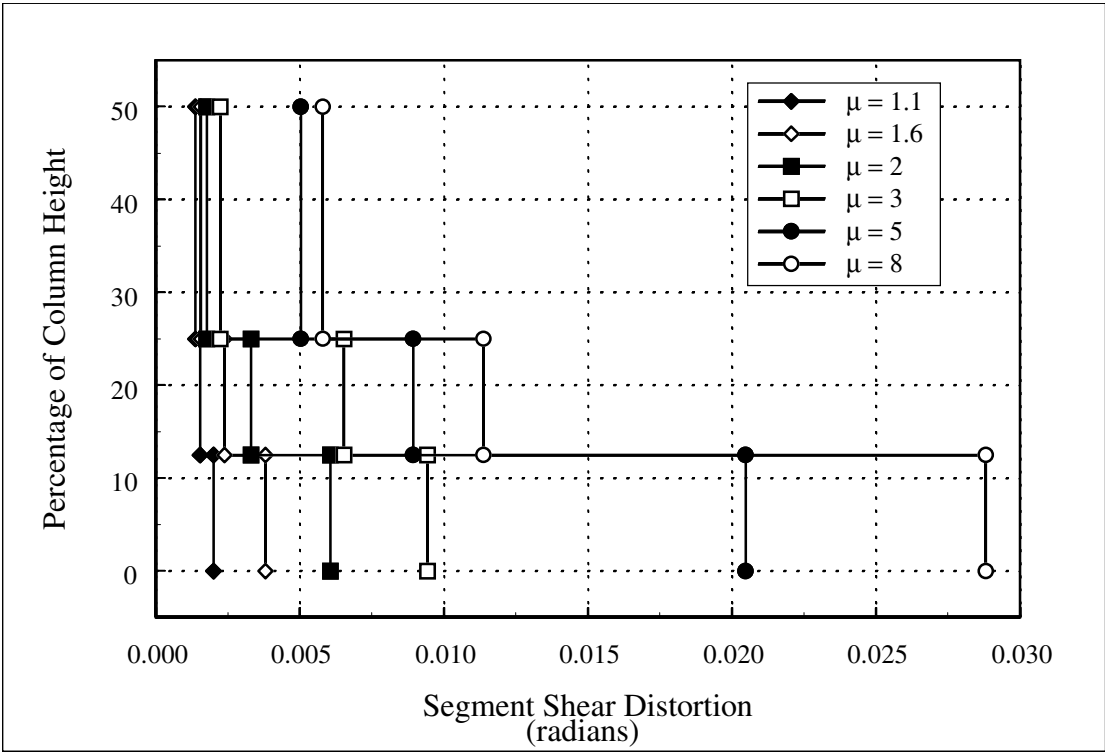


Figure C.96: Column 415 Shear-Strain Profile

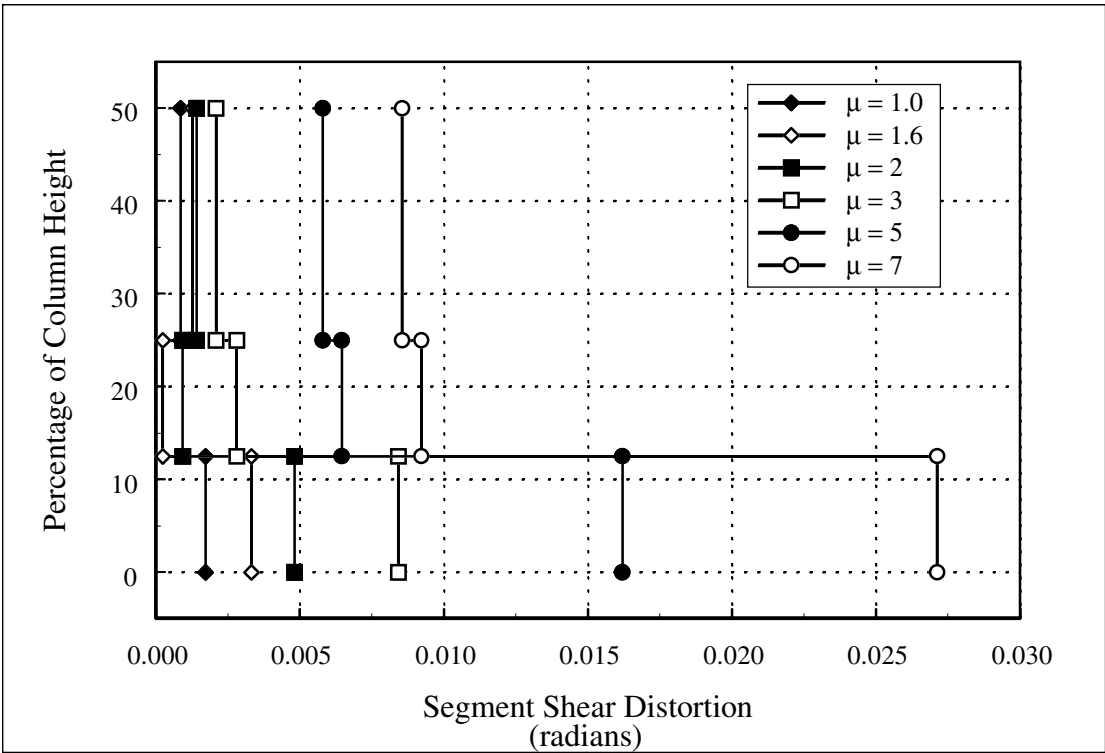


Figure C.97: Column 430 Shear-Strain Profile

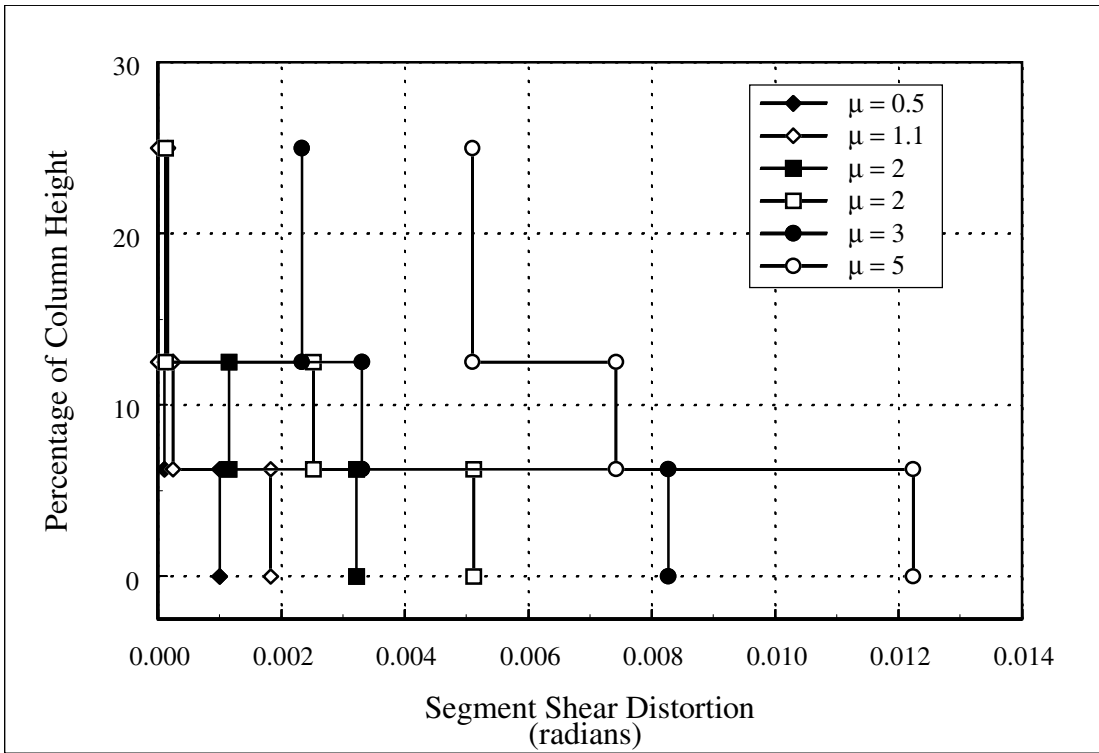


Figure C.98: Column 815 Shear-Strain Profile

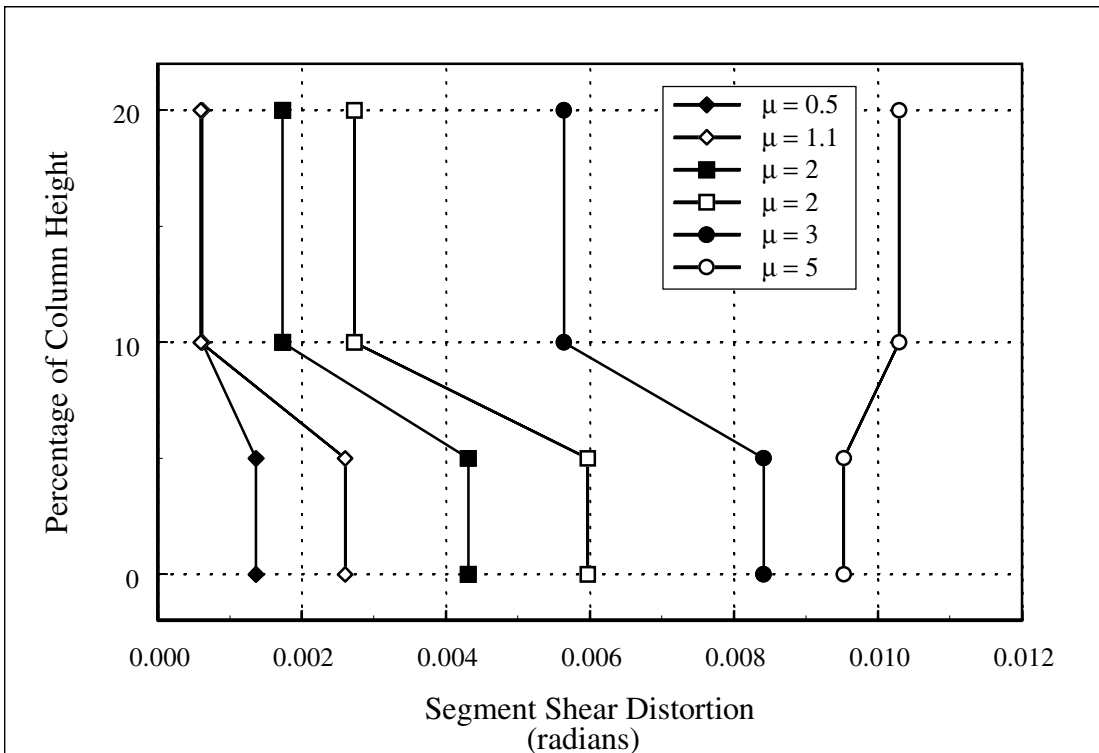


Figure C.99: Column 1015 Shear-Strain Profile

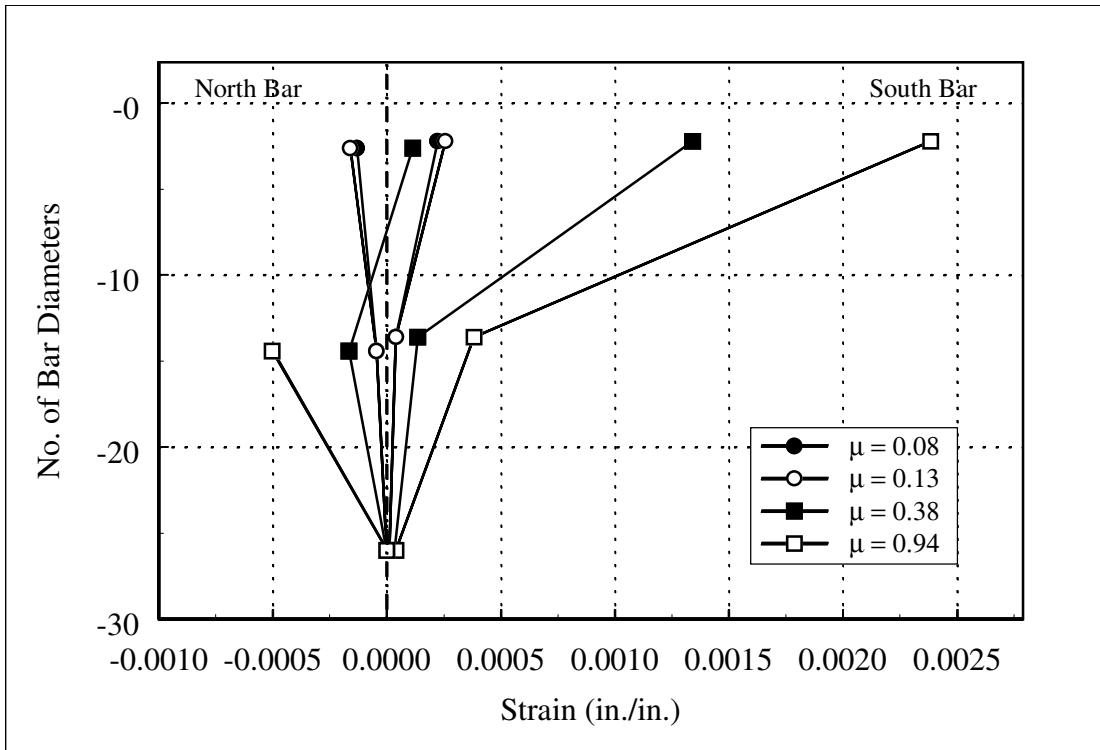


Figure C.100: Column 407 Longitudinal Strain Profile in Joint: Initial Displacement Cycles

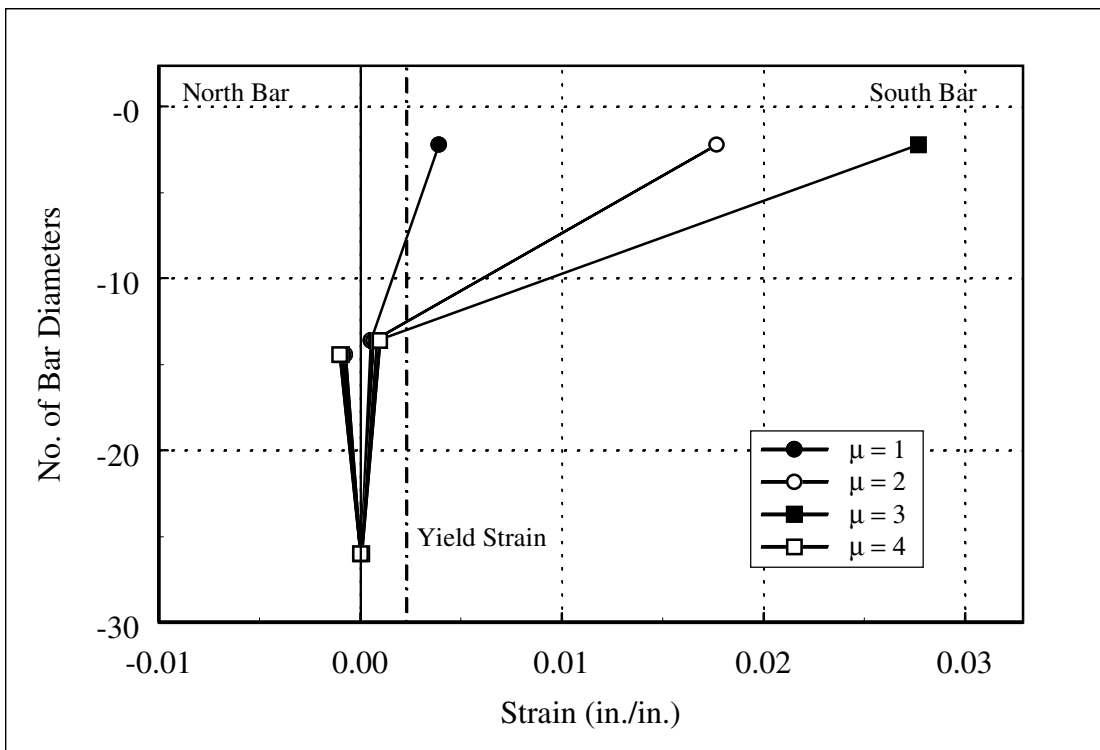


Figure C.101: Column 407 Longitudinal Strain Profile in Joint: Final Displacement Cycles

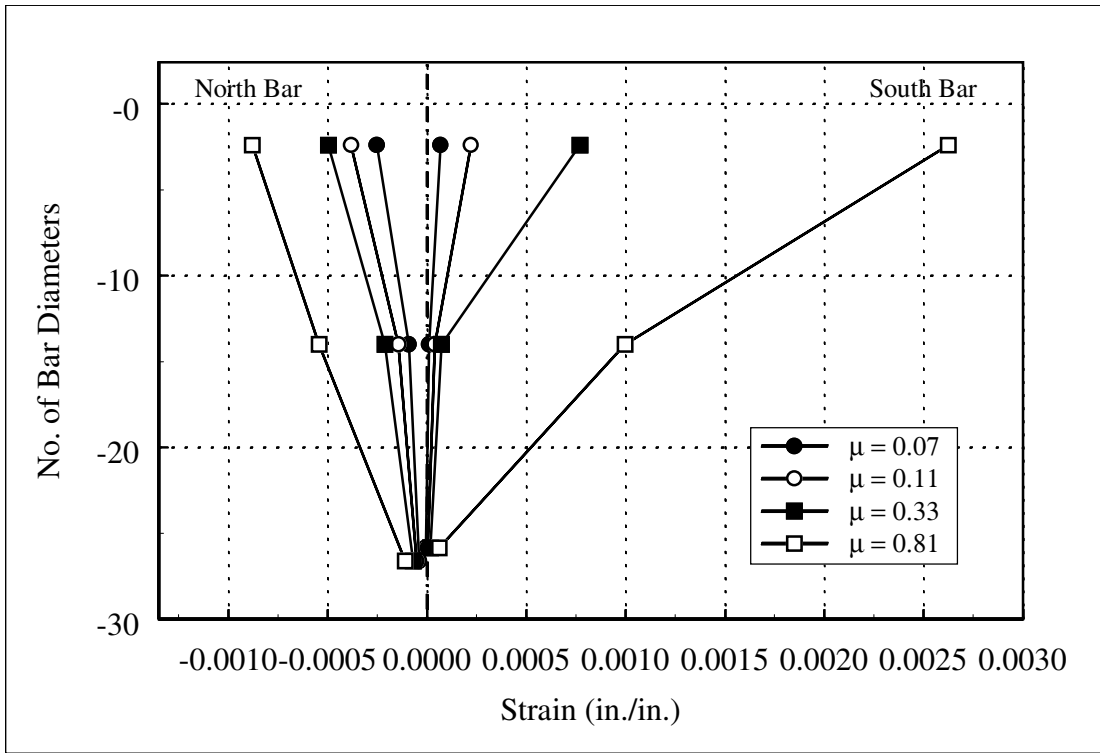


Figure C.102: Column 415 Longitudinal Strain Profile in Joint: Initial Displacement Cycles

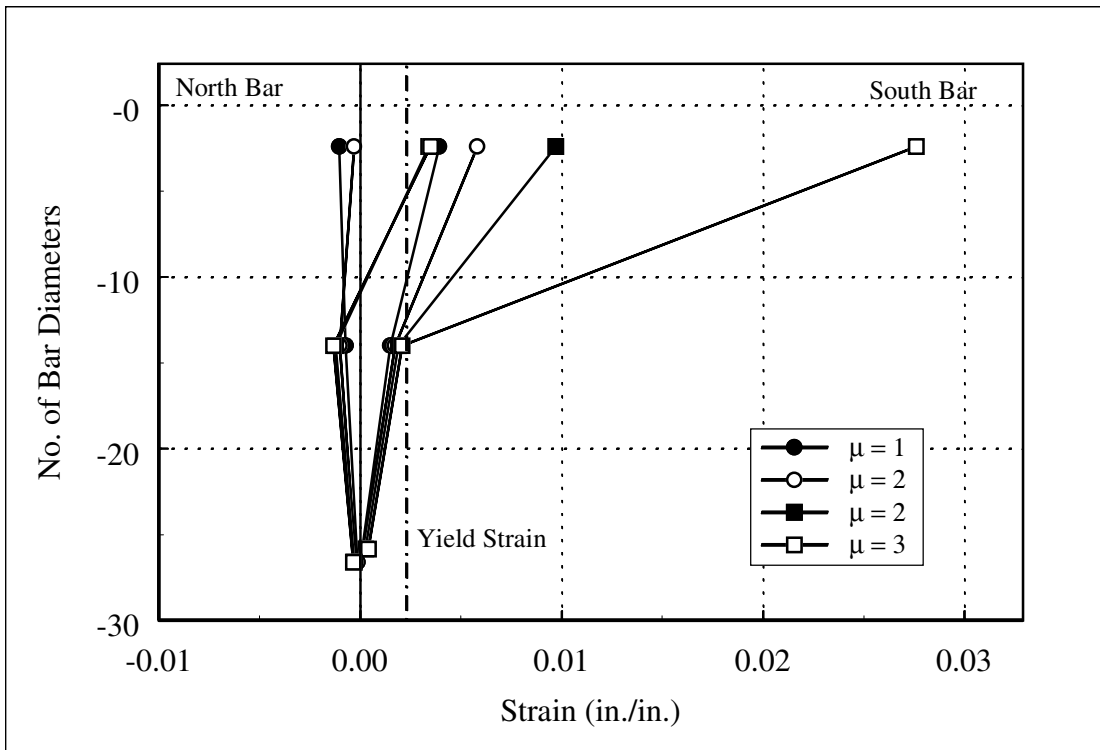


Figure C.103: Column 415 Longitudinal Strain Profile in Joint: Final Displacement Cycles

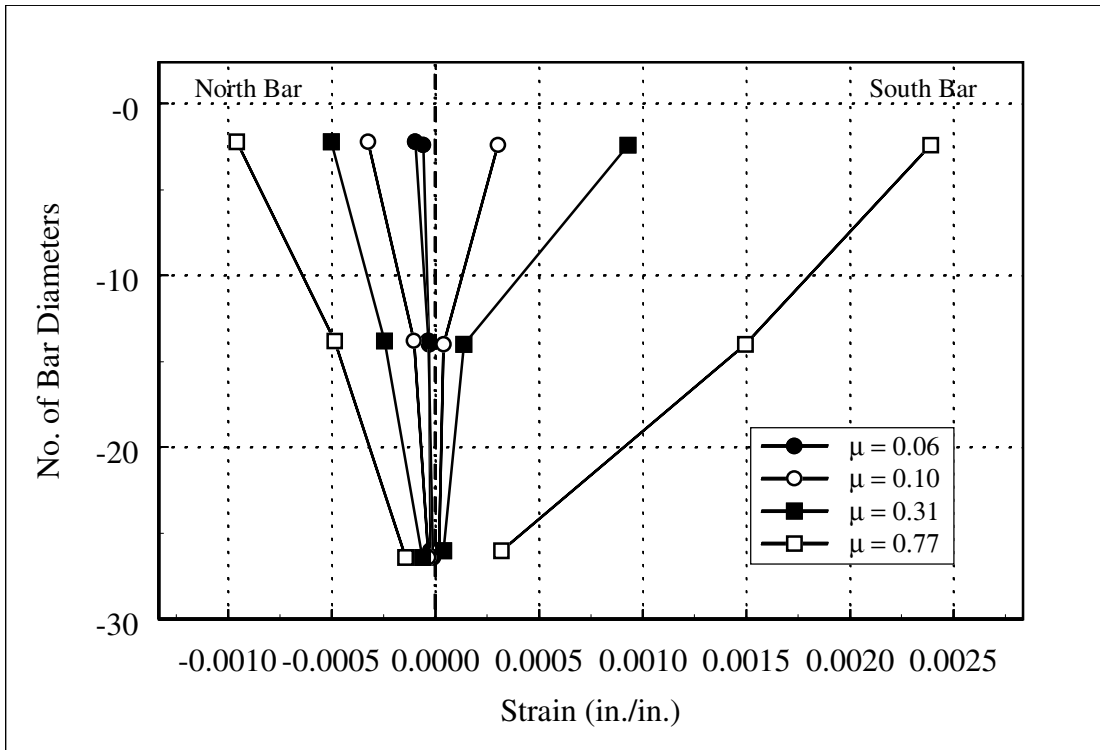


Figure C.104: Column 430 Longitudinal Strain Profile in Joint: Initial Displacement Cycles

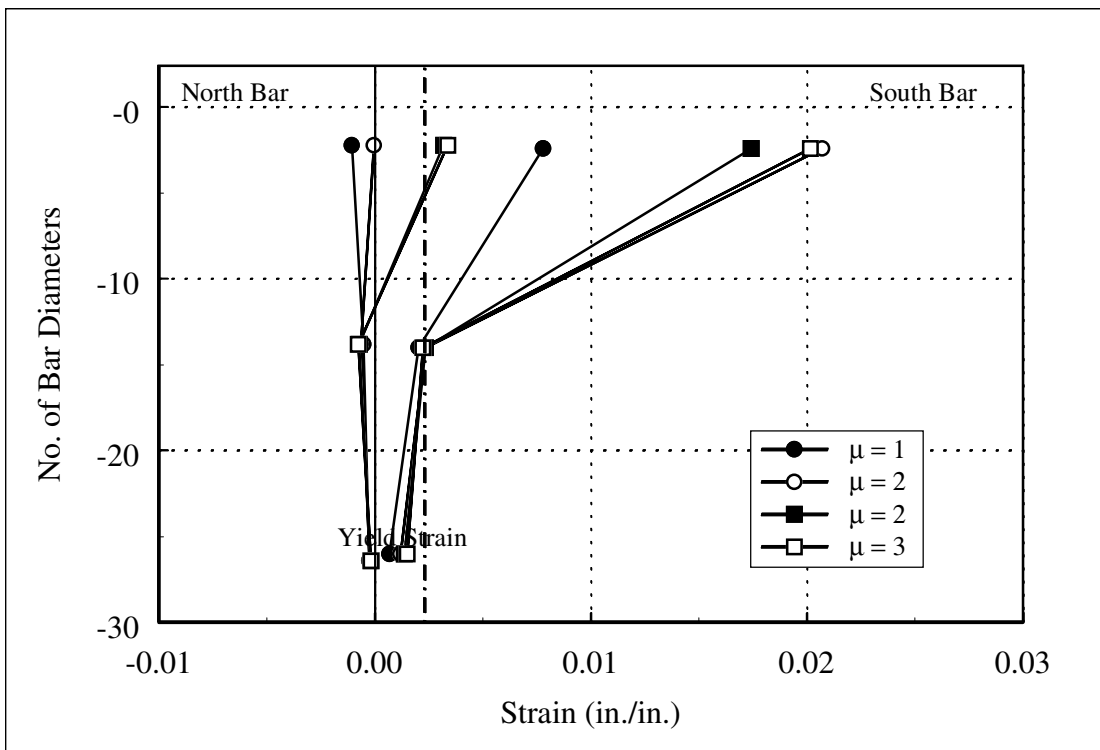


Figure C.105: Column 430 Longitudinal Strain Profile in Joint: Final Displacement Cycles

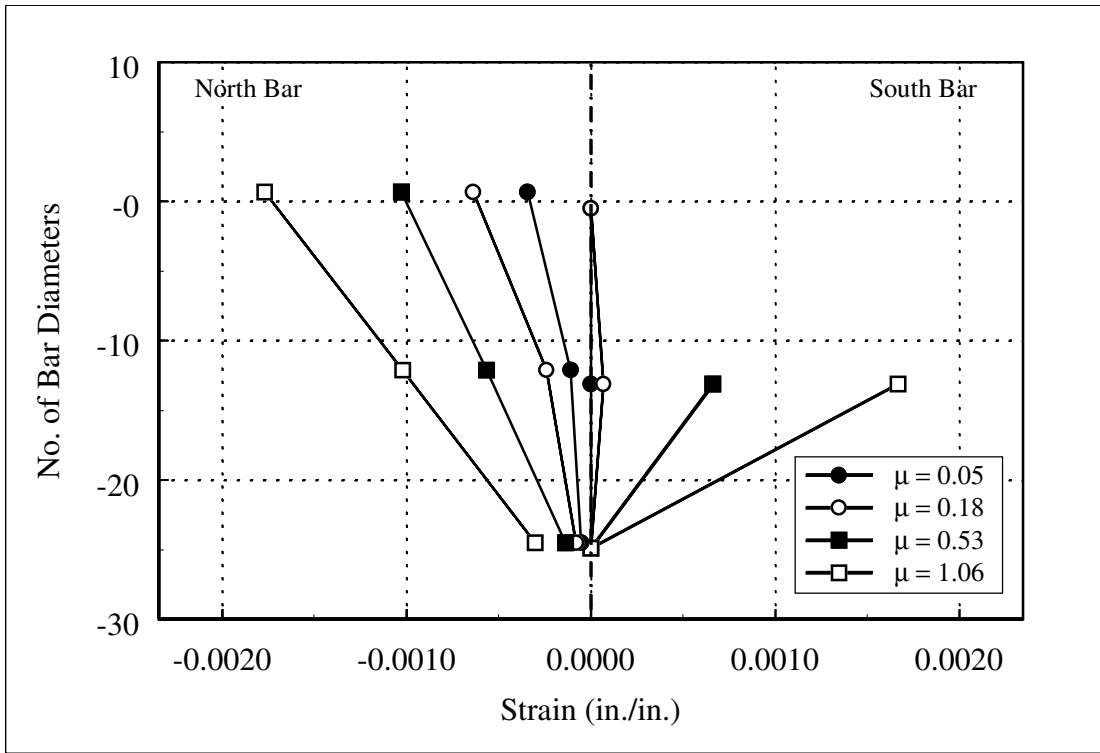


Figure C.106: Column 815 Longitudinal Strain Profile in Joint: Initial Displacement Cycles

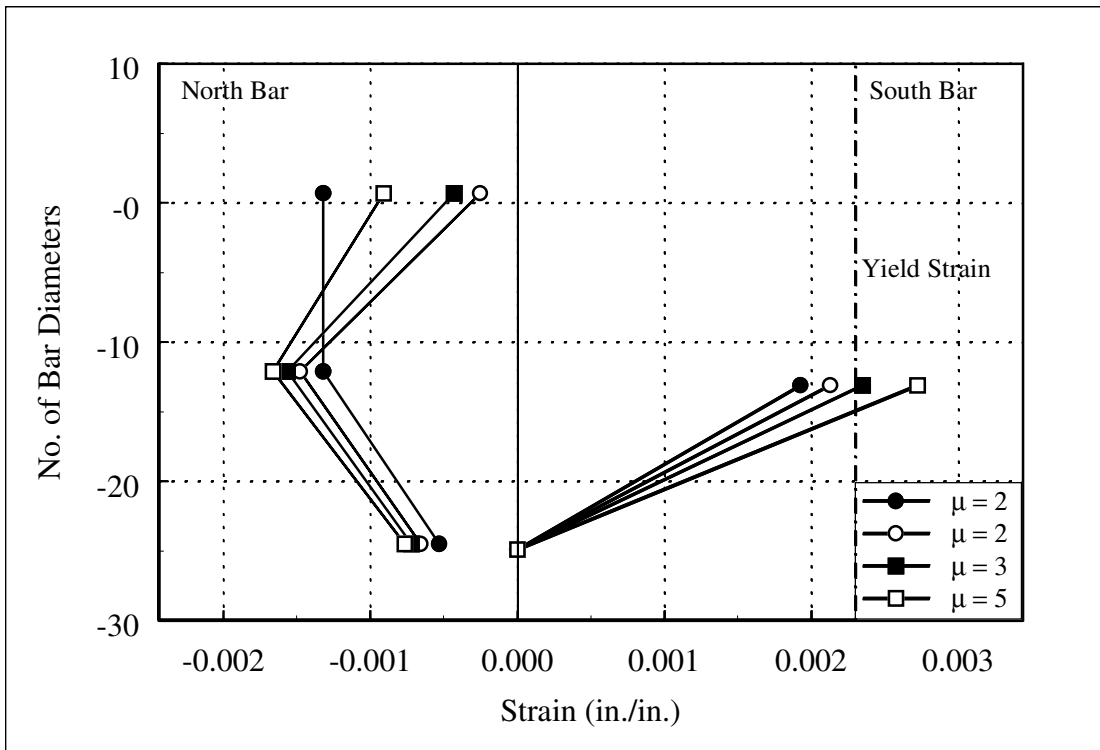


Figure C.107: Column 815 Longitudinal Strain Profile in Joint: Final Displacement Cycles

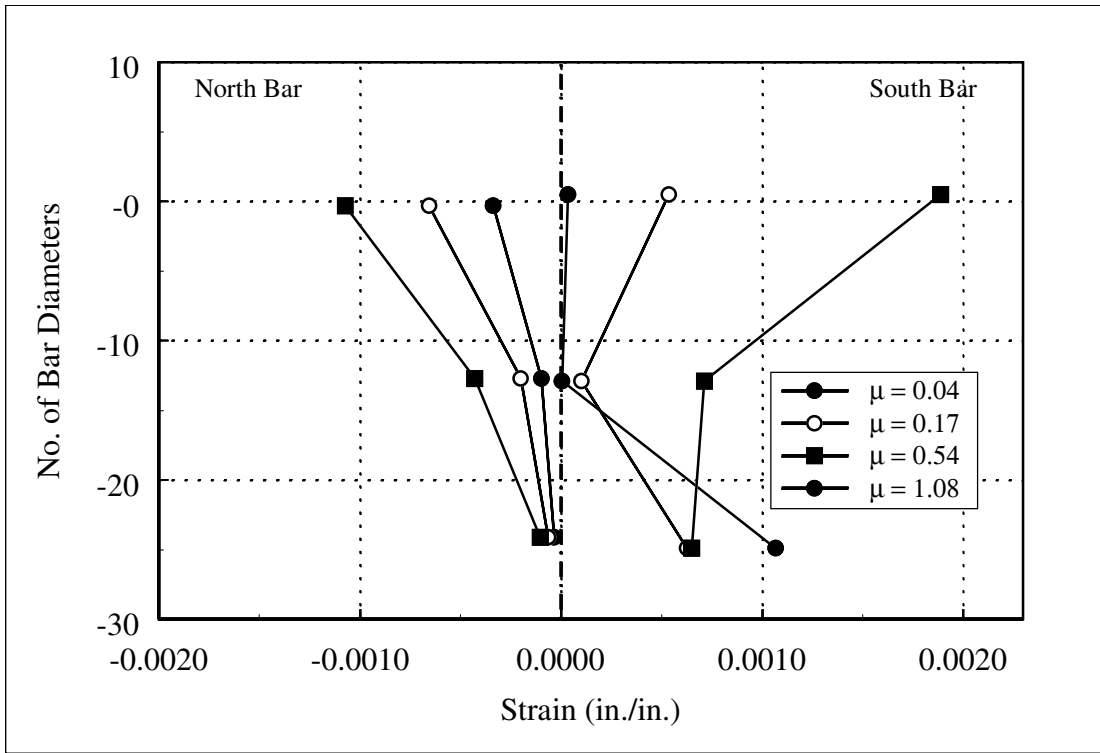


Figure C.108: Column 1015 Longitudinal Strain Profile in Joint: Initial Displacement Cycles

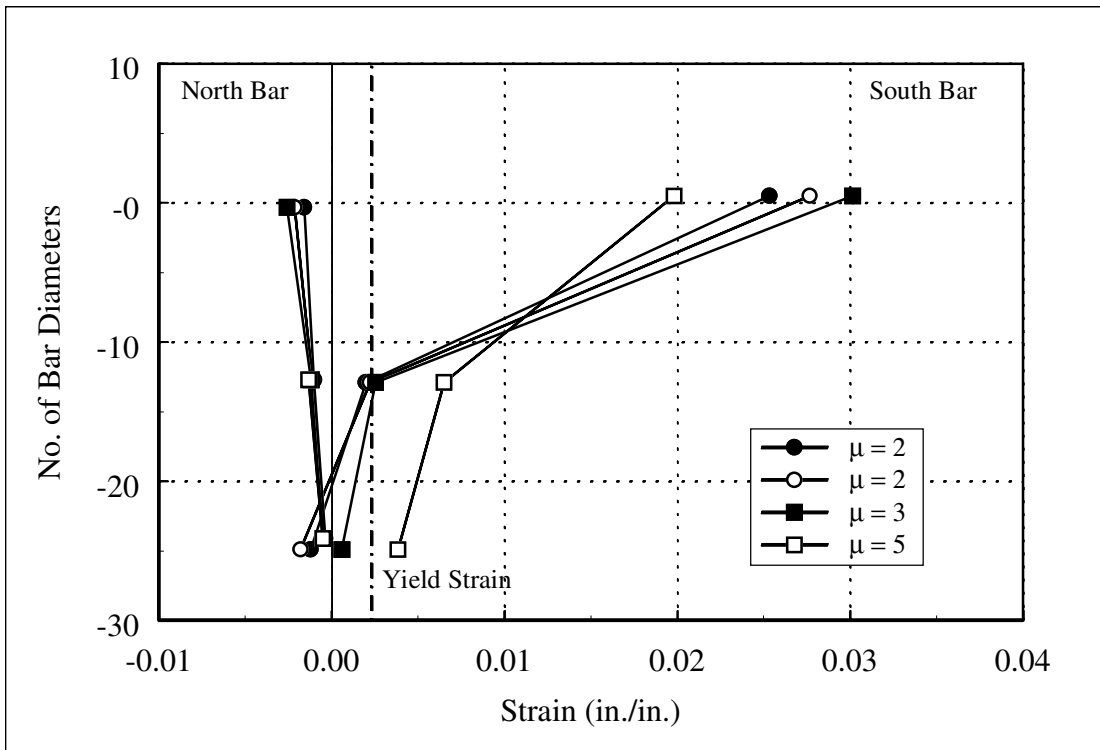


Figure C.109: Column 1015 Longitudinal Strain Profile in Joint: Final Displacement Cycles

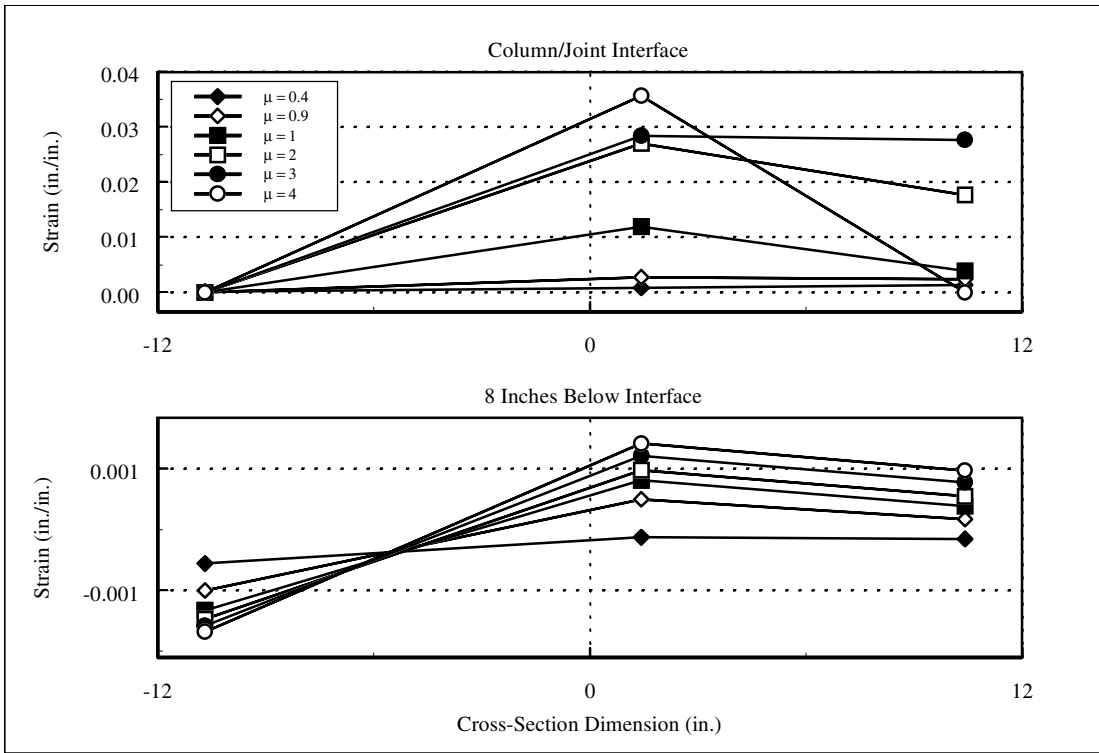


Figure C.110: Column 407 Strain Profile over Column Cross Section

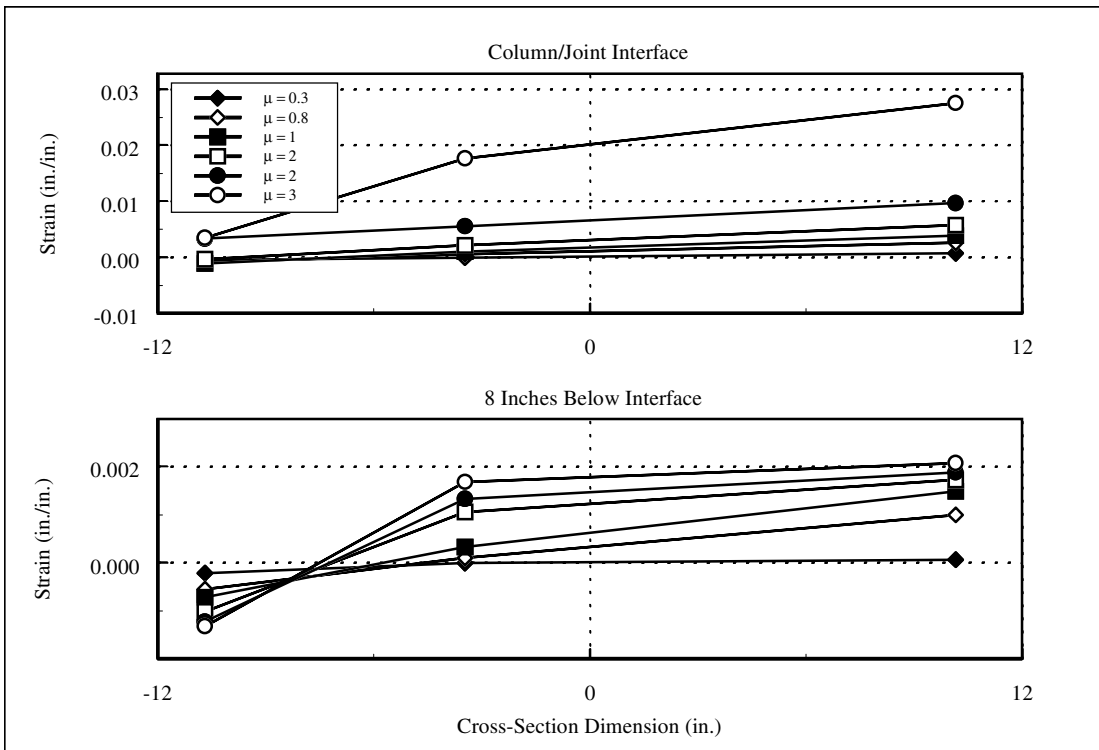
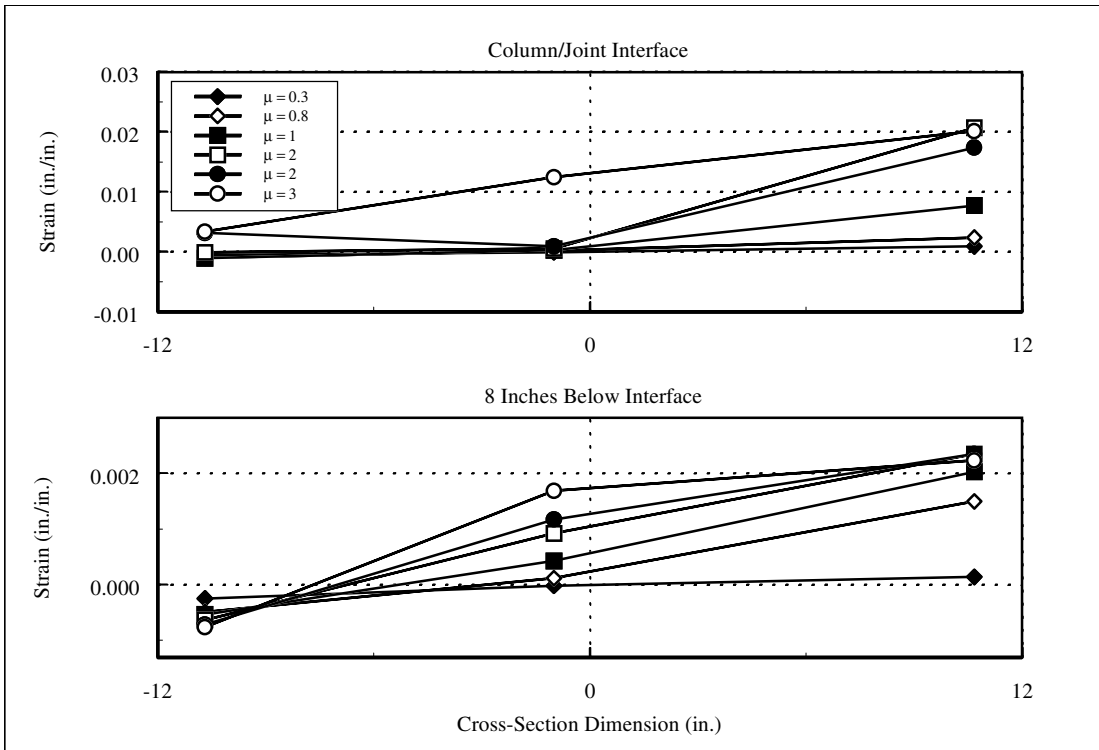
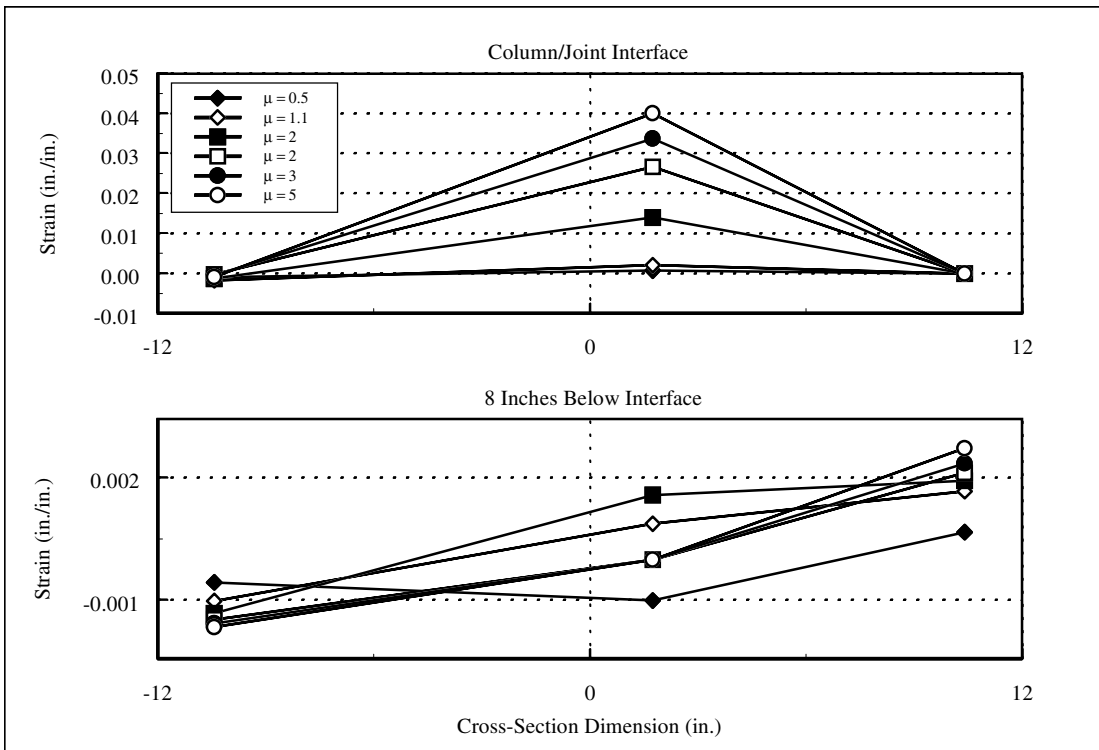


Figure C.111: Column 415 Strain Profile over Column Cross Section



**Figure C.112: Column 430 Strain Profile over Column Cross Section**



**Figure C.113: Column 815 Strain Profile over Column Cross Section**

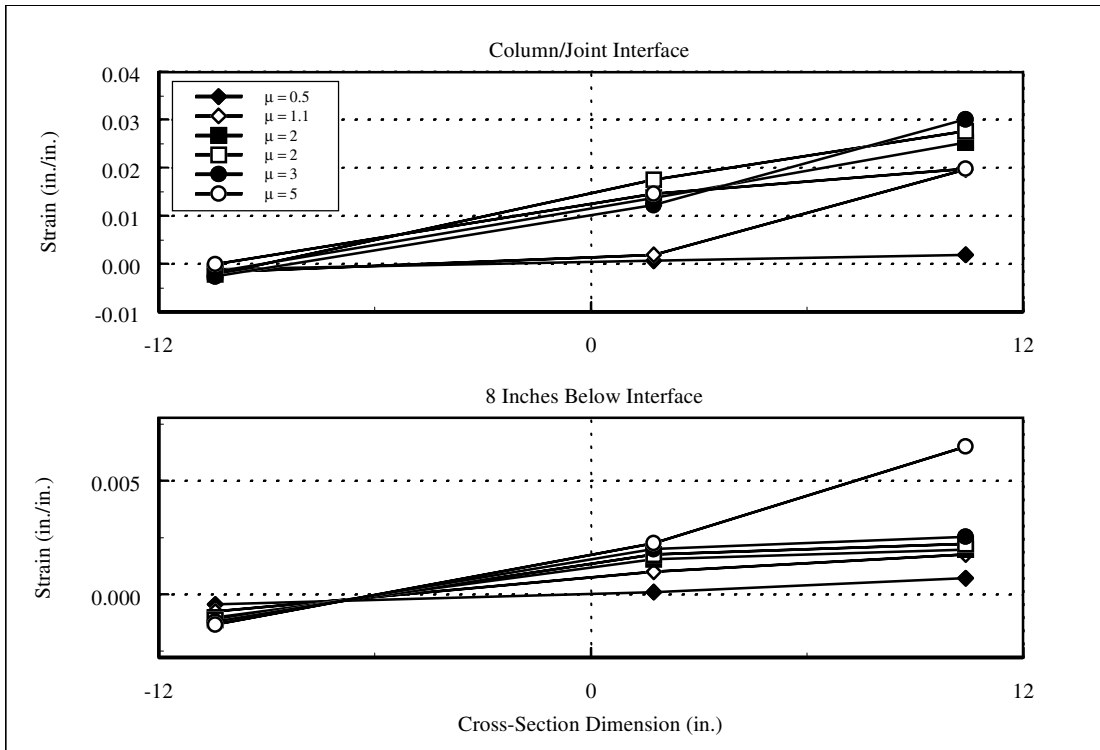


**Figure C.114: Column 1015 Strain Profile over Column Cross Section**

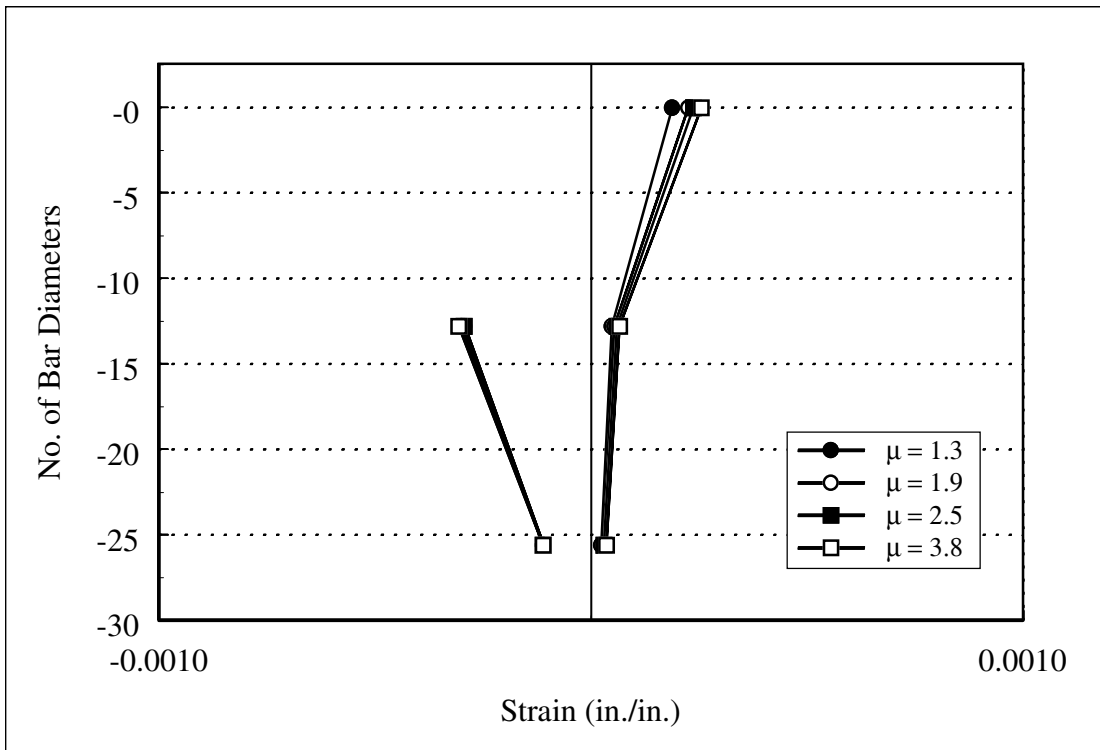


**Figure C.115: Column 407 Concrete Strain Profile in Joint**

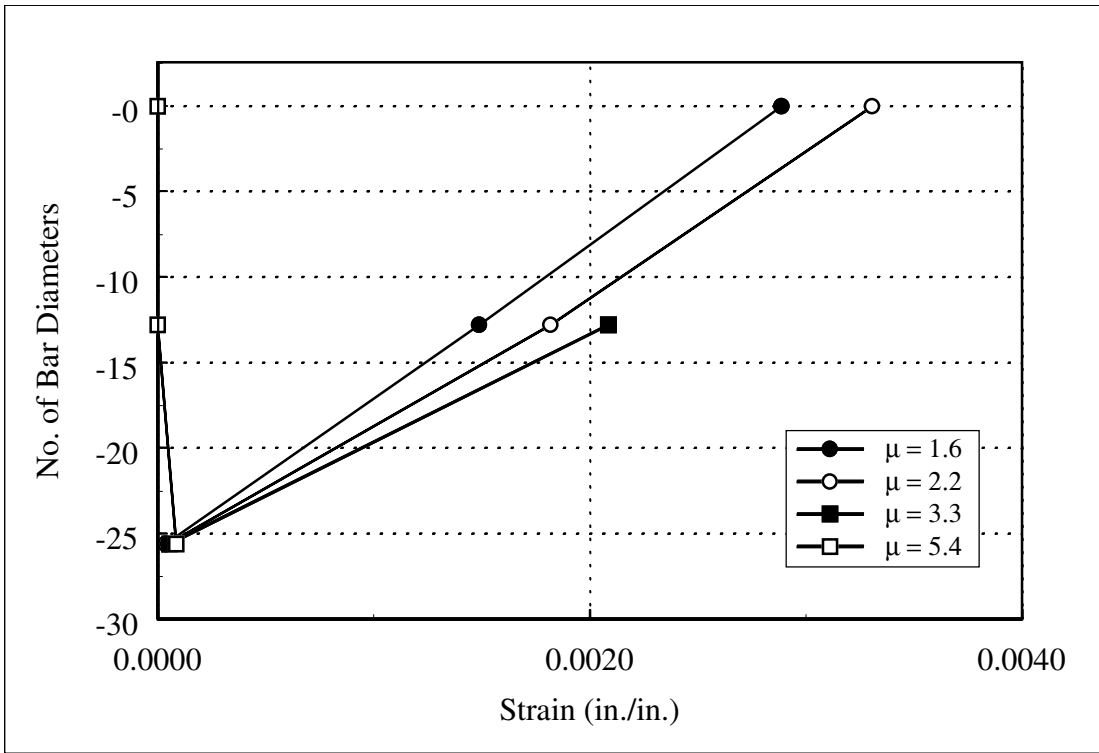


**Figure C.116: Column 415 Concrete Strain Profile in Joint**

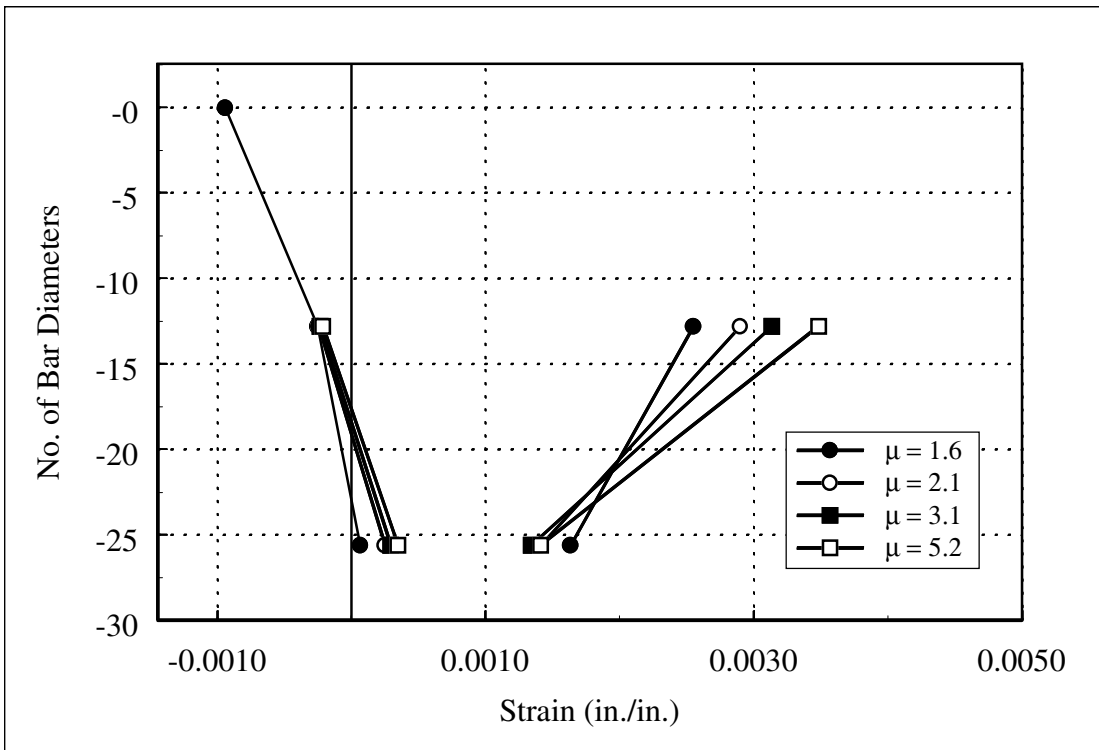


**Figure C.117: Column 430 Concrete Strain Profile in Joint**

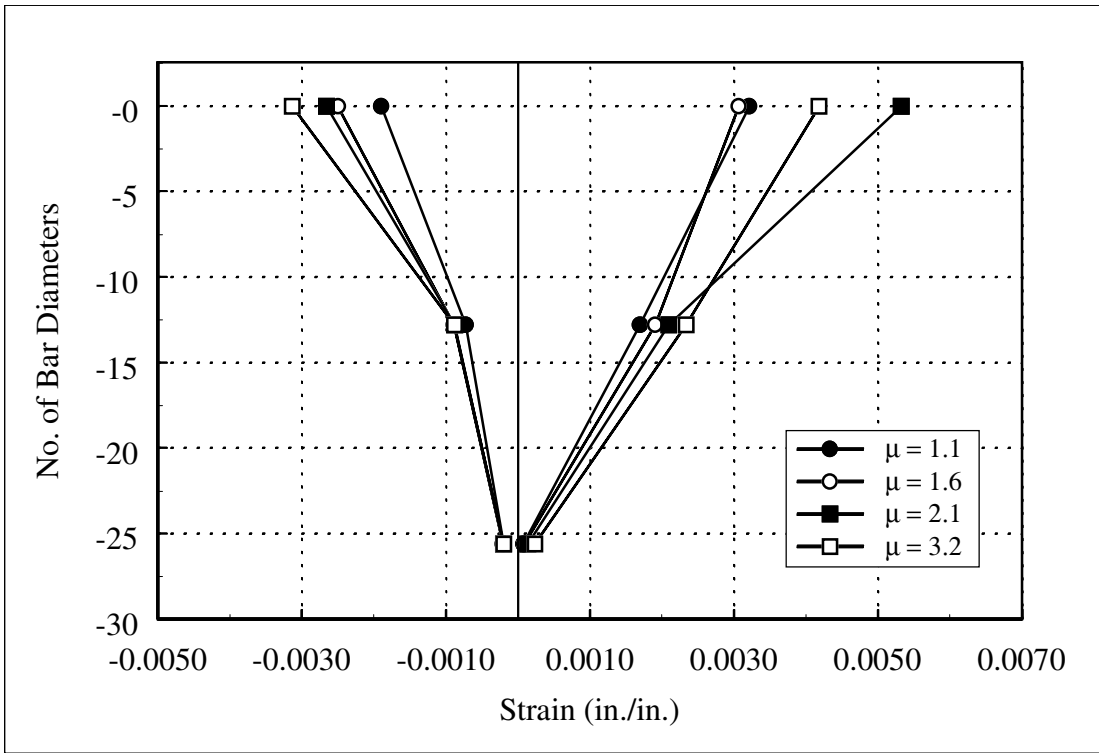


**Figure C.118: Column 815 Concrete Strain Profile in Joint**

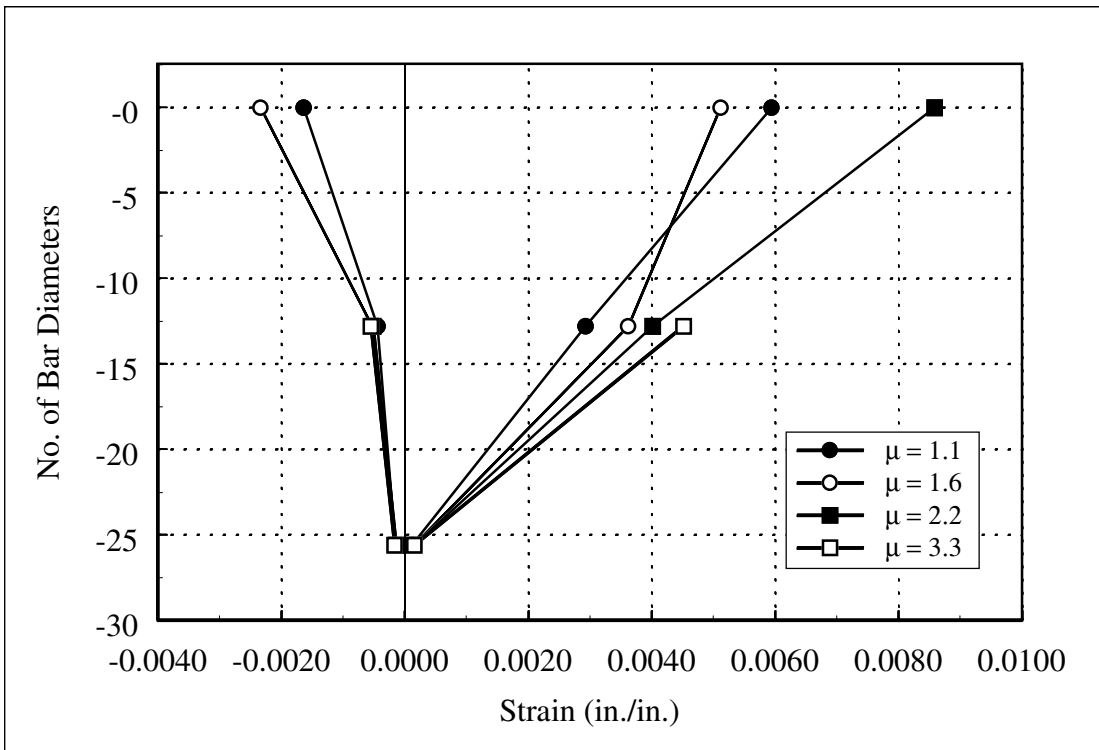


**Figure C.119: Column 1015 Concrete Strain Profile in Joint**

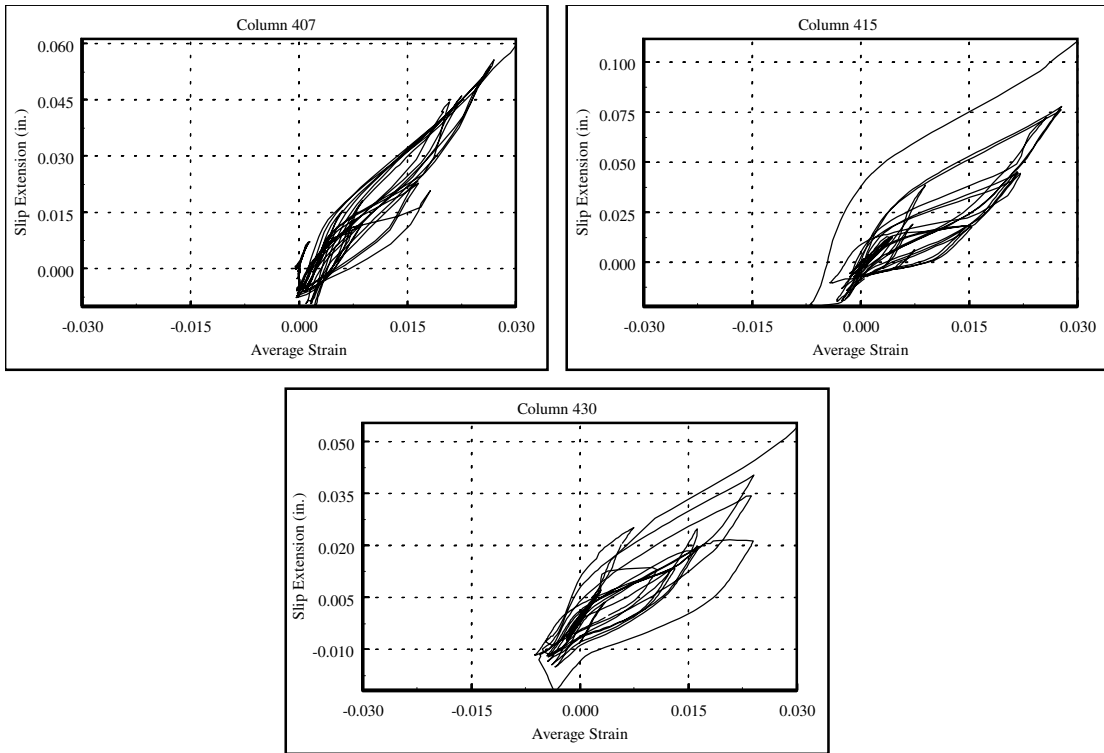


**Figure C.120: Column Series I Slip-Strain Response**

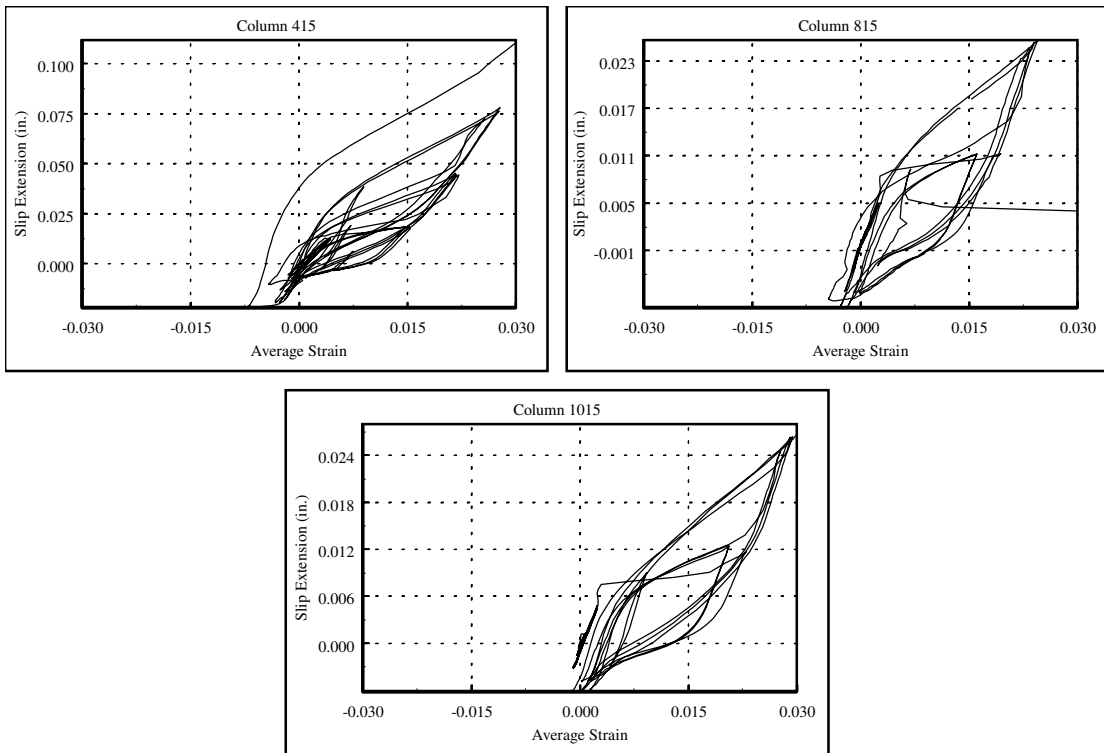


**Figure C.121: Column Series II Slip-Strain Response**

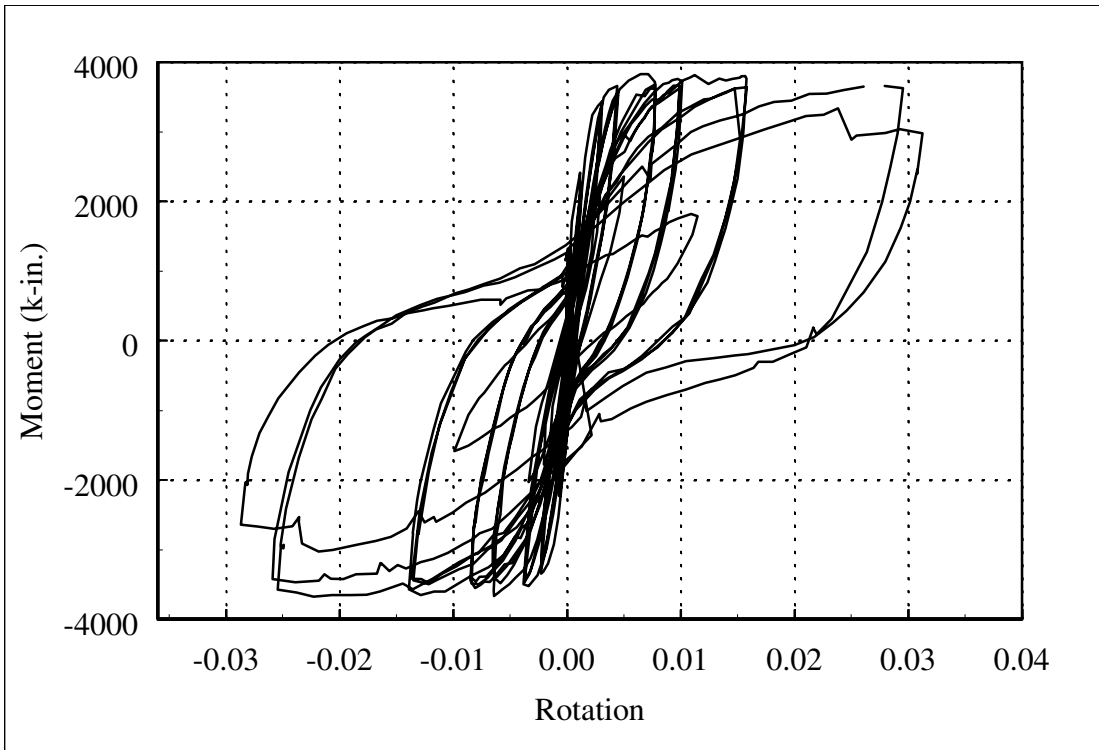


**Figure C.122: Column 407 Moment-Rotation Response of Bottommost Segment**

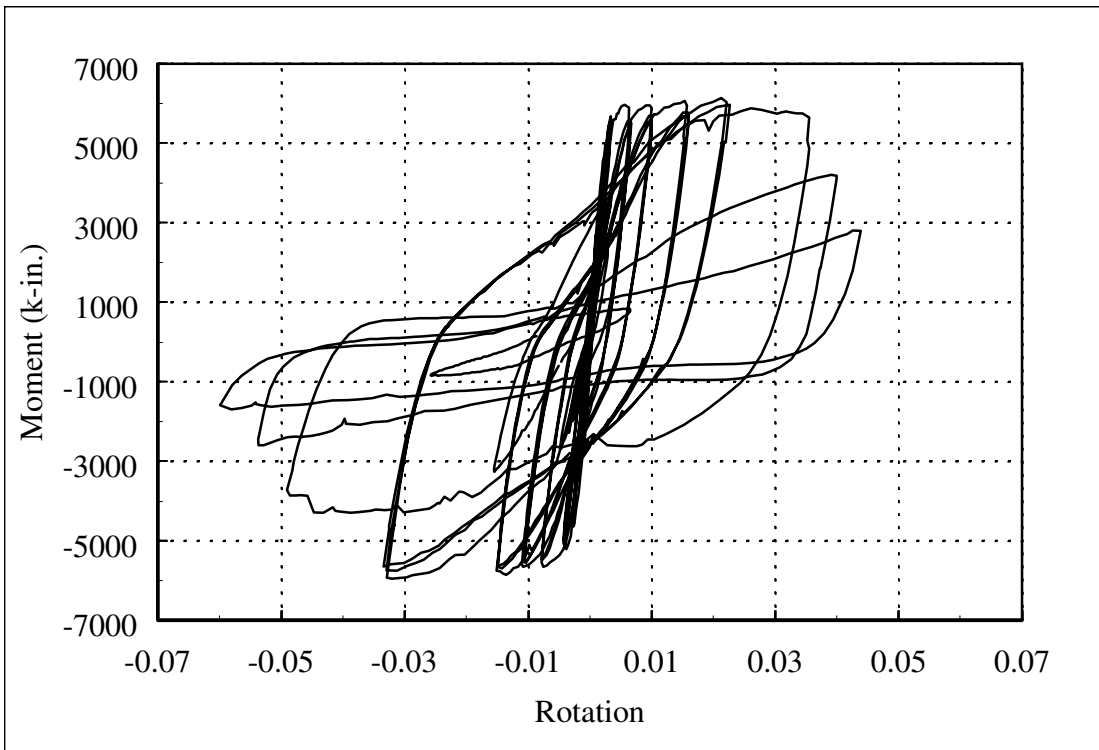


**Figure C.123: Column 415 Moment-Rotation Response of Bottommost Segment**

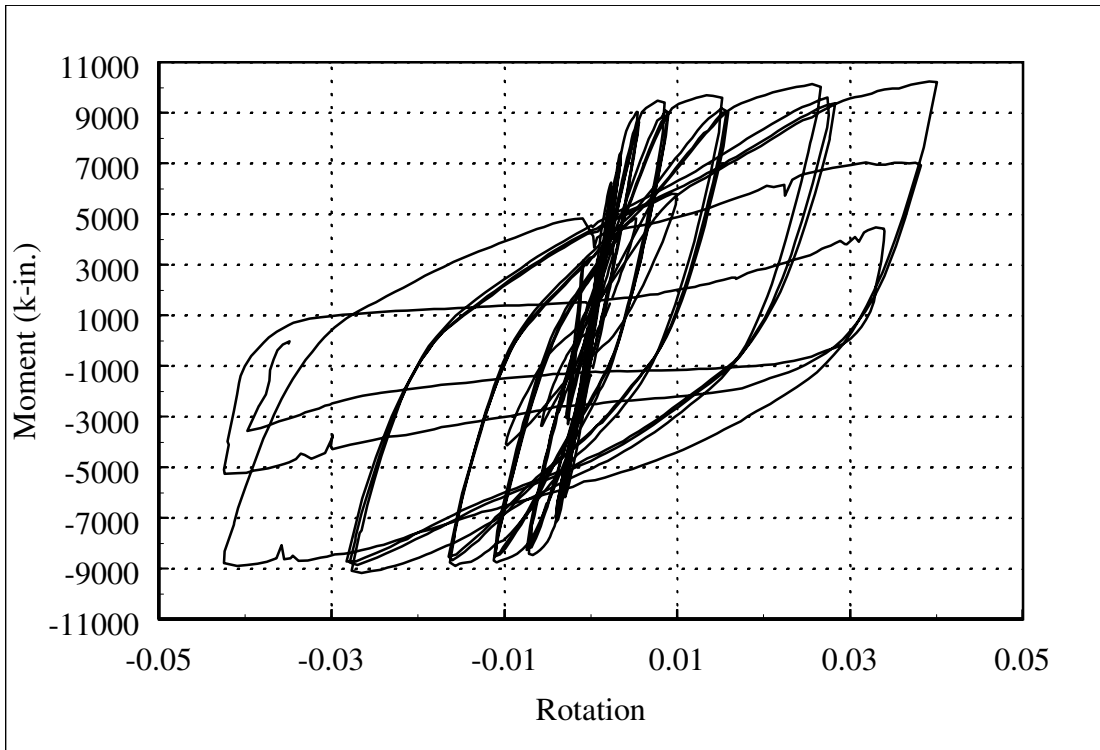


**Figure C.124: Column 430 Moment-Rotation Response of Bottommost Segment**

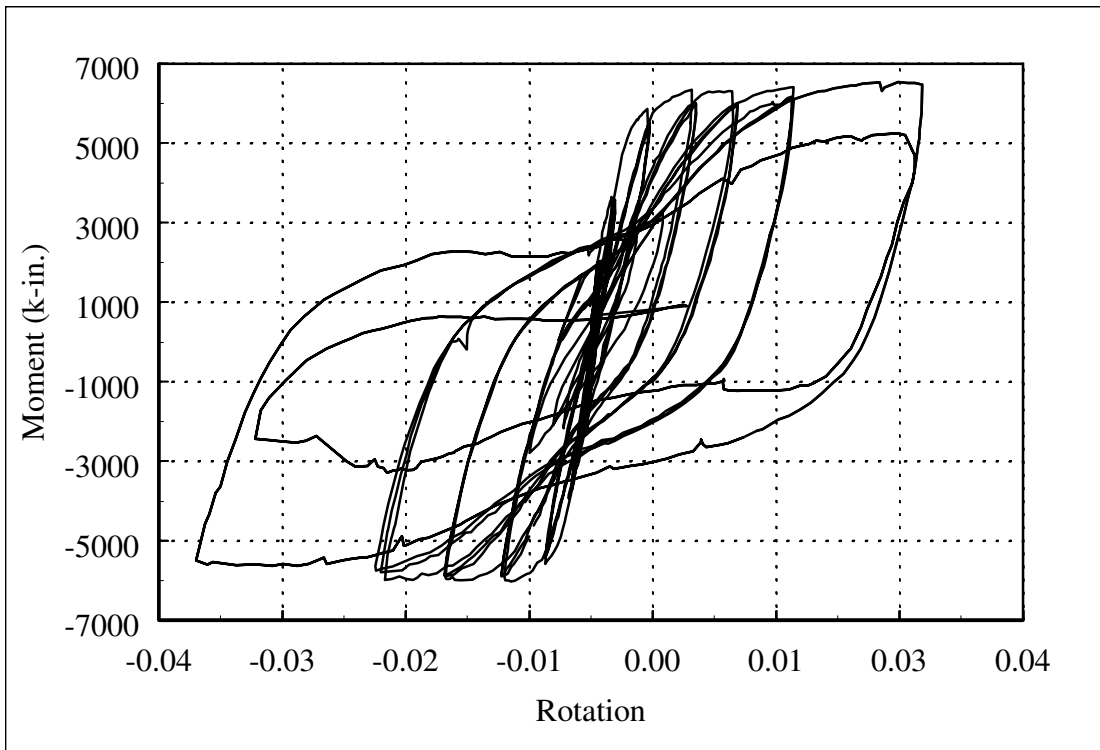


**Figure C.125: Column 815 Moment-Rotation Response of Bottommost Segment**

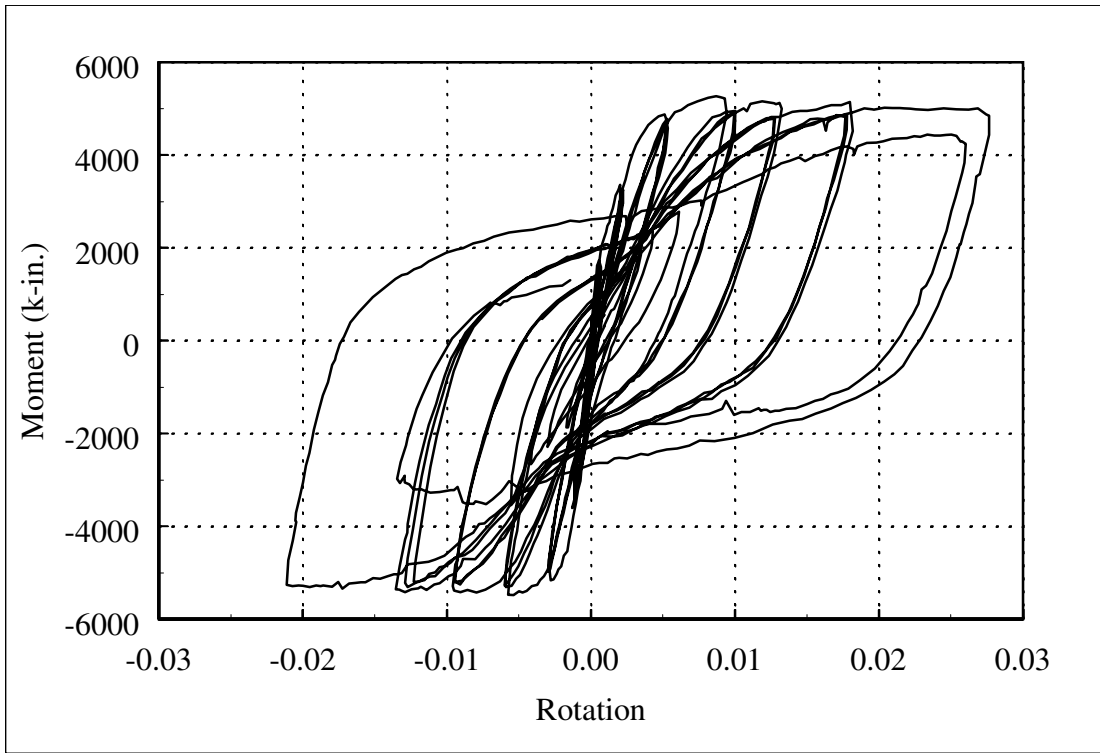


Figure C.126: Column 1015 Moment-Rotation Response of Bottommost Segment

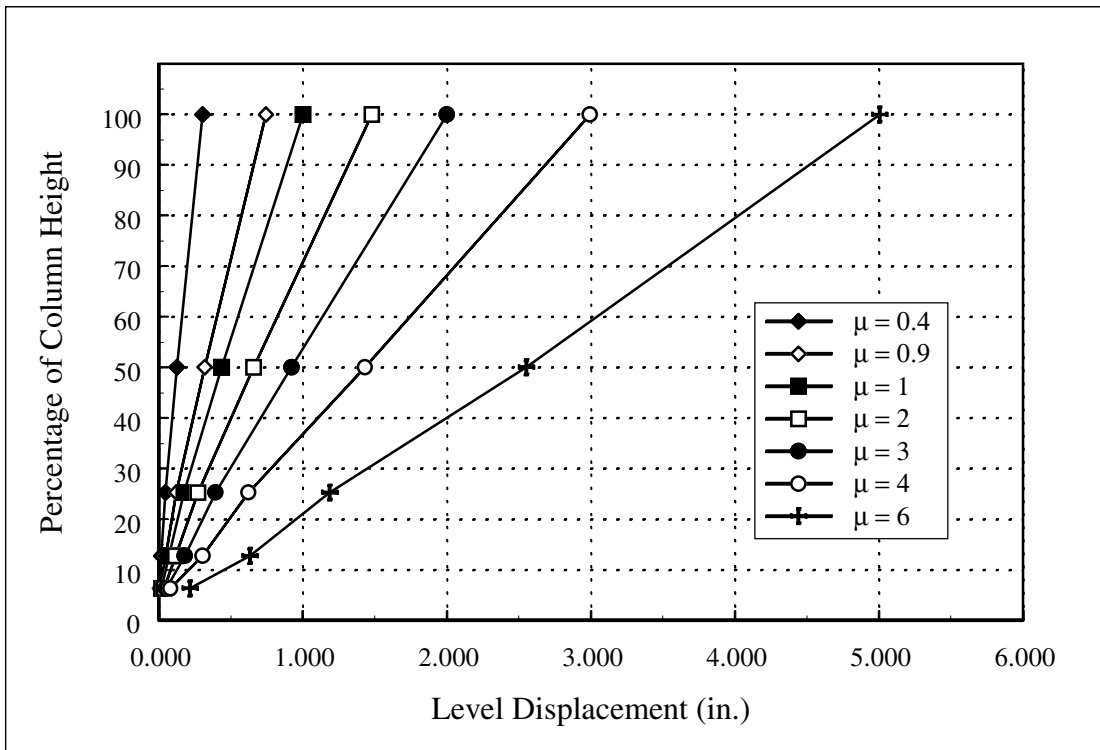


Figure C.127: Column 407 Displacement Profile

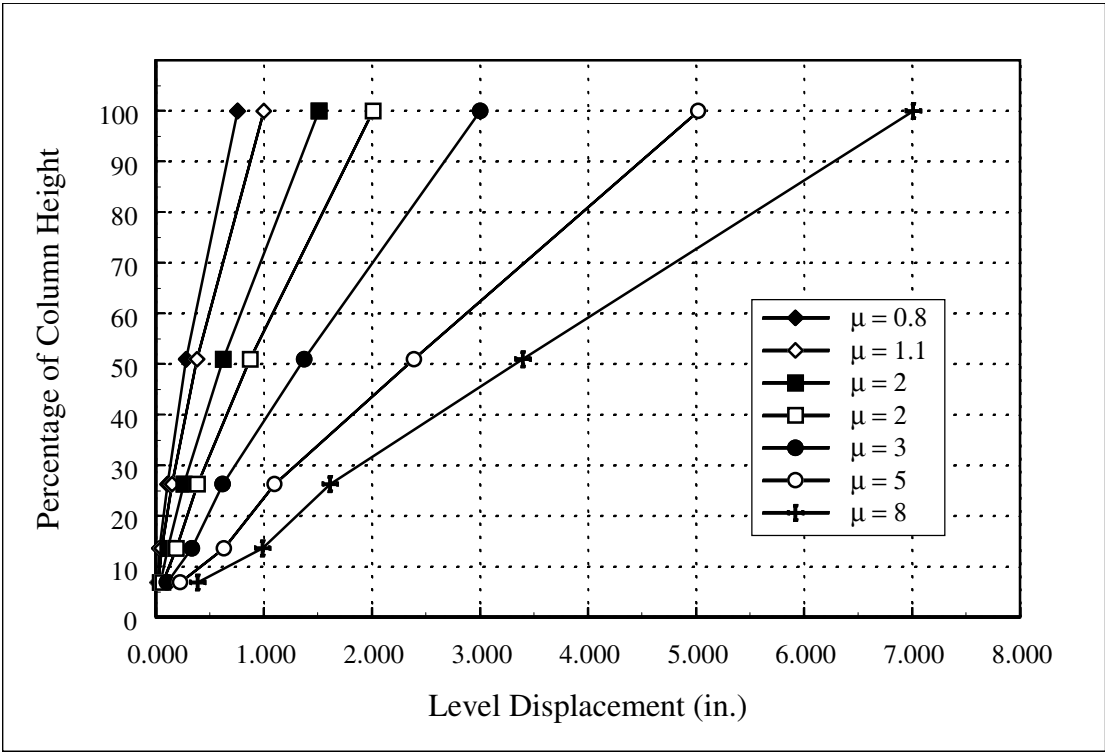


Figure C.128: Column 415 Displacement Profile

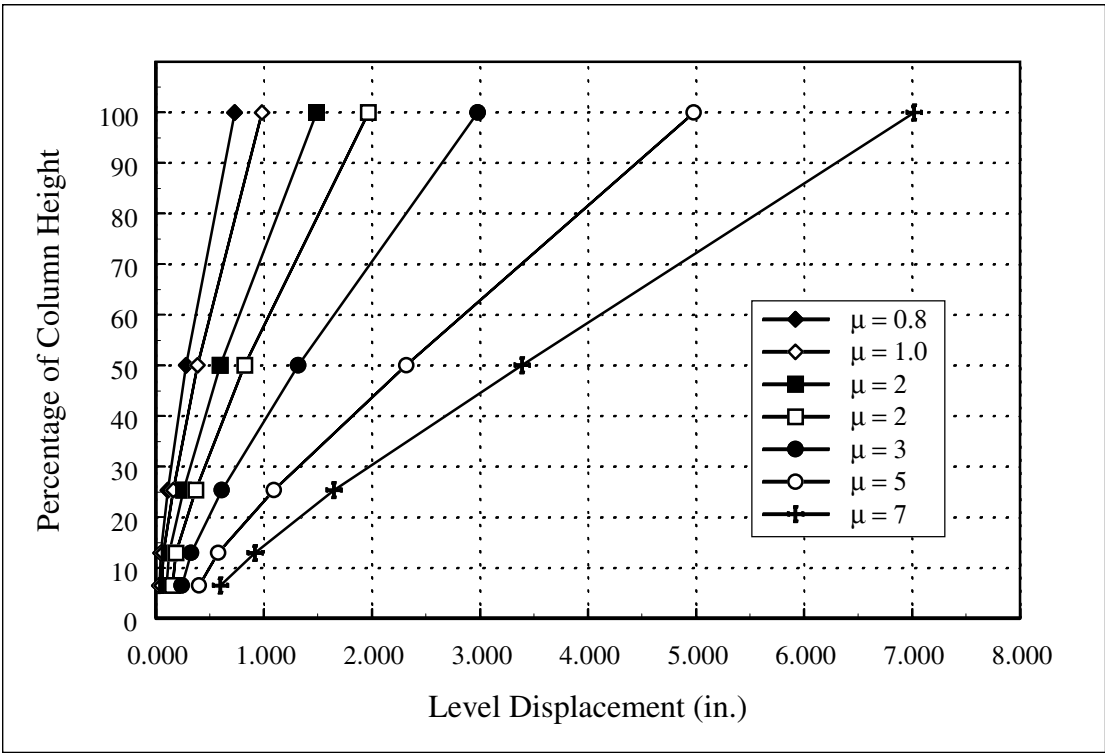


Figure C.129: Column 430 Displacement Profile

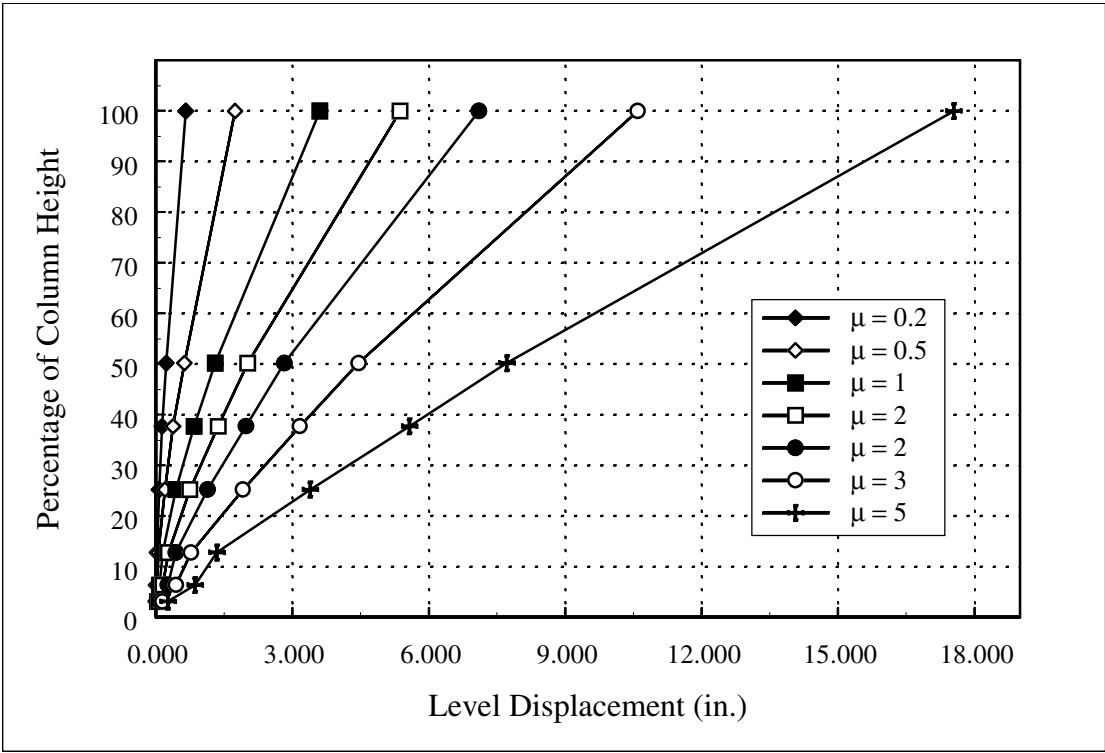


Figure C.130: Column 815 Displacement Profile

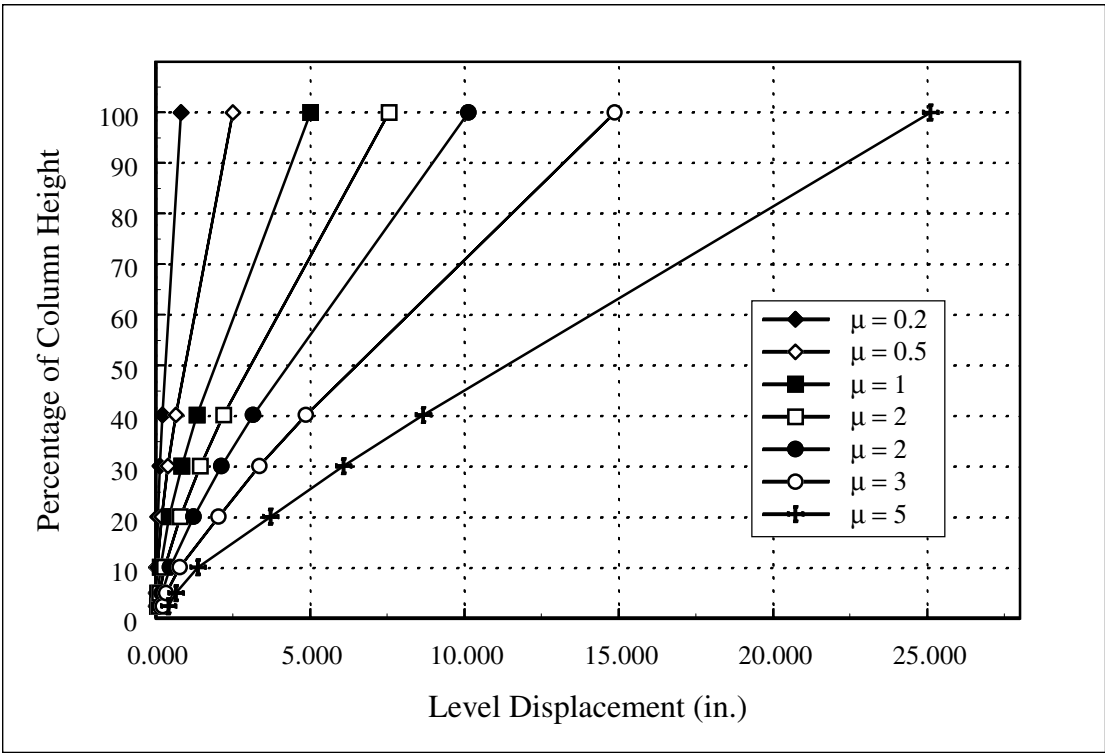
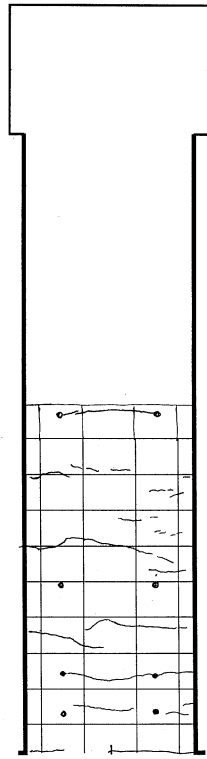


Figure C.131: Column 1015 Displacement Profile

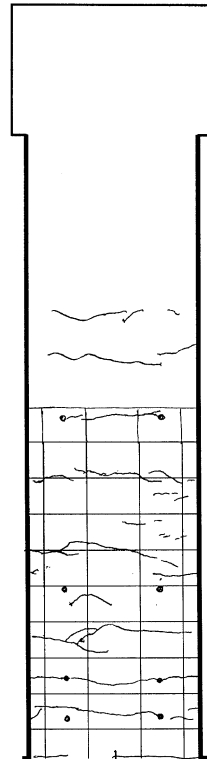
## Appendix D Crack Patterns

Crack patterns were marked on the columns during the first displacement cycle to the north and the south at each displacement level. The progression of cracking was monitored by updating crack sheets for each cycle. In the following figures, the cracks marked during the first south cycle for four displacement levels are provided for each column. The crack patterns shown were those marked on the north face.

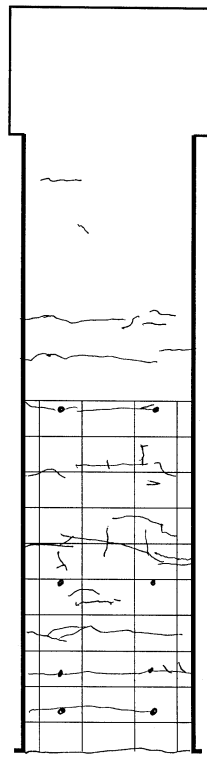
Each figure shows the column outline. Within the outline vertical and horizontal interior lines are drawn; the lines correspond to the lines drawn on the column prior to testing. On the column, the lines were spaced at 5 inches horizontally and 7.5 inches in circumference.



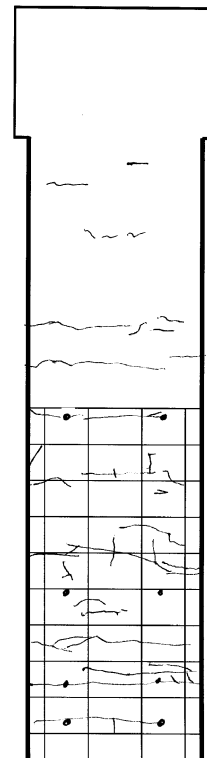
(a) 0.3-Inch Cycle



(b) 0.75-Inch Cycle

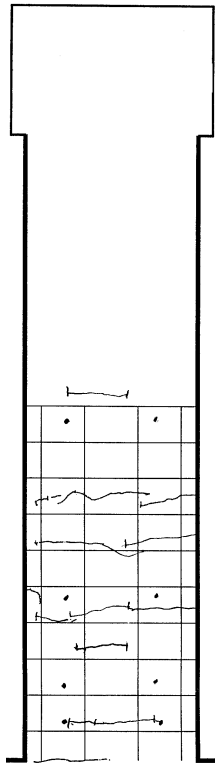


(c) 2.0-Inch Cycle

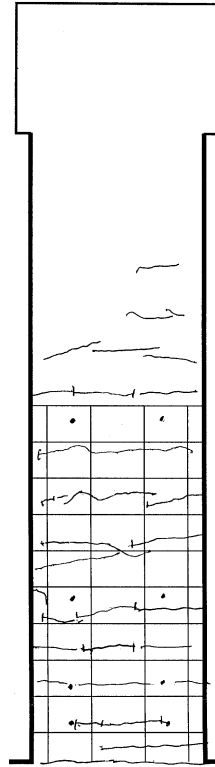


(d) 5.0-Inch Cycle

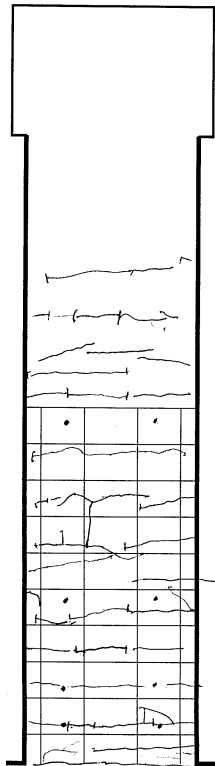
**Figure D.1: Crack Patterns for Column 407**



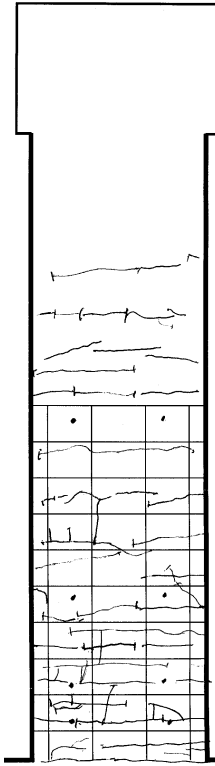
(a) 0.3-Inch Cycle



(b) 0.75-Inch Cycle

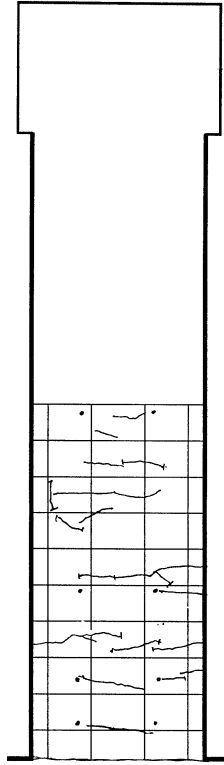


(c) 2.0-Inch Cycle

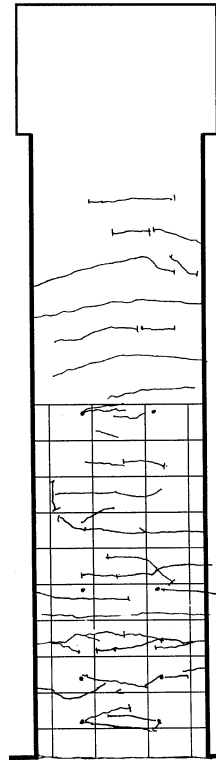


(d) 5.0-Inch Cycle

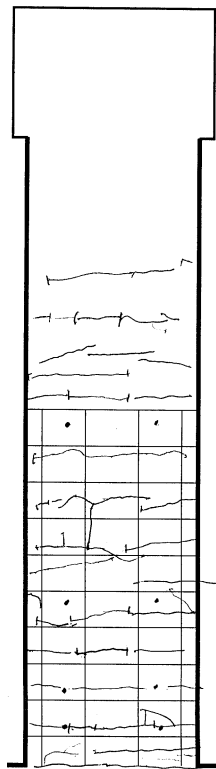
**Figure D.2: Column 415 Crack Patterns**



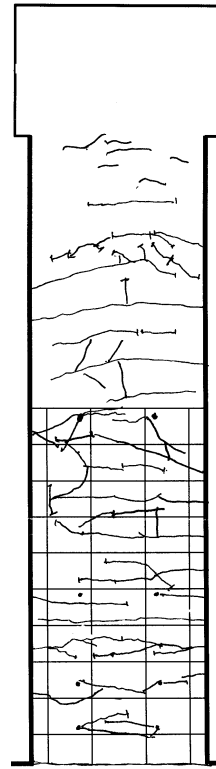
(a) 0.3-Inch Cycle



(b) 0.75-Inch Cycle

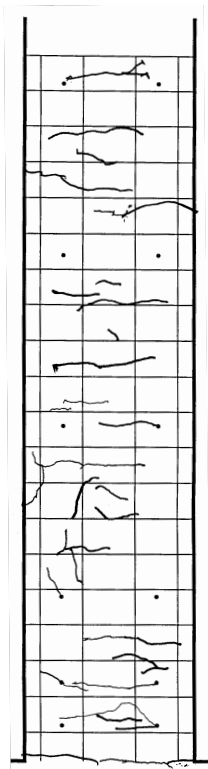


(c) 2.0-Inch Cycle

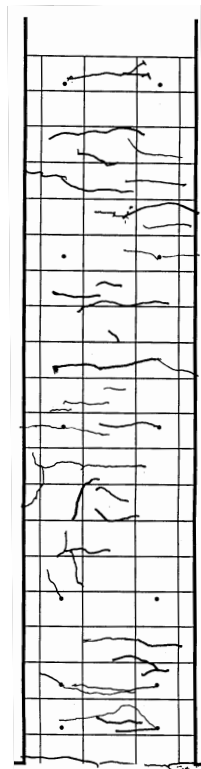


(d) 5.0-Inch Cycle

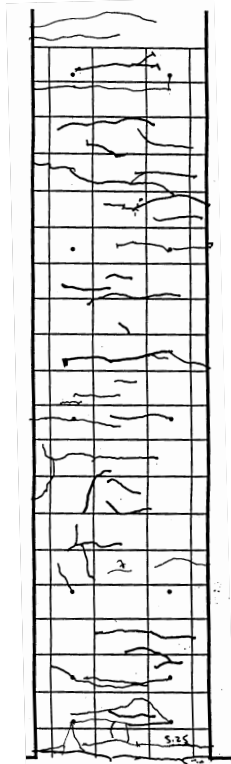
**Figure D.3: Column 430 Crack Patterns**



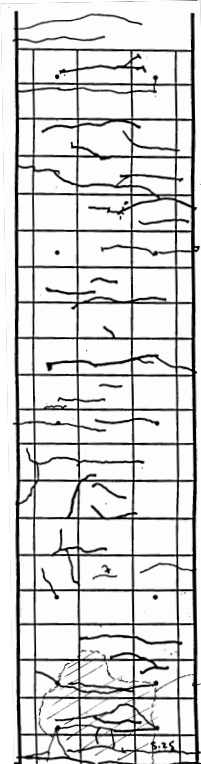
(a) 1.75-Inch Cycle



(b) 3.5-Inch Cycle

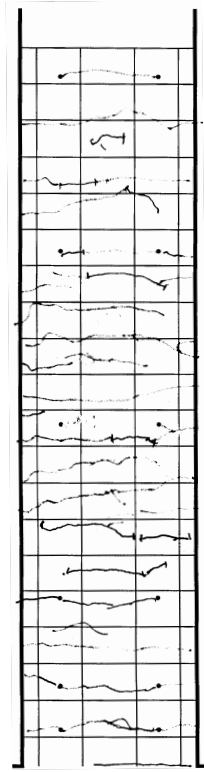


(c) 7-Inch Cycle

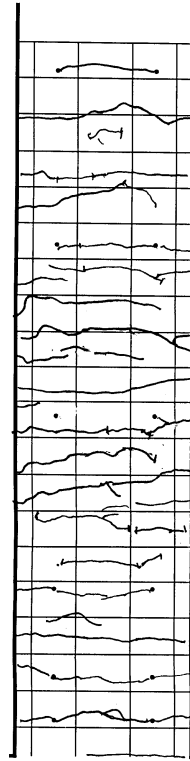


(d) 17.5-Inch Cycle

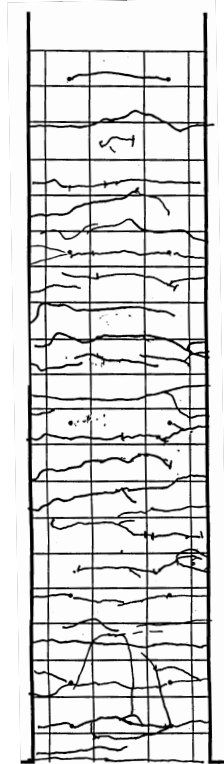
**Figure D.4: Column 815 Crack Patterns**



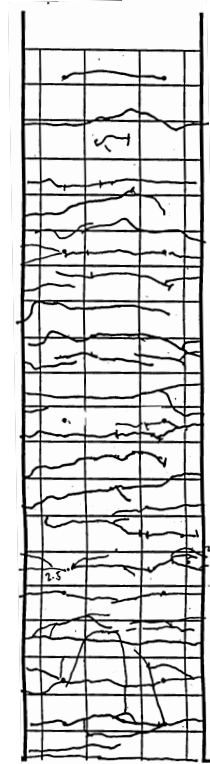
(a) 2.5-Inch Cycle



(b) 5.0-Inch Cycle



(c) 10-Inch Cycle



(d) 25-Inch Cycle

**Figure D.5: Column 1015 Crack Patterns**

## REFERENCES

- ACI.1995. American Concrete Institute. *Building Code Requirements for Reinforced Concrete (ACI 318-89) and Commentary*. Detroit, Mich.: ACI 318-95.
- AIJ. 1994. *AIJ Structural Design Guidelines for Reinforced Concrete Buildings*. Architectural Institute of Japan.
- Ang. 1981. Ghee, A. B. *Ductility of Reinforced Concrete Bridge Piers under Seismic Loading*. Christchurch, N.Z.: University of Canterbury, Department of Civil Engineering.
- Ang, Ghee, A. B.1985. *Seismic Shear Strength of Circular Bridge Piers*. University of Canterbury. Department of Civil Engineering Report 85-5. Christchurch, N.Z.: University of Canterbury, Department of Civil Engineering.
- Aschheim, M., Moehle, J. P., and Mahin, S. A. 1997. *Design and Evaluation of Reinforced Concrete Bridges for Seismic Resistance*. UCB/EERC-97/04. Berkeley, Calif.: Earthquake Engineering Research Center, University of California.
- Atalay, M. B., Penzien, J. 1975. *The Seismic Behavior of Critical Regions of Reinforced Concrete Components as Influenced by Moment, Shear and Axial Force*. Report No. EERC 75-19. Berkeley, Calif.: Earthquake Engineering Research Center, University of California.
- ATC. 1996. Applied Technology Council. *Improved Seismic Design Criteria for California Bridges: Provisional Recommendations*. Report ATC 32.
- Baker, A. L. L. 1956. *Ultimate Load Theory Applied to the Design of Reinforced and Prestressed Concrete Frames*. London: Concrete Publications Ltd.
- Baker, A. L. L. and Amarakone, A. M. N. 1964. *Inelastic Hyperstatic Frames Analysis*. Proceedings of the International Symposium on the Flexural Mechanics of Reinforced Concrete. Miami, Fla.: ASCE-ACI.
- Banon, H., Biggs, J.M., and Irvine, H.M. 1980. *Prediction of Seismic Damage in Reinforced Concrete Frames*. Publication No. R80-16. Cambridge, Mass.: Department of Civil Engineering, Massachusetts Institute of Technology.
- Banon, H., Biggs, J.M., and Irvine, H.M. 1981. *Seismic Damage in Reinforced Concrete Frames*. Journal of Structural Division, ASCE 107 ( ST9)(September ).
- Black, E., and Aschheim, M. 1998. *Effect of Prior Earthquake Damage on Response of SDOF Structures*. Proceedings, Sixth U.S. National Conference on Earthquake Engineering. Oakland, Calif.: Earthquake Engineering Research Institute.
- Caltrans. 1986. *Bridge Design Specifications Manual*. California Department of Transportation.

- Caltrans 1991. *Bridge Design Specifications Manual*. California Department of Transportation.
- Caltrans. 1991. *Proceedings of the First Annual Seismic Research Workshop*. Sacramento, Calif.:California Department of Transportation.
- Caltrans 1992. *Standard Specifications*. State of California Department of Transportation.
- Caltrans. 1993. *Second Annual Seismic Research Workshop*. Sacramento, Calif.: Proceedings California Department of Transportation.
- Caltrans. 1994. *Proceedings of the Third Annual Seismic Research Workshop Division of Structures*. Sacramento, Calif.: California Department of Transportation.
- Caltrans. 1996. *Proceedings of the Fourth Annual Seismic Research Workshop Division of Structures*. Sacramento, Calif.: California Department of Transportation.
- Caltrans. 1998. *Proceedings of the Fifth Annual Seismic Research Workshop Division of Structures*. Sacramento, Calif.: California Department of Transportation.
- Caltrans Engineers. 1996. Private Communication.
- Celebi, M. 1976. On the Shear Pinched Hysteresis Loops. *International Symposium on Earthquake Structural Engineering*.
- Chai, Y. H., Priestley, M. J. N., and Seible, F. 1991. Seismic Retrofit of Circular Bridge Columns for Enhanced Flexural Performance. *ACI Structural Journal* 88(September-October ).
- Chai, Y.H., Priestley, M.J.N. and Seible, F. 1994. Analytical Model for Steel-Jacketed RC Circular Bridge Columns. *Journal of Structural Engineering*. ASCE 120(August).
- Chai, Y. H., Romstad, K. M., Bird, S. M. 1995. Energy-based Linear Damage Model for High-intensity Seismic Loading. *Journal of Structural Engineering* 121(May ).
- Chang, G. A., and Mander, J. B. 1994. *Seismic Energy Based Fatigue Damage Analysis of Bridge Columns: Part I—Evaluation of Seismic Capacity*. NCEER-94-0006. State Univ. of New York at Buffalo: National Center for Earthquake Engineering Research.
- Chung, Y. S., Meyer, C., and Shinozuka, M. 1987. *Seismic Damage Assessment for Reinforced Concrete Members*. Technical Report NCEER-87-0022. Buffalo, N.Y.: National Center for Earthquake Engineering Research.
- Clough, R.W. 1986. *Effect of Stiffness Degradation on Earthquake Ductility Requirements*. Technical Report SESM 66-16. Berkeley, Calif.: Structural Engineering and Structural Mechanics, Department of Civil Engineering, University of California.
- Corley, W. G. 1966. *Rotational Capacity of Reinforced Concrete Beams*. Bulletin D108. Skokie, Ill.: Portland Cement Association, Research and Development Laboratories.

- Davey, B.E., and Park, R. 1975. *Reinforced Concrete Bridge Piers under Seismic Loading*. Research Report 75-3. Christchurch, N.Z.: University of Canterbury.
- Dowell, R., Seible, F., and Priestley, M.J.N. 1996. *Practical Nonlinear Bridge Analysis. Fourth Caltrans Seismic Workshop*. Sacramento, Calif.: California Department of Transportation.
- EERI . 1990. Loma Prieta Earthquake Reconnaissance Report. *Earthquake Spectra* Supplement to Volume 6. May.
- EERI. 1995. Northridge Earthquake Reconnaissance Report. *Earthquake Spectra* Supplement to Volume 11. April 1995.
- Elkin, S. 1998. *Repair of Moderately and Severely Damaged Bridge Columns*. Masters Thesis. Berkeley, Calif.: University of California.
- Eligehausen, R., Popov, E. P., and Bertero, V. V. 1983. *Local Bond Stress-Slip Relationships of Deformed Bars under Generalized Excitation*. EERC 83-23. Berkeley, Calif.: Earthquake Engineering Research Center, University of California.
- FEMA.1997. *NEHRP Guidelines for the Seismic Rehabilitation of Buildings*. Federal Emergency Management Agency. FEMA 273.
- Filippou, F. C., Popov, E. P., and Bertero, V. V. 1983. *Effects of Bond Deterioration on Hysteretic Behavior of Reinforced Concrete Joints*. EERC 83-19. Berkeley, Calif.: Earthquake Engineering Research Center, University of California.
- French, C. W., and Schultz, A. E. 1991. Minimum Available Deformation Capacity of Reinforced Concrete Beams. ACI SP-127. *Earthquake-Resistant Concrete Structures: Inelastic Response and Design*.
- Gulkan, P., and Sozen, M. A. 1974. Inelastic Responses of Reinforced Concrete Structures to Earthquake Motions. *Journal of the American Concrete Institute* 71(December).
- Gupta, B. and Kunnath, S. K. 1998. Effect of Hysteretic Model Parameters on Inelastic Seismic Demands. *Sixth U.S. National Conference on Earthquake Engineering*.
- Higashi, Y., Ohkubo, M., and Ohtsuka, M. 1977. Influences of Loading Excursions on Restoring Force Characteristics and Failure Modes of Reinforced Concrete Columns. *Sixth World Conference on Earthquake Engineering, Meerut, India*.
- Hose, Y. D., Smith, P. E., Seible, F., Priestley, M. J. N. 1996. *Strategic Relocation of Plastic Hinges in Bridge Columns. Fourth Caltrans Seismic Workshop*. Sacramento, Calif.: California Department of Transportation.
- Ingham, J. M., Priestley, M. J. N., and Seible, F. 1994. *Seismic Performance of Bridge Knee Joints*. Report SSRP-94/17. La Jolla, Calif.: Structural Systems Research, University of California, San Diego.

- Iwasaki, T., Kawashima, K., Hagiwara, R., Hasegawa, K., Koyama, T. and Yoshida, T. 1985. Experimental Investigation on Hysteretic Behavior of Reinforced Concrete Columns. *Proceedings of the Second Joint U.S.-Japan Workshop on Performance and Strengthening of Bridge Structures and Research Needs*. San Francisco, Calif.
- Jeong, G. D., and Wilfred, I. D. 1988. The Effect of Earthquake Duration on the Damage of Structures. *Earthquake Engineering and Structural Dynamics* 16. 1988.
- Kowalsky, M. J., Priestley, M. J. N., MacRae, G. A. 1995. *Displacement-based Design of RC Bridge Columns in Seismic Regions*. *Earthquake Engineering & Structural Dynamics* 24(December).
- Kunnath, S. K., Reinhorn, A. M., and Lobo, R. F. 1992. *IDARC Version 3.0: A Program for the Inelastic Damage Analysis of Reinforced Concrete Structures*. NCEER-92-0022. Buffalo, N.Y.: National Center for Earthquake Engineering Research, State University of New York.
- Kunnath, S. K. 1997. *Cumulative Seismic Damage of Reinforced Concrete Bridge Piers*. NCEER 97-0006. Technical Report. Buffalo, N.Y.: National Center for Earthquake Engineering Research.
- Lehman, D. E. 1994. *Towards a Consistent Formulation of the Plastic Hinge Length Method*. CE 299 Report. Berkeley, Calif.: University of California.
- Lehman, Dawn E. 1998. Seismic Performance of Well-Confined Concrete Bridge Columns. Ann Arbor: University of Michigan dissertation AAT9922928.
- Lowes, L. N., and Moehle, J. P. 1995. *Seismic Behavior and Retrofit of Older Reinforced Concrete Bridge T-joints*. UCB/EERC-95/09. Berkeley, Calif.: Earthquake Engineering Research Center, University of California.
- Lybas, J., and Sozen, M. A. 1977. *Effect of Beam Strength and Stiffness on Dynamic Behavior of Reinforced Concrete Coupled Walls*. Civil Engineering Series SRS 444. Urbana, Ill.: University of Illinois.
- MacGregor, J. G. 1992. *Reinforced Concrete: Mechanics and Design*. Second ed. Prentice-Hall Inc.
- Macrae, G. A., Kawashima, K. 1997. Post-earthquake Residual Displacements of Bilinear Oscillators. *Earthquake Engineering & Structural Dynamics* 26(July)
- Mander, John B., Priestley, M. J. N., and Park, R. 1984. *Seismic Design of Bridge Piers*. Research Report 84-2. Christchurch, N.Z.: University of Canterbury, Department of Civil Engineering.
- Mander, J. B., Priestley, M. J. N., and Park, R. 1988. Theoretical Stress-Strain Model for Confined Concrete. *Journal of Structural Engineering* 114(August ).

- Mazzoni, S. *Design and Response of Lower-Level Beam-Column Joints in Ductile Reinforced-Concrete Double-Deck Bridge Frames*. Ph.D. Dissertation. Berkeley, Calif.: University of California. August.
- McCabe, S. L., and Hall, W. J. Assessment of Seismic Structural Damage. *Journal of Structural Engineering* 115(September).
- Meli, R., Baeza, J., and Rodriguez, M. 1984. Hysteretic Behavior of Concrete Flexural Members with High Strength Steel. *Eighth World Conference on Earthquake Engineering*, Vol. 6. 1984.
- Moehle, J. P., and Sozen, M. A. 1980. *Experiments to Study Earthquake Response of R/C Structures with Stiffness Interruptions*. UILU-ENG-80-2016. Urbana, Ill.: Civil Engineering Studies, Structural Research Series 482, Department of Civil Engineering, Univ. of Illinois. August.
- Moehle, J. P. 1992. Displacement-based Design of RC Structures Subjected to Earthquakes. *Earthquake Spectra* 8(August).
- Moehle, J. P. 1998. Private Communication.
- Nacamuli. 1998. *Repair of Severely Damaged Ductile Reinforced Concrete Bridge Columns*. Masters Thesis. Berkeley, Calif.: University of California.
- Nishigaki T., and Mizuhata, K. 1983. Experimental Study on Low-Cycle Fatigue of Reinforced Concrete Columns. *Transactions of the Architectural Institute of Japan*.
- NZS. 1995. New Zealand Standard. Concrete Structures Standard, Part 1 —The Design of Concrete Structures. Wellington: NZS 3101.
- Oliveira, C. S. 1975. *Seismic Risk Analysis for a Site and a Metropolitan Area*. Report No. EERC-75-3. Berkeley, Calif.: University of California.
- Otani, S., and Sozen, M. A. 1972. *Behavior of Multistory Reinforced Concrete Frames During Earthquakes*. Civil Engineering studies. Structural Research Series 392. Urbana, Ill.: University of Illinois..
- Otani, S., and Cheung, V. 1981. *Behavior of Reinforced Concrete Columns under Biaxial Lateral Load Reversals*. Toronto: University of Toronto, Department of Civil Engineering.
- Park, R., and Paulay, T. 1975. *Reinforced Concrete Structures*. New York: John Wiley and Sons.
- Park, Y.-J., and Ang, A. H.-S. 1985. Mechanistic Seismic Damage Model for Reinforced Concrete. *Journal of Structural Engineering* 111(4)(April).
- Potangaroa, R. T., and Priestley, M. J. N. 1979. *Ductility of Spirally Reinforced Concrete Columns under Seismic Loading*. Research report, 79-8. Christchurch, N.Z.: University of Canterbury, Department of Civil Engineering.

- Priestley, M.J.N., and Park, R. 1987. *Strength and Ductility of Concrete Bridge Columns under Seismic Loading*. *ACI Structural Journal* 84(January).
- Priestley, M. J. N., Seible, F., and Chai, Y. H. 1992. *Design Guidelines for Assessment Retrofit and Repair of Bridges for Seismic Performance*. Research Report SSRP-92/01. La Jolla, Calif.: Department of Applied Mechanics and Engineering Sciences, University of California, San Diego.
- Priestley, M. J. N., and Benzoni, G. 1994. Seismic Performance of Circular Columns with Low Longitudinal Steel Ratios. *ACI Structural Journal* 93(July).
- Priestley, N., Seible, F., and Calvi, G. 1996. *Seismic Design and Retrofit of Bridges*. New York: John Wiley and Sons.
- Public Works Research Institute. 1998. *Design Specifications of Highway Bridges, Part V. Seismic Design*. Earthquake Engineering Division, Earthquake Disaster Prevention Research Center.
- Razvi, S. R., and Saatcioglu, M. 1994. Strength and Deformability of Confined High-Strength Concrete Columns. *ACI Structural Journal* 91(November–December).
- Rodriguez, A. M. 1995. *Spread of Inelastic Deformations in Reinforced Concrete Columns Subjected to Flexure and Axial Compression*. Masters Thesis. Berkeley, Calif.: University of California.
- Rothe, D. H., and Sozen, M. A. 1984. *A SDOF Model to Study Nonlinear Dynamic Response of Large- and Small-Scale Reinforced Concrete Test Structures*. UILU-ENG-83-2018. Urbana, Ill.: University of Illinois.
- Roufaiel, M. S. L., and Meyer, C. 1987. Analytical Modeling of Hysteretic Behavior of R/C Frames. *Journal of Structural Engineering*, ASCE 113(9).
- Saatcioglu, M., Ozcebe, G. 1989. Response of Reinforced Concrete Columns to Simulated Seismic Loading. *ACI Structural Journal* 86(January–February).
- Saatcioglu, M., and Razvi. 1994. Behavior of High Strength Columns Subjected to Axial Load. *Fifth National Conference on Earthquake Engineering*.
- Saiidi, M., and Sozen, M. A. 1979. *Simple and Complex Models for Nonlinear Seismic Response of Reinforced Concrete Structures*. UILU-ENG-79-2013. Urbana, Ill.: University of Illinois.
- Sakai, K., and Sakai, S.A. 1989. What Do We know about Confinement in Reinforced Concrete Columns. *ACI Structural Journal* 86(March ).
- Sawyer, H. A. 1964. *Design of Concrete Frames for Two Failure States*. *Proceedings of the International Symposium on the Flexural Mechanics of Reinforced Concrete*. Miami: ASCE-ACI.

Scott, B. D., Park, R., and Priestley, M. J. N. 1982. Stress-Strain Behavior of Concrete Confined by Overlapping Hoops at Low and High Strain Rates. *Journal of the American Concrete Institute* 79(January–February).

Scribner, C. F., and Hwang, T. H. 1982. Effect of Load History Variation on Cyclic Response of Reinforced Concrete Flexural Members. *Proceedings of US-PRC Bilateral Workshop on Earthquake Engineering*. Harbin, P.R.C.: Institute of Engineering Mechanics, Academia Sinica.

Structural Engineers Assn. of California (SEAOC). 1995. *Vision 2000 Committee. Performance-Based Seismic Engineering of Buildings*. Sacramento, Calif.: Structural Engineers Assn. of California.

Sheikh, S. A., and Uzumeri, S. M. 1982. Analytical Model for Concrete Confinement in Tied Columns. *Journal of the Structural Division, ASCE* 108 (ST12)(December).

Sheikh, S. A., and Yeh, C. C. 1992. *Analytical Moment-Curvature Relations for Tied Concrete Columns*. *Journal of Structural Engineering* 188(February).

Sheikh, S. A., and Khoury, S. S. 1993. Confined Concrete Columns with Stubs. *ACI Structural Journal* 79(July).

Sheikh, S. A., Shah, D. V., and Khoury, S. S. 1994. *Confinement of High-Strength Concrete Columns*. *ACI Structural Journal* 91(January–February).

Shibata, A., and Sozen, M. A. 1976. *Substitute-Structure Method for Seismic Design in R/C*. *Journal of the Structural Division, ASCE* 102(ST1)(January).

Sozen, M. A., and Moehle, J. P. 1993. *Stiffness of Reinforced Concrete Shear Walls*. EPRI Research Project 3094-1. Palo Alto, Calif.: Electric Power Research Institute.

Sritharan, S., Priestley, M. J. N., and Seible, F. 1996. Influence of Prestress on Column/Cap Beam Tee Joints. *Proceedings of the Fourth Caltrans Seismic Research Workshop*. Sacramento, Calif.: California Department of Transportation.

Stephens, J. E., and Yao, J. T. P. 1987. Damage Assessment Using Response Measurements. *Journal of Structural Engineering, ASCE* 107(4).

Stojadinovic, B., and Thewalt, C. 1995. *Upgrading Bridge Outrigger Knee Joint Systems*. UCB/EERC-95/03. Berkeley, Calif.: Earthquake Engineering Research Center, University of California.

Stone, W. C., and Cheok, G. S. 1989. *Inelastic Behavior of Full-Scale Bridge Columns Subjected to Inelastic Loading*. Gaithersburg, Md.: National Institute of Standards and Technology. (January).

Stone, W. S., and Taylor, A.W. 1994. Integrated Approach to Seismic Design of Reinforce Concrete Structures. *Journal of Structural Engineering, ASCE* 120(December).

- Takenda, T., Sozen, M. A., and Nielsen, N. N. 1970. Reinforced Concrete Response to Simulated Earthquakes. *Journal of Structural Engineering* ASCE 96(ST12)(December).
- Tanaka, Hitoshi, and Park, R. 1990. *Effect of Lateral Confining Reinforcement on the Ductile Behavior of Reinforced Concrete Columns*. Research report 90-2. Christchurch, N.Z.: University of Canterbury, Department of Civil Engineering.
- Taylor, A.W., and Stone, William C. A. 1993. *Summary of Cyclic Lateral Load Tests on Spiral Reinforced Concrete Columns*. NISTIR 5285. Gaithersburg, Md.: Building and Fire Research Laboratory, National Institute of Standards and Technology.
- Teran-Gilmore, A., with Bertero. V. V. 1996. *Performance-Based Earthquake-Resistant Design of Framed Buildings Using Energy Concepts*. Ph.D. Thesis. Berkeley, Calif.: University of California.
- Thewalt, C. R., and Stojadinovic, B. 1994. Stable Reinforced-Concrete Section-Analysis Procedure. *Journal of Structural Engineering* 120(October).
- Verma, R., Priestley, M. J. N., and Seible, F. 1992. *Assessment of Seismic Response and Steel Jacket Retrofit of Squat Circular Reinforced Concrete Bridge Columns*. Report SSRP-92/05. La Jolla, Calif.: University of California, San Diego.
- Wakabayashi, M. 1986. *Design of Earthquake-Resistant Buildings*. New York: McGraw-Hill.
- Wang, M. L., and Shah, S. P. 1987. *Reinforced Concrete Hysteresis Model Based on the Damage Concept*. *Earthquake Engineering and Structural Dynamics* 16(8).
- Watson, S., and Park, R. 1994. Simulated Seismic Load Tests on Reinforced Concrete Columns. *Journal of Structural Engineering* 120(June).
- Williams, M. S., and Sexsmith, R. G. 1995. Seismic Damage Indices for Concrete Structures: a State-of-the-Art Review. *Earthquake Spectra* 11(May).
- Williams, M. S., Villemure, I., and Sexsmith, R. G. 1997. Evaluation of Seismic Damage Indices for Concrete Elements Loaded in Combined Shear and Flexure. *ACI Structural Journal* 94(May-June).
- Wong, Y. L., Paulay, T., and Priestley, M. J. N. *Squat Circular Bridge Columns Under Multi-Directional Seismic Attack*. Research Report 90-4 (October). Christchurch, N.Z.: University of Canterbury.
- Xiao, Y., and Martirosyan, A 1998. *Seismic Performance of High-Strength Concrete Columns*. *Journal of Structural Engineering*, Vol. 124(March).
- Yao, J. T. P., and Munse, W. H. 1962. Low-Cycle Axial Fatigue Behavior of Mild Steel. *Journal of the Structural Division*, ASCE 95(ST8)(August).

Zahn, F. A. 1986. *Design of Reinforced Concrete Bridge Columns for Strength and Ductility*. Christchurch, N.Z.: University of Canterbury, Department of Civil Engineering.

## PEER REPORTS

PEER reports are available from the National Information Service for Earthquake Engineering (NISEE). To order PEER reports, please contact the Pacific Earthquake Engineering Research Center, 1301 South 46<sup>th</sup> Street, Richmond, California 94804-4698. Tel.: (510) 231-9468; Fax: (510) 231-9461.

- PEER 2000/07** *Cover-Plate and Flange-Plate Reinforced Steel Moment-Resisting Connections.* Taejin Kim, Andrew S. Whittaker, Amir S. Gilani, Vitelmo V. Bertero, and Shakhzod M. Takhirov. September 2000. \$33.00
- PEER 2000/06** *Seismic Evaluation and Analysis of 230-kV Disconnect Switches.* Amir S. J. Gilani, Andrew S. Whittaker, Gregory L. Fenves, Chun-Hao Chen, Henry Ho, and Eric Fujisaki. July 2000. \$26.00
- PEER 2000/05** *Performance-Based Evaluation of Exterior Reinforced Concrete Building Joints for Seismic Excitation.* Chandra Clyde, Chris P. Pantelides, and Lawrence D. Reaveley. July 2000. \$15.00
- PEER 2000/04** *An Evaluation of Seismic Energy Demand: An Attenuation Approach.* Chung-Che Chou and Chia-Ming Uang. July 1999. \$20.00
- PEER 2000/03** *Framing Earthquake Retrofitting Decisions: The Case of Hillside Homes in Los Angeles.* Detlof von Winterfeldt, Nels Roselund, and Alicia Kitsuse. March 2000. \$13.00
- PEER 2000/01** *Further Studies on Seismic Interaction in Interconnected Electrical Substation Equipment.* Armen Der Kiureghian, Kee-Jeung Hong, and Jerome L. Sackman. November 1999. \$20.00
- PEER 1999/14** *Seismic Evaluation and Retrofit of 230-kV Porcelain Transformer Bushings.* Amir S. Gilani, Andrew S. Whittaker, Gregory L. Fenves, and Eric Fujisaki. December 1999. \$26.00
- PEER 1999/12** *Rehabilitation of Nonductile RC Frame Building Using Encasement Plates and Energy-Dissipating Devices.* Mehrdad Sasani, Vitelmo V. Bertero, James C. Anderson. December 1999. \$26.00
- PEER 1999/11** *Performance Evaluation Database for Concrete Bridge Components and Systems under Simulated Seismic Loads.* Yael D. Hose and Frieder Seible. November 1999. \$20.00
- PEER 1999/10** *U.S.-Japan Workshop on Performance-Based Earthquake Engineering Methodology for Reinforced Concrete Building Structures.* December 1999. \$33.00

- PEER 1999/09** *Performance Improvement of Long Period Building Structures Subjected to Severe Pulse-Type Ground Motions.* James C. Anderson, Vitelmo V. Bertero, and Raul Bertero. October 1999. \$26.00
- PEER 1999/08** *Envelopes for Seismic Response Vectors.* Charles Menun and Armen Der Kiureghian. July 1999. \$26.00
- PEER 1999/07** *Documentation of Strengths and Weaknesses of Current Computer Analysis Methods for Seismic Performance of Reinforced Concrete Members.* William F. Cofer. November 1999. \$15.00
- PEER 1999/06** *Rocking Response and Overturning of Anchored Equipment under Seismic Excitations.* Nicos Makris and Jian Zhang. November 1999. \$15.00
- PEER 1999/05** *Seismic Evaluation of 550 kV Porcelain Transformer Bushings.* Amir S. Gilani, Andrew S. Whittaker, Gregory L. Fenves, and Eric Fujisaki. October 1999. \$15.00
- PEER 1999/04** *Adoption and Enforcement of Earthquake Risk-Reduction Measures.* Peter J. May, Raymond J. Burby, T. Jens Feeley, and Robert Wood. \$15.00
- PEER 1999/03** *Task 3 Characterization of Site Response General Site Categories.* Adrian Rodriguez-Marek, Jonathan D. Bray, and Norman Abrahamson. February 1999. \$20.00
- PEER 1999/02** *Capacity-Demand-Diagram Methods for Estimating Seismic Deformation of Inelastic Structures: SDF Systems.* Anil K. Chopra and Rakesh Goel. April 1999. \$15.00
- PEER 1999/01** *Interaction in Interconnected Electrical Substation Equipment Subjected to Earthquake Ground Motions.* Armen Der Kiureghian, Jerome L. Sackman, and Kee-Jeung Hong. February 1999. \$20.00
- PEER 1998/08** *Behavior and Failure Analysis of a Multiple-Frame Highway Bridge in the 1994 Northridge Earthquake.* Gregory L. Fenves and Michael Ellery. December 1998. \$20.00
- PEER 1998/07** *Empirical Evaluation of Inertial Soil-Structure Interaction Effects.* Jonathan P. Stewart, Raymond B. Seed, and Gregory L. Fenves. November 1998. \$26.00
- PEER 1998/06** *Effect of Damping Mechanisms on the Response of Seismic Isolated Structures.* Nicos Makris and Shih-Po Chang. November 1998. \$15.00
- PEER 1998/05** *Rocking Response and Overturning of Equipment under Horizontal Pulse-Type Motions.* Nicos Makris and Yiannis Roussos. October 1998. \$15.00
- PEER 1998/04** *Pacific Earthquake Engineering Research Invitational Workshop Proceedings, May 14–15, 1998: Defining the Links between Planning, Policy Analysis, Economics and Earthquake Engineering.* Mary Comerio and Peter Gordon. September 1998. \$15.00

- PEER 1998/03** *Repair/Upgrade Procedures for Welded Beam to Column Connections.* James C. Anderson and Xiaojing Duan. May 1998. \$33.00
- PEER 1998/02** *Seismic Evaluation of 196 kV Porcelain Transformer Bushings.* Amir S. Gilani, Juan W. Chavez, Gregory L. Fenves, and Andrew S. Whittaker. May 1998. \$20.00
- PEER 1998/01** *Seismic Performance of Well-Confined Concrete Bridge Columns.* Dawn E. Lehman and Jack P. Moehle. December 2000. \$33.00